Natural and experimental kinetic studies on structural evolution of carbonaceous material in subduction zone

by
Yoshihiro Nakamura

Doctoral Program in Environmental Science and Technology
Graduate School of Science and Technology
Niigata University

February 7th, 2017

Thesis Supervisor: Professor Madhusoodhan Satish-Kumar

ABSTRACT

Carbonaceous material (CM) is a widespread accessory phase in sediments, and its composition and structure are sensitive to increasing peak metamorphic temperatures. The structural changes of CM as a function of temperature is widely applied as a geothermometry in very low- to medium-grade metamorphism. However, the fundamental process involved in the conversion of amorphous carbon to graphite exhibits complex devolatilization and recrystallization that depends not only on peak temperature, but also tectonic deformation, catalytic effects and fluid activity under a lithostatic pressure. Hence, it is key to understand the rate determining chemical reaction of CM to graphite through a combination of kinetic experiments and natural observations. In this study, I have conducted detailed observations of natural CM in Shimanto accretionary (SM) complex and Hidaka metamorphic belt (HMB), and carried out experimental kinetic studies based on X-ray diffraction (XRD), micro-Raman spectroscopy and Transmission Electron Microscopic (TEM) observations.

The natural structural evolution of CM extracted from metapelitic rocks in Hidaka metamorphic belt, Hokkaido, Japan, were initially investigated in detailed. The natural CM showed the heterogeneous recrystallization from 300 to 500 °C, suggesting the sigmoid transformation of amorphous, turbostratic and graphitic carbon. TEM observations indicated that natural CM have undergone the microstructural evolution from randomly misoriented carbon sheets to highly oriented stacking with increasing temperature. To further characterize the graphitization and carbonization process at lower temperature regimes, I have investigated the natural structural evolution of CM in the Shimanto accretionary complex, Kochi, Japan. The natural CM in mudstones systematically changed its crystallinity toward the paleo out-of-sequence thrust, ranging between 180 and 280 °C.

The devolatilization of CM represented by decrease in the aliphatic CH, aromatic CH and carboxyl peaks are well consistent with results of micro-Raman spectroscopy.

Based on the detailed field observations, I carried out high temperature high pressure (*HPHT*) experimental kinetic studies on graphitization using natural CMs in SM and HMB at various temperature of 1000 to 1450 °C for various durations (10 min to 115 hours) under a pressure of 1 GPa. Natural CMs extracted from sedimentary rocks transformed their morphology and crystallinity with increasing annealing temperatures and durations. The time-temperature relations of each crystal parameter by micro-Raman spectroscopy and XRD demonstrated sigmoidal transformations from an amorphous to a graphitic structure, suggesting the complex chemical reactions during graphitization. To assess these complex chemical processes, I adopted three different approaches for formulating the graphitization kinetics using a power rate model, a Johnson-Mehl-Avrami-Kolmogorov (JMAK) model and a superposition method. Irrespective of the models employed, the effective activation energies were estimated to lie between 259 and 339 kJ/mol, which are much lower than those reported previously for graphitization at 1 atm. In addition to the isothermal experiments at 1 GPa, kinetic experiments at various pressure of 0.5 to 8 GPa at 1200 °C for 10 min to 24 hours were also conducted. The time-pressure relations of each crystal parameter similarly demonstrated sigmoidal transformations from an amorphous to a graphitic structure, suggesting the pressure-induced recrystallization at constant temperature. In this study, we obtained the activation volumes of –22∼–44 cm^3/mol using a power rate model and a JMAK model during graphitization. Combining the effective activation energies and activation volumes, the structural evolution of CM based on experimental kinetic model can be expressed by three different factors of pressure *P*, metamorphic temperature *T* and duration *t*:

$$f(P, T, t) = C_{\min} + (C_{\max} - C_{\min}) \,/\, \{1+[((-22P + 286686)/RT)/t]^h\},$$

where C_{min} and C_{max} are respectively the maximum and minimum values of each parameter, A the intercept of the Arrhenius plot, R the gas constant, and h is the reaction rate of the sigmoid function (named as the "Hill coefficient"). It is thus possible to calculate graphitization at any *P-T-t* relations in metamorphism. Utilizing the kinetic model, I tried to compare the experimental model based crystallinity of CM with natural metamorphic *P-T-t* conditions. In the case of Hidaka metamorphic belts, the natural CMs along the field *P-T* path of HMB proceeded structural evolution of CM from around 350 °C and form a graphite at around 450 °C. On the other hand, calculated structural evolution of CM started to recrystallize at around 400 °C, and form a graphite at over 500 °C for 10 million years. Although there still exist some factors for fully understanding the natural structural evolution of CM to a graphite, the experimental kinetic model can be applicable to the thermal indicator in wide range of *P-T* conditions between 0.5 and 2 GPa at geologically reasonable temperatures (300~800 °C). The most important implication of our finding is that natural CM in the crust has proceeded fast recrystallization from an amorphous to a graphitic structure bearing upon temperature, pressure and duration of heaeting compared with the laboratory at 1 atm. Our data provide a new kinetic model for not only geothermometry but also geospeedmetry and geobarometry in subduction zone.

論文要旨

炭質物は堆積岩中の普遍的な副成分鉱物であり，化学組成や結晶構造は最高変成温度の変化に依存して敏感に変化する．この温度に依存した炭質物の結晶構造変化を利用することによって低変成から中変成度での地質温度計として広く応用されている．しかしながら非晶質炭素からグラファイトへの構造変化は変成温度だけではなく圧力・変形・触媒作用・流体が関与する複雑な脱ガス反応と再結晶化作用によって進行している．つまり反応速度実験と天然試料の観察を組み合わせるから炭質物の結晶構造進化に関する律速課程を理解することが重要である．本研究ではXRD・顕微ラマン分光分析・TEM による微細構造観察に基づく四万十帯・日高変成帯中の天然炭質物の詳細な結晶構造の解析と天然試料を用いた反応速度実験を行った．

まず初めに北海道日高変成帯の泥質岩を研究対象に詳細な炭質物の結晶構造進化に関する研究を行った．炭質物は約 300℃から 500℃にかけて非晶質構造から乱層構造をへてグラファイト構造へ不均一な再結晶化を示す．結晶度に関連するパラメーターがシグモイド曲線を描くことが特徴である．透過電子顕微鏡観察では，変成温度の増加につれて微細構造の組織も不規則な乱層構造から高い配向性を示す積層構造への連続的な変化を観察できた．一方で高知県四万十付加帯ではより低温での天然炭質物の結晶構造進化に関して詳細に研究をおこなった．泥質岩中の炭質物は過去のプレート境界断層に向かって約 180 ℃から 280 ℃の温度幅で結晶度を変化させた．顕微 FTIR 分光を利用した分析では脂肪族 CH，芳香族 CH やカルボキシル基の脱離に代表される炭質物の熱分解反応が観察でき，顕微ラマン分光分析の結果とも整合的であった．

これらの詳細な野外観察と分析に基づき，我々は四万十帯と日高変成帯中の炭質物を利用した反応速度論に基づく高温高圧実験を 1GPa, 1000~1450℃, 10 分から 115 時間の条件にて実行した．堆積岩中から抽出した天然炭質物は被熱時間と被熱温度が上昇するにつれて形態と結晶度を変化させた．各パラメーターの温度—時間関係は，非晶質炭素からグラファイト構造へシグモイド曲線を示す．これは複雑な化学反応が石墨化の時に進行していることを示唆している．そのような複雑な化学反応を評価するために，累乗則モデル・JMAK モデル・superposition 法を

利用したグラファイト化反応速度論の解析を試みた．これらのモデルを使用すると， 約 259 から 339 kJ/mol の有効活性化エネルギーを見積もった．これは従来報告されてきた常圧下での石墨化の活性化エネルギーよりも大幅に低い値である．1GPa 下での等温実験に加えて，1200℃における 0.5 GPa から 8GPa まで 10 分から 24 時間の反応速度実験を行った．各結晶構造パラメーターの時間―圧力関係も同様に非晶質炭素からグラファイト構造へシグモイド曲線を示す．これは一定温度にて炭質物が圧力に誘発されて再結晶化が進行していることを示唆する．本研究では累乗則と JMAK モデルを利用して–22～–44 cm^3/ mol の石墨化に対する活性化体積を得た．これらの有効活性化エネルギーと活性化体積を利用すると炭質物の結晶構造進化は，三つの異なる要素である圧力・変成温度・時間によって表現可能である:

$$f(P,\ T,\ t) = C_{\min} + (C_{\max} - C_{\min}) \,/\, \{1+[((\text{-}22\text{P} + 286686)/RT)/t)^{h}),$$

$C_{\min}$ と $C_{\max}$ は パラメーターの最大値と最小値. A はアレーニウスプロットの定数, R はガス定数（8.314 kJ.mol)，で h はシグモイド関数の反応次数である（Hill 係数と呼ばれる)．つまり変成帯中の温度圧力時間を利用して炭質物の石墨化をモデル計算することが可能となる．このモデルを利用し，天然の温度圧力条件と実験に基づく結晶構造進化の比較を行った．日高変成帯の場合，フィールド P-Tpath 上で天然の炭質物は約 350℃から再結晶化が進行し 450℃前後でグラファイトを形成する．一方でモデル計算を行った炭質物の結晶構造進化では，1000 万年の被熱時間にて約 400℃から再結晶化が開始し，約 500℃にてグラファイトを形成する．我々の試算では天然石墨化の完全な理解にはまだいくつかの欠陥が残っているが我々の実験に基づくカイネティクスモデルは熱指標として 400℃から 800℃, 0.5 から 2 GPa における地質学的な温度圧力条件下にて適用可能である．本研究における最も重要な点は，地殻中の天然炭質物は常圧の実験室に比べて非晶質炭素からグラファイト構造へ温度・圧力・速度に関連して早く再結晶化が進行することを発見したことである．我々の成果は今後沈み込み帯における地質温度計としてだけではなく，地質速度計・地質圧力計としての新しい反応速度モデルを提供するであろう．

Acknowledgements

I would like to acknowledge Professor M. Satish-Kumar, my supervisor, for leading and various supports on my Ph. D study. In addition, Dr. T. Yoshino were very helpful for assistance with high pressure high temperature experiments at IPM, Okayama University, Misasa.

I would like to thank Dr. H. Hara for guiding and sampling the pelitic rocks in Shimanto accretionary complex, Central Shikoku, Japan. His financial supports in sampling was grateful acknowledged. Professer H. Kagi and M. Watanabe were very helpful for assistance with micro-FTIR analysis at The University of Tokyo.

I would like to acknowledge C. Zhao, Dr. N. Tsujino, Dr. D. Yamasaki, Dr. A. Yoneda and Dr. E. Ito at IPM, Okayama University for their helps and valuable discussions.

In addition, I also thank Prof. T. Toyoshima and emeritus Professor J. Akai for their valuable discussions. Their constructive comments on the manuscripts are also grateful acknowledged. I also want to thank Dr. K. Kobayashi and seminar members of Structural geology, Petrology research for constructive and valuable discussions. Moreover, Professer H. Konishi, Dr. T. Ogawara Dr. T. Taakahashi and M. Ozawa were very helpful for assistance with HRTEM observations and ICP-MS.

Finally, part of this thesis present a result of a joint research program carried out at the Institute for Planetary Materials, Okayama University, and this work was financially supported by Grant-in-Aid for JSPS Fellows (26-3941).

7th Feburary, 2017

Yoshihiro Nakamura

TABLE OF CONTENTS

LIST OF TABLES

LIST OF FIGURES

CHAPTER I

Structural evolution of carbonaceous material to graphite in subduction zone

1.1. Overview

Elemental carbon can exist in a diverse number of forms and allotropes such as carbynes, hexagonal graphite, rhombohedral graphite, nanotubes, fullerenes, graphene, cubic and hexagonal diamond because of its ability to form linear (sp-), trigonal (sp^2-), and tetrahedral (sp^3-) coordination (Miller et al. 1997; Mao et al. 2003). Such bonding in the unit cell provides characteristic physicochemical properties in their crystal structures (Kroto et al. 1985; Iijima et al. 1992; Irihune et al. 2003; Weller et al., 2005; Balandin 2011). The crystal structure of graphite, belonging to the $P6_3/mmc(D_{6h}^4)$ space-group symmetry, shows interesting physicochemical properties. The hexagonal with ABAB… stacking and the rhombohedral form with ABCABC… stacking of graphite have π bonding along *a*-axis and *Van der Waals* bonding along *c*-axis in unit cell (Fig. 1). The planar Young's modulus is 1020 GPa and is higher than for any other substance, while in the *c*-axis direction, it is only 37 GPa at atmospheric pressure (Zhao and Spain, 1989; Gills 1984). In addition, *c*-axis resistivity (ρ_c) of graphite makes sharp contrast with those on the in-plane resistivity (ρ_a). This provides large anisotropies of thermal and electrical conductivity between *a*-axis and *c*-axis (Noto and Tsuzuku, 1970; Matsubara et al. 1990). The ideal crystal structure of graphite has triperiodic orders of graphene sheets, however, amorphous or turbostratic carbon exhibits wide variety of bonding in the structure. The structural evolution is categorized into three groups from amorphous (1D), turbostratic (2D), and graphitic

structure (3D) depending on ordering of carbon sheets. The microstructure model of their amorphous to graphitic carbon in which small graphitic domains are joined by crosslinks was firstly proposed by Franklin (1950). Utilizing X-ray diffraction, she distinguished two groups, which are called for graphitizing and non-graphitizing carbon based on the experimental studies (Buseck and Beyssac et al. 2014). This distinction has been still fundamental concept for synthesizing graphite.

It is important to synthesize well crystallized graphite from an amorphous carbon for industry applications. In particular, the discoveries of specific forms such as C_{60} fullerene by Kroto et al. (1985), carbon nanotubes by Iijima et al. (1991), graphene (e.g., Novoselov et al; 2004), and tetrahedral amorphous carbon (diamond like carbon; DLC) cased a breakthrough for nanotechnology and new carbon materials (e.g., Lazzeri and Barreiro 2014). Thanks to the developments of carbon material science and their specific dynamic properties, the structural evolution of amorphous carbon to well crystallized graphite (called for high oriented pyrolytic graphite; HOPG) were well studied for decades (Oberlin et al. 2006). For synthesis of graphite, it is well known that graphite formation required a high temperature of ~3000 K under an anoxic condition (e.g., Oberlin 1984). This indicates the difficulty of synthesis in laboratory, and large amount of literatures has been discussed on the more efficient recrystallization kinetics of amorphous carbon under a low temperature condition. Hence, the kinetics on synthesis of graphite (graphitization) has been investigated in detailed (Fischbach 1963, Murty et al. 1969). Pioneering aggressive works by Fischbach pointed out that the formation of graphite required ~1000 kJ/mol, which is identical to the theoretical value for vacancy diffusion in graphite by Kanter (1957) and Kaxiras and Pandey (1988). More detailed pervious kinetic studies were summarized in table A1. Based on the detailed experiments, some important implications have been proposed. (1) The graphitization rate and final crystal sizes are strongly depending on the nanostructures between graphitizing and non-graphitizing

carbon (Inagaki 1996; Oberlin et al. 2006). (2) The hydrostatic and non-hydrostatic stress during heat treatment drastically change their crystallinity (e.g., Ross and Bustin 1990). (3) Transitional metals that can form carbides are potential for acceleration of recrystallization as a catalyst (Oya and Marsh 1980; Marsh et al. 1983; Charon et al. 2014). These results suggest that it is possible to synthesize graphite under low-temperature conditions utilizing some important properties in graphitization. Recently, it has been investigated based on molecular dynamics (MD) simulation of graphitization from an amorphous carbon (Ma et al. 2009; Loh and Bailargeat 2013). It is expected that these studies serve as development of graphitization kinetics in the future.

In the case of natural geological condition, the characteristic physicochemical properties of graphite, carbonaceous material (CM) and organic matter (OM) are widely applied for understanding the Earth's dynamic evolution. Elemental carbon in the subduction zones is fixed within rocks as an insoluble organic matter. The organic matter is mainly derived from living organic matter such as carbohydrates, proteins, lipids, and lignin, which are estimated to about 1.2×10^{16} ton and contained from 0.28 wt. % in sandstone to 0.99 wt. % in shales (Durand, 1980). These organic matters change their crystal and chemical structures with increasing pressure and temperature through burial (Fig. 2). The natural structural evolution of organic matter to carbonaceous material (CM), and then into graphite mainly comprises two prominent processes: carbonization and graphitization (Oberlin 1984). Carbonization is characterized by release of heteroatom as functions of temperature, pressure and duration and various steps occurring in carbonization are recognized by some physicochemical properties of CM (Oberlin et al. 1999). The early stage of carbonization begins with softening and the release of aliphatic compounds and heteroatoms in coal structure with increasing temperature. Fourier Transform infrared spectroscopy (FTIR) is one of the most powerful tool for understanding the chemical evolution of primary carbonization (e.g., Ibarra et al. 1996).

Such systematic transformation by FTIR are identified using the area ratio between aliphatic CH and aromatic CH, which is named for aromaticity. Such devolatilization can be analyzed by ^{13}C-Nuclear Magnetic Resonance (NMR) spectroscopy and carbon X-ray Absorption Near Edge structure (XANES) spectroscopy (Lu et al. 2001; Cody et al. 2008; Bernard et al. 2015). After thermal degradation of aliphatic CH groups, solid-state reorganization (the formation of basic structure units, BSUs) progresses with the release of non-condensable gases (e.g., CH_4 and H_2) from the aromatic CH groups (Oberlin et al. 1999). The BSU is the minimum structural unit of the CM nanostructure. The aggregate is stacked in two or three polyaromatic layers, and acts as a nucleus for the transformation of turbostratic to a graphitic structure (Oberlin, 1984; Oberlin et al. 1999). During secondary carbonization, micro-Raman spectroscopy is a useful tool for analyzing the degree of carbonization in natural CM. Lahfid et al. (2010) reported the significant increase in intensity ratio between D band and G band from 250 to 300 °C in low grade metamorphic terrain of Glarus Alps, Switzerland. Lu et al. (2001) suggested that coal structure composed of two types of carbon structure including crystalline carbon (A_{002}) and amorphous carbon (A_γ) based on X-ray diffraction (XRD) study. The area ratio of both parameters is consistent with aromaticity in coal structure. In addition, the vitrinite reflectance (VR) is one of the most powerful tool from primary to secondary carbonization for interpreting the paleo-thermal structures in sedimentary basin and very low-grade metamorphic terrain.

The other major process, graphitization, involves crystallization from a turbostratic to a graphitic structure by the reorganization of stacking sheets. The structural change of CM to graphite has been well studied using XRD (Grew 1974; Itaya 1981; Okuyama-Kusunose and Itaya 1989; Wada et al. 1994; Nakamura 1995), transmission electron microscopy (TEM; Buseck and Huang, 1985; Nakamura and Akai 2013) and micro-Raman spectroscopy (Wopenka and Pasteris, 1993; Kribek et al. 2008).

The pioneering work on the structural evolution of CM to graphite was investigated by Landis (1971) in detail. Landis (1971) reported that natural CM obtained from New Zealand (Otago) and Japanese metamorphic rocks (Sambagawa) has grouped into five patterns: *graphite*-d_1, -d_{1A}, -d_2, -d_3, and fully ordered graphite. Based on the XRD and TEM observations, the controls of graphitization are primarily dependent upon metamorphic temperature, and pressure and variation in starting material presumably constitute secondary controls. In the low-grade metasediments, it is difficult to interpret the *P-T* condition compared with mafic rocks because of no indication of metamorphic minerals. Hence, the structural evolution of CM to graphite is one of the most useful and important parameter that can be used to determine the sensitive transition with increasing temperatures in metasediments. It is widely applied for understanding the tectonic evolution between fore arc, accretionary complex and low-grade metamorphism. However, based on detailed structural analyses of natural CM in different *P-T* conditions some problems about the kinetics of graphitization still exist (Grew 1974; Itaya 1981; Wada et al. 1994). The biggest drawback in understanding natural graphitization is that it has proceed through a very complex recrystallization process from heterogeneous starting materials. Studies have shown that temperature is the most important factor for controlling graphitization. Although the lithostatic pressure, catalytic effects, fluid activity and tectonic deformation have affected the recrystallization, it is very difficult to assess the influence of such factors in natural metamorphic process (e.g., Luque et al. 1998; Beyssac et al. 2002b). Therefore, it has been still uncertain for decades what factor is crucial for controlling graphitization in metamorphic rocks. In addition, previous studies had mainly investigated the structural evolution of CM using bulk XRD study. The XRD profile of CM provide a wide variety of crystallographic information on graphite along *a*-axis and *c*-axis, however, the natural CM before recrystallization is difficult to analyze crystal structure owing to the amorphous structure. In addition, the chemical extraction

of CM from mudstones is necessary for high-precision analysis of amorphous carbon (see Appendix I), however, it takes great effort to analyze CM by XRD. This might be receded from XRD studies on the natural graphitization.

Recently, graphitization process has been widely investigated using a micro-Raman spectroscopy because of the development of semiconductor devices (Wopenka and Pasteris 1993; Yui et al. 1996; Beyssac et al. 2002; Rahl et al. 2005; Kribek et al 2008; Aoya et al. 2010; Scharf et al. 2013; Hilchie and Jamieson 2014). In the case of micro-Raman spectroscopy, it is easy to analyze the very low to low crystallinity of CM using the polished thin sections. In addition, we are able to distinguish the spatial distributions of heterogeneous crystallinity of CM combined with the detailed SEM observations with EDS analysis (e.g., Nakamura et al. 2015). The Raman band of CM is composed of first-order (1000–1800 cm^{-1}) and second-order (2500–3100 cm^{-1}) regions (e.g. Nemanich and Solin 1979). It is recently revealed that both regions have different information on the crystal structure of CM along the *a*-axes (first-order) and the *c*-axes (second-order) (e.g. Cancado et al. 2008). Pioneering work by Tuinstra and Koenig (1970) suggested that the intensity ratio between the disorder-induced D band (~1350 cm^{-1}) and first-order allowed G band (~1580 cm^{-1}) is inversely proportional to the in-plane crystallite size L_a. On the other hand, the second harmonic of the D band, the G' band (~2700 cm^{-1}) is also very sensitive to structural changes along the *c*-axes from a turbostratic to graphitic structure (Wilhelm et al. 1998). Thus, the natural structural evolution of CM using micro-Raman spectroscopy has a sufficient potential for substitution of XRD study on crystallographic information. In addition, Beyssac et al. (2002) proposed a new geothermometry, which is named for Raman spectra of carbonaceous materials (RSCM) thermometry for low- to medium-grade metasediments. It is easy to apply for natural CM in metasediments and widely used for the interpretation of *P-T* conditions. Thereafter, several modifications in the geothermometry have been proposed by Rahl et al. (2005), Lahfid et al. (2010), Aoya et al.

(2010) and Kouketsu et al. (2014).

Owing to the developments of analysis methods and RSCM thermometry, it will become more developments of structural evolution of CM in metamorphic terrain. However, there have been still some issues on the utilization of geothermometry. The geothermometers based on the crystallinity of CM using micro-Raman spectroscopy are forced to rely on poorly constrained temperature estimations using different empirical thermometry. Some literatures argued that the structural evolution of CM proceed as functions of not only peak temperature but also annealing duration, and lithostatic pressure based on thermal activated process (Luque et al. 1998; Beyssac et al. 2002b), and other factors may proceed recrystallization of natural CM. In addition, the rapid recrystallization such as contact metamorphism or flash heating by dyke formation cannot validate the conventional RSCM thermometry because they ignored rate dependence (Mori et al. 2015; Mori et al. 2016). Therefore, it is key to understand the detailed chemical kinetics of recrystallization from organic matter to graphite based on the thermal activation process.

In this study, I attempted to assess the temperature, pressure and rate dependence of graphitization based on natural and experimental kinetic studies. The detailed investigations lead not only to a revised geothermometry but also test the potential of graphitization process for geospeedmetry, which is modelled through duration, pressure and temperature dependence.

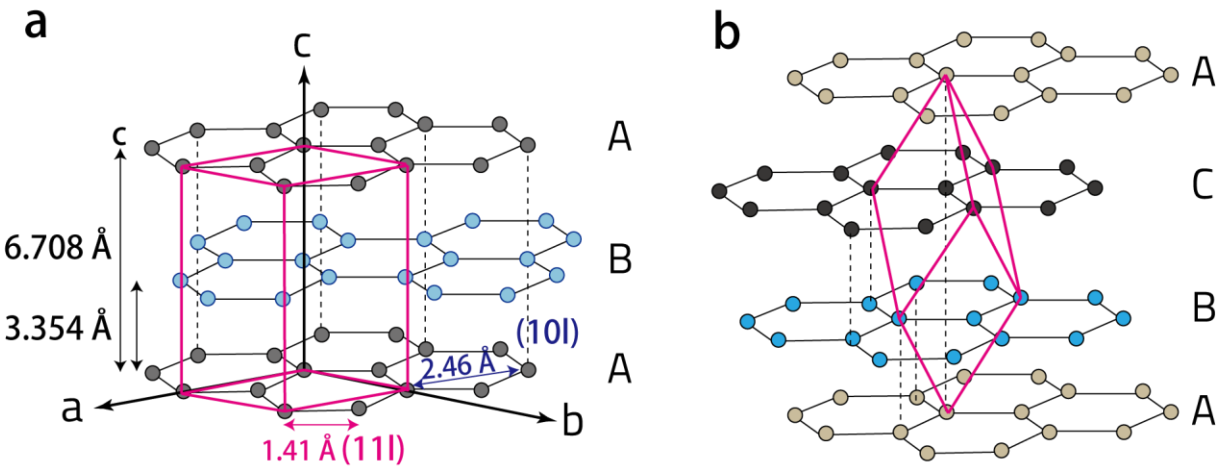

Figure 1. Crystal structure of hexagonal graphite **(a)** and rhombohedral graphite **(b)** in unit cell.

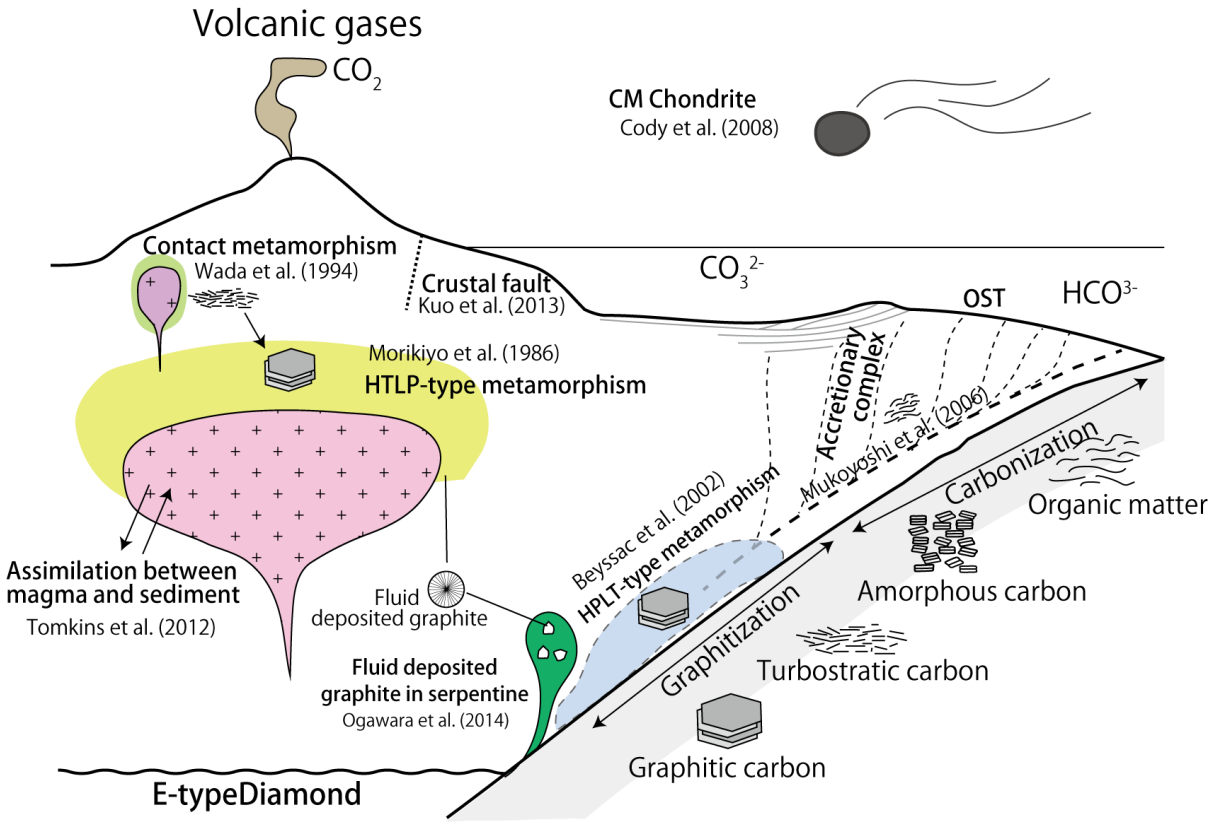

Figure 2. A schematic model of structural evolution of natural organic matter to carbonaceous material, and then graphite in subduction zone.

CHAPTER II

Structural evolution of carbonaceous material to graphite in Hidaka Metamorphic belt, Hokkaido, Japan

2.1. Introduction

Carbonaceous Material (CM) in sedimentary or metamorphic rocks transform from an amorphous carbon to a graphic carbon by complex thermal activation processes. These processes proceed irreversibly with increasing temperature, and record the maximum paleo-temperature (Landis, 1971; Buseck and Beyssac, 2014). The structural evolution of natural CM to a graphite has been widely investigated to reveal the peak metamorphic conditions in metamorphic terrains using XRD (Grew 1974; Itaya, 1981; Nakamura and Akai, 2013), micro-Raman spectroscopy (Wopenka and Pasteris, 1993; Yui et al. 1996; Beyssac et al. 2002b; Rahl et al., 2005; Aoya et al. 2010), vitrinite reflectance (Okuyama-Kusunose and Itaya, 1987) and stable carbon isotopic studies (Hoefs and Frey, 1976; Morikiyo 1986; Wada et al. 1994). In addition to these analyses, many studies have attempted to reveal the nano-structural evolution of CM from an amorphous to a graphitic structure using a High-Resolution Transmission Electron Microscopy (HRTEM; Buseck and Huang, 1985; Deurbergue et al., 1987; Buseck et al., 1988; Large et al., 1994; Beyssac et al., 2002a). These previous literatures have generally accepted that the natural graphitization during metamorphism has more complex recrystallization than that in experimental studies. The influence of lithostatic pressure, duration of heating and shear strain have been debated in many earlier studies as well (Bonijoly et al., 1982; Deurbergue et al., 1987; Bustin et al., 1995; Beyssac et al., 2002a).

In studies on industrial use of natural cokes or carbon materials by heat treatment experiments, relationships between each crystal parameter such as d_{002} spacing, crystal stacking (L_c), crystal diameter (L_a) and micro/nanostructures have been studied in detail. Oberlin (1984) has classified into four continuous stages from nano-structural changes of Local Molecular Orientation (LMO) and Basic Structure Unit (BSU) based on detailed HRTEM study on the run products annealed from 600 to 3000 °C. The CM nanostructures firstly form the BSU, which are composed of five to six stacking layers and extends up to 10 Å in CM microstructures (stage I). In stage II, the BSU's associate face to face and form distorted columns, and the adjacent columns coalesce into distorted winkled layers (stage III). The distorted layers stiffen, become flat and perfect in the last stage (stage IV). These continuous structural changes classified by Oberlin (1984) are also observed in natural samples metamorphosed by contact metamorphism (Nakamura and Akai, 2013). Other studies have also identified some stages of structural changes by XRD, micro-Raman spectroscopy, micro-FTIR study on the heating experiments (Sheng, 2007; Vazques-Santos et al. 2012). These data have suggested that the primary nanostructures of carbon material will strongly control graphitization and carbonization, especially influences of polyaromatic and aliphatic structures in heteroatoms (oxygen, hydrogen, sulphur, and so on; Bourrat et al. 1986; Inagaki, 1996). On the other hand, our previous information about structural evolution of natural CM is limited because it is uncertain what factor controlled "the natural graphitization" in metamorphism. Previous studies have concluded that the natural graphitization is controlled mainly by temperature with additional influence of pressure, duration of heating and shear strain (Landis, 1971; Wada et al., 1994; Bustin et al., 1995; Beyssac et al., 2002a). Moreover, it is well known that the low-grade CM including cokes has heterogeneous microstructures in nature, and many researchers have considered that there is a structural transitional point at around ~300 °C, represented by the release in heteroatoms (Wada et al., 1994), decrease in aliphatic chains (Lu et al.,

2007), kerogen degradation reactions (Schwab et al., 2005).

It is essential to investigate natural graphitization combined with the detailed microstructural observations from the various viewpoints of mineralogy, structural and metamorphic geology in metamorphic terrain. The previous literatures have mainly forcused on the studies on graphitization at over 350 °C in metamorphic terrain (Buseck and Huang, 1985; Large et al., 1994; Beyssac et al., 2002a), whereas the transitional point of various parameters is located at around 300 °C through regional metamorphism. Thus, it is important to reveal the structural evolution of CM at the structure transitional point throughout graphitization and carbonization combined with XRD, micro-Raman spectroscopy, HRTEM, and carbon stable isotopic study. The natural processes seem to be heterogeneous and other factors may affect the structural evolution of CM to graphite. Therefore, I have conducted detailed field observations of graphite-bearing metasediments and analyzed natural CM samples formed by simple heating events in metamorphic terrain.

2.2. Geological setting and sample locations

The study area located in central part of Hidaka Mountains, Hokkaido, Japan, belong to the Hidaka Metamorphic Belt (HMB), which is a typical high-temperature low-pressure (HTLP) type metamorphic terrain. The HMB is divided into two tectonic sequences based on the metamorphism and deformation histories; the lower sequence and the upper sequence (Fig. 3; Osanai et al., 1985; Toyoshima et al., 1994). The upper sequence of metasedimentary rocks in Figure 3 are progressively metamorphosed toward to western area, starting from very low-grade metasediments belonging to Nakanogawa Group to biotite-musicovite schist and gneiss at around the main ridge of Hidaka Mountains. The protolith, Nakanogawa Group, is composed solely of turbidities facies sediments,

including acidic tuff layers and dismembered hemipelagic red and green mudstones. Based on the lithology, biostratigraphy and radiolarian ages, they are divided into two tectonicstratigraphic units; the northern and southern unit bounded by the Nupinaigawa Fault (Kontani, 1978; Nanayama, 1992; Nanayama and Ganzawa, 1997). The southern unit of Nakanogawa Group have been folded into nearly upright tight folds with N-S trending axes, on the other hand, the northern unit showed nearly upright tight folds with NE-SE to ENE-SWS trending axes (Fig. 3).

The multiple thermal events of HMB from subduction to collision tectonics are classified into three stages (Toyoshima et al., 1994, 2004; Osanai et al., 2007). Stage-I is the tectonic thickening (M_0) of earliest Paleogene accretionary complex with fore arc sediments (Nakanogawa Group). After subduction to NE Japan island arc, the prograde metamorphism (M_1) with increasing temperatures had been caused by underplating of mafic to intermediate intrusions in back-arc basin. Almost all CM and illite have recorded the peak metamorphic event (M_1). At the peak metamorphism (M_1), the pelitic and psammitic rocks of Nakanogawa group converted to schist and gneiss from greenschist to upper amphibolite facies in the study area (Fig. 4). Stage-II is the tectonic deformation that is characterized by subhorizontal top to the south displacement and thrusting of lower to upper crustal rocks with sheet like intrusions of S-type tonalite (Toyoshima et al., 1994). Although a part of metasediments at around the intrusions affects the contact metamorphism (M_2), we have concluded that most of the metasediments have not influenced the M_2 event from the microscopic observations of metamorphic rocks. Thereafter, the graphite-bearing metasediments have undergone retrograde metamorphism (M_3), which metamorphosed greenschist to prehnite-pumpellyite facies, and mylonitization (stage-III). In this study, over 190 metasedimentary rocks were selected that have recorded the simple thermal events to avoid the deformed CM during retrograde metamorphism reported by Nakamura et al. (2015). The sampling points and

mineral assemblages are shown in Figure 4.

2.3. Analytical methods

XRD was carried out using a Rigaku ULTIMA IV diffractormeter at Niigata University, equipped with CuKα (40 kV, 40 mA) radiation, graphite monochrometer, slit system 2/3°–0.45 mm–2/3° and time constant of 0.5° min^{-1}. The diffractometer was run between 10 ° and 90 ° by step scan method (0.5 degree / min). The powdered samples of CM extracted by HF-HCl treatment were dried on a Si-low background sample holder with internal standard of high purity silicon (up to 99.99%; 10–20 wt%; Kojundo Chemical Laboratory). The detailed procedures of chemical extractions from mudstones are described in the Appendix 1. Lattice constant, crystal thickness, and crystal diameter of graphite were calculated according to the following methods. The 2θ values of the obtained peaks were calibrated using the peak positions of the internal silicon standard (Iwashita et al., 2004). The $L_c(002)$ was calculated by following Scherrer equation:

$$L_c(002) = K\lambda / \beta\cos\theta,$$

where K, constant (1.0); λ, X-ray wavelength (Cu$K\alpha$ = 1.54059292 Å); β, full width at half maximum (FWHM); θ, the Bragg angle. The K value is not a constant, but depends on the crystallite sizes (Fujimoto, 2003). Therefore, we used the constant K of 1.0 for $L_c(002)$ following JIS standards (Iwashita et al., 2004).

We also measured IC values from 87 samples of pelitic and pssamitic rocks. The samples used the same powder for CM separation, and sieved using a 100-mesh screen. 10~20 g of rocks were suspended in a test tube with distilled water. The <2 μm clay fraction was separated by gravity settling and then concentrated by a centrifuge. The clay samples were placed onto glass slides (~ 2 mg /cm^2) to produce oriented samples and left to dry overnight. XRD was carried out using Rigaku ULTIMA IV diffractometer, equipped

with CuKα (40 kV, 40 mA) radiation, graphite monochrometer, slit system 2/3° – 0.45 mm – 2/3° and time constant of 1° min^{-1}. Two slides of each sample were scanned in ordered to check and calculated the mean values of dry condition and Ethylene Glycol (EG) treatment. Based on measured values of standard samples (JIC) proposed by Hara and Kimura (2003), all IC values were calibrated to JIC values using the following correlation equation (Fig. 5):

IC (JIC, AD) = 0.8689IC (measured in Niigata Univ.) +0.0964 (R^2 = 0.997).

IC (JIC, EG) = 0.8079IC (measured in Niigata Univ.) +0.1092 (R^2 = 0.995).

In addition, Hara and Kimura (2003) have also reported measured values of standard samples (CIS) proposed by Warr and Rice (1994), and presented the following correlation equation:

IC (CIS) = 1.55 IC (JIC) – 0.07 (R^2 = 0.99).

IC values range from 0.25 to 0.76 Δ°2θ in this study, corresponding to anchizone and diagentic zones defined by Warr and Rice (1994).

Arkai (1991) has proposed that not only illite crystallinity (IC) but also chlorite crystallinity (ChC) has a potential as a thermal indicator during diagenetic process. The FWHM of chlorite (001), (002) and (003) reflections are well consistent with IC in very low-grade metamorphic terrain (Warr et al. 1996). Figure 6a shows the relationship between illite $(001)_{CIS}$ and chlorite $(001)_{EG}$, and illite $(001)_{CIS}$ and chlorite $(001)_{AD}$, respectively. The linear regression lines between illite $(001)_{raw}$, chlorite$(002)_{AD}$, and chlorite$(002)_{EG}$ showed similar correlation coefficients of 0.64~0.68. These data suggest that the swelling clay mineral such as smectite in 14 Å interferes the (001) reflection of chlorite in the case of very low grade metamorphism at over ~0.42 Δ°2θ. In order to form the chlorite as solid solution between Al, Mg and Fe, it is well known that the chemical composition of chlorite affects the degree of crystallinity (Arkai, 1991). Therefore, I tried to compare the intensity of (001), (002) and (003) reflection of chlorite in ternary diagram

(Fig. 6b). The ternary diagram of each basal reflection of chlorite is known to the "Oinuma diagram". It can be identified as Al-rich chlorite or Mg-rich chlorite from the distribution of ternary diagram. Figure 6b show the ternary diagram between (001), (002) and (003) reflection of chlorite. These data plots in a similar domain and, therefore, almost chlorite have the similar chemical compositions of Mg-chlorite.

Micro-Raman spectroscopy was applied to CM and graphite using a Jasco NRS 3100 spectrometer at Niigata University, equipped with the grating of 1800 lines/mm and CCD-detector (256×1024 pixels). The microscope objective of 100×, and Nd-YAG laser (wavelength: 532 nm) were used. Acquisition time is 10–30 s, and 3–6 spectra were cumulated for each data point. All Raman peak profiles were analyzed by using peak profile fitting Peak Fit 4.12, and G (1580 cm^{-1}), D1 (1350 cm^{-1}), D2 (1620 cm^{-1}), D3 (at around 1450 cm^{-1}), and D4 (at around 1200 cm^{-1}) bands in the first order region (1000–1800 cm^{-1}) were separated (Fig. 7). The parameters of G band FWHM, D1 band FWHM, G position (Raman shift), R1 ratio (Intensity D1 band / Intensity G band), R2 ratio (Area $_{D1\ band}$ / Area $_{G + D1 + D2\ bands}$), RA1 (Area $_{D1+D4\ band}$ / Area $_{G + D1 + D2 + D3 + D4\ bands}$) and RA2 (Area $_{D1+D4\ band}$ / Area $_{G + D2 + D3\ bands}$) were estimated. The Tuinstra and Koenig equation were applied (Tuinstra and Koenig 1970):

$$I_{D1} / I_G = C(\lambda) / L_a\ (nm)$$

where C (λ), constant (4.4); I_{D1}/I_G, Intensity D1 band / Intensity G band, R1 ratio; L_a (nm), the crystal size of lateral extent of carbon sheets. Mean values and standard deviations were calculated based on over 25 analyses.

Carbon stable isotope analysis of graphite was carried out using a Finnigan MAT 251 mass spectrometer at Niigata University. An aliquot of the graphite powder used for the XRD analysis that was extracted by the chemical extraction from the rock samples was used for isotope analyses (Bulk analysis). The samples were introduced into a preheated (1100 °C for 12 h) quartz tube. Vanadium pentoxide (V_2O_5) was used as oxidizing agent

for conversion of carbon to carbon dioxide. The quartz tubes containing graphite and V_2O_5 were again preheated at 500 °C for 30 min. to remove any surface organic contaminations in samples, and sealed under vacuum (~10^{-3} Torr). Sealed tubes were combusted at 1000 °C for 2 h for oxidizing the graphite to CO_2. The tubes were then cracked under vacuum, in a line connected to a modified high vacuum inlet system for carbon isotope measurements of micro-volume CO_2 gas (Wada et al., 1984a, 1984b, Satish-Kumar et al., 2011a).

Transmission electron microscopy (TEM) was carried out using a JEOL JEM 2010 electron microscope in Niigata University, operating at 200 kV with LaB_6 filament. CM samples extracted from the run products were ground and suspended in pure water. After ultrasonic cleaning in plastic tubes, the solution was deposited on the carbon-coated holey film of the TEM micro-grid treated by plasma cleaning. The samples were mainly observed for the d_{002} lattice fringe along the [010] direction.

2.4. Results

2.4.1. Low grade metamorphism based on RSCM thermometry and Illite crystallinity

Because of the lack of sufficient mineral assemblages and metamorphic markers in the study area, I tried to use the Raman Spectra of Carbonaceous Material (RSCM) thermometry calibrated by Beyssac et al. (2002a), Rahl et al. (2005), Aoya et al. (2010), Kouketsu et al. (2014) in combination with illite (IC) and chlorite crystallinity (ChC) for understanding the very low to low grade metamorphism. Although the calibrations used here have some issuers relating to the reference calibration data, a rough approximation of peak metamorphic temperatures can be easily obtained.

The metasediments fall into four metamorphic zones based on metamorphic

mineral assemblages of illite, chrolite, and biotite, and IC values. The mudstones with laumontite and smectite in zone Ia are limited to the confluence of the Iwanai and Minami-Iwanai Rivers (Fig. 8). The IC values range between 0.57 and 0.93, suggesting the digenetic zone. They are one of the lowest maturation and retain a framboidal pyrite within coal. The mudstones with illite and chrolite are located in the eastern area along the Karupesinape River, downstream part of the Ueda River and Iwanai River. The IC values in pelitic and psammitic rocks range from 0.37 to 0.74 Δ°2θ (mean = 0.5 Δ°2θ, 1σ = 0.099) and 0.48 to 0.53 Δ°2θ (mean = 0.51 Δ°2θ, 1σ = 0.03), respectively, suggesting the digenetic zone to anchi zone based on the Kübler index (Fig. 8 and table 1). In addition, these IC values were used to calculate the peak metamorphism by following equation; T (°C) = 353 – 206 IC (Δ°2θ), with a correlation coefficient of 0.92 and error of ±30 °C (Hara and Kurihara, 2010; Mukoyoshi et al., 2007). The estimated temperatures using IC values show the range values between approximately 200 and 276 °C (mean = 250 °C). In the case of RSCM thermometry using Kouketsu et al. (2014) and Lahfid et al. (2010), the estimated temperatures exhibited between 147 and 291 °C, and 222 and 363 °C, respectively. Other calculated temperatures are listed in table 4. The estimated temperatures by equation of Lahfid et al. (2010) overestimate by about 100 °C to compare with other thermometery, therefore, we concluded that peak metamorphism in zone Ia ranged from approximately 147 to 291 °C by very low-grade metamorphism of HMB.

The mudstones in zone Ib are distributed in the upper reach of Iwanai and the Ueda, and Pitoitoppi Rivers, and 4 no sawa and 5 no sawa area. The IC values calibrated JIC in pelitic rocks and pssamitic rocks range from 0.23 to 0.44 Δ°2θ (mean = 0.34 Δ°2θ, 1σ = 0.062) and 0.28 to 0.55 Δ°2θ (mean = 0.41 Δ°2θ, 1σ = 0.067), respectively, suggesting the Anchi zone to Epi zone based on the Kübler index (Fig. 8 and table 1). The estimated temperatures between 261 to 306 °C, and 240 to 295 °C were obtained by the equation of Mukoyoshi et al. (2007), respectively. RSCM thermometry using Beyssac et al. (2002a) and

Rahl et al. (2005) displays the values between 332 and 389 °C, and 278 and 406 °C, respectively. These estimated temperatures between IC and CM data show the wide range values, and it is difficult to estimate the peak temperature exactly. The area in zone Ic has undergone the poly-metamorphism by M_0 diagenetic process and M_1 regional metamorphism by underplating of mafic or intermediate intrusive. At least, biotite isograd between zone Ic and zone IIa, bounded at around 400 °C reported by Osanai et al. (1986) and the boundary between zone Ia and Ib is located at around 300 °C from IC and RSCM thermometry data. Therefore, zone Ib suggests that the peak metamorphism ranges from approximately 291 to 400 °C.

The mudstones from zone IIa are located along the Satsunai River, downstream of the Koikakushu Satsunai River, and 6 no sawa area. The appearance of biotite is observed in thin section. RSCM thermometry by Beyssac et al. (2002a) and Rahl et al. (2005) displays the values from 407 °C to 515 °C and 408 °C to 498 °C, respectively. Therefore, the area in zone IIa shows the ranges between approximately 400 to 500 °C. The samples from zone IIb are located in the Satsunai River, upperstream of the Koikakushu Satsunai River, and 7 no sawa area. RSCM thermometry by Beyssac et al. (2002a) and Rahl et al. (2005) displays the values from 497 °C to 596 °C and 489 °C to 643 °C, respectively. The area in zone IIa shows the estimated temperatures between approximately 500 to 640 °C.

Based on the detailed temperature estimations, we constructed the regional thermal variation diagram, which was contoured at an interval of 20 °C (Fig. 9). This figure is based on areal interpolation method using kriging. The geothermal gradient along the Route A and B are consistent with the thermal contours, which show NNW-SSE trending. These thermal contours were overprinted by the reginal geological structure, suggesting peak metamorphism had been obtained after the formation of map-scale folding.

2.4.2. Temperature estimates using different methods

The detailed *P-T* conditions based on the upper and lower sequence of Hidaka metamorphic belt (HMB) has already been investigated by Osanai et al. (1986) and Osanai et al. (2007). The zone II in HMB is characterized by the appearance of biotite in lower to middle part of amphibolite facies metamorphic rocks, suggesting the metamorphic conditions between 400 and 550 °C, at 250–380 MPa. In addition, the geothermal gradient of 35 °C/km from zone I to zone IV in HMB has been determined. In this study, we also tried to carry out a pseudosection modelling with KFMASH system for calculating the metamorphic mineral assemblages in the metapelites (e.g, Thompson, 1976; Pattison and Tracy, 1991; Spear 1993). The bulk chemistry for the pseudosection modelling were used for four different XRF whole rocks major element data of pelitic and psammitic rocks (Table 3). Although KFMASH system is commonly used for various metamorphic terrains in the past, the use of more complex chemical system such as MnKFMASH (Mahar et al. 1997) and MnNKFMASH (Symmes and Ferry 1992) have been proposed for understanding the effect of Mn on metapelite phase stability. The stability field of Mn-rich garnet is critically changed by the effect of Mn in KFMASH system (Tinkham et al. 2001). It is important to estimate the complex chemical systems for fully understanding the pseudosection modelling, however, we firstly constructed a simple KFMASH pseudosection modelling for practice using a *Perplex 6.7.1* software (Connolly and Petrini 2002) with the thermodynamic data base of Holland and Powell (2011). Figure 10 shows a KFMASH pseudosection modelling using our XRF data of metapelites (Table 2). The three-important dehydration pathes were initially identified, suggesting chlorite (green dotted line), muscovite (orange dotted line), and biotite breakdown (red dotted line). In the Hidaka metamorphic belt, the dehydration reactions in metapelites defines the metamorphic zonation from I to IV (e.g., Osanai et al. 1986). The field *P-T* path constructed

by Osanai et al (1989) were slightly out of phase stability on KFMASH pseudosection modelling (Fig. 10). The difference of first appearance of metamorphic minerals are easily identified by the estimated volume fraction of mineral phases using a perplex software (Fig. 11). Based on the thermodynamic modelling, first appearance of biotite was plotted at over ~530 °C due to the breakdown of chlorite and muscovite. On the other hand, our observations using RSCM thermometry show the appearance of biotite at over ~400 °C. The difference of metamorphic temperature may be derived from the bulk chemistry between pelitic and psammitic rocks. In this study, I also tried to construct a T-$x$$Al_2O_3$ diagram using a perplex software. The first appearance of biotite is strongly depended on the Al_2O_3 contents in pelitic rocks, therefore, it might produce the difference of mineral phases between pelitic and psammitic rocks (Tinkham et al. 2001). In the case of low Al pelitic rocks, the first appearance of biotite varied between 380 °C and 550 °C as a function of Al_2O_3 contents from15 to 19 wt.% (Fig. 12). In fact, bioite is dominant in the pssamitic layers compared with pelitic layers, which may result from the difference of stability field of biotite at low temperature. In addition to thermodynamic modelling, we tried to compare the peak temperatures of RSCM thermometry and geothermal gradients (Fig. 13). The estimated peak temperatures using the geothermal gradient of 35 °C/km were calculated from the boundary of biotite isograd between zone I and II. Figure 13 display a relationship between the peak temperatures using both RSCM thermometry ($T_{\text{Kouketsu \& Beyssac}}$) and the geotherm based peak temperatures (T_{geotherm}). The results of both temperature estimates show good correlation coefficient.

2.4.3. Optical and SEM observations of CM

In the metasediments, minor amount of CM and/or graphite are observed as an accessory phase in pelitic rocks. The morphological characteristics of CM extracted by HF-HCl

treatments in zone Ia and Ib shows the hairy and porous microstructures (Fig. 14a and 14c). These CM are usually associated with the muscovite and chlorite in sedimentary rocks (Fig. 14b) or pelitic layers in metasediments (Fig. 14d). In the biotite-muscovite schist at around boundary between zone IIa and IIb, the graphite tends to concetrate with the pelitic layers and shows the arrangement of small granular textures along schistosity (Fig. 14f), which is ~1μm width. The hexagonal shapes and stiff (001) planes are already observed by SEM (Fig. 14e). The graphite in biotite-muscovite gneiss (zone IIb) is seen the biotite and muscovite (001) cleavages, which is 10-20 μm width (Fig. 14h). These crystals in figure 14g are stiff layers and no defects under SEM observations. A part of graphitic structures glide the (001) planes parallel to the biotite and muscovite cleavages.

2.4.4. Structural evolution of natural CM to graphite

2.4.4.1. XRD study

It is well known that the CM microstructures display the structural evolution from amorphous structure (interlayer spacing = c/2 = d_{002} > 3.43 Å) to turbostratic structure (d_{002} ≈ 3.43 Å), and then finally into graphitic structure (d_{002} = <3.36 Å) based on XRD studies (Fig. 15a; table 3). The XRD profiles in this study were divided into four distinct structural changes based on characteristic d_{002}, 10 and 11 peak profiles for each metamorphic zonation. Figure 15 shows the transformation of CM observed in XRD profiles between 10 and 90 degree. In the range of 2θ values between 40 and 90 degree, there are peaks of d_{100}, d_{101} (at around 42~46 degree; Fig. 15c), d_{004} (at around 54.4 degree; Fig. 15c), d_{110}, d_{112} (at around 77~83 degree; Fig. 15d) and d_{006} (at around 86 degree; Fig. 15d) attributed to the graphitic structure. Although these intensities in XRD profiles are very small against d_{002} peak, Wada et al. (1994) have argued that these peaks gave valuable information on crystal structure including ABAB stacking of graphite along

not only *c*-axis but also *a*-axis. The tailed 10*l* reflection toward high angle side, so-called the prism reflection, and the very broad 11*l* reflection can be observed during zone Ia and Ib. Such characteristic reflections suggest random structures of carbon layers (1D or 2D structures). The 002 reflection in zone Ia shows very broad and symmetric peak, whereas in zone Ib, the 002 reflection shows the asymmetric peak contained two different crystallite peaks in figure 16. The shoulder peak at around 25.5 degree were calculated the very small crystal stacking from 17 to 38 Å by Scherrer equation, suggesting amorphous carbon in microstructure. Another peak at around 26 degree showed the typical interlayer spacing of turbostratic structures (d_{002} ≈ 3.43 Å). Although the peak display a broad and not fully ordered structure, these crystallites were having about twice L_c(002) as that of amorphous carbon. These profiles suggest the heterogeneous microstructures, which is composed of amorphous carbon (≈ 20 Å) and poorly crystalline stacking (≈ 50 Å) in zone Ib. The crystal stacking along c-axis indicates that the crystallite already grew up between 15 and 20 carbon sheets, corresponding to Local Molecular Orientation (LMO). In addition, amorphous carbon and poorly crystallized carbon in this study corresponded to the coaly material and transitional material by Itaya et al. (1997), respectively. In zone IIa, amorphous peak at around 25.5 degree was absent in XRD profiles. Instead, the asymmetric peak composed of turbostratic stacking (d_{002} ≈ 3.43 Å) and graphitic stacking (d_{002} = <3.36 Å) was newly observed (Fig. 16b). The 10 reflection splits off into d_{100} and d_{101} spacing with increase in metamorphism, and the d_{112} spacing was shown (Fig. 15a). The appearance of d_{112} spacing indicates that the CM microstructure changes from two-dimensional structures to three-dimensional structures (ABAB… sequence). Although a part of CM microstructure grow up the graphitic structure at around 400 °C with prograde regional metamorphism (M_1), the turbostratic structures in microstructure are remained until zone IIa. This heterogeneous recrystallization related to graphitic and turbostratic structures may induce the increasing of FWHM in previous

XRD studies on regional metamorphism (i.e. Itaya 1981; Nakamura 1995). In zone IIb at over 500°C, the (002) reflection changes from asymmetric to symmetric peak profile with increasing temperature. The appearance of d_{006} spacing and sharp peaks such as d_{100} and d_{110} indicate that the CM microstructure showed the transformation from turbostratic to graphitic structures with crystal growth along the *a*-axis and *c*-axis. In fact, the crystal sizes of $L_c(002)$, $L_c(004)$, $L_a(100)$ and $L_a(110)$ significantly increase from zone IIb (Table 3). In this way, the first appearance of fully order graphite (d_{002} = <3.36 Å) is at around 400 °C, similar to other localities reported by many studies (Landis 1971; Okuyama-Kusunose and Itaya 1987; Wang et al. 1989; Nakamura 1995). However, we newly found that the formation of fully ordered graphite underwent heterogeneous recrystallization with increasing peak temperatures. These data strongly indicate that the rate of graphitization was depended on the other factors during prograde metamorphism.

2.4.4.2. Micro-Raman spectroscopy

A lot of previous studies have pointed out that carbonization has been more complex recrystallization and devolatilization than graphitization by the influences of not only peak metamorphism but also lithostatic pressure, duration of heating, starting material and even deformation (e.g. Lahfid et al. 2010). On the other hand, some important common aspects during carbonization have been reported as follow. (1) D1 band FWHM (FWHM-D) is the most sensitive parameter in the first region (1000-1800 cm^{-1}) (Quirico et al. 2005; Busemann et al. 2007; Kouketsu et al. 2014). (2) The intensity ratio between D1 and G band changes the increase and decrease at the boundary of 2.4 (La ≈ 2nm by Tuinstra and Koenig equation; Ferrari and Robertson, 2000). (3) G band position shifts from 1580 to ~ 1600cm^{-1}, and D1 band also sifts from 1350 to ~1330 cm^{-1} (Ferrari and Robertson, 2000). (4) The appearance of D4 band (at around 1150 cm^{-1}) below 300 °C (Sadezky et al. 2005; Lahfid et al. 2010). These changes have been discussed for industrial

carbon materials or cokes by heating experiments, and the natural CM is also expected to grow through the same or similar recrystallization processes (Fig. 17). In order to observe the evolution in the Raman profile, I attempted to make scatter plots between D1 band FWHM, R1, RA2, and G band FWHM (Fig. 18 and table 4). However, not all plots showed linear relationship and some of them seems to have complexly trends that representing the whole process. In particular, the D1 band FWHM from 40 to 120 cm^{-1} show characteristic transformation with increasing temperature. There are some transition points of Raman parameters during carbonization at around 55-60 cm^{-1} and 100 cm^{-1} (Figs. 18a-c). The early stage of carbonization, R1 ratio and D1 band FWHM increase and decrease with increasing temperature, respectively, which show the high correlation of linear relationship. (Fig. 18a) At around 55-60 cm^{-1}, R1 ratio change to decreasing trend. The transition point corresponds to the point between carbonization and graphitization. On the other hand, D1 band FWHM and RA2 did not show a linear relationship in this area. Lahfid et al. (2010) and Kouketsu et al. (2014) have constructed the RSCM thermometry in low grade metamorphism using those parameters and peak metamorphic conditions. Our results suggest that reference peak temperatures for thermometry were not consistent with the structural evolution of CM. G band FWHM and R1 ratio have also similar discontinuous trends between carbonization and graphitization, suggesting the transformation of rate-determining chemical reaction through structural changes (Figs. 18a-d).

2.4.5. Structural transformation along the biotite isograd

Figures 19 and 20 display the relationships of each structural parameter using micro-Raman spectroscopy and XRD study along the distance from biotite isograd in this study area. The parameters continuously change from zone Ia to zone IIb with increasing

metamorphic conditions. In Satsunai River area and upper reach of Iwanai River of zone Ib are having different trends. The changes of parameters in zone Ib suggest that tectonic deformation after peak metamorphism has modified the countinuity of the thermal trend. On the other hand, other continuous trends of structural parameters from zone Ia to IIb correspond to peak metamorphism. The increase of R1 ratio and decrease of D1 band FWHM change the trend at the boundary between zone Ia and Ib (at around 300 °C; Fig. 19c). As metamorphic conditions increase, G band FWHM, R1 ratio d_{002} and FWHM in XRD systematically change to the structural parameters, suggesting the fully ordered graphite from 400 to 500 °C (Figs. 19b-c and 20a-b). The recrystallization from zone Ib and IIa show the "sigmoid transformation" from amorphous to graphitic structure in XRD study (Fig. 20). Finally, at over 500 °C, the graphitic structures have already been formed based on these structure parameters, and grow up the large hexagonal structures. In this way, the structural parameters of CM and graphite systematically change from an amorphous structure in zone Ia and Ib to a graphitic structure in zone IIa and IIb with increasing temperatures in the range of 200 to 650 °C.

2.4.6. Nanostructures of CM

In this study, I revealed the heterogeneous recrystallization of CM in zone Ib and IIa in the temperature ranges between 300 to 400 °C based on XRD study. These temperature ranges correspond to other structural changes such as carbon isotope composition and chemical composition of CM. It can be expected that the heterogeneity of structural parameters may result from the micro/nano- structure of CM, therefore, I attempt to observe the nanostructure of CM in zone Ia to IIb using TEM.

In zone Ia at around 200 to 300 °C, the porous structures that show 10, 11 002 ring in Selected Area Electron Diffraction (SAED) patterns are observed in powder

samples (Fig. 21a). Although these CM show the very broad SAED pattern in microstructure, these lattice fringes have been already formed as shown in figure 21b, which is composed of 3-4 distorted layers in non-graphitized carbon like structures. At the early stage of zone Ib, the nanostructure of CM is composed of amorphous carbon domain and Local Molecular Orientation (LMO) domain in aggregates (Fig. 21c). The amorphous carbon domain shows the typical ring pattern, suggesting random orientation of lattice fringes, whereas the LMO domain already show the spot patterns in SAED (Fig. 21b). The appearance of LMO corresponds to the boundary of zone Ia and Ib at around 300 °C. These stacking in LMO form the turbostratic structures, which have dislocations and distorted layers. In order to compare with crystal size of XRD study, I tried to observe the microstructures by 002 Dark Field (DF) mode. Using 002 DF mode, the LMO domains which selects the 002 spots in SAED pattern are selectively illuminated in microstructures (Fig. 21d), therefore, we can measure the LMO sizes from electron images. Figure 22a shows the 002DF image and SAED patterns. Light circles in SAED pattern are selected spots to image the 002DF. The samples of 5s11080606, Pt11073102 and Sn11080401 correspond to the metamorphic rocks in middle part of zone Ib, late part of zone Ib and early part of zone IIa, which are metamorphosed at 300~420 °C, respectively. The LMO domains of 5s11080606 in figure 22a are very small, which is 10 to 30 Å in stacking. As temperature increases, LMO start to grow up from 30 Å to 70 Å in microstructures of Pt11073002 and from 30 Å to 100 Å in microstructures of Sn11080401. Although two microstructures between Pt11073102 and Sn11080401 grow up over 60 Å of LMO, there is the difference of SAED pattern at the boundary of these samples. SAED pattern of Pt11073102 shows the ring pattern and arc shape of 002 patterns, whereas SAED pattern of Sn11080401 shows only the spot patterns (Figs. 22b-c). These patterns and crystal size of LMO suggest that microstructures of CM in zone Ib retained the amorphous characteristics in CM aggregates and that amorphous domain disappeared at the

boundary between zone Ib and IIa. These heterogeneous microstructuresbased on the HRTEM observations correspond to the results from structural parameters by XRD and micro-Raman spectroscopy. At the zone IIa, a part of filament like microstructures has already formed the 2H-graphite structures in LMO. These filament-like structures are observed from 400 to 500 °C during zone IIa. During zone IIb, the microstructure of CM forms the hexagonal shapes (Fig. 21g). The lattice fringe in the [010] direction display (101) and (002) reflection in graphitic LMO, suggesting a 2H-graphite (Fig. 21h). In this way, three important features are identified by HRTEM observations. (1) turbstratic LMOs in microstructures appeared at around 300 °C in the zone Ib and start to form the heterogeneous structure coexisting with amorphous domain and turbstratic LMO. (2) At the boundary of biotite isograd, the heterogeneous structures disappear from the amorphous domain and form the graphitic LMO that is already 2H-graphite. (3) The hexagonal shape of graphite has appeared at over 500 °C during zone IIb.

2.5. DISCUSSION

2.5.1. Comparison of microstructures and structural parameters

The present study has revealed that the crystal parameters have some important transitional points through carbonization and graphitization in Hidaka metamorphic belt. These structural transition points are well consistent with the nanostructural evolution of CM based on the HRTEM observations. In the zone Ia between 200 and 300 °C, the misoriented stacking of carbon sheets are dominant in amorphous domain, and the amorphous domain disappear with increasing temperature. Such nanostructural change corresponds to a decrease in the D3 and D4 band, and an increase in the D1 band by micro-Raman spectroscopy. In general, these parameters changed during carbonization process,

which are related to the amorphous sp^2-sp^3 sites in coal structure (Sheng, 2007). It is likely that the decrease in the amorphous structures results in the transformation of crystal parameters. On the other hand, the crystal parameters such as d_{002} or FWHM in XRD show less transformations than that in micro-Raman spectroscopy. Under the HRTEM observations, these microstructures already start to form the very small stackings, which corresponds to the BSU, and show the "strong" ring pattern of 002, 10, 11 reflections by SAED patterns. Thus, the change of microstructures in zone Ia were characterized by a continuous reorganization form amorphous carbon to the formation of BSU. As metamorphic condition increases, in the zone Ib between 300 and 400 °C, the amorphous carbon in microstructures disappear toward the boundary of the biotite isograd. Moreover, the progressive change of G band FWHM and R1 ratio from zone Ib to zone IIb also suggest the increase of crystal size of LMO based on the HRTEM observation. The parameters in micro-Raman spectroscopy seem to pass through an important transition point at around zone Ia and Ib rather than the boundary of fully ordered graphite at 400 °C. The data presented here suggests that these structural parameters in XRD and micro-Raman spectroscopy reflect the different information in microstructures. The structural parameters in micro-Raman spectroscopy change the trend at the boundary of 300 °C, and the change of structural parameters correspond to the appearance of LMO in microstructure. These data indicate that the structural transition points of G band FWHM and R1 ratio are closely related to the appearance of LMO in microstructure. On the other hand, two distinct peaks between amorphous and turbostratic structures in XRD study also correspond to the heterogeneous microstructure using HRTEM observations during stage Ib.

Figure 23 shows the summary of microstructure and structural changes by XRD and micro-Raman spectroscopy. Microstructures of CM are mainly composed of amorphous carbon and LMO in heterogeneous structures. The difference of crystallinity

has appeared at around 300 °C and turbostratic LMO start to grow the crystal size from 300 °C in zone Ib to 600 °C in zone IIb. On the other hand, the amorphous carbon has remained in the microstructures until around 400 °C and they disappeared at the boundary of biotite isograd. On the basis of relationships between microstructures and structural parameters, two types of nanostructures are identified that reflect different information in microstructures; LMO and amorphous carbon. The decrease of G band FWHM between 60 and 14 cm^{-1} and R1 ratio between 2.4 to 0.1 mainly reflect the growing crystal size of LMO from turbostratic to graphitic structures in microstructure. On the other hand, the D1 band FWHM and intensity of D3, D4 band mainly reflects the relative amount of amorphous carbon in microstructure. The parameters of d_{002} spacing and FWHM have different information about amorphous carbon and LMO domain.

Overall, the continuous microstructural evolution based on the structural parameters and microstructural observations between 200 and 600 °C is summarized below. (1) The primary structure in CM is mainly composed of amorphous carbon, which have some heteroatoms in edge planes. With increasing temperature, the reorganization of BSU progressively start to form in amorphous carbon. During this process, the decrease of intensity of D3 and D4 bands may be reflected in the devolatilization of CM. (2) The appearance of LMO triggers the change of parameters such as G band FWHM and R1 ratio at around 300 °C. These parameters start to decrease between 300 and 600 °C. (3) At the boundary of biotite isograd between zone Ib and IIa, the LMO in microstructures convert from turbostratic to graphitic structure. The heterogeneous microstructure of CM appeared at around 300 °C and decrease heterogeneously from 300 to 500 °C by growing both crystal sizes L_a and L_c. (4) Above 500 °C, the heterogeneous microstructures already disappeared and the crystal size starts to grow up dramatically at over micro-meter scales. The combined observations with HRTEM, XRD, and micro-Raman spectroscopy revealed that the heterogeneous recrystallization in metamorphic rocks may result from the

difference of structural evolution of CM in different *P-T* conditions. In addition, it is important to interpreted heterogeneous recrystallization for fully understanding the phenomena of natural graphitization.

Some earlier literatures reported that the origin of heterogeneous recrystallization in metamorphic rocks results from the catalytic effect in grain boundaries (Zuilen et al., 2012, Itaya et al., 1997), tectonic deformation (Ross and Bustin, 1990) and fluid activities (Nakamura 1995). However, there have been no significant evidences of promotion of recrystallization from natural graphitization. In the future, it is important to combine between natural and experimental kinetic studies of graphitization from the point of heterogeneous recrystallization of two starting materials.

2.5.2. Sigmoidal recrystallization of natural CM in metamorphic terrain

Based on the detailed structural analyses and HRTEM observations, it is revealed that the natural structural evolution of CM to graphite exhibited a sigmoidal transformation at around 300~500 °C owing to the heterogeneous recrystallization from amorphous to graphitic carbon. As the peak temperature increase, two representative parameters of unit cell height *c* and R2 ratio start to change their crystallinity at over 300 °C (Figs. 24a-b). The systematic structural changes from 300~500 °C are well consistent with the carbon stable isotopic shifts toward ^{13}C enriched values by thermal degradation of CM. The devolatilization of CM change the isotopic values at around the boundary of chlorite breakdown, shifting to the ^{13}C depleted values. This suggests that fluid deposited graphite may be produced or overgrew from metamorphic graphite due to the diffusion-controlled crystal growth (Richter et al. 2003; 2006; 2008). In the low temperatures at 300~500 °C, the dominant chemical reactions during structural evolution of CM are devolatilization of functional group and their reorganization in nanostructure. On the other hand, at high

temperatures above 500 °C, the graphitic structure starts to grow and form large hexagonal crystal with no stacking defects. During recrystallization of graphite, overgrowth rim might have lighter carbon isotopic values compared with core in graphite, and results in the ^{13}C depleted values at high grade metamorphic rocks (Satish-Kumar et al. 2011b).

In general, a sigmoid transformation can be identified as two different reactions; rapid and slow reactions that combine to form a single sigmoid curve. In the case of graphitization, two different starting materials corresponding to amorphous carbon (non-graphitizing carbon) and LMO (graphitizing carbon) may result from sigmoidal transformation. The different rate of recrystallization might produce the sigmoidal transformation curve. On the other hand, fluid activity by dehydration process might also play an important role for heterogeneous recrystallization. The carbon isotopic data suggest the formation of fluid deposited graphite in high-grade metasediments (Fig. 24c). The process has a sufficient role for the formation of heterogeneity of crystal size in metasediments. In this way, various processes of recrystallization of CM have been proceeded under natural metamorphism. It is important to understand the dominant process of structural evolution of CM as a function of each temperature regime, and it is necessary to consider a complex chemical kinetic model for graphitization.

2.6. CONCLUSION

The detailed structural studies presented here on carbonaceous material in diagenetic zone to amphibolite facies rocks of the Upper reach of Satsunai River, Hokkaido, Japan clearly shows the heterogeneous graphitization between 300 and 500 °C. Heterogeneous microstructures are mainly composed of LMO and amorphous carbon. The appearance of LMO is observed from HRTEM observation and continuous decreasing trend of G band

FWHM and R1 ratio at around 300 °C, whereas, the amorphous carbon is retained until 400 °C with decreasing D band FWHM and corresponding to the disappearance of D3 and D4 band by micro-Raman spectroscopic study. The heterogeneity in nanostructures appeared at around 300 °C, and then disappeared at around 500 °C. In addition, the appearance of fully ordered graphite is consistent with the metamorphic reaction from chlorite to biotite by dehydration process. These detailed observations suggest that heterogeneous graphitization might be closely related to the metamorphic reaction during prograde metamorphism.

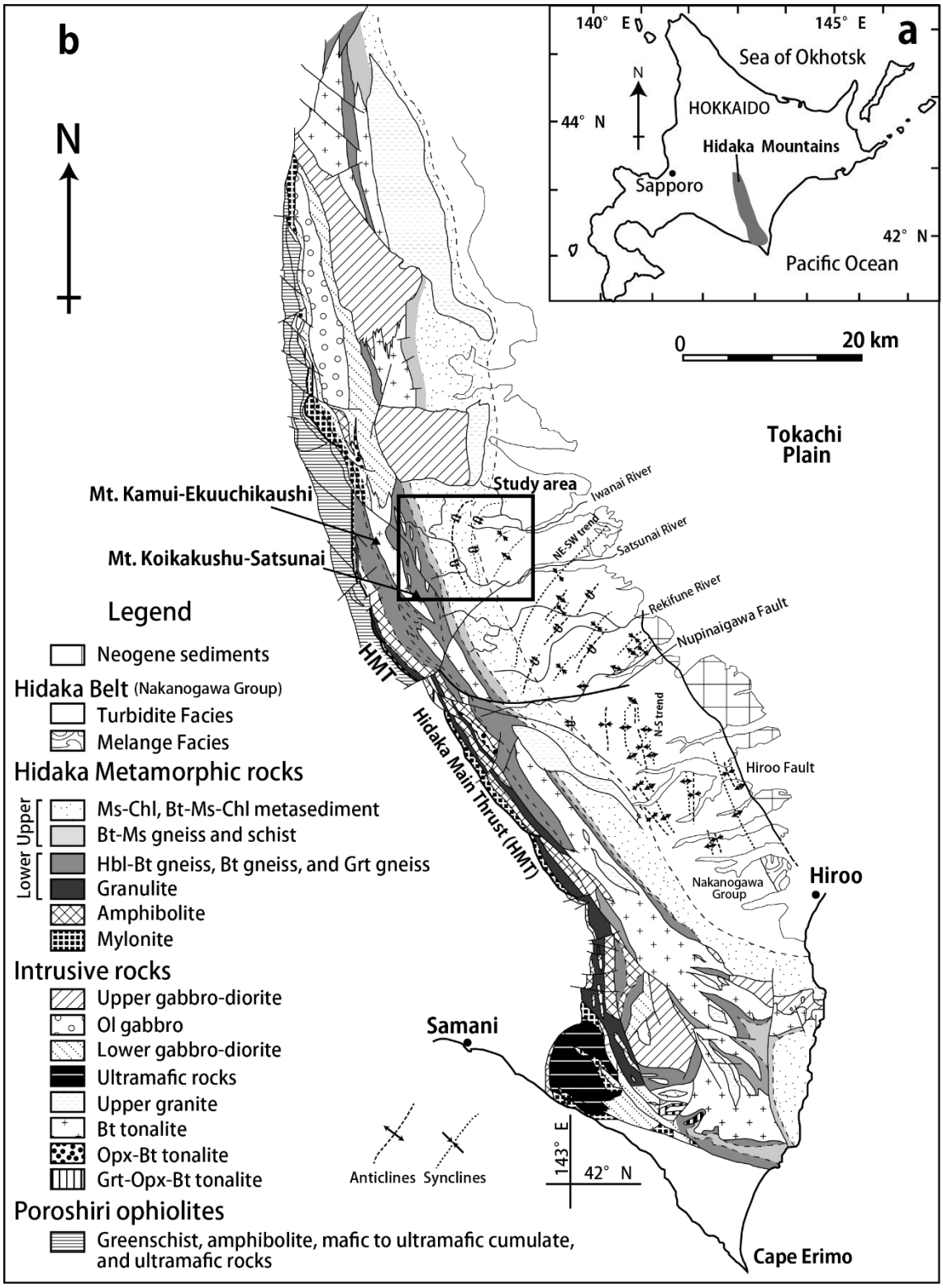

Figure 3. (a) Distribution of the Hidaka metamorphic belt (HMB) in central Hokkaido, Japan. **(b)** Location of the study area superimposed on the regional geological map of the Hidaka metamorphic belt (HMB), modified from Osanai et al. (2007). Ms, muscovite; Chl, chlorite; Hbl, hornblende; Ol, oivine; Bt, biotite; Grt; garnet.

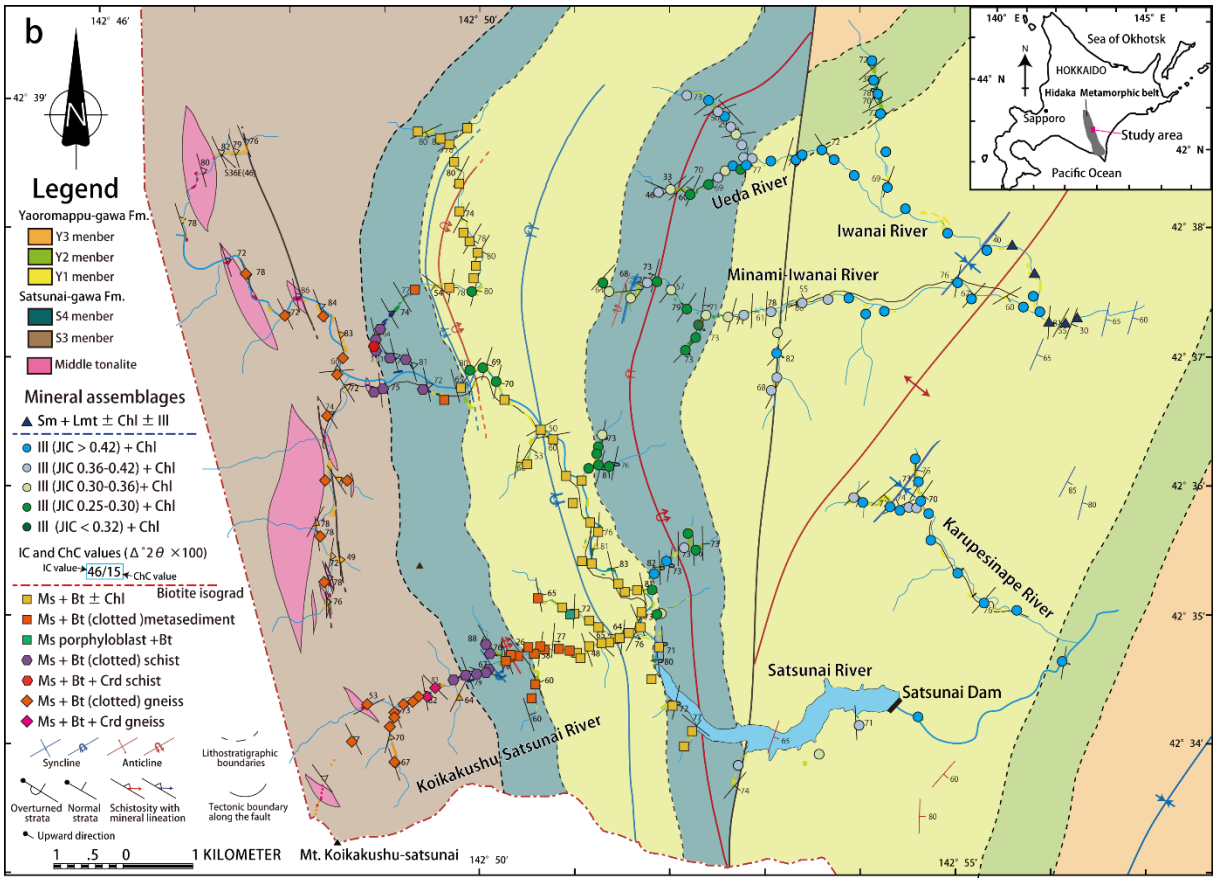

Figure 4. (a) Distribution of the Hidaka metamorphic belt (HMB) in central Hokkaido, Japan. **(b)** Geological map of the study area, showing the distribution of lithostratigraphic units of the upper sequence of the HMB and Nakanogawa group. Mineral assemblages of metamorphic rocks are plotted. The red dotted line shows the biotite isograd in the study area. Sm; semectite, Lmt; laumontite, Ill; illite, Chl, chlorite; Ms, muscovite; Bt, biotite; Crd, cordierite.

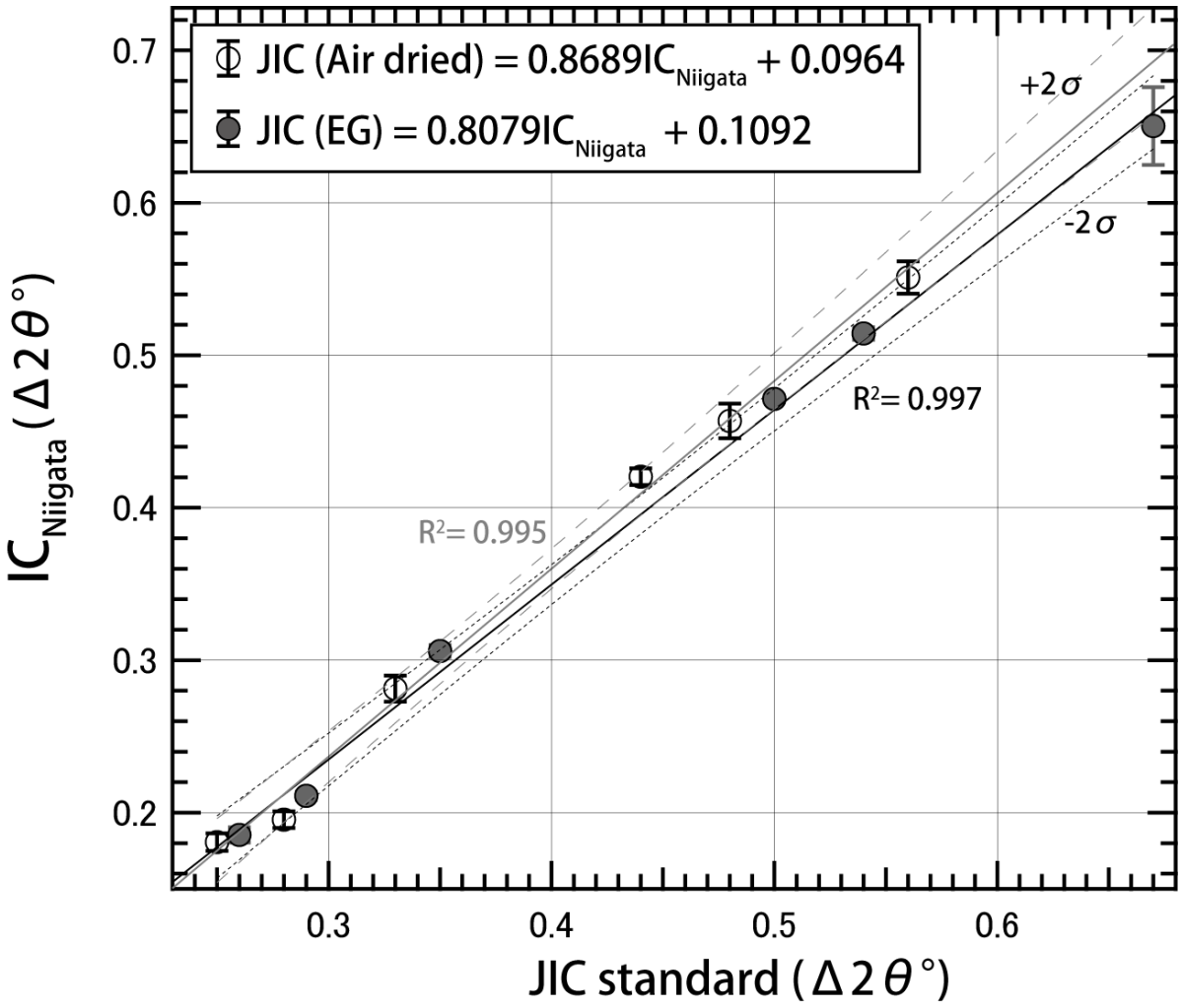

Figure 5. Relationship between reference values and the IC valued measured by XRD in Niigata University. The high correlation coefficient of 0.997 and 0.995 are obtained by regression analysis.

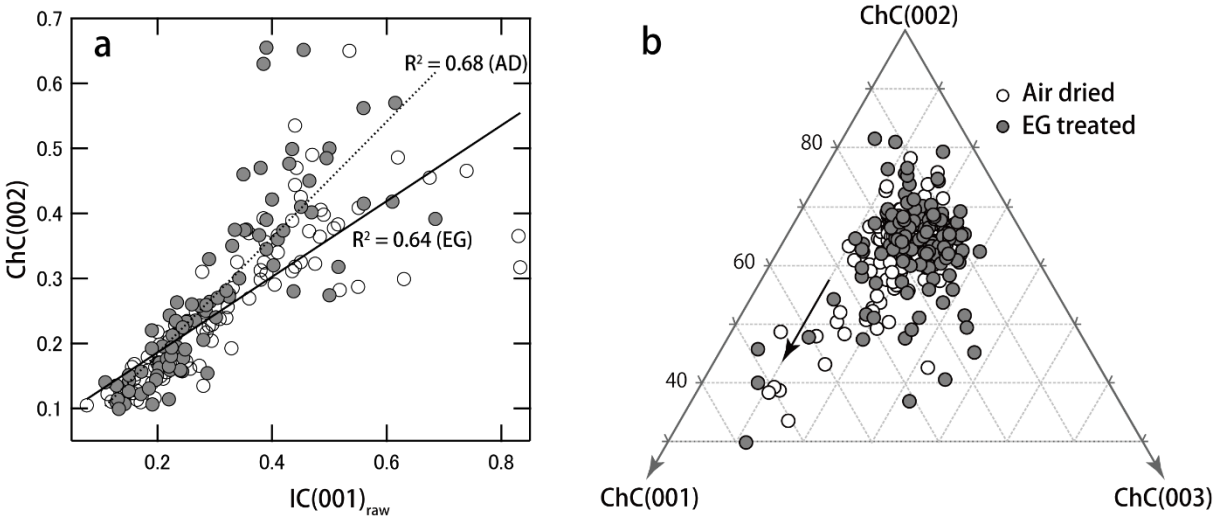

Figure 6. (a) The relationship between air dried (AD) and EG treated samples in Illite (001) and chlorite (001) plot. Both samples show slightly high correlation coefficient of 0.68 (AD) ~0.64 (EG), respectively. **(b)** Ternary diagram plot of chlorite intensity between (001), (002) and (003) reflection (Oinuma plot).

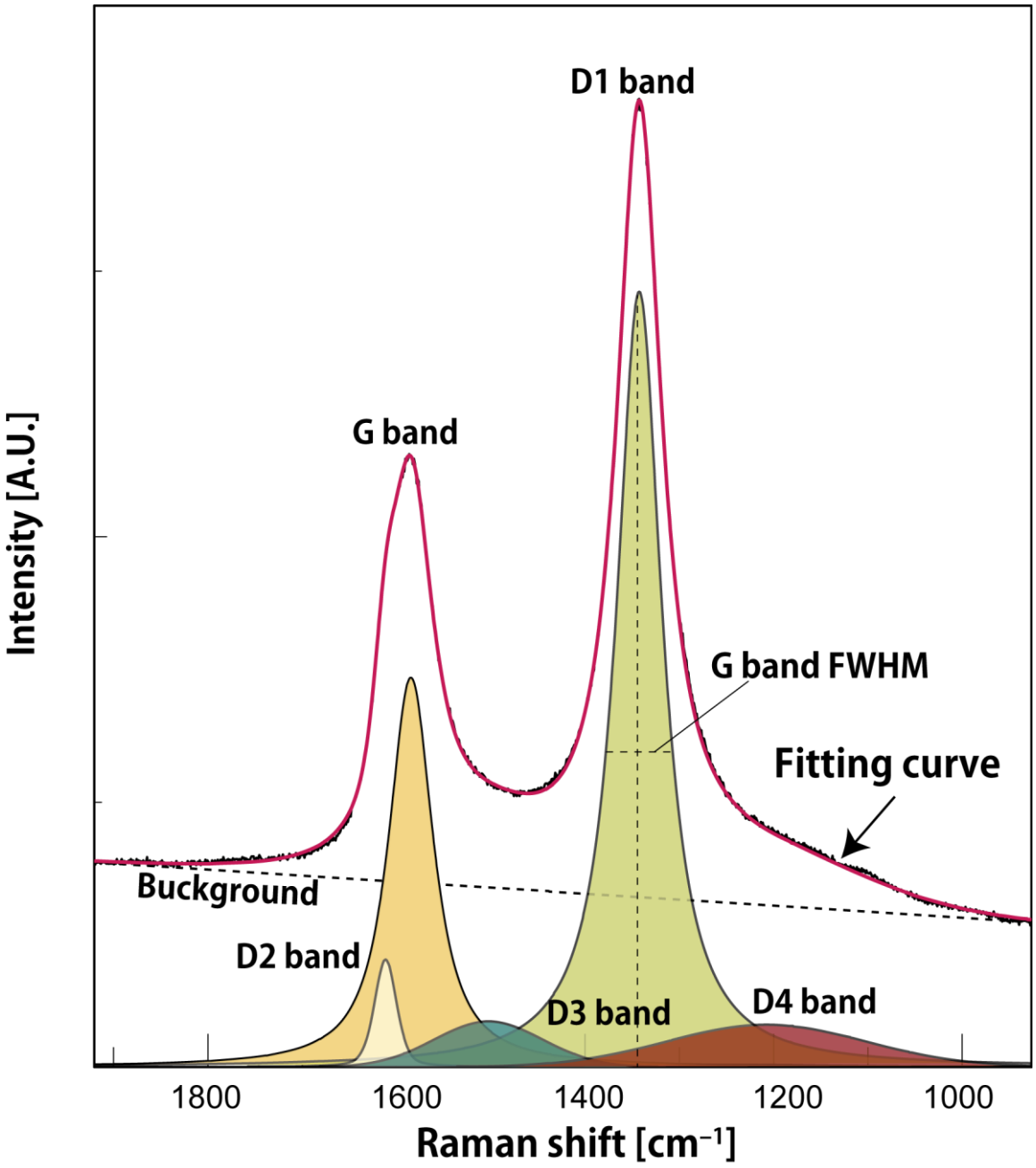

Figure 7. Peak deconvolution of CM in the first order region (1000 – 1800 cm^{-1}) of micro-Raman spectroscopy. There are four or five distinct peaks in the first order region; G (1580 cm^{-1}), D1 (1350 cm^{-1}), D2 (1600 cm^{-1}), D3 (at around 1350 cm^{-1}), and D4 (at around 1150 cm^{-1}), and they are fitted by peak fitting following Sadezky et al. (2005). In case of high grade metamorphism, D3 and D4 band of CM disappear from first order region.

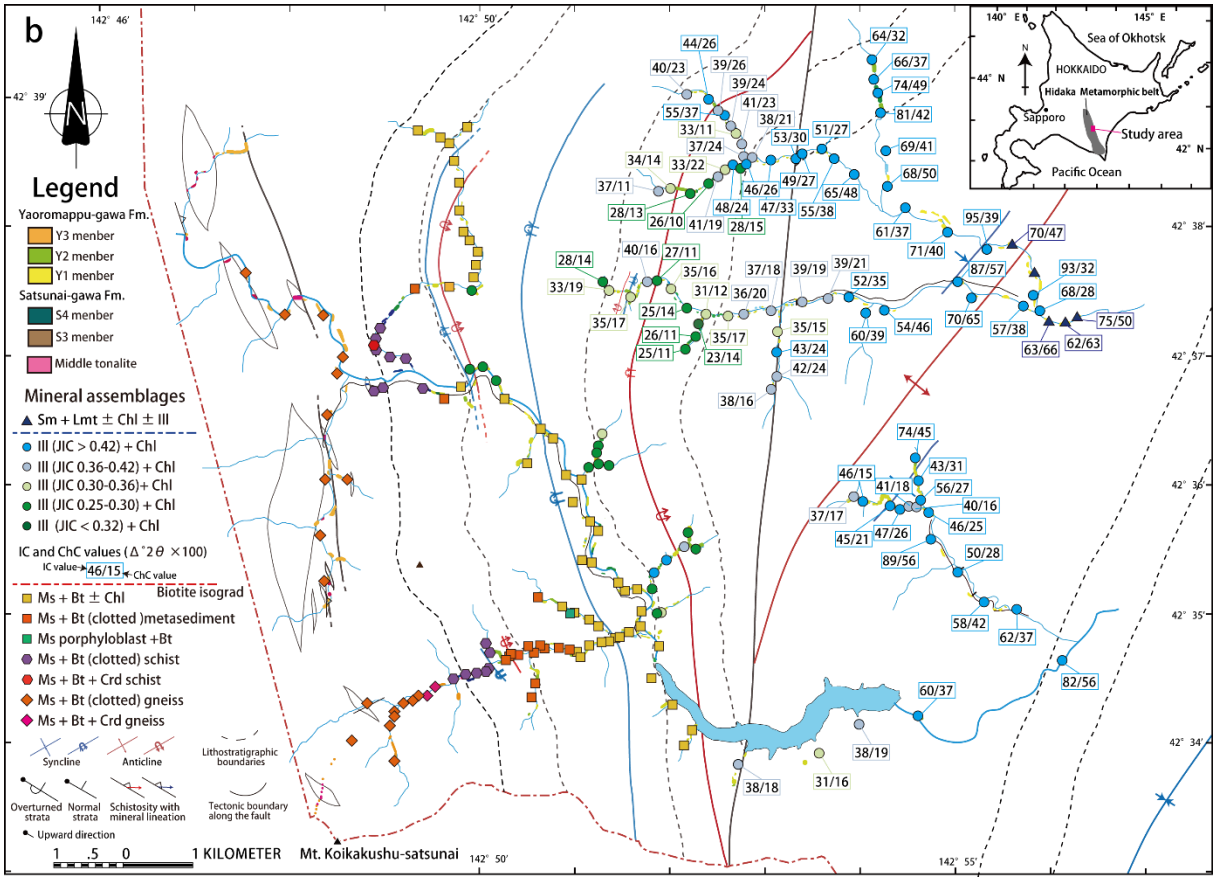

Figure 8. Mineral assemblages of metasediments in this area, showing the IC and ChC values. Sm; smectite; Lmt, laumontite; Ms, muscovite; Chl, chlorite; Bt, biotite.

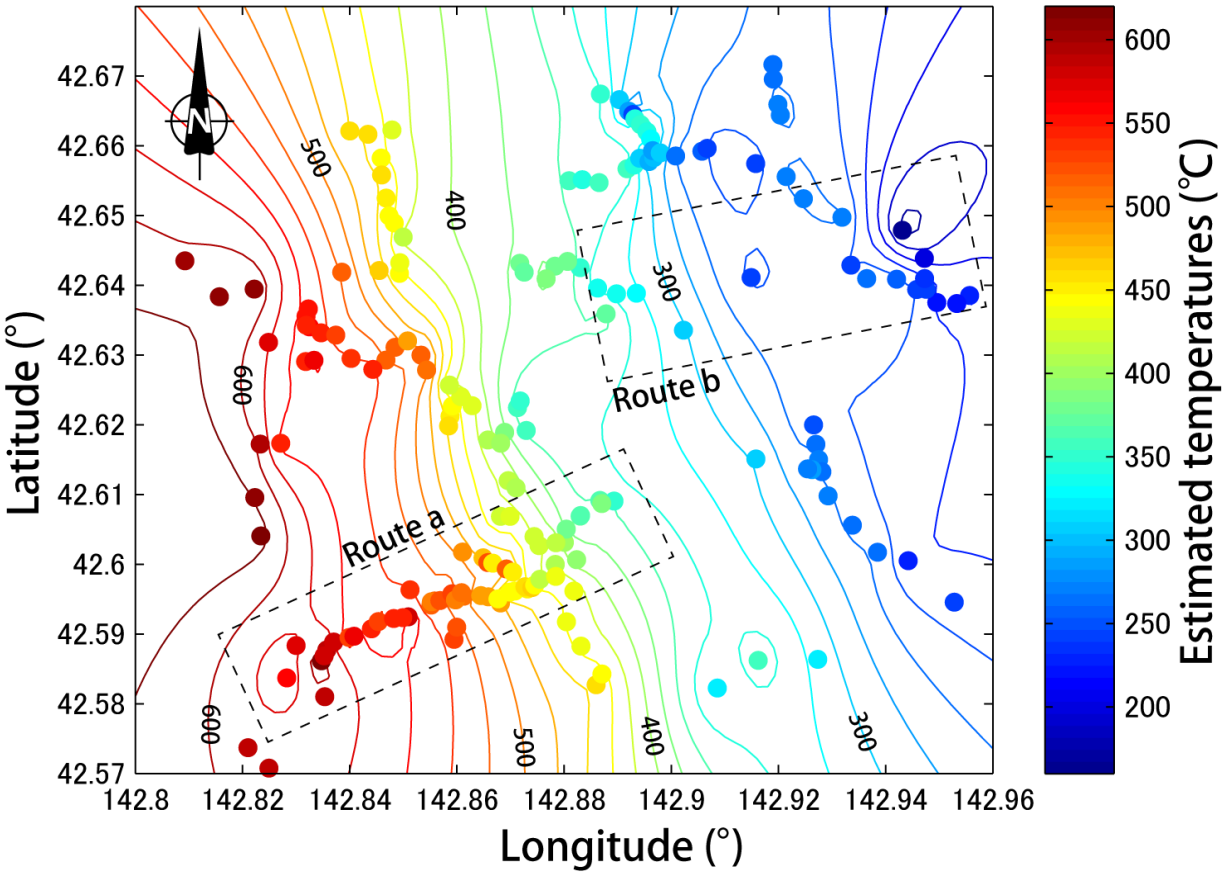

Figure 9. Peak metamorphic conditions based on the Raman spectra of carbonaceous material (RSCM) thermometry, which is contoured at an interval of 20 °C. These contours are constructed by the kriging methods (MATLAB R2014b).

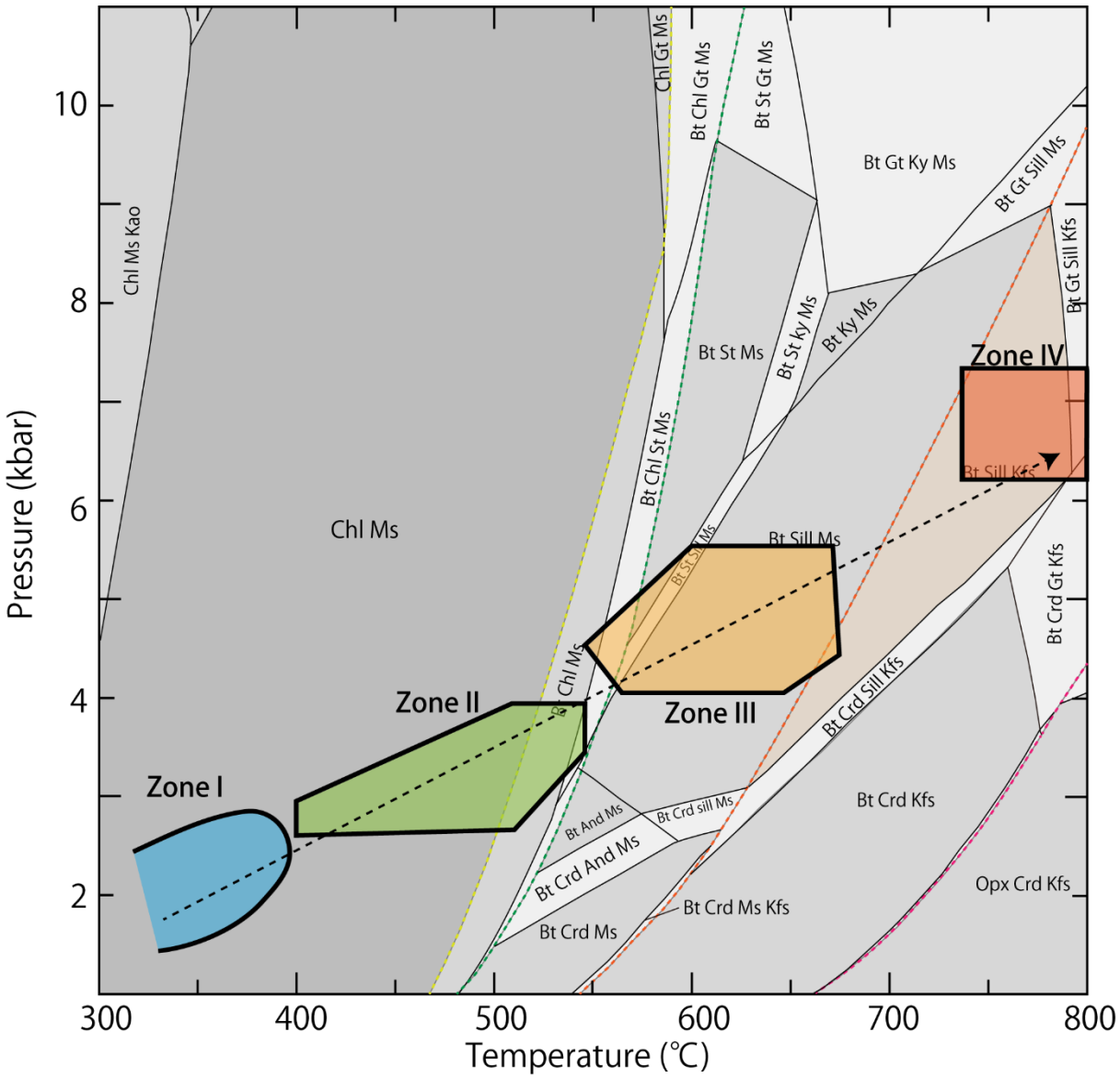

Figure 10. Relationship between field *P-T* path by Osanai et al. (2007) and KFMASH pseudosection modelling based on the mean value of XRF whole rock major elements of metasediments (Table 2). This diagram is constructed by *Perplex* 6.7.1 software (Connolly and Petrini 2002) using thermodynamic database of Holland and Powell (2011).

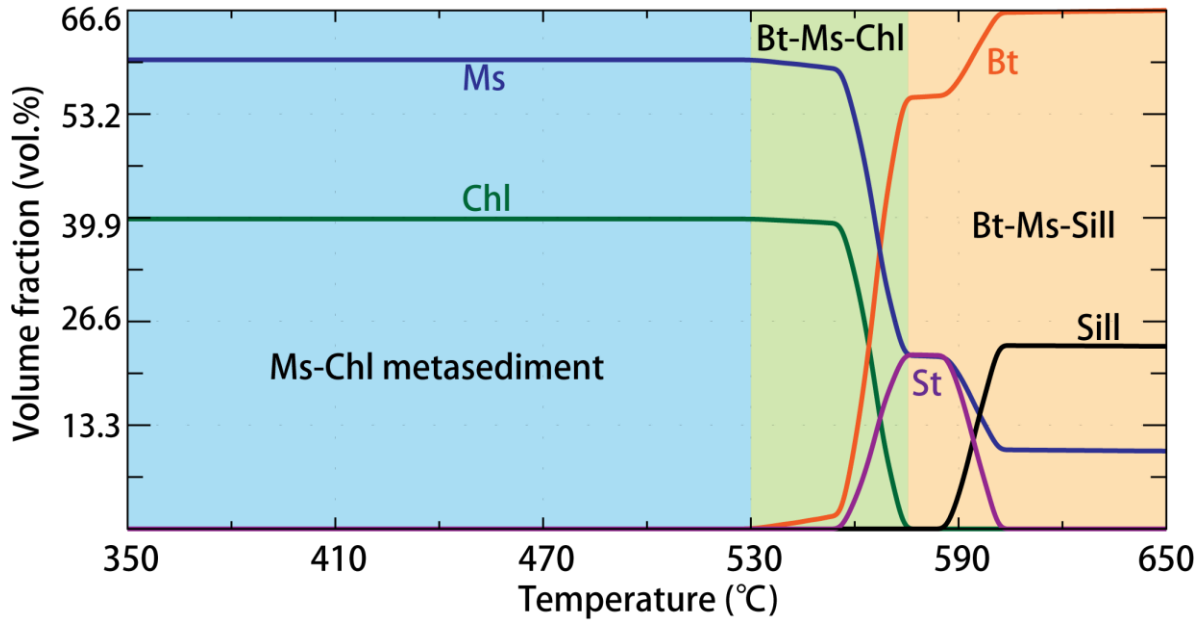

Figure 11. Calculated volume fractions of metamorphic mineral phases based on the KFMASH pseudosection modelling corrected by field *P-T* path. Chl, chlorite; Ms, muscovite; Bt, biotite; St, staurolite; Sill, sillimanite.

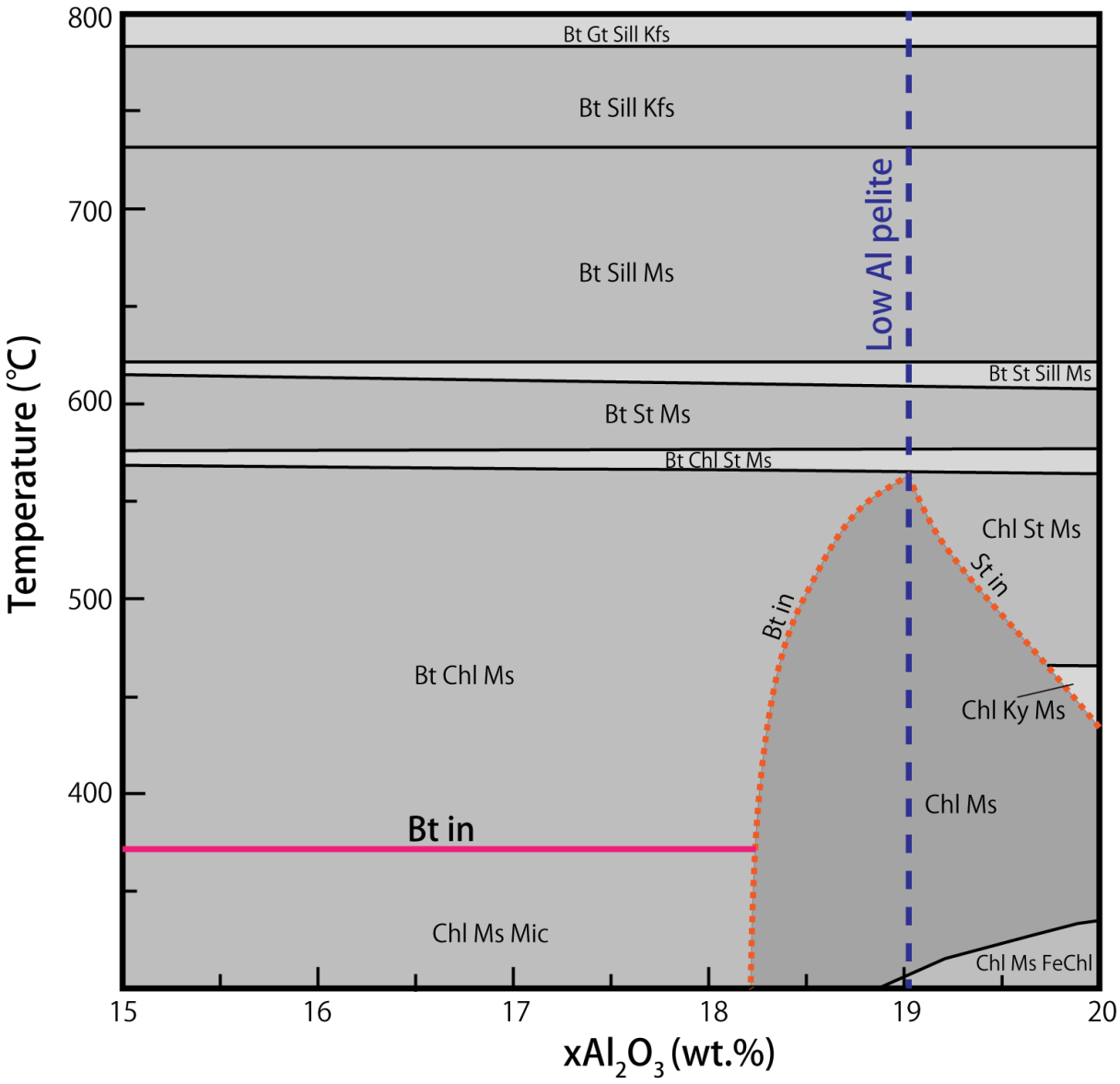

Figure 12. *T–xAl₂O₃* diagram showing the dependence of total A_2O_3 component in KFMASH system. This diagram is constructed by perplex 6.7.1 software (Connolly and Petrini 2002).

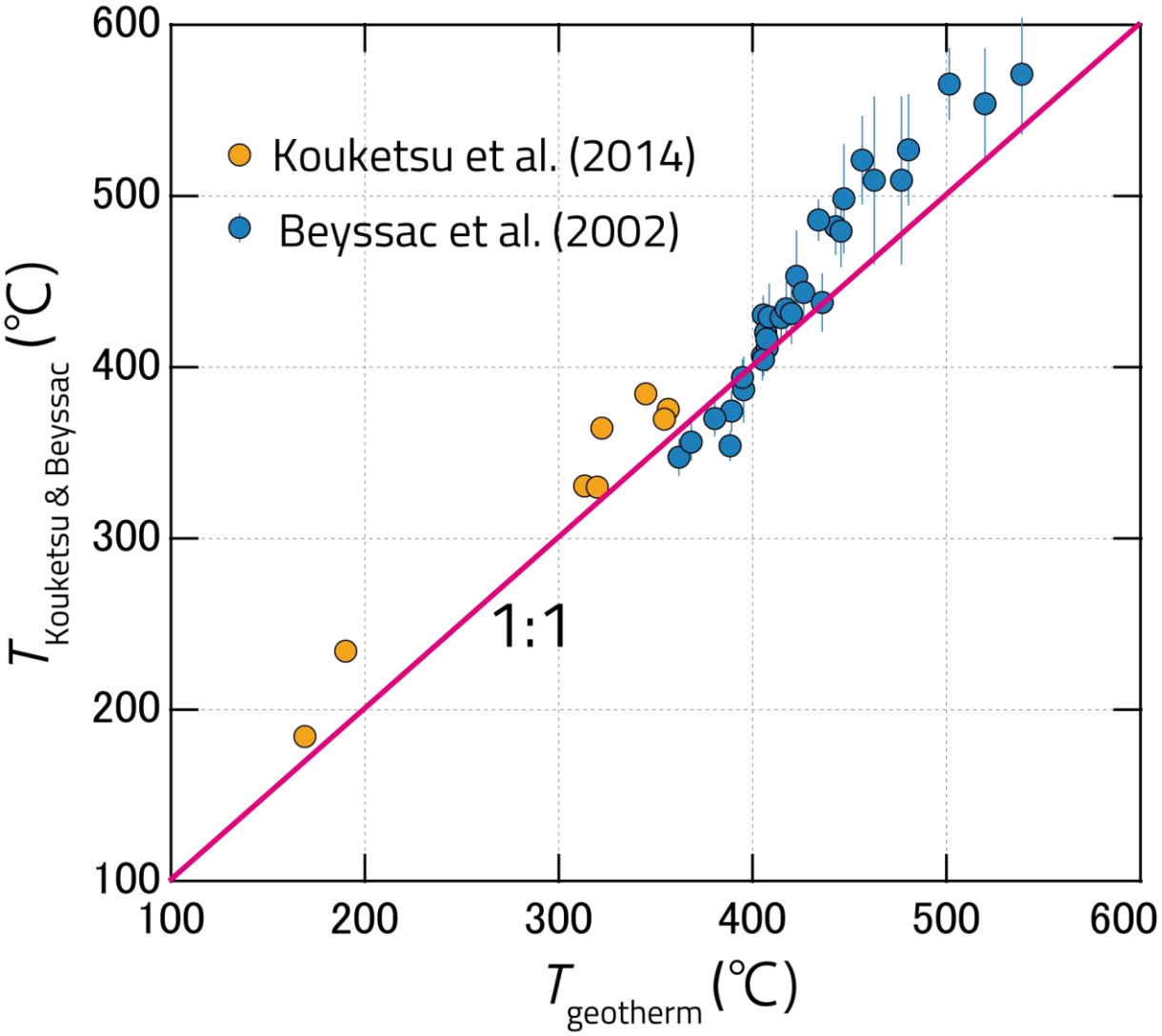

Figure 13. Relationship between peak temperatures based on geothermal gradients ($T_{geotherm}$) and RSCM thermometry ($T_{Kouketsu\ \&\ Beyssac}$).

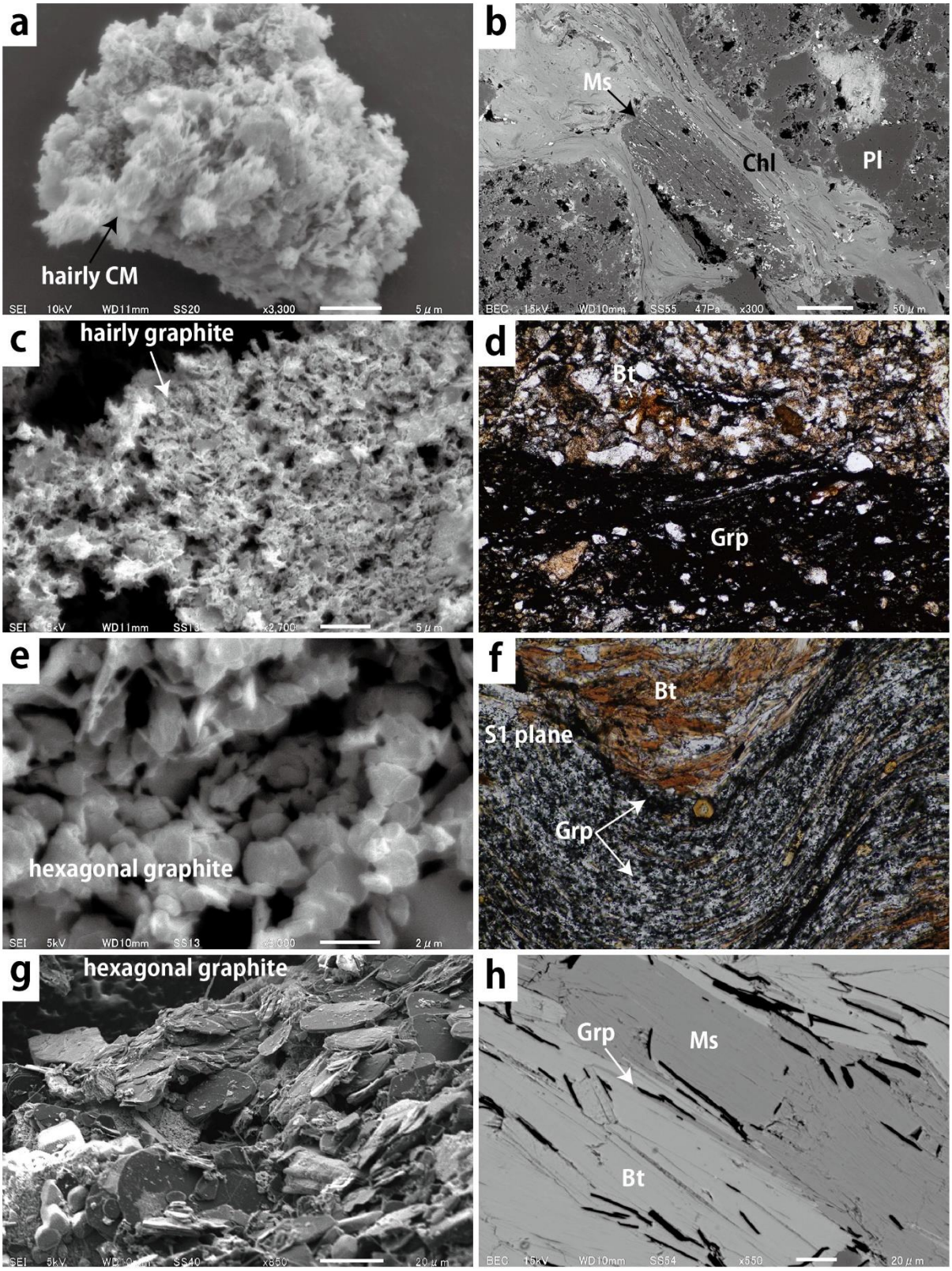

Figure 14. Optical and SEM observation of CM microstructures. **(a)** The separated CM by HCl treatment from metasediments in Zone Ia. **(b)** Muscovite-rich mud crust including CM in thin section. **(c)** The CM aggregates by HCl treatment from metasediments in zone Ib.

(d) Pelitic layers with graphite and other oxide minerals in the metasediments of zone IIa. **(e)** The aggregates of hexagonal graphite in biotite schist. **(f)** Deformed pelitic layer including a lot of graphite grains in biotite schist. **(g)** Hexagonal graphite crystals separated from biotite gneiss, which is 20-50 μm diameters. **(h)** The graphite crystals along the biotite and muscovite cleavages in biotite gneiss.

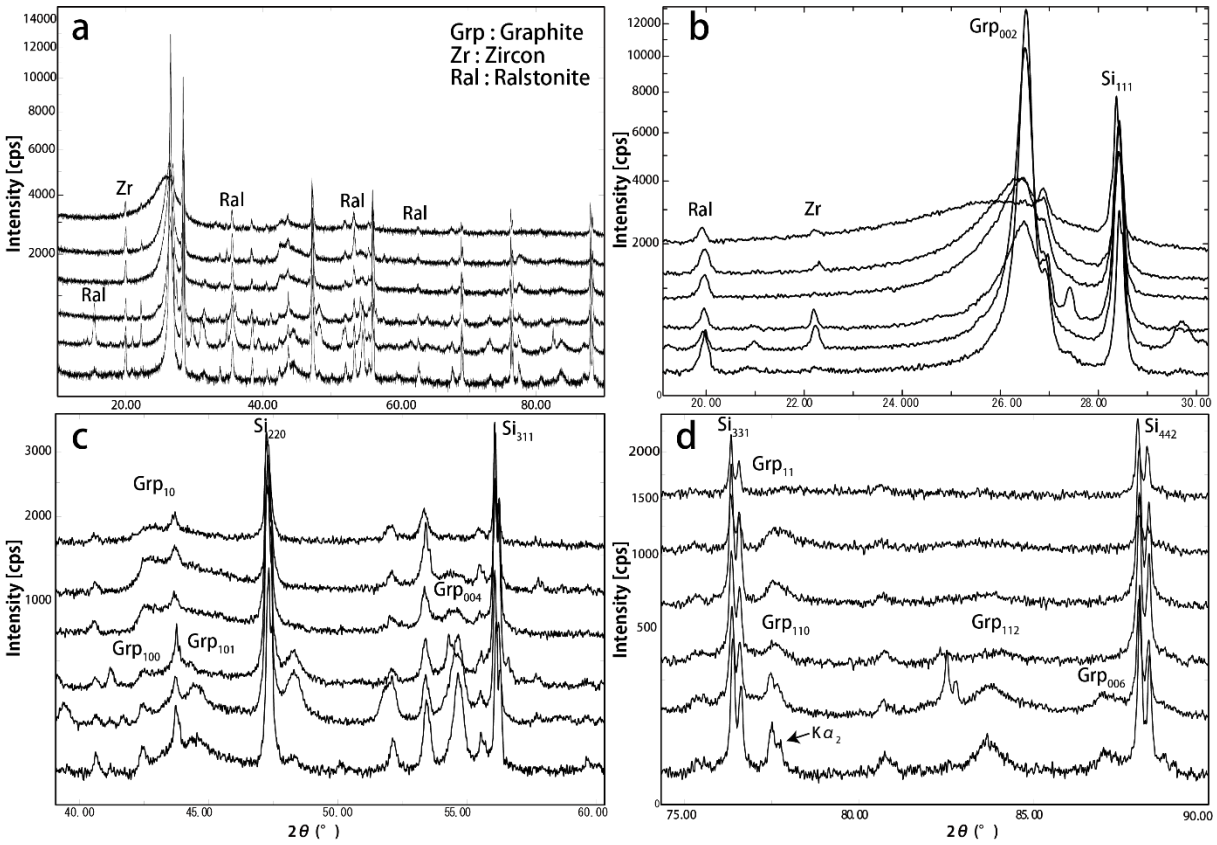

Figure 15. (a) XRD profiles from amorphous CM to graphite in 2θ range between 10 and 90°. **(b)** Gr_{002} and Si_{111} peak between 20 and 30°. **(c)** Graphite and silicon profiles between 40 and 60°. **(d)** Graphite and silicon profiles between 75 and 90°.

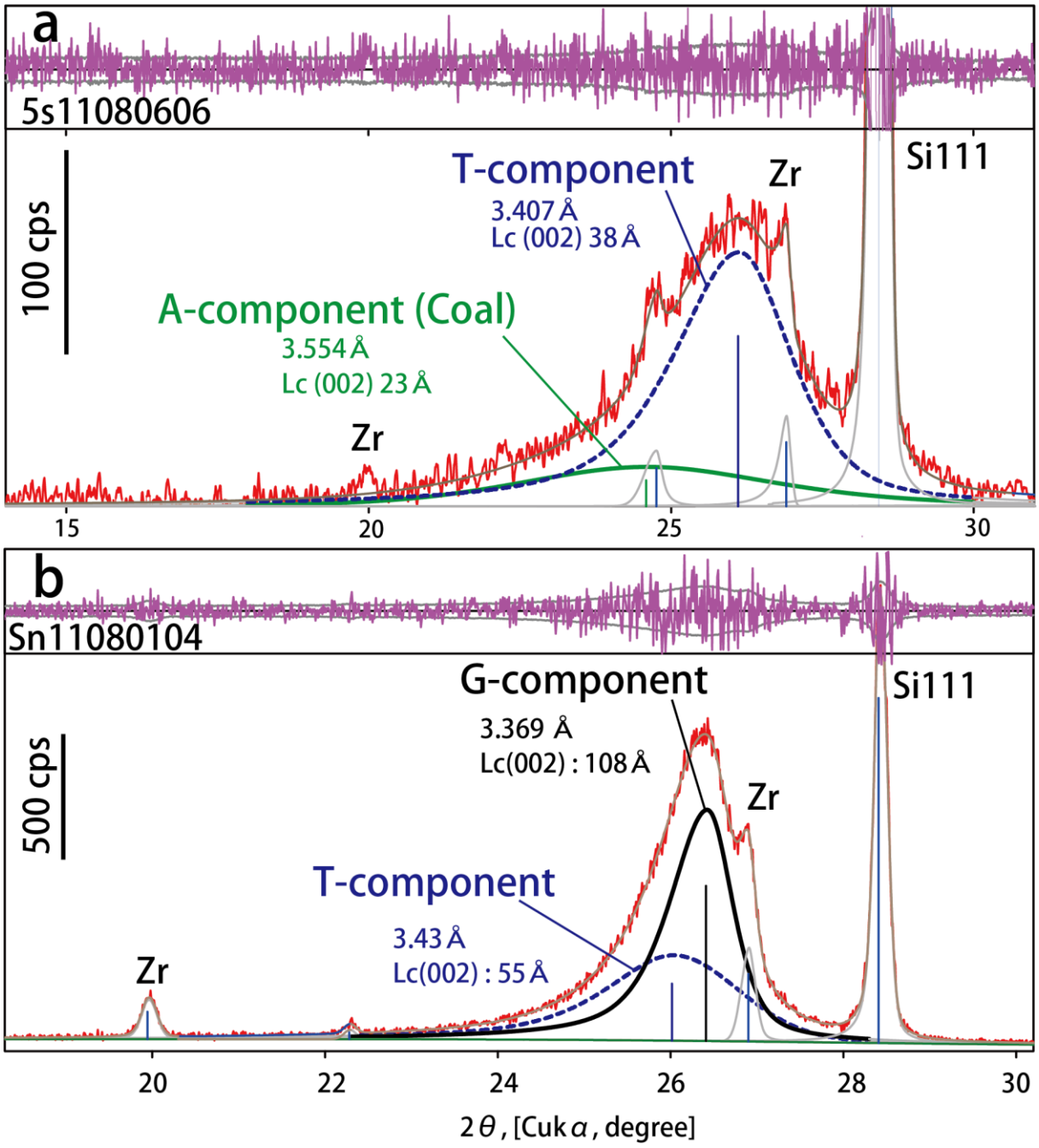

Figure 16. Peak deconvolution of XRD profiles of CM. **(a)** The asymmetric d_{002} spacing of CM in very low grade rocks that can be separated by *A*-component (amorphous carbon) and *T*-component (turbostratic carbon). **(b)** The asymmetric d_{002} spacing of CM in very low grade rocks that can be separated by T-component (turbostratic carbon) and *G*-component (graphitic carbon).

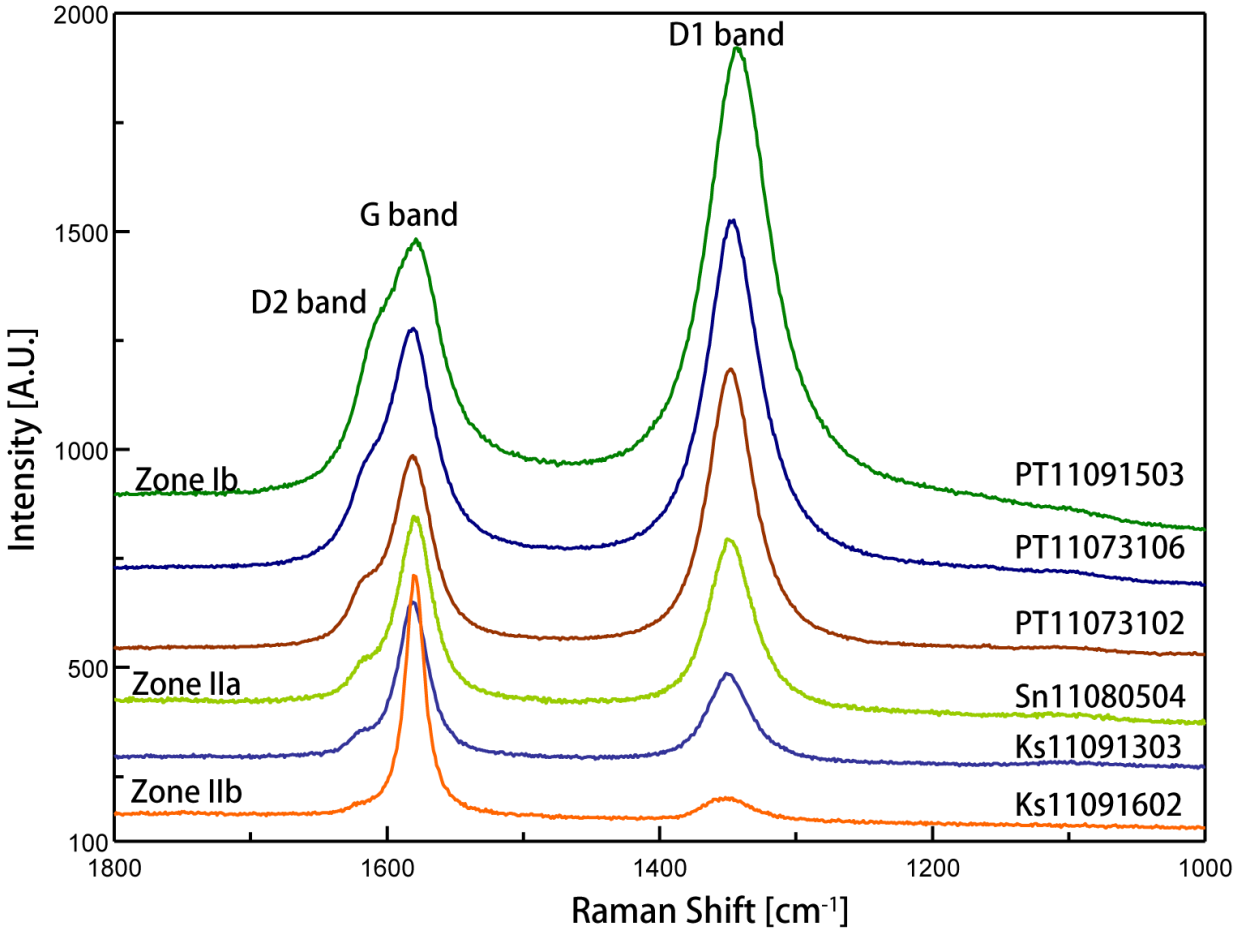

Figure 17. Profile evolution of CM during metamorphism based on micro-Raman spectroscopy. The intensities of D1 band and G band are systematically changed as a function of peak temperature.

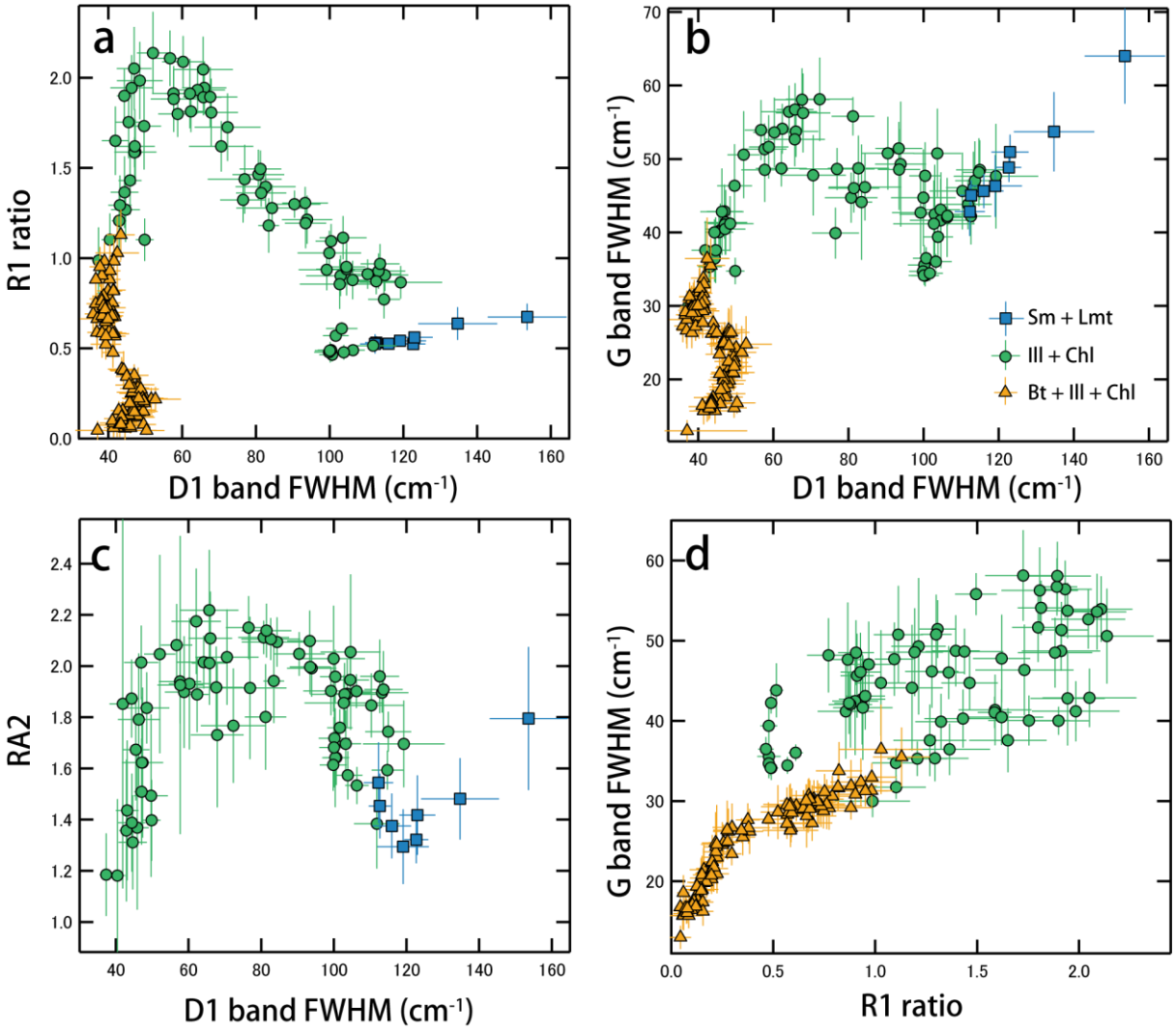

Figure 18. Relationship between D1 band FWHM and other factors such as R1 ratio **(a)**, G band FWHM **(b)**, RA2 **(c)**, and R1 ratio and G band FWHM **(d)**.

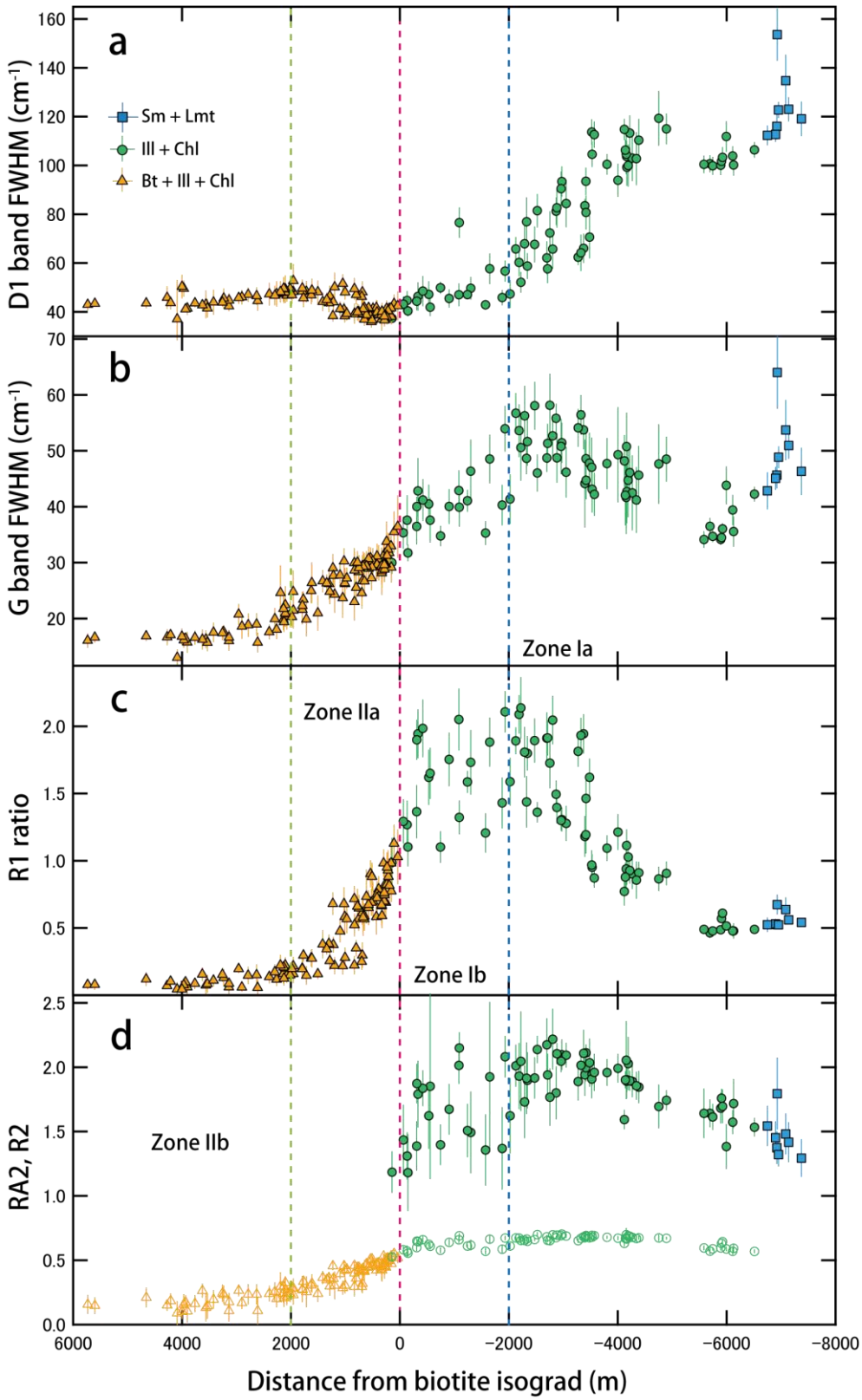

Figure 19. Structural evolution of CM as indicated by D1 band FWHM **(a)**, G band FWHM **(b)**, R1 ratio **(c)**, RA2, and R2 **(d)** along distance from the biotite isograd of metasediments.

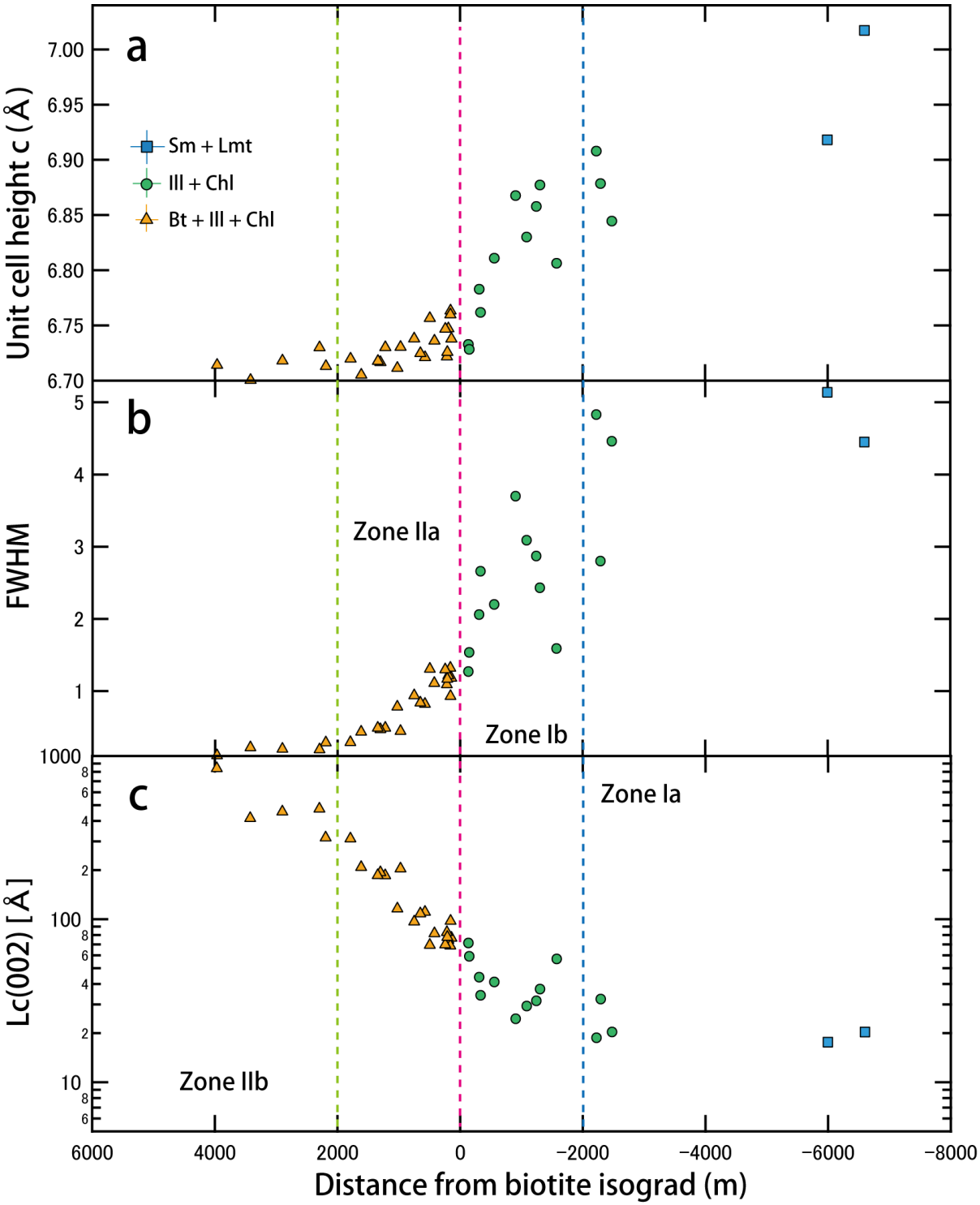

Figure 20. Structural evolution of CM as indicated by unit cell height *c* **(a)**, FWHM of d_{002} spacing **(b)**, L_c (002) **(c)** along the distance from the biotite isograd of metasediments.

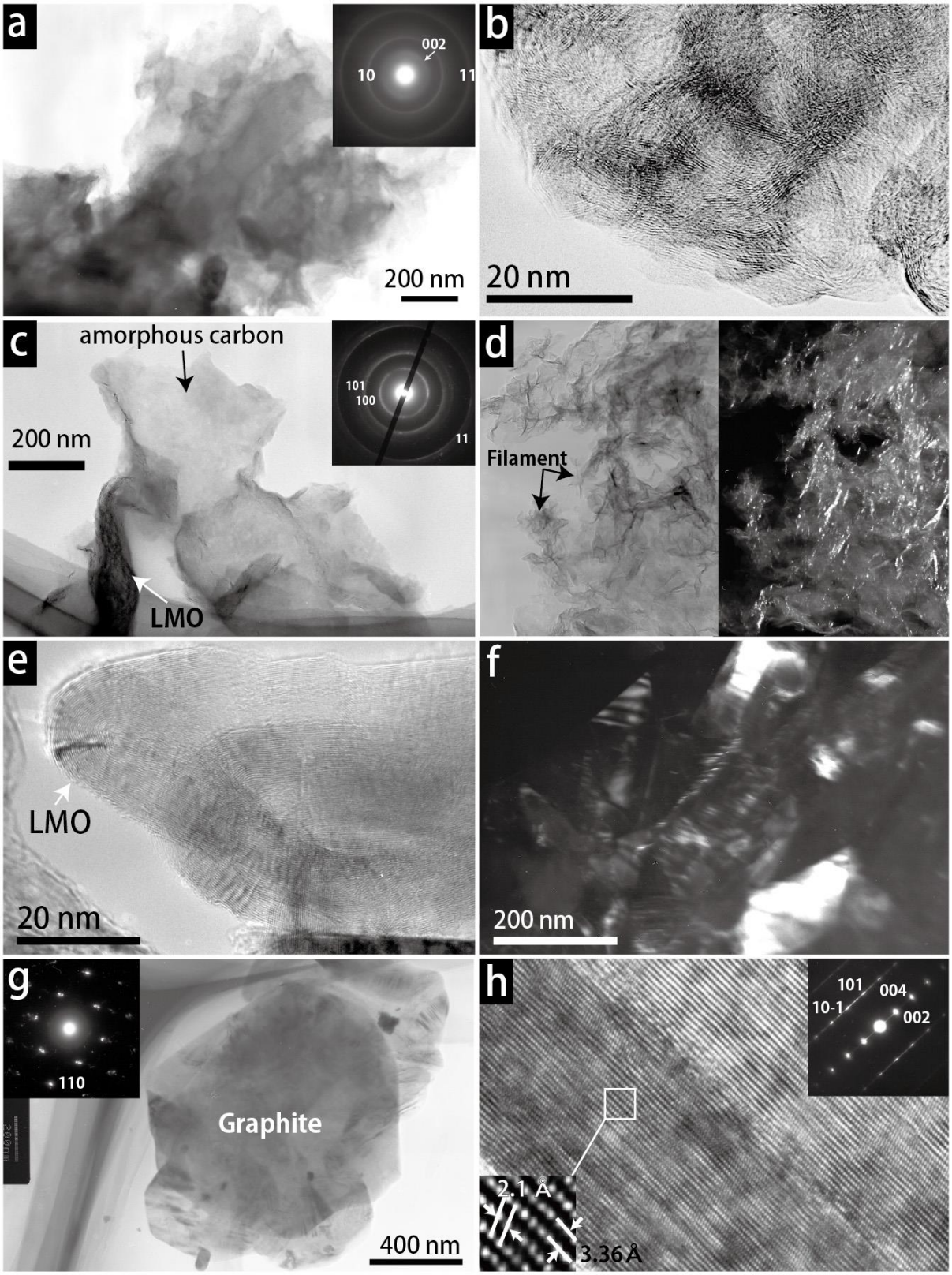

Figure 21. HRTEM observation of CM from zone Ia to IIb. **(a)** The grain like structures during zone Ia. **(b)** The lattice fringe of CM during zone Ib. **(c)** Heterogeneous structure and SAED pattern in zone Ib. (d) 002DF image and bright image of filament structure of

CM in zone Ib. **(e)** The lattice fringe of CM in zone IIa. **(f)** 110 DF image of graphite in zone IIb. **(g)** The hexagonal shape of graphite. **(h)** The lattice fringe of graphitic structure, suggesting 2H-graphite.

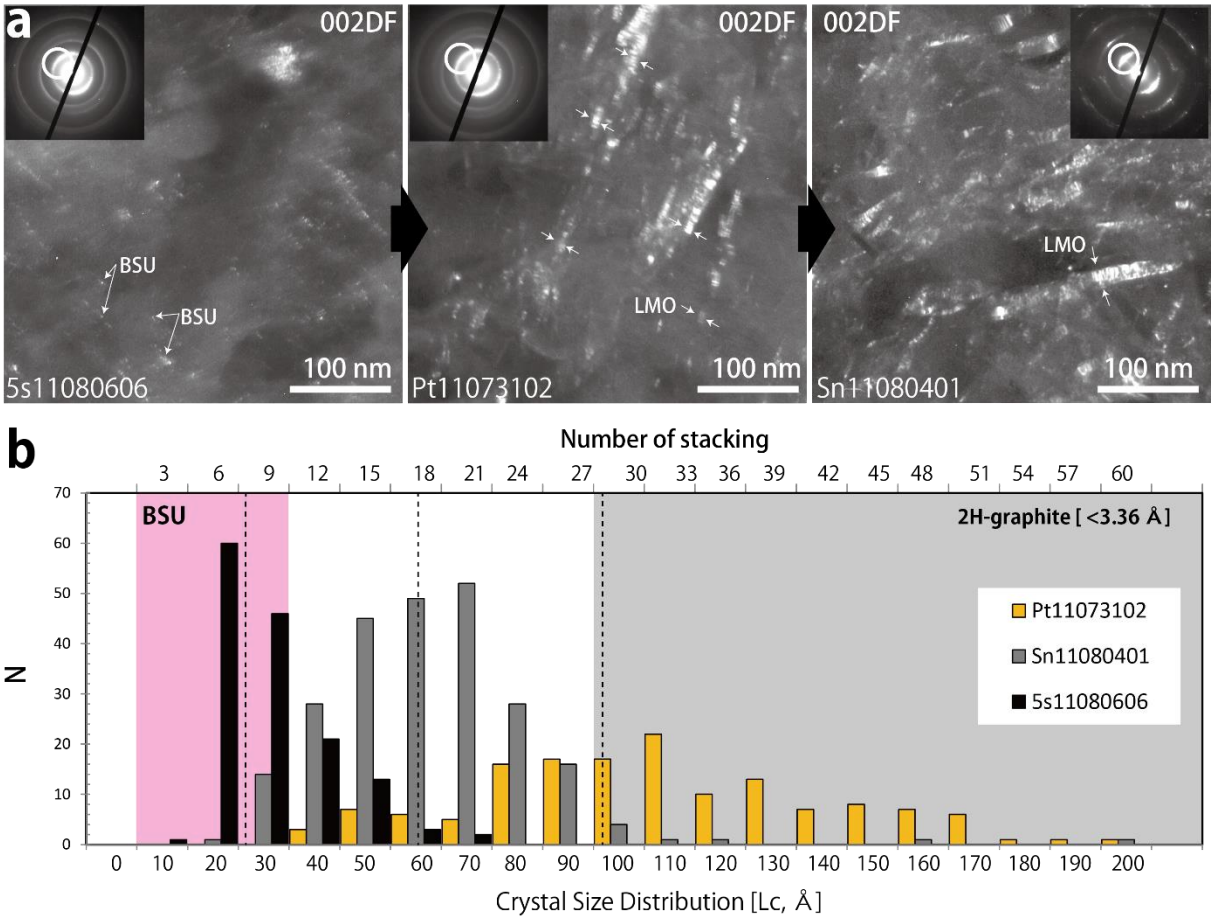

Figure 22. (a) 002 dark field (DF) images of natural CM using HRTEM. White circles are the selected area for DF mode. **(b)** Crystal size distribution of d_{002} reflections by 002 DF methods of HRTEM.

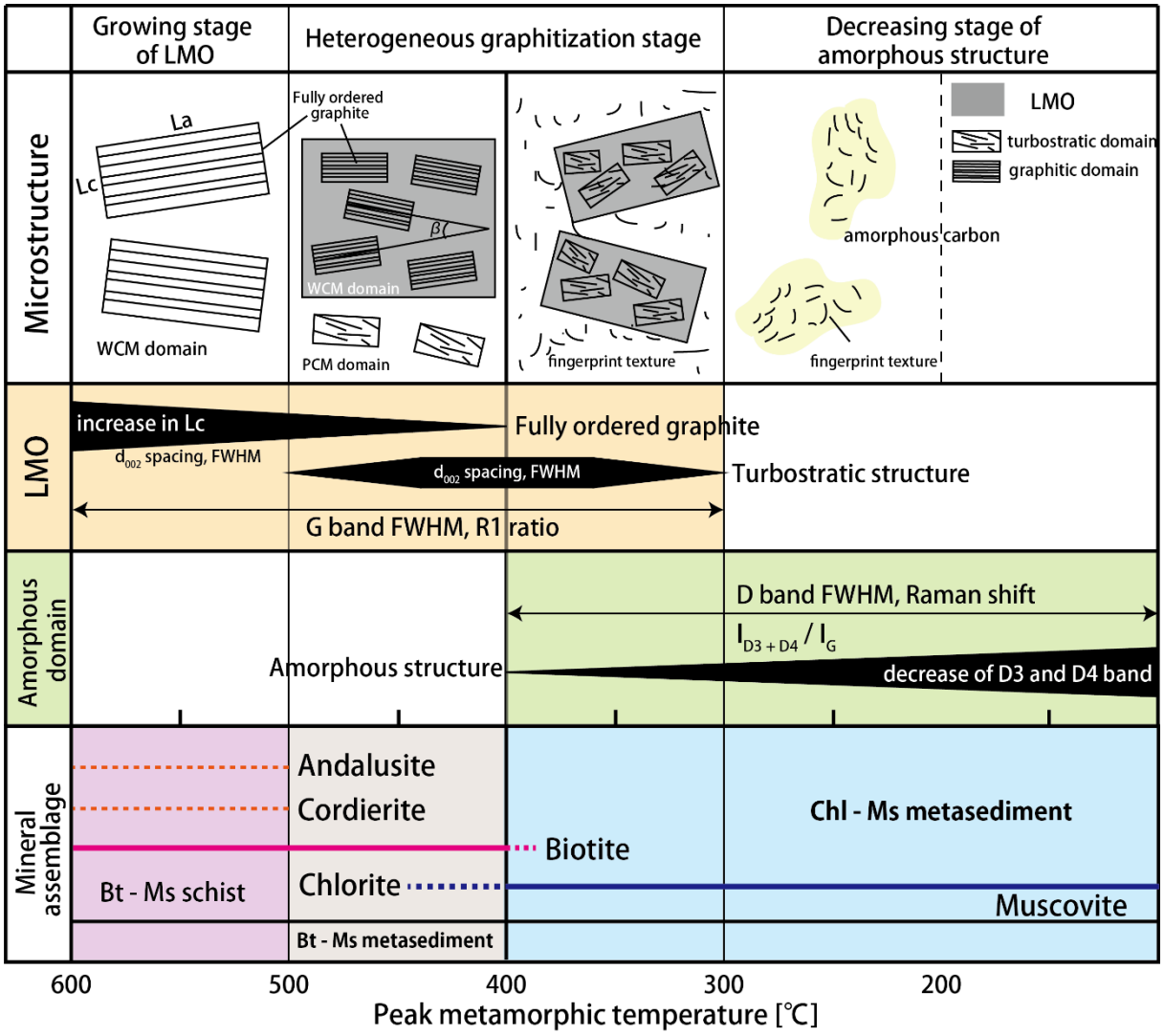

Figure 23. Summary of microstructural evolution during metamorphism in this study.

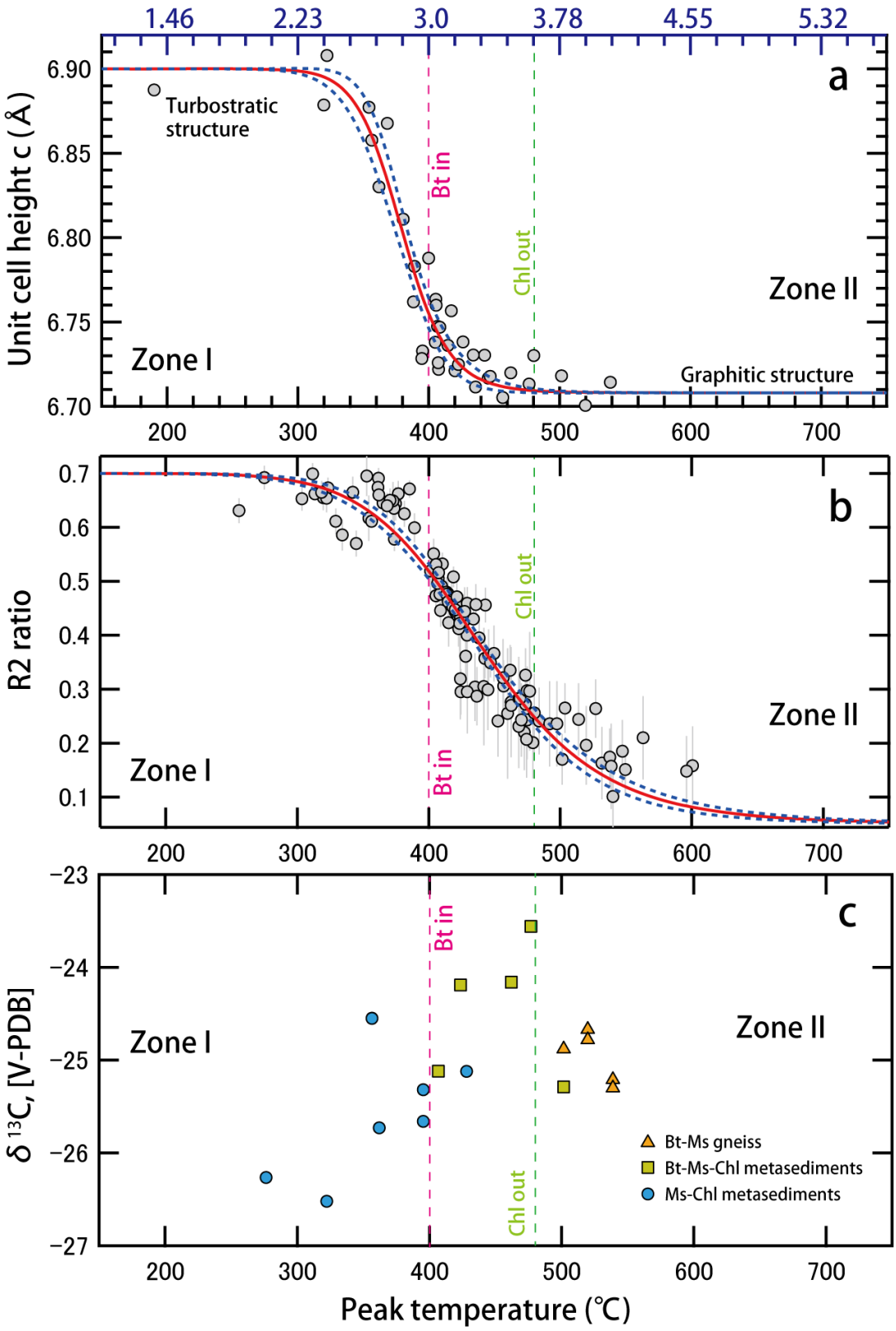

Figure 24. Structural evolution of CM as a function of peak temperatures in this study. Unit cell height *c* **(a)**, R2 ratio **(b)**, and $\delta^{13}C$ values **(c)** are systematically changed from zone I to Zone II.

CHAPTER III

Strain-induced amorphization of graphite in fault zones of the Hidaka metamorphic belt, Hokkaido, Japan

3.1. Introduction

Carbonaceous materials (CM) and graphite are common accessory minerals in sedimentary and metasedimentary rocks, and they are often present in fault rocks, associated with other sheet silicate minerals (e.g., Zulauf et al., 1990; Craw, 2002). Sheet silicate minerals and graphite have one key characteristic in common: the presence of weak bonding along the (001) planes. This weak bonding, such as hydrogen or Van der Waals bonding, potentially results in the low frictional strength of natural fault materials (Morrow et al., 2000; Moore and Lockner, 2004). In fault zones, therefore, it is important to determine the deformation mechanisms of minerals with a sheet structure based on microstructural observations.

The most common strain-induced defects of sheet silicate minerals are mainly classified under the four headings of polytypic disorder, layer flexures, dislocations, and interlayer delamination, as suggested by HRTEM studies (Kogure and Kameda, 2008; Viti and Collettini, 2009). Viti and Collettini (2009) reported that the microstructure of talc in fault rocks is affected by several strain-induced defects, among which (001) interlayer delamination results in sub-lamellae from 200–300 nm to 10–30 nm thick. On the other hand, graphite also has one of the weakest bondings in crystal structures, and it is well known as a “solid lubricant” in fault zones (Oohashi et al., 2011). Graphite gouge has a markedly low coefficient of friction of around 0.1 in experimental studies, and many

researchers have pointed out that graphite is also an important material in fault zones, potentially controlling frictional strength (Morrow et al., 2000; Oohashi et al., 2011). In the case of natural occurrences of graphite in mylonite zones, Kretz (1996) reported that the graphite underwent deformation by cleavage separation and the formation of folds and kink bands. However, most previous studies of microstructures, frictional strength, and deformation mechanisms in natural fault rocks have mainly focused on sheet silicate minerals (e.g., Collettini et al., 2009; Lockner et al., 2011), and similar studies on graphite are limited.

In addition to this general lack of data on graphite in fault rocks, it is well known that the process of graphitization during metamorphism cannot be directly explained by the Arrhenius relationship between peak metamorphic temperatures and the duration of heating (Fischbach, 1971; Bustin et al., 1995). There are many other factors that may influence the graphitization process, including fluid activity, lithostatic pressure, catalytic effects, and shear stress (Luque et al., 1998; Beyssac et al., 2002b). In particular, previous researchers have pointed out that natural graphitization during regional metamorphism is accelerated by the deformation process of rotating and reorienting the turbostratic structures in stacking (Deurbergue et al., 1987; Bustin et al., 1995). Such observations have been supported by recent experiments and studies of natural occurrences that demonstrate that the crystallinity or maturity of amorphous carbon increases as a result of shearing and short-lived frictional heating under a high-strain regime (Oohashi et al., 2011, 2012; Sakaguchi et al., 2011; Kitamura et al., 2012). On the other hand, several studies of mechanical deformation using ball milling have reported a reduction in crystal size and amorphization of graphite based on micro-Raman spectroscopy (Niwase et al., 1995; Salver-Disma et al., 1999b) as well as XRD investigations (Inagaki et al., 1973; Francke et al., 2005; Crespo et al., 2006) and HRTEM observations (Huang et al., 1999; Salver-Disma et al., 1999a). These contrasting observations on the effects of deformation

on CM and graphite suggest that deformation processes play a critical role in the graphitization or the amorphization of graphite in natural fault systems.

Despite CM and graphite being important materials in controlling the frictional strength and dynamic behavior of fault zones, there is still a lack of understanding on how deformation influences stacking and crystallinity. Here we describe the occurrences, micro/nano-structural characteristics, and mineralogical properties of graphite in a progressively metamorphosed metasedimentary terrain where mylonites, cataclasites, and pseudotachylytes occur. The study area, situated in the Hidaka metamorphic belt, Hokkaido, Japan, is suited to an investigation of the deformation-induced behavior of graphite, because various types of graphite-bearing fault rocks are present, and they formed under differing *P*–*T* conditions and deformation regimes. In this paper, we compare the microstructures and crystallinity of CM and graphite within various types of fault rocks, and we go on to interpret and integrate the various structural changes in the different deformation regimes, and graphitization during the regional metamorphism.

3.2. Geological setting

3.2.1. Geological outline

The Hidaka metamorphic belt is exposed in the Hidaka Mountains in central Hokkaido, Japan, and extends more than 100 km from north to south (Fig. 3a). The belt exposes a typical cross section of a magmatic arc, and consists of intrusive magmatic rocks and eastwards-dipping metamorphic rocks that have a NNW–SSE trending zonal distribution (e.g., Komatsu et al., 1983, 1989; Osanai et al., 1991; Toyoshima et al., 1994; Fig. 3b). The metamorphic grade of the Hidaka metamorphic rocks decreases progressively from granulite facies in the basal (western) part to very low-grade metasediments in the top

(eastern) part of the belt (Osanai, 1985; Osanai et al., 1986, 1991, 2007; Komatsu et al., 1989). The Hidaka metamorphic rocks are grouped into two sequences, lower and upper (Komatsu et al., 1983). The lower sequence is composed of amphibolite to granulite facies mafic, pelitic, and psammitic rocks, and the upper sequence, in descending order, consists of very low-grade (prehnite–pumpellyite facies) metasediments, muscovite (Ms)–chlorite (Chl) metasediments, biotite (Bt)–Ms schists, Bt–Ms gneisses, and banded Bt gneisses (Osanai et al., 1986, 1989, 1991; Komatsu et al., 1989). The uppermost (easternmost) metasediments of the Hidaka metamorphic belt are lithologically continuous with sedimentary rocks of the Nakanogawa Group that overlie the upper sequence (e.g., Komatsu et al., 1989; Osanai et al., 1989), and the Nakanogawa Group is considered to be the protolith of the upper sequence (Komatsu et al., 1983). Peak *P*–*T* conditions of metamorphism in the upper sequence have been estimated to be ca. 550 °C and ca. 350 MPa (Osanai et al., 1986, 1991).

On the basis of structural analysis of the lower sequence, the deformation history of the Hidaka metamorphic belt can be divided into three main stages (Toyoshima et al., 1994, 1997, 2004; Osanai et al., 2007). Stage I is subdivided into the D_0 and D_1 stages. D_0 is the pre-metamorphic and pre-igneous stage, and involved the tectonic thickening of an accretionary complex and forearc sediments of uppermost Cretaceous and earliest Paleogene age (Nakanogawa Group). D_1 is a stage that involved progressive metamorphism from very low grade to granulite facies conditions; it was accompanied by the thinning and vertical uplift of the metamorphic rocks, and mafic to intermediate magmatic underplating. Stage II is subdivisible into two stages of deformation (D_2 and D_3). The D_2 event was a result of top-to-the-south subhorizontal displacements, and involved the formation of high-temperature mylonites and duplex structures, and the intrusion of sheets of S-type tonalite. In the D_3 stage, low-temperature mylonitization occurred, involving dextral displacements and accompanied by retrograde metamorphism and the

formation of nappes and duplex structures. The Hidaka metamorphic belt was then uplifted and tilted steeply eastwards through the two stages of mylonitization (Toyoshima et al., 1994). Subsequently, during Stage III, the exhumed Hidaka metamorphic rocks were locally modified by ductile and brittle deformations under very low temperature conditions (Toyoshima et al., 2004).

The upper sequence and tonalite of the Hidaka metamorphic belt are exposed in the study area (Fig. 3b). The upper sequence consists of Ms–Chl metasediments, Bt–Ms–Chl metasediments, Bt–Ms schists, and Bt–Ms gneisses (Figs. 4 and 25a-b), representing a westwards progressive increase in metamorphic grade from sub-greenschist to amphibolite facies. The upper sequence rocks were originally deposited as turbidite facies pelitic and psammitic sediments, and the bedding has now been folded into nearly upright tight folds with N–S to NE–SW trending axes (Figs. 25a-b). The folding and an early stage of mylonitization under very low temperature condition occurred before the peak metamorphism. The schistosity (defined by aligned biotite) formed during the peak metamorphism and cut the folds and bedding planes (Koyasu et al., 2006; 2007). Subsequently, localized low-temperature mylonitization related to the intrusion of sheet like tonalites and brittle deformations took place during retrograde metamorphism. Koyasu et al. (2006; 2007) also summarized that most of the deformation events in the upper sequence and tonalite in the study area cannot be correlated with that of the lower sequence events reported by Toyoshima et al. (2004).

3.3. Methods

Two types of CM and graphite were prepared for this study; (1) for *in-situ* observations and analyses in petrographic thin sections, (2) CM and graphite residues separated from pelitic and psammitic rocks by HF-HCl treatment following Nakamura and Akai (2013).

The detailed procedures of chemical extractions from mudstones are described in the Appendix 1. X-ray diffractometry (XRD) was carried out using Rigaku ULTIMA IV diffractometer, equipped with CuKα (40 kV, 40 mA) radiation, graphite monochrometer, slit system 2/3°–0.45 mm–2/3° and time constant of 0.5° min^{-1}. The diffractometer was run between 10° and 90°. The powdered samples of CM and graphite were dried on a Si-low background sample holder with internal standard of silicon (10–20 wt. %). The 2θ values of the obtained peaks were calibrated using the internal silicon standard (2θ: 28.462°). Lattice constants of graphite and their crystal thickness were calculated. The thickness of $L_c(002)$, $L_c(004)$, $L_c(006)$, $L_a(100)$, and $L_a(110)$ were calculated using the Scherrer equation: Crystal size = $K\lambda$ / $\beta\cos\theta$, where K, constant (1.0); λ, X-ray wavelength ($CuK\alpha$ = 1.54 Å); β, Full width at half maximum (FWHM) of each reflection; θ, the Bragg angle of each reflection.

Micro-Raman spectroscopy was applied to CM and graphite in the first order region using Jasco NRS 3100 at Niigata University, equipped with the gratings of 1800 lines/mm and CCD-detector (256×1024 pixels). The microscope objective of 100×, and Nd-YAG laser (wavelength: 532 nm) was used. Acquisition time is 10–30 s, and 3–6 spectra are cumulated for each data point. Mean value and standard deviation were calculated based on more than 25 analyses for each sample following Aoya et al. (2010). G (1580 cm–1), D1 (1350 cm^{-1}), D2 (1600 cm^{-1}), and D3 (at around 1450 cm^{-1}) bands in the first order region (1000–1800 cm^{-1}) were separated by peak profile fitting, and the parameters of G band FWHM, G position (Raman shift), R1 ratio ($Intensity_{D1\ band}$/ $Intensity_{G\ band}$), R2 ratio ($Area_{D1\ band/Area\ G+D1+D2\ bands}$) were estimated. The crystal size of La and Raman Spectra of Carbonaceous Material (RSCM) thermometry were applied: R1 ratio = $C(\lambda)$ / La (nm) (Tuinstra and Koenig, 1970); T (°C) = –445 (R2) + 641 (Beyssac et al., 2002a), where $C(\lambda)$, constant (4.4); R1 ratio; La (nm), the crystal size of lateral extent of carbon sheets.

Scanning electron microscopy (SEM) was performed by JEOL JSM-6330F and JSM-6510LA

at Industrial Research Institute of Niigata prefecture and Niigata University, respectively. The samples were coated by Osmium or Gold for observation and imaging. In the back scattered electron (BSE) mode, SEM was operated at 15–20 kV and equipped with an energy dispersive X-ray spectrometer (EDS) to detect carbon and other elements. In the secondary electron (SE) mode, SEM was operated at 5–10 kV with a small spot size of SS10 to SS20 to get the information on the surface.

High-resolution transmission electron microscopy (HRTEM) was carried out using a JEOL JEM 2010 electron microscope in Niigata University, operating at 200 kV with LaB_6 filament. CM and graphite samples were placed on the carbon-coated holey film of the TEM micro-grid, and examined using dual-axis tilting holder. The samples were observed for the d_{002} lattice fringes along the [010] direction. The lattice fringe images were processed by noise reduction using image-J software with FFT and bandpath filter to improve the quality of images.

Carbon stable isotope analysis of graphite was carried out using a Finnigan MAT 251 mass spectrometer at Niigata University. An aliquot of the graphite powder used for the XRD analysis that was extracted by the chemical separation from the rock samples was used for isotope analyses. In addition, samples from high strain zones such as ultracataclasite and pseudotachylyte veins in cataclasite were microdrilled from polished rock slabs using a dentist diamond cutter under a binocular microscope and treated with 1N HCl acid dissolution to remove carbonate minerals. In this case, the sample powder also contains silicate minerals, which will not have any effect on carbon released by combustion. Both these samples were introduced into a preheated (1100 °C for 12 h) VYCOR® tube. Vanadium pentoxide was used as oxidizing agent for conversion of carbon to carbon dioxide. The VYCOR® tubes containing graphite and V_2O_5 were again preheated at 500 °C for 30 min. to remove any surface organic contaminations in samples, and sealed under vacuum ($\sim 10^{-3}$ Torr). Sealed tubes were combusted at 1000 °C for 2 h for oxidizing

the graphite to CO_2. The tubes were then cracked under vacuum, in a line connected to a modified high vacuum inlet system for carbon isotope measurements of micro-volume CO_2 gas (Wada et al., 1984a, 1984b, Satish-Kumar et al., 2011a; 2011b). The CO_2 gas was analyzed for carbon isotopes and is reported in δ notation relative to the V-PDB standard for carbon. Laboratory machine standard CO_2 gas measured in the beginning and end of each measurement session gave reproducibility better than 0.1 ‰.

Total organic carbon (TOC) analysis was performed by a Perkin Elmer CHNS analyzer at Niigata University. Three aliquots of samples weighing between 1.0 to 1.5 mg were prepared from HCl-treated whole rock and fault rock powders. Standard materials (acetanilide) were also measured randomly during each measurement session. Machine error for each measurement is less than 0.1 wt.%, however, natural sedimentary samples have larger error because of heterogeneous distribution of carbon within each sample (Pattison, 2006).

3.4. Results

3.4.1. Occurrence of host metamorphic rocks and fault rocks

Graphite-bearing Ms–Chl metasediments, Bt–Ms–Chl metasediments, Bt–Ms schists, and gneisses are widely exposed in the study area (Figs. 25a-b and Tables 4, 5). The low-grade metasediments contain mineral assemblage indicative of three grades of metamorphism, namely Ms–Chl, Bt–Ms–Chl, and Bt–Ms (Figs. 25a-b). The Ms-Chl and Bt–Ms–Chl metasediments show only a weak schistosity, and the prominent bedding planes roughly strike N–S (Fig. 25c), slightly oblique to the regional biotite schistosity (Fig. 25d). The Bt–Ms metasediments, metamorphosed at around 500 °C based on RSCM thermometry, still preserve sedimentary structures such as graded bedding to identify the sequence of strata

(Fig. 26a). Towards the west, as a result of the increase in metamorphism, the schistosity, which trends roughly NNW–SSE, becomes prominent in the Bt–Ms schists and gneisses.

In the study area, mylonites formed at two different stages are observed in many thin ductile shear zones (1–30 cm). Early stage of mylonites consist of elongate and asymmetrical lenses of metasandstone set in a sheared matrix of metamudstone. The long axes of the elongate metasandstone lenses define a stretching lineation that plunges north or south at moderate to low angles (Fig. 25c). The asymmetrical structures of the lenses and matrix indicate a sinistral and normal sense of shear (Figs. 25c and 25d). The asymmetric structures, foliations and lineations of the mylonites are cut by biotite porphyroblasts, suggesting that the sinistral shear zones were formed before the peak metamorphism in the study area. On the other hand, the later stage of mylonites, occurring in the Bt-Ms schists and gneisses, are characterized by stretching lineations, and S–C and S–C' structures defined by the rearrangement of biotite grains. The asymmetric fabrics of the mylonites indicate a dextral and normal sense of shear (Fig. 25d). The mylonitic foliations cut the regional schistosity and bedding planes, suggesting that the dextral shear zones were formed after peak metamorphism. The early stage of mylonites in Bt–Ms metasediments represent less recrystallization than the later stage of mylonites in Bt–Ms schists and gneisses.

Many brittle shear zones, associated with cataclasites, ultracataclasites, and/or pseudotachylytes, also occur in the study area. They are parallel (layer parallel) or oblique (layer oblique) to the bedding planes, schistosity, or mylonitic foliations of the host rocks (Figs. 25e and 26b, c, d). Retrograde metamorphic minerals such as prehnite, epidote, chlorite, and zeolite are observed in the cataclasites and ultracataclasites. The layer parallel veins of pseudotachylyte and ultracataclasite, which strike roughly N–S, are a few millimeters to a maximum of 5 cm wide (Fig. 26d), and they occur along cataclasite zones that are 0.5 to 30 m wide (Figs. 26b-d). On the other hand, the layer oblique veins of

pseudotachylyte and ultracataclasite are found within thin cataclasite zones, and they strike roughly ENE–WSW to E–W (Figs. 25e and 26c). Both types of pseudotachylyte have cryptocrystalline textures indicating rapid cooling, such as spherulites, spherules of Fe oxide, biotite microlites, and flow structures (Figs. 27e, f), consistent with the way in which the pseudotachylyte veins inject and cut their host cataclasites (Figs. 27c, e). We consider these brittle fault rocks to be comparable to the stage III fault rocks of Toyoshima et al. (1997, 2004), because of their similar modes of occurrence, deformation types, orientation, and metamorphic conditions.

3.4.2. Morphological characteristics and nanostructures of graphite

3.4.2.1. Graphite in the host metamorphic rocks

CM and graphite are usually observed along the grain boundaries of phyllosilicates (biotite, muscovite, and chlorite) or quartz and plagioclase fragments within pelitic layers of the metamorphic rocks (Fig. 27a). These CM and graphite show typical Raman Spectra which are representative of their peak metamorphic temperature condition (Fig. 28). SEM observations of graphite obtained by HCl–HF treatment show various morphologies with increasing metamorphic temperature, from fibrous graphite (Fig. 29a) in metasediments to small hexagonal-shaped grains (grain size, 1–2 μm; Fig. 29b) in Bt–Ms schists, and finally large hexagonal and platy grains (grain size, 20–30 μm; Fig. 29c) in Bt–Ms gneisses. The fibrous graphite (Fig. 29a) exhibits a filament structure under the HRTEM, and already possesses a fully-ordered structure (d_{002} spacing < 3.36 Å). Raman spectra on the basal planes of hexagonal platy graphite (Fig. 29c) show only G band in the first order region, which suggests that the plates are composed of single crystals with no crystallographic defects.

Previous researchers have reported that the nanostructures of CM transform

from a turbostratic structure to a graphitic structure (ABAB… stacking) with increasing metamorphic temperature (e.g., Nakamura and Akai, 2013). The turbostratic structure in CM is composed of a random orientation of basic structure units (BSUs), which correspond to polyaromatic layers (4–10 layers), either in isolation or piled up by two or three units. These BSUs then coalesce into distorted wrinkled layers, and finally form large coherent stacking domains through graphitization process. These coherent structure domains are either called local molecular orientation (LMO; Oberlin, 1984) or molecular orientation domain (MOD; Bustin et al., 1995). During this study, we found the large coherent structure domains (LMO) of graphite in powdered samples of Bt–Ms gneiss, and the graphite also shows the typical selected area electron diffraction (SAED) pattern of graphitic structure (Figs. 29d, e). The lattice fringes in LMO are fully ordered, and defines (002) and (101) along the [010] direction, suggesting ordered 2H-graphite (ABAB… stacking) and defect-free structures (Figs. 29d, e).

3.4.2.2. Graphite in the mylonites

The characteristic microstructures of graphite in both early and later stage of mylonites include kink structures, bending, and flexure of carbon sheets (Figs. 30a, b). In thin sections under the SEM, the graphite grains within biotite cleavages are distributed along the mylonitic foliation parallel to the regional schistosity, and the width of the glide units of the stacking layers in deformed graphite varies from 200 nm to over 1 μm. They are mainly deformed by micro-scale delamination of basal planes and bending (e.g., Fig. 30b). With an increase in deformation, the deformed graphite grains become smaller, and they are reoriented within the shear bands. HRTEM observations of bending and kink structures show that the stacking of (002) planes is inclined at different angles (Fig. 30c) or by dislocations with varying crystal sizes. We can observe some types of deformation structures along the [010] direction. One such structure is the systematic bending of the

stacking layers to intersect the (101) plane at 72° along the [010] direction (Figs. 30c, d). Both limbs of the (002) planes are systematically inclined to form "mechanical twin" (middle to lower right portion in Fig. 30d). We also observed stacking faults and defects (upper portion in Fig. 30d). These deformation structures are often observed in flexure part of bending, suggesting the release of strain by stacking defects or slip cleavage.

3.4.2.3. Graphite in the cataclasites, ultracataclasites, and pseudotachylytes

The graphite in the cataclasites and ultracataclasites forms aggregates of fine graphite powders (Fig. 31a). Using micro-Raman spectroscopy and XRD, they have a low degree of crystallinity when compared with the graphite in the host metamorphic rocks (Tables 6 and 7). The deformed graphite is formed to have accumulated within black domains of pressure solution cleavage and shear bands (Figs. 27c, d and 28). In addition, striated platy aggregates of fine graphite were also observed in residues of pseudotachylyte-bearing cataclasite (Fig. 31b). These observations suggest that the aggregates were formed by the accumulation of fragmented graphite, and reoriented by the strong shear deformation. Such aggregates of deformed graphite resemble the products observed on the shear surfaces of high-velocity, rock friction experiments (Oohashi et al., 2011, 2013).

Almost all the graphite grains observed under the HRTEM show spots and ring patterns, and distorted flake-like nanostructures, which are associated with 5–10-nm-thick stacking (Fig. 31c). In the case of the fully-ordered graphite, the 11 ring pattern is divided into 110 and 112 spot and hexagonal spots along the [001] direction, suggesting ABAB stacking in LMO. However, HRTEM observations of nanostructures and SAED patterns in cataclasites, ultracataclasites and pseudotachylytes show spots and ring patterns, suggesting the presence of both ABAB stacking (well-crystallized graphite) and misoriented stacking (poorly crystalline graphite). The microstructures and SAED patterns observed in graphite aggregates suggest that they are associated with

misoriented well-crystallized graphite, indicating the conversion of hexagonal platy crystals to fine fractured graphite. In addition, most of the graphite in fault rocks exhibits "interlayer delamination" in the stacking (Fig. 31d) and stacking defects (Fig. 31e). The interlayer delamination slips by the (002) planes within LMO of graphite, and decreases the width in stacking. This nanometer-scale delamination in the stacking observed under HRTEM is a direct evidence of decreasing graphitization parameters, as indicated by XRD and micro-Raman spectroscopy.

The HRTEM observations indicate that with increasing deformation, the stacking interval of the (001) slip plane becomes smaller. In SAED patterns along the [010] direction, the (101) spot splits into doublet peaks, suggesting hexagonal graphite with a rhombohedral mosaic distribution (Fig. 31g; Lin et al., 2012). Moreover, (10l) reflections in the SAED patterns have streaks and a few spots between (100) and (101) spots. These spots and streaks indicate that the whole stacking domains are not fully ordered 2H-graphite, and that each stacking is connected by stacking defects (Fig. 31e, f). In general, the ideal 3R-graphitic structure has ABCABC… stacking which has an angle of about 78° between the (101) and (002) planes, whereas 2H graphite has an angle of about 72° between the (101) and (002) planes, as observed along the [010] direction. Thus, the doublet spots of (101) planes in SAED pattern suggest a different stacking domain, possibly with 3R-graphite existing in a 2H-graphite domain. Figure 31f shows very thin layers, which extend rhombohedral stacking by 3–9 layers in the 2H host graphite. In general, rhombohedral graphite is only embedded in defect regions by very strong shear deformation in experimental studies (Freise and Kelly, 1963; Lin et al., 2012). The restricted occurrence of different stacking domains in the 2H host graphite suggests that the graphite in the fault rocks locally suffered intense shear deformation. In this way, the nanostructures are suggestive of deformation-induced structures in fault rocks, and they correspond well with the lowering degree of graphitization, as observed with XRD and

micro-Raman spectroscopy. They perhaps suggest a hierarchy of gliding units from a few nanometers in crystal size to as large as single layers in stacking.

3.4.3. Graphitization along the Koikakushu–Satsunai River route

Figure 32 shows the graphitization parameters along the A–A' cross section of the Koikakushu–Satsunai River route (Fig. 25b), based on Raman spectroscopy (Tables 5 and 6) and XRD (Table 7). The graphitization parameters have high correlation coefficients by the least-squares fitting (R^2 = 0.86–0.90). They gradually increase westwards and cut across the anticlines and synclines. Therefore, it is suggested that the graphitization in the metamorphic rocks records a single heating event that post-dates the development of the map-scale folding. In the lower-grade metasediments around the eastern and central parts of the Satsunai River, the mineral assemblages are dominated by muscovite and chlorite. Based on RSCM thermometry, the estimated temperature conditions were around 347–387 °C, with a maximum error of ca. 50 °C (Table 5). Crystallinity parameters show that the CM is amorphous, and the crystal sizes of L_a(110) are 21–35 Å (estimated using the equation of Tuinstra and Koenig, 1970). In the higher-grade metasedimentary schists and gneisses, found along the western part of the Koikakushu–Satsunai River, the mineral assemblages are mainly muscovite and biotite; a temperature of 404–596 °C was estimated by RSCM thermometry (Tables 5 and 6). Biotite recrystallized to form clotted textures along the schistosity when the temperatures were around 500 °C. These estimated temperatures by RSCM thermometery are consistent with temperature estimates based on garnet–biotite geothermometers in other regions of the Hidaka metamorphic belt (Osanai et al., 1986, 1991, 2007). On the other hand, the graphite in the fault rocks shows lower degrees of graphitization than that in the host metamorphic rocks. The graphite in fault veins of pseudotachylyte and ultracataclasite shows the lowest

degree of graphitization (Fig. 32). The Raman bands of graphite show the typical G and D1 bands (Fig. 28), which are identified at 1580 cm^{-1} (E_{2g} mode) and 1350 cm^{-1} (A_{1g} mode). These bands sensitively shift during the lower degree of graphitization, represented by a change in the R1 ratio from 0.1 to 1.5, and the G band FWHM from 18 to 35 cm^{-1}, as well as the crystal size in $L_a(110)$ from 200 Å to less than 40 Å (Table 6). The FWHM of d_{002} and d_{110} spacing have increased from 0.2–0.23 to 0.48–0.96 Δ°2θ and 0.12 to 0.27–0.47 Δ°2θ, when compared with the graphite in Bt–Ms gneiss and pseudotachylyte-bearing cataclasite, respectively (Fig. 32; Table 7). However, the d_{002} spacing of graphite remains constant at around 3.354 to 3.364 Å, suggesting fully-ordered graphite (d_{002} < 3.36 Å). The $L_c(002)$ and $L_a(110)$ of the graphite decrease from over 400 Å and 800 Å to 94–189 Å and 241–424 Å, respectively, from the Bt–Ms gneisses to the fault veins of pseudotachylyte and ultracataclasite (Table 7).

Beyssac et al. (2003) reported the influence of mechanical damage on well-crystallized graphite, where the R2 ratio increased due to new surface defects caused by the polishing of thin sections. Because the R2 ratio includes integrated parameters (R1 ratio and G band FWHM), the R1 ratio and the G band FWHM might be related to mechanical damages. However, the degree of amorphization indicated by such parameters, as observed during our study with micro-Raman spectroscopy, resulted in a more extensive reduction in the crystal size of L_a (from 200 Å to less than 40 Å) than was observed by Beyssac et al. (2003). Moreover, samples for our XRD study were prepared from a residue of HF–HCl treatments, and they did not undergo any mechanical damage during sample preparation. Nevertheless, the results show a significant lowering of crystallinity of the CM and graphite in the fault rocks, and it is clear, therefore, from several lines of evidence that the amorphization occurred by natural deformation as opposed to any artificially imposed defects.

Deformed graphite in the cataclasites, ultracataclasites, and pseudotachylytes is

commonly distributed along shear bands and pressure solution cleavages (Figs. 28 and 33a). Although they are very small aggregates because of size reduction due to pulverization, we could still detect the distribution of graphite from observations of thin sections and micro-Raman spectroscopy. To reveal the detailed distribution of poorly crystalline graphite, we obtained two-dimensional maps and histograms of the graphitization parameters (G band FWHM and the R1 ratio) using micro-Raman spectroscopy. G band FWHM and the R1 ratio adjacent to the shear bands exhibit a significant bimodal distribution between the shear bands and the host metamorphic rocks (Figs. 33d-e). The graphite grains in the matrix of the host rocks show a high degree of crystallinity (Fig. 33c), whereas the deformed graphite grains in the shear bands show a low degree of crystallinity. These shear bands cut the schistosity and quartz veins, and they contain secondary retrograde minerals such as chlorite, Fe oxide, and apatite (Fig. 33b).

3.4.4. Carbon isotopic compositions and TOC values

The carbon isotopic compositions of the graphite in the host metamorphic rocks, cataclasites, ultracataclasites, and pseudotachylytes all have negative $\delta^{13}C$ signatures (Fig. 34a; Table 8). The graphite in the host metamorphic rocks has a narrow range of $\delta^{13}C$ values between –23.6 ‰ and –25.8 ‰, and the graphite in the cataclasites and ultracataclasite veins have similar values of –24.7 ‰ to –25.9 ‰ and –24.1 ‰ to –25.8 ‰, respectively. In addition, the graphite in the pseudotachylyte veins shows a range of values between –25.2 ‰ to –26.2 ‰. All these data indicate that the graphite in fault rocks formed from biogenic sources, and most probably represents the remains of organic material trapped in the sediments. The analyzed samples are the same as those used for observations under the SEM and HRTEM, and these data suggest, therefore, that the

changes in morphology and nanostructure were simply induced by deformation that followed the peak metamorphism. The Bt–Ms schists and gneisses contain 0.8–0.9 and 0.3–0.6 wt.% of TOC, respectively. With increasing deformation, the CM gradually increases, with TOC values greater than 0.3 wt.% in the cataclasites and up to 1.5 wt.% in the ultracataclasites and pseudotachylytes, but the $\delta^{13}C$ values in the graphite do not shift significantly (Fig. 34b; Table 8). These data suggest that the disseminated graphite in the host metamorphic rocks was accumulated within the shear bands.

3.5. Discussion

3.5.1. Deformation mechanisms of graphite in fault zones

On the basis of detailed microstructural observations in various types of fault rock, we found that the graphite systematically deforms by layer separation, interlayer delamination, polytypic disorder (formation of *3R*-graphite), and pulverization of carbon sheets. These processes are not usually observed in the host metamorphic rocks, and we revealed the differences of microstructural evolution between recrystallization and deformation process at different stages of metamorphism. Most of the strain-induced microstructures can be classified into two groups based on the size of the delamination in the stacking. In the mylonites, the micro/nanostructures of the graphite mainly involve delamination over 200 nm thick in the stacking (micrometer-scale delamination; MMD), and there are kink bands and bending structures. The microstructures involving the flexure of carbon sheets and bending are formed without pulverization of the carbon sheets. These deformation microstructures of the graphite in mylonites formed at two different stages are similar to each other, and also compareable to those of phyllosilicates formed under relatively high *P*–*T* conditions (Escartín et al., 2008).

On the other hand, in the brittle regime, graphite mainly deforms by the pulverization of carbon sheets and interlayer delamination (nanometer-scale delamination; NMD) rather than kinking and bending. In addition, nano-scale delamination and pulverization (NMD+P) induce a grain size reduction of one to two orders of magnitude. The pulverization effect can also be detected as a decrease in crystal size using XRD and micro-Raman spectroscopic data (Fig. 35). Similar amorphization phenomena have been reported for talc (Viti and Collettini, 2009) and biotite (Bell and Wilson, 1981).

To gain a better understanding of the size reduction process, we used micro-Raman spectroscopy to compare the graphitization parameters (R1 ratio and G band FWHM) between the host rocks, cataclasites, ultracataclasites and pseudotachylytes (Fig. 35). The data obtained for the graphite in the host rocks show a very good correlation by exponential regression (best fit 2; R^2 = 0.94) because the whole study area was affected by a single thermal event. However, the data from the cataclasites, and ultracataclasite and pseudotachylyte veins show a different trend with higher R1 ratios than the graphite in the host metamorphic rocks (Fig. 35; best fit 1; R^2 = 0.78). In general, the parameters of R1 ratio and G band FWHM provide different information on the in-plane defects and D regions (Niwase, 1995). The R1 ratio is strongly controlled by the D1 band, resulting from the A_{1g} vibration mode. An A_{1g} band (1350 cm^{-1}) peak can be attributed to a breakdown of the K-selection rules for Raman activity (Tuinstra and Koenig, 1970). Therefore, this parameter reflects the relative amounts of edge planes in the carbon sheets. In contrast to the R1 ratio, G band FWHM reflects the degree of graphitization on the local surface in a smaller domain (Lespade et al., 1982). Thus, the trend of regression fit (Fig. 35; best fit 1) for deformed graphite may suggest that the deformed graphite has more edge planes in the carbon sheets than those in the host metamorphic rocks. Microstructural evidence provided by HRTEM observations supports the data of strain-induced amorphization

inferred by XRD and micro-Raman spectroscopy. In experimental studies, Niwase et al. (1995) and Inagaki et al. (1973) noted that graphitic structures are modified by two distinct deformation processes: (1) shear deformation along *c** and (2) pulverization with significant decreases in crystal size L_c(002) and L_a(110), and increases in εc (lattice strain for the *c** axis) and surface area. Thus, the data obtained from both experimental and natural occurrences suggest the graphite underwent similar mechanisms of deformation.

The above results also indicate that graphite releases strain by micro/nano-scale delamination and size reduction as a function of the degree of deformation (Fig. 36), and the results have a lot in common with other studies of strain-induced microstructures (Escartin et al., 2008; Viti and Collettini, 2009). In the brittle regime, we identified a strain-induced amorphization from the cataclasites to the pseudotachylytes. It is possible that the rupture energy during deformation corresponds to an increase in the surface area of carbon sheets by pulverization and nanometer-scale delamination. In this way, the deformation mechanism in graphite is strongly controlled by the primary crystal structure of ABAB stacking, and these microstructures may change the delamination size in the stacking according to the *P*–*T* conditions and/or strain rate. Our data imply that the microstructural and crystallinity parameters can serve as potential indicators of the deformation processes that are taking place in the crust.

3.5.2. Origin of graphite and its role in natural deformation

Graphite in deformed rocks is concentrated within shear bands or on fault surfaces, and it has generally been thought that such concentrations form by two mechanisms, namely the deposition of graphite from carbon-rich fluids (Santosh and Wada, 1993; Luque et al., 1998; Santosh et al., 2003) and the physical remobilization of pre-existing disseminated graphite (Acharya and Dash, 1984; Crespo et al., 2005; Oohashi et al., 2012).

Craw (2002) reported graphite deposition along microshears, up to 3 wt.% locally, above a background of 0.1 wt.% organic carbon. This deposition resulted from a mixing of two compositionally different fluids, H_2O–CH_4 and H_2O–CO_2. In the case of graphite precipitated from COH fluids, fractionation of the carbon isotopes between the graphite and CO_2 or CH_4 can be expected, as well as a concomitant increase in the volume fraction of total carbon. However, the carbon isotopic compositions of graphite in the host rocks, cataclasites, ultracataclasites and pseudotachylytes revealed that all samples show similar negative $\delta^{13}C$ signatures at around –24.8 +/– 0.67 ‰ (Fig. 34a; Table 8), and increase of TOC values from 0.3 to 1.5 wt.% is lower when compared with other occurrences of fluid-deposited graphite as reported by previous studies (e.g., Luque et al., 1998). Moreover, because of low temperature conditions, the activation energy might not have crossed the threshold necessary to deposit the graphite. The carbon isotopic data also indicate that the deformed graphite in fault rocks was not formed by precipitation from fluids within the fault zone, and instead the results point to the remobilization of graphite along shear surfaces during deformation. The morphological evidence from HRTEM and SEM observations also supports the proposition that the graphite in fault rocks was converted from well-crystallized graphite into small fractured graphite. In fact, graphite and CM remain immobile along the shear planes under low temperature conditions, thereby increasing in content from 0.3–0.7 wt.% to 1.0–1.5 wt.% due to the preferential solution of other silicate phases and the physical reorganization of the disseminated graphite. Our studies indicate, therefore, that it is possible for graphite to accumulate in a fault zone, and if the deformation is accompanied by the accumulation and amorphization of the graphite along shear planes, it becomes possible to explain the occurrence of large aggregates of graphite present in these fault zones.

Collettini et al. (2009) proposed that the frictional strength of fault rocks is controlled by small amounts of phyllosilicate minerals that make up the rock fabric and

are present along slip surfaces. Moreover, Oohashi et al. (2013) showed that the frictional strength of a fault rock drops significantly even in the presence of small amounts of graphite. These studies indicate that the frictional strength of graphite-bearing fault rocks is controlled by microstructures and the distribution of minerals with sheet structures such as graphite and the phyllosilicates. It is uncertain whether a small concentration of graphite (1.0–1.5 wt.%) really has the potential for directly controlling the frictional strength of a fault rock in its entirety. However, large platy aggregates of graphite, which were observed in the shear bands (Fig. 31b), are composed mostly of graphite, and in such cases these aggregates may effectively reduce the frictional strength and cause preferential deformation within the fault zone.

3.6. Conclusions

I have shown that graphite in fault rocks has a different microstructure and crystallinity from graphite produced by metamorphic processes. I was able to identify two distinct deformation processes for the graphite in fault zones, based on its microstructures, morphology, crystallinity and stable carbon isotopic compositions; namely, the micrometer-scale delamination (MMD) in the stacking and nanometer-scale delamination (NMD) in the stacking plus pulverization (P) of carbon sheets to a grain size of less than 10 nm (NMD + P) (Fig. 36). These two processes are represented by the differences in scale of the delamination in the stacking (micrometer to nanometer scale), which is a function of P–T conditions and/or strain rates. In addition, the graphite of sedimentary origin has negative $\delta^{13}C$ signatures (–24.8 ± 0.67 ‰), and it has preferentially undergone strain-induced amorphization and accumulation (from 0.3 to 1.5 wt.%) within shear bands. Under low *P*–*T* conditions, the graphite acts as an immobile mineral in the fault rocks, because it does not react with other silicate minerals or fluids to activate

recrystallization. The way in which graphite preferentially deforms and releases stress by slip parallel to the (001) planes may play a key role in fault zone processes.

Our observations indicate that the crystal structure of graphite records not only the peak metamorphic temperatures but also deformation. This indicates that the graphite in many geological occurrences has the potential for strain-induced amorphization, and we need to pay more attention to the microstructures of graphite in order to discuss further the details of graphitization in metamorphic terrains.

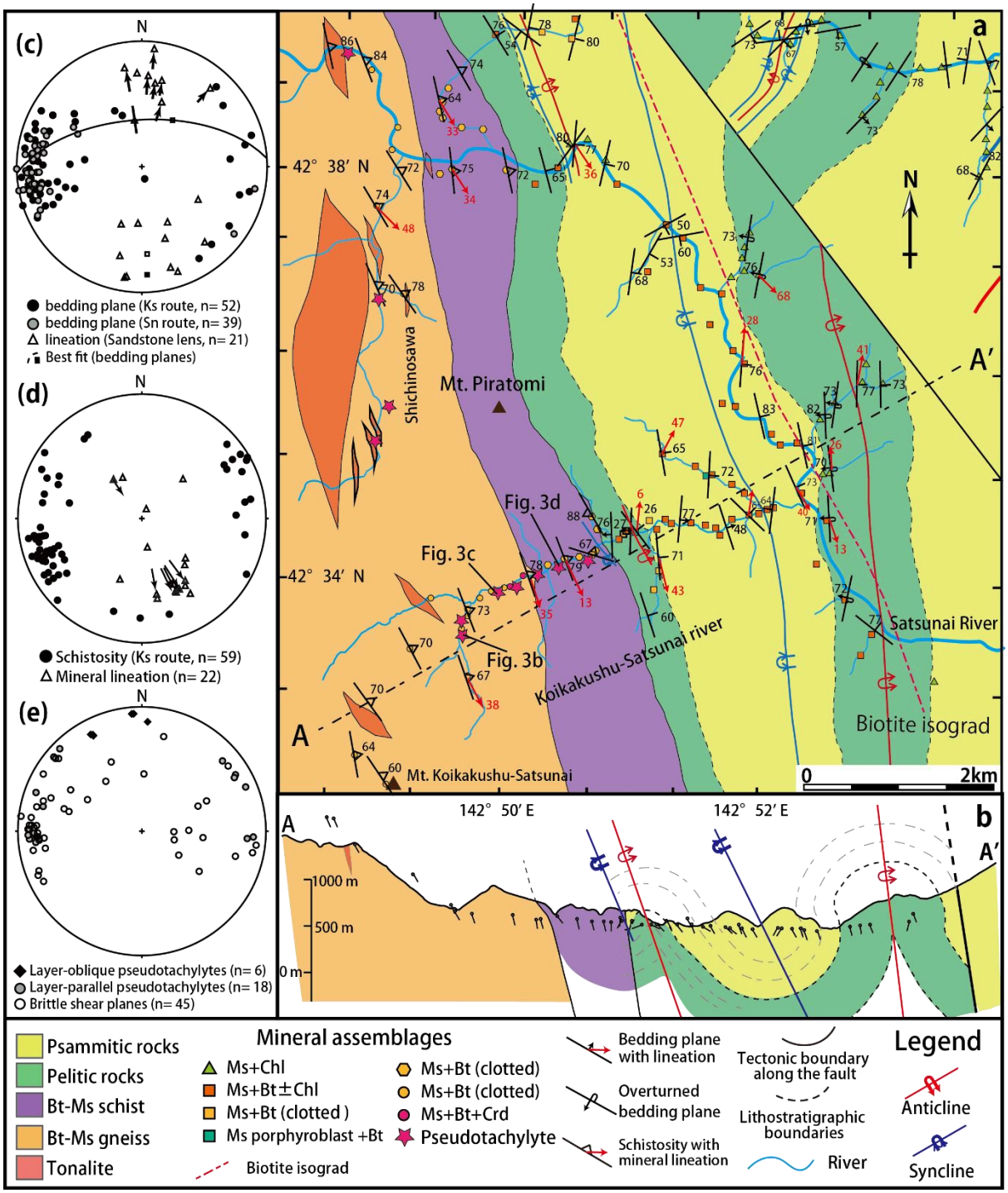

Figure 25. (a) Geological map of the study area, showing the distribution of lithostratigraphic units of the upper sequence of the HMB. Mineral assemblages of metamorphic rocks and the localities of pseudotachylyte-bearing cataclasite are plotted. The red dotted line shows the biotite isograd in the study area. Chl, chlorite; Ms, muscovite; Bt, biotite; Crd, cordierite. **(b)** A–A' cross section transverse to the

Koikakushu–Satsunai River. **(c)** Equal-area and lower-hemisphere projections of poles to bedding planes in the Koikakushu–Satunai River (Ks route) and Satsunai River routes (Sn route). Cylindrical best-fit great circle for the bedding planes and its rotational axis are also shown. The arrows attached on the lineation data indicate the movement direction of the hanging wall. **(d)** Equal-area and lower-hemisphere projections of poles to the regional biotite schistosity in the study area. The arrows attached on the lineation data indicate the movement direction of the hanging wall. **(e)** Equal-area and lower-hemisphere projections of poles to brittle shear planes (circles), and poles to fault planes of layer oblique pseudotachylytes (gray-filled circles) and layer parallel pseudotachylytes (black-filled diamonds)

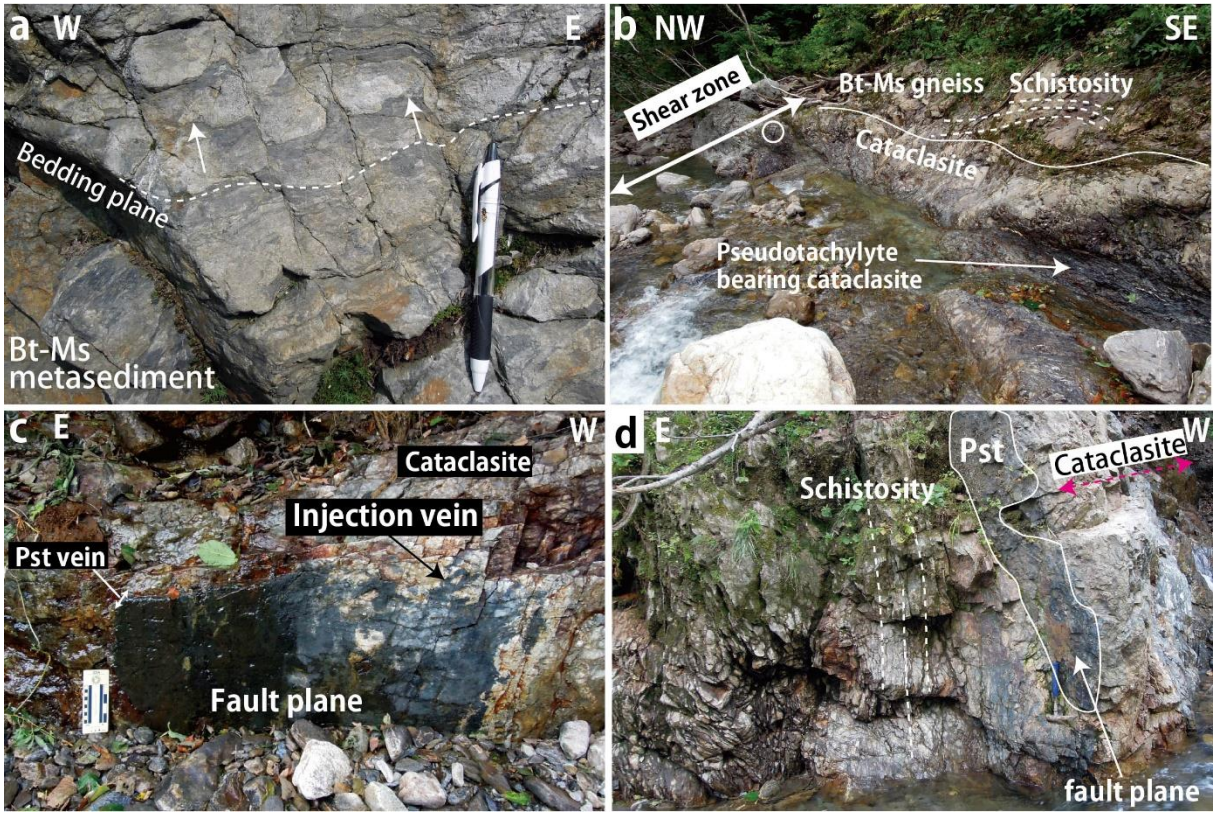

Figure 26. Occurrences of graphite-bearing cataclasites, ultracataclasites, and pseudotachylytes (Photographs of outcrops). The field localities of those occurrences are shown in the geological map of Fig. 2a. **(a)** The Bt–Ms metasediments, showing normal graded bedding. **(b)** A brittle shear zone containing graphite-bearing mylonite, cataclasite, and pseudotachylyte. The white circle shows a hammer for scale. **(c)** Layer oblique pseudotachylyte in a shear zone. The black domain represents a fault plane of pseudotachylyte. The pseudotachylyte vein cuts the NNW–SSE striking biotite schistosity. **(d)** Relationships between layer parallel pseudotachylyte (Pst), host biotite–muscovite schist, and cataclasite.

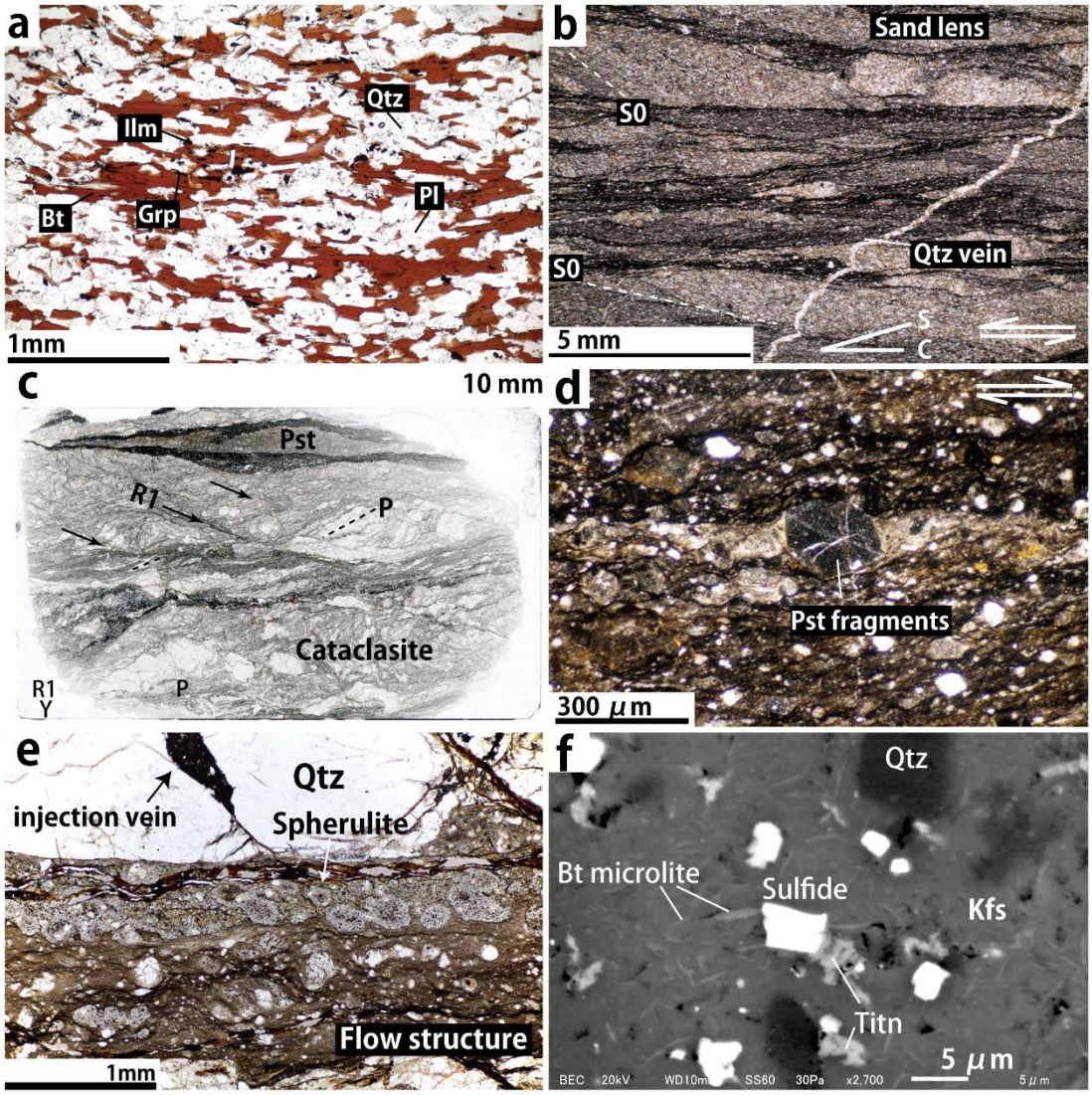

Figure 27. Photomicrographs of the host metamorphic rocks and fault rocks (a-e, are taken under plane-polarized light and f, is a BSE image). **(a)** Bt–Ms gneiss showing the growth of graphite (Grp) along the cleavage of biotite (Bt) with other oxide minerals (Ilm, ilmenite) and plagioclase (Pl). **(b)** Mylonitic texture in Bt–Ms metasediments, showing the S–C–C' fabric of the sand lenses. **(c)** Pseudotachylyte-bearing cataclasite in the XZ plane. R1 and P shear bands can be recognized, and the pseudotachylyte vein cuts these shear bands. **(d)** Ultracataclasite (Ulcat) vein in cataclasite. The fragments include δ-type porphyroclasts with strain shadows, demonstrating dextral shearing in the XZ plane. **(e)** Pseudotachylyte injection, spherulitic textures, and flow structure in pseudotachylyte veins. **(f)** Secondary minerals (biotite microlites and sulfides) in pseudotachylyte matrix.

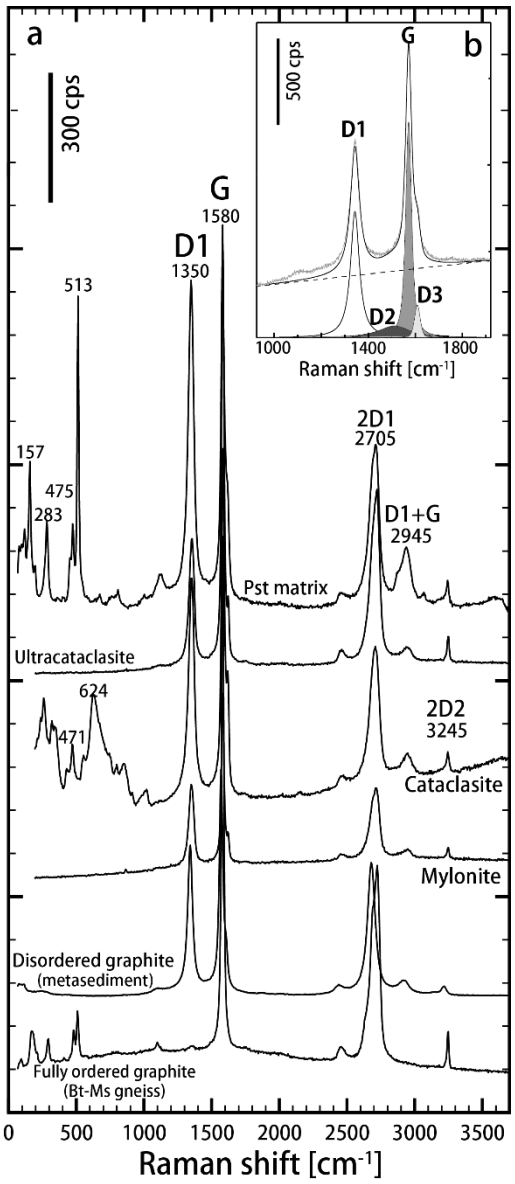

Figure 28. Raman spectra of each black domain in the cataclasite, a mylonite band, an ultracataclasite vein and the pseudotachylyte matrix (Pst matrix), and disseminated graphite grains in host metamorphic rock. All spectra show the typical graphite spectra of the D1 and the G bands in the first order region (1000–1800 cm^{-1}) and overtone peaks (2D1, D1 + G, 2D2) in the second order region (2000–3500 cm^{-1}). Raman spectra at 157, 283, 451, 475, and 513 cm^{-1} belong to sanidine or orthoclase in the Pseudotachylyte matrix. The three (or two) bands at 451, 475, and 513 cm^{-1} are identified as TO_4 tetrahedra of feldspars with a four-membered ring, and these peaks changed from triplets to doublets by Si–Al ordering (Freeman et al., 2008).

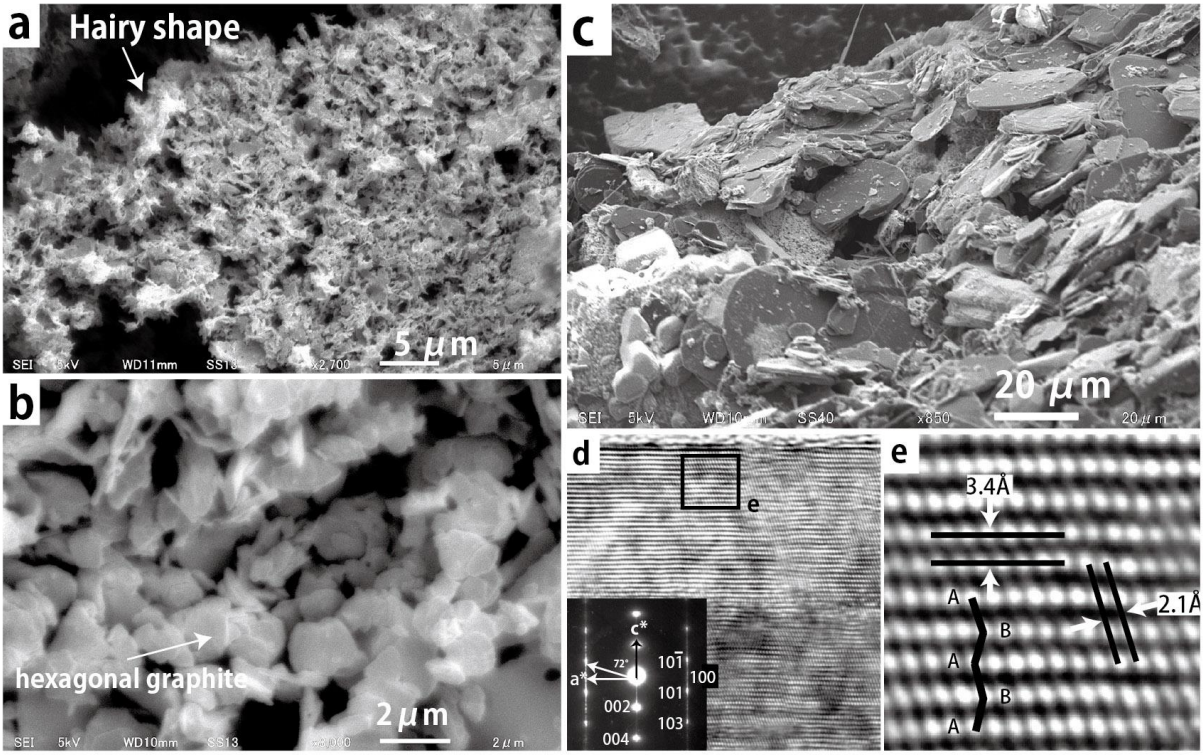

Figure 29. Morphological characteristics of graphite in metamorphic rocks. **(a)** Secondary electron image of fibrous graphite that formed in metasediments at around 400 °C, with the temperature estimated using the equation of Beyssac et al. (2002a). **(b)** Secondary electron image of hexagonal and platy graphite (1–2 μm thick) that formed in biotite schist at around 500 °C. **(c)** Secondary electron image of hexagonal platy graphite that formed in biotite gneiss at around 600 °C. **(d)** HRTEM image and SAED pattern of fully-ordered graphite in Bt–Ms gneiss along the [010] direction. **(e)** Lattice fringe of the graphitic structure along the [010] direction, showing the (101) and (002) planes.

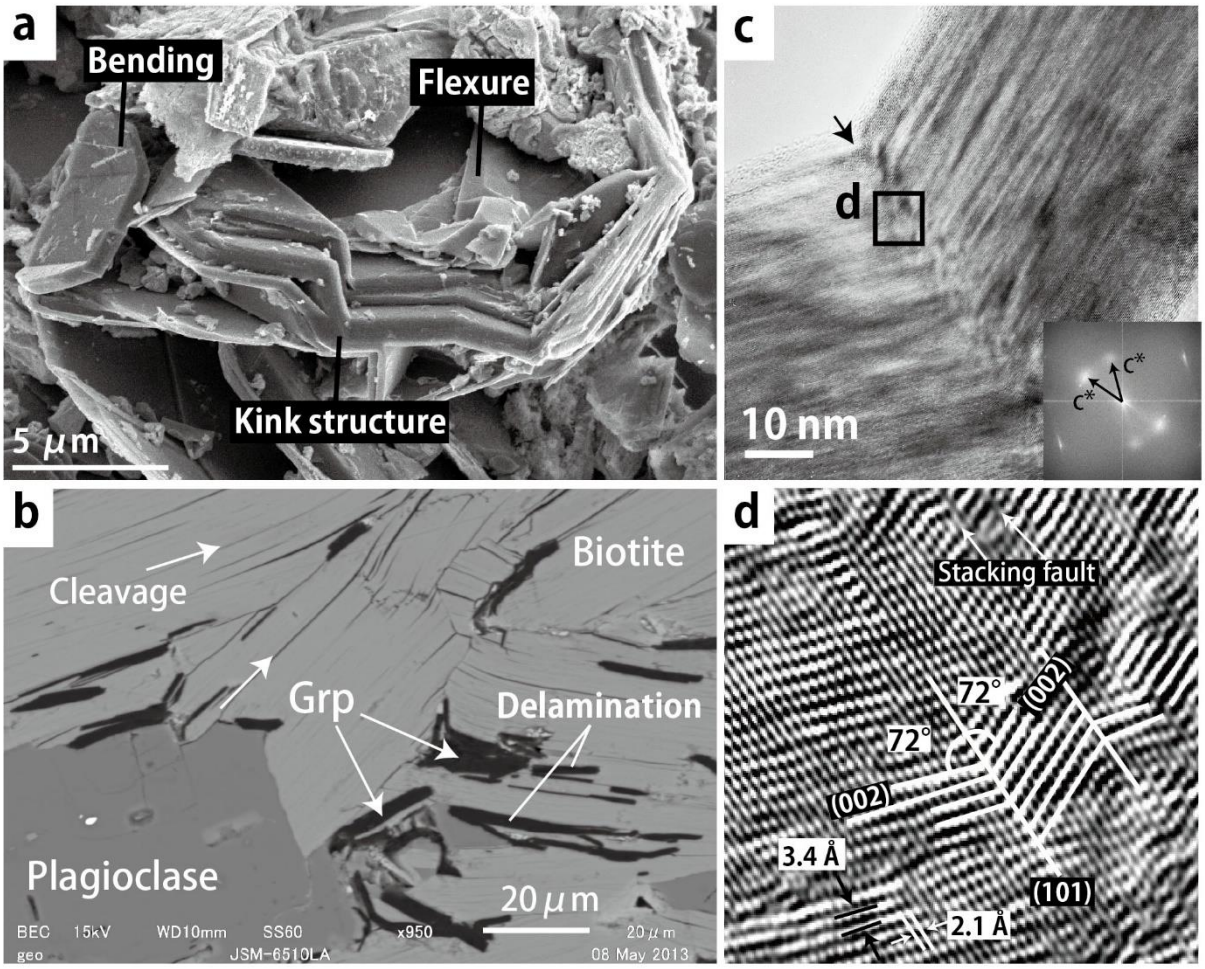

Figure 30. Morphological characteristics of graphite in the mylonites. **(a)** Secondary electron image of kink structure, bending structure and layer flexure in the graphite separated using HF–HCl treatment. **(b)** The graphite (Grp) in mylonitic metasediments shows deformation by delamination, kink structures, and bending structures along the biotite cleavage. **(c)** HRTEM image and corresponding SAED pattern of bending structure. **(d)** High-magnification view of the bending structure in Fig. 30 along the [010] direction. (002) planes intersect the (101) planes at 72°.

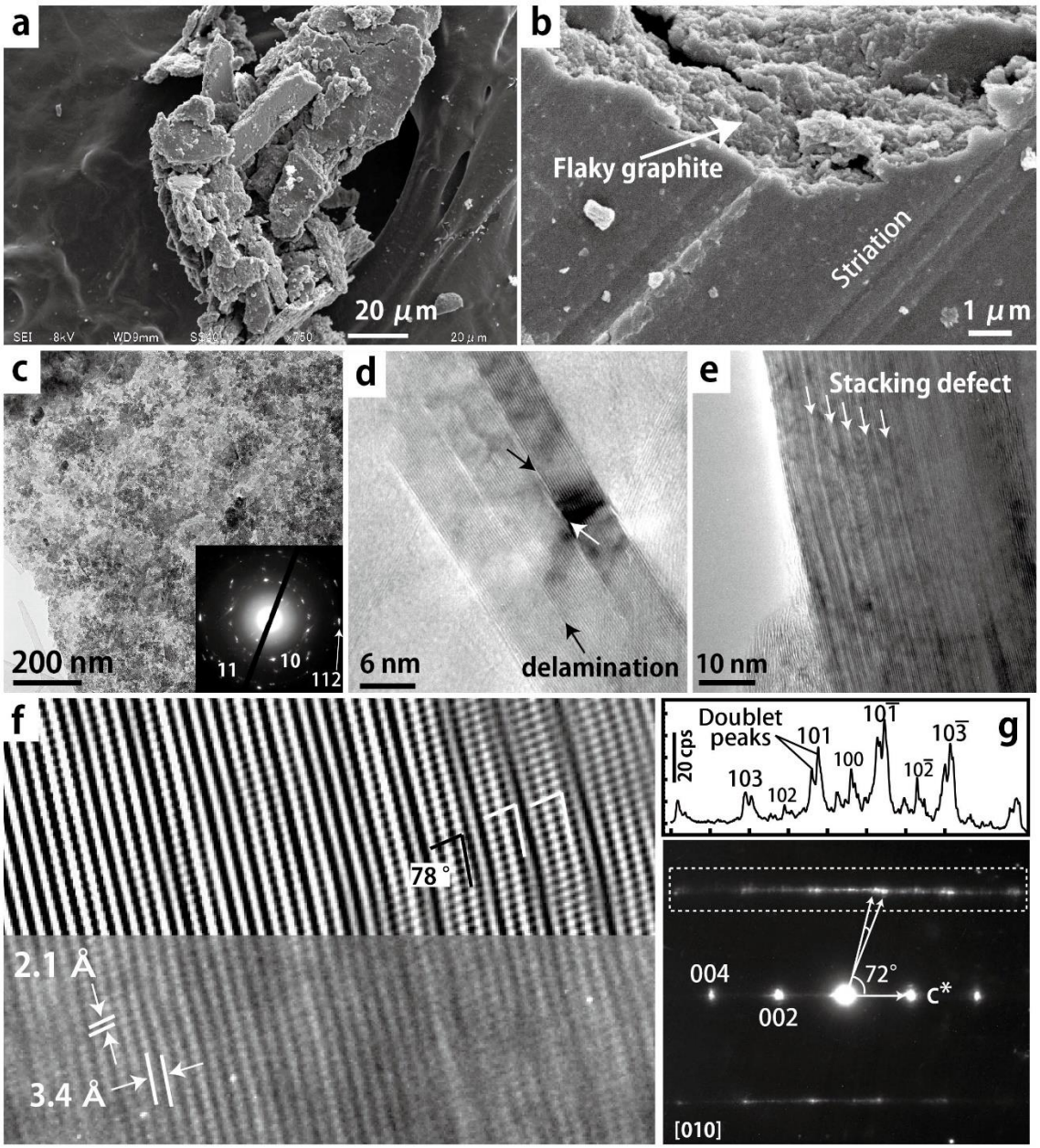

Figure 31. Morphological characteristics of graphite in cataclasites, ultracataclasites, and pseudotachylytes. **(a)** Powdered aggregations of deformed graphite in cataclasite separated using HCl–HF treatment. **(b)** Secondary electron (SE) image of an aggregation of graphite under high magnification using FE–SEM. The fractures are closely associated with fine flaky graphite. **(c)** HRTEM image of the microstructure of graphite in cataclasite. **(d)** Typical microstructure of deformed graphite in fault rocks. The structures show the interlayer delamination in the stacking. **(e)** Deformed graphitic lamellae with stacking defects. **(f)** Lattice fringes of graphite along the [010] direction in fault rocks. The upper half of the image shows the processed lattice fringes of graphite along the [010] direction. **(g)** SAED pattern of graphite along the [010] direction (lower diagram) and intensity profile of the 10*l* spot pattern (upper diagram). Note that most of the spots have doublet peaks.

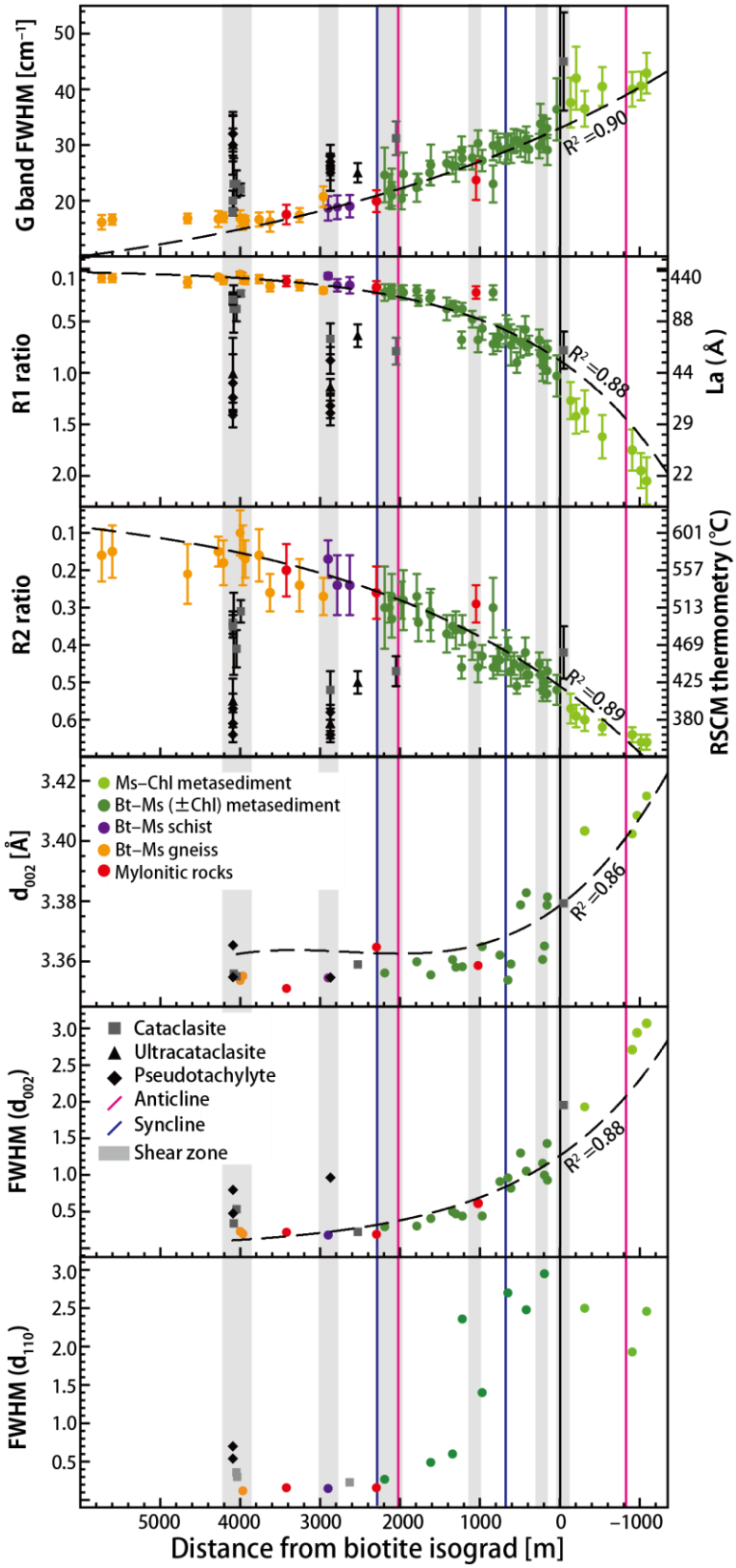

Figure 32. Graphitization parameters obtained from host rocks and fault rocks along the Koikakushu–Satsunai River route. Black line shows the biotite isograd on the

Koikakushu–Satsunai River route. Black dotted lines give the least-squares fit to the data from metamorphic rocks and mylonites with exponential regression. The peak metamorphic temperatures and La (Å) were calculated for the formulas of Beyssac et al. (2002a) with the R2 ratio and Tuinstra and Koeing (1970) with the R1 ratio, respectively. G band FWHM, R1 ratio, and R2 ratio show error bars with a range of 1σ. Chl, chlorite; Ms, muscovite; Bt, biotite.

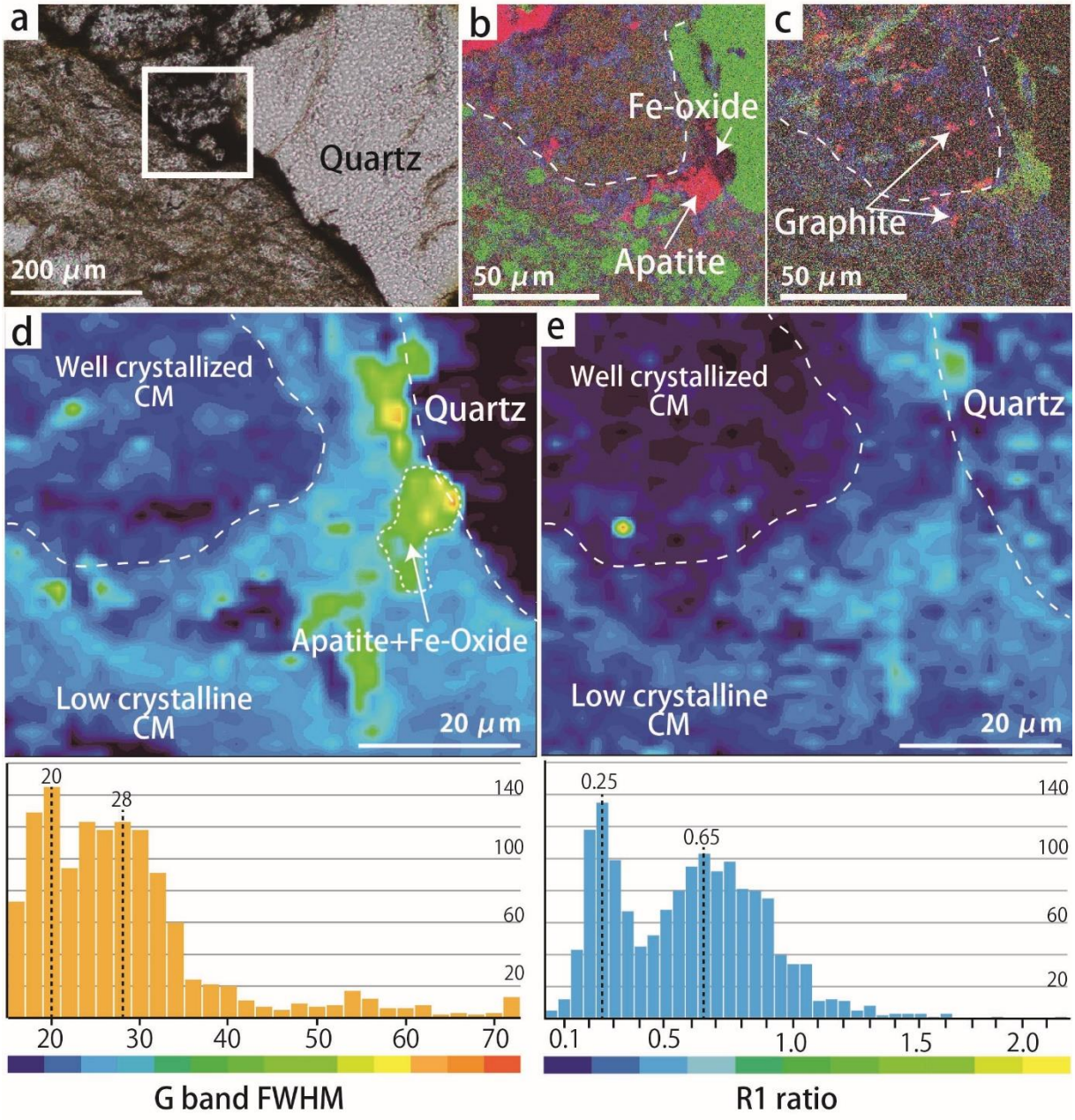

Figure 33. Maps showing chemical compositional variations and the graphitization parameters in the shear band. **(a)** Plane-polarized light image of shear band in ultracataclasite sample. White box shows the analysis area for EDS and Raman mapping. **(b)** Qualitative map by EDS analysis constructed with Si (green), Ca (red), and K (blue). **(c)** Qualitative map by EDS analysis constructed with Fe (green), C (red), and K (blue). **(d, e)** Raman mapping and histogram of the graphitization parameters of G band FWHM **(d)** and R1 ratio **(e)**

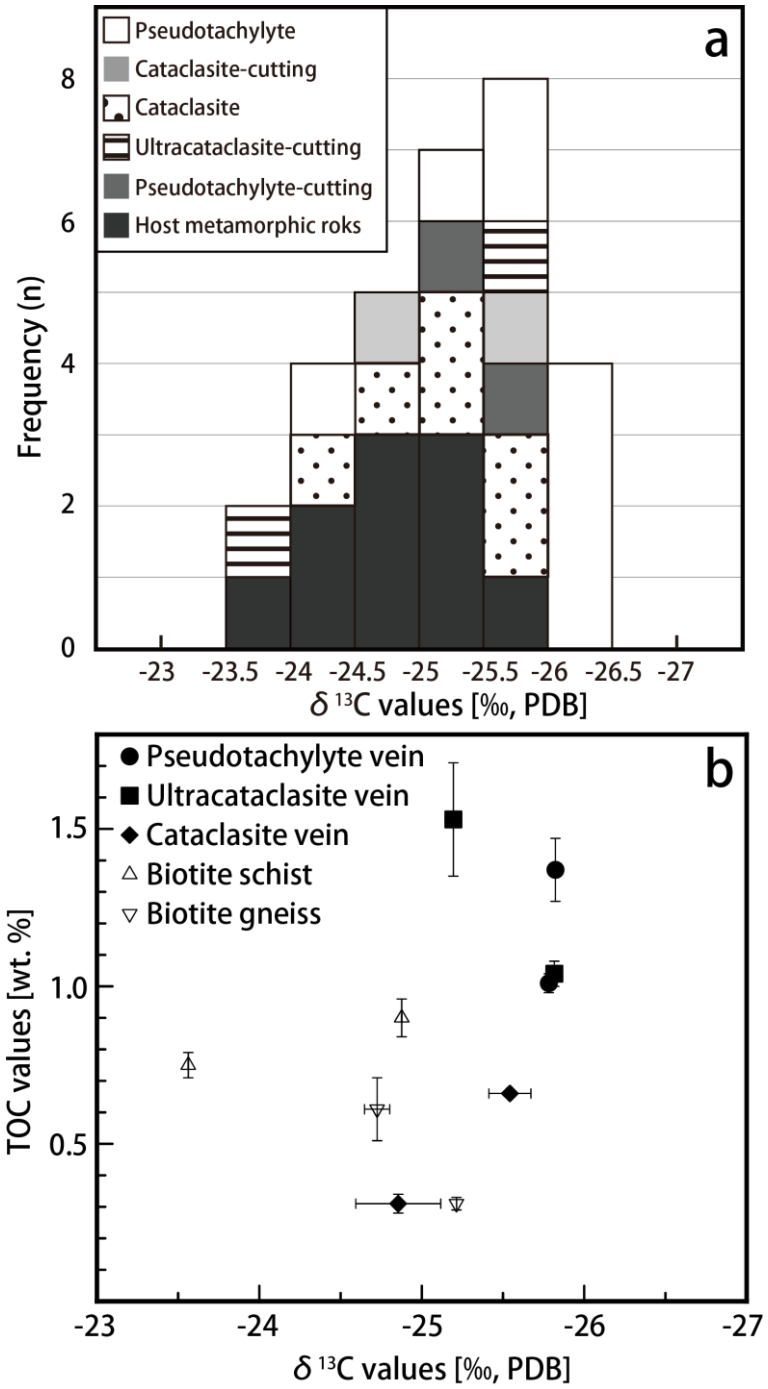

Figure 34. (a) Histogram of stable carbon isotope results from fault rocks (cataclasite, ultracataclasite, and pseudotachylyte) and host metamorphic rocks (*n = 30*). The graphite separated by HF–HCl treatment was used for the measurements. The data annotated "cutting" after the sample code were analyzed using the graphite separated from the slab under a binocular microscope. **(b)** Relationships between total organic carbon (TOC, wt.%) results and stable carbon isotope results.

.

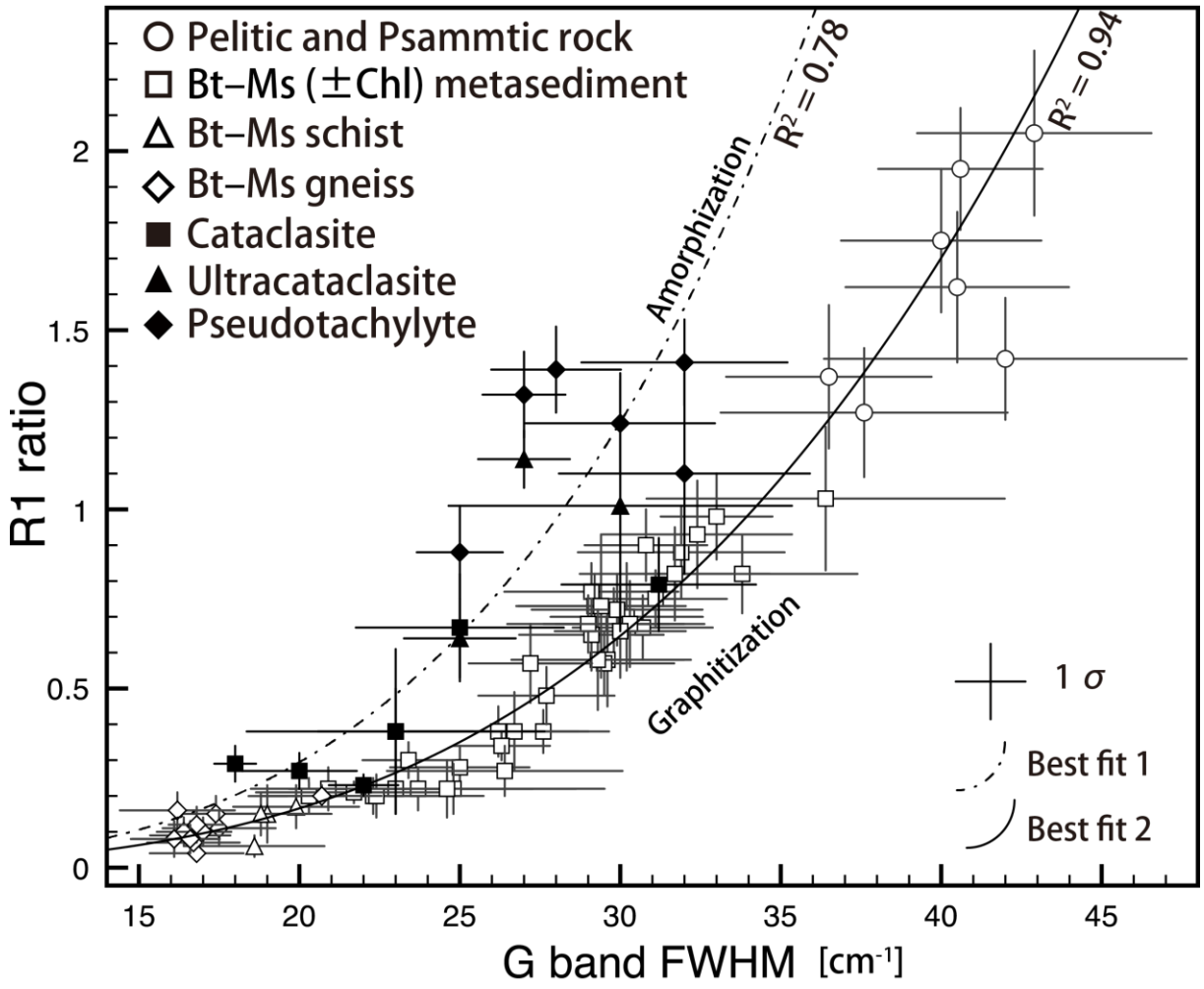

Figure 35. Relationships between R1 ratio and G band FWHM in fault rocks and host metamorphic rocks. All samples show mean values and error bars of 1σ, calculated on the basis of more than 25 analyses for each sample following Aoya et al. (2010). The exponential regression lines are calculated for fault rocks (best fit 1) and host metamorphic rocks (best fit 2). Chl, chlorite; Ms, muscovite; Bt, biotite.

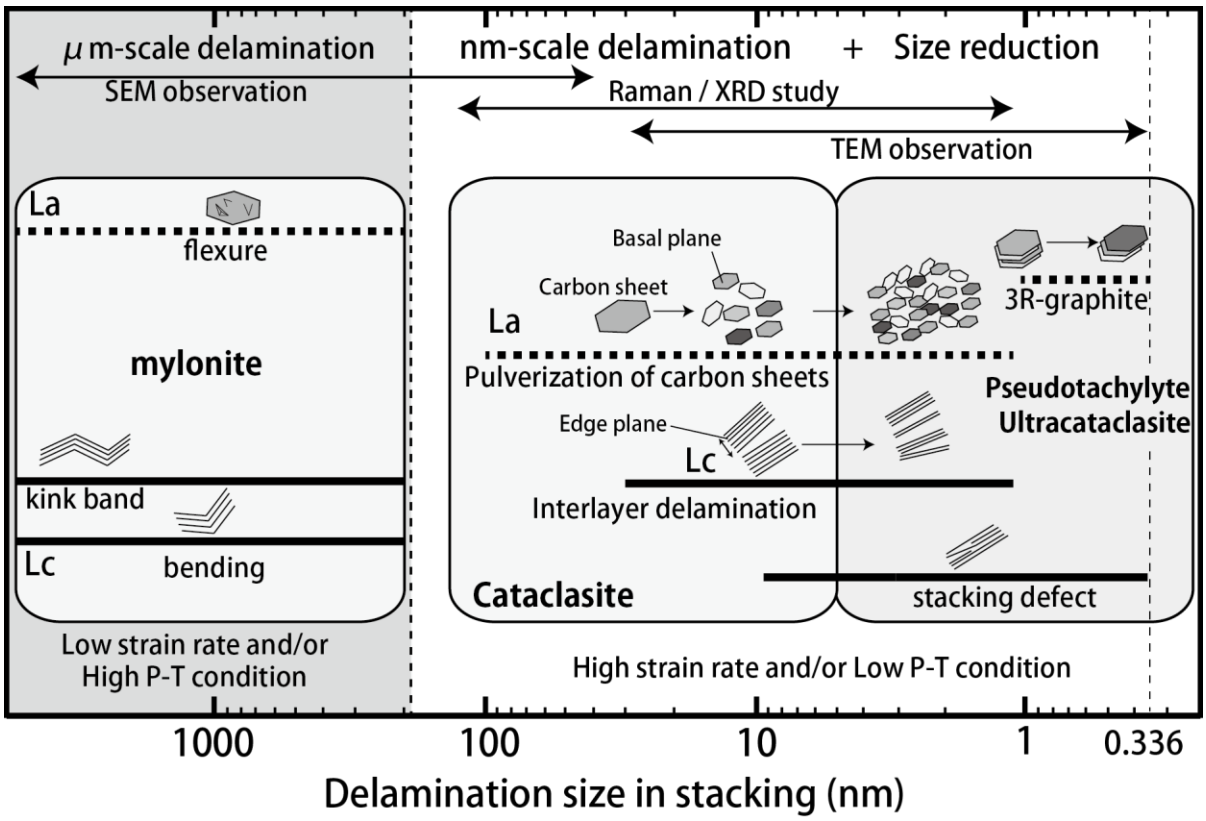

Figure 36. Schematic diagram of deformation structures of graphite as a function of the delamination size in the stacking, which corresponds to the thickness of carbon sheets.

CHAPTER IV

Fault degassing and graphite precipitation in pseudotachylytes during paleoseismicity

4.1. Introduction

Tectonic pseudotachylytes are solidified silicate melt produced by frictional melting during coseismic slip, and one of the few geological information that records dynamic Earthquake rupture process (Sibson, 1975; Cowan, 1999; Di Toro et al., 2009). In general, the pseudotachylyte occur as blackish veins and comprised of a mixture of survived lithic fragments and glassy-cryptocrystalline matrix (Shand, 1916). Bulk composition of most pseudotachylyte tend to change to more mafic components than that of protolith (Philpotts, 1964; Maddock, 1992). This arises from the selective dis-equilibrium melting of hydrous and ferromagnesian minerals in host rock (Maddock, 1992; Spray, 1993). Based on the detailed observations of pseudotachylytes, the frictional melting temperatures during coseismic slip are deduced to be in the range of 750–1450 °C, based on the mineralogy of the newly grown microlites (Toyoshima et al., 1990; Austrheim and Boundy, 1994; Lin 1994; Moecher and Brearly, 2004; Moechar and Steltenpohl, 2009), minimum melting point of survived minerals (Maddock, 1983; Spray, 1992; Ujiie et al., 2007), and numerical modelling (Di Toro et al., 2004). The peak frictional temperatures and microstructures in pseudotachylyte vein provide a valuable information on the physicochemical properties during an earthquake. In fact, the most frictional work of pseudotachylyte-bearing faults during seismic slip is converted into heat energy (Sibson, 1975; Lockner and Okubo, 1983; Wenk, 2000), and the viscosity of pseudotachylyte melt

is controlled by bulk chemistry and frictional melting of disequilibrium melting (Spray, 1993). On the other hand, the behavior of aqueous fluids in fault plane also play a fundamental role of above physicochemical properties during seismic slip (e.g., O'hara and Sharp, 2001). The fluids generated by selective melting of hydrous minerals may change pore pressure in fault plane, and result in thermal pressurization of pore fluid or lowering the breakdown temperature at frictional melting (Sibson, 1975; Allen, 1979; Magloughlin, 1992). In addition, infiltration of fluid during interseismic period lead to fault strengthening (healing) owing to sealing of fluid deposited minerals (Marone et al., 1995; Bos and Spiers, 2000; Tenthorey et al., 2003). These laboratory and theoretical implications suggest the importance of fluid activities during dynamic Earthquake process, however, the direct clues in natural observations are very limited to those obtained from fluid inclusion studies (e.g. Boullier et al., 2001) or estimation of fluid concentration in pseudotachylyte glass using a micro-FTIR (e.g. Famin et al., 2008). It is usually difficult to distinguish between syngenetic and postgenetic fluid activities from altered and hydrated pseudotachylytes (Kirkpatrick and Rowe, 2013). Notably, glass in almost all pseudotachylytes are replaced by secondary minerals such as epidote, chlorite and zeolite because the depth of pseudotachylyte generation (3 to 15 km) is unfavorable for its preservation (Maddock, 1987; Di Toro et al., 2009).

Instead of direct estimations, as in previous studies, it is also possible to understand the fluid composition and redox state indirectly, based on the activity of fluid buffering minerals such as magnetite, hematite, pyrrhotite and graphite. These minerals are common secondary minerals generated by frictional melting and their isotopic and chemical compositions sensitively change as a function of local redox state during the generation of pseudotachylyte (O'hara and Huggins, 2005). Here we characterized the detailed occurrence and geochemistry of the secondary minerals for understanding the dynamic fluctuations of oxygen fugacity (fO_2) and resulting fluid compositional variations

during paleoseismicity. Especially, we focused graphite and sulfide minerals, which are important redox tracers to estimate the COHS fluids in pseudotachylyte melt. (Poulson and Ohmoto et al., 1989; Ohmoto and Kerrick, 1977). Our fluid estimations combined with the chemical and isotopic compositions of buffering minerals lead to constrain the dynamic aspects of fluid activity during paleoseismicity.

4.2. Geological outline and field description

Pseudotachylyte bearing faults belonging to the Hidaka Metamorphic belt (HMB) were examined in this study. The HMB is a north-south trending high-temperature low-pressure (*HTLP*) type metamorphic terrain in the central Hokkaido, Japan (Fig. 3b). The metamorphic terrain extending for more than 100 km was formed by the oblique collision between paleo Kuril and Northeast Japan island arc (Komatsu et al., 1989; Osanai et al., 1991; Toyoshima et al., 1994). The Hidaka metamorphic rocks are grouped into two sequences, lower and upper (Komatsu et al., 1983). The lower sequence is composed of amphibolite to granulite facies mafic, pelitic, and psammitic rocks, and the upper sequence, in descending order, consists of very low-grade (prehnite–pumpellyite facies) metasediments, muscovite (Ms)–chlorite (Chl) metasediments, biotite (Bt)–Ms schists, Bt–Ms gneisses, and banded Bt gneisses (Osanai, 1985, 1991; Komatsu et al., 1989; Figs. 37a-b). The upper sequence of very low grade metamorphic rocks in HMB is gradually changed to Nakanogawa group (Fig. 37a). The Nakanogawa Group is composed solely of turbidities facies sediments, including acidic tuff layers and dismembered hemipelagic red and green mudstones (Nanayama, 1992; Nanayama and Ganzawa, 1997). Various types of fault rock such as graphite-bearing cataclasite, ultracataclasite and pseudotachylyte derived from Bt–Ms schist or banded Bt gneisses were widely observed in this study area (Nakamura et al., 2015). They are parallel (layer parallel) or oblique (layer oblique) to the

bedding planes, schistosity, or mylonitic foliations of the host rocks. The layer parallel veins of pseudotachylyte and ultracataclasite, which strike roughly N–S, are a few millimeters to a maximum of five cm width, and they occur along brittle shear zones of 0.5 to 30 m width. On the other hand, the layer oblique veins of pseudotachylyte and ultracataclasite are found within thin cataclasite zones, and they strike roughly ENE–WSW to E–W (Fig. 37c). Such brittle fault rocks were mainly deformed by uplifting and steeply tilting of HMB after peak metamorphism (Toyoshima et al., 2004; Nakamura et al., 2015).

4.3. Analytical methods

Detailed microstructures in the fault rocks were investigated by optical and electron microscopy. Scanning electron microscopic (SEM) observations were carried out using a JEOL 6510LA at Niigata University. Chemical compositions of mineral phases were determined by energy dispersive spectroscopy (EDS: semi-quantitative analysis) and electron microprobe analysis (EPMA) using a JEOL JXA-8600SX, at Niigata University. Analyses were obtained using a focused beam of 1 or 3 μm diameters, with an accelerating voltage of 15kV and a beam current of 13 nA. The whole rock major elements for representative samples were analyzed using an X-ray fluorescence (XRF: Rigaku RIX-3000) at Niigata University. Analytical procedures have been described by Takahashi and Shuto (1997). Total organic carbon (TOC) analysis was performed by a Perkin Elmer CHNS analyzer at Niigata University. Three aliquots of samples weighing between 1.0 to 1.5 mg were prepared from HCl-treated rock powders in selected area. Standard materials (acetanilide) and blank lead (Pb) foils were also measured randomly during each measurement session. Micro-Raman spectroscopy was applied to crystallinity of graphite and identification of inclusions using Jasco NRS 3100 at Niigata University, equipped with the gratings of 1800 lines/mm and CCD-detector (256×1024 pixels). The microscope

objective of 100×, and Nd-YAG laser (wavelength: 532 nm) was used (Nakamura et al. 2015).

Quantification of volume fraction between lithic fragments and melting area in pseudotachylyte veins were measured by two methods; (1) X-ray diffraction (XRD) semi-quantitative analysis, (2) image analysis using SEM-Back Scattered Electron (BSE) with EDS mapping. XRD semi-quantitative analysis was used for WPPF (Whole Powder Pattern Fitting) method to identify volume fraction of each mineral phase. This method is depended on the accuracy of Rietveld analysis for each mineral phase, therefore, they have about 2–5 % of measurement errors. XRD was carried out using a Rigaku ULTIMA IV diffractometer, equipped with Cu*K*α (40 kV, 40 mA) radiation. The diffractometer was run between 3° and 90°. In the case of image analysis, BSE images are automatically binarized between fragments and matrix by changing the threshold of gray value using image J software. This method is strongly depended on accuracy of threshold. Therefore, we carefully checked the binary images, which changed their values for comparing the EDS mapping and original BSE images. In addition to automatic image analysis, we manually identified the lithic fragments in pseudotachylyte matrix using BSE images with EDS mapping. The mean values of volume fractions and matrix were measured from the three to four binary images for each sample.

Given that pseudotachylytes show heterogeneous microstructures in the millimeter scale, the powder samples for trace elements and carbon stable isotopic analyses were microdrilled from polished rock slabs using a tungsten micro drill under a binocular microscope. Because the powder samples were having only extremely low concentrations of target elements, we have done some preparations before geochemical analyses. The powder samples for trace element analysis were initially heated at 900 °C for 24 h to remove volatile components before dissolution. To avoid incomplete dissolution of zircon and other refractory minerals, we prepared sample solution using a

combined Na_2CO_3 fusion and acid digestion procedure. Powdered samples were fused with Na_2CO_3 at 1050 °C. The solution was neutralized with HNO_3 + HCl and diluted by a factor of 5000 with a mixture of HF-HNO_3-HCl. The concentrations of trace element were measured with an inductively coupled plasma mass spectrometer (ICP-MS; Agilent 7500a). Variation during the analytical runs was corrected by three internal standards (In, Re and Bi). External standardization was performed for single elements in unknown samples by interpolation of results for replicate analyses of BHVO–2 (U.S. Geological Survey; Eggins et al. 1997), repeated after 5–6 unknown samples. We carefully check the blank and sample values for comparing the contamination of tungsten (W) from microdrill.

Carbon stable isotope analysis of the powder samples including graphite was carried out using a Finnigan MAT 251 mass spectrometer. The powder samples were introduced into a preheated (1100°C for 12 h) VYCOR® tube. Vanadium pentoxide (V_2O_5) was used as oxidizing agent for conversion of carbon to carbon dioxide. The VYCOR® tubes containing graphite and V_2O_5 were again preheated at 500 °C for 30 min. to remove any surface organic contaminations in samples, and sealed under vacuum (~10^{-3} Torr). Sealed tubes were combusted at 1000 °C for 2 h for oxidizing the graphite to CO_2. The tubes were then cracked under vacuum, in a line connected to a modified high vacuum inlet system for carbon isotope measurements of micro-volume CO_2 gas (Wada et al., 1984a, 1984b, Satish-Kumar et al., 2011). The CO_2 gas was analyzed for carbon isotopes and is reported in δ notation relative to the V-PDB standard for carbon. Laboratory machine standard CO_2 gas measured in the beginning and end of each measurement session gave reproducibility better than 0.1 ‰. Although this system can be analyzed for stable carbon isotope ratio of even micro-volume CO_2 gas (~0.05 μmol), ~0.4 μmol of CO_2 gas are adequate for avoiding pressure effect between standard gas and sample gas, as well as to nullify the effect of minor contamination from quartz tube during combustion (Wada et al., 1984a). In this study, CO_2 gas for carbon stable isotopic analysis was ranged between 0.05 μmol

and 41.5 μmol depending on the graphite concentration of treated powder samples (Fig. 38). We carefully check the carbon isotopic values obtained from very small CO_2 gas (< 0.05 μmol), however, there is no significant fluctuation depending on CO_2 gas volume. For the reason, we also used the carbon stable isotopic values obtained from very small CO_2 gas (0.05 ~ 0.4 μmol).

4.4. Results

4.4.1. Microstructures of protolith and pseudotachylytes

4.4.1.1. Host metamorphic rocks

Host metamorphic rocks in this area mainly consist of biotite, chlorite, muscovite, plagioclase, and quartz with minor amount of carbonaceous material, ilmenite and pyrite. 15~18 vol. % of phyllosilicates are contained in the host rocks based on the XRD semi-quantitative analysis. The main phase of phyllosilicates, biotite, has an Annite content in the range of 42 to 50% [Fe / (Fe + Mg)], depending on peak metamorphic condition and bulk geochemistry (Table 9). Plagioclase in the protolith show mean chemical composition of $Or_{0.9}Ab_{72.5}An_{26.6}$, suggesting an oligoclase composition in the ternary diagram of feldspar (Fig. 39, Table 9). In biotite gneiss, metamorphic graphite was usually observed along the cleavages of phyllosilicates or grain boundaries of quartz and plagioclase. Peak metamorphic temperatures of the Bt–Ms schist or gneiss have been estimated to be 523~596 °C using a Raman spectra of carbonaceous material thermometry (Nakamura et al. 2015).

4.4.1.2. Pseudotachylytes in fault rocks

The pseudotachylytes in fault rocks can be grouped into two types; Pst I and Pst II based on the occurrences, SEM observations, geochemical and spectroscopic analyses of lithic

and secondary minerals.

The Pst I veins are often observed as blackish injections and fault veins in cataclasite. Under the microscope, their blackish veins exhibit a cryptocrystalline texture, which are cut by a network of veins or open cracks with quartz filling (Fig. 41a). The Pst I matrix is composed of K-feldspar ($Or_{90}Ab_5An_5$, Table 9), hydroxide, titanite, pyrrhotite (N[FeS] = 0.92~0.93; Fig. 40, Table 10) and vesicles that hosted volatiles as secondary minerals, and lithic fragments of plagioclase and quartz as minerals that survived melting (Fig. 41b). The pressure solution cleavage in cataclasite demonstrated the concentration of titanite and other oxide minerals with phyllosicates, however, k-feldspar matrix cannot ovserved (Fig. 43a). Image analysis using BSE and EDS mapping indicate that the volume fraction of lithic fragments (φ) in Pst I matrix is relatively higher than that of the other types (φ: 18~52 vol. %, Fig 42). The microstructures and secondary minerals progressively change with increasing degree of frictional melting in each domain. The Pst II matrix have complex microstructures with biotite microlites (Figs. 41c-d), plagioclase spherulites (Figs. 41e-f) and numerous vesicles (Figs. 41g-h) within a restricted area of pseudotachylyte veins. Therefore, the microstructures in Pst II are subdivided into three microtextural domains; biotite microlite-dominant (MD), spherulite-dominant (SD) and vesicle-dominant domain (VD). The MD and SD in Pst II matrix systematically decrease the volume fractions of lithic fragments and secondary minerals (Fig 42). The partial melting textures such as embayment textures and spherulites of plagioclase are usually observed in K-feldspar matrix ($Or_{93}Ab_4An_3$, Fig. 43b; Table 9). Apatite shows a droplet texture. The chemical compositions of pyrrhotite slightly changes from Fe_7S_8 to Fe_9S_{10} structures (N[FeS] = 0.93~0.95; Fig. 40, Table 10). Notably, a characteristic melting texture that composed of "plagioclase-mantled K-feldspar ovoid" was observed in the spherulite-dominant domain (SD) of Pst II matrix (Figs. 41f and 43c). The spherulitic texture is similar to the “rapakivi texture” in igneous rocks (e.g. Eklund and Shebanov, 1999). The

cores of Rapakivi texture display a K-feldspar component ($Or_{94}Ab_4An_2$; Table 9) with the rim of plagioclase components ($Or_{10}Ab_{78}An_{12}$: Figs. 39 and 43c-d). The "pseudo-rapakivi texture" in pseudotachylyte is only observed near to the partially melted-plagioclase fragments (Figs. 43c-d), however, they do not form the microlitic textures due to a rapid cooling. Finally, almost all fragments are melted in vesicle-dominant domain (VD) of Pst II, where even the secondary minerals have also disappeared.

The Pst I veins are usually cut or injected by Pst II or other Pst I veins that have irregular boundaries in cataclasite (Figs. 44a-b). These wavy boundaries imply that the pseudotachylyte melt flowed due to the rapid volume increase of a fluid phase under a high fluid pressure exceeding local normal stress (Hadizadeh et al. 2012). The microstructures in pseudotachylyte are usually modified by networked or reworked dilation jogs with quartz filling in the fracture opening (Fig. 44c). In the dilation jogs with quartz filling, we could observe fluid inclusions of CH_4-H_2O composition (Fig. 44d). These observations suggest that the pseudotachylytes were generated by multiple frictional melting with large amount of fluids under a high fluid pressure and relatively low fO_2 during interseismic period. The cross-cutting relation between each subdomain in Pst II could not be distinguished. This suggests that the microstructural subdomains may have resulted from the heterogeneity of primary mineral assemblages and microstructures within a single rupturing stage.

4.4.2. Major and trace elements

XRF whole-rock major-element analyses of pseudotachylytes and cataclasite were carried out to assess the changes in bulk rock geochemistry within fault rocks during frictional melting. All major-elements were normalized by mean values of host metamorphic rocks (n = 4; Table 2). There are significant gains in CaO (+70 ~ +110 %), K_2O (+16 ~ +103 %),

and volatile components (LOI; +33 ~ +78 %) and depletion in Na_2O (–50 ~ –69 %), suggesting the breakdown of phyllosilicates and plagioclase by frictional melting (Fig. 45). The degree of mobilization of above major elements slightly changed from cataclasite to pseudotachylyte.

Given that various types of microstructures in pseudotachylytes are distributed in the millimeter scale, it is necessary to distinguish each melting domain from slab sections and prepare the powder samples using a microdrill under a binocular microscope. The concentrations of trace element obtained in the selected millimeter scale area are listed in Table 11. All trace elements were normalized by data of protolith, which were concurrently prepared using same producers (Table 11). Our data exhibited significant enrichments of Rb (+195 ~ +258 %), Sr (+119 ~ +213 %) and Ba (+153 ~ +532 %) in Pst I matrix (Fig. 46a). Similar enrichments of Rb (+129 ~ +309 %), Sr (+70 ~ +201 %), and Ba (+84 ~ +275 %) were also observed in Pst II matrix (Fig. 46b). In general, Rb, Sr and Ba represent large-ion lithophile (LIL) elements, which are enriched in biotite. Such significant gain of Ba from 662 to 4187 ppm can be suggested by selective non-equilibrium melting and solidification from biotite melt. In addition to LIL elements, significant gain of high field strength (HFS) elements were partly observed. The HFS elements are difficult to move between melt and minerals, therefore, relative enrichments HFS elements by volume increase are deduced. In fact, the microstructures of open crack and dilation jogs with quartz filling are key evidence for volume increase during paleoseismicity. On the other hand, the fluctuations of trace elements in cataclasite is much less than that in pseudotachylytes (Fig. 46a). This suggest that the significant fluctuations of trace elements arise from the selective frictional melting of phyllosilicates in pseudotachylytes. This may be a potential indicator to identify the evidence of frictional melting in altered pseudotachylytes.

4.4.3. Carbon isotopic variation of graphite

I found that graphite inclusions occur as micrometer size inclusions in plagioclase spherulites of Pst II matrix (Figs. 47a-b). Such graphite inclusions are associated with titanite and hydroxyapatite, which are identified using micro-Raman spectroscopy (Fig. 47c). Host metamorphic graphite has already transformed into large hexagonal platy graphite by graphitization (Nakamura et al. 2015), whereas those graphite inclusions occurring in the spherulitic domain display a globular shape (Fig. 47b). Micro-Raman spectroscopy of the graphite inclusions revealed lower crystallinity than those in the host rock (Fig. 47d). These data imply a prominent difference in morphological characteristics between metamorphic graphite and graphite inclusions, similar to those reported in earlier studies (e.g. Barrenechea et al. 2009).

Bulk analyses of powdered samples in pseudotachylyte-bearing cataclasites demonstrated wide ranges of carbon stable isotopic values between –22.5 and –27.1 ‰, therefore, we conducted the rock powder analyses including graphite obtained from the polished slab in protolith, cataclasite, Pst I and Pst II domains (Fig. 48a). Carbon stable isotopic compositions of disseminated graphite in protolith range between between –24.2 and –25.9 ‰, suggesting the biogenic origin. Likewise, the graphite in the cataclasite, ultracataclasite, and Pst I matrix show the similar carbon isotopic values between –24.6 and –25.8 ‰ (Fig. 48a; Table 12). On the other hand, the carbon isotopic values of graphite inclusions in Pst II ranged between –18.2 and –25.4 ‰. On the other hand, the carbon isotopic values of graphite inclusions in Pst II ranged between –18.2 and –25.4 ‰. On average these values are heavier in the order of +2 ~ +3 ‰ than those from the host metamorphic graphite. The volume fraction of elemental carbon (TOC) systematically increases with the shifts in the $\delta^{13}C$ values from Pst I to Pst II (Fig. 48b). In addition, the majority of the graphite having higher $\delta^{13}C$ values are selectively distributed in the

restricted domains, such as spherulite, microlite and vesicle domain (Fig. 49). These data suggest that the metamorphic graphite in the protolith was incorporated into the COHS fluid phase in pseudotachylyte silicate melt by frictional melting, and then re-precipitated as a "fluid deposited graphite" with hydrous minerals during quenching stage. The carbon isotopic variations of fluid deposited graphite in pseudotachylyte veins in this study are well consistent with the distribution of the fluid-deposited graphite in magmatic sulfide deposits of HMB (Oshirabetsu mine: Tsuchiya et al., 1991; Luque et al., 2014; Horoman mine: Tomkins et al., 2012; Fig. 48a). Those graphite mines were located in the southern part of HMB and formed by crustal contamination between mudstone in Nakanogawa group and Oshirabetsu gabbro through magma mixing and assimilation process (Tomkins et al., 2012). Both fluid deposited graphite spherules are originated from the biogenic carbon in Nakanogawa group and regarded as the same source in graphite-bearing pseudotachylyte of HMB (Tsuchiya et al., 1991). These data may suggest that the precipitation process of fluid deposited graphite in both samples underwent the similar redox state and fluid speciation owing to supersaturation from COHS fluids.

4.5. Temperature estimates during frictional melting

The temperature estimates during frictional melting are essential to deduce the COHS fluid speciation in pseudotachylyte melt and their redox state. Based on the microstructures of the survived and melted minerals in each type of pseudotachylyte matrix, I tried to estimate the minimum frictional melting temperatures. In the Pst I matrix, the phyllosilicates are completely melted by frictional melting, whereas the plagioclase and quartz has remained as relicts. Trace element analysis strongly supports these microstructural observations. Our observations suggest that the Pst I veins are mainly generated by dehydration melting of biotite and muscovite between 650 and 1100 °C

utilizing the experimental data of Spray (1992) and Mariani et al. (2006). In contrast, not only phyllosilicates but also quartz, plagioclase, and apatite are absent in Pst II. These minerals have been completely melted or partially melted to form embayment textures. The only phase that is remaining is zircon. These observations suggest that the Pst II pseudotachylytes are generated at temperatures of around 1100~1400 °C by breakdown of plagioclase and apatite (Spray, 1992). In addition, the minimum melting temperatures of 1077~1192 °C, independently estimated using *MELTS* software is also consistent (Table 2; Ghiorso and Sack 1995).

A significant evidence for the variations in the melting conditions is the presence of the pseudo-rapakivi texture in Pst II, which provide additional constraints on quenching temperature from the exsolution of two feldspars in pseudotachylyte silicate melt. Assuming that the plagioclase and K-feldspar are in equilibrium during the formation of pseudo-rapakivi textures, two feldspar thermometry in Pst II matrix gave exsolution temperatures between 554 and 616 °C (Putirka, 2008).

4.6. Discussion

4.6.1. Dynamic fluctuation of redox state during paleoseismicity

Numerous studies have suggested that frictional melting during seismicity is a disequilibrium process. Such a selective frictional melting will generate different pseudotachylyte melts as a function of bulk chemistry of melting minerals (Spray 1992; DiToro et al. 2009). On the other hand, O'hara and Huggins (2005) has pointed out that the disequilibrium melting is a whole rock scale phenomenon and can be regarded as "local equilibrium melting" on the grain scale or in texturally isolated micro domains. In fact, this concept has been the basis for several studies including successful application of

geothermometers (Toyoshima et al. 1990; Moecher and Steltenpohl, 2009), oxygen isotopic study (O'hara and Sharp, 2001) and ^{40}Ar / ^{39}Ar dating method (Wenk et al. 2000).

We have also adopted the "local equilibrium" concept for estimating the redox state and carbon isotopic compositions in each microstructural domain within the pseudotachylyte using the *P-T-f*O_2-*f*S_2 phase diagram (Fig. 50). The microstructures and secondary mineral assemblages are strongly driven by the redox state and *f*S_2 in each domain. Under a low-temperature condition (650–1100 °C) in the Pst I matrix, biotite and muscovite in the host metamorphic rocks are selectively melted by frictional melting and generate the mafic melt enriched in Fe and H_2O. The thermal decompositions of biotite coexisting with graphite and sulfide minerals are deduced by following reactions (Tracy and Robinson, 1988);

Annite in biotite + 3Pyrite = Sanidine + 6Pyrrhotite + H_2O + 1.5O_2 or (1)

Annite in biotite + 3Pyrite + 1.5Graphite = Sanidine + 6Pyrrhotite + H_2O + 1.5 CO_2 (2)

In the case of breakdown of biotite and pyrite in pseudotachylytes, it is important to distinguish the breakdown of graphite because it acts as a reducing agent. There are two possibilities for dehydration-redox reactions: graphite-free (1) or graphite-bearing (2) (Fig. 50). Former process arises from the oxidation of pseudotachylyte melt, whereas latter results from the reduction owing to graphite oxidation which serves as a redox buffer. In experimental studies, chemical kinetics of graphite oxidation is strongly depended on temperature, *f*O_2, active surface area and activation energies for the adsorption of oxygen and the desorption of CO and CO_2 gasification. Notably, CO_2 gasification from graphite exponentially increases at over 800 °C, changing the rate determining step of graphite oxidation (El-Genk and Tournier 2011). Hence, it is suggested that the graphite-bearing dehydration reaction is depended on the peak

frictional melting temperature. In the case of Pst I matrix, there are no clear evidence for reduction by breakdown of graphite, suggesting the possibility of graphite-free dehydration-redox reaction. This indicates that the selective frictional melting of biotite and pyrite produced relatively oxidized pseudotachylyte melt due to the production of $H_2O + O_2$ (Fig. 50). According to fO_2-fS_2 diagram at 700 °C (Fig. 50), the dehydration of biotite is mainly driven by melting temperature, fS_2, and fO_2. Pressure dependence, especially between 1 kbar and 2 kbar, has much less influence than other factors. In the case of pseudotachylytes originated from metasedimentary rocks, phyllosilicates and sulfide minerals were converted into pyrrhotite + Kfs assemblages by sulfidation rather than oxidation (Fig. 50). This suggests that the stable phase of ferric minerals derived from pseudotachylyte melt is controlled by not only fO_2 but also fS_2. Similar mineral assemblages in pseudotachylytes were also reported by Maglouhlin (2005), and such dehydration-redox reactions incorporating sulfide minerals might be common in metasediments.

Under a high-temperature condition (1100–1400 °C) in the Pst II matrix, not only mafic minerals but also other felsic minerals such as quartz and feldspars begin to melt by frictional heating. Because oxidation rate of graphite exponentially increases by temperature, the host metamorphic graphite could be rapidly converted to CO_2–H_2O or CH_4–H_2O fluids by graphite-bearing dehydration-redox reaction (2). The oxidation of graphite changes the redox state to a reduced pseudotachylyte melt as a result of absorption of free oxygen. In fact, pyrrhotite + Kfs assemblages change to Bt microlite + Kfs in Pst II matrix (Fig. 41c). In the *P-T*-fO_2-fS_2 phase diagram, the stable phases should shift to lower fO_2-fS_2 space than those in the Pst I. Unfortunately, it was difficult to directly estimate the fluid species and redox state at peak temperature of frictional melting, instead they were estimated during the precipitation stage of fluid deposited graphite. The moderate carbon isotopic shift of + 2 to + 3‰ from host metamorphic graphite, could be

interpreted by supersaturation from COHS fluids in pseudotachylyte melt. The effects on the carbon isotope fractionation can be evaluated from graphite-fluid fractionation factors (Poulson, 1996) and the expression for fluid-composition dependence (Duke and Rumble, 1986). Assuming the carbon isotopic composition of newly formed graphite equilibrated at 600 °C (quenching temperature), the calculated mole fraction of xCO_2 (= CO_2 / CH_4 + CO_2) ranges between 0.12 and 0.03, suggesting H_2O-CH_4 is the dominant fluid, based on the estimated ideal fluid mixing model using *Perplex* 6.7.1 software (Connolly and Cesare 1993). The calculated fO_2 based on fluid speciation is estimated to be between –21.6 and –22.0 $\log_{10}$ units (Fig. 51a). When COH fluid encounters the graphite saturation surface with the decrease in temperature, graphite begins to precipitate along with hydrous silicates such as hydroxyapatite and titanite by supersaturation (Figs. 51b-c). A wide range of carbon isotopic variation is possible in fluid deposited graphite by small fluctuations of mole fraction H_2O (xH_2O) (Duke and Rumble 1986). The co-precipitation of graphite with hydrous minerals have been often reported in igneous occurrences (e.g. Papineau et al. 2010; Tomkins et al. 2012). Such a similar process in pseudotachylyte is reported here for the first time. Altogether, the data suggest that the redox state in the Pst II matrix was relatively in a low fO_2 environment, which ranges between ΔFMQ –1.6 and – 2.0 (Figs. 51a-c).

Overall, the fluid estimations based on the breakdown of graphite and hydrous minerals provided an important evidence for a frequent fluctuation of local redox state and fluid speciation during paleoseismicity. In general, reduced fluid were generated by the mechanochemical reaction on the fault slip surface and serpentinization of mantle and oceanic crust beneath the accretionary complex owing to the production of H_2 (Kita et al. 1982; Yamaguchi et al. 2011). In this study, I revealed that the breakdown of graphite and organic materials also act as a reducing agent and one of the source for reduced fluids during seismic cycle.

4.6.2. Implication for fault degassing and precipitation during seismicity

The most important implication of this study is that the redox state in both types of pseudotachylyte is controlled by graphite breakdown. The data suggest that graphite requires a minimum melting temperature of ~ 1100 °C by frictional heating. This may result from the rate of graphite oxidation which controlled by peak frictional temperature. Based on the microstructural observations and microscale-geochemical analyses, we present two possibilities of redox state in pseudotachylytes (Fig. 52). For graphite-free pseudotachylyte of igneous origin, magnetite + Kfs or hematite + Kfs assemblages were usually observed as secondary minerals (e.g. Petrik et al. 2003; Takagi et al. 2000). These oxide mineral assemblages can be expressed by ASM (Annite = Sanidine + Magnetite + H_2) equilibrium in O–H fluid (Wones and Eugster 1965). It can be estimated that the pseudotachylyte without a reducing agent becomes oxidized and produce CO_2 + H_2O in COH fluids. In fact, O'hara and Huggins (2005) have reported that magnetite-bearing pseudotachylytes plot at about +2 ~ +4 $\log_{10}$ units above fayalite-magnetite-quartz buffer (ΔFMQ +2 ~ +4), and hematite-bearing pseudotachylytes plot +3.5 $\log_{10}$ units above the hematite-magnetite (HM) buffer. On the other hand, the graphite-bearing pseudotachylyte of metasedimentary origin in this study obtained –1.6 ~ –2.0 $\log_{10}$ units below the FMQ buffer (ΔFMQ –1.6 ~ –2.0). These fO_2 suggest that the local redox state and fluid speciation in pseudotachylyte melt are driven by presence of graphite. As graphite begin to oxidize, the dehydration-redox reaction produces relatively reducing COHS fluid, suggesting CH_4–H_2O fluid. These processes result in the fault degassing during frictional melting and reprecipitation of fluid deposited graphite during quenching. Note that it is difficult to deduce the carbon budget based on the bulk CHN analysis of fault rocks because the relative deviations of major and trace elements suggest volume increase. However,

Tomkins et al. (2012) has reported that reduced felsic magma has a sufficient potential for the reduction of oxidized mafic magma by even small amounts of graphite (0.5–1.0 %) based on magma mingling model. The variations in the TOC values of ~1.0 wt. % by frictional melting in our samples suggest a potential for control of the redox state in pseudotachylyte melt by mingling of compositionally differing felsic and Fe-enriched mafic melts. Pseudo-rapakivi textures might be an evidence for mixing between quartz and plagioclase-origin melt and phyllosilicate-origin melt in millimeter scale. In addition, the TOC values also fluctuate between protolith and pseudotachylytes, therefore, a part of COHS fluids may have discharged to the fault zones as H_2O–CO_2 or H_2O–CH_4 fluids (Fig. 52). Pattison (2006) has reported that COH fluid is easily buffered by conversion of even small amount of graphite to fluid phase (less than 0.1 wt. %). Our study demonstrates that small amount of graphite (including carbonaceous materials) in sedimentary rocks can also act as a CO_2 or CH_4 source during fault degassing, in addition to carbonate minerals as reported by Famin et al. (2008). If the precursor of graphite is organic materials, it is expected to produce ^{12}C enriched carbon by frictional melting of sediments. The presence of reduced carbon by frictional melting can also substantiate the production of wide variety of carbon fluid species and isotopic variations by mixing with the available oxidized carbon-bearing fluid species (e.g. CO_2^{3-}, HCO_3^{2-}) derived from carbonate minerals. In fact, previous studies have reported that isotopically light carbon as well as varying carbon speciation are monitored along active fault zones (Lewicki and Brantley, 2000) and geochemical anomalies after large earthquakes (Sato and Takahashi, 1997; Miller et al. 2004). Thus, graphite breakdown by frictional melting is key to understanding carbonic fluid migration and fluid speciation along active fault zone and potential source for ^{12}C enriched carbon during seismic activity.

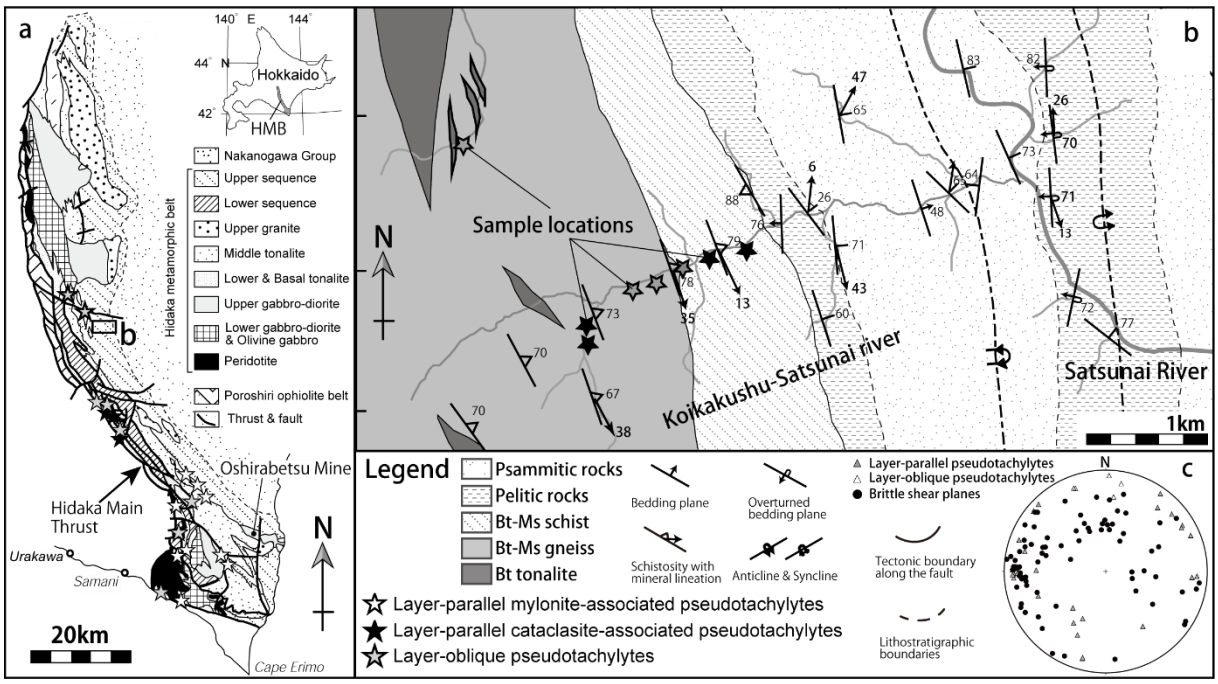

Figure 37. (a) Simplified Geological map of Hidaka metamorphic belt in Hokkaido, compiled from Toyoshima et al. (2004) and Nakamura et al. (2015). **(b)** The detailed route map and **(c)** lower-hemisphere projections of poles to brittle shear planes (black-filled circles), layer oblique pseudotachylytes (triangles) and layer parallel pseudotachylytes (grey-filled triangles).

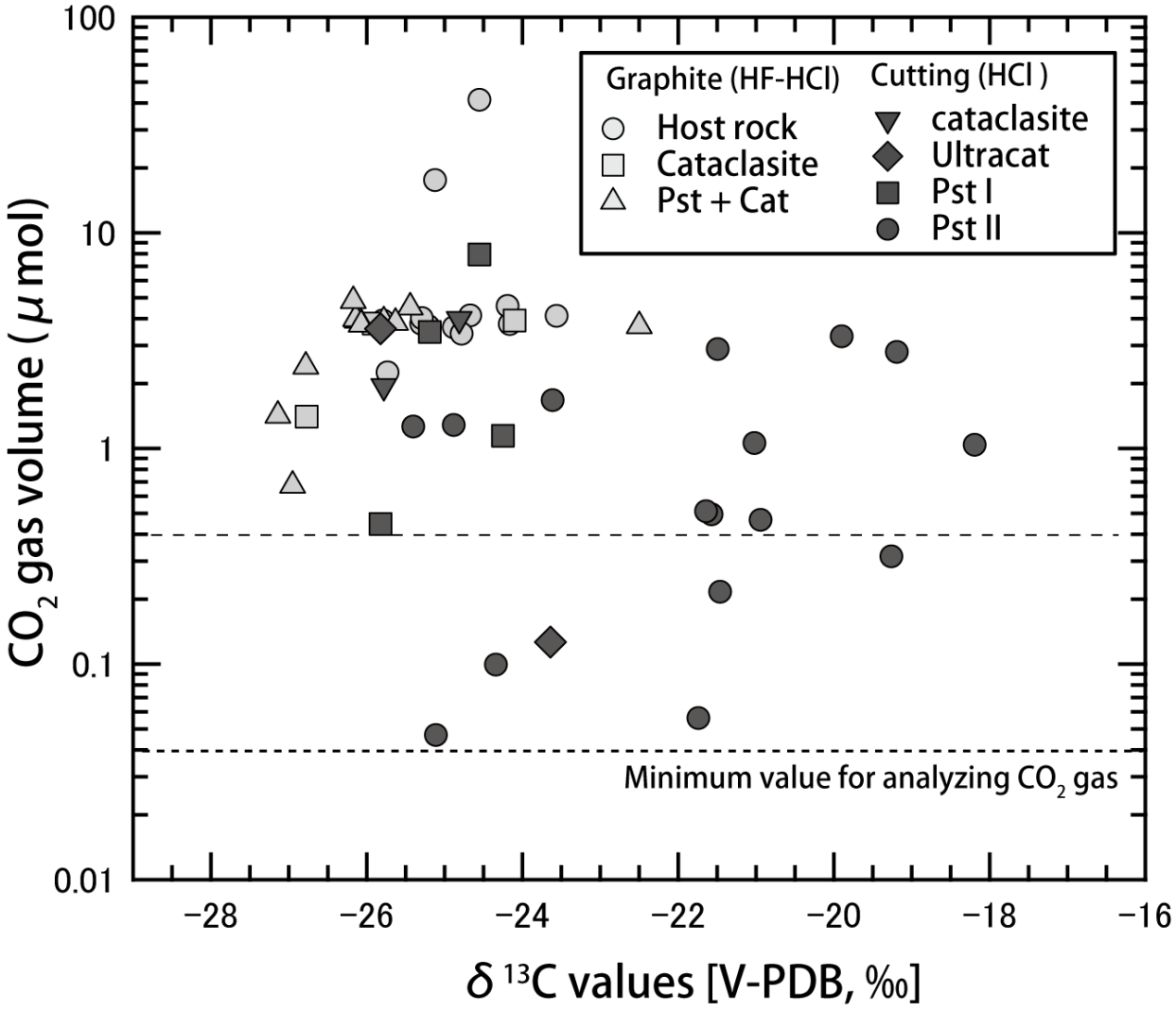

Figure 38. Relationship between CO_2 gas volume and $\delta^{13}C$ values. There are no significant trend depending on the gas volume.

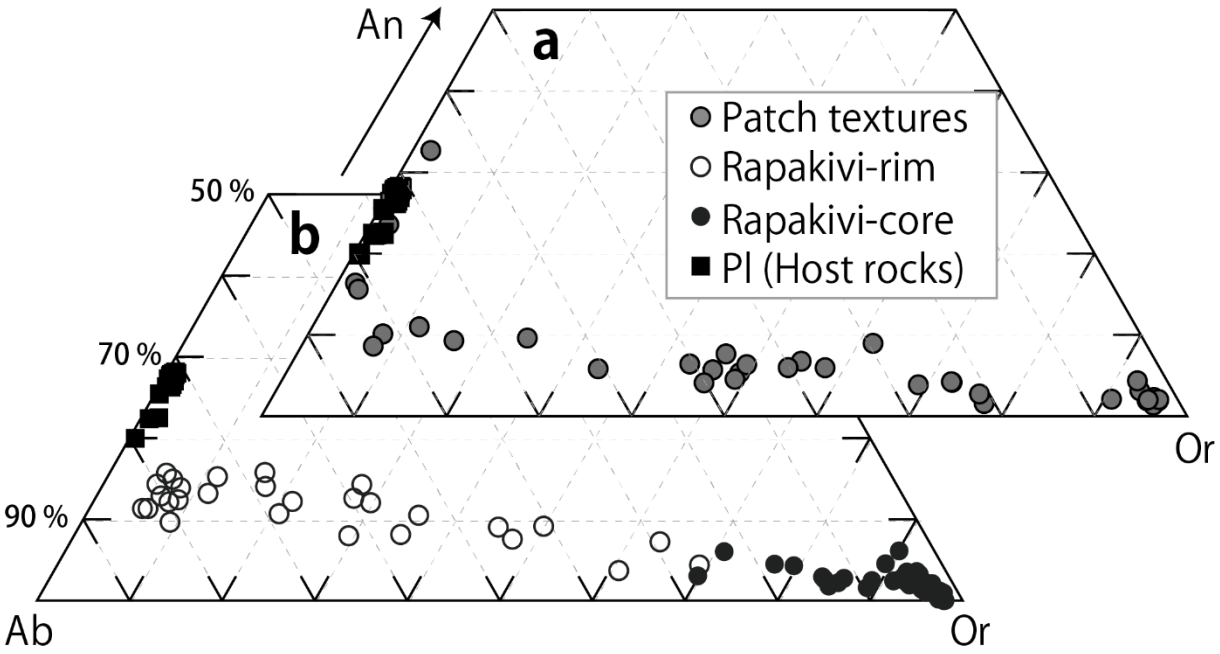

Figure 39. Ternary composition diagram for the patch textures **(a)** and pseudo-Rapakivi textures **(b)**. Four different areas are analyzed; gray circle, patch texture; white circle, core of Rapakivi texture; black circle, rim of Rapakivi texture; black square, plagioclase in host rocks.

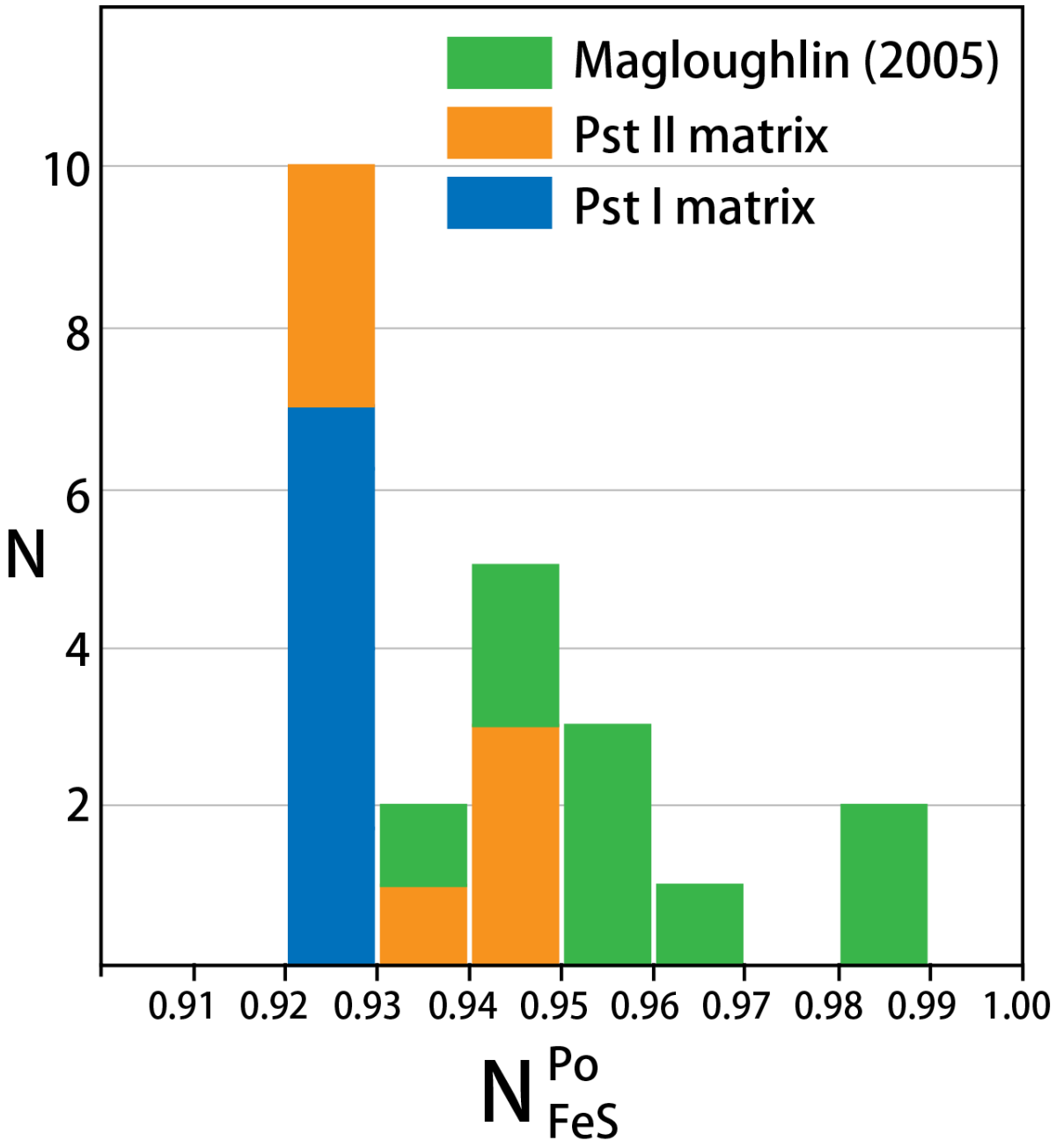

Figure 40. Histogram of pyrrhotite components (N[FeS]) in pseudotachylyte matrix. Green blocks are listed by Magloughlin (2005) for reference.

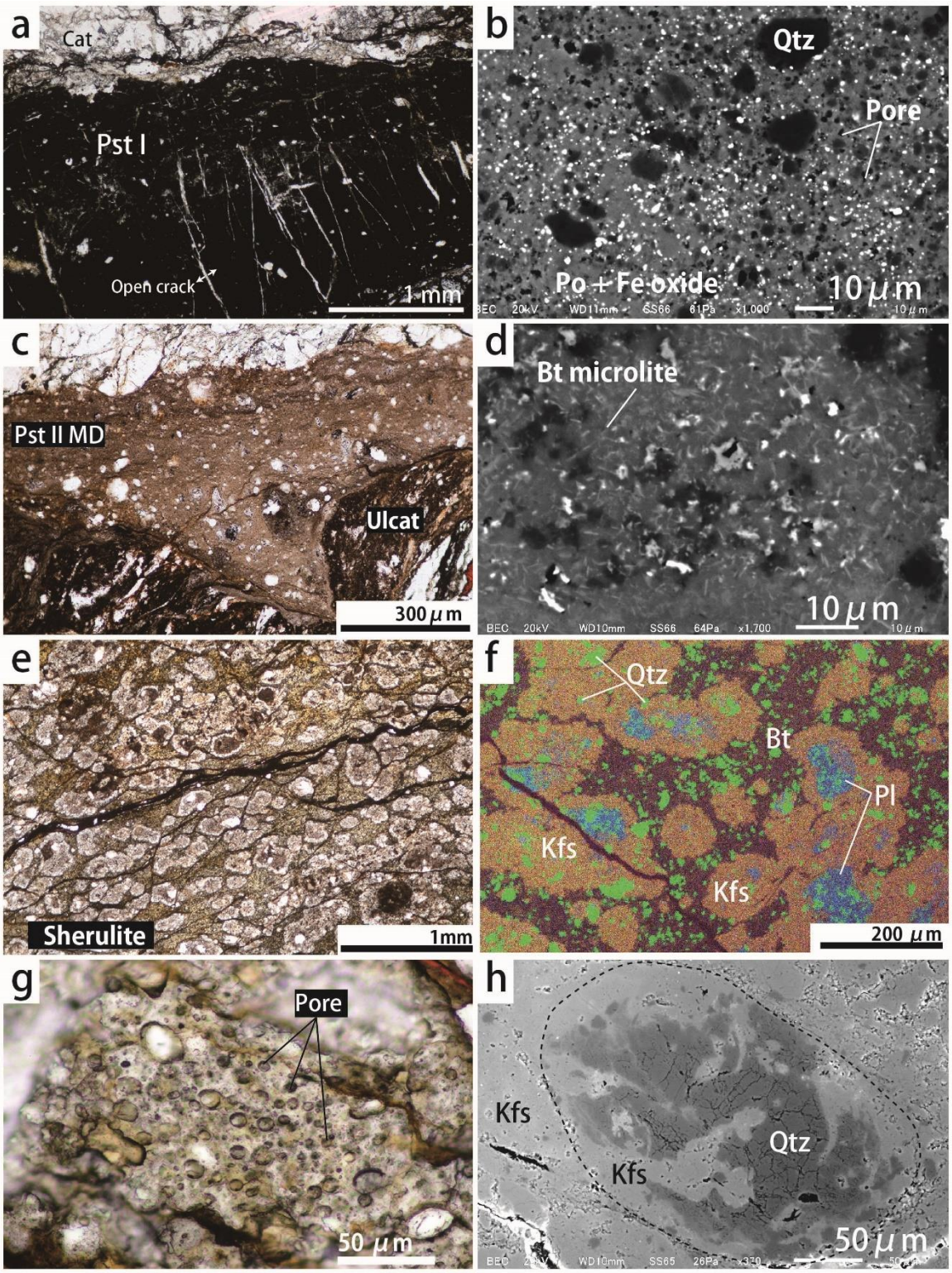

Figure 41. Photomicrographs and back-scatted electron images of representative microstructures in the pst I domain **(a-b)**, pst II microlite dominant domain **(c-d)**, pst II spherulitic dominant domain **(e-f)**, and pst II vesicle dominant domain **(g-h)**, respectively.

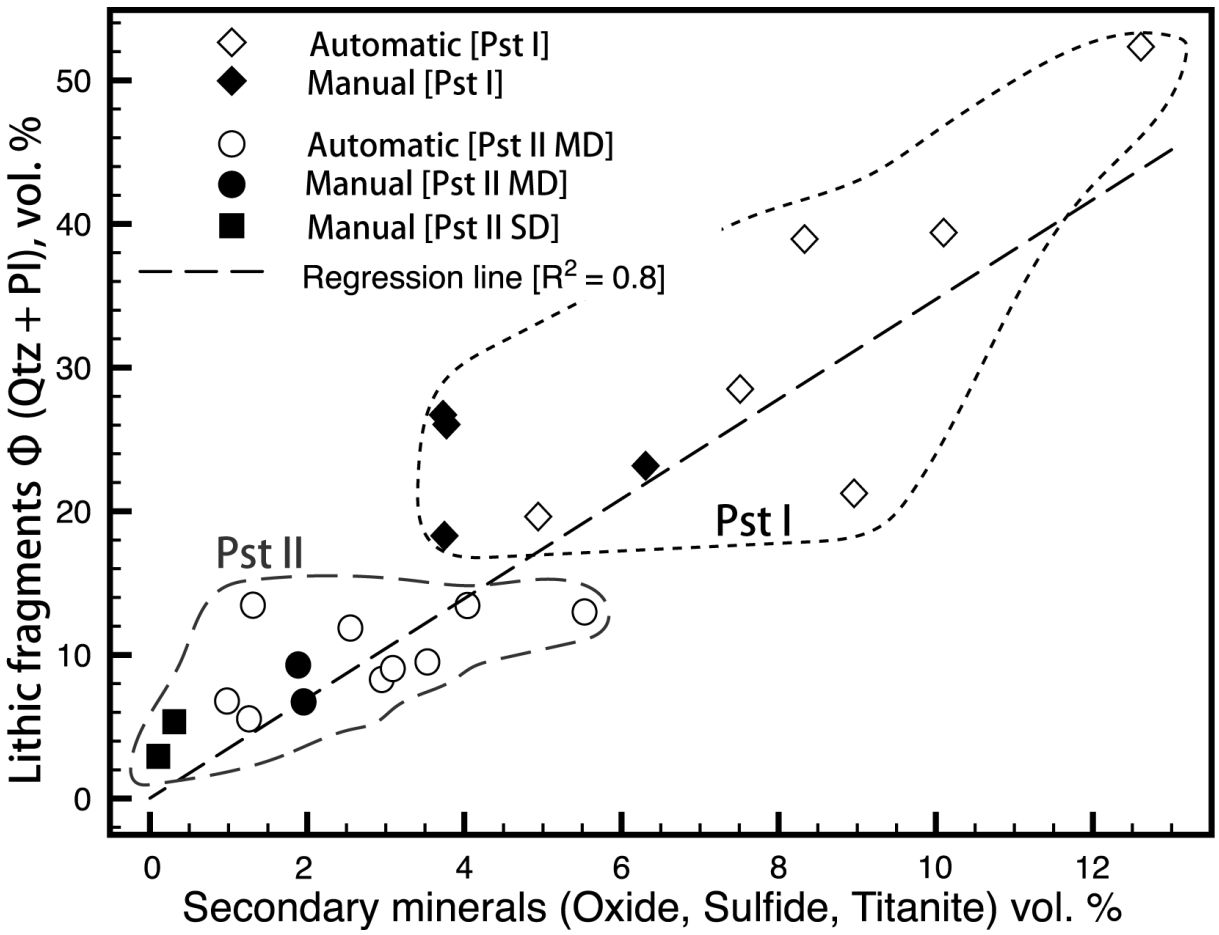

Figure 42. Relationship between lithic fragments of quartz and plagioclase (φ) and secondary minerals (oxide, sulfide and titanite). Dotted line is the regression line of all data.

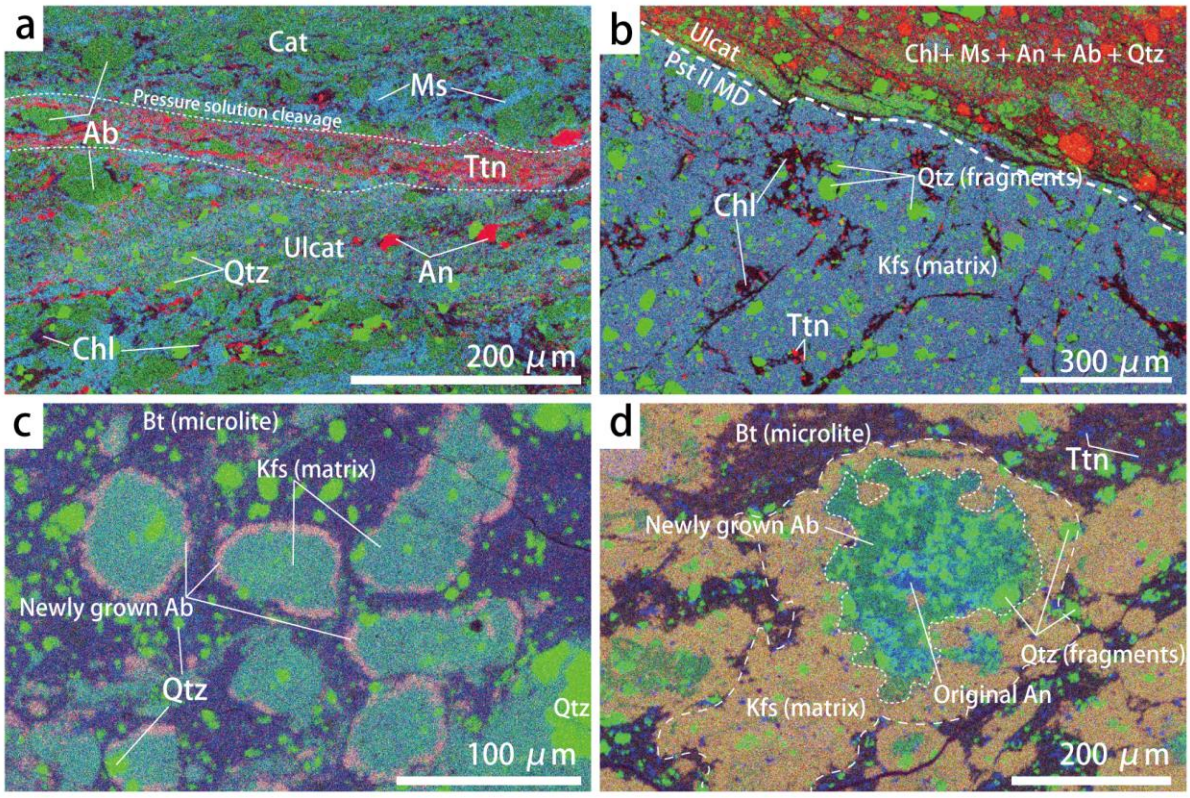

Figure 43. (a) Qualititative map of pressure solution cleavage by EDS analysis constructed with Ca (red), Si (green) and Al (blue). **(b)** Qualititative map of Pst II matrix by EDS analysis constructed with Ca (red), Si (green) and K (blue). **(c)** Qualititative map of pseudo Rapakivi textures by EDS analysis constructed with Na (red), Si (green) and K (blue). **(d)** Qualititative map of pseudo spherulites by EDS analysis constructed with K (red), Si (green) and Na (blue).

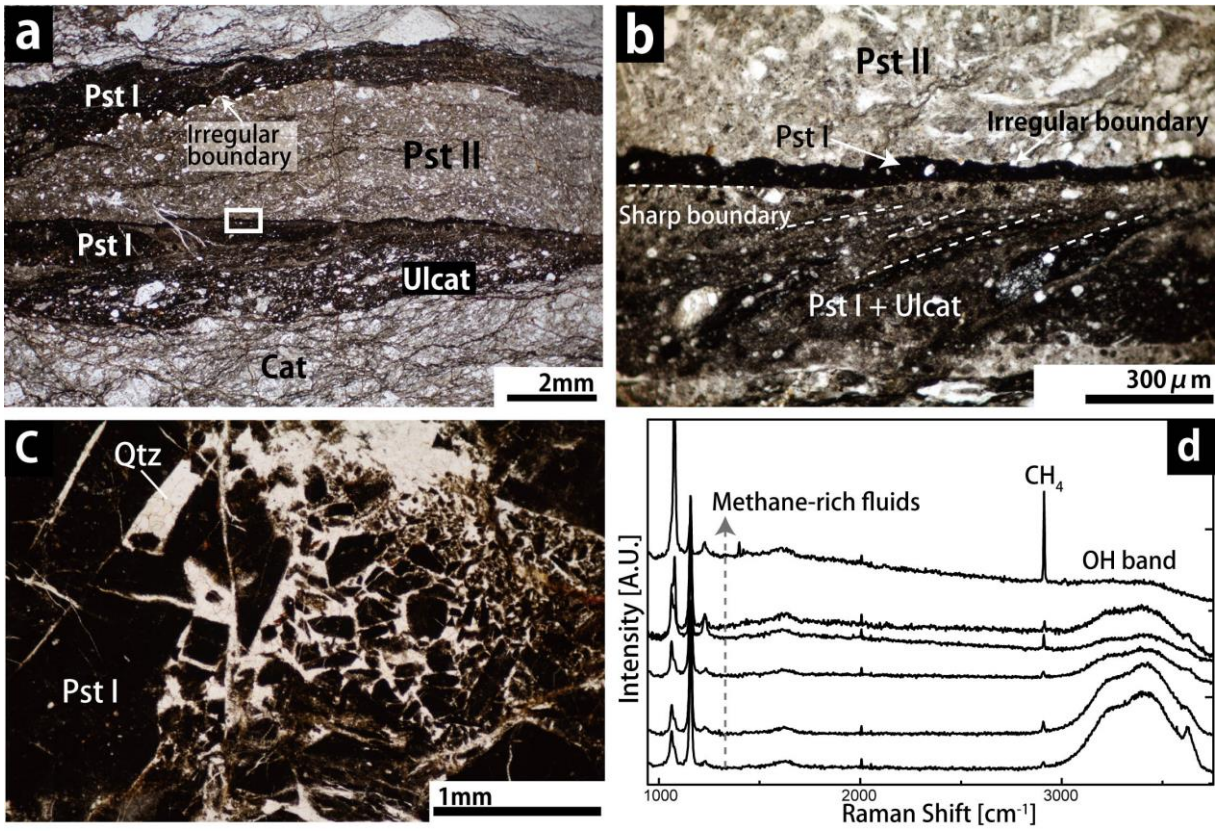

Figure 44. Optical images of pseudotachylyte textures and cross-cutting relationships between Pst I and Pst II in cataclasite. **(a)** Pst II fault vein cutting a Pst I vein. Irregular boundaries are observed between Pst I and Pst II fault veins. **(b)** High magnification image of cross-cutting relation between Pst I and Pst II fault veins. Ultracataclasite with Pst I fragments are sharply cut by Pst I vein, whereas, illegular boundary between Pst I and Pst II veins are observed. **(c)** A reworked dilattion jog with quartz filling in Pst I matrix. In the quartz filling, a lot of fluid inclusions of CH_4-H_2O **(d)** are found using micro-Raman spectroscopy.

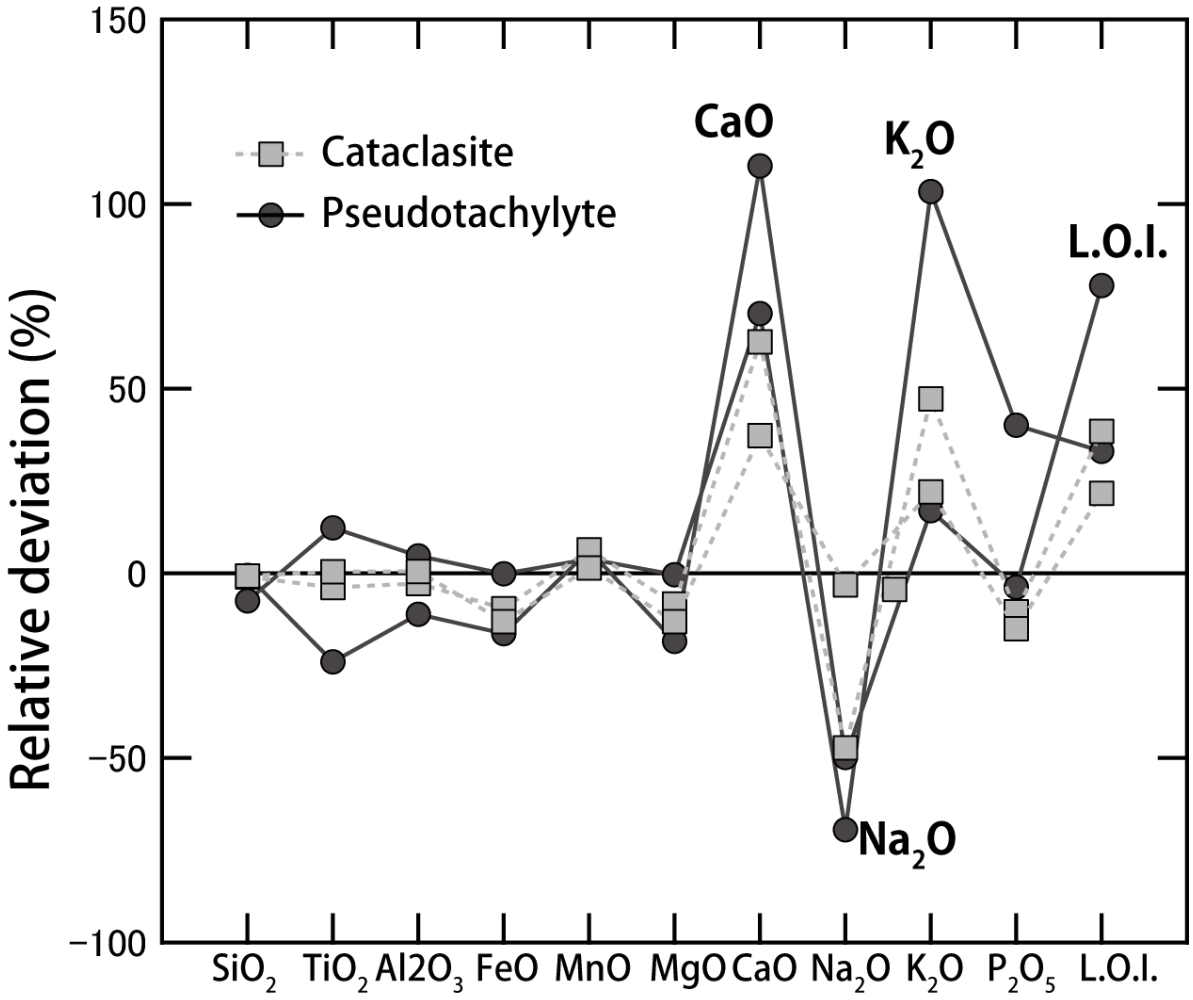

Figure 45. Major element anomalies of pseudotachylyte and cataclasite normalized by averaged host rock bulk chemistry (n = 4).

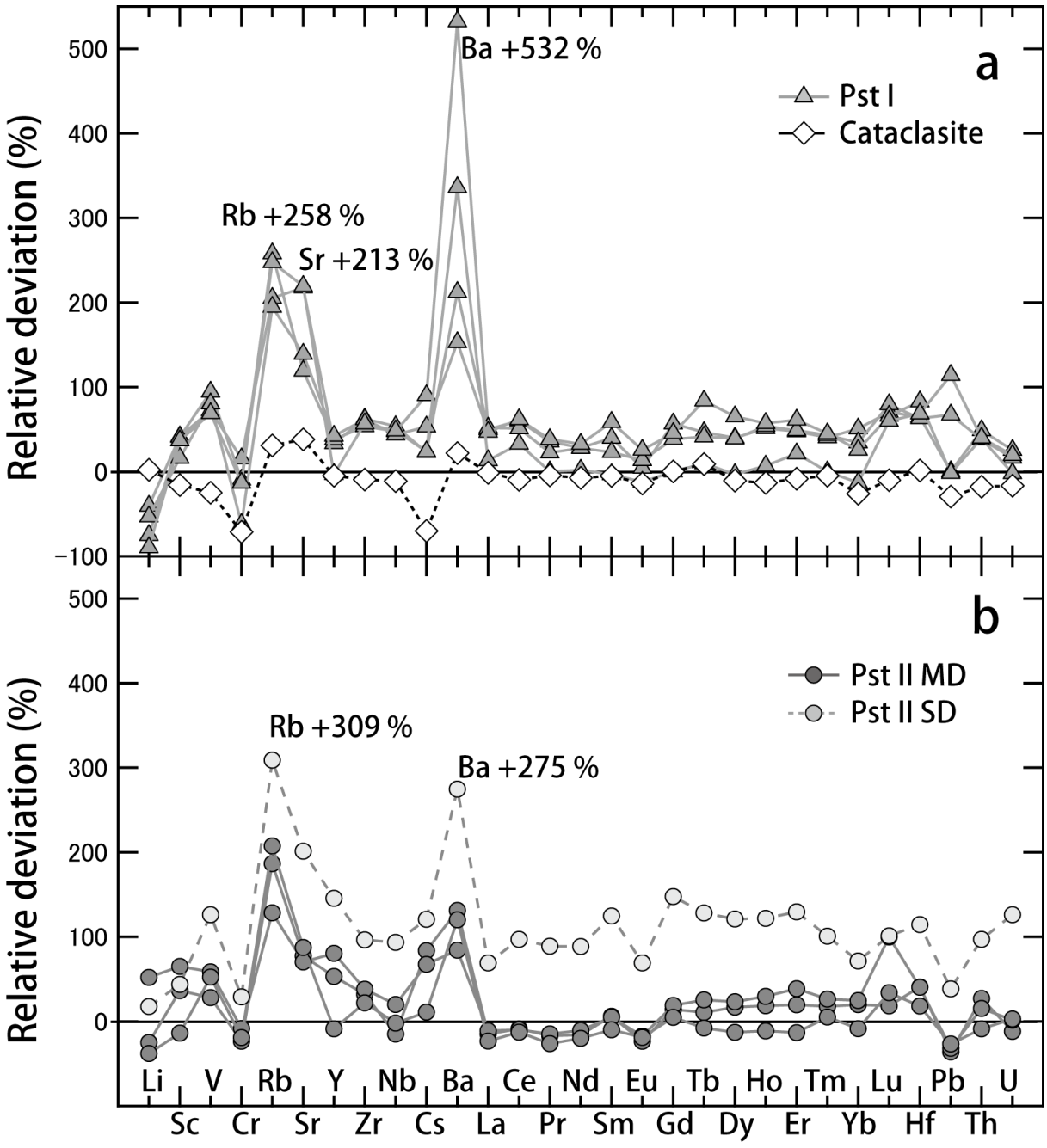

Figure 46. Trace element anomalies of representative Pst I and cataclasite, normalized by bulk geochemistry of biotite gneiss. Relative deviation (%) of each trance elements was calculated as follows: [(pseudotachylyte – protolith) / protolith] × 100.

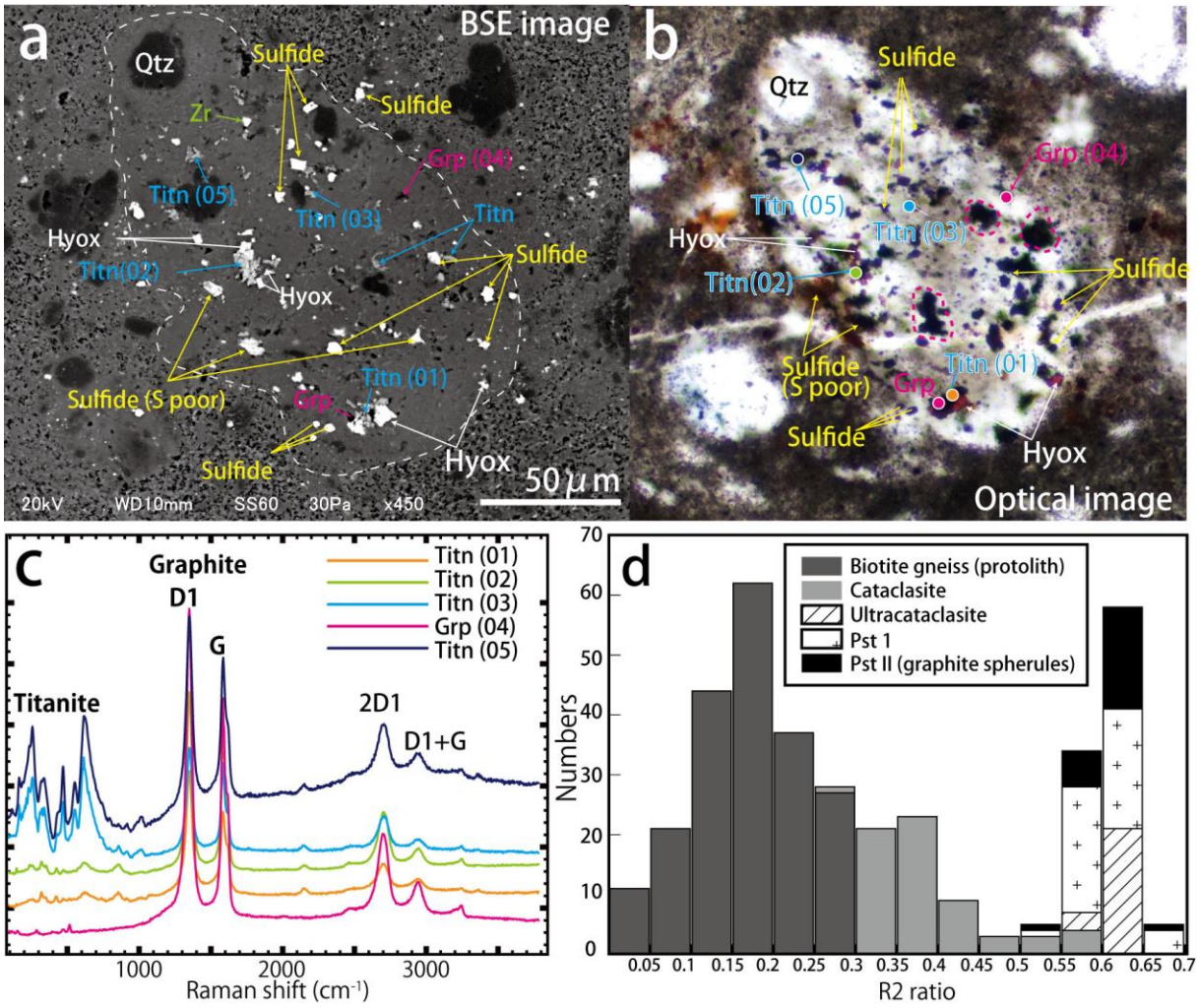

Figure 47. Microstructural characteristics of solid inclusions in pseudotachylyte matrix. BSE image **(a)** and optical image **(b)** of sulfide minerals, graphite (Grp), titanite (Titn), hydroxide (Hyox), and zircon (Zr) in K-feldspar with biotite microlite. Graphite spherules in pseudotachylyte show a lowest *Z* contrast in BSE images and blackish color in optical image. Dotted circles are also identified as graphite spherules. **(c)** Raman spectra of selected points in fig. 46b, showing G (~ 1580 cm^{-1}) and D1 bands (~ 1350 cm^{-1}) with titanite and hydroxyapatite. **(d)** Degree of graphitization of each graphite grain. R2 ratio is calculated from area ratio of (D1 band) / (G + D1 + D2 band). Spherulitic graphite grains show different crystallinity to the host metamorphic graphite and pulverized graphite in cataclasite (data from Nakamura et al. 2015).

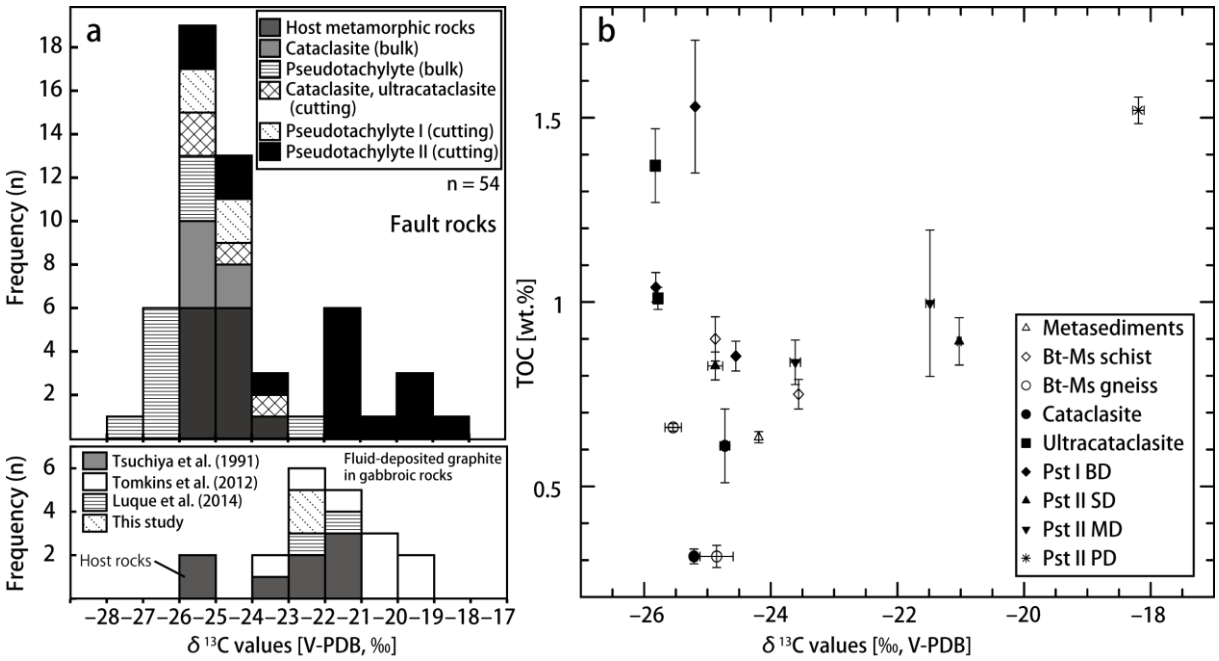

Figure 48. (a) Distribution of carbon isotopic compositions of the graphite, cutting from different microstructural domains. The lower portion of histogram is shown in the carbon isotopic compositions of fluid-deposited graphite from graphite mines in Hidaka Metamorphic Belt (Oshirabetsu mine; Tsuchiya et al. 1991 and Luque et al. 2014; Horoman mine; Tomkins et al. 2012). The fluid deposited graphite in both areas is derived from same host biogenic graphite in Nakanogawa formation. **(b)** Relationship between Total of Organic Carbon (TOC) values and carbon isotopic composition in each microstructural domain

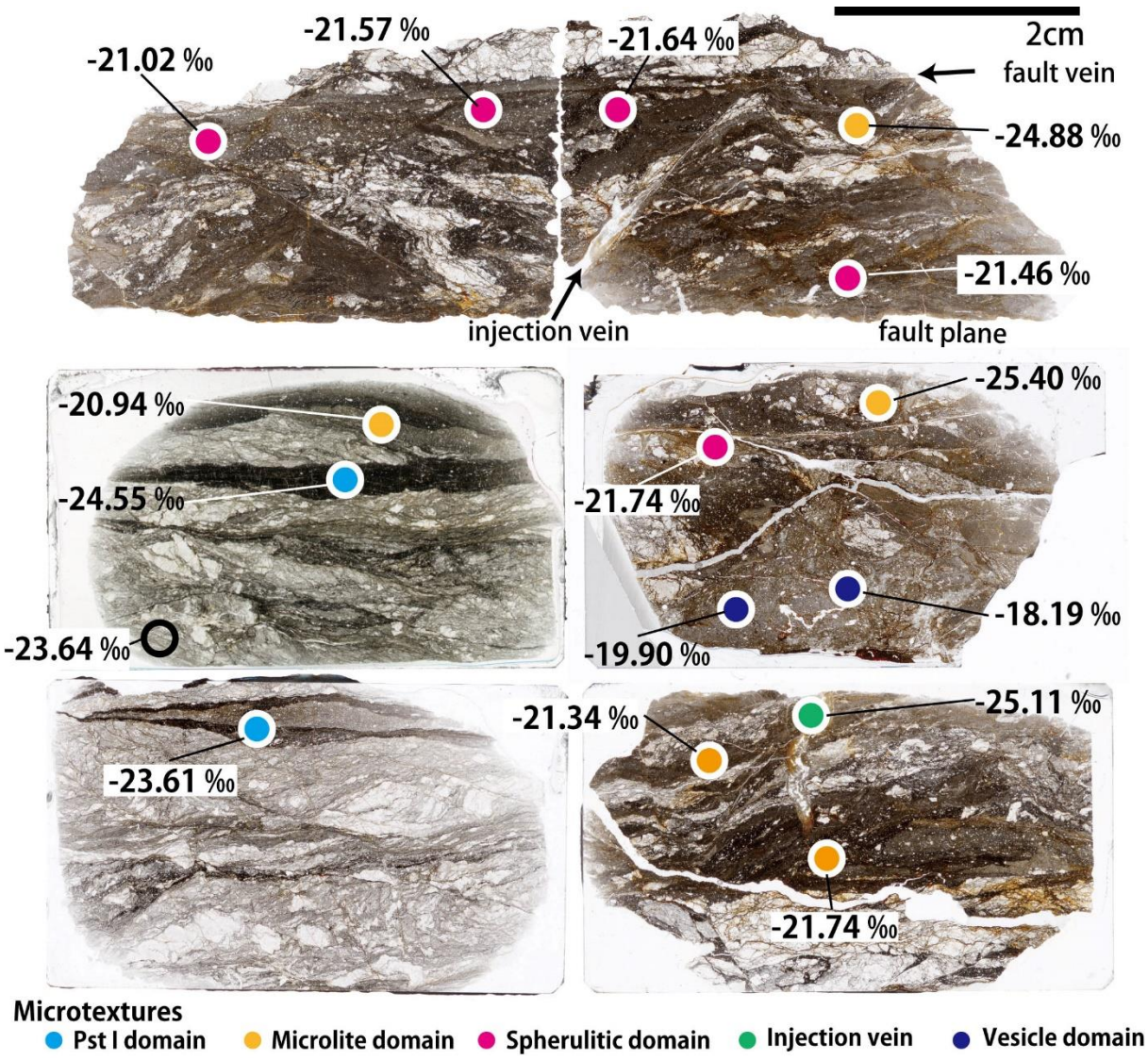

Figure 49. Spatial distributions of representative $\delta^{13}C$ values of graphite on the polish slab sections. These thin sections were prepared for same polishing slab sections that was cut for carbon isotopic analyses.

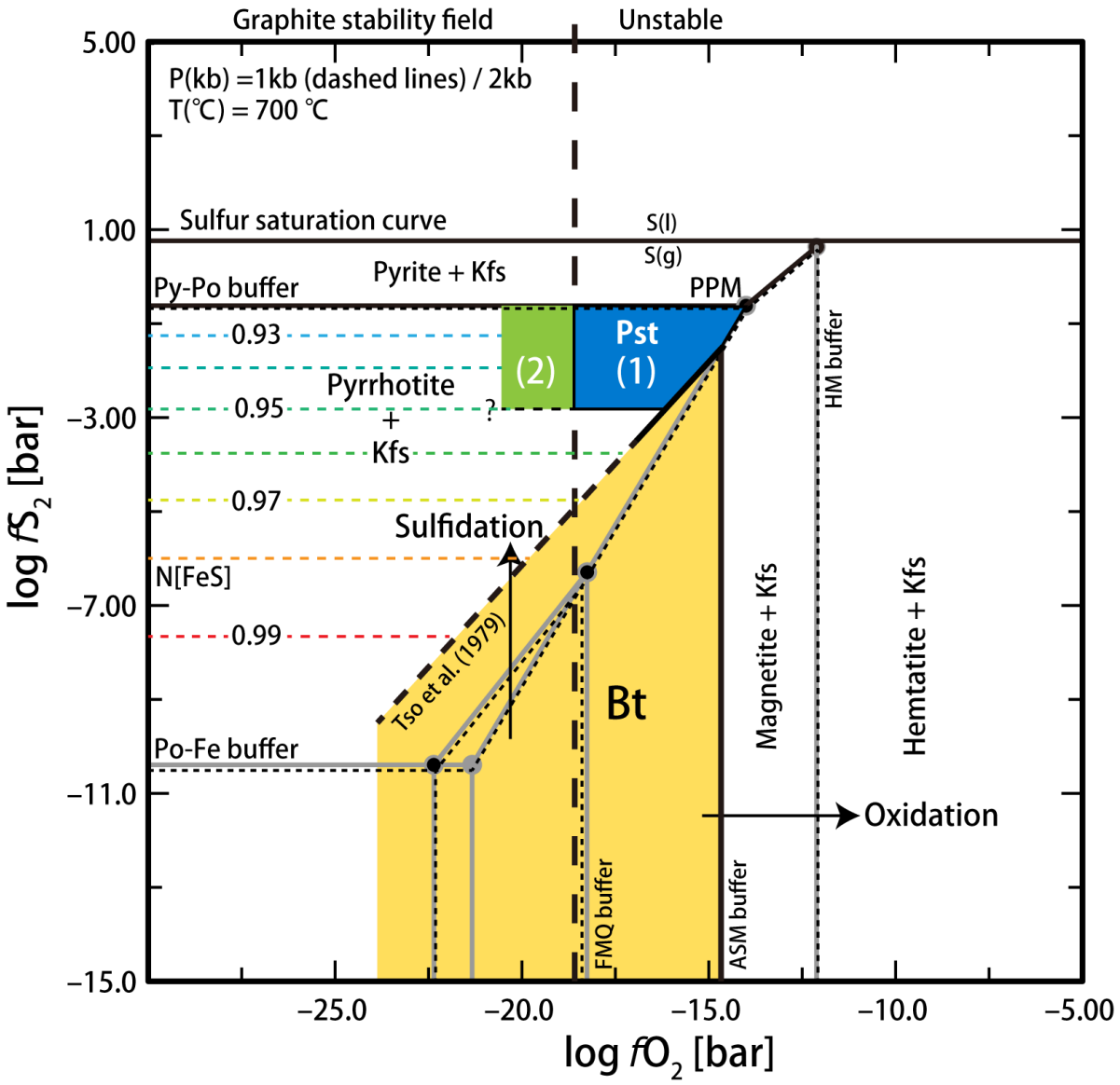

Figure 50. The fO_2–fS_2 phase diagram (chemical potential diagram) of biotite and graphite stabilities at 700 °C, 1kbar (Dashed lines) and 2kbar (Solid lines) modified by Shi (1992) and the experimental data of Tso et al. (1979). This diagram is constructed by *Perplex* 6.7.1 using thermodynamic database of SUPCRT 92 (Connolly and Petrini 2002; Johnson et al., 1992). The stability field of graphite is calculated from the thermodynamic data of Ohmoto and Kerrick (1977), and the fS_2 at target temperature is calculated by the equations of Toulmin and Barton (1964) and Froese and Gunter (1976).

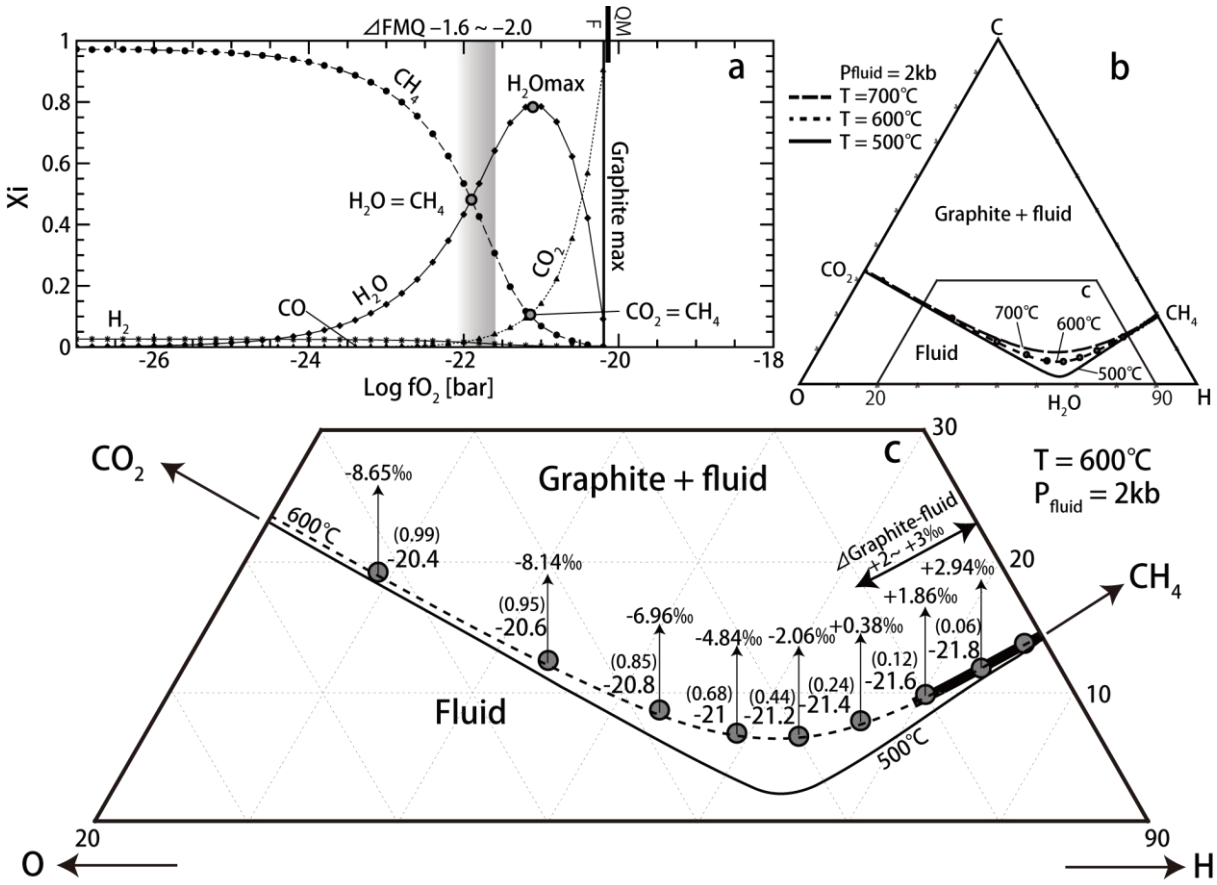

Figure 51. Estimated ideal fluid mixing model **(a)**, phase diagram of entire C-O-H diagram **(b)**, and enlarged C-O-H diagram with showing graphite-fluid isotopic fractionation as a function of fluid composition and fO_2 **(c)** at 2kb and 600 °C. These diagrams are constructed by *Perplex* 6.7.1 using the thermodynamic database of SUPCRT 92 (Connolly and Petrini 2002; Johnson et al., 1992). Values of $\Delta_{graphite\text{-}fluid}$ and xCO_2 (CO_2 / CO_2 + CH_4) are labeled in C-O-H diagram.

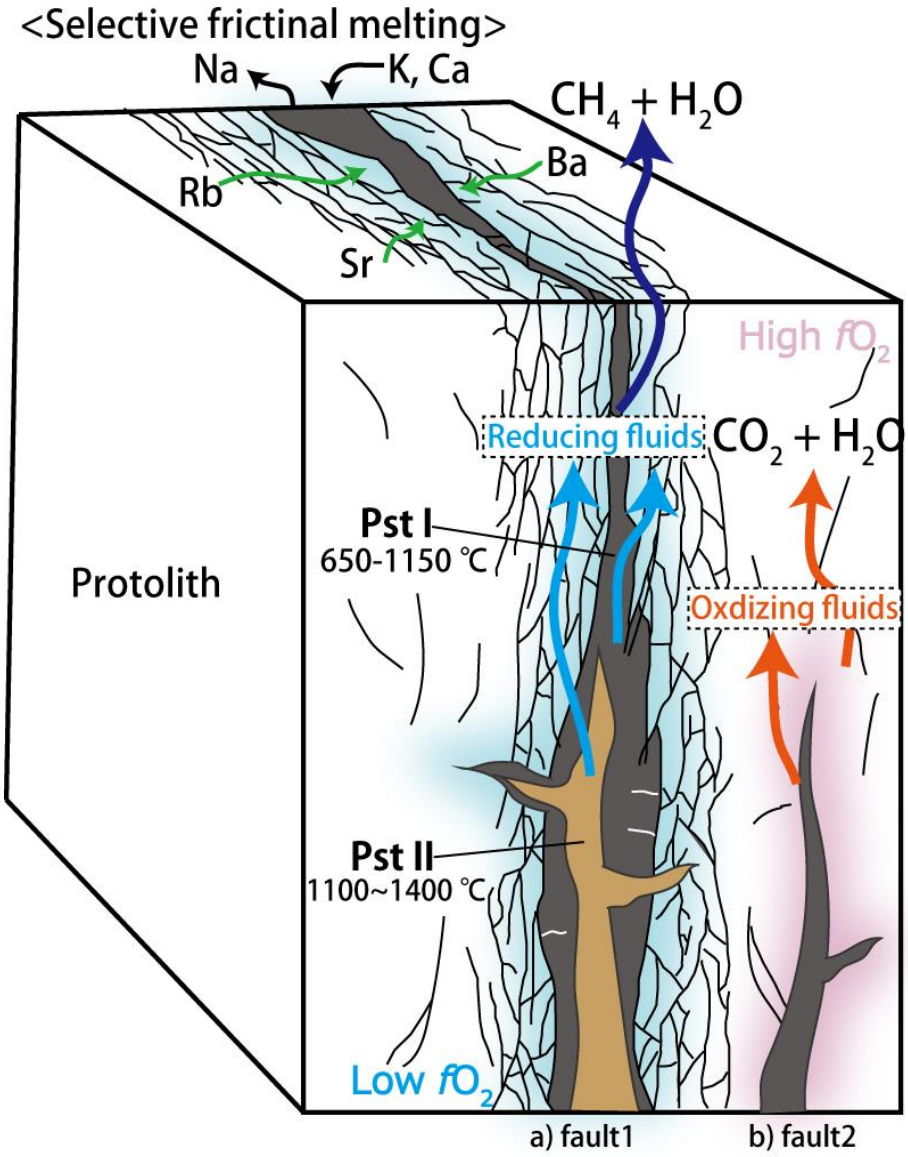

Figure 52. Simplified schematic diagram of two possible models of pseudotachylyte generation modified after Storti et al. (2003). **(a)** Graphite-bearing pseudotachylyte (Reducing type). **(b)** Graphite-free pseudotachylyte (Oxidizing type).

CHAPTER V

Structural and chemical evolutions of natural carbonaceous material during carbonization: An example from Shimanto accretionary complex

5.1. Introduction

Thermal degradation of carbonaceous material (CM) through burial is mainly controlled by thermally activated process, which depends on metamorphic (or maturation) temperatures and durations (Oberlin et al. 1999). The chemical reaction in subduction zone, carbonization, is widely applied not only as a thermal indicator for very low to low grade metamorphism but also as an exploration tool for oil and gas generation in sedimentary basin. Fully understanding the natural carbonization of CM with respect to the chemical kinetic approaches can lead to a powerful indicator for *time-Temperature (t-T)* conditions in Earth's dynamic evolution.

It is generally accepted that temperature is a major factor controlling natural carbonization (Lopatin 1971; Hower and Gayer, 2002). The process is irreversible, and well reflected as transformations of physicochemical properties in coal. It has been proposed that carbonization comprised two major processes with increasing temperature; primary and secondary carbonization (Oberlin et al. 1999). During the primary carbonization, macromolecular breakage, cracking, polymerization and cyclization of organic matter with softening has proceeded (Schwab et al. 2005). The processes were well identified as degradations of functional groups based on experimental studies (Guo and Bustin 1998). After liberation of volatile compounds, the

secondary carbonization is characterized by solid-state reorganization with the production of noncondensable gases (CH_4, H_2) due to the loss of aromatic CH groups. These series of devolatilization reactions through both stages of carbonization was widely investigated by transmission or reflectance micro-Fourier Transform Infrared spectroscopic (FTIR) studies (Landais et al. 1993; Chen et al. 2012; Li et al. 2013), X-ray diffraction (XRD) studies (Lu et al. 2001; Sonibare et al. 2010), column and gas chromatography (Price and DeWitt 2001), thermogravimetric analysis (TGA; Di Blasi 2008) and Vitrinite Reflectance studies (VR; Lopatin 1971; Hood et al. 1975; Huang et al. 1996; Le Bayon et al. 2011; 2012). In particular, it is well known that the VR in mudstones is well consistent with coal rank and C/H ratio in coal through burial (Vandenbroucke and Largeau, 2007). The optical properties of coal are easy to measure using a reflectance microscopy, and have been used for understanding the chemical kinetics of carbonization. Sweeney and Burnham (1990) and later kinetic studies have compiled the chemical kinetic models for carbonization and grouped them into five categories; (1) models that describe vitrinite maturation only as a function of temperature (Price 1983; Barker and Pawlewicz 1986), (2) models that incorporate time as a rule of thumb (Hood et al. 1975; Barker 1989), (3) models that describe vitrinite maturation as an Arrhenius first-order chemical reaction with a single activation energy (Middleton 1982; Antia 1986; Wood 1988), (4) models that describe vitrinite maturation with parallel Arrhenius first-order chemical reactions with a Gaussian distribution or weighting distribution of activation energies (Larter 1988; Burnham and Sweeney 1989; Sweeney and Burnham 1990). (5) Direct estimation of activation energy, rate constant, pre-exponential factor and reaction order (Ea, k, A, n) based on experimental kinetic studies (e.g., Huang et al. 1996; Ernst and Ferreio Mahlmann, 2004; Le Bayon et al. 2011; 2012). Former models in the first and second categories are empirically determined using burial history and thermal maturation index, and depended on the poorly constrained estimations of peak

temperatures. Latter models in the third, fourth and fifth categories are based on the assumptions of Arrhenius relation between peak temperature and geological time scale. These Arrhenious-type kinetic models are characterized by the differences between perceptions of activation energy during carbonization. In general, the various types of CM that have heterogeneous macro molecular structures are complexly included in mudstone (Price and DeWitt 2001; Schwab et al. 2005). This makes it difficult to assume the Arrhenious-type kinetic modelling and extrapolation to natural carbonization. In the case of simple chemical reaction, single rate constant *k* and reaction order can be estimated by experimental kinetic study using a differential (log-log plot) or integration methods (e.g., Khawam and Flanagan 2006), whereas, complex chemical reactions such as parallel or series reactions exhibit different rate constants and reaction orders, under certain temperature condition, which are driven by rate-determining chemical reaction in whole process. Moreover, the rate-determining chemical reaction might change as a function of peak temperature, fluid activity, and lithostatic pressure during burial. The first-order parallel-reaction model with a distribution of activation energies is one of the most suitable way to understanding the complex chemical reactions of CM than the assumption using a single effective activation energy. However, the original activation energies are based on the chemical kinetic studies of bond-dissociation energies such as C-H or C-C bonding in laboratory, and it is difficult to incorporate the effect of other factors such as tectonic deformation and fluid activity in low-grade metamorphic terrain into the vitrinute maturation (EASY%R_o) model proposed by Sweeney and Burnham (1990). Recently, several studies reported that the effect of other factors on the vitrinite maturation have been debated. Huang (1996) suggested that increasing pressure has no influence on VR, whereas Dalla Torre et al. (1997) and Le Bayon et al. (2011; 2012) suggested that the vitrinite maturation is suppressed by increased pressure. In addition, Monthioux et al. (1986) and Huang (1996) proposed that the original hydrogen content

in the starting material is crucial for the evolution of VR. High shear stresses have also been shown to further promotion of VR in natural rocks (Stach et al. 1982) and experimental studies (Ross and Bustin 1989). These studies suggest that it is necessary to assess the effect of other factors during carbonization for fully understanding natural carbonization.

The contradiction of carbonization in various types of *P-T* condition stems from the lack of understanding the kinetics of chemical reaction. In this study, we aimed to investigate the detailed rate-determining chemical process of CM in subduction zone, and conducted for pyrolysis experiments using natural starting materials. The study area, situated in the Shimanto accretionary complex, Shikoku, Japan, is suited to detailed investigation of structural and chemical evolution of CM though accretion and subduction. Based on natural and experimental studies on carbonization, I attempt to interpret and integrate chemical kinetics in subduction zone.

5.2. Geological outline

The Shimanto accretionary complex is exposed in the Nansei Islands, south Kyushu, south Shikoku, Kii Peninsula, Akaishi and Kanto Mountains and on the Boso Peninsula (Fig. 53a). In southern region of Shikoku, Japan, the Cretaceous Shimanto accretionary complex and Jurassic Chihibu accretionary complex are bounded by Butsuzo Tectonic Line (BTL; Fig.53b). The narrow belt in southwestern Japan is divided into two major tectonostratigraphic units; Northern Shimanto Belt and Southern Shimanto Belt (Teraoka 1979; Taira 1982). The northern belt in this study, the Cretaceous Shimanto accretionary complex, consists of seven units from north to south: Tochidani, Izuhara, Hinotani, Osodani, Taniyama, Hiwasa and Mugi units based on lithology, biostratigraphy and radioactive dating of detrital zircon (Fig. 54). Tochidani, Hinotani, Osodani and Hiwasa

units show coherent turbidite facies of massive and bedded sandstone, interbedded sandstone and mudstone, and mudstone with minor amounts of felsic tuff (Figs. 55a-b, d). On the other hand, Izuhara, Taniyama and Mugi units are melange facies that contains basaltic blocks, chert and red mudstone in an argillaceous matrix with sandstone and mudstone broken beds (Fig. 55c). The southern belt, the Paleogene accretionary complex, consists solely of the Naharigawa unit that is a coherent Eocene turbidite facies.

The thermal history of the Shimanto accretionary complex in Shikoku has been well studied based on vitrinite reflectance (Mori and Taguchi 1988; Laughland and Underwood 1993; Sakaguchi 1996; Ohmori et al. 1997), Illite crystallinity (Underwood et al. 1993; DiTullio et al. 1993), fluid inclusion (Sakaguchi 1999) and fission track studies (Hasebe et al. 1993). The Paleogene accretionary complex was overprinted by an unusual thermal event related to the acidic and mafic intrusions in Shikoku basin (Underwood et al. 1993), whereas the Cretaceous Shimanto accretionary complex display a systematic thermal distribution along to the paleo out of sequence thrust (OST) during accretion (Sakaguchi 1996; Ohmori et al. 1997; Mukoyoshi et al. 2006). In the eastern part of the Cretaceous Shimanto accretionary complex, Shikoku, two different paleo OSTs are already identified: Fukase fault and Aki Tectonic Line (ATL). The Fukase fault is a prominent fault boundary between Taniyama mélange unit and coherent unit of Hiwasa unit. The maximum thermal variation between Taniyama and Hiwasa units bounded by the Fukase fault were estimated at ca. 80 °C based on VR study (Ohmori et al. 1997). In addition, Aki Tectonic Line also shows a thermal discontinuity between Mugi and Naharigawa unit, which was estimated at ca. 110 °C.

5.3. Structural relations and fault rocks surrounding Aki tectonic line

It is well known that Aki tectonic line (ATL) is one of the most distinct pale-out of sequence

thrust between Cretaceous Shimanto and Paleogene Shimanto accretionary complex (e.g. Kimura et al. 2013). The thrust is traceable for over 800 km in the Shimanto Belt and is parallel to the modern Nakai Trough. ATL is called for Nobeoka Thrust in Kyushu and has different displacements and dip angle (Kondo et al. 2005). At Umaji area, similar thermal structures and deformation history can be seen. Although it is not good exposure of outcrop compared with coastline, it is possible to observe the aspect of regional thermal structures along the ATL. Figure 56 shows a detailed geological map in Higashi-gou area, Umaji, Kochi, exposing the Cretaceous Shimanto accretionary complex and Paleogene Shimanto accretionary complex bounded by ATL. Based on the detailed field survey, Mugi unit in Cretaceous Shimanto accretionary complex and Naharigawa unit in Paleogene Shimanto accretionary complex were lithologically subdivided into 5 subunits. Mugi subunit1 (Mg1) composed of mélange facies that contains basaltic blocks, chert and red mudstone in an argillaceous matrix with broken beds of sandstone and mudstone. Mugi subunit2 (Mg2) consists of phyllite, which is highly sheared and deformed toward the ATL (Fig. 55e). Mugi subunit 3 (Mg3) consists of mélange facies, which has a thick shear zone of ~500 m width in the side of hanging wall (Fig. 55f). In particular, the fault core with fault gauge (~ 30 cm; Fig. 55g) can been seen along the ATL, suggesting the active faulting after accretion stage. Naharigawa subunit 1 (Nr1) is also highly sheared and deformed sandstone and mudstone compared with other units of Paleogene Accretionary complex. On the other hand, Naharigawa subunit 2 (Nr2) composed of solely of turbidide facies and thick sandstones (Hara et al. 2006 under review).

Many brittle shear zones associated with phyllites, cataclasite and fault gauges occur in the study area (Figs. 55e-h). The fault planes and schistosity are parallel to the bedding planes, which trend roughly E-W and dip at high angles (Figs. 57a-b, 58). The lineations on the fault planes have different trends that indicate dextral and reverse sense of shear (Fig. 57c). At the fault core of ATL, the fibrous slicken lines indicated a reverse

sense of shear. Our observations are consistent with the kinematics of out of sequence thrust during subduction (Fig. 55h). On the other hand, minor faults indicating normal and sinistral shearing are also observed in the brittle shear zone (Fig. 57c).

5.4. Analytical method

72 mudstones were collected for this study (Figs. 54 and 59). After making the polished thin sections, we observed for CM microstructures. Under a microscopy, two different macerals (vitrinite and inertinite) are identified, however, almost all dispersed macerals are smaller than 10 μm in diameter. The small grains of dispersed vitrinite are selectively analyzed for micro-Raman spectroscopy as much as possible.

Raman spectra of CM were obtained using a Jasco NRS 3100 spectrometer at Niigata University, equipped with the grating of 1800 lines/mm and CCD-detector (256×1056 pixels). The microscope objective of 100×, and Nd-YAG laser (wavelength: 532 nm) were used. For Raman analysis, it is well known to modify the crystallinity of CM by the effect of polishing thin section due to inducing structural defects in graphitic structures (Pasteris, 1989; Beyssac et al. 2003). On the other hand, for compounds that are much less organized CM than graphite, polishing has no significant effect of the CM microstructure (Quirico et al. 2009). However, we found that CM microstructure were seriously damaged by Nd-YAG laser power per irradiation area. Previous researchers reported that the laser powers of 1–3 mW (Kouketsu et al. 2014), 1 mW (Lahfid et al. 2010), 0.45 mW (Wilkins et al. 2014), 0.4–0.8 mW (Quirico et al. 2009), 0.5 mW (Bonal et al. 2016) were selected for non-destructive analyses of poorly ordered CM. These studies were used for different objective lens (40× ~ 100×), acquisition time, cumulated numbers and spot sizes with a pinhole or slit. In addition, the crystallinity of CM microstructure is also depended on resistibility of CM to the laser irradiation. Hence, it is important to find

most suitable condition empirically for reproducible measurements of natural CM. In this study, the irradiation laser powers with a 50 μm pinhole between 7.7 mW and 0.01 mW were compared using a single CM grain (Figs. 60a-b). Raman spectra of CM were modified by the irradiation laser powers between 1.0 and 7.7 mW (Fig. 60a). The Raman peaks obtained from damaged spots tend to be more amorphous carbon compared with that in non-destructive spots (Fig. 60c). The small depressions from φ1.03 to 3.71 μm after Raman measurements suggested irradiation-induced amorphization at over 1 mW had undergone (Fig. 60a; Niwase 1995). For these reasons, we conducted Raman measurements at 0.1 mW with a 50 μm pinhole to avoid laser-induced amorphization and fluorescence at around 5000 cm^{-1}. Acquisition time and cumulated numbers of analyzing CM changed in each case for non-destructive measurements.

Many peak fitting models such as two-band peak fitting with Lorentzian profiles (Quirico et al. 2003) or a Lorentzian profile for the D band and a Breit-Wigner-Fano profile for the G band (LBWF fit; Bonal et al. 2006; Busemann et al. 2007; Quirico et al. 2009), and multi-peak fitting with Lorentzian and Gaussian-shaped profiles (e.g. Sadezky et al. 2005; Lahfid et al. 2010; Kouketsu et al. 2014) have been proposed in many literatures. Some studies have argued that G, D2 and D3 bands of CM are separated at around 1600 cm^{-1}, however, it is difficult to deconvolute the overlapping three bands. Therefore, we selected the peak deconvolution method of CM based on Kouketsu et al. (2014). All Raman peak profiles deconvoluted using *Peak Fit 4.12* software. G (or termed G_L, D2; ~1600 cm^{-1}), D1 (~1350 cm^{-1}), D3 (~ 1450 cm^{-1}), and D4 (~ 1200 cm^{-1}) bands in the first order region (1000–1800 cm^{-1}) were separated. The parameters of G band FWHM, D1 band FWHM, G position (Raman shift), I_{D1}/I_G (Intensity $_{D1\ band}$ / Intensity $_{G\ band}$), and AR (Area $_{D1\ +\ D4\ bands}$ / Area $_{G\ +\ D3\ bands}$) were estimated. Mean values and standard deviations were calculated based on over 25 analyses for each natural sample. In the case of the run products, we analyzed 13~20 points for each sample on the powder surface.

Representative CM samples are done for chemical extraction using HF-HCl treatments. The detailed procedures of chemical extractions from mudstones are described in the Appendix 1. After chemical treatments, Infrared (IR) absorption spectra of CM were obtained using a Fourier-transform infrared (FTIR) spectrometer (Spectrum 2000; Perkin-Elmer Inc.), equipped with an IR microprobe in the Geochemical Research Centre, The University of Tokyo. Before we analyze by micro-FTIR spectrometer, the powder samples crushed using a diamond anvil to transmit infrared light. After crushing, infrared spectra for each sample between 750 and 4000 cm^{-1} were collected for 200 scans per sample at a resolution of 4 cm^{-1}. Micro-FTIR measurements were performed at five different areas with 15 × 15 μm aperture size for each sample. The obtained IR profiles were calibrated forbackground and peak deconvolution done using *Peak Fit 4.12* software.

5.5. Experimental method

The starting materials for the heat treatment were prepared from mudstone in Hinotani unit (Figs. 54 and 55a). The CM samples in mudstones were already treated by above chemical extractions. The CM samples are of the lowest maturity in this area and systematically change their Raman and IR profiles with increasing the paleo-thermal gradient toward the out of sequence thrusts, ranging between 1.3 and 3.0 % of vitrinite reflectance (Ohmori et al. 1997).

Before heating experiments, the natural CM powders were introduced into a preheated (1100 °C for 12 h) quartz tube and sealed under vacuum (~10^{-3} Torr). In general, poorly ordered CM easily converts to carbon dioxide at over ~500 °C under atmospheric condition (Cetinkaya and Yurum 2000), therefore, we performed kinetic experiments using sealed quartz tubes under vacuum. Five or six sealed tubes were placed in a mantle furnace and run between 10 min to 48 hours at 500~900 °C for experimental

kinetic study. Experimental temperature in mantle furnace was measured by two type-K thermocouples independently. The run products were quenched by taking out the quartz tubes from the mantle furnace.

5.6. Results

5.6.1. Structural evolution of CM in the Cretaceous Shimanto accretionary complex

Several significant aspects of Raman and IR profiles of CM were observed in different units of Shimanto accretionary complex (Fig. 61; Table 13). These profiles were rearranged lowest to highest maturity (upper portion) based on the previous VR, IC values, and our results (Ohmori et al. 1997; Hara et al. under review). Two prominent bands corresponding to the G (~1600 cm^{-1}) and D1 band (1350 cm^{-1}) are observed in the first order region (1000~1800 cm^{-1}). The disordered bands of D3 and D4 bands are also identified by the peak deconvolution of two prominent bands (Fig. 61a). Both disordered bands are originated from amorphous sp^2 or sp^3-sp^2 mix sites in organic molecules (Dippel and Heintzenberg 1999; Sadezky et al. 2005). For the early stage of carbonization, the D1 and G bands display a large full width at half maximum (FWHM), and characteristic shoulder peak in the left side of D1 band. The band was identified as D5 band at about 1480 cm^{-1} (Deldicque et al. 2016). It was reported that the D5 band was attributed to hydrocarbons trapped in the organic nanoporosity (Romero-Sarmiento et al. 2014). With increasing temperature, the D5 band is eliminated or difficult to identify. D1 and G band FWHM systematically become smaller, and increase in intensity ratio between D1 and G band (I_{D1}/I_G) are observed. In the case of FTIR study, FTIR profiles are characterized by the presence of intense bands at around 3400- 3300 cm^{-1}, 3050 – 2800 cm^{-1}, 1700 cm^{-1}, 1615 cm^{-1}, 1300 cm^{-1} and 780 cm^{-1} in prominent in CM extracted from mudstones (Fig.

61b). The broad band at 3400–3300 cm^{-1}, representing the –OH stretching vibration of water. The three bands at 3050–2800 cm^{-1} are derived from aliphatic CH_x and aromatic CH stretching vibration. The area ratio of aliphatic CH and aromatic CH, which is named for aromaticity, is one of the thermal indicator for carbonization. The aromatic C=C ring stretching vibrations at around 1615 cm^{-1} is the most prominent bands developed through carbonization. The carboxyl C=O stretching at around 1700 cm^{-1} systematically decreases the intensity, and then disappears with increasing temperature. Chen et al. (2012) argued that the IR peak evolution of functional group in vitrinite, liptinite and inertinite were similar to each other and show sensitive transformation between low and high-rank coal (R_0 < 1.50 %). On the other hand, they also reported that the trends of the IR profiles are difficult to trace in high rank coal (R_0 > 1.50 %). Such peak evolution of CM was also observed in this area.

Figures 62 and 63 display structural evolution of natural CM along to the ATL. In this study, I have compared the illite crystallinity (IC) values in mudstone as a different thermal indicator in the Cretaceous Shimanto accretionary complex (Fig. 62a; data from Hara et al. under review). The crystal parameters exhibit significant “saw tooth” aspects bounded by two OSTs (Figs. 62a-c). Such characteristic structural change of D1 band FWHM was obviously observed (Fig. 62b). These structural changes analyzed by micro-Raman spectroscopy are well consistent with the thermal variations based on previous studies and these parameters are useful tools for understanding the detailed paleothermal structure in accretionary complex. In addition, we found some important differences of structural changes at different temperature regimes. In the low maturity area, G band FWHM show a significant transformation as a function of paleo-thermal variation (Fig. 62c), on the other hand, I_{D1}/I_G, G and D1 band position are much sensitive structural change at around ATL than that at the Fukase fault (Figs. 62d-e). The difference of peak evolution may result from the attribution of chemical reaction in whole process.

Applying the Raman spectra of carbonaceous material (RSCM) thermometry proposed by Kouketsu et al. (2014), the temperature variations in this area were range between 180~300 °C (Fig. 62f). It is important to note that the evolution profile of CM changed sensitively changed as a function of temperature even at a restricted range in the accretionary complex.

5.6.2. Pyrolysis kinetic experiments of CM under vacuum

Pyrolysis kinetic experiments of CM are crucial for understanding the temperature dependence of carbonization directly. Numerous earlier studies have argued that the natural carbonization is controlled by not only temperature but also lithostatic pressure, fluid activity, and tectonic deformation. It is therefore key to find the rate-determining chemical process for comparing natural and experimental evolution by micro-FTIR and Raman studies. Simple temperature dependence of carbonization is easily identified by the determination of activation energy based on the pyrolysis experimental kinetic studies. Thereafter, we attempt to comparison between natural and experimental structural evolution of CM (Table 14).

I conducted for 26 heating experiments using natural starting materials which are introduced into quartz tubs at 500~900 °C for 10 min to 2880 min. Figure 64 display time-crystal parameter relations as a function of annealing temperature. The intensity ratio of D1 and G band (I_{D1}/I_G) shows a power relationship to the heat treatment time (Fig. 64a). On the other hand, D1 and G band FWHM are not simple transformations with an increase in annealing temperatures and durations (Figs. 64b-c). In the low-temperature conditions at 500~600 °C, the values of D1 band FWHM tend to be increasing trend with increasing temperature, and turn over decreasing trend at 600 °C for 60 min. These changes strongly suggest that the rate-determining chemical reaction of carbonization by pyrolysis

experiments were changed by experimental temperature. Such changes of rate-determining chemical reaction are also reflected by slopes of power rate model in D1 band FWHM between 600 and 700 °C (Fig. 64a). In addition, micro-FTIR data supported the change of rate-determining chemical reaction at each temperature. At low temperature of 500 °C, the aliphatic CH, carboxyl C=O stretching, and OH stretching vibration of water in CM are selectively liberated with increasing heating durations (Figs. 65a-b). The liberations of volatiles proceeded with increasing annealing durations, which were reflected by area ratio between aliphatic CH_x and aromatic CH. At high temperature condition (Fig. 65c; > 700 °C), almost all functional groups are decrease in intensity or disappeared, suggesting the termination of devolatilization or thermal degradation. From the point of view, I revealed that two different chemical reactions were identified by micro-Raman and FTIR studies. The early stage of carbonization has been progressed by selective devolatilization of volatiles such as aliphatic CH, carboxyl C=O stretching, and OH stretching vibration of water. Thereafter, the thermal degradation of CM, which are mainly observed as I_{D1}/I_G is prominent process at high temperature conditions (> 700 °C).

5.7. Discussion

5.7.1. Chemical kinetics of carbonization

Our data on pyrolysis kinetic experiments suggested that the structural changes of natural CM were subjected to thermal activation process between annealing temperatures and durations. I therefore assessed the kinetic approaches for carbonization of natural CM using the power rate model (Huang 1996; Muirhead et al. 2012), and the Avrami-Erofeev model (e.g., Kebukawa et al. 2010). The detailed kinetic models are described in the Appendix II. In this study, I selected the I_{D1}/I_G ratio as a kinetic indicator because it

demonstrated a most sensitive transformation between 500 and 900 °C for long annealing durations in pyrolysis experiments (Fig. 64a). Before we adopted these kinetic models, the experimental data were converted to the degree of carbonization (α) by following the equation (Khawam and Flanagan, 2006; Table 14);

$$\alpha = (I_t - I_0) / (2.4 - I_0) \quad (1)$$

where I_0 is the initial intensity ratio of starting materials (I_{D1}/I_G: 0.5447, Table 13), I_t is the analyzed experimental data, and the value of 2.4 shows the maximum value of I_{D1}/I_G, which were previously reported by Ferrari and Robertson (2000). After conversions to nondimensional parameter α, we attempted to fit the following power law of time as;

$$\alpha = k_p t^{-n} \quad (2)$$

where k_p is the rate constant, t time (sec), n a reaction order at that temperature. In addition to power rate model, we also attempted to calculate the best fitting using a Avrami-Erofeev model to understand the complex chemical reaction. The Avrami-Erofeev model is especially suitable for a sigmoid transformation as functions of two factors for controlling carbonization. The equation was expressed as follows;

$$\alpha = 1 - \exp(-k_a t^{-l}) \quad (3)$$

where k_a is the rate constant of Avrami-Erofeev model, l is the reaction order named as "Avrami index", t is the duration of heating (sec). Taking the natural logarithm of equation (3), it can be also written by;

$$\ln[-\ln(1-\alpha)] = \ln k_a + m \ln t. \quad (4)$$

Plotting the left side of equation ($\ln[-\ln(1-\alpha)]$) and natural logarithm of time $\ln t$, the rate constant $\ln k_a$ and Avrami index l are estimated from the linear regression of intercept and slope in this Avrami plot, respectively. Figure 66 shows the degree of carbonization (α) as a function of time (sec) fitted by the power rate and Avrami-Erofeev models, respectively. The regression in both the kinetic models are in good agreement with the experimental results, showing high correlation coefficients of 0.949–0.989. This indicates that the

structural change of I_{D1}/I_G ratio has taken place by the thermal activation process in the pyrolysis experiments. In particular, we revealed the specific aspects of reaction orders (n and l) with increasing heating temperature (Fig. 67a). In general, the overall rate constants and reaction orders in complex chemical reaction results from a sum of reaction orders and rate constants in simple chemical reaction, respectively. Hence, those values fluctuate by changing the rate-determining chemical process at each temperature. Previous kinetic studies have regarded that the change of reaction order stems from experimental uncertainly, and used the mean values (Huang et al. 1996) or linear regression values from the least squares of experimental data (Muirhead et al. 2012) for the determination of activation energy. However, our data imply that the reaction orders systematically changed by not only experimental uncertainty but also annealing temperatures (Fig. 67a). The termination of devolatilization that can be analyzed by micro-FTIR study was observed between 500 and 700 °C, and then systematic change of I_{D1}/I_G ratio started at over 700 °C by micro-Raman spectroscopy. These profile changes based of spectroscopic studies may be reflected by change in the kinetic parameters of complex chemical reaction.

Based on the model fittings, we attempted to fit the Arrhenius relation using the following equation:

$$k_{p,a} = A\exp(-E_a / RT) \qquad (5)$$

where $k_{a,p}$ are the rate constant of both models, A the pre-exponential factor, E_a the effective activation energy (kJ/mol), R the gas constant (8.314598 kJ/mol), and T the absolute temperature (K) of the experiment. Using the Arrhenius equation (5), we calculated the effective activation energies of 106 ± 16 kJ/mol and 106 ± 17 kJ/mol, respectively (Fig. 67b; Table 15). Both effective activation energies by power rate and Avrami-Erofeev models demonstrated good least square correlation coefficients of 0.928-0.932 (Table 16). In this study, we superimposed the Arrhenius plots of previous pyrolysis experiments of CM, biomass, coal and Murchison inorganic matter for reference (Fig. 67b).

The cellulose, hemicellulose and Kraft lignin, which serve as endmembers of CM in mudstone, demonstrated similar slopes in Arrhenius plots (Di Blasi 2008; Fig. 67b). This suggests that natural CM in accretionary complex has undergone similar chemical evolution of the organic materials during pyrolysis experiments. Previous kinetic data on thermogravimetric and micro-FTIR studies corresponds to the aspect of weight loss and degradation of aliphatic CH. The peak evolution in this study may bear on the thermal degradation of CM by heat treatment. In addition, previous pyrolysis experiments also reported the significant increase in I_{D1}/I_G ratio with increasing annealing temperatures at over 600 °C (Muirhead et al. 2012; Deldicque et al. 2015; Kaneki et al. 2016). Such structural changes are in good agreement with aromatization of amorphous carbon, which is proportional to the square of crystal diameter L_a (Ferrari and Robertson, 2000; Ferrari 2007; Deldicque et al. 2015).

5.7.2. Relationship between natural and experimental carbonization

Our kinetic results revealed that natural carbonization in the Shimanto accretionary complex and pyrolysis kinetic experiments exhibited different structural evolution of CM using even same starting materials. Many previous studies have regarded the D1 band FWHM and I_{D1}/I_G ratio as a sensitive thermal indicator in low-grade metamorphism (Fig. 68; Busemann et al. 2007; Cody et al. 2008; Kouketsu et al. 2014; Muirhead et al. 2012; Deldicque et al. 2015; Rouzaud et al. 2015). However, the CM obtained from experimental kinetic studies could not reconstruct the trend of D1 band FWHM in natural CM (Figs. 62 and 63). In the Shimanto accretionary complex, wide variation of D1 band FWHM between 90 and 140 cm^{-1} was recognized along the paleo thermal structure from ATL. The structural change of I_{D1}/I_G ratio were only observed at the restricted lithology of mélange and phyllite unit. On the other hand, the synthesized CM systematically changed their

I_{D1}/I_G ratio with increasing annealing temperature and it is expected to construct the prospective thermal indicator for Arrhenius-type thermometry. It is well known that characteristic variation of the I_{D1}/I_G ratio with increasing L_a diameter has the transitional point at ~20 Å. The I_{D1}/I_G ratio will increase with increasing disorder until ~20 Å between a graphitic and turbostratic carbon, according to the *TK* relationship (the equation of Tuinstra and Koenig 1970). On the other hand, the TK relationship will no longer hold for more disorder under ~20 Å, and the D1 band intensity is proportional to the probability of finding a six-fold ring in the cluster (Ferrari and Robertson, 2000). In other words, D1 band intensity arises from the ordering during carbonization. Thus, it is assumed that the thermal variation detected by D1 band FWHM in the Shimanto accretionary complex underwent different processes, which rely on the structural ordering in amorphous carbon. In the case of natural carbonization, there are stronger intensity of G band case than that of run products. G band is related to the clustering of the sp^2 phase, and the polymerization and cyclization of sp^2 phase in the cluster may be selectively developed. In this study, our kinetic experiment using a sealed tube is a solid state chemical reaction which involves the loss of water from reactant. On the other hand, organic chemical reactions are essential for presence of water to react with organic material (Price and DeWitt 1993). Under hydrous pyrolysis conditions, water acts as an external source of hydrogen, which facilitates organic matter cracking and inhibits cross-linking reactions (Lewan 1997; Schwab et al. 2005). Hence, our solid-state reactions might not produce a hydrocarbon related chemical reaction in the solution because of low concentration of hydrogen. In any case, the systematic change of I_{D1}/I_G ratio in micro-Raman spectroscopy arises from the temperature dependence of kinetic experiments in solid state reaction of CM, and it has a potential as a thermal indicator of matured CM which already completed the devolatilization in coal structure.

5.7.3. Application and limitation to natural carbonization in accretionary complex

Our kinetic experiments combined with assessment of natural carbonization in accretionary complex represents a systematic aspect of I_{D1}/I_G ratio depending on the peak temperature. The process is proportional to the reorganization of CM in amorphous carbon and potential prospective indicator for natural geological condition. Based on the experimental results, we attempted to a simplified isothermal calculation of Arrhenius-type carbonization during subduction. If carbonization rate is subject to Arrhenius temperature dependence, the sigmoid and power curves can be extrapolated to represent low-temperature conditions in geological time scale. Both extrapolation curves were tested using the parameter of I_{D1}/I_G ratio:

$$f(t) = C_{min} + (C_{max} - C_{min}) / \{1 + (t_{half}/t)^h\}, \text{ or} \qquad (8)$$

$$f(t) = kt^n \qquad (9)$$

where C_{min} and C_{max} are respectively the maximum and minimum values of each parameter, t is the annealing duration during metamorphism, t_{half} is the inflection point obtained from this function, and h is the order of reaction of the sigmoid function (called "Hill coefficient"), k the rate constant, and n the exponent. The values of C_{min} and C_{max} correspond to the starting and termination points of natural carbonization, respectively, and h and n is used for 0.2145 and 0.0753, respectively. The value of t_{half} changes as functions of time and temperature, which correspond to rate constant. Therefore, its value was calculated at target temperature and time from the Arrhenius plots. The t_{half} can also be described following the Arrhenius relation:

$$t_{half} = A_1 \exp(-m/T), \qquad (10)$$

where A_1 is the intercept and m is the slope of the Arrhenius plot. Combining equation (8) and (10), (9) and (10):

$$f(T, t) = C_{min} + (C_{max} - C_{min}) / [1 + \{A_1 \exp(-m/T)/t\}^h], \qquad (11)$$

$$f(T, t) = A_1 \exp(-m/T) t^n \qquad (12)$$

The equations are expressed as sigmoid (11) and power extrapolations (12) relying upon the peak temperature and duration of heating (Fig. 69). The trends of calculated I_{D1}/I_G ratio are driven by the extrapolation method for rate constants and reaction orders. Using both *t-T* relation, we attempted to extrapolate the structural evolution of CM at very low temperature (150–450 °C) during annealing for 1–10^{10} years. Previous studies on low-grade metamorphism reported the significant increase of I_{D1}/I_G ratio in Glarus Alps (Lahfid et al. 2010) and Hidaka metamorphic belt (Nakamura et al. 2015). An attempt was made to estimate for the I_{D1}/I_G ratio between 150 and 450 °C (Fig. 69). If CM underwent prograde metamorphism for a duration of 10~50 Ma, the systematic increasing of I_{D1}/I_G are shown in the range of green area. In this study, we superposed the natural CM in Hidaka metamorphic belt, which is a high-temperature low-pressure type metamorphic terrain (Fig. 70; Chapter II, Nakamura et al. 2015). The peak temperatures of natural CM were calculated based on the RSCM thermometry (Kouketsu et al. 2014). The natural CM in zone Ia of Hidaka metamorphic belt (HMB) only demonstrate good correlation between estimated extrapolation curves and peak temperatures by RSCM thermometry. The CM in zone Ib of HMB already change to the *TK* relation ($I_{D1}/I_G \propto 1/L_a$), and is out of our extrapolation based on experimental kinetic study. Nevertheless, the evolution of natural CM in Shimanto accretionary complex is not consistent with both extrapolation curves. This results from the possible overestimation of peak temperatures compared with metamorphic terrain, or limitations in the extrapolation method based on pyrolysis experiments in the solid-state reaction. Our results suggest that the difference of *P-T* condition and effect of water may produce a large difference of structural evolution CM during carbonization. It is necessary for more detailed estimations combined with natural observations and experimental kinetic studies.

5.8. Conclusion

I assessed the structural evolution of natural CM based on the two different approaches; natural and experimental kinetic studies using the detailed micro-Raman spectroscopy and FTIR studies. Based on the detailed field survey and spectroscopic analyses, the structural evolution of natural CM in the Shimanto accretionary complex demonstrate the systematic changes of crystal parameters. These structural changes of D1 band FWHM and I_{D1}/I_G ratio are well consistent with the thermal variations bounded by paleo out of sequence thrust, and G band FWHM show a significant transformation in the low maturation area. In addition, the natural CM modified their chemical structure by liberation of heteroatom in functional group. In the case of experimental kinetic studies, our kinetic results using natural starting materials exhibited characteristic structural evolution of CM as functions of annealing temperature and duration. The intensity ratio of I_{D1}/I_G ratio shows a power relationship to the heat treatment time. On the other hand, D1 and G band FWHM are not simple transformations with an increase in annealing temperature and duration. Hence, an attempt was made to fit the kinetic models using the I_{D1}/I_G ratio. Using the rate constants obtained from model fitting, the effective activation energies of 106 ± 16 kJ/mol and 106 ± 17 kJ/mol were estimated using an Arrhenius equation, respectively. Both effective activation energies by power rate and Avrami-Erofeev model demonstrated good least square correlation coefficients of 0.928-932, suggesting the temperature dependence of carbonization. In this way, the I_{D1}/I_G ratio demonstrate the systematic structural change during natural and experimental carbonization as a function of peak temperature. Other factors such as D1 band FWHM did not show a clear correlation to the peak temperature, suggesting the interplay of different factors during carbonization. It is important to distinguish the crystal parameters for applying the thermal indicator in subduction zone.

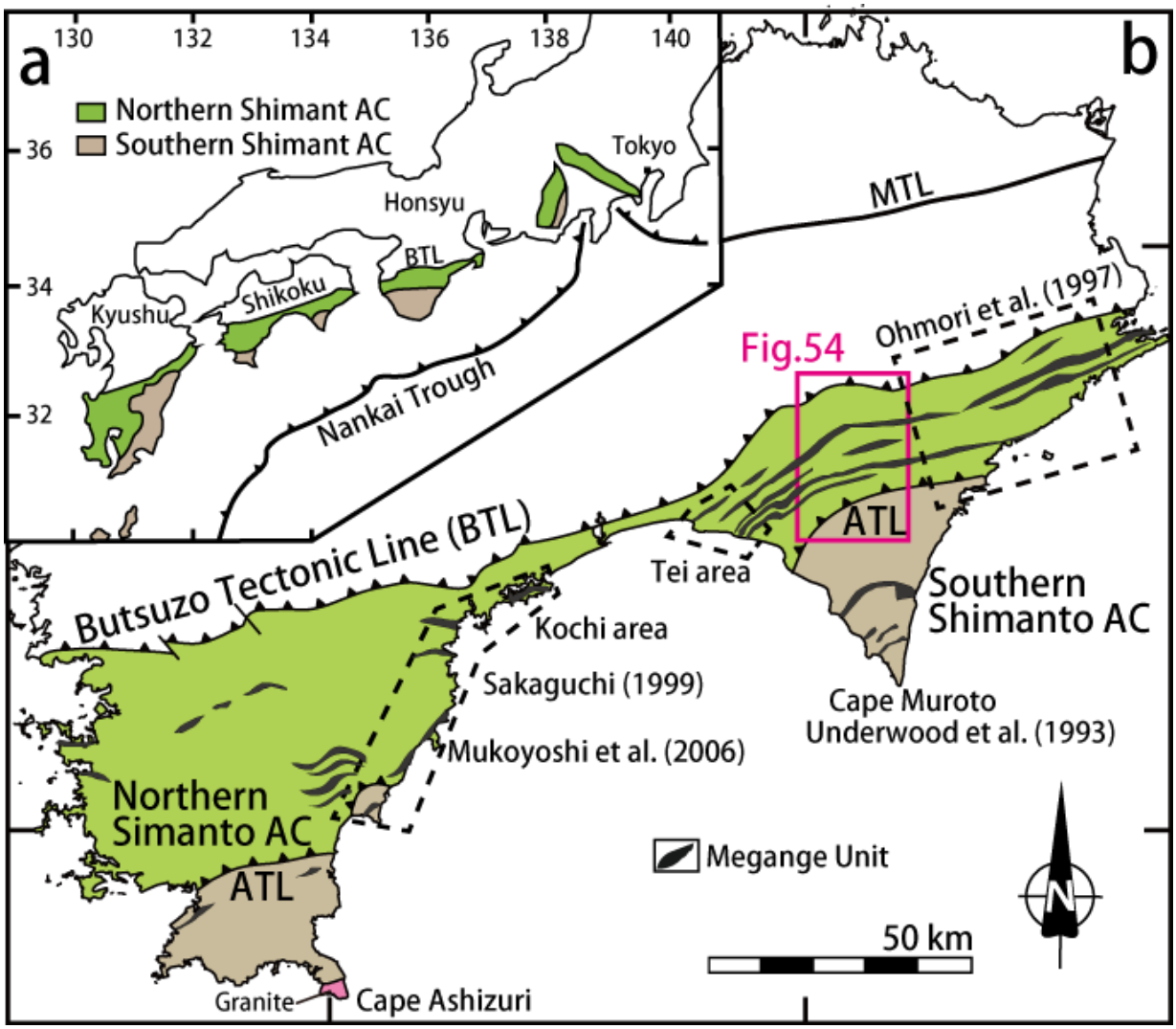

Figure 53. (a) Location map of the Shimanto accretionary complex in the Southwest and Central Japan. **(b)** Geological outline of the Shimanto accretionary complex in Shikoku, Japan, showing two tectonostratigraphitc unit pf Northern Shikoku and Southern Shikoku accretionary complex modified after Ohmori et al. (1997). Representative areas where previously investigated on the paleothermal structures of vitrinite reflectance by Ohmori et al. (1997), Underwood et al. (1993), Sakaguchi (1999) and Mukoyoshi et al. (2006) are described in this figure. BTL, Butsuzo Tectonic Line; ATL, Aki Tectonic Line.

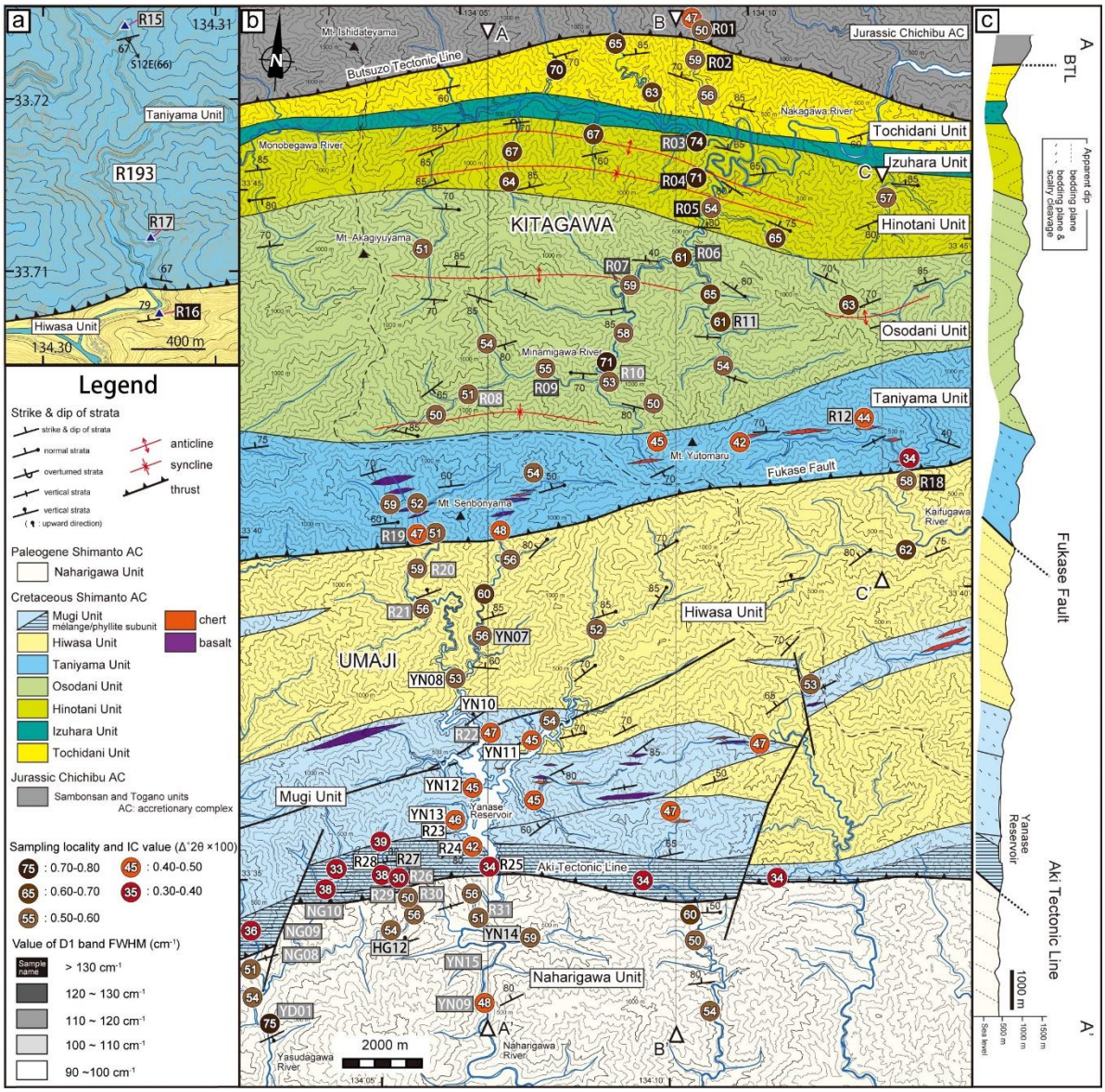

Figure 54. (a) Geological map of the Cretaceous Shimanto accretionary complex along route 193. **(b)** Geological map of the Cretaceous and Paleogene Shimanto accretionary complex in Shikoku, Japan, showing illite crystallinity (IC) values. Circle symbols indicate sample localities of IC, accompanying IC values modified after Hara et al. (under review). Squared symbols indicate those samples analyzed by micro-Raman spectroscopy. The gray colors of box are changed by the values of D1 band FWHM (cm^{-1}). **(c)** Geological cross section along A-A' line after Hara et al. (under review).

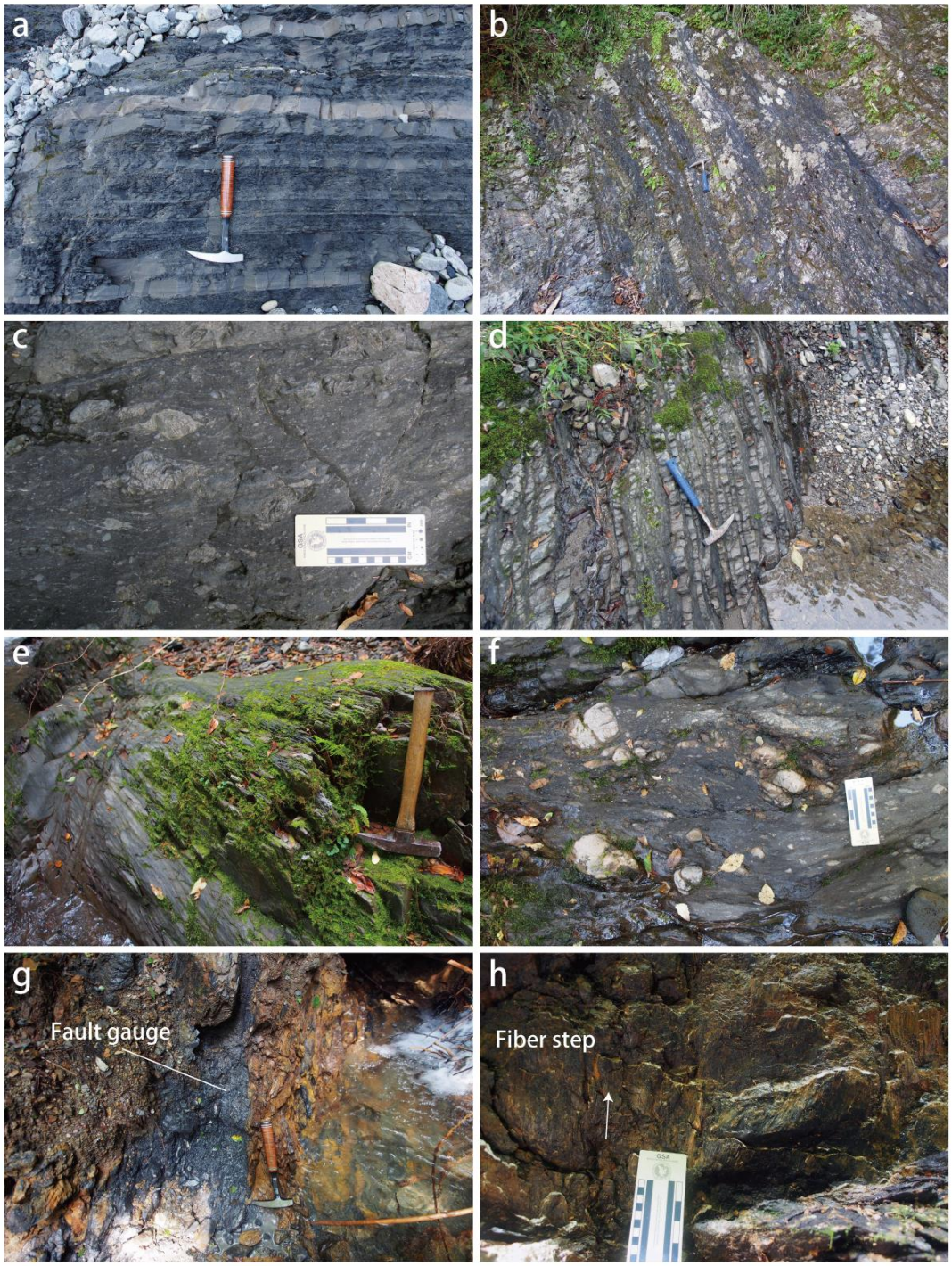

Figure 55. Occurrences of coherent turbidite facies in **(a)** Hinotani Unit and **(b)** Osodani unit. **(c)** Melange facies that contains basaltic blocks, sandstone and mudstone broken beds **(d)** Occurrence of coherent turbidite facies in Hiwasa Unit. **(e)** Occurrence of phyllite in Mugi subunit 2. **(f)** Broken mudstone with sandstone and basaltic blocks in Mugi subunit 3. **(g)** A fault core with fault gauge along the ATL. **(h)** The fiberous slicken sides on the fault planes, indicating the reverse sense of shear.

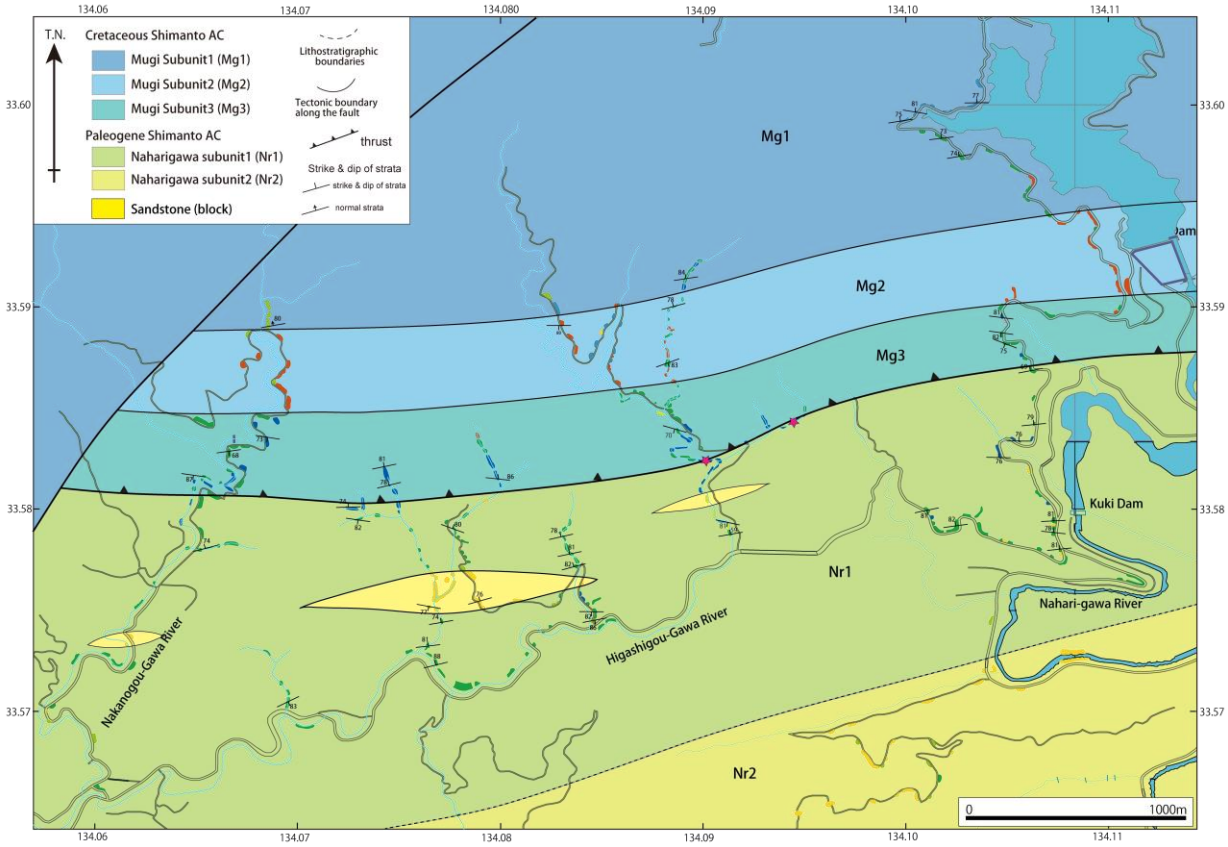

Figure 56. Detailed geological map of the Cretaceous Shimanto accretionary complex and Paleogene Shimanto accretionary complex bounded by Aki Tectonic line in Higashigou-gawa River are, Umaji, Kochi, Japan.

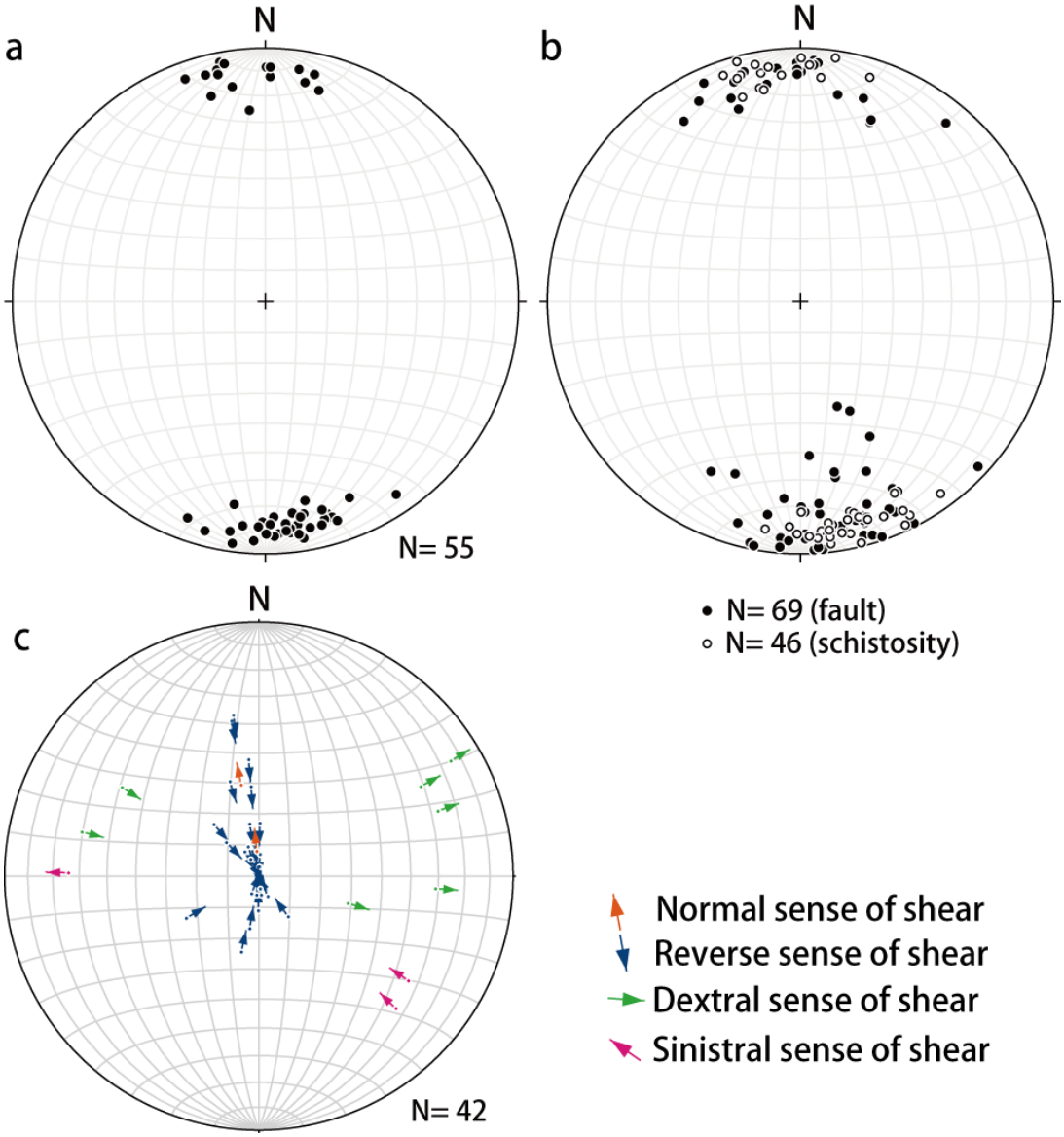

Figure 57. (a) Lower hemisphere projections of bedding planes in Higashigou-gawa River area. **(b)** Lower hemisphere projections of fault plnes and schistosity in Higashigou-gawa River area. **(c)** Lower hemisphere projections of lineations on the fault planes. The arrows indicate a sense of shear.

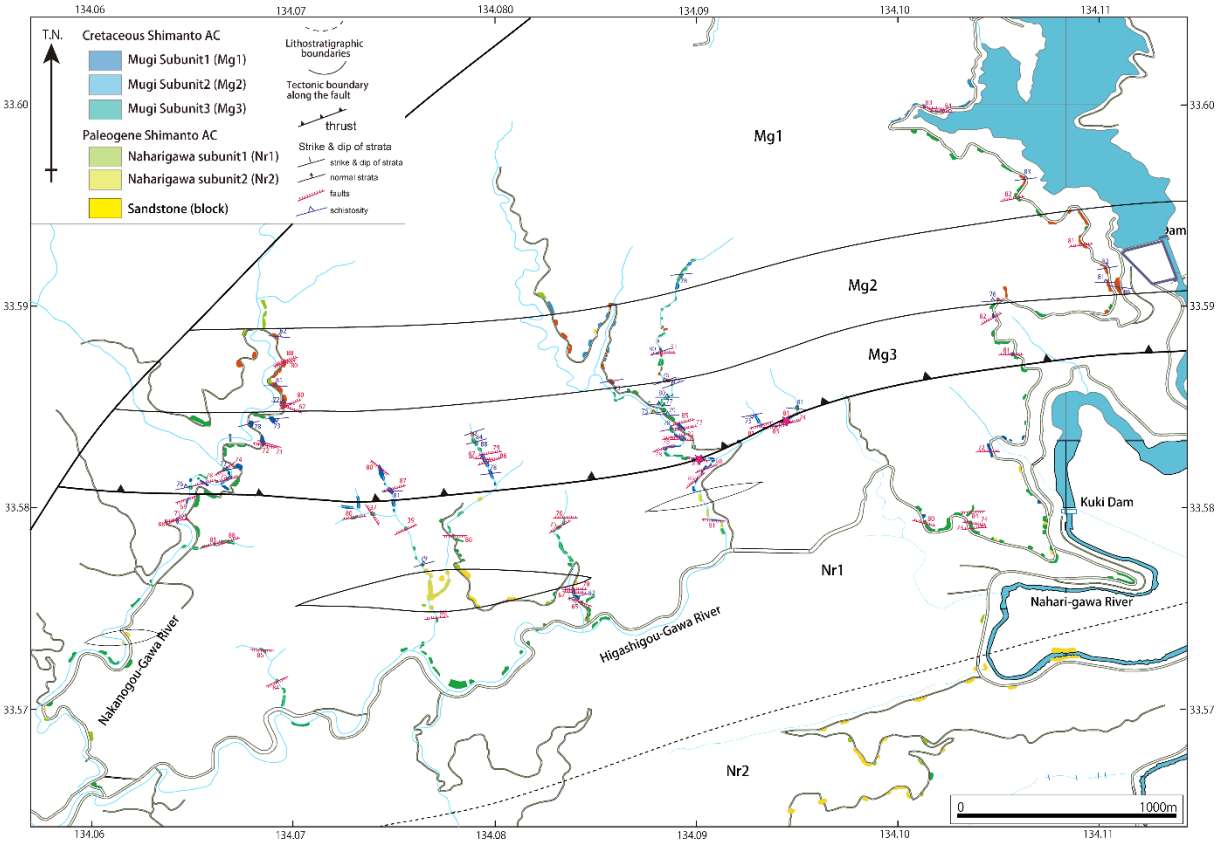

Figure 58. Detailed route map in Higashigou-gawa River are, Umaji, Kochi, Japan.

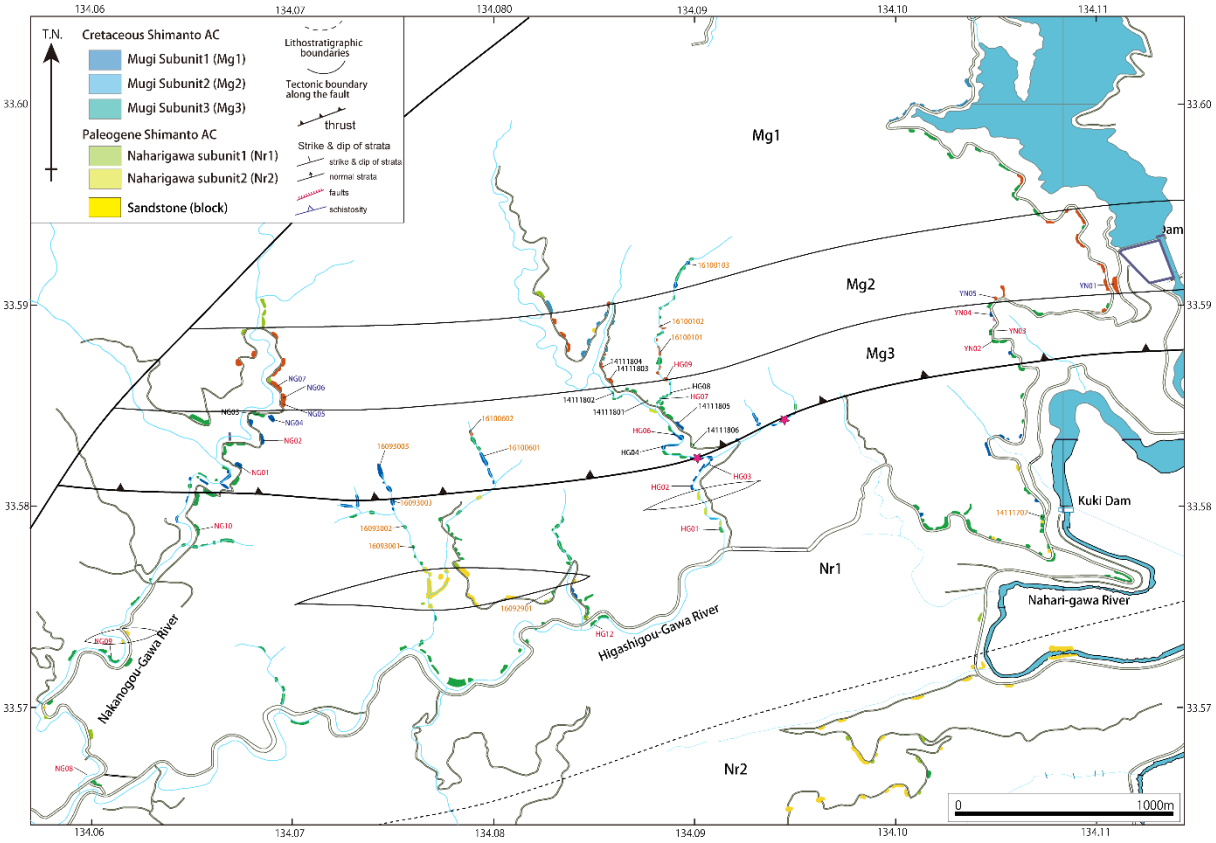

Figure 59. The locations of analysis sampls in Higashi-gou River area.

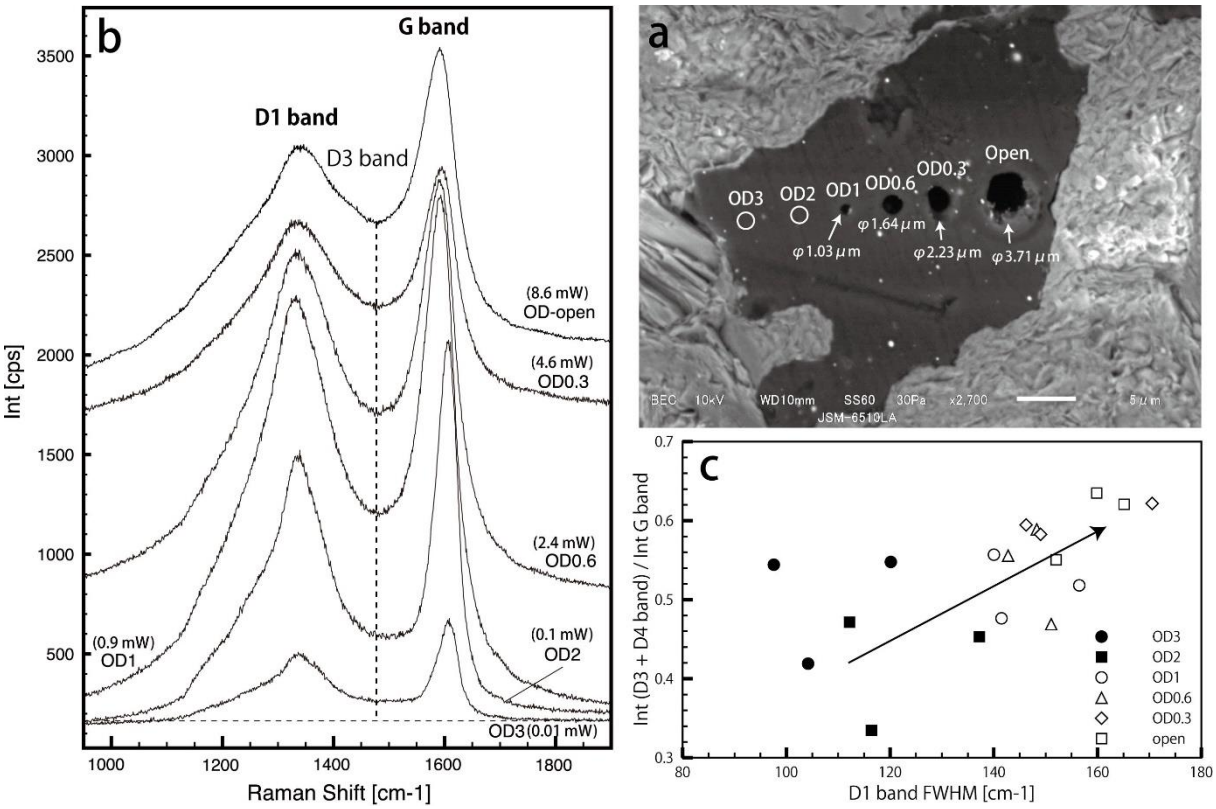

Figure 60. Influence of laser irradiation in coal structure by micro-Raman spectroscopy. **(a)** SEM image of the small holes from φ1.03 to 3.71 μm after Raman measurements. **(b)** Raman spectra of CM by laser-induced amorphization. **(c)** Structural changes of CM by laser-induced amorphization.

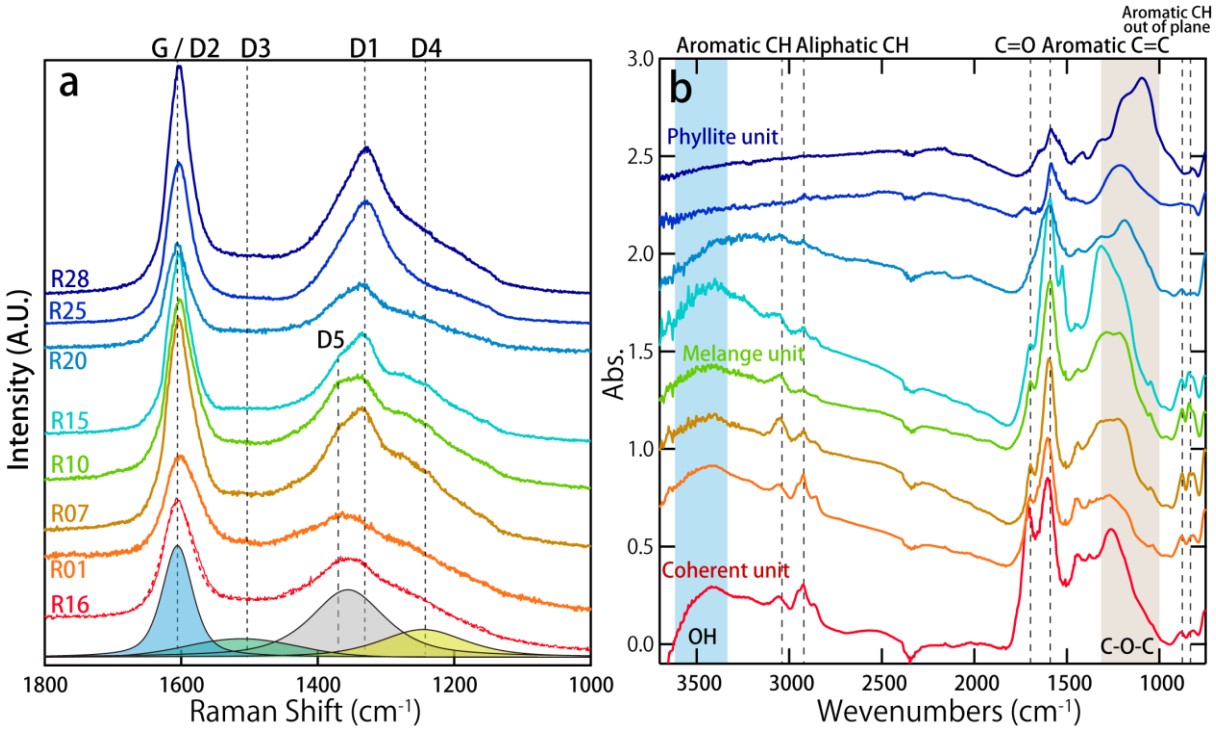

Figure 61. Representative Raman **(a)** and IR **(b)** spectra of carbonaceous material along the Aki tectonic line.

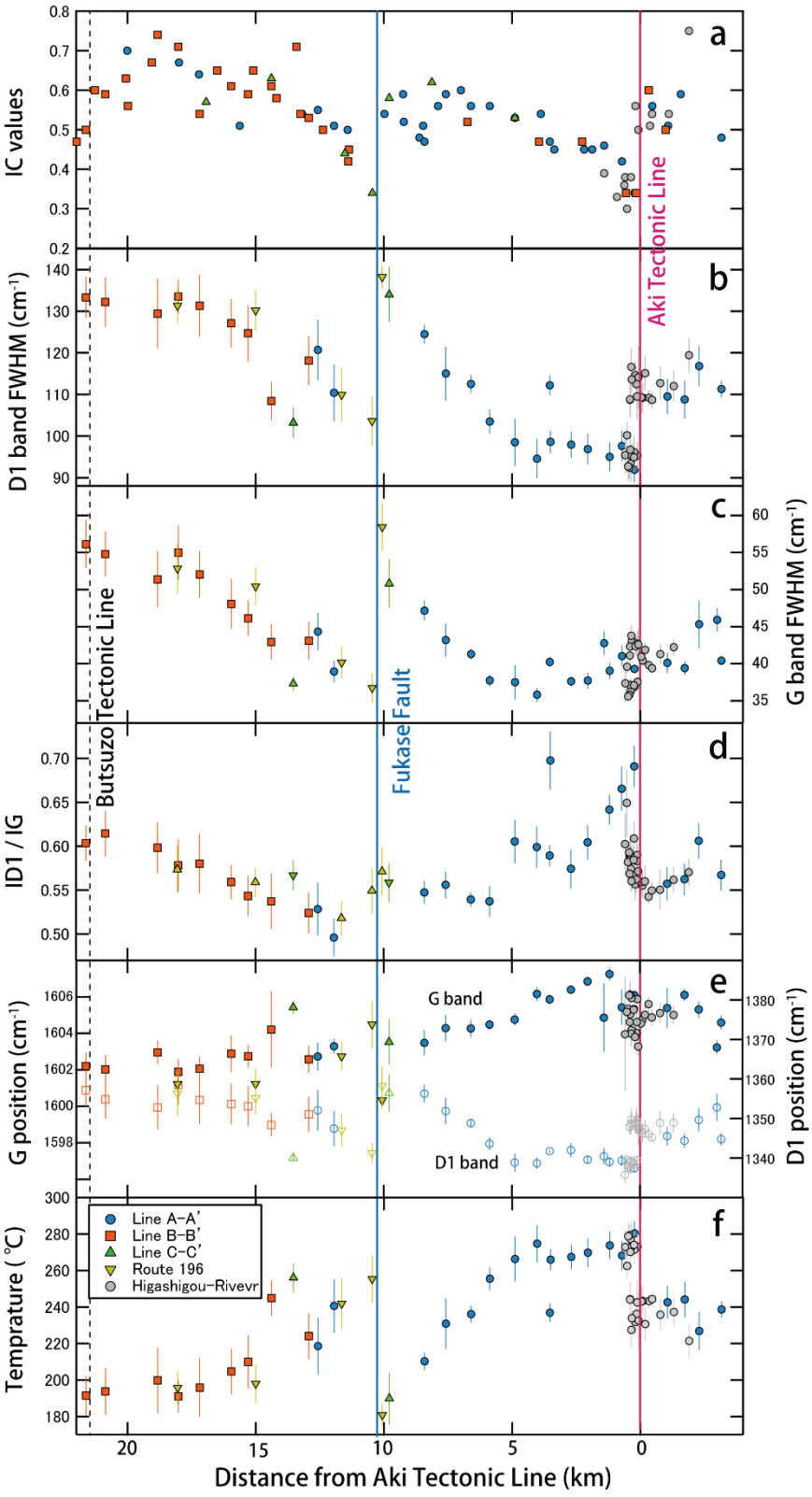

Figure 62. Structural changes of CM in mudstones along the distance from Aki tectonic line. Symbols are divided into five areas; Line A-A', B-B', C-C', Route 196, and Higashigou-River area.

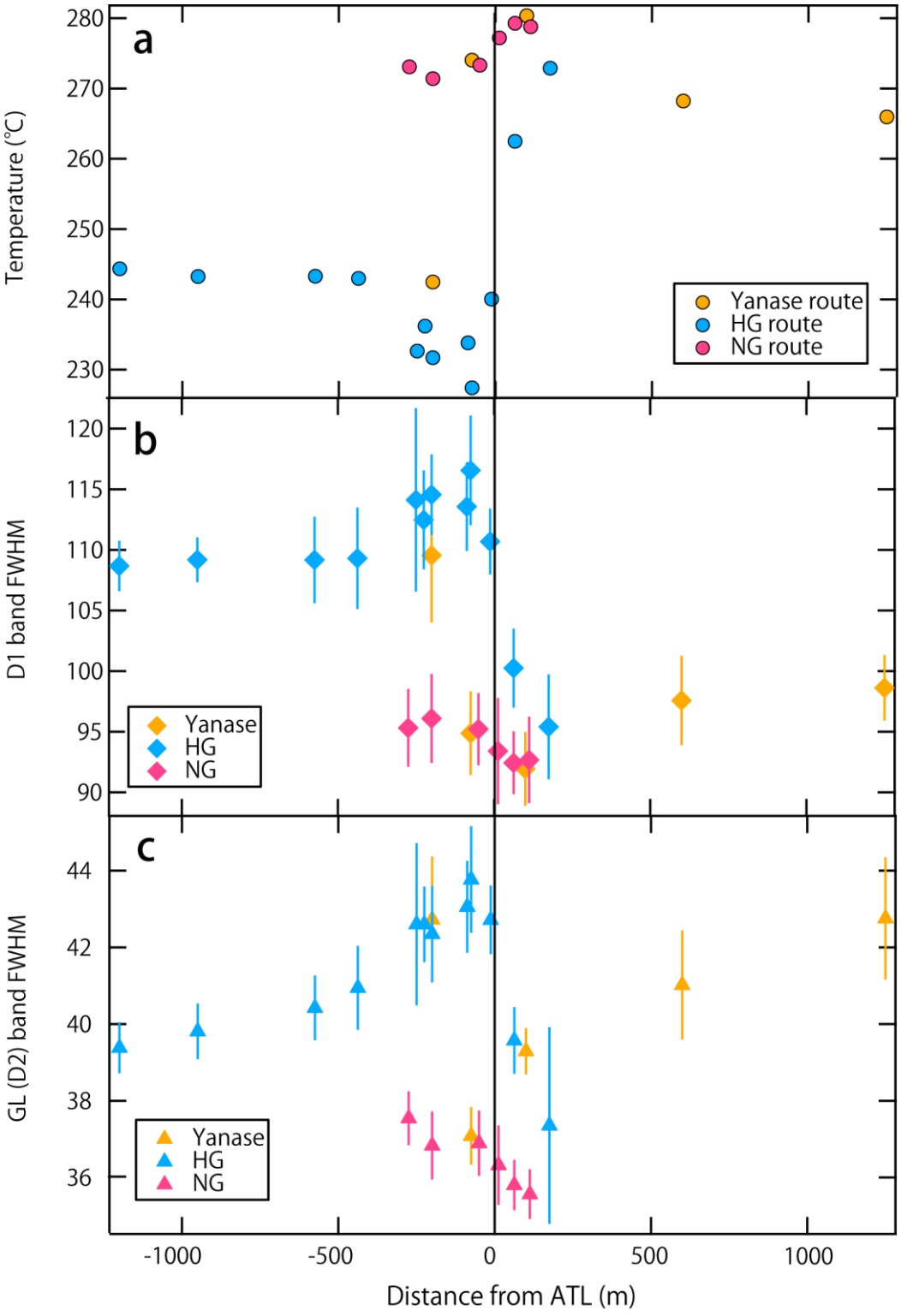

Figure 63. Detailed structural changes of CM in mudstones at around Aki tectonic line.

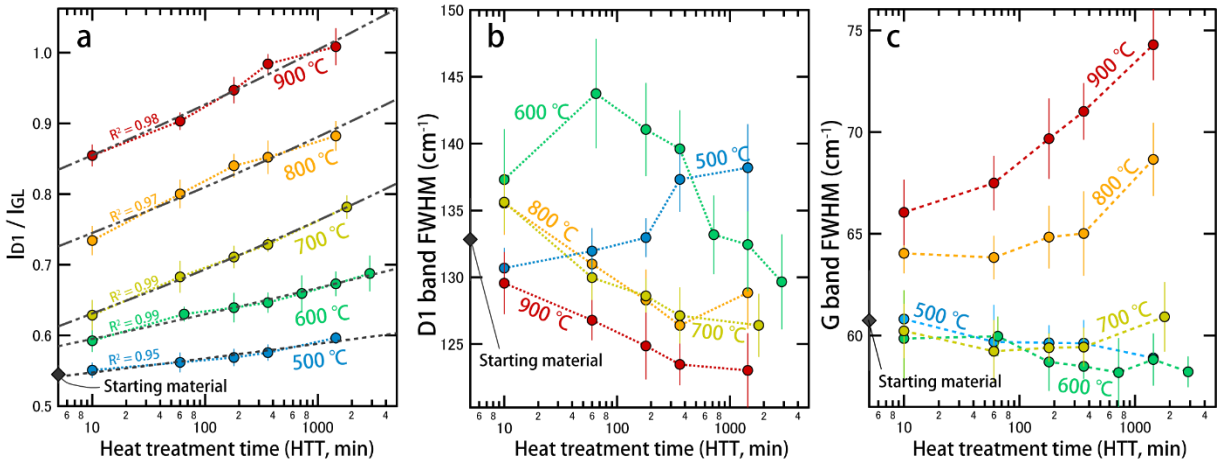

Figure 64. Time-temperature relations between 10 and 5000 min. The parameters **(a)** I_{D1}/I_G, **(b)** D1 band FWHM, **(c)** G band FWHM are systematically changed as a heating temperatures from 500~900 °C.

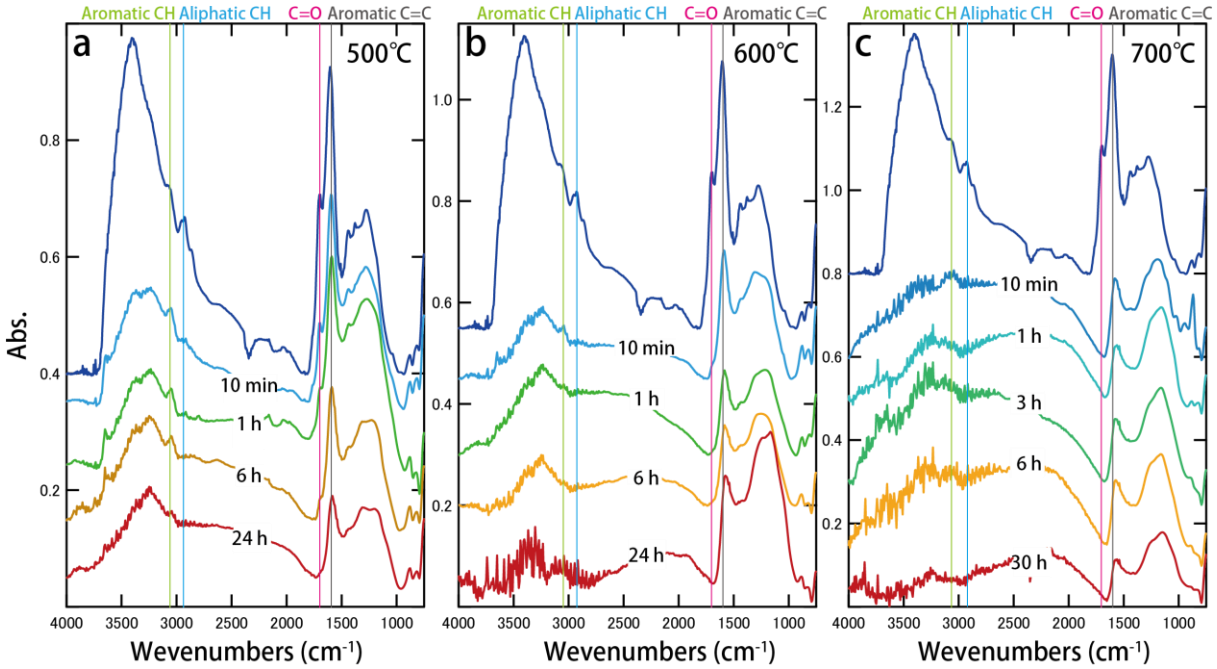

Figure 65. Structural changes of functional groups by micro-FTIR study. The different heating temperatures from **(a)** 500 °C, **(b)** 600 °C, and **(c)** 700 °C are described as a function of heating duration for 10 min to 30 hours.

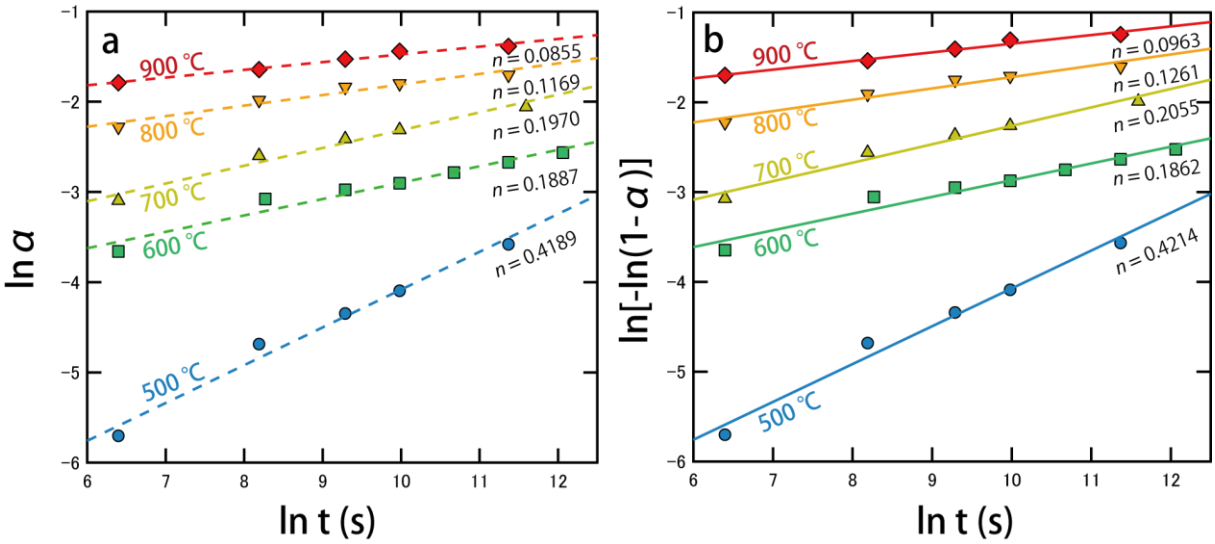

Figure 66. The relationship between natural logarithm of experimental time (sec) and natural logarithm of degree of carbonization α fitted by power rate **(a)** and Avrami-Erofeev models **(b)**.

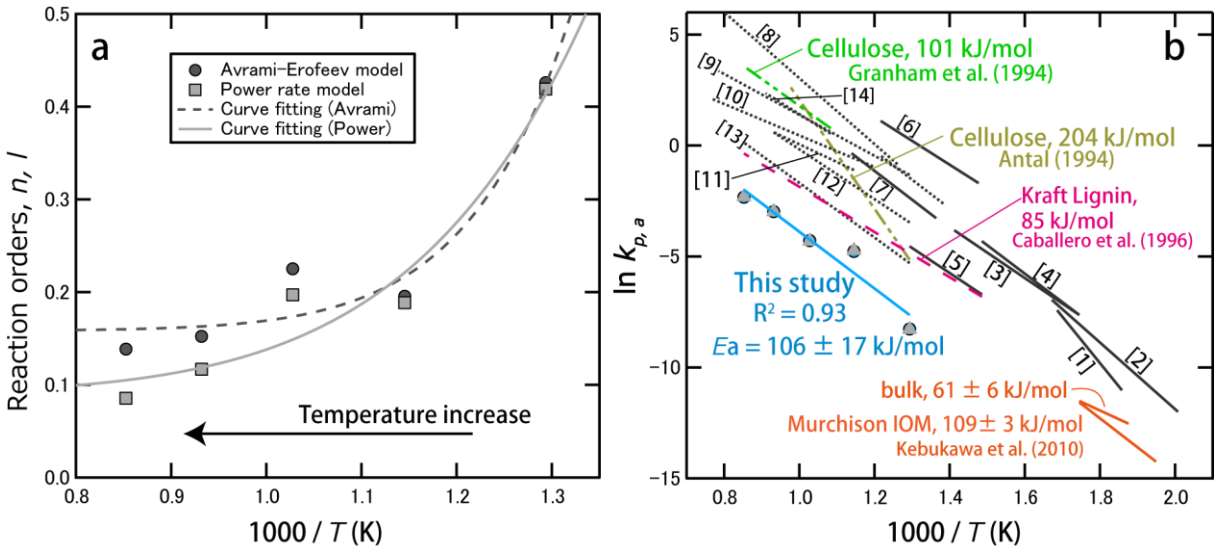

Figure 67. (a) The systematic changes of reaction order n and l as a function of experimental temperature. **(b)** Arrhenius plot of rate constants k_p and k_a with the previous data on pyrolysis experiments by [1], Ward and Brashlaw, (1985); [2], Reina et al., (1998); [3], Di Blasi and Branca, (2001); [4], Thuner and Mann (1981); [5], Samolada and Vasalos (1991); [6], Gorton and Knight (1984); [7], Font et al. (1990); [8], Lede (2000); [9], Morf et al., (2002); [10], Baumlin et al. (2005); [11], Rath and Staudinger (2001); [12], Boroson et al. (1989); [13], Cozzani et al. (1995); Diebold, (1985); Celluose, Graham et al., (1994), Antal (1983); kraft lignin, Caballero et al. (1996); Murchison insoluble organic matter, Kebukawa et al. (2010).

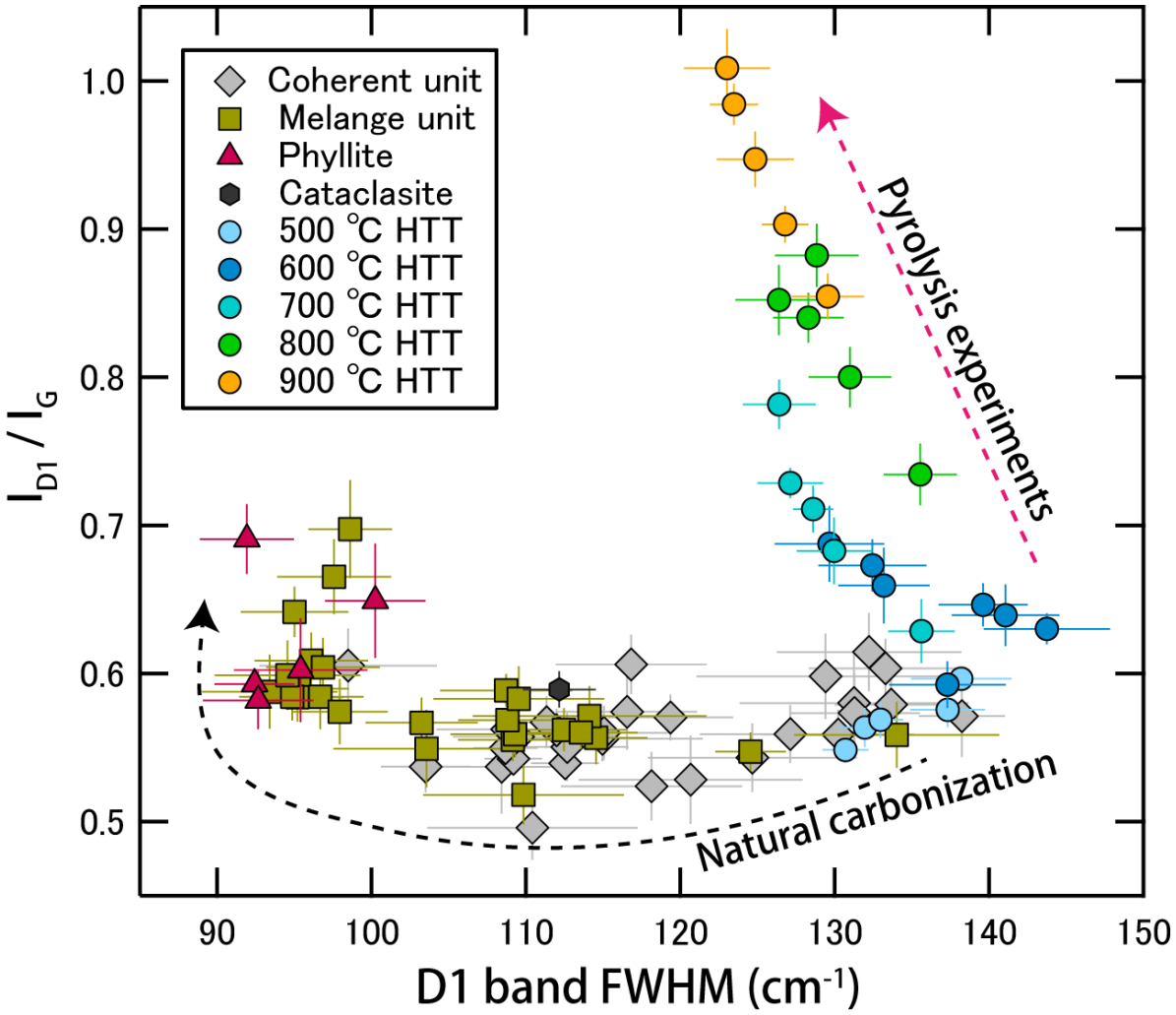

Figure 68. Relationship between D1 band FWHM and I_{D1}/I_G ratio during natural carbonization and pyrolysis experiments.

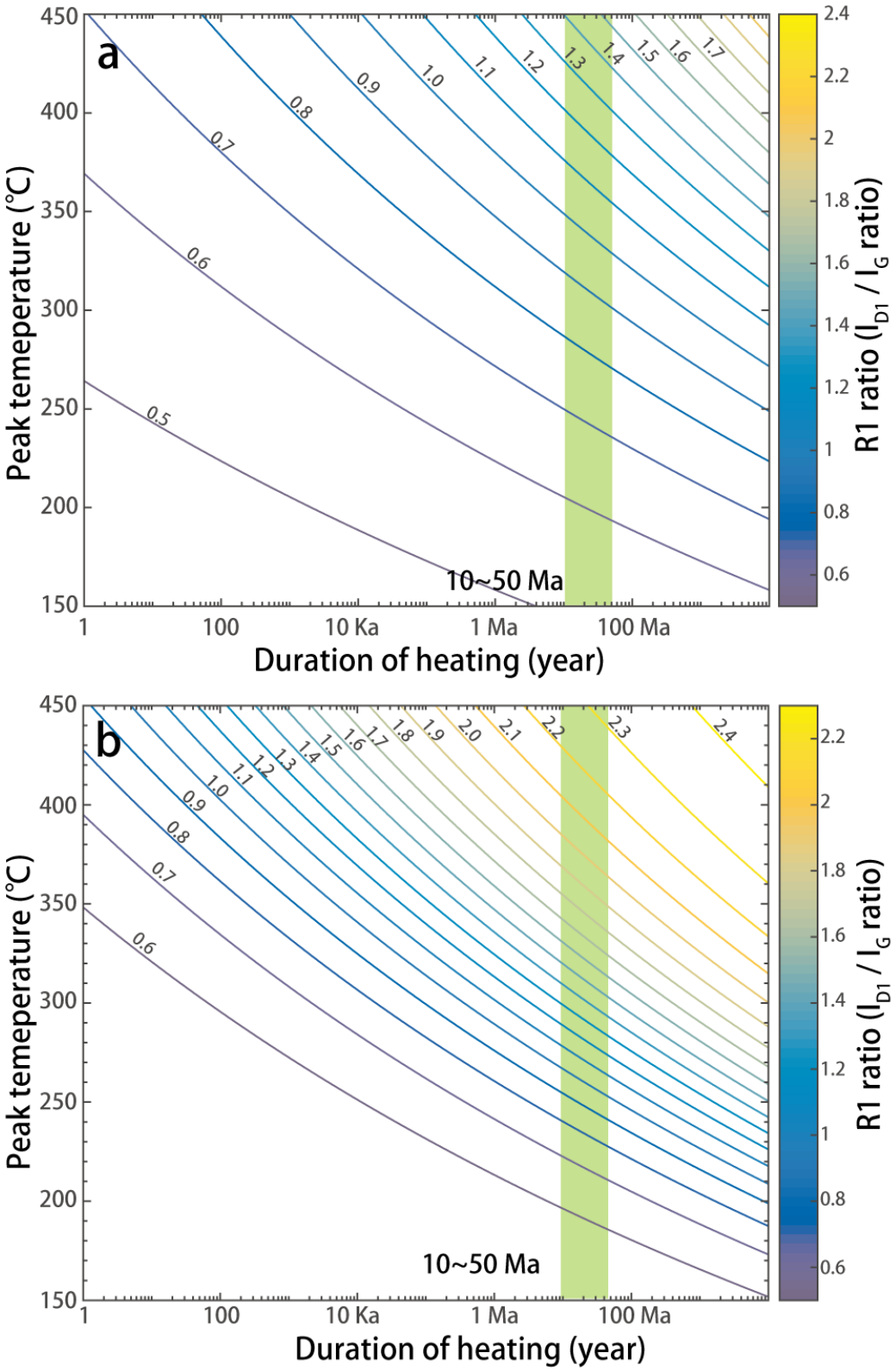

Figure 69. Structural change of I_{D1}/I_G ratio as a function of peak temperature utilizing **(a)** power rate model and **(b)** sigmoid model. Green area indicates the range of duration of heating for 10~50 Ma.

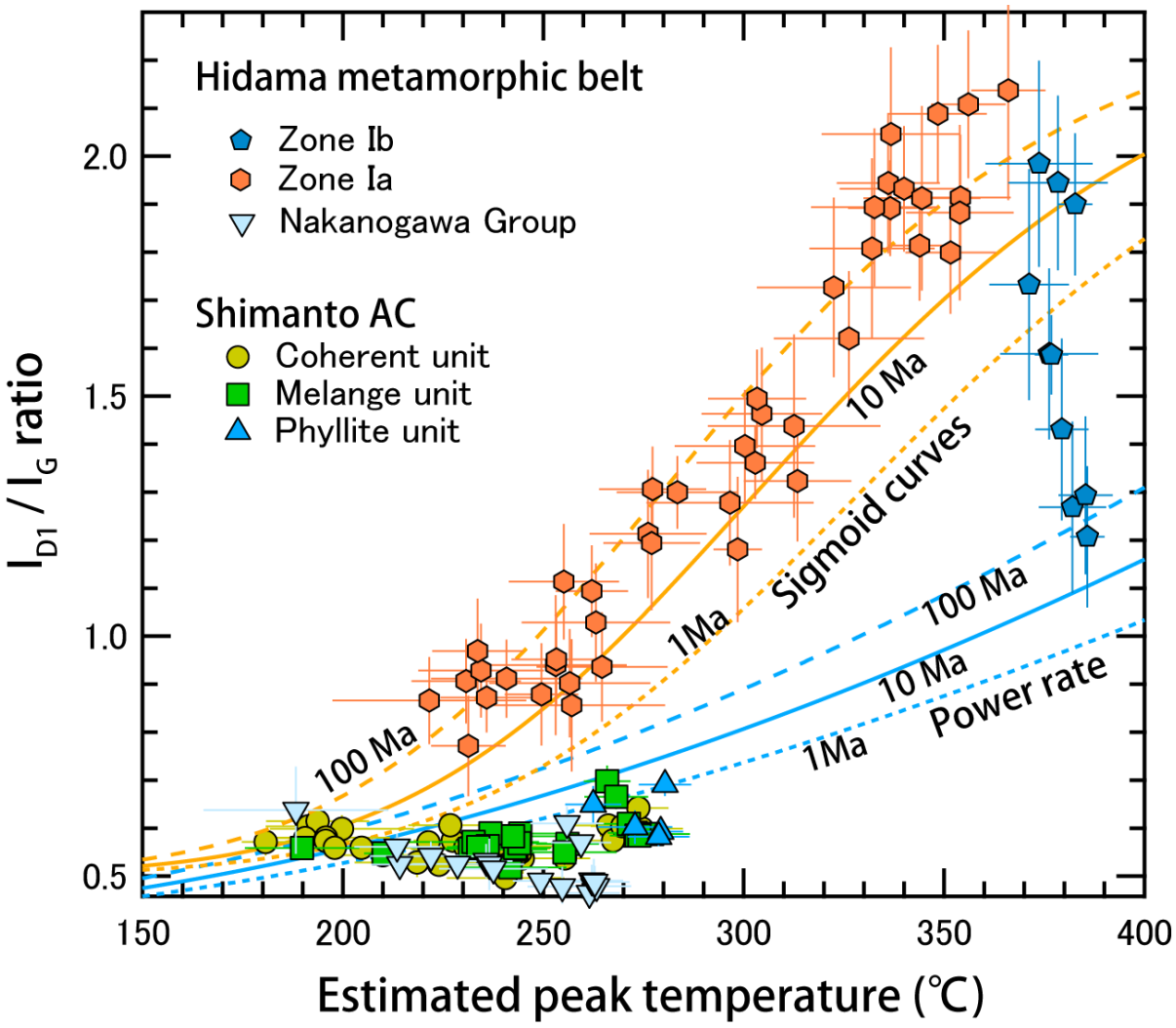

Figure 70. Estimated peak temperatures based on the power rate and sigmoid models. The plots in Shimanto accretionary complex and Hidaka metamorphic belt are superposed for reference.

CHAPTER VI

An experimental kinetic study on the structural evolution of natural carbonaceous material to graphite

6.1. Introduction

Carbonaceous material (CM) is a widespread accessory phase in sediments, and its composition and structure are sensitive to change during metamorphism (Buseck and Beyssac 2014). The structural evolution of CM to graphite is one of the most important thermal indicators for geological regimes of low to medium metamorphic temperatures, and is widely used as a geothermometer (Beyssac et al. 2002; Kouketsu et al. 2014). However, the process *sensu stricto* is not a simple recrystallization that depends only on metamorphic temperature. The organic precursor materials of CM in sediments have complex supramolecular structures (Oberlin et al. 1999; Schwab et al. 2005), and their evolutions in chemical composition, microstructure, and crystallinity depend not only on thermal maturation but also on tectonic deformation, catalytic effects, and fluid activity under lithostatic pressure (Luque et al. 1998). Such complex transformations during the transition of organic matter to graphite make it difficult to understand the natural structural evolution of CM, and proper assessments of these factors during graphitization have been seldom achieved. Therefore, it is essential to consider a fundamental kinetic model for natural graphitization under geological timescales and crustal temperatures.

The natural structural evolution of organic matter to CM, and then into graphite, mainly comprises two prominent processes: carbonization and graphitization (Oberlin 1984). The early stage of carbonization begins with softening and the release of aliphatic

compounds and heteroatoms with increasing temperature. After degradation of aliphatic CH groups, solid-state reorganization (the formation of basic structure units, BSUs) progresses with the release of non-condensable gases (e.g., CH_4 and H_2) from the aromatic CH groups (Oberlin et al. 1999). The BSU is the minimum structural unit of the CM nanostructure. The aggregate is stacked in two or three polyaromatic layers, and acts as a nucleus for the transformation of turbostratic to a graphitic structure (Oberlin, 1984; Oberlin et al. 1999). The natural and experimental kinetic approaches on carbonization have been widely investigated using vitrinite reflectance (Hood et al. 1975; Burnhan and Sweeney, 1989; Sweeney and Burnham, 1990; Huang 1996), biomarker thermal maturity (Sheppard et al. 2015), carbon X-ray absorption near-edge structure spectroscopy (C-XANES: Cody et al. 2008), micro-Raman spectroscopy (Muirhead et al. 2012) and *in-situ* micro-Fourier transform infrared spectroscopy (Kebukawa et al. 2010). These kinetic studies have reported wide ranges of apparent activation energies between 98 and 345 $kJmol^{-1}$ (Marsh et al. 1999), some of which are comparable to the dissociation energies of C–H bonds (346–421 kJ mol^{-1}) and C–C bonds (254–346 kJ mol^{-1}). The other major process, graphitization, involves crystallization from a turbostratic to a graphitic structure by the reorganization of stacking sheets. The structural change of CM to graphite has been well studied using X-ray diffraction (Grew 1974; Wada et al. 1994), transmission electron microscopy (Buseck and Huang, 1985) and micro-Raman spectroscopy (Wopenka and Pasteris, 1993). On the other hand, the experimental studies on the kinetics of graphitization are scarce in the literature. The biggest drawback in synthesizing graphite is that it requires very high treatment temperature (~ 3000 K) in a low fO_2 environment under ambient pressure. Early kinetic studies in the 1960s–1970s already reported an effective activation energy of ~ 1000 kJ mol^{-1} for the formation of graphite (e.g., Fischbach 1963, 1971; Murty et al. 1969). These values are in good agreement with activation energies of vacancy diffusion from experiments with natural graphite (Kanter, 1957) and

first principles calculation (Kaxiras and Pandey, 1988). However, such a high effective activation energy based on experimental results points to notable differences between natural and experimental structural evolution of CM. For instance, extrapolation based on previous experimental kinetic data at 1 atm suggests that even at 700 °C, graphite would require durations of the order 10^{40} min (1.9×10^{34} years; Fischbach 1971; Bustin et al. 1995). Therefore, it is required that we should provide more realistic experimental kinetic model and more realistically constrained experimental data to understand the kinetics behind natural graphitization.

The large divergence between experimental and natural graphitization results from neglecting other factors such as lithostatic pressure (Noda et al. 1968; Beyssac et al. 2003), tectonic deformation (Ross and Bustin, 1990; Bustin et al. 1995) and catalytic effects (Marsh et al. 1983). This work constructs a revised kinetic model for natural graphitization through an experimental exploration of the synthesis of graphite under relatively low temperature and pressure conditions (1000–1450 °C and 1 GPa), when compared with early kinetic studies. Previous studies on the synthesis of graphite have noted that the structural evolution of CM to graphite depends greatly on the nanostructure of the precursor materials (graphitizing and non-graphitizing carbon) (Oberlin 1984; Oberlin et al. 2006). Therefore, we used two different CM samples extracted from representative pelitic rocks in a low-grade metamorphic terrain and an accretionary complex to compare the influence of the nanostructure of the precursor. Our findings lead to a revised kinetic model for the natural structural evolution of CM, which advances our understanding of graphitization in natural environments over geological timescales.

6.2. Method

6.2.1. Starting materials

The natural CMs in pelitic rocks are complex aggregates of two CM end-members (non-graphitizing and graphitizing carbon; Oberlin 1984). The heterogeneity of nanostructures is one of the most important factors to discuss in the recrystallization during the high pressure high temperature (HPHT) experiments. It is difficult to quantify the heterogeneity of nanostructures in transmission electron microscopy observations and reconstruct the natural heterogeneity of CM using the two end-members. Therefore, the starting materials for the HPHT experiments were prepared from two different naturally occurring sedimentary rocks: one from the Hidaka metamorphic belt (HMB) and the other from the Cretaceous Shimanto accretionary complex (SM). Both starting materials extracted by HF-HCl treatments were expected to demonstrate behavior closer to that in nature than observed in previous experiments using cokes and other commercial carbon materials, and especially suitable starting materials, because their localities have been well studied in terms of structural geology, metamorphic geology, and organic geochemistry (Nakamura et al. 2015; Ohmori et al. 1997).

The CM in HMB were sampled from muscovite-chlorite grade metasediments, which are located near to the boundary of the biotite isograd (see Nakamura et al. 2015 for detailed geological relations). Under the microscope, the CM was observed along the grain boundaries of quartz or plagioclase within pelitic layers, and along cleavage planes in chlorite and muscovite. The CM showed a turbostratic (sample HMB, d_{002} spacing = 3.431 ± 0.007 Å) structure in XRD profiles and high R2 ratio (R2 ratio = 0.62 ± 0.01) in micro-Raman spectroscopy.

The CM in SM were sampled from mudstone in the Hinotani unit of the Cretaceous Shimanto accretionary complex. The Hinotani unit is dominated by coherent turbidite units containing massive and bedded sandstone, interbedded sandstone and mudstone,

and mudstone. The CMs in this area show the lowest maturity and systematically change their crystallinity with increasing the paleo-thermal gradient toward the out-of-sequence thrusts (Fukase fault and Aki Tectonic line), ranging between 1.3 and 3.0 % of vitrinite reflectance (Ohmori et al. 1997). In addition, these sediments are considered as a candidate precursor for high pressure metamorphic rocks such as Sambagawa metamorphic belt (e.g., Aoki et al. 2011; low temperature high pressure type metamorphic terrain). Therefore, these rocks have another benefit, to compare different geothermal gradients in metamorphic regimes. Under the microscope, the CM was identified optically as two different macerals (vitrinite and inertinite), and it coexists with illite, plagioclase, quartz, and framboidal pyrite in pelitic layers. The CM showed an amorphous (sample SM, d_{002} spacing = 3.505 ± 0.013 Å) structure in XRD profiles and a broad D1 band FWHM in micro-Raman spectroscopy (D1 band FWHM = 129.4 ± 8.4 cm^{-1}). The two samples we have selected cover a wide range of crystallinity, and are suitable for applying experimental graphitization of natural CM back to the temperature–time scale of metamorphic rocks.

6.2.2. Chemical extraction from pelitic rocks

Given that the sedimentary rocks have low concentrations of organic carbon (total organic carbon values of 0.3–0.7 wt%; Nakamura et al. 2015), we followed the chemical extraction for preparing the required aliquots of CM samples (Nakamura and Akai, 2013). The presence of silicate or oxide minerals in the starting materials may form various carbides at high temperature (> 900 °C; e.g., Charon et al. 2014), therefore it is important to eliminate these minerals as much as possible by chemical extraction.

The rock samples (500–800 g) were crushed by a Jaw crusher and sieved using a 200–mesh screen. The sieved powder was initially treated with 2N HCl to remove

carbonate, sulfide, sulfate and hydroxides (Vandenbroucke and Largeau, 2007), and then the solution was treated by HF (48 %) in several large Teflon vessels (500 ml) and dried on a hot plate at 120 °C. Dried residues in Teflon vessels were composed of CMs and newly formed fluorides such as ralstonite and other complex fluorides (Durand and Nicaise, 1980). These fluorides are difficult to redissolve once precipitated and they interfere with further analysis of CM (Vandenbroucke and Largeau, 2007), therefore, we performed repeated rinsing with hot deionized water between acid treatments (Durand and Nicaise, 1980). The residues were dissolved again in 2N HCl at 60 °C. The chemical treatments were repeated several times until the CM floated in the solution. This floatation is a signal of the complete decomposition of fluorides (Itaya, 1981; Itaya 1985). The supernatant of CM was filtered and dried on a watch glass. Note that the CM residues retained small amounts of minerals such as zircon, rutile, ilmenite, and pyrite even after HF–HCl acid treatments. Both starting materials of SM and HMB are slightly matured or metamorphosed during diagenesis and low grade metamorphism, respectively. Many researchers have concluded that the HF–HCl acid treatments do not alter the CM structure and do not generate newly formed solvent soluble organic materials except in the case of very immature sediments (Durand and Nicaise, 1980; Larsen et al. 1989; Vandenbroucke and Largeau, 2007). More detailed procedures of chemical extractions from mudstones are described in the Appendix 1.

6.2.3. HPHT experiments

HPHT experiments were performed at the Institute for Planetary Materials (IPM), Okayama University, Misasa, Japan. The two starting materials were encapsulated and stamped in platinum tubes of 2.0 and 3.0 mm outer diameter. Experiments were carried out with both starting materials together in a single run so as to reduce any apparent

difference in absolute temperature conditions. After welding and encapsulating, the platinum capsules were placed in two different pressure apparatus for appropriate treatment of temperature and time; (1) The piston-cylinder (PC) apparatus (2) The DIA-type apparatus (AMAGAEL). For the PC experiments, the assembly was composed of a talc-Pyrex-graphite furnace with MgO disks as pressure medium (19.05 mm (3/4 inch diameter)). Two platinum capsules were placed at the center of graphite heater. Experimental temperature was measured by type S ($Pt\text{-}Pt_{90}\text{-}Re_{10}$) thermocouples. For experiments using the DIA-type apparatus, the cubic pyrophyllite with edge length of 21 mm was adopted as pressure medium and the tungsten carbide anvils with top edge length was 15 mm. Temperature was monitored using $W_{97}Re_3\text{-}W_{75}Re_{25}$ thermocouples with Al_2O_3 insulating sleeves, whose junction was placed in contact with the center of MgO disk. We used DIA-type apparatus for high temperature conditions (1325 and 1450 °C). Previous studies on HPHT experiments already reported that the conversion of graphite at 1 GPa required at least 1200 °C for 100 h (Beyssac et al. 2003). Therefore, our experiments were carried out at four different temperature conditions between 1000 °C and 1450 °C, and different annealing durations at peak temperature from 10 min to 115 h. Short experiments of 1s duration (PC 481 and PC 482) were also carried out for reference, however, these were not used for kinetic analysis due to uncertainties in time-temperature estimates. Both experiments were carried out with a heating rate of about 100 °C / min and quenching by switching off the furnace power.

6.2.4. Analytical methods

The recovered platinum capsules were mounted into epoxy resin and cut into two halves. One half was used for SEM observations and micro-Raman spectroscopy. The other half was separated from the slab section of platinum capsule using a dentist diamond cutter

under a binocular microscope. The powder was used for X-ray diffraction and transmission electron microscopy observations.

X-ray diffraction (XRD) was obtained using a Rigaku ULTIMA IV diffractometer at Niigata University, equipped with CuKα (40 kV, 40 mA) radiation, graphite monochromator, slit system 2/3 °–0.45 mm–2/3 ° and time constant of 0.5 ° min^{-1}. The diffractometer was run between 10 ° and 90 °. The powdered samples of CM were dried on a Si-low background sample holder with internal standard of silicon (10–20 wt%). Lattice constant and crystal thickness of graphite were calculated according to the following methods. The 2θ values of the obtained peaks were calibrated using the peak positions of the internal silicon standard (Iwashita et al. 2004). The $L_c(002)$ was calculated using the Scherrer equation: $L_c(002) = K\lambda / \beta\cos\theta$, where K, constant (1.0); λ, X-ray wavelength (Cu$K\alpha$ = 1.5419 Å); β, full width at half maximum (FWHM); θ, the Bragg angle. The K value is not a constant, but depends on the crystallite sizes (Fujimoto 2003). Therefore, we used the constant K of 1.0 for $L_c(002)$ following JIS standards (Iwashita et al. 2004).

Micro-Raman spectroscopy was applied to CM and graphite in the first order region using a Jasco NRS 3100 spectrometer at Niigata University, equipped with the grating of 1800 lines/mm and CCD-detector (256×1024 pixels). The microscope objective of 100×, and Nd-YAG laser (wavelength: 532 nm) were used. Acquisition time is 10–30 s, and 3–6 spectra were cumulated for each data point. All Raman peak profiles were analysed by using peak profile fitting, and G (1580 cm^{-1}), D1 (1350 cm^{-1}), D2 (1620 cm^{-1}), D3 (at around 1450 cm^{-1}), and D4 (at around 1200 cm^{-1}) bands in the first order region (1000–1800 cm^{-1}) were separated. The parameters of G band FWHM, D1 band FWHM, G position (Raman shift), R1 ratio (Intensity $_{D1\ band}$ / Intensity $_{G\ band}$), R2 ratio (Area $_{D1\ band}$ / Area $_{G + D1 + D2\ bands}$), and Area ratio (AR; Area $_{D1 + D4\ bands}$ / Area $_{G + D2 + D3\ bands}$) were estimated. The Tuinstra and Koenig equation were applied: $I_{D1} / I_G = C(\lambda) / L_a$ (nm) (Tuinstra and

Koenig 1970); where C (λ), constant (4.4); I_{D1}/I_G, Intensity $_{D1\ band}$ / Intensity $_{G\ band}$, R1 ratio; L_a (nm), the crystal size of lateral extent of carbon sheets. Mean values and standard deviations were calculated based on 11–20 analyses for both edge and center part of samples.

Scanning electron microscopic (SEM) observations were carried out using a JEOL 6510LA, equipped with an energy dispersive X-ray spectrometer (EDS) at Niigata University. Both samples were observed without coating under low vacuum pressure.

Transmission electron microscopy (TEM) was carried out using a JEOL JEM 2010 electron microscope in Niigata University, operating at 200 kV with LaB_6 filament. CM samples extracted from the run products were ground and suspended in pure water. After ultrasonic cleaning in plastic tubes, the solution was deposited on the carbon-coated holey film of the TEM micro-grid treated by plasma cleaning. The samples were mainly observed for the d_{002} lattice fringe along the [010] direction.

6.3. Results

6.3.1. Morphological characteristics of run products

Both CM samples show gradually changing surface optical properties (i.e., relative reflectance) as annealing occurs at increasing temperatures and for longer durations. Short annealing (1 s to 10 min) leads to the formation of many voids and cracks of 1 to 10 μm width in some areas of the run products (Fig. 71a). Such pores are rare in the HMB samples (Fig.71b). Previous studies have also reported the presence of voids or porous structures on polished coal surfaces, suggesting the release of volatile matter from the precursor (Rodrigues et al. 2011; Zhou et al. 2014). Our observations also suggest a change in the bulk density of the CM due to the release of volatile matter during

carbonization (Inagaki and Meyer 1999). In addition, the morphological characteristics of the CM gradually change in response to both annealing duration and temperature. Treatment at 1000 °C leads to CM samples consisting of small grains of 1–10 μm diameter with porous structures observable by SEM (Fig. 71c). Treatment at higher temperatures changes the CM to aggregates with planar structures (Fig. 71d), which do not show the hexagonal morphology commonly seen by SEM in well crystallized graphite.

6.3.2. XRD analysis

Both CM samples extracted from Pt capsules show systematically changing XRD profiles with respect to temperature and duration (Fig. 72a; Table 17). Crystal parameters derived from the XRD patterns reveal the evolution of three types of microstructure: amorphous (1D), turbostratic (2D), and graphitic (3D) structures. At the early stage (1 s to 10 min), SM shows a broad and symmetric reflection at the 2θ range of 40–45° in XRD profiles. This single broad reflection (named as 10 reflection) is a composite of d_{100} and d_{101} reflections, suggesting the presence of randomly oriented small stacks in amorphous structure. Longer annealing (1 to 6 h, Fig. 72a) makes the broad peaks asymmetric owing to the formation of turbostratic structure. This asymmetric peak starts to split into the d_{100} and d_{101} reflections with increasing temperature and time. The d_{112} and d_{006} reflections also appear, suggesting the formation of a graphitic structure (Fig. 72a). Both samples show such progressive structural changes from amorphous to graphitic with increasing temperature.

6.3.3. Micro-Raman spectroscopy

Two prominent bands corresponding to the G band (1580 cm^{-1}) and D1 band (1350 cm^{-1})

appear in the first-order region (1000–1800 cm^{-1}; Fig.72b; Table 18). Their intensity and area ratio gradually change with increasing temperature and longer treatment. In addition to the first-order region, the overtone and combinations of the G and D bands (2D1, D1+G, 2D2) in the second-order region (2500–3200 cm^{-1}) show similar changes to the main bands, as reported by Wopenka and Pasteris (1993). At the early stage of annealing at low temperature, disordered bands such as D3 and D4 are identified by the peak deconvolution of two prominent bands (Fig. 72b). The 1500 cm^{-1} D3 band generally appears broad, suggesting that it originates from amorphous sp^2-bonded carbon from organic molecules, fragments, or functional groups in poorly organized materials (Cuesta et al. 1994; Sadezky et al. 2005). The 1200 cm^{-1} D4 band is also derived from poorly organized organic materials, and is attributed to sp^3–sp^2 mixed sites at the peripheries of crystallites or to C–C and C=C stretching vibrations of polyene-like structures (Dippel et al. 1999; Sadezky et al. 2005; Shen 2007). These two bands indicate that the CM samples at the early stage of annealing at low temperatures have many dangling bonds on polyaromatic layers. Higher temperatures and longer annealing change the CM into a graphitic structure, as shown by the decreasing intensity of the disordered bands. These structural changes observed by micro-Raman spectroscopy are in a good agreement with those observed by XRD. Beyssac et al. (2003) reported that the crystal parameters in micro-Raman spectroscopy display strong heterogeneous distributions in microscopic scale. To assess the microtextural heterogeneity, we compared the area ratio of the center with the edge part of non-polished slab section of platinum capsules (Fig. 73). The edges of both samples annealed at lower temperatures show slightly lower crystallinity compared with the central part of the capsule. This may have resulted from the temperature and microstructural heterogeneity within the assembly as reported by Beyssac et al. (2003). However, almost all data obtained in the temperature range exhibited a strong squared correlation coefficient of 0.978 in the center vs. the edge parts

of area ratio plot (Fig. 73).

6.3.4. TEM observations

The starting materials of HMB and SM show different microstructural signatures. Although the CMs of HMB display broad 002, 10, and 11 rings in the selected area electron diffraction (SAED) patterns, poorly crystallized parallel fringes are locally observed in the tissue-like aggregates (Fig. 74a). Under high magnification, poorly organized fringes surrounded by disordered graphitic layers are discernible. The distorted graphitic layers already have anisotropy in lateral direction. The SAED pattern in the distorted graphitic layers shows arc-like spots of 002 reflections, suggesting turbostratic structures within graphitic layers (Fig. 74b). Such aggregates of CM were also observed in the chlorite zone (Buseck and Huang, 1985). On the other hand, the CMs of SM also show broad 002 rings in the SAED patterns and granular aggregates (Fig. 74c). Under high magnification, poorly organized fringes that are composed of 2–3 carbon layers are observed. In contrast to the CM in HMB, the poorly organized fringes are isotropically oriented in the aggregates (Fig. 4d). The isotropic distributions of poorly organized fringes generally correspond to the nanostructure of BSU in coal (Oberlin et al. 1999). Longer and higher-temperature annealing converts these nanostructures to a graphitic structure (Figs. 74e–h). Under the 11 dark-field (DF) mode, the platy graphite displays a typical Moiré fringe, suggesting a fully ordered and stiff layer in lateral direction (Fig. 74e; Oberlin 1984). In addition, the 10 ring in the SAED pattern starts to split into two diffraction patterns of 100 and 101 spots, while the 11 ring splits into 110 and 112 spots (Fig. 74g). The lattice fringes of the d_{002} spacing are fully ordered, and define (002) and (101) in the SAED pattern along the [010] direction (Figs. 74f and 74h). These microstructural observations suggest that heat treatment converted both CM samples to a graphitic structure. However, the SAED

patterns still display ring and spotted patterns, suggesting the presence of turbostratic or amorphous structures in the graphitic carbon. In fact, some of the XRD peak profiles show asymmetric d_{002} peaks, which included signatures of both the turbostratic and graphitic components in the microstructure. Previous studies using XRD (Inagaki and Meyer 1999), micro-Raman spectroscopy, and TEM observations (Beyssac et al. 2003) have reported that graphitization under HPHT conditions induces heterogeneous recrystallization. In this study, similar patterns regarding microstructural evolution observed by TEM supports their results observed in XRD and micro-Raman spectra.

6.3.5. Time–temperature relations inferred from heat treatment

The time–temperature relations of both CM samples display changes in crystallinity with increasing annealing duration (Figs. 75a–l). Similar to the observations of Beyssac et al. (2003), structural changes at 1000 °C were limited when annealing lasted between 10 min and 48 h. However, structural changes of CM to graphite occurred at 1200, 1325, and 1450 °C as the heat treatment progressed. In particular, almost all the crystal parameters indicated a graphitic structure even at the early stage of heating (1 to 6 h), and most of the parameters became constant or showed only extremely slow change after 6 h, suggesting either the termination of crystal growth or only sluggish growth. In addition, each parameter obtained from XRD and micro-Raman spectroscopy displays some important signatures in the time–temperature relations. The d_{002} spacing (Figs. 75a and 75d) and FWHM (Figs. 75b and 75e) for both CM samples terminate at around 3.36 Å and 0.4°, respectively. The L_c(002) of SM (Fig. 75f) also indicates the termination of crystal growth at around 200 Å, whereas that of HMB (Fig. 75c) still grow up over 200 Å in crystal thickness. The unchanging d_{002} spacing indicates the formation of graphitic structures in the microstructures, but the termination of crystal growth shows a different signature

from both samples. In general, the final crystal sizes of carbon materials such as carbon black and soft carbon directly depends on the primary nanostructures (spherical or platy) during graphitization (Inagaki 1996). The starting material of SM displayed isotropic poorly organized fringes (Fig. 75d), whereas that of HMB already had developed the anisotropic distorted layers (Figs. 75a and 75b). The different primary nanostructures considered here may have influenced the final crystal sizes and morphological characteristics of the run products.

6.4. Discussion

6.4.1. Kinetic models of graphitization

The results of the HPHT experiments at 1 GPa for both CM samples suggest that their changes in crystallinity, morphology, and nanostructures were directly related to both the duration and temperature of treatment. We therefore assessed three different kinetic approaches of graphitization using the power rate model (e.g., Murty et al. 1969), the Johnson-Mehl-Avrami (JMA) model (e.g., Sung 2001; Khawam and Flanagan, 2006) and the superposition method (e.g., Fischbach 1963; Inagaki et al. 1968). Before we adopted these kinetic models, the experimental data were converted to the degree of graphitization (g) by following the equation (Murty et al. 1969; Khawam and Flanagan, 2006; Table 17):

$$g = (d_0 - d_1) / (d_0 - d_f), \quad (1)$$

where d_0 is the initial value of d_{002} spacing (Figs. 76a and 77d; Fischbach, 1971), d_1 is the observed experimental data, and the d_f show the final value of d_{002} spacing (Figs. 76a and 76d; Fischbach, 1971). The power rate model is the most robust kinetic model for carbonization and widely applied for extrapolating the geological time-temperature

regime using the rate constant and pre-exponential factor (e.g., Huang 1996). After conversions to nondimensional parameters, we attempted to fit the following power law of time as:

$$g = k_p t^{-n}, \qquad (2)$$

where k_p is the rate constant, t time (s), n an order of reaction at that temperature. The experimental data fitted by the equation (2) show squared correlation coefficient of 0.584–0.952 depending on the treatment temperatures (Figs.76a–b). The rate constant k_p and order of reaction n also demonstrate distributions as a function of the treatment temperature. In particular, the logarithm of rate constant $\ln k_p$ and order of reaction n show strong squared correlation coefficient of 0.979 (Fig. 77). This suggests that the kinetics of graphitization under low and high temperature underwent different chemical reactions. Some previous studies have used the mean values of order of reaction (Huang 1996) or linear regression values from the least squares of experimental data (Muirhead et al. 2012) to avoid the experimental uncertainty of the complex chemical reactions. The differences of experimental uncertainty are permissible in the range of order of reaction (n) between 0.062 and 0.09 (Huang, 1996). On the other hand, the orders of reaction in this study vary widely (n = 0.007 to 0.82), and it is difficult to apply the previous methods directly (Fig. 77). The results imply that graphitization is not a simple chemical reaction and that various reactions progress simultaneously (concurrent reaction) and/or successively (successive reaction). In this study, we attempted to fit the Arrhenius relation using following equation:

$$k_{p,} = A\exp(-E_a/RT), \qquad (3)$$

where k_p is the rate constant, A the pre-exponential factor, E_a the effective activation energy, R the gas constant, and T the absolute temperature of the experiment. Using the Arrhenius equation (3), we calculated the effective activation energy. The values of SM and HMB samples partly demonstrate good squared correlation coefficients of 0.903 and 0.981,

however, have a large uncertainty spread in the average of activation energies of 259 ± 26 kJ mol^{-1} and 271 ± 63 kJ mol^{-1} (Fig. 76c; Table 19). Consistent with the results of earlier experimental studies, we concluded that graphitization does not follow a simple power rate model (e.g., Fischbach 1971).

Instead of a power rate model, we tried to calculate the best fitting using a JMA model to apply for the complex "sigmoid" transformation from an amorphous to a graphitic structure (Figs. 75a-l). The JMA equation is suitable to heterogeneous nucleation and recrystallization and widely applied in material science (e.g., Khawam and Flanagan, 2006). The equation was expressed as follows:

$$g = 1 - \exp(-k_a t^l), \qquad (4)$$

where k_a is the rate constant of JMA equation, l is the order of reaction termed "Avrami index", t is the duration of heating (s). Taking the natural logarithm of equation (4), it can be also expressed as:

$$\ln[-\ln(1-g)] = \ln k_a + l \ln t, \qquad (5)$$

Plotting the left side of equation ($\ln[-\ln(1-g)]$) and natural logarithm of time $\ln t$, the rate constant k_a and Avrami index l are estimated from the linear regression of intercept and slope in this Avrami plot, respectively. The model fitting by a JMA equation displays squared correlation coefficient between 0.555 and 0.963 depending on the temperatures (Figs.76d–e). The rate constant k_a and order of reaction l also demonstrate distributions as a function of the temperature (Fig. 77). Such variations are consistent with the results of the power rate model, suggesting complex chemical reactions. Using the $\ln k_a$ values vs. $1/T$, we obtained the effective activation energies of 269 ± 59 kJ mol^{-1} and 273 ± 47 kJ mol^{-1} for HMB and SM samples, respectively (Fig. 76f; Table 19). Both models are not in good agreement with the experimental structural changes from CM to graphite. These misfits to model fitting result from the large variation of the effective activation energies. Thus, we concluded that the structural change of CM to graphite cannot follow a

simple power rate model nor a simple JMA model.

We therefore applied the superposition method to propose a kinetic model for natural graphitization. The effective activation energy is usually obtained from the slope of the Arrhenius plot, which is the logarithm of the rate constant vs. the reciprocal of absolute temperature (i.e., ln$k$ vs. $1/T$). Arrhenius plots using a power rate model and a JMA model empirically provide only one intercept value (ln$k$) for each treatment temperature, whereas the superposition method has an advantage in its determination of the activation energy using two or more slopes derived from all experimental data. This is an effective method to predict the kinetics of complex chemical reactions. The superposition method is well known to describe the mechanical and electrical relaxation behavior of polymers, and some earlier studies have successfully applied the Arrhenius approach to graphitization (e.g., Fischbach 1971; Feng et al. 2002). The fitting curves of the measured crystal parameters vs. the logarithmic treatment time at different temperatures can be superposed by proper scale changes on the time axis. The shift in distance is called the time–temperature shift factor a_T, which is given by:

$$a_T = t_T / t_{ref}, \qquad (6)$$

where t_{ref} is the reference time at a certain reference temperature (Fig. 78a), and t_T is the time required to give the same response at the reference temperature (Fig. 78a). For every reference temperature chosen, a fully superimposed curve generated by the shift factors is called the master curve. The above equation (6) also can be written by combining the Arrhenius equation (3):

$$a_T = \exp\{E_a/R\,(1/T - 1/T_{ref})\}, \qquad (7)$$

where both T and T_{ref} are absolute temperatures. Plotting ln(a_T) vs. $1/T$ is another way to calculate E_a values and to predict crystal changes at low temperatures. The crystal properties with regression curves obtained by the superposition method are shown in Figure 78 and Table 20. The experimental reference temperature here is 1000 °C. To find

the best-fitting non-linear regression curve, some sigmoid functions and power functions were chosen to determine the shift values (Table 20). The fitting considered four parameters: the unit-cell height c, the FWHM of the d_{002} peak, $L_c(002)$, and the area ratio of the Raman bands. The master curves obtained for both samples show good squared correlation coefficients of 0.878 to 0.982 (Figs. 78a–d; Table 20). In particular, these sigmoid functions accurately reflect the three different processes of the successive reactions from carbonization to graphitization. The first stage of heat treatment corresponds to the formation of BSUs by the release of aliphatic and aromatic C–H bonding. After devolatilization, they start to crystallize from turbostratic to graphitic structures as the temperature and duration increase. The final transformation to graphite suggests the termination of crystal growth. Our extrapolations using sigmoid fitting have an advantage over the linear or power law fitting models used in previous studies, because we can extrapolate from the starting point to the termination point using a single sigmoid master curve. The effective activation energy was calculated from the relationship between $\ln(a_T)$ and $1/T$. The plot of the mean values and their linear regression lines show good squared correlation coefficients of 0.984–0.999 (Table 20), suggesting that the relation between annealing duration and temperature can be described as a thermal activation process. The mean values of effective activation energies were 274 ± 9 and 339 ± 6 kJ mol^{-1} for HMB and SM, respectively (Fig. 79).

The estimated activation energies between 259 and 339 kJ mol^{-1} using a power rate model, a JMA model and a superposition method are remarkably lower than the previously determined activation energies (~ 1000 kJ mol^{-1}) under 1 atm. Summarizing the previous studies and our results, we found that the effective activation energies systematically decrease as a function of pressure (Fig. 80). Some previous studies pointed out that the structural evolution of CM to graphite rapidly progress by additional pressure (Beyssac et al., 2003; Zhao et al. 2009). However, these studies only noted the possibility

of fast graphitization under high pressure and detailed investigation of kinetics under high pressure is limited. Noda et al. (1968) argued that graphitization under high pressure changes the E_a values from 1000 kJ mol^{-1} to 330–500 kJ mol^{-1} by additional pressure of 0.3–0.5 GPa. Such a large pressure dependence on graphitization was also observed in this study. According to the results of Lynch and Drickamer (1966) and Hanfland et al. (1989), the crystal thickness (L_c) and diameter (L_a) in a graphitic structure decrease by about 2.2 % and 0.17 % at 1 GPa at room temperature, respectively. The interlayer spacing of graphite decreases by about 2.5 % with development of the graphitic structure. Thus, the decrease at 1GPa is comparable to the total decrease of interlayer spacing during graphitization. Such a large effect on compression along the *c*-axis may result from a "negative" activation volume under HPHT experiments. In the light of pressure dependence, the activation energy under high pressure is strictly expressed by the equation: $\Delta H = \Delta E\mathrm{a} + P\Delta V^{\neq}$, where ΔH is the activation enthalpy, ΔEa the activation energy at 1 atm, P the pressure, $\Delta V^{\neq}$ the activation volume. If the ΔH values are correlatable to a single effect on pressure dependence, the ΔEa values and pressure P will show a linear relationship, and the ΔH and $\Delta V^{\neq}$ values can be calculated from the intercept and slope, respectively. In this study, the relation between the effective activation energy and pressure seems to display a logarithmic curve rather than a linear regression line (Fig. 80). This may suggest that the different factors are included in the whole "effective" activation energies. For instance, Marsh et al. (1983) reported that catalytic effects largely change the activation energy from 1000 kJ mol^{-1} to ~ 400 kJ mol^{-1} without addition of pressure. Although it is uncertain to calculate the activation volume using our results, we found that the activation energies between ambient pressure and 1 GPa decrease by a factor of over 2. Thus, almost all natural graphitization in the earth's crust undergoes a faster transformation than estimated in previous studies.

6.5. Implications

Our experimental kinetic study on the structural evolution of CM to graphite gave remarkably low activation energies for the natural precursor materials, and natural graphitization in the Earth's crust may proceed much more quickly than suggested by previous calculations based on large activation energies (~ 1000 kJ mol^{-1}) because of "negative" activation volume during graphitization. This suggests that extrapolation using our kinetic model at 1 GPa is expected to model well the conditions of geological environments and produce better results than previous studies. Based on the experimental results in this study, we attempted a simplified isothermal calculation of graphitization rate depending on temperature. If graphitization rate is subject to Arrhenian temperature dependence, the sigmoid master curves can be extrapolated to represent low-temperature conditions. For instance, sigmoid fitting was tested using the parameters of unit-cell height *c*, and the area ratio (AR) of Raman spectra:

$$f(t) = C_{min} + (C_{max} - C_{min}) / \{1 + (t_{half}/t)^h\}, \quad (8)$$

where C_{min} and C_{max} are respectively the maximum and minimum values of each parameter, t is the annealing duration during metamorphism, t_{half} is the inflection point obtained from this function, and h is the order of reaction of the sigmoid function (called "Hill coefficient"). The values of C_{min} and C_{max} correspond to the starting and termination points of natural graphitization, respectively, and h is used for the experimental data (Table 20). The value of t_{half} changes as functions of time and temperature. Therefore, we calculate its value at target temperature and time from the Arrhenius plots. The t_{half} can also be described following the Arrhenius relation:

$$t_{half} = A_1 \exp(-m/T), \quad (9)$$

where A_1 is the intercept and m is the slope of the Arrhenius plot. Combining equation (8) and (9):

$$f(T, t) = C_{min} + (C_{max} - C_{min}) / [1 + \{A_1 \exp(-m/T)/t\}^h], \qquad (10)$$

It is thus possible to predict the structural evolution of CM to graphite by the above function of peak temperature T (K) and annealing duration t (min) during metamorphism. Using the above equation (10), we attempted to extrapolate the structural evolution of CM to graphite at low temperatures (300–800 °C) during annealing for 10^0–10^{10} years. For instance, the master curve at 1000 °C extended to ~ 10^6 min (~ 2 years) for the formation of graphite (Figs. 8a–d). With decreasing temperature, the time required for conversion to graphite exponentially increases. Figure 11 shows the calculated time–temperature transformation diagrams using the parameters of unit-cell height c (Figs. 81a and 81c) and the area ratio (AR) of Raman spectra (Figs. 81b and 81d). If CM in HMB underwent prograde metamorphism for about 10,000 years, it would show initial crystallinity changes at ~ 500 °C and conversion to the fully ordered graphite (d_{002} spacing ~ 3.36 Å) at over ~ 640 °C (Path 1 of Fig. 81a). Longer metamorphism for ~1 m.y. would convert CM to fully ordered graphite at temperatures over ~ 520 °C (Path 2 of Fig. 81a). The CM in SM shows a similar change in its crystallinity as a function of duration (Path 5 and 6 of Fig. 81c), however, the estimated temperatures at the conversion of graphite are slightly higher than that in HMB. This difference results from the difference in the initial activation energy required to form a graphite. Wang (1989) reported that almost fully ordered graphite (d_{002} spacing ~ 3.36 Å) in high-pressure low-temperature and high-temperature low-pressure metamorphic rocks can form at temperatures between 410 and 440 °C in various metamorphic terrains. Our kinetic model suggests that annealing following metamorphism requires ~ 10^8 years (Fig. 81a). The results are not in good agreement with natural and calculated graphitization rates. In addition to unit-cell height c, the area ratio (AR) in HMB and SM also displays similar behavior as a function of heating duration (Figs. 81b and 81d). If CM in HMB underwent prograde metamorphism for about 10,000 years, it would show initial crystallinity changes at 350 °C and conversion to

graphite (AR < 0.2) at over 800 °C (Path 3 of Fig. 81b). Longer metamorphism for ~ 1 m.y. would convert CM to graphite at temperatures over ~ 720 °C (Path 4 of Fig. 81b). The CM in SM displays initial crystallinity changes at 350 °C and conversion to graphite at over 590 °C for duration of ~ 1 m.y. (Path 8 of Fig. 81d). In contrast to the unit-cell height *c*, the contour of AR tends to extend over a wide interval in time-temperature space (Figs. 81b and 81d). The difference is driven by the calculated Hill coefficient *h* in equation (10), making AR a more sensitive measure for graphitization progress over a wide temperature range. In the case of micro-Raman spectroscopic studies, almost all CM changed into graphite at around 650 °C based on the detailed observations of various types of metamorphic terrains (Beyssac et al. 2002; Aoya et al. 2010; Hilchie and Jamieson 2014). If CMs changed into graphite at 650 °C by graphitization, the durations of heating required would be about 100,000 years (SM) and 10 m.y. (HMB), respectively. These estimations suggest that natural CMs are rapidly able to change their crystallinity as functions of realistic duration and peak temperature. In particular, the structural change of CMs in SM are consistent with previously reported examples of natural graphitization (Beyssac et al. 2002; Aoya et al. 2010), where crystallinity increased at temperature between 350 and 650 °C. This suggests that the Raman spectra of carbonaceous materials (RSCM) thermometry have potential to be calibrated to use the Arrhenius-type *t*-*T*-dependence of graphitization as a tool for extracting kinetic information from natural rocks. On the other hand, we found that the two CM samples display a large divergence of recrystallization. This difference results from the sigmoid *t*-*T*-relation descried by the Hill coefficient *h*, and suggests that further detailed evaluation of the chemical reaction under natural and laboratory conditions are required for a complete understanding of structural evolution of CM.

Overall, our kinetic model demonstrates that graphitization can proceed at relatively low temperatures (520 ~ 720 °C) in generally more realistic timescales (~ 1

m.y.) than expected from previous experimental kinetic studies (e.g., Fischbach 1971). In addition, our new kinetic data suggests that activation energies as reported previously (e.g., Fischbach 1971) do not suitably describe natural graphitization in crustal settings. Under a lithostatic pressure of 1 GPa, we were able to demonstrate the structural evolution of CM at geologically reasonable temperatures (300–800 °C) and durations (1–10^{10} years). Further refining and a better understanding of the kinetics of graphitization might provide new pathway to use it not only as a tool for geothermometry but also for geospeedometry in order to resolve petrogenetic processes occurring over geologic timescales. However, there exist slight mismatch between our experimental results and natural graphitization in metamorphic rocks. It can be deduced that the actual activation energies for natural graphitization could be even slightly lower than that estimated here due to the influence of other factors (e.g., catalytic effects, tectonic deformation and fluid activity), and further experiments will help to constrain the influence of additional factors to refine our kinetic model for natural graphitization.

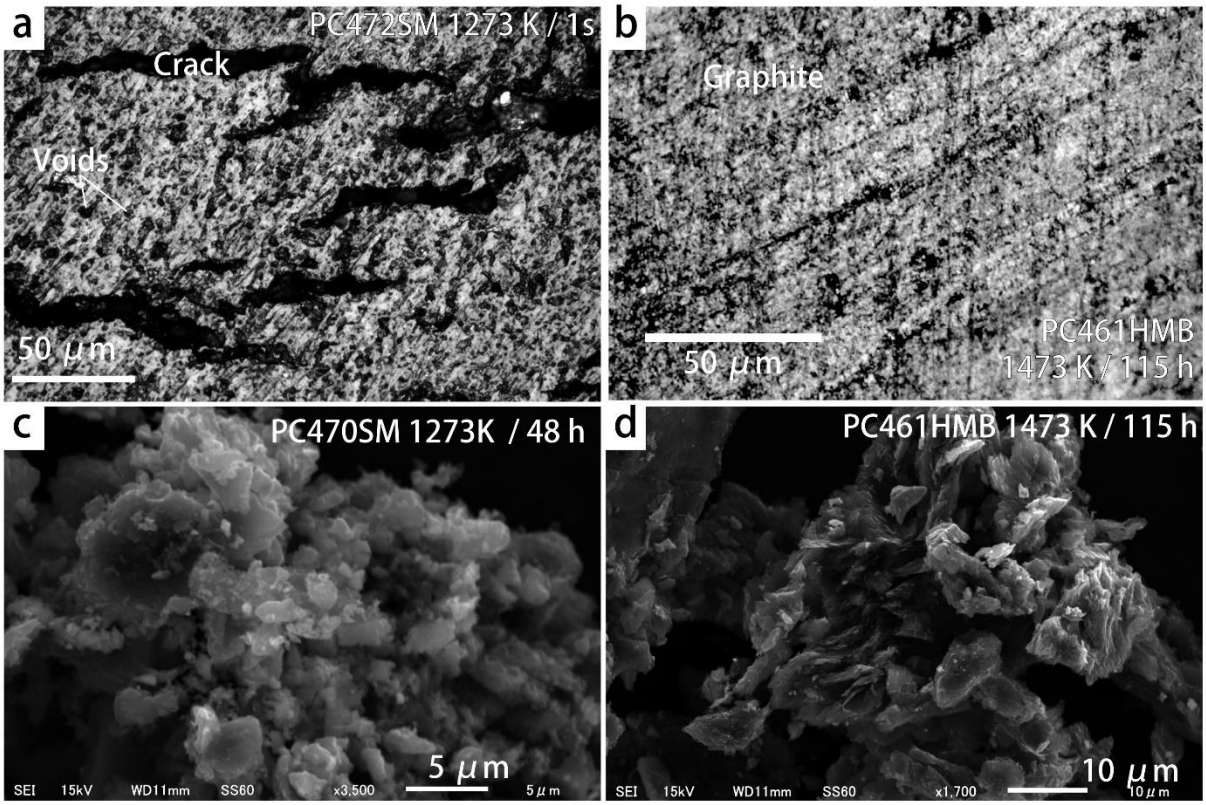

Figure 71. Optical and backscattered images of the run products extracted from various time–temperature experiments. **(a)** Photomicrograph of a polished slab section of sample PC 472SM showing many voids and cracks (1000 °C, 1 GPa, 1 s). **(b)** Photomicrograph of the smooth surface of sample PC 461HMB (1200 °C, 1 GPa, 115 h). **(c)** Porous structure of powder CM extracted from the Pt capsule for sample PC470SM (1000 °C, 1 GPa, 48 h). **(d)** Planar structure of powder CM extracted from the Pt capsule for sample PC461HMB (1200 °C, 1 GPa, 115 h).

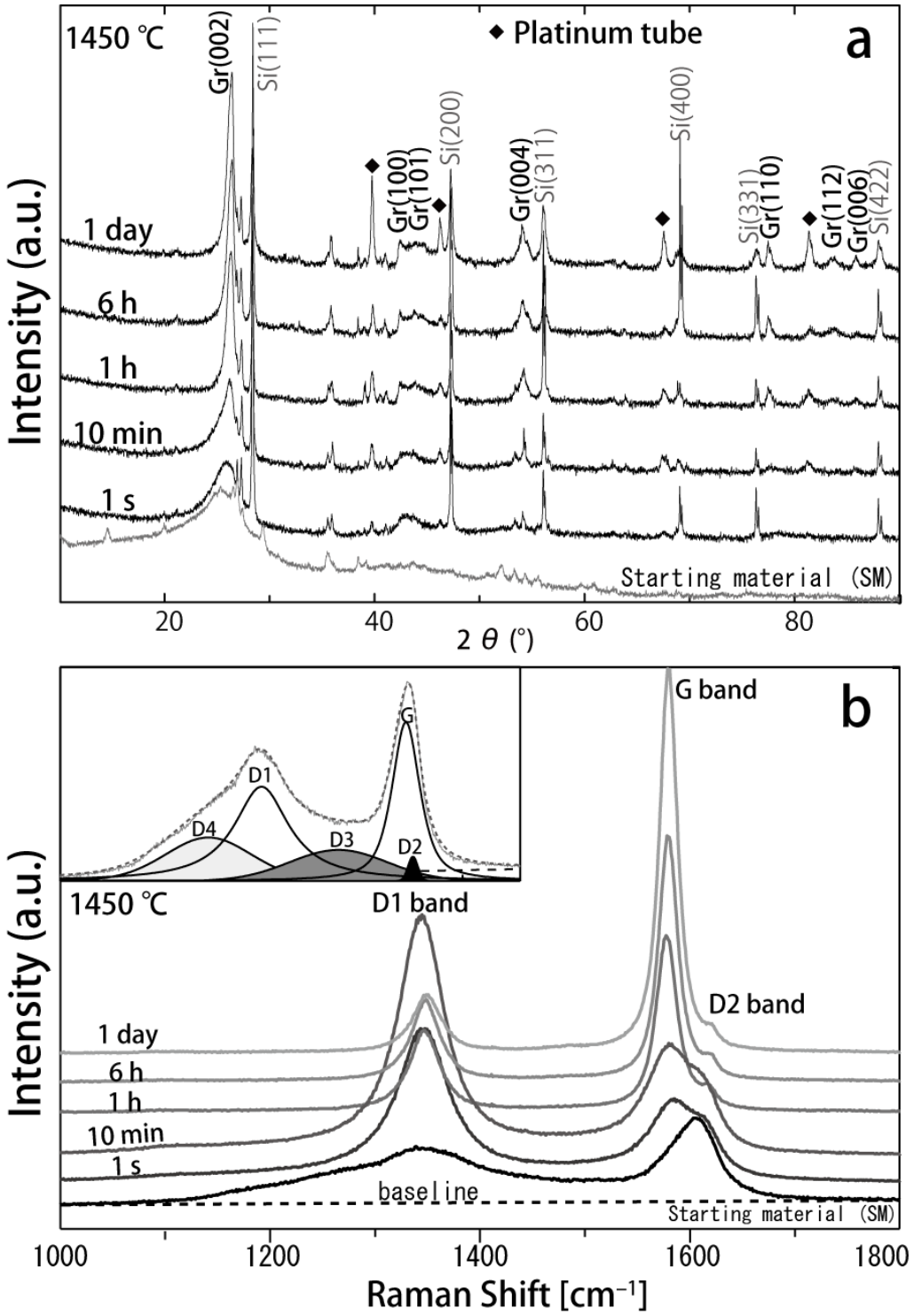

Figure 72. Structural evolutions from 1 s to 24 h of CM and starting material in SM to graphite at 1450 °C as observed by **(a)** X-ray diffractometry and **(b)** micro-Raman spectroscopy. The Raman spectra of CM are fitted by five peaks of D1, D2, D3, D4, and G band. Silicon peaks in XRD profile are an internal standard for calibrating the interlayer spacing of disordered graphite.

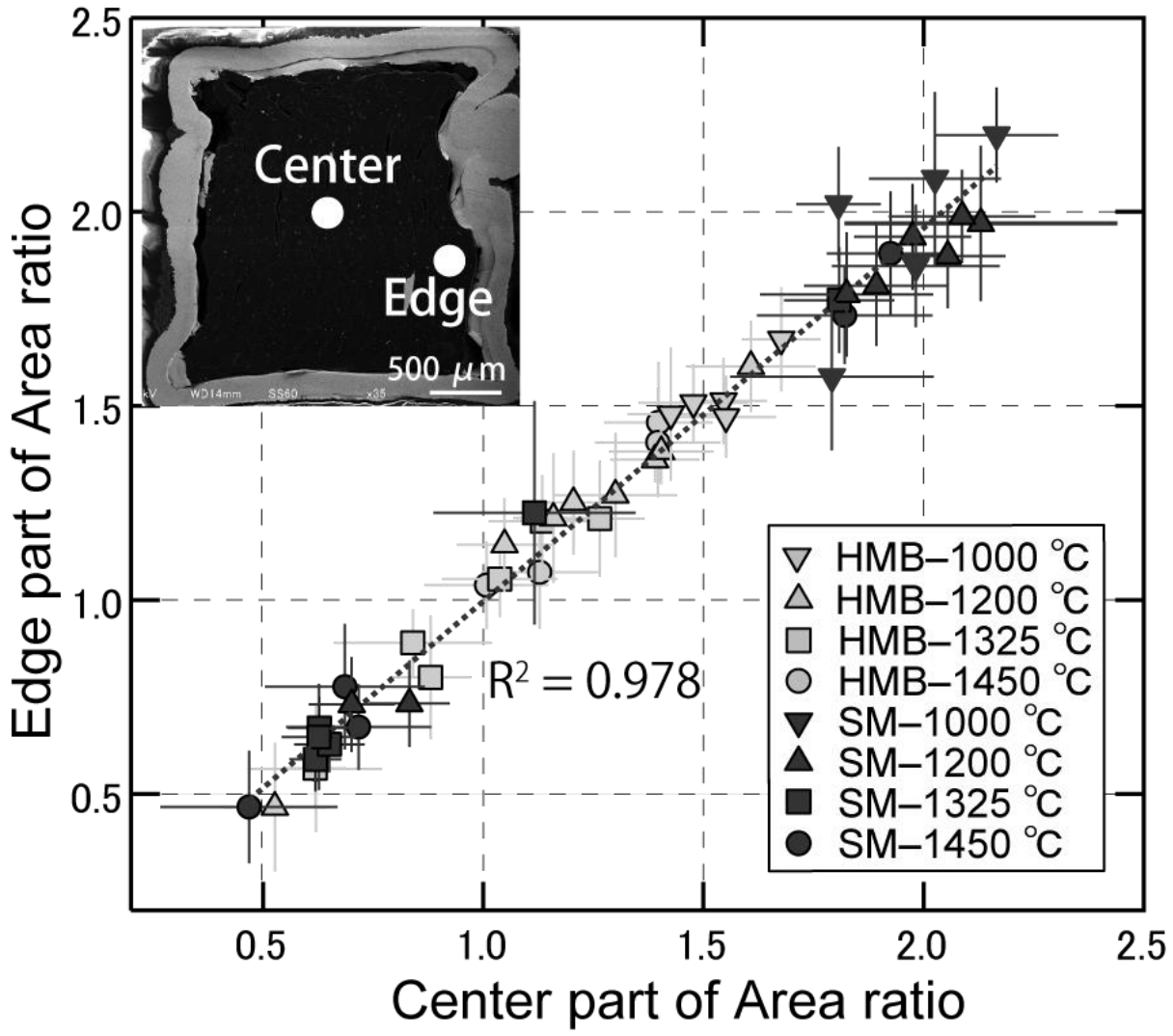

Figure 73. Relationship between center and edge parts of area ratio (D1 + D4 bands) / (D2 + D3 + G bands). The dashed line is calculated by linear regression.

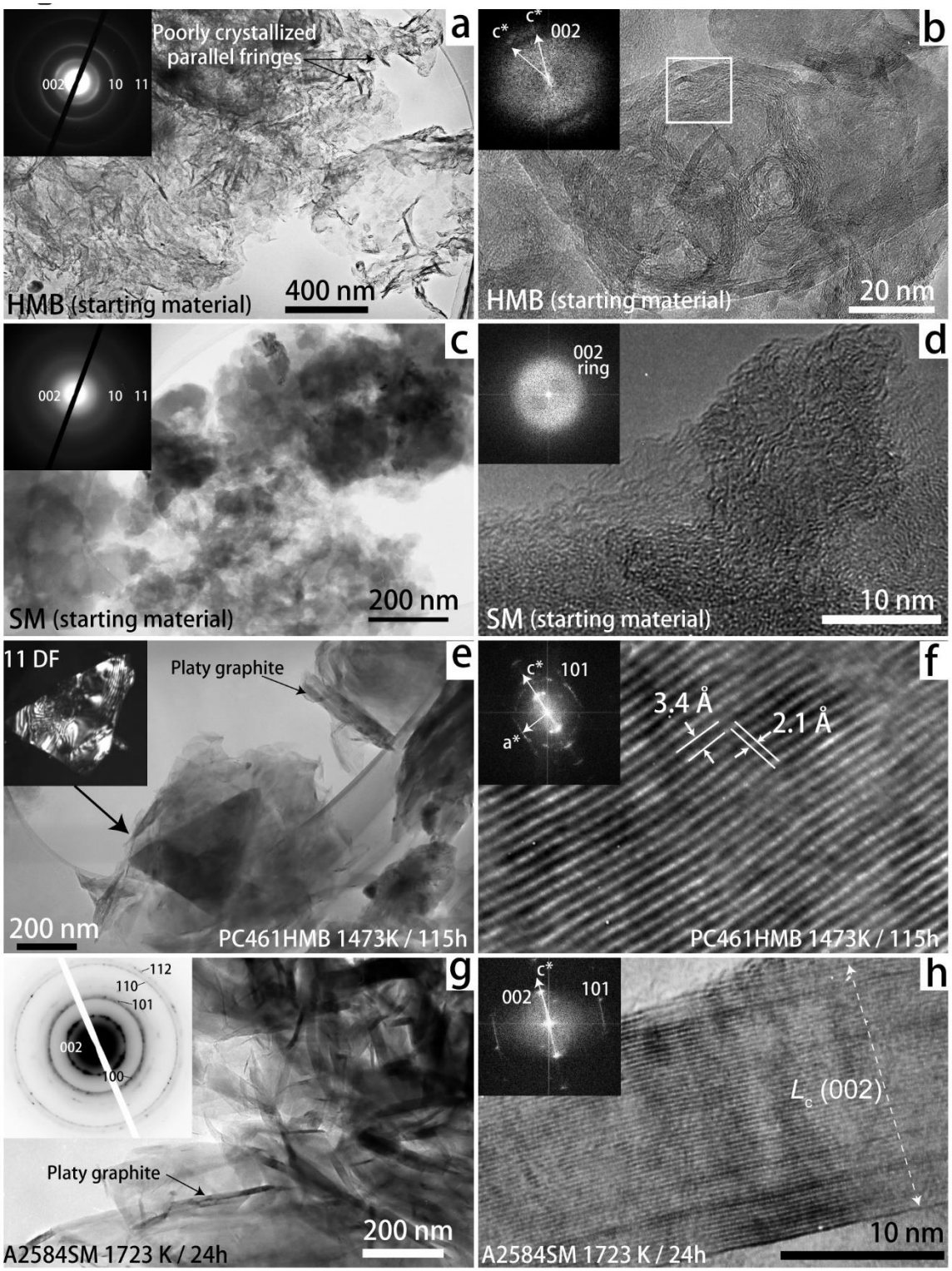

Figure 74. Microstructural evolutions of the CM in HMB and SM to graphite. **(a)** TEM image and corresponding SAED pattern of the starting material in HMB. The distorted graphitic layers are locally observed in the tissue-like aggregates. **(b)** High-magnification image of the poorly crystalline carbon surrounded by the distorted graphitic layers. The

SAED pattern is compiled from the area outlined by the white square. **(c)** TEM image and corresponding SAED pattern of the starting material in SM. **(d)** High-magnification image and SAED pattern of poorly organized fringes. **(e)** TEM image of ordered graphite and its 11 dark-field image (PC461HMB, 1200 °C and 115 h). **(f)** Lattice fringes of graphite corresponding to (002) and (101) along the [010] direction. **(g)** Nanostructures and corresponding SAED pattern of ordered graphite (A2584SM, 1200 °C and 48 h). **(h)** Lattice fringes and corresponding SAED pattern of ordered graphite.

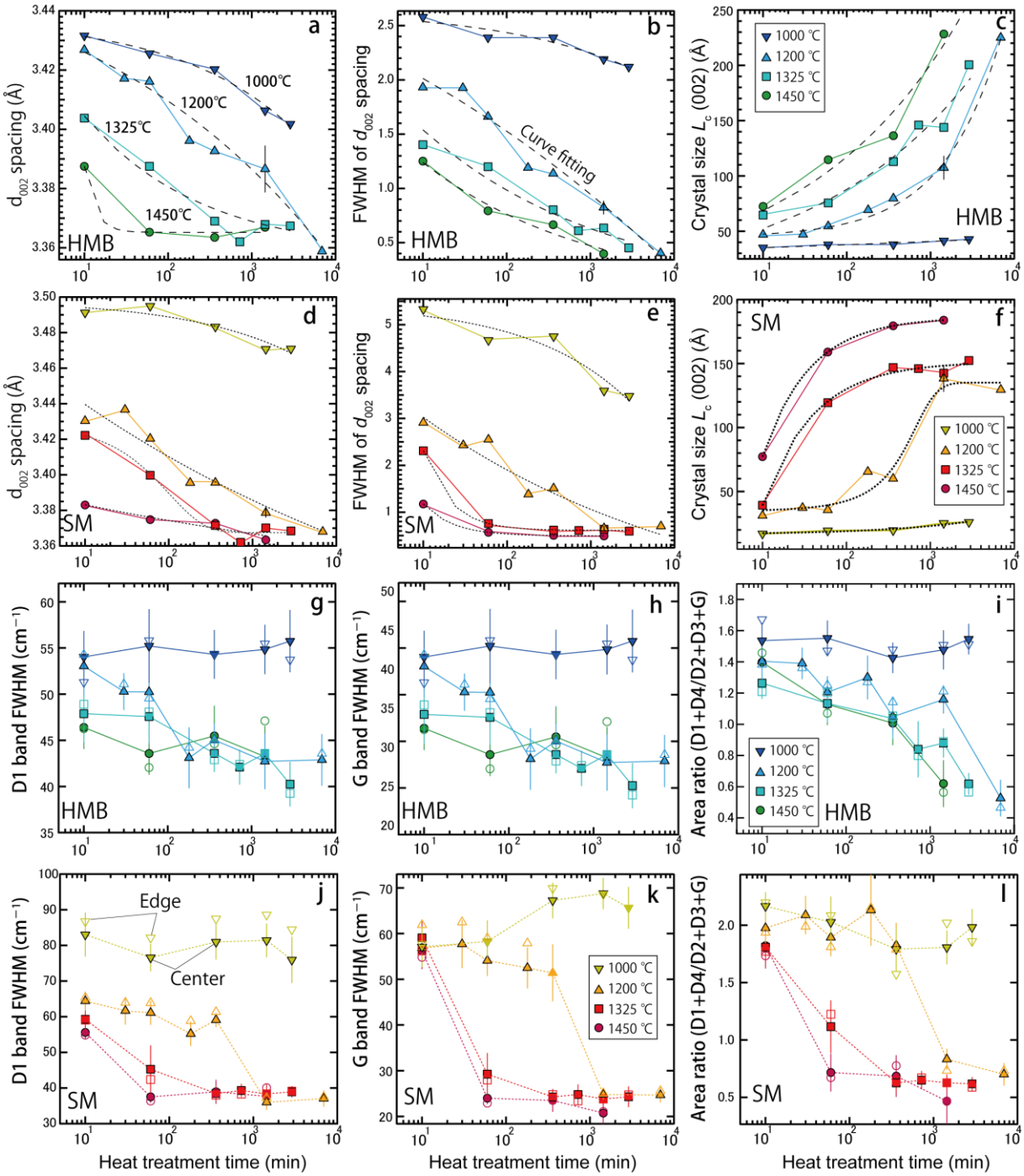

Figure 75. Time–temperature relations between 10 and 10^4 min. The parameters **(a)** d_{002} spacing, **(b)** FWHM of d_{002} peak, and **(c)** $L_c(002)$ from XRD, and also **(g)** D band FWHM, **(h)** G band FWHM, and **(i)** area ratio are based on data for the CM in HMB. **(d), (e), (f), (j), (k),** and **(l)** show the same parameters, respectively, for the CM in SM. Data from XRD are used to calculate the non-linear best fitting of sigmoid functions and power functions for reference.

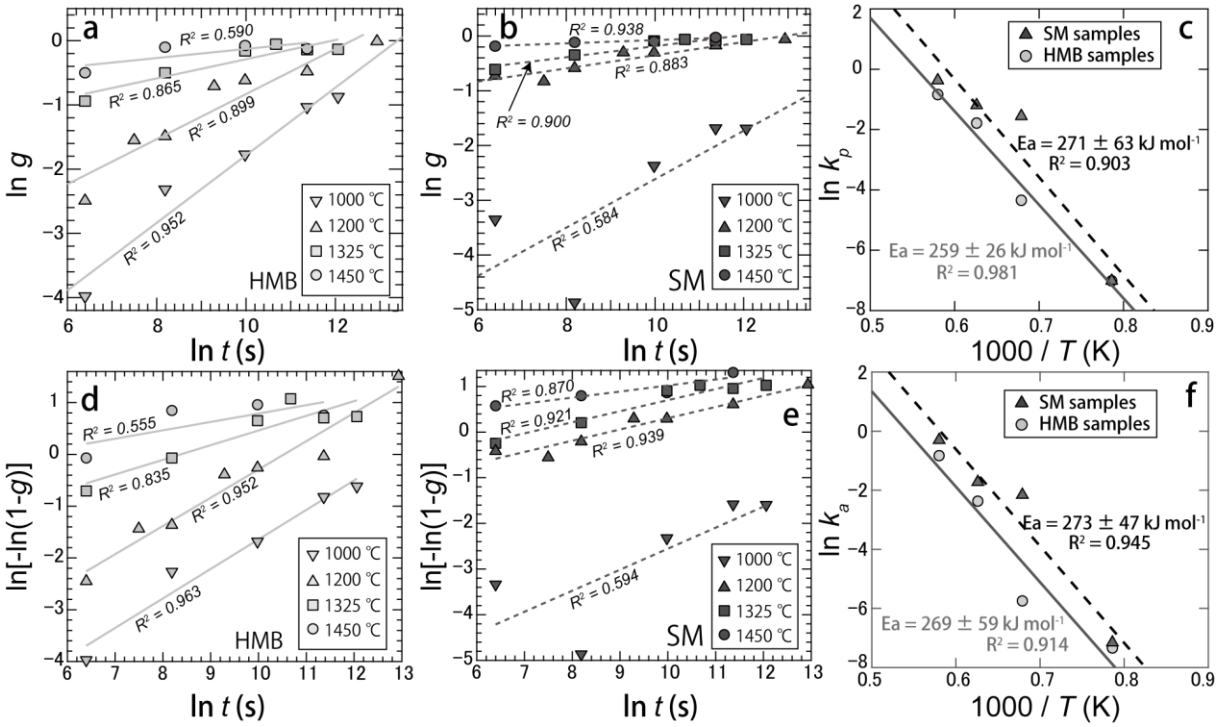

Figure 76. The relationship between experimental ln*t* (s) and ln*g* of HMB **(a)** and SM samples **(b)** fitted by a power rate model. **(c)** Arrhenius plot of HMB and SM samples. The relationship between experimental ln*t* and ln[–ln(1–*g*)] of HMB **(d)** and SM samples **(e)** fitted by a JMAK model. **(f)** Arrhenius plot of HMB and SM samples.

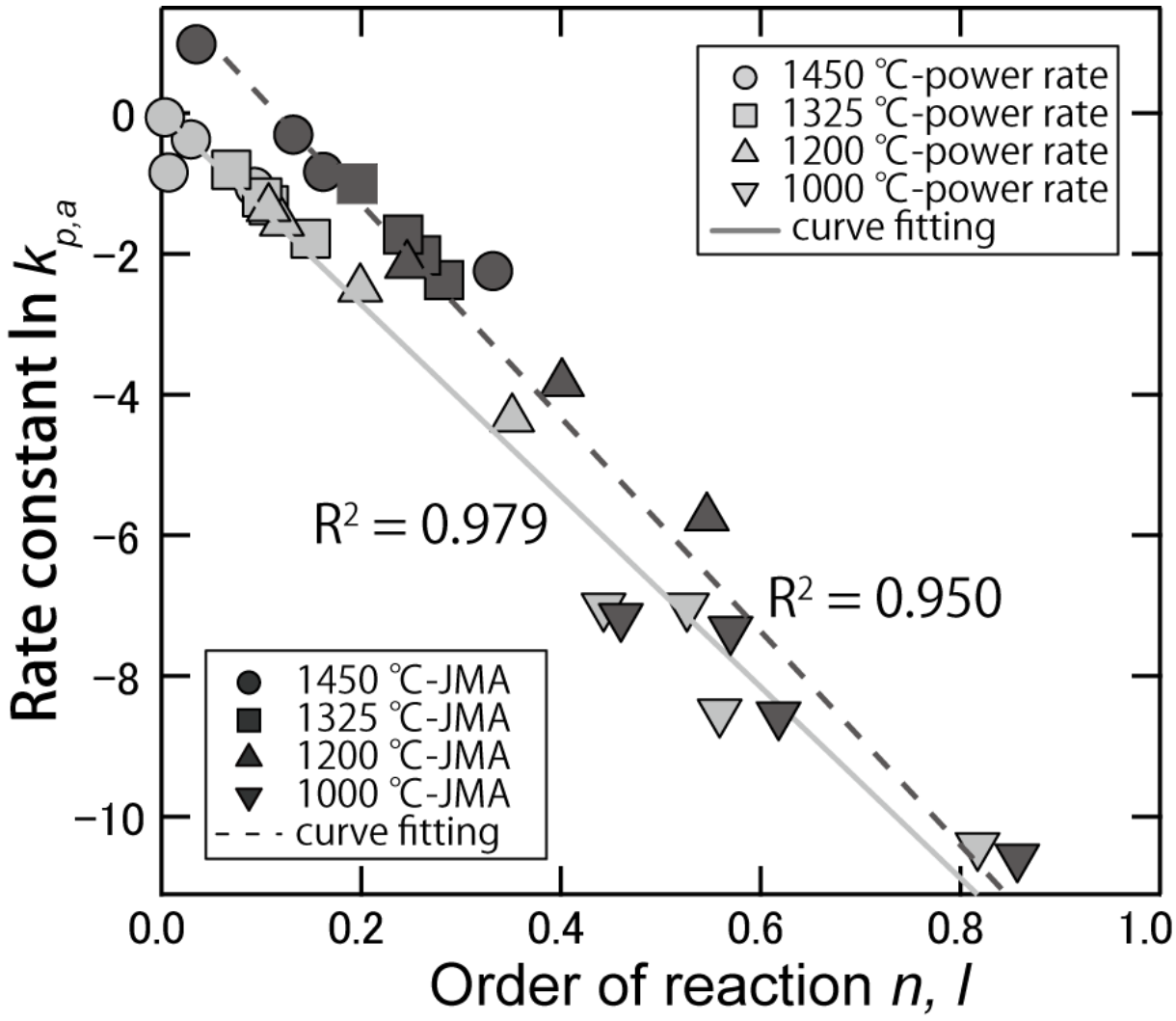

Figure 77. The relationship between the rate constants ln$k_{p,\,a}$ and the orders of reaction n, l of power rate and JMA models. All of rate constants and orders of reaction including d_{002} spacing, FWHM of d_{002} peak, L_c(002), and Area ratio and are plotted.

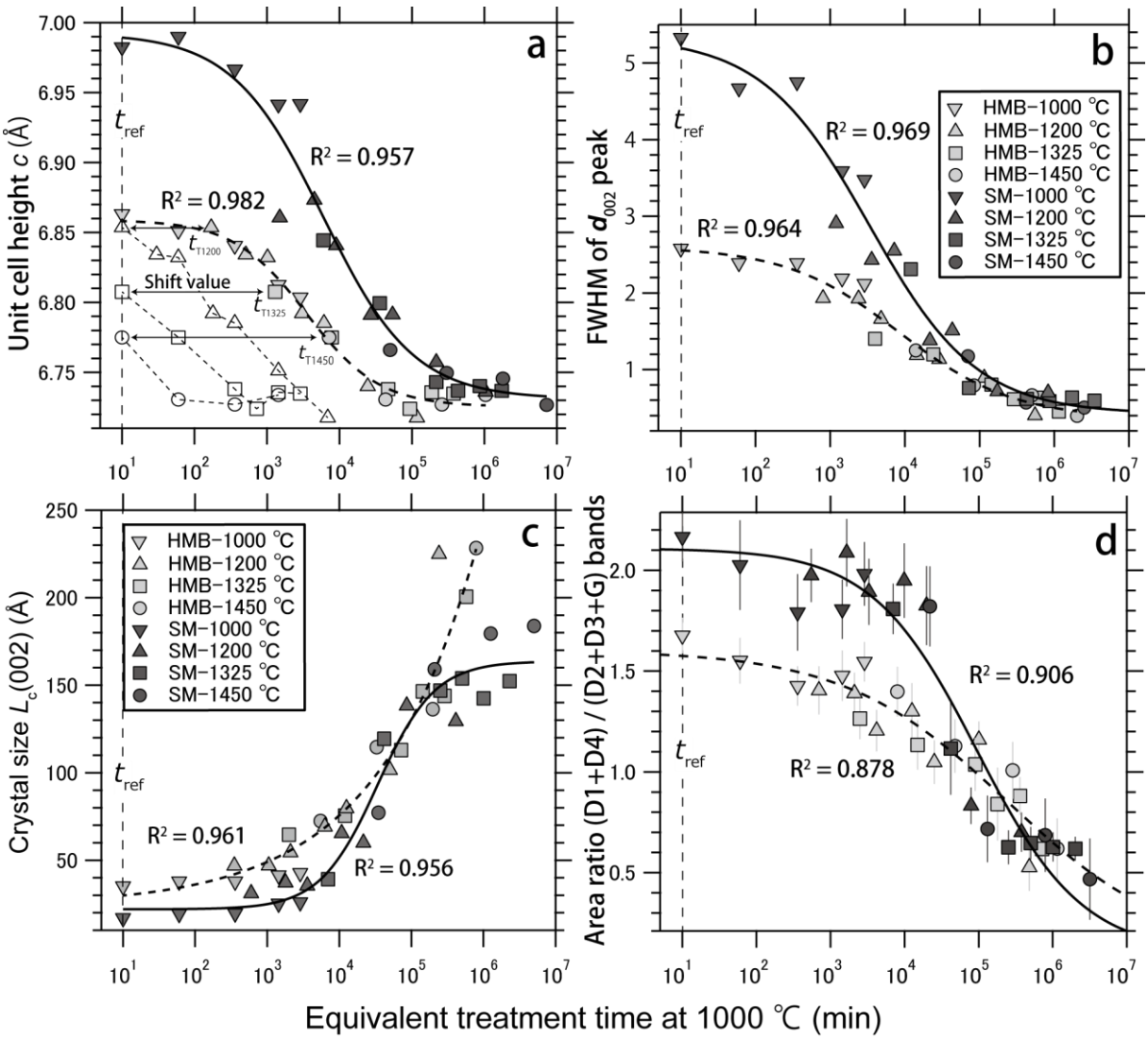

Figure 78. Composite master curves for CM samples SM and HMB obtained by shifting the 1200, 1325 and 1450 °C curves to combine smoothly with the 1000 °C (reference temperature) curve from time–temperature relations. All master curves are calculated by non-linear best fitting of sigmoid functions and power functions. Master curves of both CM samples are fitted by the values of **(a)** unit-cell height *c*, **(b)** FWHM of d_{002} peak, **(c)** $L_c(002)$, and **(d)** area ratio.

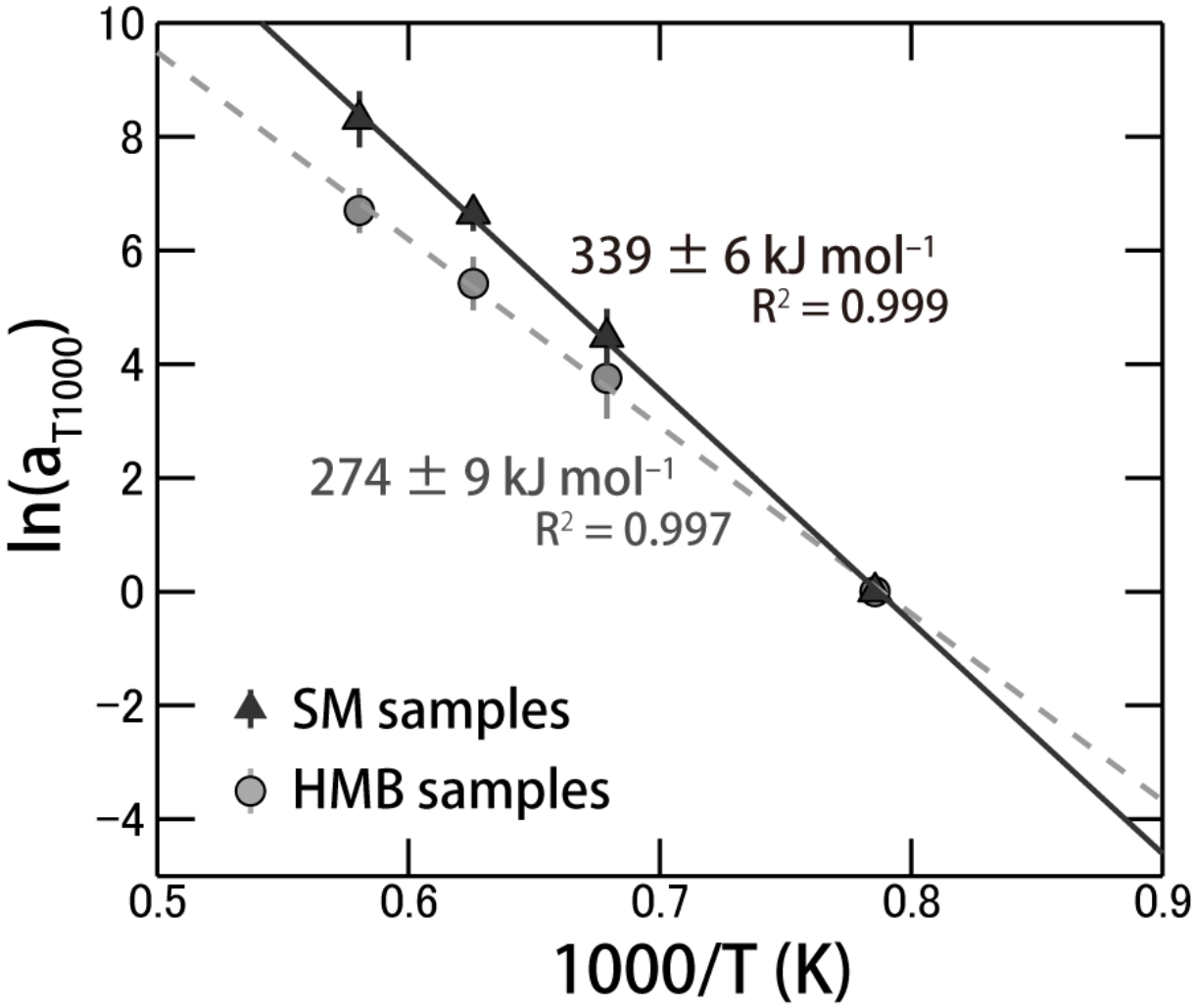

Figure 79. Arrhenius plot of shift values using the average of four different parameters by XRD and micro-Raman spectroscopy. Error bars show one standard deviation.

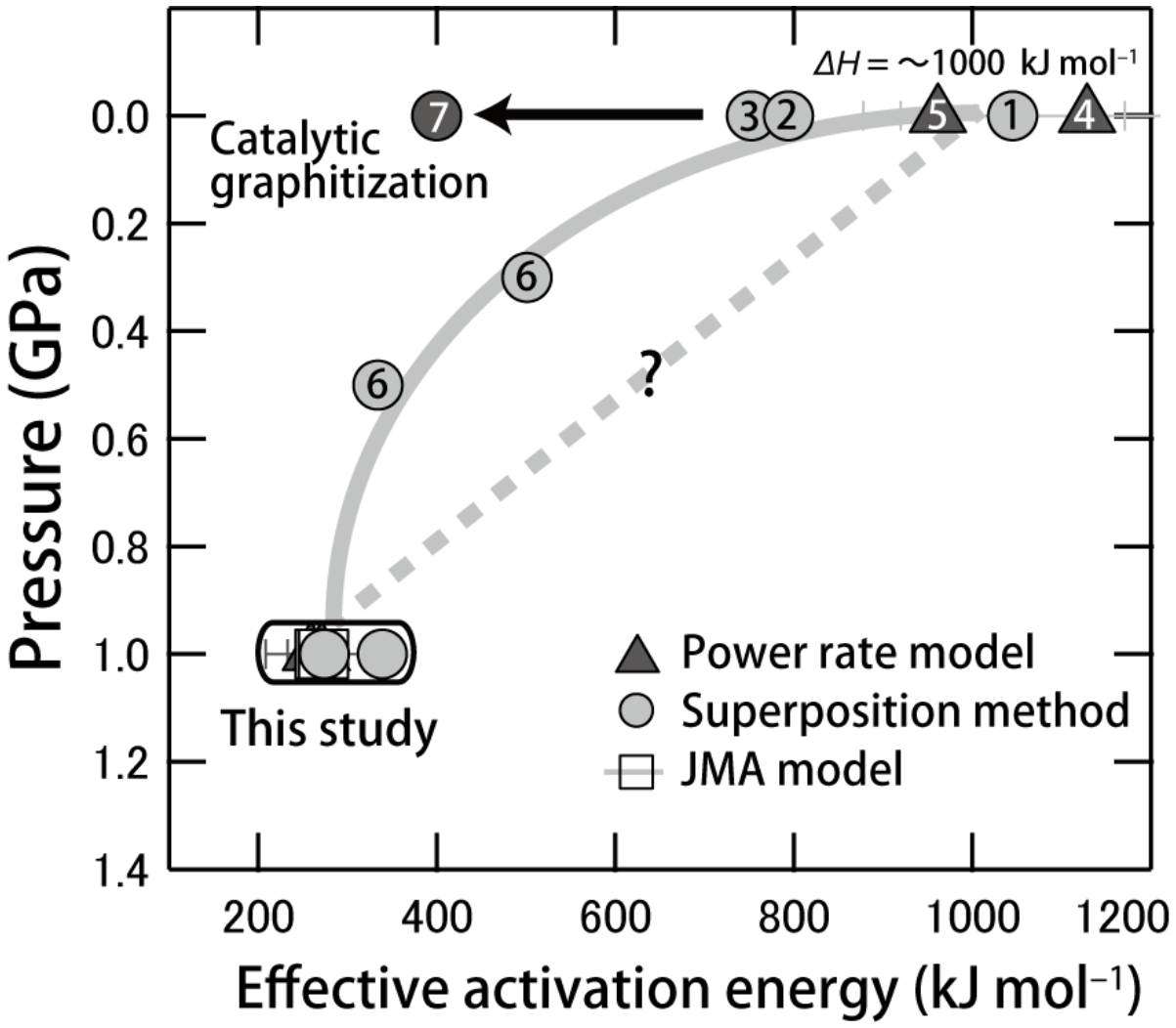

Figure 80. Compilation of effective activation energies (kJ/mol) at various pressures (GPa) obtained in this study and published values using power rate model, JMAK model and superposition method. The effective activation energies of previous studies are cited from 1, Fischbach (1963); 2, Inagaki et al. (1968); 3, Noda et al. (1965); 4, Fischbach (1971); 5, Murty et al. (1969); 6, Noda et al. (1968); and 7, Marsh et al. (1983).

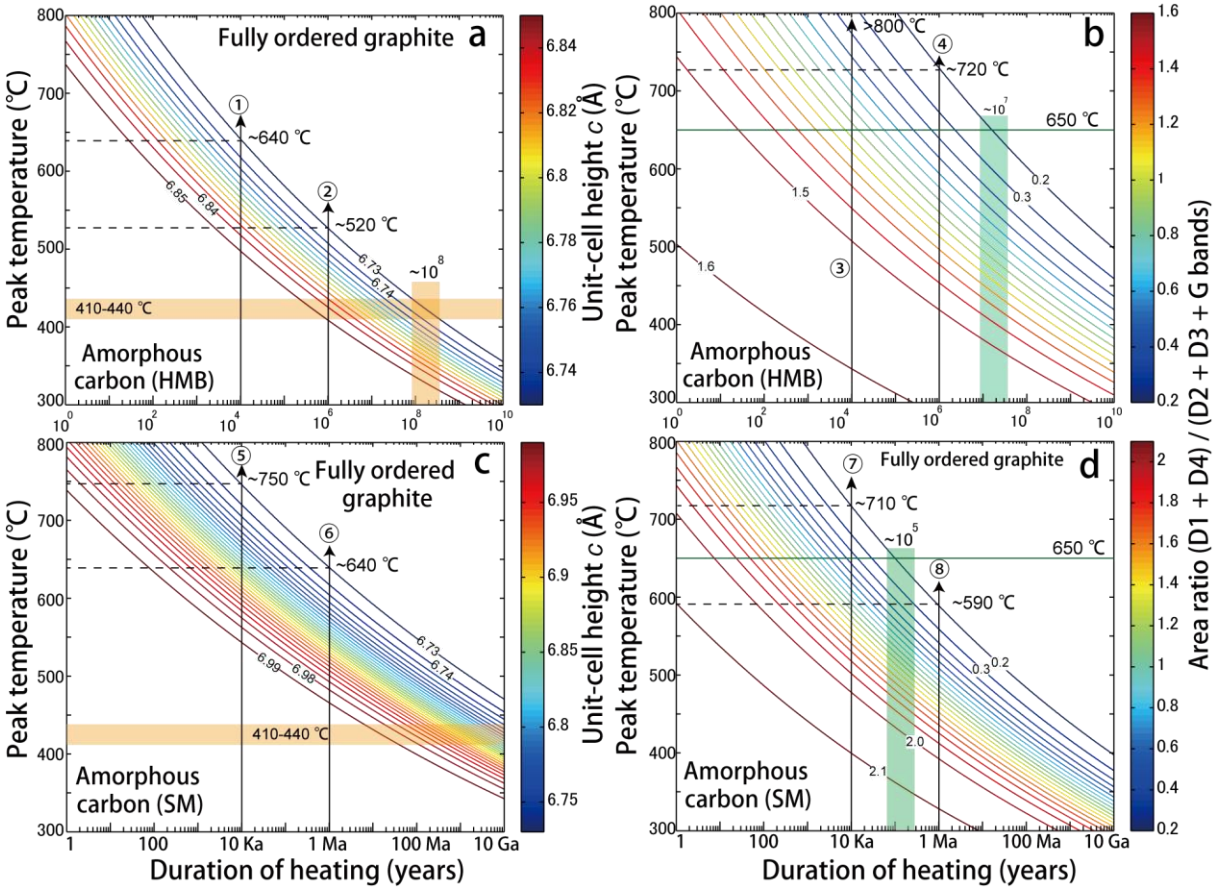

Figure 81. Time–temperature–transformation diagram of HMB **(a)** and SM samples **(c)** using the unit-cell height *c* (Å). Orange area indicates the first appearance of fully ordered graphite (d_{002} spacing ~ 3.36 Å) as reported by Wang (1989). Numerals indicate the unit-cell height *c* (Å), which is contoured at an interval of 0.01 Å. Time–temperature–transformation diagram of HMB **(b)** and SM samples **(d)** using the area ratio of (D1 + D4 bands) / (D2 + D3 + G bands). Numerals indicate the area ratio, which is contoured at an interval of 0.1. Green area indicates the range of intersection at 650 °C.

CHAPTER VII

Pressure dependence of structural evolution of carbonaceous material to graphite: Implication for fast recrystallization in subduction zone

7.1 Introduction

The structural evolution of carbonaceous material (CM) to graphite is the one the most important and sensitive thermal indicator that can be used to determine very low to medium metamorphism in subduction zone. The process is irreversible with temperature, and retains as indication of peak temperature in the crystal structure (Buseck and Beyssac et al. 2014). Hence, many researchers devoted the detailed investigations of CM to graphite from the various standpoints of crystal structure by X-ray diffraction (XRD; Landis 1971; Grew 1974; Itaya 1981; Okuyama-Kusunose and Itaya 1987), micro-Raman spectroscopy (Wopenka and Pasteris, 1993; Yui et al. 1996; Bayssec et al. 2002a), stable carbon isotopic study (Hoefs and Frey, 1976; Morikiyo 1986; Wada et al. 1994), microstructural observation by transmission electron microscopy (TEM; Buseck and Huang 1985; Nakamura and Akai 2013) and optical properties (Diessel et al. 1978; Kříbek et al. 2008). There are many reasons for investigation of the structural evolution of CM, however, all are ultimately related to the user-friendly thermal indicator in metamorphic terrain that is a lack of metamorphic indicator. Moreover, the developments of Raman spectra of carbonaceous material (RSCM) thermometry has made more powerful and useful tools again for better understanding the geodynamic evolution in metamorphic

terrain (Beyssac et al. 2002; Rahl et al. 2005; Aoya et al. 2010; Lahfid et al. 2010; Kouketsu et al. 2014). On the other hand, the natural structural evolution of CM has some issures related to the kinetics of recrystallization in metamorphism for decades. The previous RSCM thermometry has been constructed only based on the temperature dependence of metamorphic rocks estimated the different geothermometers or thermal modelling (e.g., Beyssac et al. 2002; Aoya et al. 2010). The temperature dependence of the process is most prominent effect during metamorphism. Nevertheless, previous literatures have ignored the effect of duration of heating and other factors to estimate the RSCM thermometry. It has been also known that the synthesis of graphite from an amorphous carbon at 1 atm required a very high activation energy of ~1000 kJ/mol by laboratory experiments. For example, extrapolation based on previous experimental kinetic data at 1atm suggests that even at 700 °C, synthesizing graphite would require durations of the order 10^{40} min (~$1.9*10^{34}$ years; Fischbach 1971; Bustin et al. 1995). This strongly suggests that we should consider the various effects of not only temperature dependence but also pressure dependence, rate dependence, fluid activity and tectonic deformation for controlling structural evolution of CM during metamorphism. In addition, it is essential for more realistic kinetic model for recrystallization of CM in various metamorphic terrains.

The structural evolution of CM to graphite is a combination of into two prominent processes; carbonization and graphitization (Oberlin 1984). Carbonization takes place by the devolatilization of heteroatom in coal structure, whereas, graphitization involves recrystallization from a turbostratic to a graphitc structure by the reorganization of graphene sheets. Both processes have been well studied by laboratory experiments for synthesizing wide variety of carbon materials (Inagaki and Meyer, 1999; Oberlin et al. 1999; Oberlin et al. 2006). In particular, the pressure effect on graphitization has been debated based on the experimental studies (Noda and Kato, 1965; Kamiya et al. 1970; Beyssac et al. 2003; Zhao et al. 2009). Pioneering works by Inagaki and coworkers

revealed that graphitization under high pressure condition dramatically progressed structural evolution of CM by heterogeneous recrystallization, which they termed as stress graphitization (e.g., Inagaki and Meyer 1999). In addition, it has been well known that tectonic deformation also progressed recrystallization of CM by modification of CM microstructure (Ross and Bustin, 1990; Bustin et al. 1995). The non-hydrostatic stress by deformation lead to arise from the breakdown of pore wall and rearrangement of turbostratic structures. Such dynamic modification underwent recrystallization in the crystal structure. These experimental data imply that both promotion effects of non-hydrostatic and hydrostatic stress stem from the crystallographic anisotropy of graphitic structure. In general, the hexagonal form with ABAB… stacking of graphite have π bonding along *a*-axis and *Van der Waals* bonding along *c*-axis in the unit cell. This large difference of bond strength produced the large crystal anisotropy and characteristic physical properties in graphitic structure. In fact, the crystal thickness (L_c) and diameter (L_a) in a graphitic structure decreases by about 2.2 % and 0.17 %, respectively, at 1 GPa at room temperature (Fig. 82; Lynch and Drickamer, 1966; Hanfland et al. 1989). Thus, hydrostatic and non-hydrostatic stresshas an important role in the structural evolution of natural CM, especially in high-pressure geological condition. Nakamura et al. (2017) has revealed that the effective activation energy for graphitization in~300 kJ/mol under a pressure of 1 GPa, which has dramatically decrerased from ~1000 kJ/mol as reported in previous studies (e.g., Fischbach 1971). This suggests that the natural conditions in the crust show a different recrystallization kinetics of CM to graphite compared with laboratory kinetic experiments at 1 atm, and it is essential for the determination of the pressure dependence in geological condition. In this study, I have focused on the geologically reasonable pressures between 0.5 and 2.0 GPa in subduction zone for calculating the activation volume of reaction. Our experiments provide an important information on kinetics of graphitization by tectonic deformation, and lead to a revised kinetic model for the natural

structural evolution of CM, which incorporate a pressure-temperature-time (*P-T-t*) relation.

7.2. Methods

7.2.1. Starting materials

The starting materials for the HPHT experiments were identical to that employed in Nakamura et al. (2017). They were prepared from two different naturally occurring sedimentary rocks: one from the Hidaka metamorphic belt (HMB) and the other from the Cretaceous Shimanto accretionary complex (SM). Both starting materials extracted by HF-HCl treatments were expected to demonstrate behavior closer to that in nature than observed in previous experiments using cokes and other commercial carbon materials. Further, these CM were especially suitable starting materials, because their localities have been well studied in terms of structural geology, metamorphic geology, organic geochemistry and experimental kinetic study (Nakamura et al. 2015; Ohmori et al. 1997; Hara et al. under review; Nakamura et al. 2017). The CM in HMB showed a turbostratic (sample HMB, d_{002} spacing = 3.431 ± 0.007 Å) structure in XRD profiles and high R2 ratio (R2 ratio = 0.62 ± 0.01) in micro-Raman spectroscopy. The CM in SM were sampled from mudstone in the Cretaceous Shimanto accretionary complex. These sediments are considered as a candidate precursor for high pressure metamorphic rocks such as Sambagawa metamorphic belt (e.g., Aoki et al. 2011; low temperature high pressure type metamorphic terrain). Under the microscope, the CM was identified optically as two different macerals (vitrinite and inertinite), and it coexists with illite, plagioclase, quartz, and framboidal pyrite in pelitic layers. The CM showed an amorphous (sample SM, d_{002} spacing = 3.505 ± 0.013 Å) structure in XRD profiles and a broad D1 band FWHM in micro-

Raman spectroscopy (D1 band FWHM = 129.4 ± 8.4 cm^{-1}). The two samples we have selected cover a wide range of crystallinity, and are suitable for applying experimental graphitization of natural CM back to the temperature–time scale of metamorphic rocks.

Before kinetic experiments, we conducted for chemical extraction was carried out using HF-HCl solution because the sedimentary rocks have low concentrations of organic carbon (0.3-0.7 wt.%; Nakamura et al. 2015). The chemical procedures were identical to those described in Nakamura et al. (2017). The rock samples were crushed by a Jaw crusher and sieved using a 200–mesh screen. The sieved powder was initially treated with 2N HCl to remove carbonate, sulfide, sulfate and hydroxides (Vandenbroucke and Largeau, 2007), and then the solution was treated by HF (48 %) in several large PFA vessels and dried on a hot plate at 120 °C. We performed repeated rinsing with hot deionized water between acid treatments for eliminating the newly formed fluorides (Durand and Nicaise, 1980). After rinsing with hot water, the residues were dissolved again in 2N HCl at 60 °C. The procedures of HCl treatments and rinsing with water were repeated several times until the CM floated in the solution. This floatation is a signal of the complete decomposition of fluorides (Itaya, 1981; Itaya 1985). The supernatant of CM was filtered and dried on a watch glass. Note that the CM residues retained small amounts of minerals such as zircon, rutile, ilmenite, and pyrite even after HF–HCl acid treatments. Both starting materials of SM and HMB are slightly matured or metamorphosed during diagenesis and low grade metamorphism, respectively. It has been generally accepted that the HF–HCl acid treatments do not alter the CM structure and do not generate newly formed solvent soluble organic materials except in the case of very immature sediments (Durand and Nicaise, 1980; Larsen et al. 1989; Vandenbroucke and Largeau, 2007). More detailed procedures of chemical extraction are described in Appendix I.

7.2.3. HPHT experiments

HPHT experiments were performed at the Institute for Planetary Materials (IPM), Okayama University, Misasa, Japan. The two starting materials were encapsulated and stamped in platinum tubes of 2.0 and 3.0 mm outer diameter. All experiments were carried out with both starting materials together in a single run so as to reduce any apparent difference in absolute temperature conditions. After welding and encapsulating, the platinum capsules were placed in three different pressure apparatus for appropriate treatment of temperature and time; (1) The piston-cylinder (PC) high-pressure apparatus (2) The DIA-type high-pressure apparatus (AMAGAEL) (3) The Kawai-type high-pressure apparatus. For the PC experiments, the assembly was composed of a talc-Pyrex-graphite furnace with MgO disks as pressure medium (3/4 inch diameter). Two platinum capsules were placed at the center of graphite heater. Experimental temperature was measured by type S (Pt-Pt_{90}-Re_{10}) thermocouples. For experiments using the DIA-type high-pressure apparatus, the cubic pyrophyllite with edge length of 21 mm was adopted as pressure medium and the tungsten carbide anvils with top edge length was 15 mm for runs at 1 and 2 GPa. Temperature was monitored using $W_{97}Re_3$-$W_{75}Re_{25}$ thermocouples with Al_2O_3 insulating sleeves, whose junction was placed in contact with the center of MgO disk. For experiments using the Kawai-type high-pressure apparatus, pressure media was composed of a Cr_2O_3-doped MgO octahedron with 18 mm edge length for run at 4 and 8 GPa. The powder samples encapsulated by Pt tube were placed at the center of graphite heater with MgO disk. Temperature was monitored using $W_{97}Re_3$-$W_{75}Re_{25}$ thermocouples with Al_2O_3 insulating sleeves, whose junction was placed at the contact between two Pt tubes. The pressure cell assembly was compressed using tungsten carbide cubes with 11 mm truncation edge lengths for runs at 4 and 8 GPa. The different types of high-pressure apparatuses were used for each pressure condition. Altogether, 12 kinetic experiments

were carried out at varying pressure conditions between 0.5 and 8 GPa at 1200 °C, and different annealing duration at peak temperature from 10 min to 24 hours. These experiments were carried out with a heating rate of about 100 °C / min and quenching by switching off the furnace power. More detailed procedures of *HPHT* experiments are described in Appendix III.

7.3. Analytical methods

The recovered platinum capsules were mounted into epoxy resin and cut into two halves. One half was used for SEM observations and micro-Raman spectroscopy. The other half was separated from the slab section of platinum capsule using a dentist diamond cutter under a binocular microscope. The powder samples were used for X-ray diffraction.

X-ray diffraction (XRD) was obtained using a Rigaku ULTIMA IV diffractometer at Niigata University, equipped with CuKα (40 kV, 40 mA) radiation, graphite monochromator, slit system 2/3 °–0.45 mm–2/3 ° and time constant of 0.5 ° min^{-1}. The diffractometer was run between 10 ° and 90 °. The powdered samples of CM were dried on a Si-low background sample holder with internal standard of silicon (10–20 wt%). Lattice constant and crystal thickness of graphite were calculated according to the following methods. The 2θ values of the obtained peaks were calibrated using the peak positions of the internal silicon standard (Iwashita et al. 2004). The $L_c(002)$ was calculated using the Scherrer equation: $L_c(002) = K\lambda / \beta\cos\theta$, where K, constant (1.0); λ, X-ray wavelength (Cu$K\alpha$ = 1.5419 Å); β, full width at half maximum (FWHM); θ, the Bragg angle. The K value is not a constant, but depends on the crystallite sizes (Fujimoto 2003). Therefore, we used the constant K of 1.0 for $L_c(002)$ following JIS standards (Iwashita et al. 2004).

Micro-Raman spectroscopy was applied to CM and graphite in the first order

region using a Jasco NRS 3100 spectrometer at Niigata University, equipped with the grating of 1800 lines/mm and CCD-detector (256×1024 pixels). The microscope objective of 100×, and Nd-YAG laser (wavelength: 532 nm) were used. Acquisition time is 10–30 s, and 3–6 spectra were cumulated for each data point. All Raman peak profiles were analyzed by using peak profile fitting, and G (1580 cm^{-1}), D1 (1350 cm^{-1}), D2 (1620 cm^{-1}), D3 (at around 1450 cm^{-1}), and D4 (at around 1200 cm^{-1}) bands in the first order region (1000–1800 cm^{-1}) were separated. The parameters of G band FWHM, D1 band FWHM, G position (Raman shift), R1 ratio (Intensity D1 band / Intensity G band), R2 ratio (Area D1 band / Area G + D1 + D2 bands), and Area ratio (AR; Area D1 + D4 bands / Area G + D2 + D3 bands) were estimated. The Tuinstra and Koenig equation were applied: ID1 / IG = C(λ) / L_a (nm) (Tuinstra and Koenig 1970); where C (λ), constant (4.4); ID1/IG, Intensity D1 band / Intensity G band, R1 ratio; L_a (nm), the crystal size of lateral extent of carbon sheets. Mean values and standard deviations were calculated based on 11–20 analyses for both edge and center part of samples.

Scanning electron microscopic (SEM) observations were carried out using a JEOL 6510LA, equipped with an energy dispersive X-ray spectrometer (EDS) at Niigata University. CM samples extracted from the run products were ground and suspended in pure water. After ultrasonic cleaning in plastic tubes, the solution was deposited on the SEM sample stage. Both samples were observed without coating under low vacuum pressure.

7.4. Results

7.4.1. Morphological characteristics of run products

The optical properties of CM powders extracted from Pt capsules gradually changed with

increasing pressure and for longer durations. In order to assess the pressure dependence of morphological characteristics in the CM samples, the run products were compared for constant duration (1h) at constant temperature of 1200 °C. At a low pressure of 0.5 GPa, both CM samples consist of small grains of 1~10 μm diameter based on SEM observations (Fig. 83a). Compressing at higher pressures (> 1.5 GPa) changes the CM to aggregates with planar structures (Fig. 83b), which do not show hexagonal platy structure yet. The appearance of fibrous graphite has occurred in the aggregates with planar structure at 4 GPa (Fig. 83c). These aggregates convert to a scaly structure, whichgrow a few μm width by compressing at 8 GPa (Fig. 83d). The morphological changes from 0.5 to 8 GPa could be well consistent with the appearance of d_{004}, d_{110}, and d_{006} in XRD profiles, suggesting a formation of graphitic structure owing to the pressure dependence.

7.4.2. Structural change of both CM by XRD and micro-Raman spectroscopy

Both CM samples display systematic changes of XRD and Raman profiles with respect to pressure and heating duration at 1200 °C (Figs. 84a and 85a; Table 21). For the starting materials of SM, the broad 002 reflection, 10 reflection and Raman profile that have a characteristic inclined background were indetified by XRD and micro-Raman spectroscopy, respectively. These characteristic profiles result from an amorphous carbon in nanostructure. Although similar structures were also observed in the CM of HMB, they have already converted from an amorphous structure to a turbostratic structure, showing the d_{002} spacing of ~3.43 Å in XRD. With increasing pressure, the characteristic structural evolution of CM, showing the sigmoid transformation are identified. At low pressure conditions between 0.5 and 2.0 GPa, the CM displays a broad and symmetrical reflection at the 2θ range of 40–45° in XRD profiles (Figs. 84a and 85a). This single broad reflection suggests the aggregation of randomly oriented small staking in the amorphous structure.

Longer heating duration or higher pressure makes the broad asymmetric peak owing to the formation of a turbostratic structure. The asymmetric peak starts to split into two reflections of d_{100} and d_{101} at 8 GPa, suggesting the formation of a graphitic structure. In addition to changes in the XRD profile, the Raman spectra of two prominent bands in the first-order region (1000–1800 cm^{-1}) systematically changed their intensity and area ratio as functions of increasing pressure and heating duration (Figs. 84b and 85b). The disordered bands of D3 and D4 gradually disappeared at over 4 GPa, suggesting the disappearance of amorphous structure in the microstructure.

7.4.3. Time-pressure relations inferred from HPHT treatment

The time–pressure relations of both CM samples demonstrate significant change in crystallinity with increasing annealing duration at 1200 °C (Figs. 86a–l; Table 22). Almost all the crystal parameters became constant or distinguished only extremely slow change even after 1000 min, suggesting either the termination of crystal growth or only sluggish growth. These structural changes indicate slower transformation than temperature dependence for same annealing duration reported by Nakamura et al. (2017). On the other hand, we found that the CM in SM progress more rapid recrystallization of CM than that in HMB (Fig. 86). The crystal parameters of XRD and micro-Raman spectroscopy in HMB is difficult to identify the structural chages as a function pressure (Figs. 86a-c, g-i), whereas, that in SM show a significant change as a function of pressure (Figs. 86d-e, j-l). In addition, the CM in SM change their crystallinities by a sigmoid transformation from an amorphous to a graphitic structure in the time-pressure relations. These parameters such as d_{002} spacing, FWHM of d_{002} spacing, D1 band and area ratio rapidly changed at the inflection point of a sigmoid curve, and then gently terminate to a graphitic structure. The CM in HMB can be only observed as a deceleration curve as a function of annealing duration. These data suggest that the CM in SM progress recrystallization more

rapidly by pressure dependence. Previous study reported that CM in SM shows a more random orientation of carbon sheets in the CM nanostructure based on transmission electron microscopy (TEM) observations compared with the nanostructure in HMB (Nakamura et al. 2017). These nanostructural differences may arise from the graphitization depending on the pressure effect.

7.5. Discussion

7.5.1. Estimation of activation volume of graphitization

The kinetic results of the *HPHT* experiments at 1200 °C for both CM samples suggest that their changes in crystallinity, morphology were proportional to both the duration and pressure. Hence, we assessed the activation volume of graphitization using the power rate model (Jones et al. 1972; House 2007) and Johnson-Mehl-Avrami-Kolmogorov model (JMAK model; e.g., Sung 2001; Khawam and Flanagan 2006). The experimental kinetic data first converted to the degree of graphitization (g) by following the equation (Khawam and Flanagan 2006):

$$g = (d_0 - d_1) / (d_0 - d_f), \quad (1)$$

where d_0 is the initial value of d_{002} spacing (Table 21; Murty et al. 1969; Fischbach 1971), d_1 is the observed experimental data, and the d_f show the final value of d_{002} spacing (Table 21; Fischbach, 1971). After conversions to nondimensional parameters, an attempt was made to fit the following power law of time as:

$$g = k_p t^{-n}, \quad (2)$$

where k_p is the rate constant, t time (s), n a reaction order at that pressure. Using the differential method (ln-ln plot), the rate constant k_p are obtained under each pressure. The experimental data fitted by the equation (2) show least square correlation coefficient

of 0.656–0.975 depending on the pressures (Figs. 87a–b). Almost all crystal parameters demonstrated the sigmoid transformation from an amorphous to a graphitic structure (Fig. 86), therefore, we tried to calculate the best fitting using a JMAK model to apply for the complex "sigmoid" transformation of graphitization (Figs. 86a-l). The JMAK equation is especially suitable to the transformation kinetics of heterogeneous nucleation and recrystallization, and widely utilized in material science and mineralogy (e.g., Sung et al. 2003; Francisco et al. 2016). The equation was expressed as follows:

$$g = 1 - \exp(-k_a t^l), \qquad (4)$$

where k_a is the rate constant of JMAK equation, l is the order of reaction named for "Avrami index", t is the duration of heating (s). Taking the natural logarithm of equation (4), it can be also expressed as:

$$\ln[-\ln(1-g)] = \ln k_a + l \ln t, \qquad (5)$$

Plotting the left side of equation ($\ln[-\ln(1-g)]$) and natural logarithm of time ($\ln t$), the rate constant k_a and Avrami index l are estimated from the linear regression of intercept and slope in this Avrami plot, respectively. The model fitting by a JMAK equation displays squared correlation coefficient between 0.681 and 0.962 depending on the pressures (Figs. 87d–e). The rate constants $k_{p,a}$ and reaction orders n, l obtained from both model fitting systematically change as function of pressure (Fig. 88). The exponential transformation with increasing pressure are in good agreement with the variation in temperature dependence reported by Nakamura et al. (2017). This suggests that temperature dependence and pressure dependence progress similar transformation kinetics, showing sigmoid recrystallization from an amorphous to a graphitic structure by HPHT experiments.

The pressure dependence in experimental kinetic study is termed as activation volume $\Delta V^{\neq}$, which describes the influence of the pressure on the rate constant (House 2007). The activation volume $\Delta V^{\neq}$ is expressed as:

$$(\partial \ln k_{p,a} / \partial P)_T = -\Delta V^{\neq} / RT \qquad (3)$$

where P is the pressure, R the gas constant, T the absolute temperature at $1473K$ (1200 °C). This equation indicates that a plot of $\ln k_{p,a}$ vs. P should be linear relationship with a slope of $-\Delta V^{\neq} / RT$ if $\Delta V^{\neq}$ is independent of pressure, within the experimental uncertainty. Using the $\ln k_p$ values vs. pressures between 0.5 and 2 GPa, we obtained the activation volumes of – 22 ± 3.4 cm^3/ mol and – 36 ± 19.5 cm^3/ mol for HMB and SM samples, respectively (Fig. 87c; Table 23). Likewise, the activation volumes of – 25 ± 9.6 cm^3/ mol and – 44 ± 17.5 cm^3/ mol for HMB and SM samples using a JMAK model, respectively (Fig. 87f; Table 23). Regarding to the activation volume, pioneering works were only reported by Noda et al. (1968), who proposed the activation volumes of – 7 and – 9 cm^3/ mol for graphitization under the pressure of 1, 3 and 5 kbar. However, they did not cite the detailed experimental data on pressure dependence and referred to the activation volume as approximate values in the literature. Hence, our experimental kinetic results are the first systematic kinetic data on the pressure dependence of graphitization under the pressures between 0.5 and 2 GPa at 1200 °C. For decades, large amount of literatures argued that a hydrostatic stress accelerates the graphitization rate (Onodera et al. 1991; Beyssac et al. 2003; Zhao et al. 2009). This means that the activation volume is negative, and our activation volumes matches well with the kinetic results in previous *HPHT* experiments. On the other hand, we found that a large discontinuouity of apparent activation energy between ambient and high pressure condition. Strictly speaking, the activation enthalpy ΔH increases with increasing pressure as given by;

$$\Delta H = \Delta E\mathrm{a} + P\Delta V^{\neq}, \qquad (4)$$

where ΔH is the activation enthalpy, ΔEa the activation energy at 1 atm, P the pressure, $\Delta V^{\neq}$ the activation volume. The equation (4) imply that activation enthalpy at any pressure conditions are obtained using the linear relationship between pressure and apparent activation energy. The ΔH value is equal to ΔEa value at 1 atm. In the CM in HMB, we

already reported the effective activation energy of 265 ± 19 kJ/mol under a pressure of 1GPa based on same kinetic experiments (Nakamura et al. 2017). Utilizing the activation energy and activation volumes in HMB, the estimated effective activation energy at 0.5 GPa demonstrate between 276 and 277 kJ/mol. Likewise, the estimated effective activation energy at 2.0 GPa demonstrate between 240 and 243 kJ/mol. These estimations suggest that the wide ranges of pressure condition progress the fast graphitization obeying our low activation energy of 240 ~ 280 kJ/mol under the pressures between 0.5 and 2.0 GPa. Noda et al. (1968) pointed out that fast graphitization under a high pressure proceeded at least at pressures of 0.3 GPa (300 MPa) compared with graphitization at 1 atm. It is expected that our extrapolation of effective activation energy might be true at over 0.3 GPa. In addition, the apparent activation energy of ~124 kJ/mol for graphitization was reported, which are significantly smaller than that for the graphitization at 0.5 GPa and 1 GPa (Onodera et al. 1991). These data suggest that the negative volume of activation was retained until phase transition of graphite to diamond between 0.3 and 15 GPa. On the other hand, the estimated activation energy at 1 atm based on our experimental kinetic data show 287 and 290 kJ/mol, respectively. These data have large difference of activation energy of ~1000 kJ/mol at 1 atm. This suggests that pressure dependence dose not have linear relation between pressure and effective activation energy, and some important dynamic process on hydrostatic stress might be happened at around 1~3 kbar.

7.5.2. Deformation induced graphitization under a hydrostatic pressure

The kinetic experiments demonstrated the importance of hydrostatic pressure in graphitization. In particular, I found the difference of pressure effects in both starting materials. The CM in SM has a larger activation volume than that in HMB, suggesting the promotion of recrystallization with confining pressure in crust. The CM in HMB already

formed oriented stackings termed local molecular orientation in amorphous carbon, however, the CM in SM display a random orientation of carbon sheets in amorphous carbon. These nanostructural aspects may arise from the difference of activation volume resulting from the realignment of random orientation of carbon sheets with confining pressure. Previous deformation experiments pointed out that the rotation and rearrangements of carbon sheets by non-hydrostatic stress yield fast recrystallization of CM. Their experiments also reported that it is difficult to realign the random orientation of carbon sheets by coaxial and hydrostatic stress (Bustin et al. 1995). However, we found that hydrostatic pressure also acts as an important factor for promotion of graphitization based on experimental kinetic study, and randomly oriented stacking in amorphous carbon is easier to realign the carbon sheets by the pressure effect than those in turbostratic carbon. This might be related to the realignment mechanism of recrystallization under a hydrostatic pressure. In general, amorphous carbon and graphite have a large difference of physical property in their crystal structures (Zhao and Spain 1989). It is well known that amorphous carbon has sp^2-sp^3 hybrid sites in the cluster and sp^3 bonding increase with increasing pressure (Kelires 1994). The fraction of sp^3 is directly proportional to the Young's modulus, yielding the bond strengthening in amorphous carbon (Schultrich et al. 1996). On the other hand, the release of compressive stress by heat treatments results from sp^3 to sp^2 conversion (Ferrari et al. 1999; Robertson 2002). Such sp^3 to sp^2 conversion accompanying heat treatment might resulted in the realignment and recrystallization of CM under a high-pressure condition. In any case, the hydrostatic pressure accompanying heat treatment drastically change the crystallinity of CM and lead to a graphitic structure without non-hydrostatic stress. In the wide variety of geological contexts, it is important to assess the effect of not only tectonic shearing but also hydrostatic pressure during graphitization. Our experimental data provide a detailed *P-T-t* relation of graphitization and lead to an ideal Arrhenius-type thermometry in various

types of low-grade metamorphic terrains.

7.6. Implication

The estimated activation volumes between – 22 and – 44 cm^3/ mol using a power rate model and a JMAK model demonstrated the large negative values, suggesting the promotion of recrystallization in amorphous carbon under the pressure between 0.5 and 2 GPa. I therefore attempted to extrapolate the *P-T-t* relation of graphitization in various types of metamorphic terrains. Based on the previous kinetic studies on graphitization, it is possible to estimate the effective activation energies with respect to pressure effect empirically (Fig. 89). The pressure dependence of effective activation energy was given by:

$$Ea = -71.66\ln(P) + 789 \ (R^2 = 0.98) \qquad (5)$$

Thus, I can express the effective activation energy *Ea* at any pressure conditions using the above regression curve. In addition to empirical estimation of effect activation energy at any pressure, we also attempted to extrapolate the effective activations using the equation (4) under a pressure of 0.3 to 2 GPa. The equations (4) and (5) are named for linear and log-linear models in this study. Utilizing these activation energies and activation volumes, the relationship between temperature and pressures dependence during graphitization were shown in Figure 90. In this study, I superposed the KFMASH pseudosection modelling with field *P-T* path in Hidaka metamorphic belt for reference (Fig. 10). In the case of log-linear model for heating duration of 100 m.y., the natural CM in HMB start to recrystallized at over 550 °C and form a graphitic carbon at around 650 °C in zone III of HMB (Fig. 90a). On the other hand, the linear model demonstrates the lower recrystallization from 400 °C, and then form a graphite at around ~ 500 °C at even 10 million years (Fig. 90b). Our extrapolation based on the linear model is well consistent

with natural graphitization in various type of metamorphic terrain. For more detailed extrapolations, I attempted to construct the parameter-temperature relations with time along the field *P-T* path in HMB (Fig. 91). The extrapolation curves of log-linear model for 1 Ma, 10 Ma and 100 Ma cannot superpose the natural transformation curve by natural graphitization (Fig. 91a). In addition, the extrapolation curves of linear model are also difficult to fit the natural transformation curve utilizing even changing the heating duration from 1 Ma to 100 Ma (Fig. 91b). The difference of activation energies between natural structural changes of CM and experimental *P-T-t* model make up to 10~15 % (–32 kJ/mol). Although the *P-T-t* kinetic model has lacking some factors, both sigmoid curves of natural and experimental model show similar exponents and inflection points, suggesting the accurate extrapolation.

Moreover, I attempted to calculate the unit cell height *c* and R2 ratio at different *P-T* conditions utilizing the linear and log-normal models. Figure 92 represents typical geothermal gradients from 10 °C/km to 80 °C/km. The typical high pressure, medium pressure, and low pressure metamorphic terrains can be extrapolated by such geothermal gradients (Miyashiro 1994). In the case of log-normal model, the sigmoid curves of each geothermal gradient that transform an amorphous to a graphitic structure demonstrated a large difference owing to the pressure dependence. This suggest that pressure dependence results in the difference of graphitization rate. On the other hand, the calculated sigmoid curves based on the linear model proceeded faster recrystallization of CM to a graphitic structure than log-normal model. In particular, graphitization is attained for all of geothermal gradients at ~550 °C for unit cell height c and 650 °C for R2 ratio. The geothermal gradients between 30~80 °C/km show similar sigmoid curves as a function of peak temperature, suggesting the similar graphitization process in medium to low pressure metamorphic terrain. The difference of extrapolations results in the dP/dT slope of graphitization due to the model fittings. In general, pressure dependence of

graphitization has not been reported in natural metamorphic terrain (Landis 1971, Beyssac et al. 2002a). Considering the previous studies on natural graphitization, the latter model is more suitable for extrapolation of natural graphitization. The termination point of each geothermal gradient corresponds to a maximum value at 650 °C and the temperature range between 400 to 550 °C is reasonable for natural graphitization. Our extrapolation by linear model indicates that graphitization proceeds in greenschist to lower amphibolite facies. In addition, I also attempted to calculate the rate dependence of graphitization in natural *P-T* conditions. Previous empirical thermometry could not consider the effect of duration of heating, however, with the Arrhenius-type equation I propose here it is possible to estimate the rate dependence from contact to regional metamorphism. In the case of linear models (Figs. 94a and c), for hundred thousand years, it would require conversion of a fully ordered graphite at ~650 °C under a pressure of 500 MPa. Longer metamorphism for ~10 m.y. would convert CM to fully ordered graphite at temperatures of ~550 °C. A potential application in the future is to use such difference of graphitization rate that can distinguish between contact and regional metamorphism using the degree of crystallinity.

Overall, our experimental kinetic model corrected by pressure dependence demonstrated that graphitization can proceed at very low temperature (400~ 500 °C) for long duration (~10 Ma) under a realistic pressure conditions of 0.3 ~ 2 GPa in crust. In addition, the *P-T-t* extrapolation indicate that it is possible to calculate the degree of graphite utilizing my equation at any pressure and duration. Figure 95 show compilation of effective activation energy based on our kinetic model and previous kinetic studies. The data imply that the mechanism of graphitization is completely different between ambient and pressure. In particular, natural CM rapidly recrystallize to a graphite based on Arrhenius-type equation at over 0.3 GPa. The fast graphitization is reasonable for understanding the structural evolution of natural CM in subduction zone, where

metamorphosed under high pressure. However, we also found the discordance of model fitting in HMB. This suggest that realistic graphitization is more rapid recrystallization, and further refining of kinetics of graphite is needed for providing new tool for Arrhenius-type geothermometry and geospeedometry in the future.

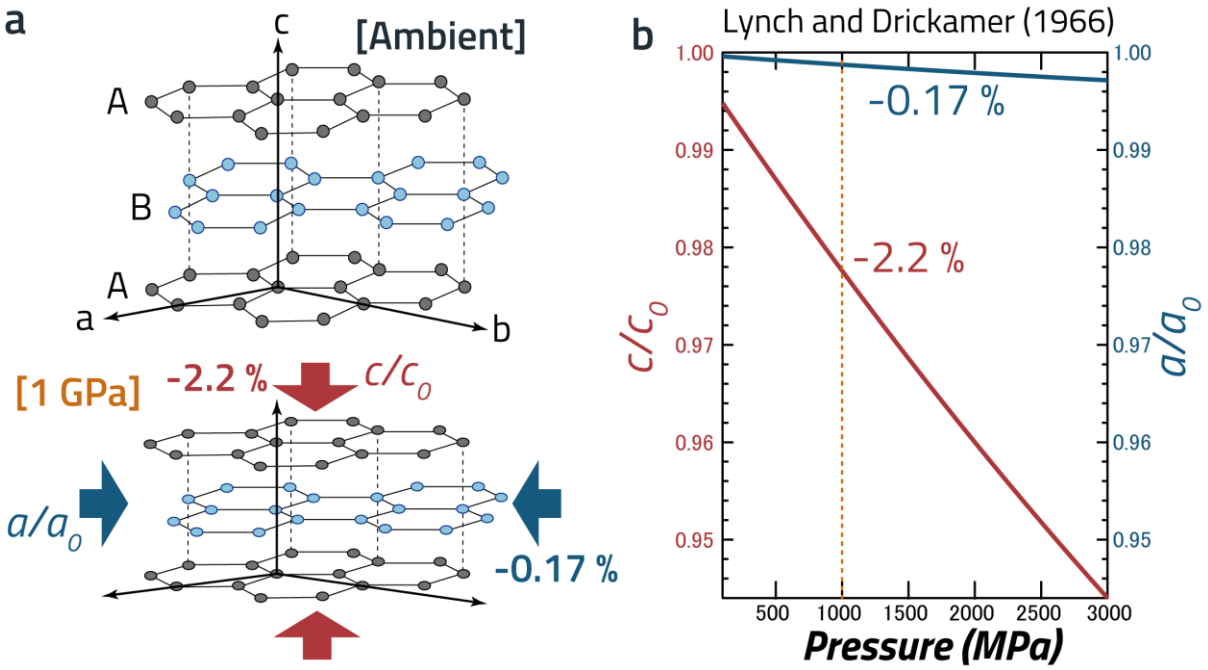

Figure 82. (a) Schematic model of compressed graphite under a 1 GPa. Graphitic structure compresses to 2.2 % along c-axis and 0.17 % along a-axis, respecitively. **(b)** Relationship of compression between pressure, c/c_0, and a/a_0 referred from Lynch and Drickamer (1966).

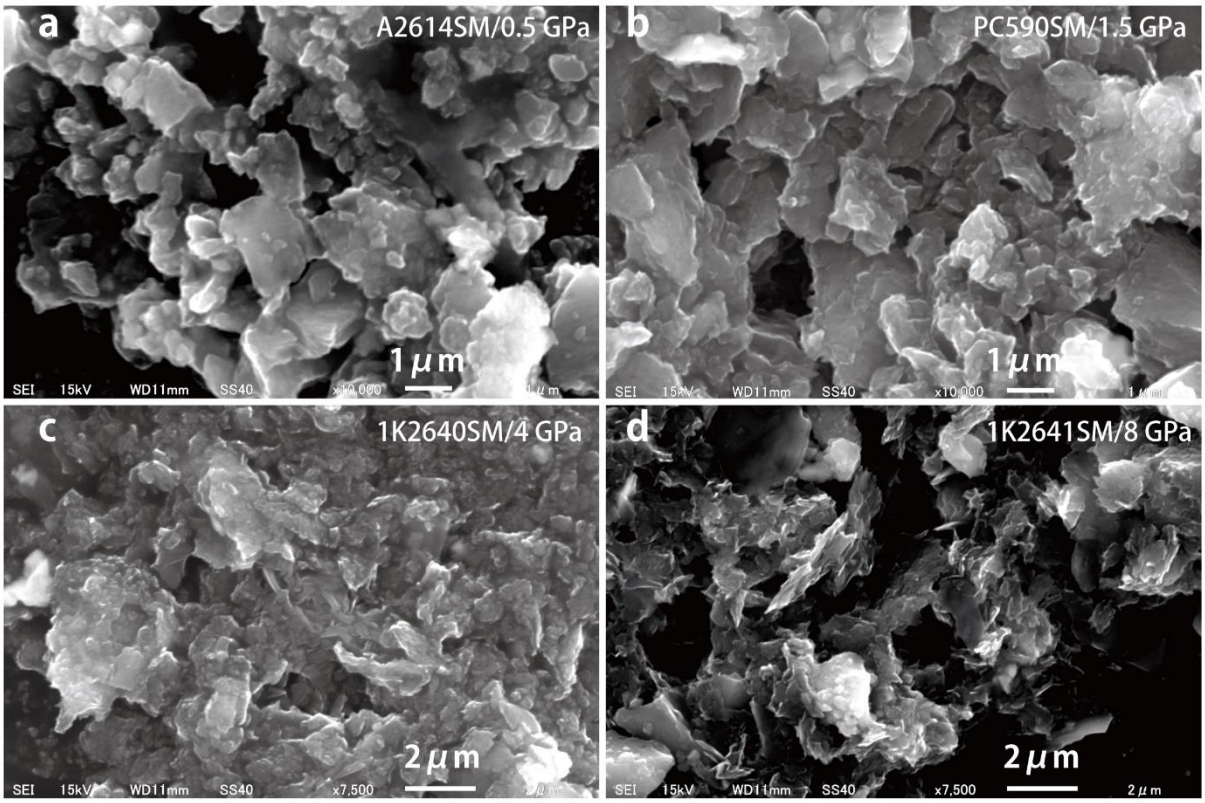

Figure 83. Morphological change of run products as a function of pressure between 0.5 and 8 GPa at constant temperature of 1200 °C for 1 hour. **(a)** SEM observation of CM at 0.5 GPa, showing small grain of CM (A2614SM, 0.5 GPa). **(b)** Planer structure in the CM microstructure for PC590SM (1.5 GPa). **(c)** Fibrous structure with planar grains at 4 GPa (1K2640SM). **(d)** Scaly graphite in powder sample of 1k2641SM at 8GPa.

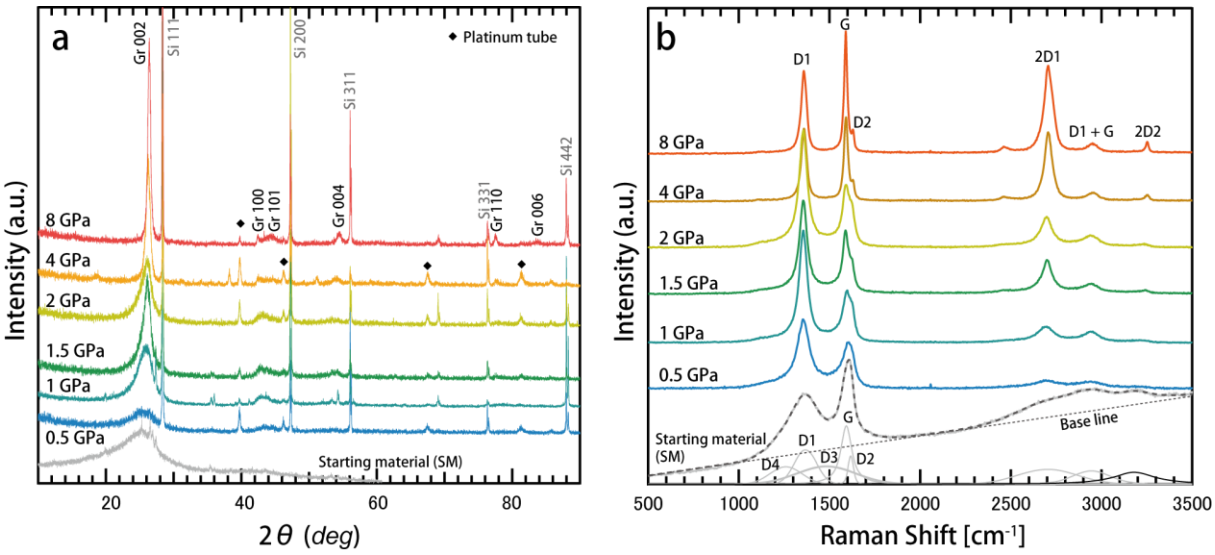

Figure 84. Structural evolutions under a pressure of 0.5 and 8 GPa of CM and starting material in SM to graphite at 1200 °C as observed by **(a)** X-ray diffractometry and **(b)** micro-Raman spectroscopy. The Raman spectra of CM are fitted by five peaks of D1, D2, D3, D4, and G band. Silicon peaks in XRD profile are an internal standard for calibrating the interlayer spacing of disordered graphite.

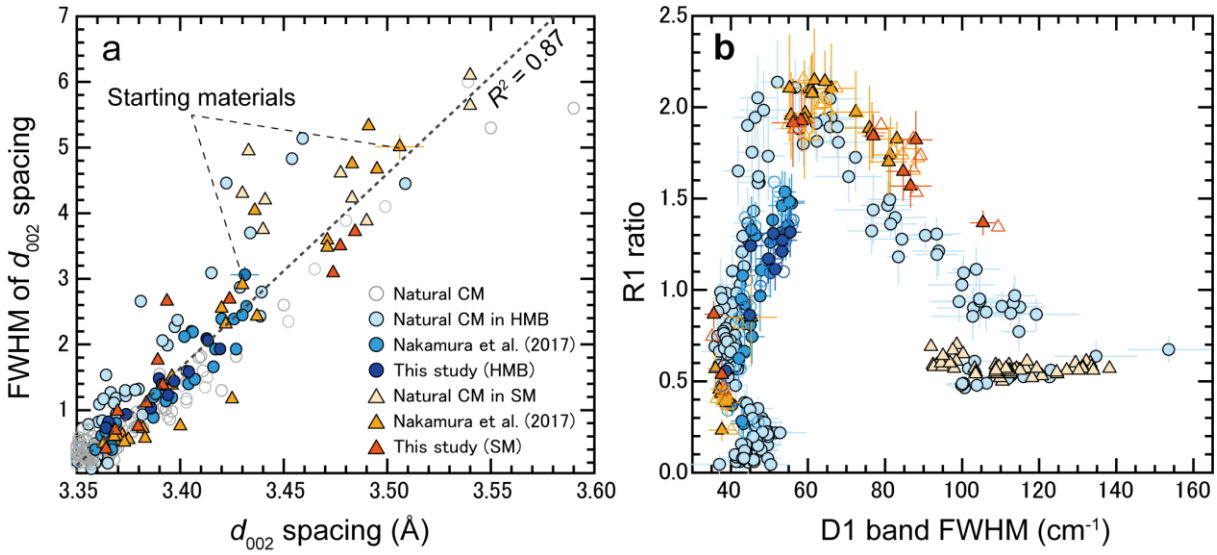

Figure 85. Structural evolution of each crystal parameter of both samples and natural CM by **(a)** X-ray diffraction and **(b)** micro-Raman spectroscopy obtained from various types of metamorphic terrain in Hidaka metamorphic belt (Nakamura et al. 2015; Nakamura et al. 2017), Sambagawa (Itaya 1981), Ryoke (Wang 1989), and so on (Grew 1974; Kříbek et al. 2008).

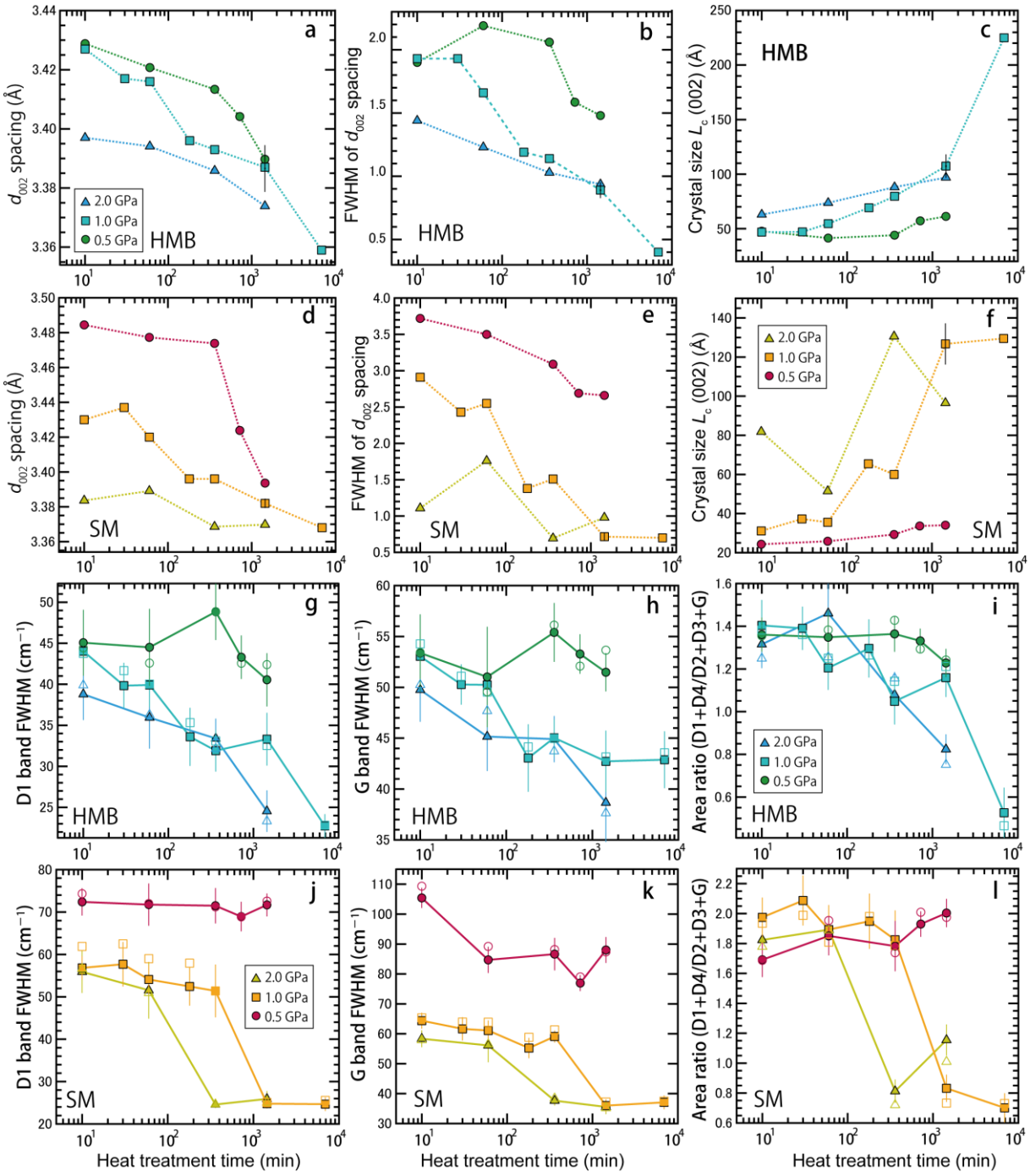

Figure 86. Time–pressure relations between 10 and 10^4 min. The parameters **(a)** d_{002} spacing, **(b)** FWHM of d_{002} peak, and **(c)** L_c(002) from XRD, and also **(g)** D1 band FWHM, **(h)** G band FWHM, and **(i)** area ratio are based on data for the CM in HMB. **(d), (e), (f), (j), (k),** and **(l)** show the same parameters, respectively, for the CM in SM.

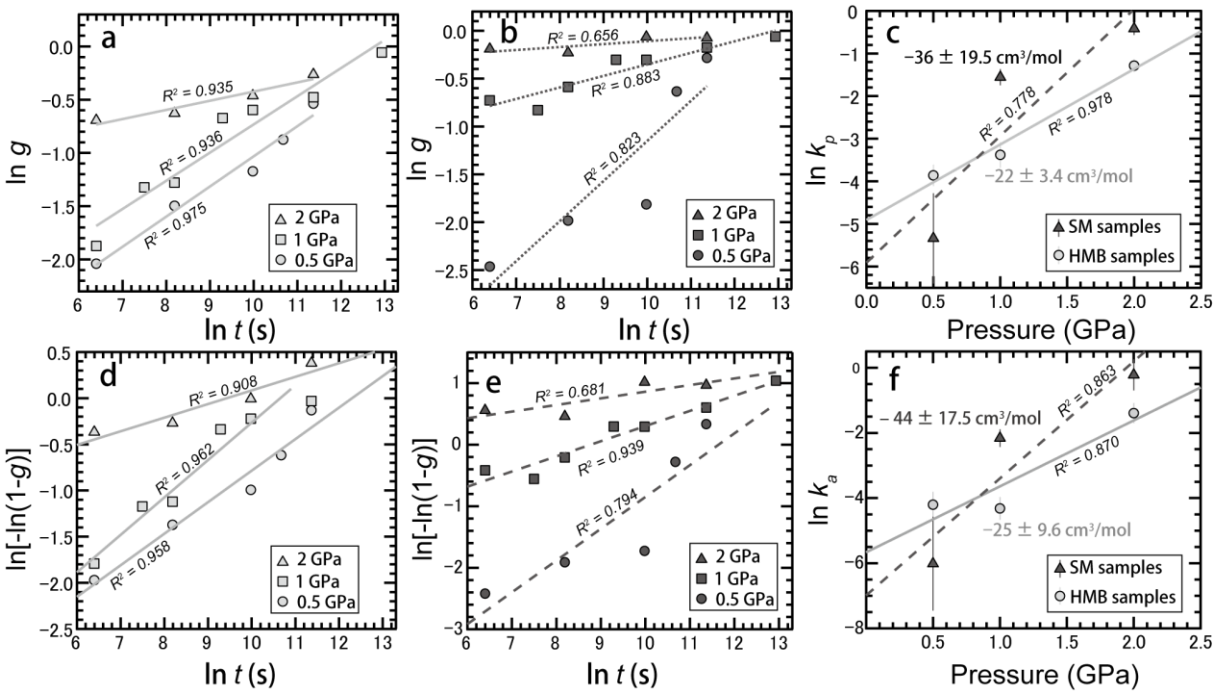

Figure 87. The relationship between experimental ln*t* (s) and ln*g* of HMB **(a)** and SM samples **(b)** fitted by a power rate model. **(c)** The relationship between lnk_p and pressure (GPa) of HMB and SM samples. The relationship between experimental ln*t* and ln[–ln(1–*g*)] of HMB **(d)** and SM samples **(e)** fitted by a JMAK model. **(f)** The relationship between lnk_p and pressure (GPa) of HMB and SM samples.

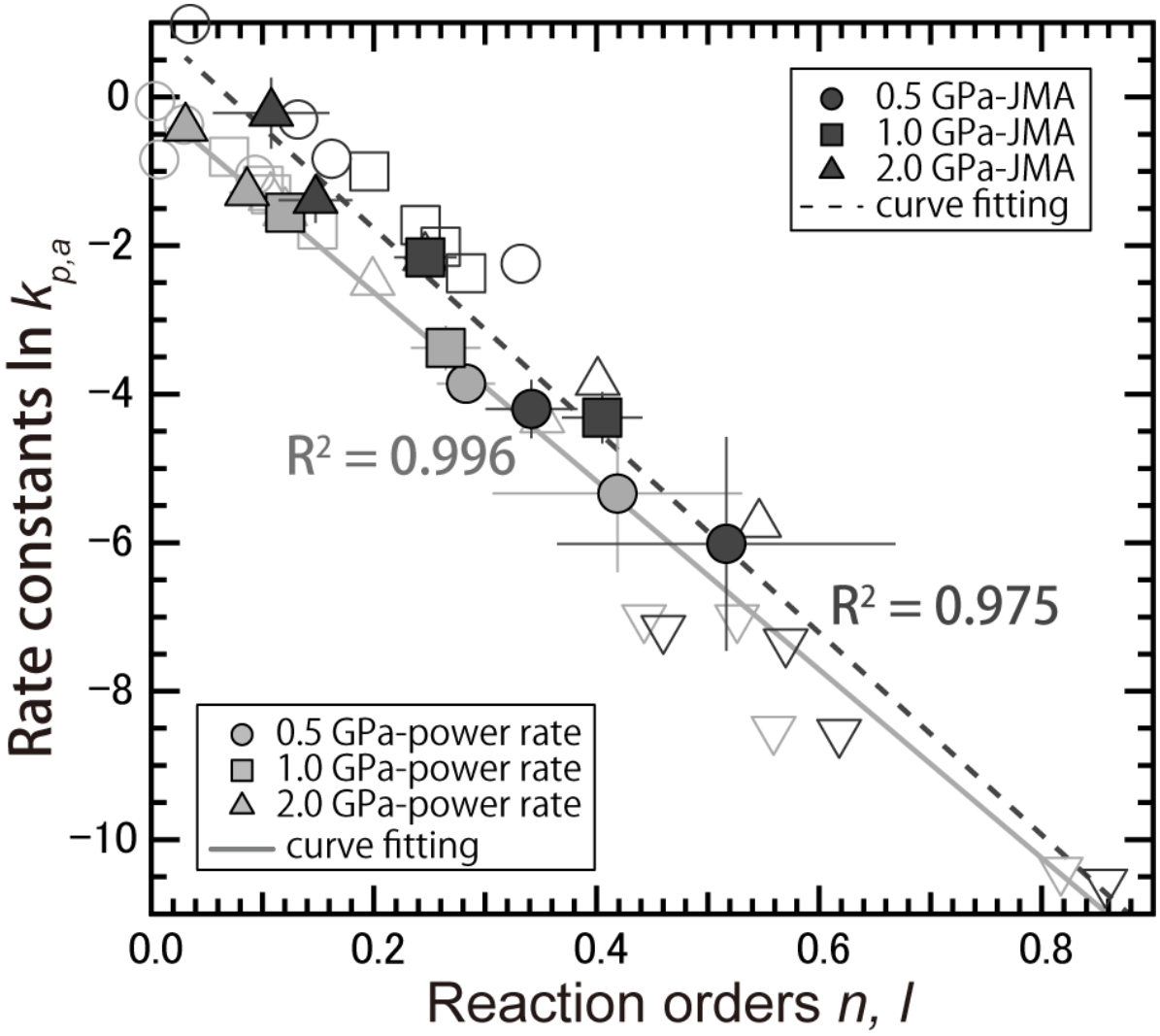

Figure 88. The relationship between the rate constants ln$k_{p,\,a}$ and the orders of reaction n, l of power rate and JMAK models. All of rate constants and reaction orders in this study are plotted. White circules, squares, upper triangular, and lower triangular are utilized for the data on Nakamura et al. (2017).

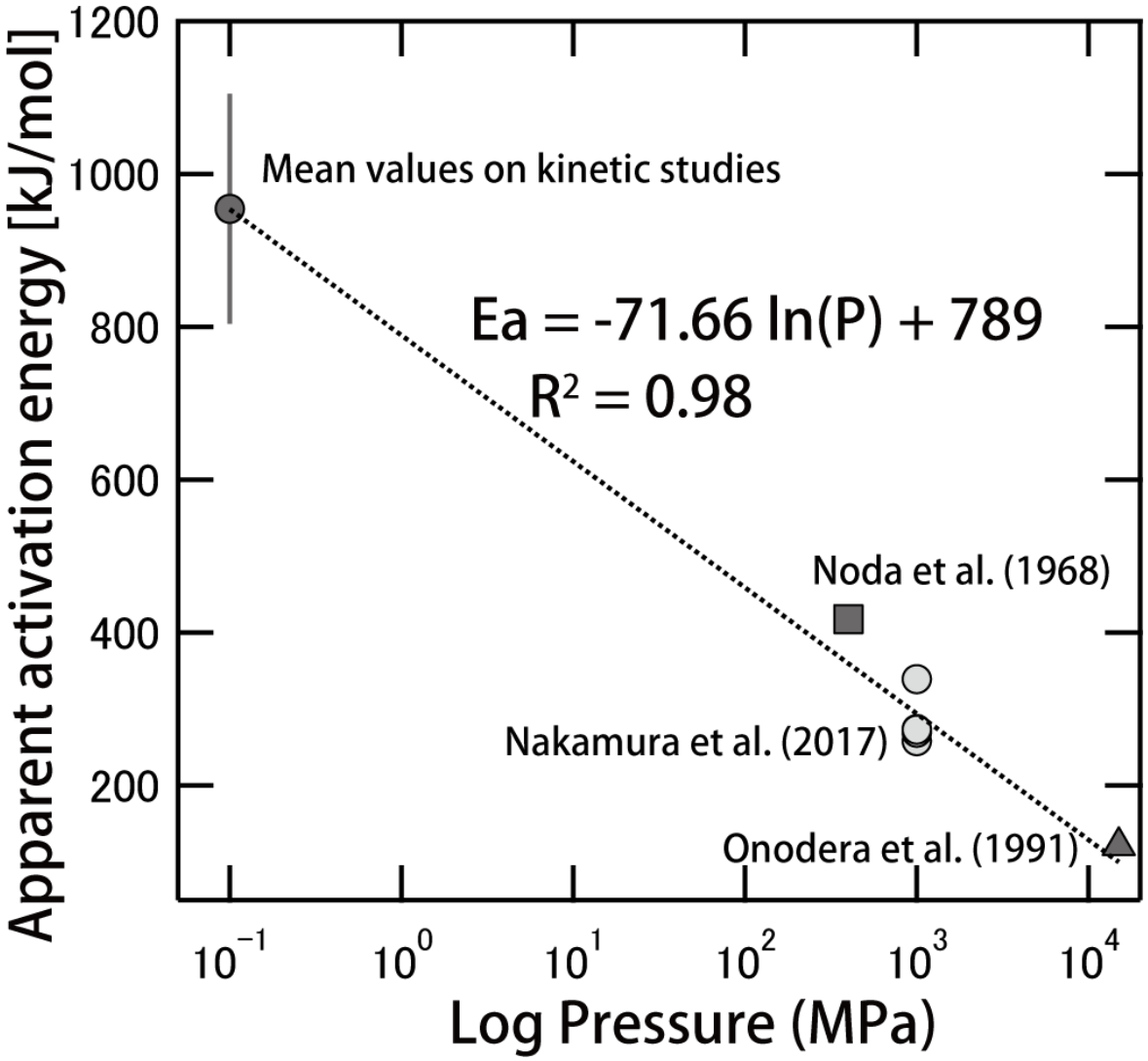

Figure 89. Relationship between effective activation energy and log pressure based on the previous kinetic studies (Murty et al. 1969; Fischbach et al. 1971; Noda et al. 1968; Nakamura et al. 2017; Onodera et al. 1991).

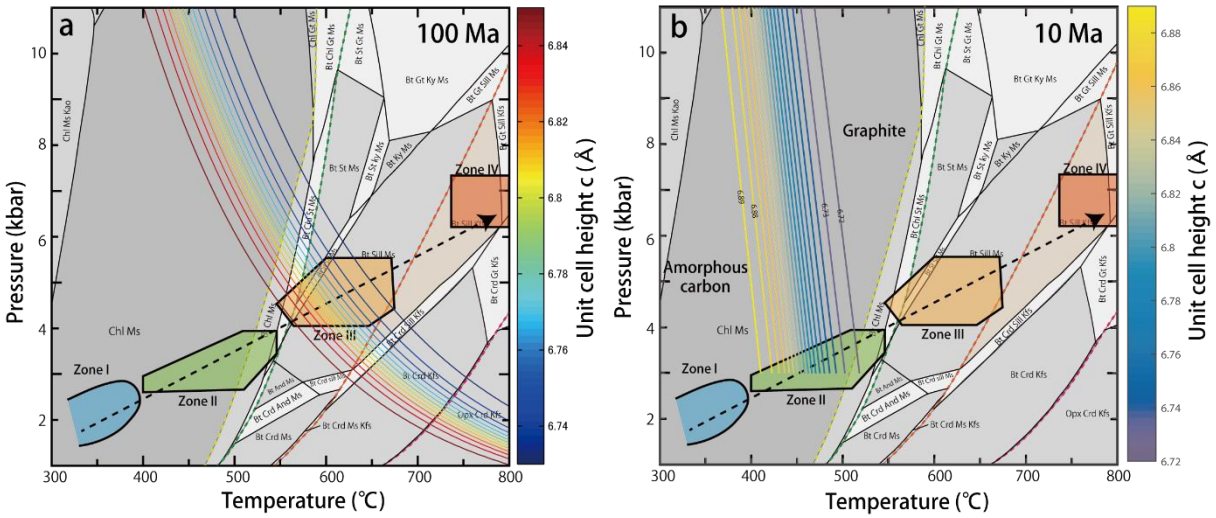

Figure 90. KFMASH pseudosection modelling with field P-T path and calculated unit cell height c using **(a)** the equation (5) for100 Ma and **(b)** the equation (4) for 10 Ma. The phase diagram is constructed by perplex 6.7.1 software (Connolly and Petrini 2002) using thermodynamic database of Holland and Powell (2011).

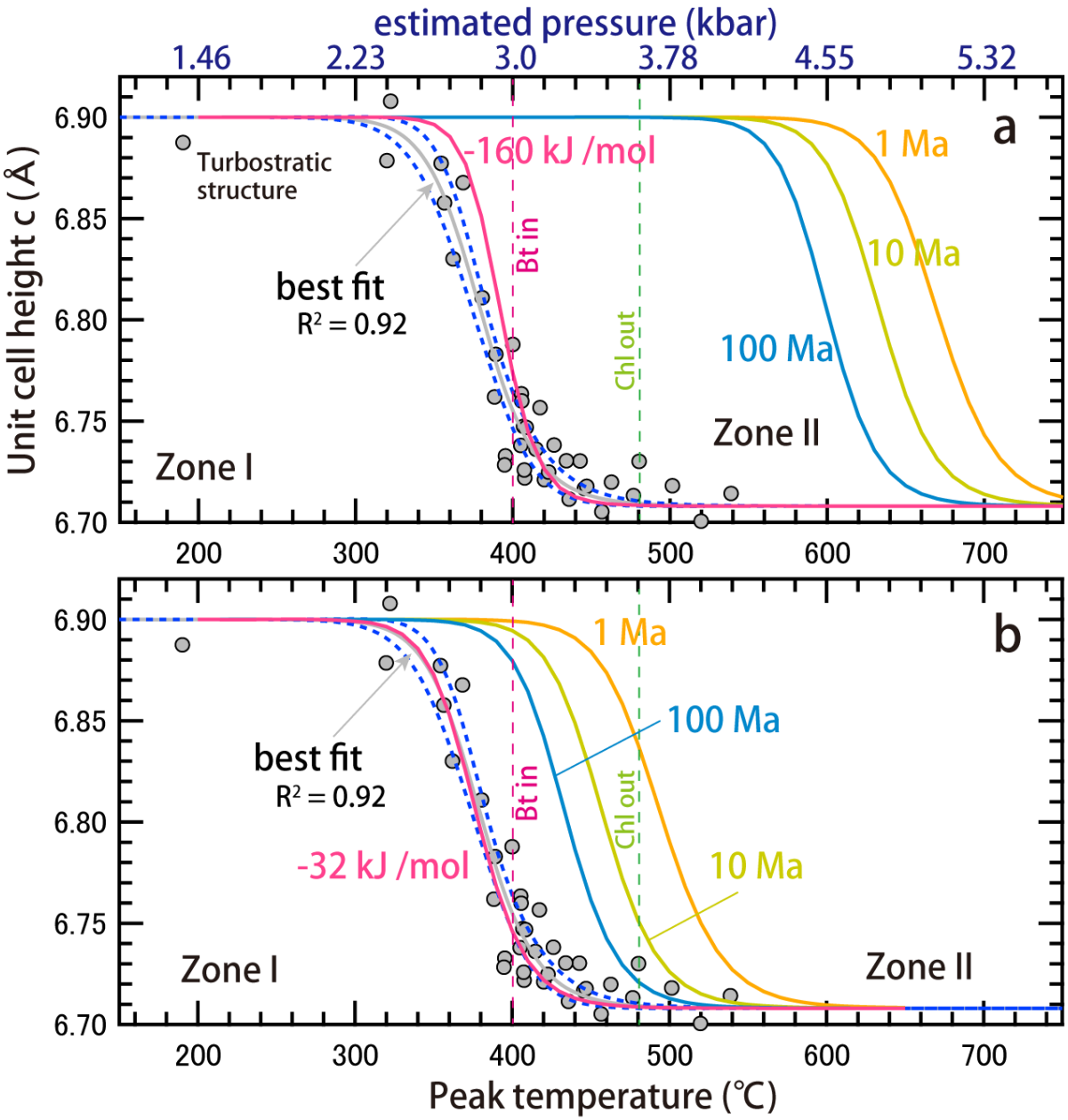

Figure 91. Structural evolution of CM as a function of peak temperatures with calculated unit cell height c based on our kinetic model. The estimated sigmoid curves utilized **(a)** the equation (5), and **(b)** the equation (4) for 1Ma to 100 Ma. Pink sigmoid curves are superposed to the best fitting of measured d_{002} spacing in natural CM, sifting the effective activation energy.

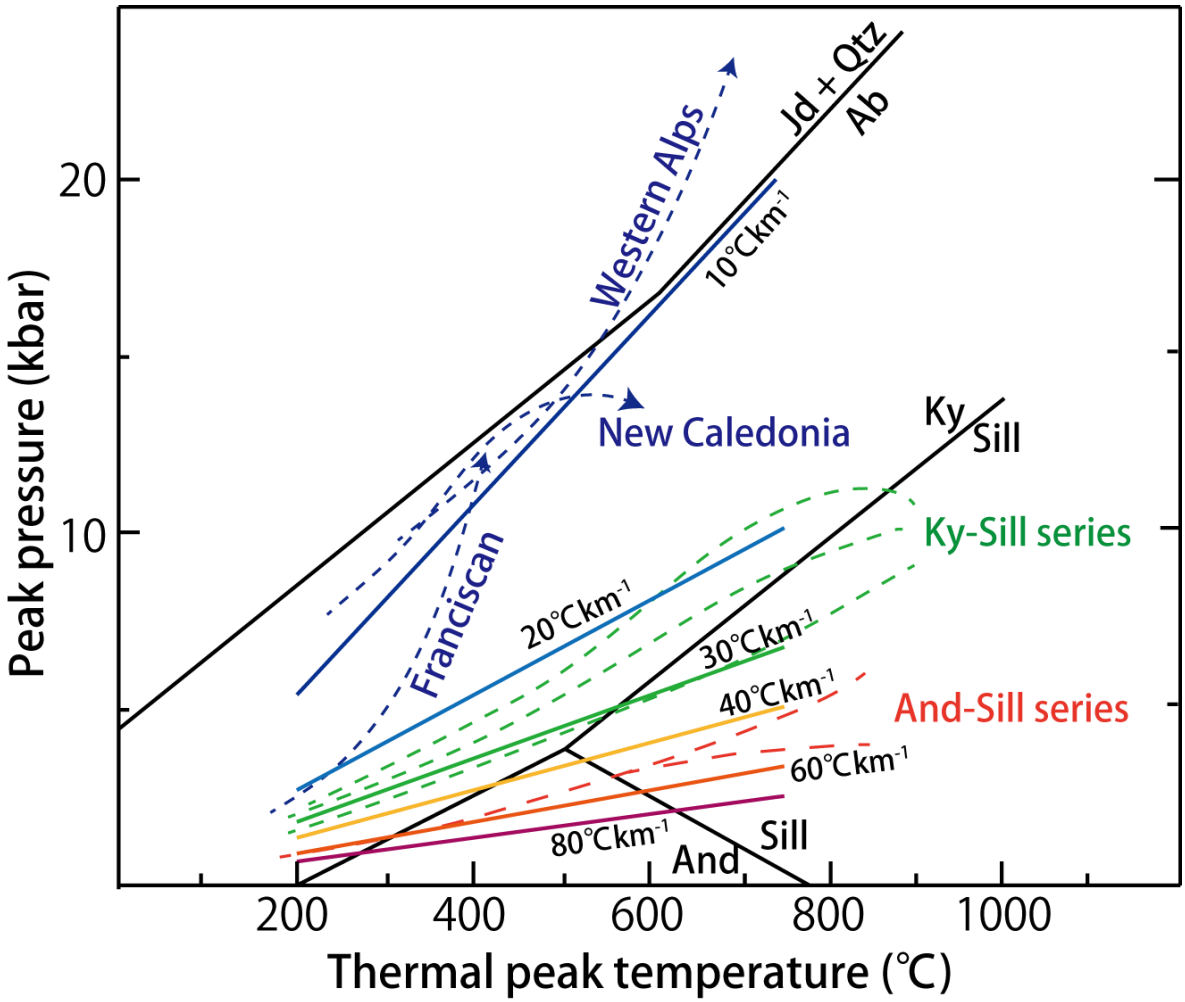

Figure 92. Representative *P-T* conditions in High pressure (blue), medium pressure (green), low pressure type metamorphic terrain (red) (modified after Miyashiro 1994).

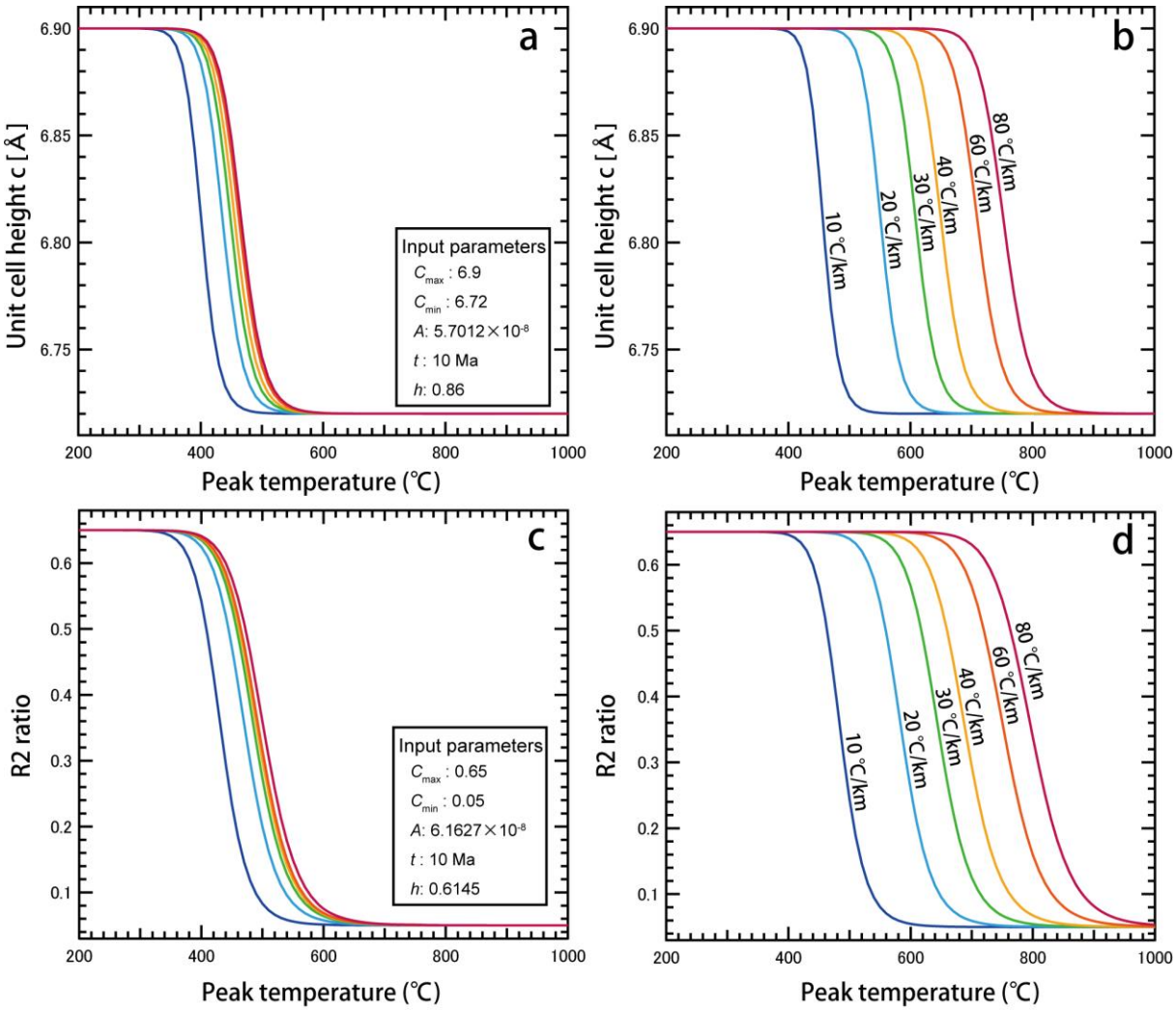

Figure 93. Calculated unit cell height *c* and R2 ratio as a function of peak temperature utilizing a linear model **(a, c)** and a log-linear model **(b, d)**, respectively. Input parameters for calculations are described in the figures. Each color from red to blue corresponds to the geothermal gradient in Fig. 93.

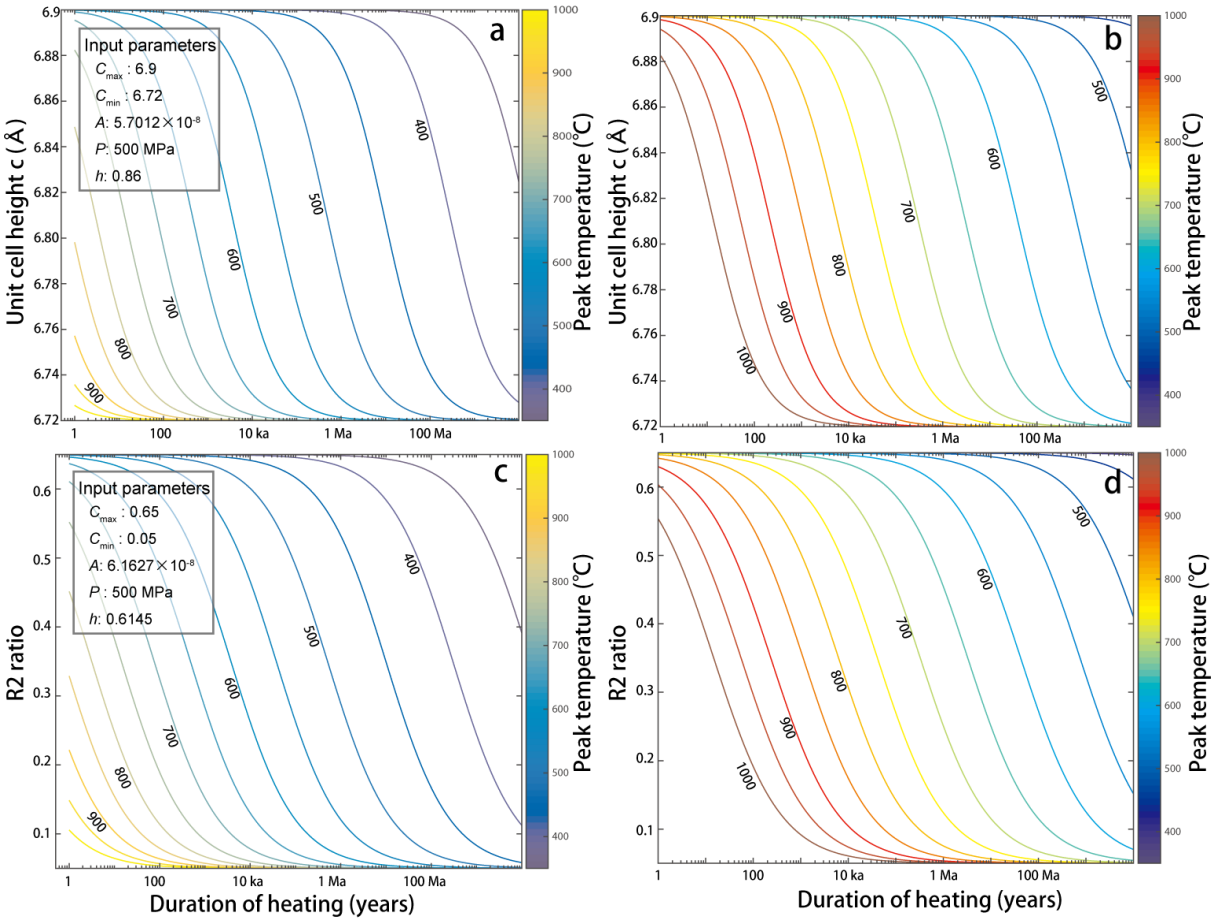

Figure 94. Calculated unit cell height *c* and R2 ratio as a function of duration of heating utilizing a linear model **(a, c)** and a log-linear model **(b, d)**, respectively. Input parameters for calculations are described in the figures. Numbers indicate the peak temperatures, which are contoured at an interval of 50 °C.

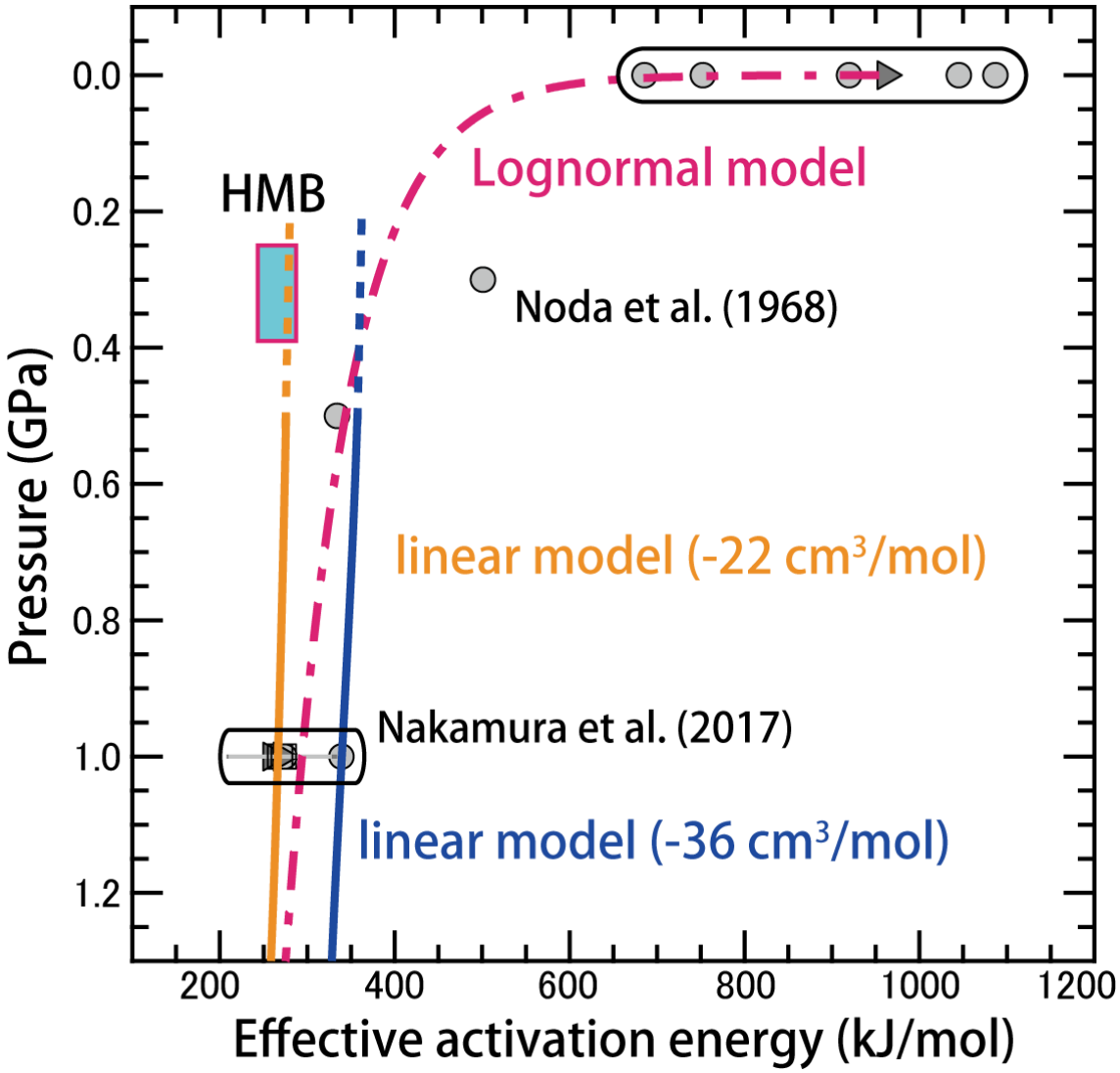

Figure 95. Compilation of effective activation energies (kJ mol^{-1}) at various pressures (GPa) obtained in this study and published values using power rate model, JMAK model and superposition method. The effective activation energies of previous studies are cited from 1, Fischbach (1963); 2, Inagaki et al. (1968); 3, Noda et al. (1965); 4, Fischbach (1971) 5, Murty et al. (1969); 6, Noda et al. (1968); and 7, Marsh et al. (1983). These linear and exponential curves are calculated using the equation (4) and (5).

CHAPTER VIII

8.1 Conclusion

I assessed the detailed rate, pressure, and temperature dependence of structural evolution of natural CM to graphite combining experimental kinetic studies and natural observations in metamorphic terrain. Based on the kinetic experiments and natural observations, important findings of the study are summarized as follows.

1) The structural evolution of natural CM to graphite in Hidaka metamorphic belt (HMB) demonstrated the heterogeneous nature of recrystallization from an amorphous to turbostratic and finally to a graphitic structure with increasing peak temperature. The heterogeneous structural changes based on micro-Raman spectroscopy and X-Ray Diffraction (XRD) show a sigmoid transformation, which derived from the heterogeneous nanostructures of natural CM by transmission electron microscopy (TEM) observations. It is important to reconstruct the heterogeneous recrystallization of CM for fully understanding the kinetics of graphitization in metamorphic terrains.

2) The time-temperature relations of each crystal parameter obtained using XRD analysis and micro-Raman spectroscopy in HPHT kinetic experiments demonstrated sigmoidal transformations from amorphous to graphitic structure, suggesting the complexity of chemical reactions undergoing during graphitization. Irrespective of the models employed, the effective activation energies were estimated to lie between 259 and 339 kJ mol^{-1}, which are much lower than those reported previously for

graphitization. Summarizing the previous studies and our results between 0.1 and 1000 MPa, we found that the effective activation energies systematically decrease as a function of pressure.

3) The estimated activation volumes between – 22 and – 44 cm^3/ mol using a power rate model and a JMAK model demonstrated the large negative values, suggesting the promotion of recrystallization in amorphous carbon under the pressure conditions between 0.5 and 2 GPa. In particular, linear regression model using the activation volumes demonstrate rapid recrystallization from 400 °C, and then form a graphite at ~ 500 °C for even 10 million years. This extrapolation by experimental kinetic results is well consistent with natural graphitization in various type of metamorphic terrain.

Note that there exists slight mismatch between the experimental *P-T-t* kinetic model and natural graphitization in metamorphic rocks. It is thought that the more realistic activation energies for natural graphitization could be slightly lower by about 10% than that estimated in this study, perhaps owing to the influence of other factors. In the future, further detailed experiments and natural observations of graphitization will help to constrain the more realistic *P-T-t* kinetic modelling for graphitization.

REFERENCE CITED

Acharya, B.C., and Dash, B., 1984, Graphite in Eastern Ghats Precambrian migmatites, Orissa, India: Transactions of the Royal Society of Edinburgh: Earth Sciences, v. 75, no. 4, p. 391–406, doi: 10.1017/S0263593300014024.

Allen, A.R., 1979, Mechanism of frictional fusion in fault zones: Journal of Structural Geology, v. 1, p. 231–237.

Antal, M.J., 1983, Effects of reactor severity on the gas-phase pyrolysis of cellulose- and kraft lignin-derived volatile matter: Industrial & Engineering Chemistry Product Research and Development, v. 22, no. 2, p. 366–375, doi: 10.1021/i300010a039.

Antia, D.D.J., 1986, Kinetic method for modeling vitrinite reflectance: Geology, v. 14, no. 7, p. 606–608, doi: 10.1130/0091-7613(1986)14<606:KMFMVR>2.0.CO;2.

Aoki, K., Maruyama, S., Isozaki, Y., Otoh, S., and Yanai, S., 2011, Recognition of the Shimanto HP metamorphic belt within the traditional Sanbagawa HP metamorphic belt: New perspectives of the Cretaceous–Paleogene tectonics in Japan: Journal of Asian Earth Sciences, v. 42, no. 3, p. 355–369, doi: 10.1016/j.jseaes.2011.05.001.

Aoya, M., Kouketsu, Y., Endo, S., Shimizu, H., Mizukami, T., Nakamura, D., and Wallis, S., 2010, Extending the applicability of the Raman carbonaceous-material geothermometer using data from contact metamorphic rocks: Journal of Metamorphic Geology, v. 28, no. 9, p. 895–914, doi: 10.1111/j.1525-1314.2010.00896.x.

Arkai, P., 1991, Chlorite crytallinty: an emprical approach and correlation with illite crystalliny, coal rank and mineral facies as exemplified by Palaeozoic and Mesozoic rocks of rotheast Hungary: Journal of Metamorphic Geology, v. 9, p. 723–734.

Austrheim, H., and Boundy, T.M., 1994, Pseudotachylytes generated during seismic faulting and eclogitization of the deep crust.: Science (New York, N.Y.), v. 265, no. 5168, p. 82–83, doi: 10.1126/science.265.5168.82.

Barker, C.E., 1989, Temperature and time in the thermal maturation of sedimentary organic matter (N. D. Naeser & T. H. McCulloch, Eds.): Springer-Verlag, New York.

Barker, C.E., and Pawlewicz, M.J., 1986, The correlation of vitrinite reflectance with maximum temperature in humic organic matter - Paleogeothermics: Evaluation of Geothermal Conditions in the Geological Past, *in* Buntebarth, G. and Stegena, L. eds., Springer Berlin Heidelberg, Berlin, Heidelberg, p. 79–93.

Barrenechea, J.F., Luque, F.J., Millward, D., Ortega, L., Beyssac, O., and Rodas, M., 2009, Graphite morphologies from the Borrowdale deposit (NW England, UK): Raman and SIMS data: Contributions to Mineralogy and Petrology, v. 158, no. 1, p. 37–51, doi: 10.1007/s00410-008-0369-y.

Baumlin, S., Broust, F., Ferrer, M., Meunier, N., Marty, E., and Lédé, J., 2005, The continuous self stirred tank reactor: Measurement of the cracking kinetics of biomass pyrolysis vapours: Chemical Engineering Science, v. 60, no. 1, p. 41–55, doi: 10.1016/j.ces.2004.07.057.

Bell, I.A., and Wilson, C.J.L., 1981, Deformation of biotite and muscovite: Tem microstructure and deformation model: Tectonophysics, v. 78, no. 1–4, p. 201–228, doi: http://dx.doi.org/10.1016/0040-1951(81)90014-7.

Bernard, S., Benzerara, K., Beyssac, O., Balan, E., and Brown, G.E., 2015, Evolution of the macromolecular structure of sporopollenin during thermal degradation: Heliyon, v. 1, no. 2, p. 1–28, doi: 10.1016/j.heliyon.2015.e00034.

Beyssac, O., Goffé, B., Chopin, C., and Rouzaud, J.N., 2002, Raman spectra of carbonaceous material in metasediments: a new geothermometer: Journal of Metamorphic Geology, v. 20, no. 9, p. 859–871, doi: 10.1046/j.1525-1314.2002.00408.x.

Beyssac, O., Goffé, B., Petitet, J.-P., Froigneux, E., Moreau, M., and Rouzaud, J.N., 2003, On the characterization of disordered and heterogeneous carbonaceous materials by Raman spectroscopy: Spectrochimica Acta Part A: Molecular and Biomolecular Spectroscopy, v. 59, no. 10, p. 2267–2276, doi: 10.1016/S1386-1425(03)00070-2.

Bonal, L., Quirico, E., Bourot-Denise, M., and Montagnac, G., 2006, Determination of the petrologic type of CV3 chondrites by Raman spectroscopy of included organic matter: Geochimica et Cosmochimica Acta, v. 70, no. 7, p. 1849–1863, doi: 10.1016/j.gca.2005.12.004.

Bonal, L., Quirico, E., Flandinet, L., and Montagnac, G., 2016, Thermal history of type 3 chondrites from the Antarctic meteorite collection determined by Raman

spectroscopy of their polyaromatic carbonaceous matter: Geochimica et Cosmochimica Acta, v. 189, p. 312–337, doi: 10.1016/j.gca.2016.06.017.

Bonijoly, M., Oberlin, M., and Oberlin, A., 1982, A possible mechanism for natural graphite formation: International Journal of Coal Geology, v. 1, no. 4, p. 283–312, doi: http://dx.doi.org/10.1016/0166-5162(82)90018-0.

Boroson, M.L., Howard, J.B., Longwell, J.P., and Peters, W.A., 1989, Product yields and kinetics from the vapor phase cracking of wood pyrolysis tars: AIChE Journal, v. 35, no. 1, p. 120–128, doi: 10.1002/aic.690350113.

Bos, B., and Spiers, C.J., 2000, Effect of phyllosilicates on fluid-assisted healing of gouge-bearing faults: Earth and Planetary Science Letters, v. 184, no. 1, p. 199–210, doi: 10.1016/S0012-821X(00)00304-6.

Boullier, A., Ohtani, T., Fujimoto, K., Ito, H., and Dubois, M., 2001, Fluid inclusions in pseudotachylytes from the Nojima fault, Japan: Journal of Geophysical Research, v. 106, no. B10, p. 21965, doi: 10.1029/2000JB000043.

Bourrat, X., Oberlin, A., and Escalier, J.., 1987, Sulphur behaviour treatment during asphalt: FUEL, v. 66, p. 542–550.

Buseck, P.R., and Beyssac, O., 2014, From Organic Matter to Graphite: Graphitization: Elements, v. 10, no. 6, p. 421–426, doi: 10.2113/gselements.10.6.421.

Buseck, P.R., Bo-Jun, H., and Miner, B., 1988, Structural order and disorder in Precambrian kerogens: Organic Geochemistry, v. 12, no. 3, p. 221–234, doi: http://dx.doi.org/10.1016/0146-6380(88)90260-4.

Buseck, P.R., and Huang, B.-J., 1985, Conversion of carbonaceous material to graphite during metamorphism: Geochimica et Cosmochimica Acta, v. 49, no. 10, p. 2003–2016, doi: http://dx.doi.org/10.1016/0016-7037(85)90059-6.

Busemann, H., Alexander, C.M.O., and Nittler, L.R., 2007, Characterization of insoluble organic matter in primitive meteorites by microRaman spectroscopy: Meteoritics & Planetary Science, v. 1416, no. 7, p. 1387–1416, doi: 10.1111/j.1945-5100.2007.tb00581.x.

Bustin, R.M., Ross, J. V., and Rouzaud, J.N., 1995, Mechanisms of graphite formation from kerogen: experimental evidence: International Journal of Coal Geology, v. 28, no. 1, p. 1–36, doi: 10.1016/0166-5162(95)00002-U.

Caballero, J.A., Font, R., and Marcilla, A., 1996, Kinetic study of the secondary thermal decomposition of Kraft lignin: Journal of Analytical and Applied Pyrolysis, v. 38, no. 1, p. 131–152, doi: http://dx.doi.org/10.1016/S0165-2370(96)00953-9.

Cançado, L.G., Takai, K., Enoki, T., Endo, M., Kim, Y. a., Mizusaki, H., Speziali, N.L., Jorio, a., and Pimenta, M. a., 2008, Measuring the degree of stacking order in graphite by Raman spectroscopy: Carbon, v. 46, no. 2, p. 272–275, doi: 10.1016/j.carbon.2007.11.015.

Çetinkaya, S., and Yürüm, Y., 2000, Oxidative pyrolysis of Turkish lignites in air up to 500 °C: Fuel processing technology, v. 67, no. 3, p. 177–189, doi: 10.1016/S0378-3820(00)00105-3.

Charon, E., Rouzaud, J.N., and Aléon, J., 2014, Graphitization at low temperatures (600-1200 C) in the presence of iron implications in planetology: Carbon, v. 66, p. 178–190, doi: 10.1016/j.carbon.2013.08.056.

Chen, Y., Mastalerz, M., and Schimmelmann, A., 2012, Characterization of chemical functional groups in macerals across different coal ranks via micro-FTIR spectroscopy: International Journal of Coal Geology, v. 104, p. 22–33, doi: 10.1016/j.coal.2012.09.001.

Cody, G.D., Alexander, C.M.O., Yabuta, H., Kilcoyne, A.L.D., Araki, T., Ade, H., Dera, P., Fogel, M., Militzer, B., and Mysen, B.O., 2008, Organic thermometry for chondritic parent bodies: Earth and Planetary Science Letters, v. 272, no. 1–2, p. 446–455, doi: 10.1016/j.epsl.2008.05.008.

Collettini, C., Niemeijer, A., Viti, C., and Marone, C., 2009, Fault zone fabric and fault weakness.: Nature, v. 462, no. 7275, p. 907–10, doi: 10.1038/nature08585.

Connolly, J.A.D., and Petrini, K., 2002, An automated strategyfor calculation of phase diagram sections and retrieval of rockproperties as a function of physical conditions (0.4 Mb).: Journal of Metamorphic Geology, v. 20, p. 697–708, doi: 10.1046/j.1525-1314.2002.00398.x.

Connolly, J.A.D., and Cesare, B., 1993, C-O-H-S fluid composition and oxygen fugacity in graphitic¥rmetapelites: Journal of Metamorphic Geology, v. 379–388, p. 379–388.

Cowan, D.S., 1999, Do faults preserve a record of seismic slip? A field geologist's opinion: Journal of Structural Geology, v. 21, no. 8–9, p. 995–1001, doi: http://dx.doi.org/10.1016/S0191-8141(99)00046-2.

Cozzani, V., Nicolella, C., Petarca, L., Rovatti, M., and Tognotti, L., 1995, A Fundamental Study on Conventional Pyrolysis of a Refuse-Derived Fuel: Industrial & Engineering Chemistry Research, v. 34, no. 6, p. 2006–2020, doi: 10.1021/ie00045a010.

Crespo, E., Luque, F.J., Barrenechea, J.F., and Rodas, M., 2006, Influence of grinding on graphite crystallinity from experimental and natural data: implications for graphite thermometry and sample preparation: Mineralogical Magazine, v. 70, no. 6, p. 697–707, doi: 10.1180/0026461067060358.

Crespo, E., Luque, J., Barrenechea, J.F., and Rodas, M., 2005, Mechanical graphite transport in fault zones and the formation of graphite veins: Mineralogical Magazine, v. 69, no. 4, p. 463–470, doi: 10.1180/0026461056940266.

Cuesta, A., Dhamelincourt, P., Laureyns, J., Martínez-Alonso, A., and Tascón, J.M.D., 1994, Raman microprobe studies on carbon materials: Carbon, v. 32, no. 8, p. 1523–1532, doi: 10.1016/0008-6223(94)90148-1.

Dalla Torre, M., Ferreiro Mahlmann, R., and Ernst, W.G., 1997, Experimental study on the pressure dependence of vitrinite maturation: Geochimica et Cosmochimica Acta, v. 61, no. 14, p. 2921–2928.

Deldicque, D., Rouzaud, J.-N., and Velde, B., 2016, A Raman e HRTEM study of the carbonization of wood: A new Raman-based paleothermometer dedicated to archaeometry: Carbon, v. 102, p. 319–329, doi: 10.1016/j.carbon.2016.02.042.

Deurbergue, A., Oberlin, A., Oh, J.H., and Rouzaud, J.N., 1987, Graphitization of Korean anthracites as studied by transmission electron microscopy and X-ray diffraction: International Journal of Coal Geology, v. 8, no. 4, p. 375–393, doi: http://dx.doi.org/10.1016/0166-5162(87)90074-7.

Di Blasi, C., 2008, Modeling chemical and physical processes of wood and biomass pyrolysis: Progress in Energy and Combustion Science, v. 34, no. 1, p. 47–90, doi: 10.1016/j.pecs.2006.12.001.

Di Blasi, C., and Branca, C., 2001, Kinetics of Primary Product Formation from Wood Pyrolysis: Industrial & Engineering Chemistry Research, v. 40, no. 23, p. 5547–5556, doi: 10.1021/ie000997e.

Di Toro, G., and Pennacchioni, G., 2004, Superheated friction-induced melts in zoned pseudotachylytes within the Adamello tonalites (Italian Southern Alps): Journal of Structural Geology, v. 26, no. 10, p. 1783–1801, doi: 10.1016/j.jsg.2004.03.001.

Di Toro, G., Pennacchioni, G., and Nielsen, S., 2009, Pseudotachylytes and Earthquake Source Mechanics, *in* Fault-Zone Properties and Earthquake Rupture Dynamics, Elsevier Inc., p. 87–133.

Diebold, J., 1985, The cracking kinetics of depolymerized biomass vapors in a continuous, tubular reactor: Colorado School of Mines, Golden.

Diessel, C.F.K., Brothers, R.N., and Black, P.M., 1978, Coalification and graphitization in high-pressure schists in New Caledonia: Contributions to Mineralogy and Petrology, v. 68, no. 1, p. 63–78, doi: 10.1007/BF00375447.

Dippel, B., and Heintzenberg, J., 1999, Soot characterization in atmospheric particles from different sources by NIR FT Raman spectroscopy: Journal of Aerosol Science, v. 30, p. S907–S908, doi: 10.1016/S0021-8502(99)80464-9.

DiTullio, L., and Hada, S., 1993, Regional and local variations in the thermal history of the Shimanto Belt, southwest Japan: Geological Society of America Special Papers, v. 273, p. 103–114, doi: 10.1130/SPE273-p103.

Duke, E.F., and Rumble, D., 1986, Textural and isotopic variations in graphite from plutonic rocks, South-Central New Hampshire: Contributions to Mineralogy and Petrology, v. 93, no. 4, p. 409–419, doi: 10.1007/BF00371711.

Durand, B., 1980, Sedimentary organic matter and kergen. Difinition and quantitative imprtance of kerogen (B. Durand, Ed.): Techniq, Paris.

Durand, B., and Nicaise, G., 1980, Kerogen Insolbule organic matter from sedimentary rokcs (B. Durand, Ed.): Techniq, Paris.

Eggins, S.M., Woodhead, J.D., Kinsley, L.P.J., Mortimer, G.E., Sylvester, P., McCulloch, M.T., Hergt, J.M., and Handler, M.R., 1997, A simple method for the precise determination of ≥ 40 trace elements in geological samples by ICPMS using enriched isotope internal standardisation: Chemical Geology, v. 134, no. 4, p. 311–326, doi: http://dx.doi.org/10.1016/S0009-2541(96)00100-3.

Eklund, O., and Shebanov, A.D.D., 1999, The origin of rapakivi texture by sub-isothermal decomporession: Precanbrian Research, v. 95, p. 129–146.

El-Genk, M.S., and Tournier, J.-M.P., 2011, Development and validation of a model for the chemical kinetics of graphite oxidation: Journal of Nuclear Materials, v. 411, no. 1–3, p. 193–207, doi: 10.1016/j.jnucmat.2011.01.129.

Ernst, W.G., and Mählmann, R.F., 2004, Vitrinite alteration rate as a function of temperature, time, starting material, aqueous fluid pressure and oxygen fugacity—Laboratory corroboration of prior work, *in* Ronald J. Hill Zeev Aizenshtat, Mary Jo Baedecker, George Claypool, Robert Eganhouse, Martin Goldhaber and Kenneth Peters. The Geochemical Society Special Publications, J.L. ed., Geochemical Investigations in Earth and Space Science: A Tribute to Isaac R. Kaplan, Elsevier, p. 341–357.

Escartín, J., Andreani, M., Hirth, G., and Evans, B., 2008, Relationships between the microstructural evolution and the rheology of talc at elevated pressures and temperatures: Earth and Planetary Science Letters, v. 268, no. 3–4, p. 463–475, doi: 10.1016/j.epsl.2008.02.004.

Famin, V., Nakashima, S., Boullier, A.-M., Fujimoto, K., and Hirono, T., 2008, Earthquakes produce carbon dioxide in crustal faults: Earth and Planetary Science Letters, v. 265, no. 3–4, p. 487–497, doi: 10.1016/j.epsl.2007.10.041.

Feng, B., Bhatia, S.K., and Barry, J.C., 2002, Structural ordering of coal char during heat treatment and its impact on reactivity: Carbon, v. 40, no. 4, p. 481–496, doi: 10.1016/S0008-6223(01)00137-3.

Ferrari, A.C., Kleinsorge, B., Morrison, N.A., Hart, A., Stolojan, V., and Robertson, J., 1999, Stress reduction and bond stability during thermal annealing of tetrahedral amorphous carbon: Journal of Applied Physics, v. 85, no. 10, p. 7191, doi: 10.1063/1.370531.

Ferrari, A.C., and Robertson, J., 2000, Interpretation of Raman spectra of disordered and amorphous carbon: Physical Review B, v. 61, no. 20, p. 14095–14107, doi: 10.1103/PhysRevB.61.14095.

Fischbach, D.B., 1963, Kinetics of graphitization of a petroleum coke.: Nature, v. 200, no. 4913, p. 1281–1283, doi: 10.1038/2001281a0.

Fischbach, D.B., 1971, The Chemistry and Physics of Carbon: Marcel Dekker, New York.

Font, R., Marcilla, A., Verdu, E., and Devesa, J., 1990, Kinetics of the pyrolysis of almond shells and almond shells impregnated with cobalt dichloride in a fluidized bed reactor and in a pyroprobe 100: Industrial & Engineering Chemistry Research, v. 29, no. 9, p. 1846–1855, doi: 10.1021/ie00105a016.

Francisco, P.C.M., Sato, T., Otake, T., and Kasama, T., 2016, Kinetics of Fe 3+ mineral crystallization from ferrihydrite in the presence of Si at alkaline conditions and implications for nuclear waste disposal: American Mineralogist, v. 101, no. 9, p. 2057–2069, doi: 10.2138/am-2016-5589.

Franklin, R., 1950, The interpretation of diffuse X-ray diagrams of carbon: Acta Crystallographica, v. 3, no. 2, p. 107–121.

Freeman, J.J., Wang, A., Kuebler, K.E., Jolliff, B.L., and Haskin, L.A., 2008, Characterization of natural feldspars by raman spectroscopy for future planetary exploration: Canadian Mineralogist, v. 46, no. 6, p. 1477–1500, doi: 10.3749/canmin.46.6.1477.

Freise, E.J., and Kelly, A., 1963, The deformation of graphite crystals and the production of the rhombohedral form: Philosophical Magazine, v. 8, no. 93, p. 1519–1533, doi: 10.1080/14786436308207315.

Froese, E., and Gunter, A.E., 1976, A note on the pyrrhotite-sulfur vapor equilibrium: Economic Geology, v. 71, no. 8, p. 1589–1594, doi: 10.2113/gsecongeo.71.8.1589.

Fujimoto, H., 2003, Theoretical X-ray scattering intensity of carbons with turbostratic stacking and AB stacking structures: Carbon, v. 41, no. 8, p. 1585–1592, doi: 10.1016/S0008-6223(03)00116-7.

Ghiorso, M.S., and Sack, R.O., 1995, Chemical mass transfer in magmatic processes IV. A revised and internally consistent thermodynamic model for the interpolation and extrapolation of liquid-solid equilibria in magmatic systems at elevated temperatures and pressures: Contributions to Mineralogy and Petrology, v. 119, no. 2, p. 197–212, doi: 10.1007/BF00307281.

Gillis, P.P., 1984, Calculating the elastic constants of graphite: Carbon, v. 22, no. 4–5, p. 387–391, doi: http://dx.doi.org/10.1016/0008-6223(84)90010-1.

Graham, R.G., Bergougnou, M.A., and Freel, B.A., 1994, The kinetics of vapour-phase cellulose fast pyrolysis reactions: Biomass and Bioenergy, v. 7, no. 1, p. 33–47, doi: http://dx.doi.org/10.1016/0961-9534(94)00045-U.

Grew, E.S., 1974, Carbonaceous Material in Some Metamorphic Rocks of New England and Other Areas: The Journal of Geology, v. 82, no. 1, p. 50–73.

Guo, Y., and Bustin, R.M., 1998, FTIR spectroscopy and reflectance of modern charcoals and fungal decayed woods: implications for studies of inertinite in coals:

International Journal of Coal Geology, v. 37, no. 1–2, p. 29–53, doi: 10.1016/S0166-5162(98)00019-6.

Hadizadeh, J., Mittempergher, S., Gratier, J.P., Renard, F., Di Toro, G., Richard, J., and Babaie, H.A., 2012, A microstructural study of fault rocks from the SAFOD: Implications for the deformation mechanisms and strength of the creeping segment of the San Andreas Fault: Journal of Structural Geology, v. 42, p. 246–260, doi: 10.1016/j.jsg.2012.04.011.

Hanfland, M., Beister, H., and Syassen, K., 1989, Graphite under pressure: Equation of state and first-order Raman modes: Physical Review B, v. 39, no. 17, p. 12598–12603, doi: 10.1103/PhysRevB.39.12598.

Hara, H., 2003, New proposal of standard specimens for illite crystallinity measurement: its usefulness as paleo-geothermal indicator: Bulletin of the geological survey of Japan, v. 54, p. 239–250.

Hara, H., and Kurihara, T., 2010, Tectonophysics Tectonic evolution of low-grade metamorphosed rocks of the Cretaceous Shimanto accretionary complex, Central Japan: Tectonophysics, v. 485, no. 1–4, p. 52–61, doi: 10.1016/j.tecto.2009.11.017.

Hilchie, L.J., and Jamieson, R.A., 2014, Graphite thermometry in a low-pressure contact aureole, Halifax, Nova Scotia: Lithos, v. 208–209, p. 21–33, doi: 10.1016/j.lithos.2014.08.015.

Hoefs, J., and Frey, M., 1976, The isotopic composition of carbonaceous matter in a metamorphic profile from the Swiss Alps: Geochimica et Cosmochimica Acta, v. 40, no. 8, p. 945–951, doi: http://dx.doi.org/10.1016/0016-7037(76)90143-5.

Holland, T.J.B., and Powell, R., 2011, An improved and extended internally consistent thermodynamic dataset for phases of petrological interest, involving a new equation of state for solids: Journal of Metamorphic Geology, v. 29, no. 3, p. 333–383, doi: 10.1111/j.1525-1314.2010.00923.x.

Hood, A., Gutjahr, C.C.M., and Heacock, R.L., 1975, Organic Metamorphism and the Generation of Petroleum: AAPG Bulletin, v. 59, no. 6, p. 986–996.

House, J.E., 2007, Principle of Chemical kinetics: Elsevier.

Hower, J.C., and Gayer, R.A., 2002, Mechanisms of coal metamorphism: Case studies from Paleozoic coalfields: International Journal of Coal Geology, v. 50, no. 1–4, p. 215–245, doi: 10.1016/S0166-5162(02)00119-2.

Huang, J.Y., Yasuda, H., and Mori, H., 1999, Highly curved carbon nanostructures produced by ball-milling: Chemical Physics Letters, v. 303, no. 1–2, p. 130–134, doi: 10.1016/S0009-2614(99)00131-1.

Ibarra, J. V., Muñoz, E., and Moliner, R., 1996, FTIR study of the evolution of coal structure during the coalification process, *in* Organic Geochemistry, p. 725–735.

Iijima, S., 1991, Helical microtubules of graphitic carbon: Nature, v. 354, p. 56–58, doi: 10.1038/350055a0.

Inagaki, M., 1996, Carbon materials Structure, texture and intercalation: Solid State Ionics, v. 86–88, no. PART 2, p. 833–839, doi: 10.1016/0167-2738(96)00337-2.

Inagaki, M., and Meyer, R.A., 1999, Stress graphitization, *in* Chemistry and Physics of Carbon, p. 149–243.

Inagaki, M., Mugishima, H., and Hosokawa, K., 1973, Structural change of graphite with grinding: Tanso, v. 74, p. 76–82.

Inagaki, M., Murase, Y., and Noda, T., 1968, Effect of Pre-Heat-Treatment on Kinetics of Graphitization: Journal of the Ceramic Association, Japan, v. 76, no. 874, p. 184–189, doi: 10.2109/jcersj1950.76.874_184.

Itaya, T., Tomuro, M., and Ninagawa, K., 1997, Asymmetric X-ray diffraction peak of metamorphosed carbonaceous material: The Island Arc, v. 6, p. 228–232.

Itaya, T., 1981, Carbonaceous material in pelitic schists of the Sanbagawa metamorphic belt in central Shikoku, Japan: Lithos, v. 14, no. 3, p. 215–224, doi: 10.1016/0024-4937(81)90043-8.

Irifune, T., Kurio, A., Sakamoto, S., and Sumiya, H., 2003, Ultrahard polycrystalline diamond from graphite: Nature, v. 421, no. 6 February 2003, p. 599–600, doi: 10.1038/421599b.

Iwashita, N., Park, C.R., Fujimoto, H., Shiraishi, M., and Inagaki, M., 2004, Specification for a standard procedure of X-ray diffraction measurements on carbon materials: Carbon, v. 42, no. 4, p. 701–714, doi: 10.1016/j.carbon.2004.02.008.

Johnson, J.W., Oelkers, E.H., and Helgeson, H.C., 1992, SUPCRT92: A software package for calculating the standard molal thermodynamic properties of minerals, gases, aqueous species, and reactions from 1 to 5000 bar and 0 to 1000°C: Computers & Geosciences, v. 18, no. 7, p. 899–947, doi: http://dx.doi.org/10.1016/0098-3004(92)90029-Q.

Jones, W.E., Carey, L.R., and Swaddle, T.W., 1972, Mechanistic Information on the Aquations of Complexes of the Pentaamminecobalt (III) Series from Kinetic Studies at High Pressures: Canadian Journal of Chemistry, v. 50, no. 17, p. 2739–2746.

Kamiya, K., Inagaki, M., Saito, H., and Noda, T., 1970, Effect of Pressure on Graphitization of Carbon. VII. Effect of Preheat treatment on graphitization of carbon under High pressure: Bullitin of the chelical society of Japan, v. 43, p. 926–930.

Kaneki, S., Hirono, T., Mukoyoshi, H., Sample, Y., and Ikehara, M., 2016, Organochemical characterisitics of carbonaceous materials as indicators of heat recorded on an ancient plate-subduction fault: Geochemistry, Geophysics, Geosystems, v. 17, no. 7, p. 2855–2868, doi: 10.1016/j.epsl.2016.09.038.

Kanter, M.A., 1957, Diffusion of Carbon Atoms in Natural Graphite Crystals: Physical Review, v. 107, no. 3, p. 655–663, doi: 10.1103/PhysRev.107.655.

Kaxiras, E., and Pandey, K., 1988, Energetics of defects and diffusion mechanisms in graphite: Physical Review Letters, v. 61, no. 23, p. 2693–2696, doi: 10.1103/PhysRevLett.61.2693.

Kebukawa, Y., Nakajima, S., and Zolensky, M.E., 2010, Kinetics of organic matter degradation in the Murchison meteorite for the evaluation of parent-body temperature history: Meteoritics & Planetary Science, v. 45, no. 1, p. 99–113, doi: 10.1111/j.1945-5100.2009.01008.x.

Kelires, P.C., 2000, Intrinsic stress and local rigidity in tetrahedral amorphous carbon: Physical Review B - Condensed Matter and Materials Physics, v. 62, no. 23, p. 15686–15694, doi: 10.1103/PhysRevB.62.15686.

Kelires, P.C., 1994, Elastic properties of amorphous carbon networks: Physical Review Letters, v. 73, no. 18, p. 2460–2463, doi: 10.1103/PhysRevLett.73.2460.

Khawam, A., and Flanagan, D.R., 2006, Solid-State Kinetic Models: Basics and Mathematical Fundamentals: The Journal of Physical Chemistry B, v. 110, no. 35, p. 17315–17328, doi: 10.1021/jp062746a.

Kirkpatrick, J.D., and Rowe, C.D., 2013, Disappearing ink: How pseudotachylytes are lost from the rock record: Journal of Structural Geology, v. 52, p. 183–198, doi: 10.1016/j.jsg.2013.03.003.

Kimura, G., Hamahashi, M., Okamoto, S., Yamaguchi, A., Kameda, J., Raimbourg, H., Hamada, Y., Yamaguchi, H., and Shibata, T., 2013, Hanging wall deformation of a seismogenic megasplay fault in an accretionary prism: The nobeoka thrust in southwestern japan: Journal of Structural Geology, v. 52, no. 1, p. 136–147, doi: 10.1016/j.jsg.2013.03.015.

Kita, I., Matsuo, S., and Wakita, H., 1982, H_2 generation by reaction between H_2O and crushed rock: an experimental study on H_2 degassing from the active fault zone: Journal of Geophysical Research: Solid Earth, v. 87, p. 10789–10795, doi: 10.1029/JB087iB13p10789.

Kitamura, M., Mukoyoshi, H., Fulton, P.M., and Hirose, T., 2012, Coal maturation by frictional heat during rapid fault slip: Geophysical Research Letters, v. 39, no. 16, p. 1–3, doi: 10.1029/2012GL052316.

Knight, J.A., Gorton, C.W., and Kovac, R.J., 1984, Oil production by entrained flow pyrolysis of biomass: Biomass, v. 6, no. 1, p. 69–76, doi: http://dx.doi.org/10.1016/0144-4565(84)90009-X.

Kogure, T., and Kameda, J., 2008, High-resolution TEM and XRD simulation of stacking disorder in 2:1 phyllosilicates: Zeitschrift für Kristallographie - Crystalline Materials, v. 223, p. 69, doi: 10.1524/zkri.2008.0004.

Komatsu, M., Osanai, Y. Toyoshima, T. Miyashita, S., 1989, Evolution of the Hidaka metamorphic belt, northern Japan, in Evolution of Metamorphic Belts, edited by J. S. Daly, R. A. Cliff, and B.W. Yardley: Geological Society Special Publication, p. 487–493.

Komatsu, M., Miyashita, S., Maeda, J., Osanai, Y., and Toyoshima, T., 1983, Disclosing of a deepest section of continental type crust up-thrust as the final event of collision of arcs in Hokkaido, north Japan (M. and U. S. Hashimoto, Ed.): TERRA-PUB, Tokyo.

Kondo, H., Kimura, G., Masago, H., Ohmori-Ikehara, K., Kitamura, Y., Ikesawa, E., Sakaguchi, A., Yamaguchi, A., and Okamoto, S., 2005, Deformation and fluid flow of a major out-of-sequence thrust located at seismogenic depth in an accretionary complex: Nobeoka Thrust in the Shimanto Belt, Kyushu, Japan: Tectonics, v. 24, no. 6, p. 1–16, doi: 10.1029/2004TC001655.

Kontani, Y., 1978, Geological study of the Hidaka Supergroup distributed on the east side of the Hidaka metamorphic belt: Journal of Geological Society of Japan, v. 84, no. 1, p. 1–14.

Kouketsu, Y., Mizukami, T., Mori, H., Endo, S., Aoya, M., Hara, H., Nakamura, D., and Wallis, S., 2014, A new approach to develop the Raman carbonaceous material geothermometer for low-grade metamorphism using peak width: Island Arc, doi: 10.1111/iar.12057.

Kretz, R., 1996, Graphite deformation in marble and mylonitic marble, Grenville Province, Canadian Shield: Journal of Metamorphic Geology, v. 14, p. 399–412.

Kříbek, B., Sýkorová, I., Machovič, V., and Laufek, F., 2008, Graphitization of organic matter and fluid-deposited graphite in Palaeoproterozoic (Birimian) black shales of the Kaya-Goren greenstone belt (Burkina Faso, West Africa): Journal of Metamorphic Geology, v. 26, no. 9, p. 937–958, doi: 10.1111/j.1525-1314.2008.00796.x.

Kroto, H.W., Allaf, A.W., and Balm, S.P., 1991, C60: Buckminsterfullerene: Chemical Reviews, v. 91, no. 14, p. 1213–1235, doi: 10.1017/CBO9781107415324.004.

Lahfid, A., Beyssac, O., Deville, E., Negro, F., Chopin, C., and Goffé, B., 2010, Evolution of the Raman spectrum of carbonaceous material in low-grade metasediments of the Glarus Alps (Switzerland): Terra Nova, v. 22, no. 5, p. 354–360, doi: 10.1111/j.1365-3121.2010.00956.x.

Landais, P., Rochdi, A., Largeau, C., and Derenne, S., 1993, Chemical characterization of torbanites by transmission micro-FTIR spectroscopy: Origin and extent of compositional heterogeneities: Geochimica et Cosmochimica Acta, v. 57, no. 11, p. 2529–2539, doi: http://dx.doi.org/10.1016/0016-7037(93)90415-S.

Landis, C.A., 1971, Graphitization of dispersed carbonaceous material in metamorphic rocks: Contributions to Mineralogy and Petrology, v. 30, no. 1, p. 34–45, doi: 10.1007/BF00373366.

Large, D.J., Christy, A.G., and Fallick, A.E., 1994, Poorly crystalline carbonaceous matter in high grade metasediments: implications for graphitisation and metamorphic fluid compositions: Contributions to Mineralogy and Petrology, v. 116, no. 1–2, p. 108–116, doi: 10.1007/BF00310693.

Larsen, J.W., Pan, C.S., and Shawver, S., 1989, Effect of demineralization on the macromolecular structure of coals: Energy & Fuels, v. 3, no. 5, p. 557–561, doi: 10.1021/ef00017a004.

Larter, S., 1988, Some pragmatic perspectives in source rock geochemistry: Marine and Petroleum Geology, v. 5, no. 3, p. 194–204, doi: http://dx.doi.org/10.1016/0264-8172(88)90001-3.

Laughland, M.M., and Underwood, M.B., 1993, Vitrinite reflectance and estimates of paleotemperature within the Upper Shimanto Group, Muroto Peninsula, Shikoku, Japan: Geological Society of America Special Papers, v. 273, p. 25–44, doi: 10.1130/SPE273-p25.

Lazzeri, M., and Barreiro, A., 2014, Carbon-Based Nanoscience: Elements, v. 10, no. 6, p. 447 LP-452.

Le Bayon, R., Adam, C., and Ferreiro Mählmann, R., 2012, Experimentally determined pressure effect on vitrinite reflectance at 450°C: International Journal of Coal Geology, v. 92, p. 69–81, doi: 10.1016/j.coal.2011.12.007.

Lédé, J., 2000, The Cyclone: A Multifunctional Reactor for the Fast Pyrolysis of Biomass: Industrial & Engineering Chemistry Research, v. 39, no. 4, p. 893–903, doi: 10.1021/ie990623p.

Lespade, P., Al-Jishi, R., and Dresselhaus, M.S., 1982, Model for Raman scattering from incompletely graphitized carbons: Carbon, v. 20, no. 5, p. 427–431, doi: http://dx.doi.org/10.1016/0008-6223(82)90043-4.

Lewan, M.D., 1997, Experiments on the role of water in petroleum formation: Geochimica et Cosmochimica Acta, v. 61, no. 17, p. 3691–3723, doi: http://dx.doi.org/10.1016/S0016-7037(97)00176-2.

Lewicki, J.L., and Brantley, S.L., 2000, CO_2 degassing along the San andreas fault, Parkfield, California: Geophysical Research Letters, v. 27, no. 1, p. 5–8.

Li, W., Zhu, Y., Chen, S., and Zhou, Y., 2013, Research on the structural characteristics of vitrinite in different coal ranks: Fuel, v. 107, p. 647–652, doi: 10.1016/j.fuel.2012.10.050.

Li, Z.Q., Lu, C.J., Xia, Z.P., Zhou, Y., and Luo, Z., 2007, X-ray diffraction patterns of graphite and turbostratic carbon: Carbon, v. 45, no. 8, p. 1686–1695, doi: 10.1016/j.carbon.2007.03.038.

Lin, A., 1994, Microlite Morphology and Chemistry in Pseudotachylite, from the Fuyun Fault Zone, China: The Journal of Geology, v. 102, no. 3, p. 317–329.

Lin, Q., Li, T., Liu, Z., Song, Y., He, L., Hu, Z., Guo, Q., and Ye, H., 2012, High-resolution TEM observations of isolated rhombohedral crystallites in graphite blocks: Carbon, v. 50, no. 6, p. 2369–2371, doi: 10.1016/j.carbon.2012.01.054.

Lockner, D.A., Morrow, C., Moore, D., and Hickman, S., 2011, Low strength of deep San Andreas fault gouge from SAFOD core: Nature, v. 472, no. 7341, p. 82–85.

Loh, G.C., and Baillargeat, D., 2013, Graphitization of amorphous carbon and its transformation pathways: Journal of Applied Physics, v. 114, no. 3, doi: 10.1063/1.4816313.

Lopatin, N.V., 1971, Time and temperature as factor in colification: Izvestia Akademiya Nouk USSR: Serya Geologickeskya, v. 3, p. 95–106.

Lowitzer, S., Winkler, B., and Tucker, M., 2006, Thermoelastic behavior of graphite from in situ high-pressure high-temperature neutron diffraction: Physical Review B - Condensed Matter and Materials Physics, v. 73, no. 21, p. 1–8, doi: 10.1103/PhysRevB.73.214115.

Lu, L., Sahajwalla, V., Kong, C., and Harris, D., 2001, Quantitative X-ray diffraction analysis and its application to various coals: Carbon, v. 39, no. 12, p. 1821–1833, doi: 10.1016/S0008-6223(00)00318-3.

Luque, F.J., Pasteris, J.D., Wopenka, B., Rodas, M., and Barrenechea, J.F., 1998, Natural fluid deposited grapihte: Mineralogical characteristics and mechanism of formation: American Journal of Science, v. 298, p. 471–498.

Luque, J., Tsuchiya, N., Crespo, E., Wada, H., and Fernández, J., 2014, Graphite mineralization in the Oshirabetsu Gabbroic Complex (Hokkaido, Japan): , no. 3, p. 12–13.

Lynch, R.W., and Drickamer, H.G., 1966, Effect of High Pressure on the Lattice Parameters of Diamond, Graphite, and Hexagonal Boron Nitride: The Journal of Chemical Physics, v. 44, no. 1, p. 181–184, doi: 10.1063/1.1726442.

Ma, T.-B., Hu, Y.-Z., and Wang, H., 2009, Molecular dynamics simulation of shear-induced graphitization of amorphous carbon films: Carbon, v. 47, no. 8, p. 1953–1957, doi: 10.1016/j.carbon.2009.03.040.

Maddock, R.H., 1983, Melt origin of fault-generated pseudotachylytes demonstrated by textures: Geology, v. 11, no. 2, p. 105–108, doi: 10.1130/0091-7613(1983)11<105:MOOFPD>2.0.CO;2.

Maddock, R.H., 1992, Effects of lithology, cataclasis and melting on the composition of fault-generated pseudotachylytes in Lewisian gneiss, Scotland: Tectonophysics, v. 204, no. 3–4, p. 261–278, doi: http://dx.doi.org/10.1016/0040-1951(92)90311-S.

Magloughlin, J.F., 1992, Microstructural and chemical changes associated with cataclasis and frictional melting at shallow crustal levels: the cataclasite-pseudotachylyte connection: Tectonophysics.

Magloughlin, J.F., 2005, Immiscible sulfide droplets in pseudotachylyte: Evidence for high temperature (>1200 °C) melts: Tectonophysics, v. 402, no. 1–4, p. 81–91, doi: 10.1016/j.tecto.2004.11.011.

Mahar, E.M., Baker, J.M., Powell, R., Holland, T.J.B., and Howell, N., 1997, The effect of Mn on mineral stability in metapelites: Journal of Metamorphic Geology, v. 15, no. 2, p. 223–238, doi: 10.1111/j.1525-1314.1997.00011.x.

Mao, W.L., 2003, Bonding Changes in Compressed Superhard Graphite: Science, v. 302, no. 5644, p. 425–427, doi: 10.1126/science.1089713.

Mariani, E., Brodie, K.H., and Rutter, E.H., 2006, Experimental deformation of muscovite shear zones at high temperatures under hydrothermal conditions and the strength of phyllosilicate-bearing faults in nature: Journal of Structural Geology, v. 28, no. 9, p. 1569–1587, doi: 10.1016/j.jsg.2006.06.009.

Marone, C., Vidale, J.E., and Ellsworth, W.L., 1995, Fault healing inferred from time dependent variations in source properties of repeating earthquakes: Geophysical Research Letters, v. 22, no. 22, p. 3095–3098, doi: 10.1029/95GL03076.

Marsh, H., Crawford, D., and Taylor, D.W., 1983, Catalytic graphitization by iron of isotropic carbon from polyfurfuryl alcohol, 725–1090 K. A high-resolution electron microscope study: Carbon, v. 21, no. 1, p. 81–87, doi: 10.1016/0008-6223(83)90160-4.

Matsubara, K., Sugihara, K., and Tsuzuku, T., 1990, Electrical resistance in the c direction of graphite: Physical Review B, v. 41, no. 2, p. 969–974, doi: 10.1103/PhysRevB.41.969.

Middleton, M.F., 1982, Tectonic history from vitrinite reflectance: Geophysical Journal International, v. 68, p. 121–132.

Miller, E.D., Nesting, D.C., and Badding, J. V., 1997, Quenchable Transparent Phase of Carbon: Chemistry of Materials, v. 9, no. 14, p. 18–22, doi: 10.1021/cm960288k.

Miller, S. a, Collettini, C., Chiaraluce, L., Cocco, M., Barchi, M., and Kaus, B.J.P., 2004, Aftershocks driven by a high-pressure CO2 source at depth.: Nature, v. 427, no. 6976, p. 724–727, doi: 10.1038/nature02251.

Miyashiro, A., 1994, Metamorphic Petrology: Oxford University Press.

Moecher, D.P., and Steltenpohl, M.G., 2009, Direct calculation of rupture depth for an exhumed paleoseismogenic fault from mylonitic pseudotachylyte: Geology, v. 37, no. 11, p. 999–1002, doi: 10.1130/G30166A.1.

Moecher, D.P., and Brearley, A.J., 2004, Mineralogy and petrology of a mullite-bearing pseudotachylyte: Constraints on the temperature of coseismic frictional fusion: American Mineralogist.

Monthioux, M., Landais, P., and Durand, B., 1986, Comparison between extracts from natural and artificial maturation series of Mahakam delta coals: Organic Geochemistry, v. 10, no. 1, p. 299–311, doi: http://dx.doi.org/10.1016/0146-6380(86)90031-8.

Moore, D.E., and Lockner, D.A., 2004, Crystallographic controls on the frictional behavior of dry and water-saturated sheet structure minerals: Journal of Geophysical Research, v. 109, p. B03401.

Morf, P., Hasler, P., and Nussbaumer, T., 2002, Mechanisms and kinetics of homogeneous secondary reactions of tar from continuous pyrolysis of wood chips: Fuel, v. 81, no. 7, p. 843–853, doi: 10.1016/S0016-2361(01)00216-2.

Mori, H., Mori, N., Wallis, S., Westaway, R., and Annen, C., 2016, The importance of heating duration for Raman CM thermometry: evidence from contact metamorphism around the Great Whin Sill intrusion, UK: Journal of Metamorphic Geology, p. n/a-n/a, doi: 10.1111/jmg.12225.

Mori, H., Wallis, S., Fujimoto, K., and Shigematsu, N., 2015, Recognition of shear heating on a long-lived major fault using Raman carbonaceous material thermometry: Implications for strength and displacement history of the MTL, SW Japan: Island Arc, v. 24, no. 4, p. 425–446, doi: 10.1111/iar.12129.

Mori, K., and Taguchi, K., 1988, Examination of the low-grade metamorphism in the Shimanto Belt by vitrinite reflectance: Modern Geology.

Morikiyo, T., 1986, Hydrogen and carbon isotope studies on the graphite-bearing metapelites in the northern Kiso district of central Japan: Contributions to Mineralogy and Petrology, v. 94, no. 2, p. 165–177, doi: 10.1007/BF00592933.

Morrow, C. a., Moore, D.E., and Lockner, D. a., 2000, The effect of mineral bond strength and adsorbed water on fault gouge frictional strength: Geophysical Research Letters, v. 27, no. 6, p. 815–818, doi: 10.1029/1999GL008401.

Muirhead, D.K., Parnell, J., Taylor, C., and Bowden, S.A., 2012, A kinetic model for the thermal evolution of sedimentary and meteoritic organic carbon using Raman spectroscopy: Journal of Analytical and Applied Pyrolysis, v. 96, p. 153–161, doi: 10.1016/j.jaap.2012.03.017.

Mukoyoshi, H., Hara, H., and Ikehara, K., 2007, Quantitative estimation of temperature conditions for illite crystallinity: comparision to vitrinite reflectance form Chichibu and Shimanto accretionary complexes, eastern Kyushu, Southwest Japan: Bullitin of Geological Survey of Japan, v. 58, p. 23–31.

Mukoyoshi, H., Sakaguchi, a, Otsuki, K., Hirono, T., and Soh, W., 2006, Co-seismic frictional melting along an out-of-sequence thrust in the Shimanto accretionary complex. Implications on the tsunamigenic potential of splay faults in modern subduction zones: Earth and Planetary Science Letters, v. 245, no. 1–2, p. 330–343, doi: 10.1016/j.epsl.2006.02.039.

Murty, H.N., Biederman, D.L., and Heintz, E.A., 1969, Kinetics of graphitization-I. Activation energies: Carbon, v. 7, no. 6, p. 667–681, doi: http://dx.doi.org/10.1016/0008-6223(69)90522-3.

Nakamura, D., 1995, Comparison and interpretation of graphitization in contact and regional metamorphic rocks: The Island Arc, v. 4, p. 112–127.

Nakamura, Y., and Akai, J., 2013, Microstructural evolution of carbonaceus material during graphitization in the Gyoja-yama contact aureole: HRTEM, XRD, Raman

spectroscopic study: Journal of Mineralogical and Petrological Sciences, v. 108, p. 131–143.

Nakamura, Y., Oohashi, K., Toyoshima, T., Satish-Kumar, M., and Akai, J., 2015, Strain-induced amorphization of graphite in fault zones of the Hidaka metamorphic belt, Hokkaido, Japan: Journal of Structural Geology, v. 72, p. 142–161, doi: 10.1016/j.jsg.2014.10.012.

Nakamura, Y., Yoshino, T., and Satish-Kumar, M., 2017, An experimental kinetic study on the structural evolution of natural carbonaceous material to graphite: v. 102, p. 135–148.

Nanayama, F., 1992, Stratigraphy and facies of the Paleocene Nakanogawa Group in the southern part of central Hokkaido, Japan: Journal of the Geological Society of Japan, v. 92, no. 11, p. 1041–1059.

Nanayama, F., and Ganzawa, Y., 1997, Sedimentary stratigraphy, environment and age of the northern unit of Nakanogawa Group in the Hidaka belt, central Hokkaido, Japan: The memoirs of the geological society of japan, v. 47, p. 279–293.

Nemanich, R.J., and Solin, S.A., 1977, Observation of an anomolously sharp feature in the 2nd order Raman spectrum of graphite: Solid State Communications, v. 23, no. 7, p. 417–420, doi: http://dx.doi.org/10.1016/0038-1098(77)90998-X.

Niwase, K., 1995, Irradiation-induced amorphization of graphite: Physical Review B, v. 52, no. 22, p. 15785–15798.

Noda, T., Inagaki, M., and Sekiya, T., 1965, Kinetic studies of the graphitization process—I Effect of ambient gas phase on the rate of graphitization: Carbon, v. 3, no. 2, p. 175–180, doi: http://dx.doi.org/10.1016/0008-6223(65)90045-X.

Noda, T., and Kato, H., 1965, Heat treatment of carbon under high pressure: Carbon, v. 3, no. 3, p. 289–297, doi: http://dx.doi.org/10.1016/0008-6223(65)90063-1.

Noda, T., Kamiya, K., and Inagaki, M., 1968, Effect of Pressure on Graphitization of Carbon. I. Heat Treatment of Soft Carbon under 1,3 and 5 kbar: Bulletin of the Chemical Society of Japan, v. 41, no. 2, p. 485–492, doi: 10.1246/bcsj.41.485.

Noto, K., and Tsuzuku, T., 1973, On the pressure dependence of Electrical Conductivity of Graphite: Journal of the Physical Society of Japan, v. 35, no. 6, p. 1649–1653, doi: 10.1209/epl/i2006-10401-5.

Oberlin, A., 1984, Carbonization and Graphitization: Carbon.

Oberlin, A., Bonnamy, S., and Oshida, K., 2006, Landmarks for graphitization: TANSO, v. 2006, no. 224, p. 281–298, doi: 10.7209/tanso.2006.281.

Oberlin, A., Bonnamy, S., and Rouxhet, P.G., 1999, Colloidal and supermolecular aspect of carbon:

O'Hara, K.D., and Sharp, Z.D., 2001, Chemical and oxygen isotope composition of natural and artificial pseudotachylyte: role of water during frictional fusion: Earth and Planetary Science Letters, v. 184, p. 393–406.

O'Hara, K.D., and Huggins, F.E., 2005, AMo¨ssbauer study of pseudotachylytes: redox conditions during seismogenic faulting: Contributions to Mineralogy and Petrology, v. 148, p. 602–614.

Ohmori, K., Taira, A., Tokuyama, H., Sakaguchi, A., Okamura, M., and Aihara, A., 1997, Paleothermal structure of the Shimanto accretionary prism, Shikoku, Japan: Role of an out-of-sequence thrust: Geology, v. 25, no. 4, p. 327, doi: 10.1130/0091-7613(1997)025<0327:PSOTSA>2.3.CO;2.

Ohmoto, H., and Kerrick, D., 1977, Devolatilization equilibria in graphitic systems: American Journal of Science, v. 277, p. 1013–1044.

Okuyama-Kusunose, Y., and Itaya, T., 1987, Metamorphism of carbonaceous material in the Tono contact aureole, Kitakami Mountains, Japan: Journal of Metamorphic Geology, v. 5, no. 2, p. 121–139, doi: 10.1111/j.1525-1314.1987.tb00375.x.

Onodera, A., Irie, Y., Higashi, K., Umemura, J., and Takenaka, T., 1991, Graphitization of amorphous carbon at high pressures to 15 GPa: Journal of Applied Physics, v. 69, no. 4, p. 2611–2617, doi: 10.1063/1.348652.

Oohashi, K., Hirose, T., and Shimamoto, T., 2011, Shear-induced graphitization of carbonaceous materials during seismic fault motion: Experiments and possible implications for fault mechanics: Journal of Structural Geology, v. 33, no. 6, p. 1122–1134, doi: 10.1016/j.jsg.2011.01.007.

Oohashi, K., Hirose, T., and Shimamoto, T., 2013, Graphite as a lubricating agent in fault zone: An insight from low- to high-velocity friction experiments on a mixed graphite-quartz gouge: Journal of Geophysical Research, v. 118, p. 1–18, doi: 10.1002/jgrb.50175.

Osanai, Y., 1985, Geology and metamorphic zoning of the Main Zone of the Hidaka Metamorphic Belt in the Shizunai River region, Hokkaido: Journal of Geological Society of Japan, v. 91, no. 4, p. 259–278.

Osanai, Y., Komatsu, M., and Owada, M., 1991, Metamorphism and granite genesis in the Hidaka metamorphic belt, Hokkaido, Japan: Journal of Metamorphic Geology, v. 9, no. 111–124.

Osanai, Y., Owada, M., and Toyoshima, T., 2007, Metamorphic and deformation processes of lower crustal rocks in the Hidata collision zone, Hokkaido, northern Japan: The Journal of the Geological Society of Japan, v. 113, no. Supplement, p. 29–50.

Osanal, Y., Arita, K., and Bamba, M., 1986, *P-T* conditions of granulite-facies rocks from the Hidaka Metamorphic Belt, Hokkaido, Japan: journal of the geologial society of Japan, v. 92, no. 11, p. 793–808.

Papineau, D., De Gregorio, B.T., Stroud, R.M., Steele, A., Pecoits, E., Konhauser, K., Wang, J., and Fogel, M.L., 2010, Ancient graphite in the Eoarchean quartz-pyroxene rocks from Akilia in southern West Greenland II: Isotopic and chemical compositions and comparison with Paleoproterozoic banded iron formations: Geochimica et Cosmochimica Acta, v. 74, no. 20, p. 5884–5905, doi: 10.1016/j.gca.2010.07.002.

Pasteris, J.D., 1989, In situ analysis in geological thin-sections by laser Raman microprobe spectroscopy: A cautionary note: Applied Spectroscopy, v. 43, no. 3, p. 567–570, doi: 10.1366/0003702894202878.

Pattison, D., 2006, The fate of graphite in prograde metamorphism of pelites: An example from the Ballachulish aureole, Scotland: Lithos, v. 88, no. 1–4, p. 85–99, doi: 10.1016/j.lithos.2005.08.006.

Pattison, D.R.M., and Tracy, R.J., 1991, Phase equilibria and thermobarometry of metapelites: Reviews in Mineralogy and Geochemistry, v. 26, no. 1, p. 105 LP-206.

Petrik, I., Nabelek, P.I., Jana, M., and Plasienka, D., 2003, Conditions of Formation and Crystallization Kinetics of Highly Oxidized Pseudotachylytes from the High Tatras (Slovakia): Journal of Petrology, v. 44, no. 5.

Philpotts, A.R., 1964, Origin of pseudotachylites: American Journal of Science, v. 262, no. 8, p. 1008–1035, doi: 10.2475/ajs.262.8.1008.

Poulson, S., 1996, Equilibrium mineral-fluid stable isotope fractionation factors in graphitic metapelites: Chemical Geology, v. 131, p. 207–217, doi: 10.1016/0009-2541(95)00153-0.

Poulson, S.R., and Ohmoto, H., 1989, Devolatilization equilibria in graphite-pyrite-pyrrhotite bearing pelites with application to magma-pelite interaction. Contributions to Mineralogy and Petrology, v. 95, p. 418–425.

Price, L.C., 1983, GEOLOGIC TIME AS A PARAMETER IN ORGANIC METAMORPHISM AND VITRINITE REFLECTANCE AS AN ABSOLUTE PALEOGEOTHERMOMETER: Journal of Petroleum Geology, v. 6, no. 1, p. 5–37, doi: 10.1111/j.1747-5457.1983.tb00260.x.

Price, L.C., and DeWitt, E., 2001, Evidence and characteristics of hydrolytic disproportionation of organic matter during metasomatic processes: Geochimica et Cosmochimica Acta, v. 65, no. 21, p. 3791–3826, doi: 10.1016/S0016-7037(01)00762-1.

Putirka, K.D., 2008, Thermometers and Barometers for Volcanic Systems: Reviews in Mineralogy & Geochemistry, v. 69, p. 61–120.

Quirico, E., Montagnac, G., Rouzaud, J.N., Bonal, L., Bourot-Denise, M., Duber, S., and Reynard, B., 2009, Precursor and metamorphic condition effects on Raman spectra of poorly ordered carbonaceous matter in chondrites and coals: Earth and Planetary Science Letters, v. 287, no. 1–2, p. 185–193, doi: 10.1016/j.epsl.2009.07.041.

Quirico, E., Raynal, P.-I., and Bourot-Denise, M., 2003, Metamorphic grade of organic matter in six unequilibrated ordinary chondrites: Meteoritics & Planetary Science, v. 38, no. 5, p. 795–811, doi: 10.1111/j.1945-5100.2003.tb00043.x.

Quirico, E., Rouzaud, J.-N., Bonal, L., and Montagnac, G., 2005, Maturation grade of coals as revealed by Raman spectroscopy: Progress and problems: Spectrochimica Acta Part A, v. A61, p. 2368–2377.

Rahl, J., Anderson, K., Brandon, M., and Fassoulas, C., 2005, Raman spectroscopic carbonaceous material thermometry of low-grade metamorphic rocks: Calibration and application to tectonic exhumation in Crete, Greece: Earth and Planetary Science Letters, v. 240, no. 2, p. 339–354, doi: 10.1016/j.epsl.2005.09.055.

Rath, J., and Staudinger, G., 2001, Cracking reactions of tar from pyrolysis of spruce wood: Fuel, v. 80, no. 10, p. 1379–1389, doi: 10.1016/S0016-2361(01)00016-3.

Reina, J., Velo, E., and Puigjaner, L., 1998, Thermogravimetric study of the pyrolysis of waste wood: Thermochimica Acta, v. 320, no. 1–2, p. 161–167, doi: 10.1016/S0040-6031(98)00427-4.

Richter, F.M., Davis, A.M., DePaolo, D.J., and Watson, E.B., 2003, Isotope fractionation by chemical diffusion between molten basalt and rhyolite: Geochimica et Cosmochimica Acta, v. 67, no. 20, p. 3905–3923, doi: http://dx.doi.org/10.1016/S0016-7037(03)00174-1.

Richter, F.M., Mendybaev, R.A., Christensen, J.N., Hutcheon, I.D., Williams, R.W., Sturchio, N.C., and Beloso Jr., A.D., 2006, Kinetic isotopic fractionation during diffusion of ionic species in water: Geochimica et Cosmochimica Acta, v. 70, no. 2, p. 277–289, doi: http://dx.doi.org/10.1016/j.gca.2005.09.016.

Richter, F.M., Watson, E.B., Mendybaev, R.A., Teng, F.-Z., and Janney, P.E., 2008, Magnesium isotope fractionation in silicate melts by chemical and thermal diffusion: Geochimica et Cosmochimica Acta, v. 72, no. 1, p. 206–220, doi: http://dx.doi.org/10.1016/j.gca.2007.10.016.

Robertson, J., 2002, Diamond-like amorphous carbon: Materials Science and Engineering: R: Reports, v. 37, no. 4–6, p. 129–281, doi: 10.1016/S0927-796X(02)00005-0.

Rodrigues, S., Suárez-Ruiz, I., Marques, M., Camean, I., and Flores, D., 2011, Microstructural evolution of high temperature treated anthracites of different rank: International Journal of Coal Geology, v. 87, no. 3–4, p. 204–211, doi: 10.1016/j.coal.2011.06.009.

Romero-Sarmiento, M.F., Rouzaud, J.N., Bernard, S., Deldicque, D., Thomas, M., and Littke, R., 2014, Evolution of Barnett Shale organic carbon structure and nanostructure with increasing maturation: Organic Geochemistry, v. 71, p. 7–16, doi: 10.1016/j.orggeochem.2014.03.008.

Ross, J. V., and Bustin, R., 1990, The role of strain energy in creep graphitization of anthracite: Nature, v. 343, no. 6253, p. 58–60, doi: 10.1038/343058a0.

Sadezky, A., Muckenhuber, H., Grothe, H., Niessner, R., and Pöschl, U., 2005, Raman microspectroscopy of soot and related carbonaceous materials: Spectral analysis and structural information: Carbon, v. 43, no. 8, p. 1731–1742, doi: 10.1016/j.carbon.2005.02.018.

Sakaguchi, A., 1999, Thermal maturity in the Shimanto accretionary prism, southwest Japan, with the thermal change of the subducting slab: Fluid inclusion and vitrinite

reflectance study: Earth and Planetary Science Letters, v. 173, no. 1–2, p. 61–74, doi: 10.1016/S0012-821X(99)00219-8.

Sakaguchi, A., 1996, High paleogeothermal gradient with ridge subduction beneath the Cretaceous Shimanto accretionary prism, southwest Japan: Geology, v. 24, no. 9, p. 795–798, doi: 10.1130/0091-7613(1996)024<0795:HPGWRS>2.3.CO;2.

Sakaguchi, A., Chester, F., Curewitz, D., Fabbri, O., Goldsby, D., Kimura, G., Li, C.F., Masaki, Y., Screaton, E.J., Tsutsumi, A., Ujiie, K., and Yamaguchi, A., 2011, Seismic slip propagation to the updip end of plate boundary subduction interface faults: Vitrinite reflectance geothermometry on integrated ocean drilling program nantro SEIZE cores: Geology, v. 39, no. 4, p. 395–398, doi: 10.1130/G31642.1.

Salver-Disma, F., Du Pasquier, a., Tarascon, J.-M., Lassègues, J.-C., and Rouzaud, J.-N., 1999, Physical characterization of carbonaceous materials prepared by mechanical grinding: Journal of Power Sources, v. 81–82, p. 291–295, doi: 10.1016/S0378-7753(99)00205-0.

Salver-Disma, F., Tarascon, J.-M., Clinard, C., and Rouzaud, J.-N., 1999, Transmission electron microscopy studies on carbon materials prepared by mechanical milling: Carbon, v. 37, p. 1941–1959.

Samolada, M.C., and Vasalos, I.A., 1991, A kinetic approach to the flash pyrolysis of biomass in a fluidized bed reactor: Fuel, v. 70, no. 7, p. 883–889, doi: http://dx.doi.org/10.1016/0016-2361(91)90200-T.

Santosh, M., and Wada, H., 1993, Microscale isotopic zonation in graphite crystals: Evidence for channelled CO influx in granulites: Earth and Planetary Science Letters, v. 119, no. 1, p. 19–26, doi: http://dx.doi.org/10.1016/0012-821X(93)90003-R.

SantoshM, Wada, H., Satish-Kumar, M., and Binu-Lal S, 2003, Carbon isotope “stratigraphy” in a single graphite crystal: Implications for the crystal growth mechanism of fluid-deposited graphite: American Mineralogist, v. 88, p. 1689, doi: 10.2138/am-2003-11-1208.

Satish-Kumar, M., Hayato, S., Yoshino, T., Kato, M., and Hiroi, Y., 2011a, Experimental determination of carbon isotope fractionation between iron carbide melt and carbon: 12C-enriched carbon in the Earth’s core? Earth and Planetary Science Letters, v. 310, p. 340–348.

Satish-Kumar, M., Jaszczak, J.A., Hamamatsu, T., and Wada, H., 2011b, Relationship between structure, morphology, and carbon isotopic composition of graphite in marbles: Implications for calcite-graphite carbon isotope thermometry: American Mineralogist, v. 96, no. 4, p. 470 LP-485.

Scharf, A., Handy, M.R., Ziemann, M. a., and Schmid, S.M., 2013, Peak-temperature patterns of polyphase metamorphism resulting from accretion, subduction and collision (eastern Tauern Window, European Alps) - a study with Raman microspectroscopy on carbonaceous material (RSCM): Journal of Metamorphic Geology, v. 31, no. 8, p. 863–880, doi: 10.1111/jmg.12048.

Schultrich, B., Scheibe, H.J., Grandremy, G., Drescher, D., and Schneider, D., 1996, Elastic modulus as a measure of diamond likeness and hardness of amorphous carbon films: Diamond and Related Materials, v. 5, no. 9, p. 914–918, doi: 10.1016/0925-9635(95)00439-4.

Schwab, V., Spangenberg, J.E., and Grimalt, J.O., 2005, Chemical and carbon isotopic evolution of hydrocarbons during prograde metamorphism from 100°C to 550°C: Case study in the Liassic black shale formation of Central Swiss Alps: Geochimica et Cosmochimica Acta, v. 69, no. 7, p. 1825–1840, doi: 10.1016/j.gca.2004.09.011.

Shand, S.J., 1916, The Pseudotachylyte of Parijs (Orange Free State), and its Relation to “Trap-Shotten Gneiss” and “Flinty Crush-Rock”: Quarterly Journal of the Geological Society, v. 72, no. 1–4, p. 198–221, doi: 10.1144/GSL.JGS.1916.072.01-04.12.

Sheng, C., 2007, Char structure characterised by Raman spectroscopy and its correlations with combustion reactivity: Fuel, v. 86, no. 15, p. 2316–2324, doi: 10.1016/j.fuel.2007.01.029.

Shi, P., 1992, Fluid fugasities and phase equilibria in the Fe-Si-O-H-S system: American Mineralogist, v. 77, p. 1050–1066.

Sibson, R.H., 1975, Generation of pseudotachylyte by ancient seismic faulting: GEophysical Journal of the Royal Astronomical Society, v. 43, no. 3, p. 775–794.

Spray, J.G., 1992, A physical basis for the frictional melting of some rock-forming minerals: Tectonophysics, v. 204, p. 205–221.

Spray, J.G., 1993, Viscosity determinations of some frictionally generated silicate melts: Implications for fault zone rheology at high strain rates: Journal of Geophysical Research, v. 98, no. B5, p. 8053, doi: 10.1029/93JB00020.

Stach, E., Mackowsky, M.T., Teichmuller, M., Taylor, G.H., Chandra, D., and Teichmulluer, R., 1982, Coal Petrology:

Storti, F., Billi, A., and Salvini, F., 2003, Particle size distributions in natural carbonate fault rocks: Insights for non-self-similar cataclasis: Earth and Planetary Science Letters, v. 206, no. 1–2, p. 173–186, doi: 10.1016/S0012-821X(02)01077-4.

Sung, J., 2000, Graphite->diamond transition under high pressure: A kinetics approach: Journal of Materials Science, v. 35, p. 6041–6054.

Sweeney, J.J., and Burnham, A.K., 1990, Evaluation of a simple model of vitrinite reflectance based on chemical kinetics: AAPG BulletinG, v. 74, no. 10, p. 1559–1570.

Symmes, G.H., and Ferry, J.M., 1991, Evidence from mineral assemblages for infiltration of pelitic schists by aqueous fluids during metamorphism: Contributions to Mineralogy and Petrology, v. 108, no. 4, p. 419–438, doi: 10.1007/BF00303447.

Taira, A., Okada, H., Whitaker, J.H.M., and Smith, A.J., 1982, The Shimanto Belt of Japan: Cretaceous-lower Miocene active-margin sedimentation: Geological Society, London, Special Publications, v. 10, no. 1, p. 5–26, doi: 10.1144/GSL.SP.1982.010.01.01.

Takagi, H., Goto, K., and Shigematsu, N., 2000, Ultramylonite bands derived from cataclasite and pseudotachylyte in granites, northeast Japan: Journal of Structural Geology, v. 22, no. 9, p. 1325–1339, doi: 10.1016/S0191-8141(00)00034-1.

Takahashi, T., and Shuto, K., 1997, Major and Trace element analysis of silicate rocks using X-ray fluorescence spectrometer RIX 3000: Rgaku Journal, v. 28, no. 2, p. 25–37.

Tenthorey, E., Cox, S.F., and Todd, H.F., 2003, Evolution of strength recovery and permeability during fluid-rock reaction in experimental fault zones: Earth and Planetary Science Letters, v. 206, no. 1–2, p. 161–172, doi: 10.1016/S0012-821X(02)01082-8.

Teraoka, Y., 1979, Provence of the Shimanto geosyclinal sediments inferred from sandstone compositions: Bullitin of Geological Survey of Japan, v. 85, p. 753–769, doi: 10.1248/cpb.37.3229.

Thompson, A.B., 1976, Mineral reactions in pelitic rocks; II, Calculation of some P-T-X(Fe-Mg) phase relations: American Journal of Science, v. 276, no. 4, p. 425–454.

Thurner, F., and Mann, U., 1981, Kinetic investigation of wood pyrolysis: Industrial & Engineering Chemistry Process Design and Development, v. 20, no. 3, p. 482–488, doi: 10.1021/i200014a015.

Tinkham, D.K., Zuluaga, C.A., and Stowell, H.H., 2001, Metapelite phase equilibria in MnNCKFMASH: The effect of variable Al2O3 and MgO/(MgO+FeO) on mineral stability: Geological Materials Research, v. 3, no. 1, p. 1174-.

Tomkins, A.G., Rebryna, K.C., Weinberg, R.F., and Schaefer, B.F., 2012, Magmatic sulfide formation by reduction of oxidized arc basalt: Journal of Petrology, v. 53, no. 8, p. 1537–1567, doi: 10.1093/petrology/egs025.

Toulmin, P., and Barton, P.B., 1964, A thermodynamic study of pyrite and pyrrhotite: Geochimica et Cosmochimica Acta, v. 28, no. 5, p. 641–671, doi: 10.1016/0016-7037(64)90083-3.

Toyoshima, T., 1990, Pseudotachylite from the main zone of the Hidaka metamorphic belt, Hokkaido, northern Japan: Journal of Metamorphic Geology, v. 8, p. 507–523.

Toyoshima, T., Obara, T., Niizato, T., Tanaka, H., Shimada, K., Komatsu, M., Wada, Y., and Koyasu, T., 2004, Pseudotachylytes, related fault rocks, asperities, and crustal structures in the Hidaka metamorphic belt, Hokkaido, northern Japan: Earth Pranets Space, v. 56, p. 1209–1215.

Toyoshima, T.T., Masayuki, K., and Toshiaki, S., 1994, Tectonic evolution of lower crustal rocks in an exposed magmatic arc section in the Hidaka metamorphic belt, Hokkaido , northern Japan: The Island Arc, v. 3, p. 182–198.

Tracy, R.J., and Robinson, P., 1988, Silicate-sulfide-oxide-fluid reactions in granulite-grade pelitic rocks, central Massachusetts: American Mineralogist, v. 288–A, p. 45–74.

Tso, J.L., Gilbert, M.C., and Craig, J.R., 1979, Sulfidation of synthetic biotites: American Mineralogist, v. 64, p. 304–316.

Tsuchiya, N., Suzuki, N., and Chiba, T., 1991, Origin of graphite in the Oshirabetsu gabbroic body, Hokkaido, Japan: Journal of Mineralogy, Petrology and Economic Geology, v. 86, p. 264–272.

Tuinstra, F., and Koenig, L., 1970, Raman Spectrum of Graphite: The Journal of Chemical Physics, v. 53, no. 1970, p. 1126–1130, doi: 10.1063/1.1674108.

Uher, C., Hockey, R.L., and Ben-Jacob, E., 1987, Pressure dependence of the c-axis resistivity of graphite: Physical Review B, v. 35, no. 9, p. 4483–4488, doi: 10.1103/PhysRevB.35.4483.

Ujiie, K., Yamaguchi, H., Sakaguchi, A., and Toh, S., 2007, Pseudotachylytes in an ancient accretionary complex and implications for melt lubrication during subduction zone earthquakes: Journal of Structural Geology, v. 29, no. 4, p. 599–613, doi: 10.1016/j.jsg.2006.10.012.

Underwood, M.B., Hibbard, J.P., and DiTullio, L., 1993, Geologic summary and conceptual framework for the study of thermal maturity within the Eocene-Miocene Shimanto Belt, Shikoku, Japan: Geological Society of America Special Papers, v. 273, p. 1–24, doi: 10.1130/SPE273-p1.

van Zuilen, M.A., Fliegel, D., Wirth, R., Lepland, A., Qu, Y., Schreiber, A., Romashkin, A.E., and Philippot, P., 2012, Mineral-templated growth of natural graphite films: Geochimica et Cosmochimica Acta, v. 83, no. 0, p. 252–262, doi: http://dx.doi.org/10.1016/j.gca.2011.12.030.

Vandenbroucke, M., and Largeau, C., 2007, Kerogen origin, evolution and structure: Organic Geochemistry, v. 38, no. 5, p. 719–833, doi: 10.1016/j.orggeochem.2007.01.001.

Vázquez-Santos, M.B., Geissler, E., László, K., Rouzaud, J.N., Martínez-Alonso, A., and Tascón, J.M.D., 2012, Comparative XRD, Raman, and TEM study on graphitization of PBO-derived carbon fibers: Journal of Physical Chemistry C, v. 116, no. 1, p. 257–268, doi: 10.1021/jp2084499.

Viti, C., and Collettini, C., 2009, Growth and deformation mechanisms of talc along a natural fault: a micro / nanostructural investigation: Contributions to Mineralogy and Petrology, v. 158, p. 529–542, doi: 10.1007/s00410-009-0395-4.

Wada, H., Ito, R., and Akiyama, F., 1984, Preparation and measurement of carbon dioxide for stable isotope analysis of small amount of graphite.: Geoscience Reports of Shizuoka University, v. 10, p. 133–141.

Wada, H., Tomita, T., Matsuura, K., Tuchi, K., Ito, M., and Morikiyo, T., 1994, Graphitization of carbonaceous matter during metamorphism with references to carbonate and pelitic rocks of contact and regional metamorphisms, Japan: Contributions to Mineralogy and Petrology, v. 118, no. 3, p. 217–228, doi: 10.1007/BF00306643.

Wang, G.-F., 1989, Carbonaceous material in the Ryoke metamorphic rocks, Kinki district, Japan: Lithos, v. 22, no. 4, p. 305–316, doi: 10.1016/0024-4937(89)90032-7.

Ward, S.M., and Braslaw, J., 1985, Experimental weight loss kinetics of wood pyrolysis under vacuum: Combustion and Flame, v. 61, no. 3, p. 261–269, doi: http://dx.doi.org/10.1016/0010-2180(85)90107-5.

Warr, L.N., and Rice, A.H.N., 1994, Interlaboratory standardization and calibration of day mineral crystallinity and crystallite size data: Journal of Metamorphic Geology, v. 12, no. 2, p. 141–152, doi: 10.1111/j.1525-1314.1994.tb00010.x.

Warr, L.N., Greiling, R.O., and Zachrisson, E., 1996, Thrust-related very low grade metamorphism in the marginal part of an orogenic wedge, Scandinavian Caledonides: Tectonics, v. 15, no. 6, p. 1213–1229, doi: 10.1029/96TC00983.

Weller, T.E., Ellerby, M., Saxena, S.S., Smith, R.P., and Skipper, N.T., 2005, Superconductivity in the intercalated graphite compounds C6Yb and C6Ca: Nature Physics, v. 1, no. 1, p. 39–41, doi: 10.1038/nphys0010.

Wenk, H.-R., Johnson, L.R., and Ratschbacher, L., 2000, Pseudotachylites in the Eastern Peninsular Ranges of California: Tectonophysics, v. 321, p. 253–277.

Wilhelm, H., Lelaurain, M., McRae, E., and Humbert, B., 1998, Raman spectroscopic studies on well-defined carbonaceous materials of strong two-dimensional character: Journal of Applied Physics, v. 84, no. 12, p. 6552–6558, doi: 10.1063/1.369027.

Wilkins, R.W.T., Boudou, R., Sherwood, N., and Xiao, X., 2014, Thermal maturity evaluation from inertinites by Raman spectroscopy: The “RaMM” technique: International Journal of Coal Geology, v. 128–129, p. 143–152, doi: 10.1016/j.coal.2014.03.006.

Wones, D.R., and Eugster, H.P., 1965, Stability of biotite: Experiment, Theory, and Application: The American mineralogist, v. 50, p. 1228–1272.

Wood, D.A., 1988, Relationships between thermal maturity indices calculated using Arrhenius equation and Lopatin method; implications for petroleum exploration: AAPG Bulletin, v. 72, no. 2, p. 115 LP-134.

Wopenka, B., and Pasteris, J.D., 1993, Structural characterization of kerogens to granulite-facies graphite: Applicability of Raman microprobe spectroscopy: American Mineralogist, v. 78, p. 533–557.

Yamaguchi, A., Cox, S.F., Kimura, G., and Okamoto, S., 2011, Dynamic changes in fluid redox state associated with episodic fault rupture along a megasplay fault in a subduction zone: Earth and Planetary Science Letters, v. 302, no. 3–4, p. 369–377, doi: 10.1016/j.epsl.2010.12.029.

Yui, T.-F., Huang, E., and Xu, J., 1996, Raman spectrum of carbonaceous material: a possible metamorphic grade indicator for low-grade metamorphic rocks: Journal of Metamorphic Geology, v. 14, p. 115–124.

Zhao, J., Yang, L., Li, F., Yu, R., and Jin, C., 2009, Structural evolution in the graphitization process of activated carbon by high-pressure sintering: Carbon, v. 47, no. 3, p. 744–751, doi: 10.1016/j.carbon.2008.11.006.

Zhao, Y.X., and Spain, I.L., 1989, X-ray diffraction data for graphite to 20 GPa: Physical Review B, v. 40, no. 2, p. 993–997.

Zulauf, G., Kleinschmidt, G., and Oncken, G., 1990, Brittle Deformation and Graphitic Cataclasites in the Pilot Reseach Well KTB-VB (Oberpfalz, FRG): Geological Society, London, Special Publications, v. 54, p. 97–103.

APPENDIX I

Chemical extraction of CM using HF-HCl treatments

A1.1. General method for HF-HCl treatments

The rock samples (500–800 g) were crushed by a Jaw crusher and sieved using a 200–mesh screen. The sieved powder was initially treated with 2N HCl to remove carbonate, sulfide, sulfate and hydroxides (Vandenbroucke and Largeau, 2007), and then the solution was treated by HF (48 %) in several large Teflon (perfluoro alkoxy alkane; PFA) vessels (300 ml) and dried on a hot plate at 120 °C. Dried residues in PFA vessels were composed of CMs and newly formed fluorides such as ralstonite and other complex fluorides (Durand and Nicaise, 1980). These fluorides are difficult to redissolve once precipitated and they interfere with further analysis of CM (Vandenbroucke and Largeau, 2007), therefore, we performed repeated rinsing with hot deionized water between acid treatments (Durand and Nicaise, 1980). The residues were dissolved again in 2N HCl at 60 °C. The chemical treatments were repeated several times until the CM floated in the solution. This floatation is a signal of the complete decomposition of fluorides (Itaya, 1981; Itaya 1985). The supernatant of CM was filtered and dried on a watch glass. Note that the CM residues retained small amounts of minerals such as zircon, rutile, ilmenite, and pyrite even after HF–HCl acid treatments. Both starting materials of SM and HMB are slightly matured or metamorphosed during diagenesis and low grade metamorphism, respectively. Many researchers have concluded that the HF–HCl acid treatments do not alter the CM structure and do not generate newly formed solvent soluble organic materials except in the case of very immature sediments (Durand and Nicaise, 1980; Larsen et al. 1989; Vandenbroucke and Largeau, 2007).

A1.2. Origin of interference residues

Unfortunately, it is very difficult to extract CM from sedimentary rocks by only above procedures. In many cases, we must check eliminations of interference minerals using a XRD again and again. Figure A1 displays relative fraction of interference minerals in incomplete CM residues. Ralstonite (Fig. A2a) is the most common interference minerals, which is an aluminous fluoride [$Na_xMg_xAl_{2-x}(F, OH)_6(H_2O)$]. Hieratite ($K_2SiF_6$; Fig. A2b) is also common potassium fluoride produced by HF-HCl treatments. Both fluorides are white powders and can be easily identified using XRD (Figs. A2a-b). Such fluorides are observed as the residues depending on bulk chemistry. In the case of carbonate, large amount of calcium fluorides (CaF_2) are produced as the residues. Since fluorides are difficult to dissolve into solution, I performed repeated HCl (2N) treatments in a large plastic bottle (250 ml; iboy manufactured by AS ONE is the most suitable vessels for durability and cost effectiveness) and then, rinsing with hot deionized water. This procedure was repeated until decomposition of fluorides is completely achieved. I usually replace the HCl (2N) treatments twice during shaking in water bath at 60 °C. It takes about 1 weeks to eliminate the fluorides completely. The timing of eliminations is depending on the concentration of fluorides in the residue. Perhaps, the capacity of eliminations using HCl treatment is driven by the dissolved concentration of fluorides. For examples, we can usually judge the degree of relative concentration of dissolved fluorides by “color” of solution. Orange or yellowish solutions is incomplete for HCl decomposition, whereas transparent solution is sign for completeness of decomposition.

Secondary, quartz and some oxide minerals are also major minerals that interfere the XRD analysis. Although HF treatment decompose the almost silicate minerals, “highly” crystalline quartz is often retained as residues (Fig. A2c). Pyrite, rutile, anatase and zircon

can also resist HF-HCl treatments. The quartz crystals are able to decompose using a second round of HF treatment. Pyrite can decompose in HNO_3 treatments after HF-HCl treatment. In general, HNO_3 is oxidizing agent and may modify the natural CM structure. However, large amounts of pyrite are retained in the residue of Shimanto sedimentary rocks and it is very important to eliminate the pyrite as much as possible for XRD and micro-FTIR analysis.

A1.3. More detailed procedures for chemical extractions

Based on the experiences of chemical extractions, I propose the best chemical extraction procedures in our laboratory as follows.

[1st treatment]

Firstly, the rock powder which crushed using a Jaw crusher. In the case of psammitic rocks, it is better to separate the clay component by elutriation. After powdering, the sample powders treated with 2N HCl to remove carbonate, sulfide, sulfate and hydroxides. The solution was treated by HF (48 %) in several large Teflon vessels (300 ml). Because HF solution within silicate minerals reacts explosively, it is better to introduce into a large vessel little by little. The solution is completely dried on a hot plate at 120 °C.

[2nd treatment]

2N HCl and HF solution filled in the Teflon vessels again to decompose highly crystallized silicates such as quartz and fluorides. (3) After drying, the residues are introduced into large plastic bottles (iboy 250 ml) with 2N HCl solution and deionized hot water, and then shaking in water bath at 60 °C for 1 day. In the case of low concentration of fluoride, a colloidal CM will be floating in the solution. It is a sign of completion of chemical extraction

(Itaya 1985). However, samples have to be processed with different chemical treatments to remove large amount of fluoride depending of relative concentration of fluorides. After shaking, HCl solution with CM and fluoride moves into disposal vessel, and hot deionized water added in the vessel. Itaya (1985) suggested that solution with CM and fluorides are separated by "decantation method". The aluminous fluorides slightly dissolve in water; therefore, it is important to repeat rinsing with hot deionized water until it has a clear transparency (5~6 times). After rinsing with hot water, it is better to repeat HCl treatment and rinsing with hot water again until floatation of CM in the solution. It takes time and effort to eliminate fluoride during this procedure completely.

[3rd treatment]

Previous studies reported that HNO_3 treatments might damage its chemical structure in the case of poorly organized CM, therefore, it should be avoided for chemical analyses such as CHNS or carbon stable isotopic analysis. However, in the case of XRD analysis, it is difficult to identify the broad peak of amorphous carbon by the interference with peak of pyrite. For this reason, Itaya (1985) recommended the HNO_3 treatments when the samples contained large amount of pyrite. If the HNO_3 treatments are conducted on a hot plate at 120 °C, it should be completed within one hour because, or else the poorly organized CM will easily be decomposed by oxidizing agent. Thereafter, the solution with CM and undisolved oxide minerals remain as residue in PTF vessel. The solution with CM and some oxide are separated by "decantation method" in water. The pure solutions with CM are dried on the watched glass in incubator at 120 °C.

Based on our chemical extraction procedures, 100 mg of CM powder can be obtained from 10-15g of rock powders. Although the CM powder is small amount, almost all analyses such as XRD, micro-Raman spectroscopy, micro-FTIR, HRTEM, carbon stable isotopic studies can be done from the extract of only single procedure. In the case of HPHT

experiments, it is necessary for large amount of CM (~5 g) for starting materials, therefore, about 500 g of rock powder was used for chemical extraction in this study. My chemical extraction is just one example for suitable procedures in our lab. Cody et al. (2002) reported that CsF treatment is the best way to eliminate silicate mineral without production of fluoride. In the future, we should make a lot of effort for more revised chemical extraction of CM from silicate rocks.

Figures in APPENDIX I

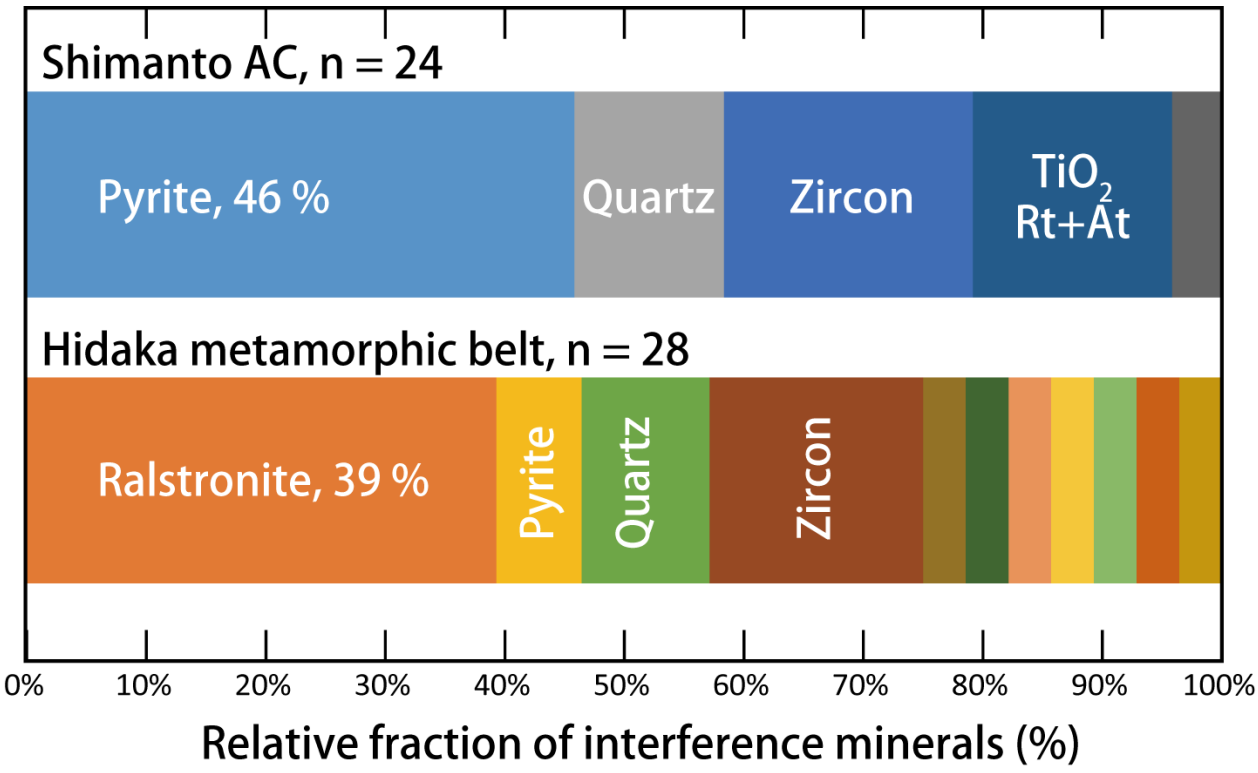

Figure A1. Relative fraction of various types of interference minerals in Shimanto accretionary complex (*n*=24) and Hidaka metamorphic belt (*n*=28). Pyrite is most prominent interference minerals (48 %) in Shimanto and ralstonite is most prominent minerals (39 %) in Hidaka.

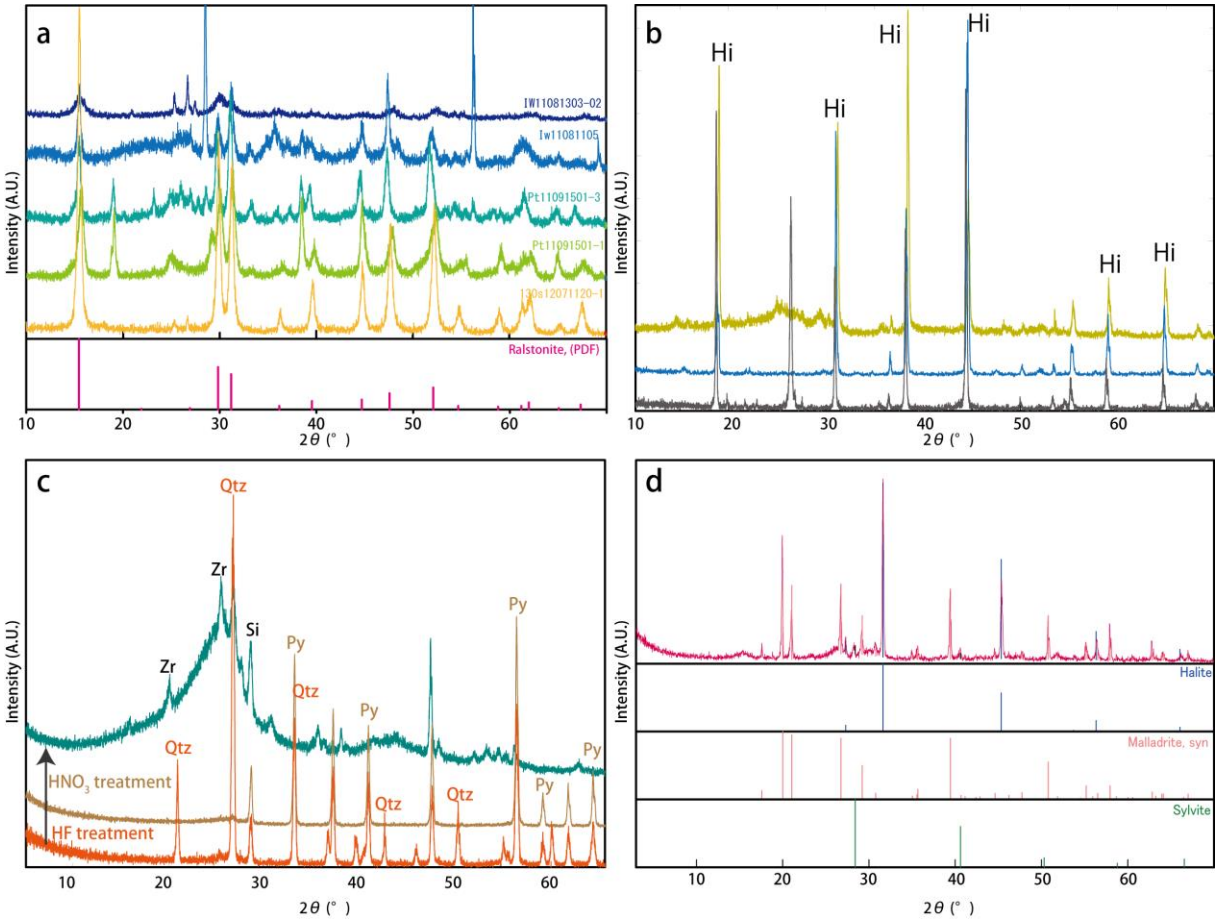

Figure A2. Representative peak profiles of interference minerals during chemical extraction. **(a)** Ralstonite **(b)** Hieratite **(c)** pyrite and quartz with amorphous carbon **(d)** Other fluorides and minerals produced by chemical extraction of CM.

APPENDIX II

Principle of chemical kinetics in Earth science

Chemical reaction of minerals is widely investigated for inferring the pressure-temperature conditions in igneous or metamorphic rocks. Such reactions are mainly driven by stoichiometry from “reactants” to “products” in closed system, and calculated based on the pressure-temperature-activity of minerals under thermodynamic models. In geology, almost all chemical reactions are considered as equilibrium reactions because rate dependence is much less effect than temperature or pressure dependence in geological time scale. However, rate dependence in chemical reactions are also key to understanding the tectonic evolutions of multiple metamorphism and deformation history. For examples, several geospeedometry methods based on diffusion have been widely developed (Zhang 1994). Another important one is that involves diffusive loss of radiogenic nuclides in accessory minerals such as zircon, monazite, apatite, and titanite (e.g., Dodson, 1973). The cation exchange diffusion between two phases such as plagioclase, pyroxine, and so on has also much applications in geological research (e.g., Lesga, 1983). A third method uses exsolution of an originally homogeneous phase (e.g., Spear et al. 2014). The determination of constants such as diffusion, partition, and decay constant lead to apply for geological extrapolation.

In the case of carbonaceous material, it has been widely studied with respect to the time-temperature relation in geological time scale. Detailed review and discussions are presented in the above sections. In the case of solving the kinetic model, it is important to follow chemical model fitting based on the chemical process or model free methods. Large number of chemical models have been proposed for understanding the complex

chemical reaction. In this study, representative kinetic models and procedures of experimental study were carried out.

A2.1. Chemical reaction of isothermal rate law

The rate of chemical reaction is described as a change in concentration of some species with time (House 2007). Basic principle of chemical reaction from chemical species "A" to "B" can be generally expressed as:

$$[A] \Rightarrow [B] \qquad (1)$$

where, [A] and [B] are concentration or partial pressure of chemical species, which are the reaction rate per unit area. These concentration or degree of chemical reaction are often studied by thermogravimetry (TG), differential scanning calorimetry (DSC), powder X-Ray Diffraction (XRD), and nuclear magnetic resonance (NMR). For examples, the rate of chemical reaction r is described using the absolute value of slope between conversion factors α, β and time t (Fig. A3).

$$r = -\frac{\mathrm{d}[\alpha]}{\mathrm{d}t} = \frac{\mathrm{d}[\beta]}{\mathrm{d}t} \qquad (2)$$

The reaction rates are described as a differential form, which are driven by the concentration, and the concentration systematically changes with progress of the reaction. For instance, α is defined by:

$$\alpha = \frac{m_0 - m_t}{m_0 - m_\infty} \qquad (3)$$

Where, m_0 is initial concentration (or partial pressure) of reactant [A], m_t is concentration at time t, and m_∞ is final concentration. It is important to transform into a conversion fraction (α) that can be used in the kinetic equations. The relation of conversion factor and duration is expressed using a rate constant k:

$$-\frac{\mathrm{d}[\alpha]}{\mathrm{d}t} = k[\alpha] \qquad (4)$$

The equation (4) can be also converted by integration methods;

$$[\alpha] = A_0 e^{-kt} \qquad (5)$$

where, A_0 is the pre-exponential factor. Combining the equations (2), (4) and (5), the reaction rate *r* is also written by as follow:

$$r = -\frac{d[\alpha]}{dt} = k[A]_0 e^{-kt} = A_0 e^{-\left(\frac{Ea}{RT}\right)} f(\alpha) \qquad (6)$$

Where, *E*a is the activation energy, *T* is absolute temperature *R* is the gas constant, *f*(α) is the "reaction model", and α is the conversion factor (see a A2.2 for detail). In general, chemical reactions are expressed by:

$$r = k[\alpha]^l[\beta]^m[\gamma]^n \ldots \qquad (7)$$

The equation (7) is named as the rate equation or rate law, which consists of rate constant *k* and order of reaction *l*+*m*+*n*. The order of reaction *l*, *m*, and *n* are also simply called the exponents. The overall order of the reaction is the sum of the exponents *l*, *m*, and *n.* We speak of a second-order reaction, a third-order reaction, etc., when the sum of the exponents in the rate law is 2, 3 etc., respectively (House 2007). Kinetic parameters can be obtained from isothermal kinetic data by applying the above rate law (6).

A2.2. Model classification

The reaction models are generally grouped into four curves; acceleratory, decelerator, linear, and sigmoidal based on the graphical shape of their isothermal curve or on their mechanical assumptions (Table A2). Acceleratory models are those in which the reaction rate is increasing as the reaction proceeds; similarly, decelerator reaction rates decrease with reaction progress. The rate of linear model remains constant and sigmoid models exhibit a S-shaped relationship between rate and α. In addition, these models are subdivided into nucleation, geometrical contraction, diffusion and reaction-order (Table

A2).

On the other hand, it is possible to estimate the activation energy without modelistic assumptions. The model free methods such as isoconventional method and superposition method, which are specifically utilized for the complex chemical reactions in a non-isothermal kinetic study. The model free and model fitting methods have some advantages and disadvantages (e.g., Khwam and Flanagan 2005). Hence, it is important to distinguish the rate-determining process in solid state kinetic reaction.

A2.3. Chemical reaction of non-isothermal rate law

Alternatively, the equation (6) can be transformed into a nonisothermal rate expression describing reaction rate as a function of temperature at a constant heating rate (B) by utilizing the following:

$$\frac{\mathrm{d}\alpha}{\mathrm{d}T} = \frac{\mathrm{d}\alpha}{\mathrm{d}t}\frac{\mathrm{d}t}{\mathrm{d}T} \qquad (8)$$

where, $\mathrm{d}\alpha/\mathrm{d}T$ is the nonisothermal reaction rate, $\mathrm{d}\alpha/\mathrm{d}t$ is the isothermal reaction rate, and $\mathrm{d}T/\mathrm{d}t$ is the heating rate (B). Nonisothermal rate law is also described by combining the equation (7) and (8):

$$\frac{\mathrm{d}\alpha}{\mathrm{d}T} = \frac{A_0}{B} e^{-\left(\frac{Ea}{RT}\right)} f(\alpha) \quad (9)$$

Both equations of isothermal (6) and nonisothermal rate laws (9) can be converted from differential to integral form, respectively.

$$g(\alpha) = \; Aexp\left(\frac{-Ea}{RT}\right) t \qquad (10)$$

and

$$g(\alpha) = \; \frac{A_0}{B}\int_0^T \exp\left(\frac{-Ea}{RT}\right)\mathrm{d}T \qquad (11)$$

Where, $g(\alpha)$ is the integral reaction model, defined by:

$$g(\alpha) = \int_0^{\alpha} \frac{d\alpha}{f(\alpha)} \qquad (12)$$

Based on the above equation (11), it is possible to estimate activation energy using the heating rate B and model fitting. In case of non-isothermal methods, the heating rate change from 1 °C /min to 100 C /min to identify the difference of reaction.

A2.3 Effect of temperature

In general, the rate of chemical reaction changes exponentially with increasing temperature. The temperature dependence is the most important feature. *Svante August Arrhenius* suggested in the late 1800s that such temperature dependences can be expressed as:

$$k = A_0 e^{-Ea/RT} \qquad (13)$$

Where k is the rate constant, A_0 is the frequency factor (or pre-exponential factor), R is the molar gas constant, Ea is the activation energy, and T is the absolute temperature (K). This equation is generally referred to as the "Arrhenius equation". Taking natural logarithm of both side of eq. (13), we obtain;

$$\ln k = -\frac{Ea}{RT} + \ln A \qquad (14)$$

By rearrangement, this equation can be put in the form of a linear regression;

$$\ln k = -\frac{Ea}{R}\frac{1}{T} + \ln A$$

$$y = mx + b \qquad (15)$$

Therefore, the activation energy Ea and pre-exponential factor A can be obtained from the slope (m) and intercept ($\ln A$) of linear regression between ln k and $1/T$ at several temperatures (Fig. A4).

A2.4. Effect of pressure

Thermodynamically, pressure multiplied by volume has the dimensions of work or energy based on the "principle of Le Chatelier". The value of the reaction rate also displays variation with confining pressure, but the effect of pressure is smaller than the effect of temperature. The variation in free energy G with pressure P at that temperature is given by:

$$(\frac{\partial G}{\partial P})_T = V \qquad (16)$$

where V is the partial molar volume. For a chemical reaction, the free energy of activation, $\Delta G^{\ddagger}$ can be written as:

$$\Delta G^{\ddagger} \;=\; G^{\ddagger} - \Sigma \mathrm{G}_R \qquad (17)$$

where $G^{\ddagger}$ is the free energy of transition state and $\Sigma \mathrm{G_R}$ represents the sum of the molar free energies of the reactants. Science the volume of activation, $\Delta V^{\ddagger}$, is given by:

$$\Delta V^{\ddagger} \;=\; V^{\ddagger} - \Sigma V_R \qquad (18)$$

where $V^{\ddagger}$ is the volume of transition state and ΣV_{R} represents the sum of the molar volume of the reactants, we can express the in free energy with pressure at constant temperature as:

$$[\frac{\partial G^{\ddagger}}{\partial P}]_T = V^{\ddagger} - \;\Sigma V_R = \;\Delta V^{\ddagger} \qquad (19)$$

For a reaction carried out at constant temperature, we know that formation of the transition state is governed by:

$$\Delta G^{\ddagger} \;=\; -RT\ln K^{\ddagger} \qquad (20)$$

Where $K^{\ddagger}$ is the equilibrium constant for formation of the transition state. The equation relating the rate constant to temperature can be written as:

$$[\frac{\partial \ln k}{\partial P}]_T = -\frac{\Delta V^{\ddagger}}{RT} \qquad (21)$$

Therefore, replacing the partial derivatives and solving for $V^{\ddagger}$ gives:

$$\Delta G^{\ddagger} = -RT\frac{d\ln k}{dP} \quad (22)$$

By rearranging this equation, we obtain:

$$d\ln k = -\frac{\Delta V^{\ddagger}}{RT}dP \quad (23)$$

This equation is now in a form that allows integration, which when performed gives:

$$\ln k = -\frac{\Delta V^{\ddagger}}{RT}P + C \quad (24)$$

where C is a constant of integration. This equation indicates that a plot of $\ln k$ versus P should be linear with a slope of $-\Delta V^{\ddagger}/RT$. Therefore, the volume of activation can be determined if the reaction is carried out to determine the rate constant at several (usually quite high) pressures (Fig. A5). The interpretations of volumes of activation are always unambiguous, but generally if $\Delta V^{\ddagger}$ is negative, the rate of the reaction increases as pressure is increased.

A2.5. Complex chemical kinetics

Almost all chemical reactions in natural diagenesis or metamorphic process take place more complex systems than simple systems in experiments. For examples, wood, which is the starting material of coal is a composite material, constituted by a mixture of hemicellulose, cellulose, lignin and extractives (Di Blasi, 2008). Therefore, chemical reactions of wood pyrolysis are usually discussed by successive reactions and/or parallel reactions from wood to char, tars and gas phase based on the nonisothermal experiments using thermal gravimetric analysis (TGA). In the same manner of wood pyrolysis, coal has very complex chemical structures. For these reasons, it is expected that rate constants in natural process are controlled by "*rate-determining step*" in major chemical reactions.

A2.5.1. Parallel reactions

A single reactant may be converted into several different products simultaneously. There are numerous examples of such reaction in organic chemistry (House 2007). Suppose a compound, A, undergoes reactions to form several products, B, C, and D, at different rate. The systems can be described as:

$$\mathrm{A} \xrightarrow{k_1} \mathrm{B} \qquad (25)$$

$$\mathrm{A} \xrightarrow{k_2} \mathrm{C} \qquad (26)$$

$$\mathrm{A} \xrightarrow{k_3} \mathrm{D} \qquad (27)$$

The rate of disappearance of *A* is the sum of the rates for the three processes, so it can be expressed by:

$$-\frac{\mathrm{d}[\alpha]}{\mathrm{d}t} = k_1[\alpha] + k_2[\alpha] + k_3[\alpha] = (k_1 + k_2 + k_3)[\alpha] \qquad (28)$$

Prior to integration, this equation can be written as:

$$-\int_{[\mathrm{A}]_0}^{[A]} \frac{d[\alpha]}{[\alpha]} = (k_1 + k_2 + k_3)\int_0^t dt \qquad (29)$$

The sum of the three rate constants are simply a constant, so integration is analogous to that of the first-order case and yields:

$$\ln\frac{[A]_0}{[\alpha]} = \ (k_1 + k_2 + k_3)t \qquad (30)$$

In the case of *N*th- order case, we can be described as:

$$\ln\frac{[A]_0}{[\alpha]} = \ (k_1 + k_2 + k_3)t^{(l+m+n)} \qquad (31)$$

Equation (30) can also be written in exponential form as:

$$[\alpha] = [A]_0\exp(-(k_1 + k_2 + k_3))t^{(l+m+n)} \qquad (32)$$

A2.5.2. Successive reaction (Series reaction)

In the case of complex reaction, reactant [A] may systematically change from [A] to [B] and finally [C] in a series of steps as follow (Fig. A6a):

$$A \xrightarrow{k_1} B \xrightarrow{k_2} C \qquad (33)$$

Such a sequence of chemical reaction is named for successive, consecutive or series reactions. B is known as an intermediate because it is not the final product. Suppose chemical reaction show a first-order reaction, the rate of appearance of C with decreasing A and intermediate can be described as:

$$[C] = A_0\left(1 + \frac{k_2}{k_1 - k_2}e^{-k_1 t} + \frac{k_1}{k_2 - k_1}e^{-k_2 t}\right) \qquad (34)$$

The systematic change of [C] display a sigmoid curve, which has an inflection point. In the case of very low concentration of [B], the reaction (33) can be regarded as simple first order reaction by following equation;

$$A \xrightarrow{k_2} C, \quad [C] \gg [B] \quad (35)$$

This method is termed as "*pseudo-first-order reaction*". It is useful for the determination of rate determining step of complex chemical reaction. Based on the pseudo-fist-order reaction, it can be just expressed as;

$$[C] = A_0(e^{-k_2 t}) \qquad (36)$$

The chemical reaction of intermediate can be omitted in series reaction (Fig. A6b).

A2.6. Rate determining step in complex chemical reaction

This concept is simple, but important to estimate the complex chemical reaction of rate constant and reaction order. The complex chemical reaction is driven by the biggest energy gap in whole process, therefore, it is key to identify the rate determine step at any

temperature. Almost all series reactions change their rate determining step with proceeding reaction. In this study, we found the aspect of reaction orders with increasing annealing temperature in HPHT experiments (section VI and VII). This suggests that rate determining step of graphitization systematically change at different temperature.

Reference Cited in Appendix II

House, J.E., 2007, Principle of Chemical kinetics: Elsevier.

Lasaga, A.C., 1983, Geospeedometry: An extension of geothermometry, *in* Saxena, S.K. ed., Kinetics and Equilibrium in mineral reactions, Springer, New York, p. 81–114.

Ptáček, P., Šoukal, F., Opravil, T., Bartoníčková, E., and Wasserbauer, J., 2016, The formation of feldspar strontian (SrAl2Si2O8) via ceramic route: Reaction mechanism, kinetics and thermodynamics of the process: Ceramics International, v. 42, no. 7, p. 8170–8178, doi: 10.1016/j.ceramint.2016.02.024.

Spear, F.S., 2014, The duration of near-peak metamorphism from diffusion modelling of garnet zoning: Journal of Metamorphic Geology, v. 32, no. 8, p. 903–914, doi: 10.1111/jmg.12099.

Youxue Zhang, 1994, Reaction kinetics, geospeedometry, and relaxation theory: Earth and Planetary Science Letters, v. 122, no. 3–4, p. 373–391, doi: 10.1016/0012-821X(94)90009-4.

Figures in APPENDIX II

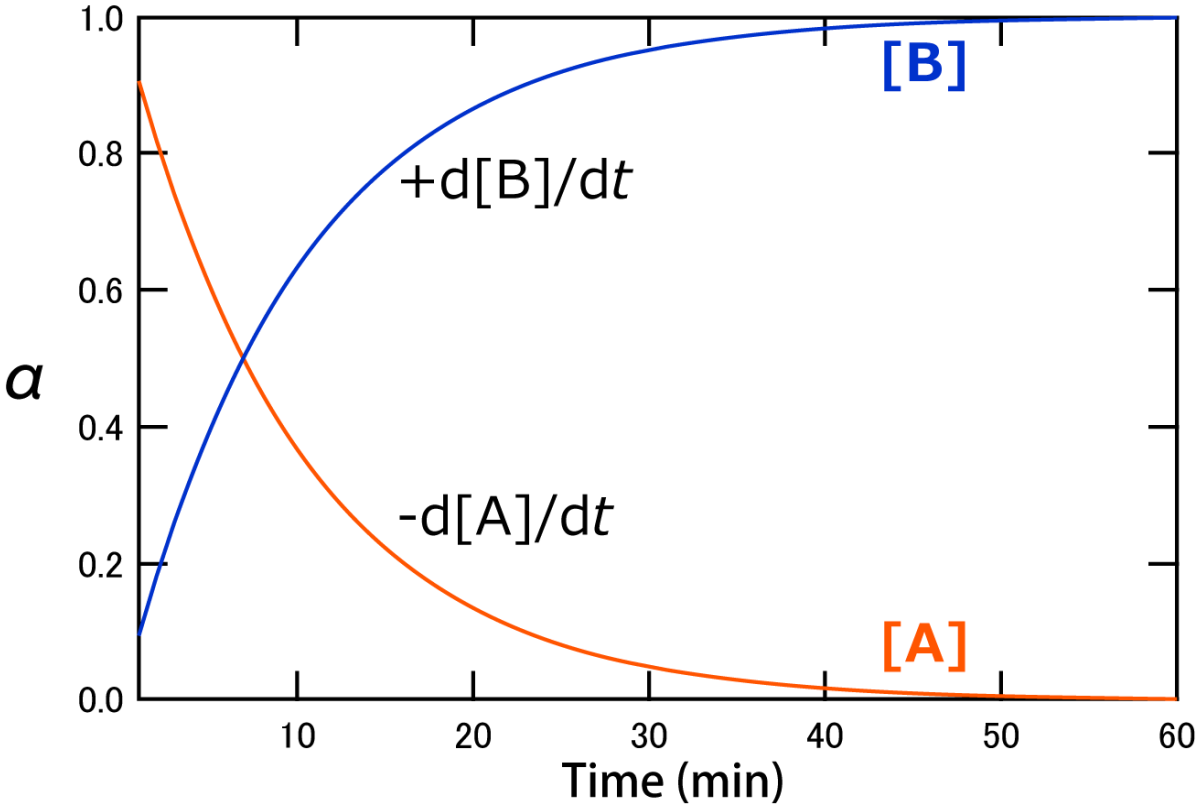

Figure A3. Simple aspects in concetration of A and B for the reaction A => B.

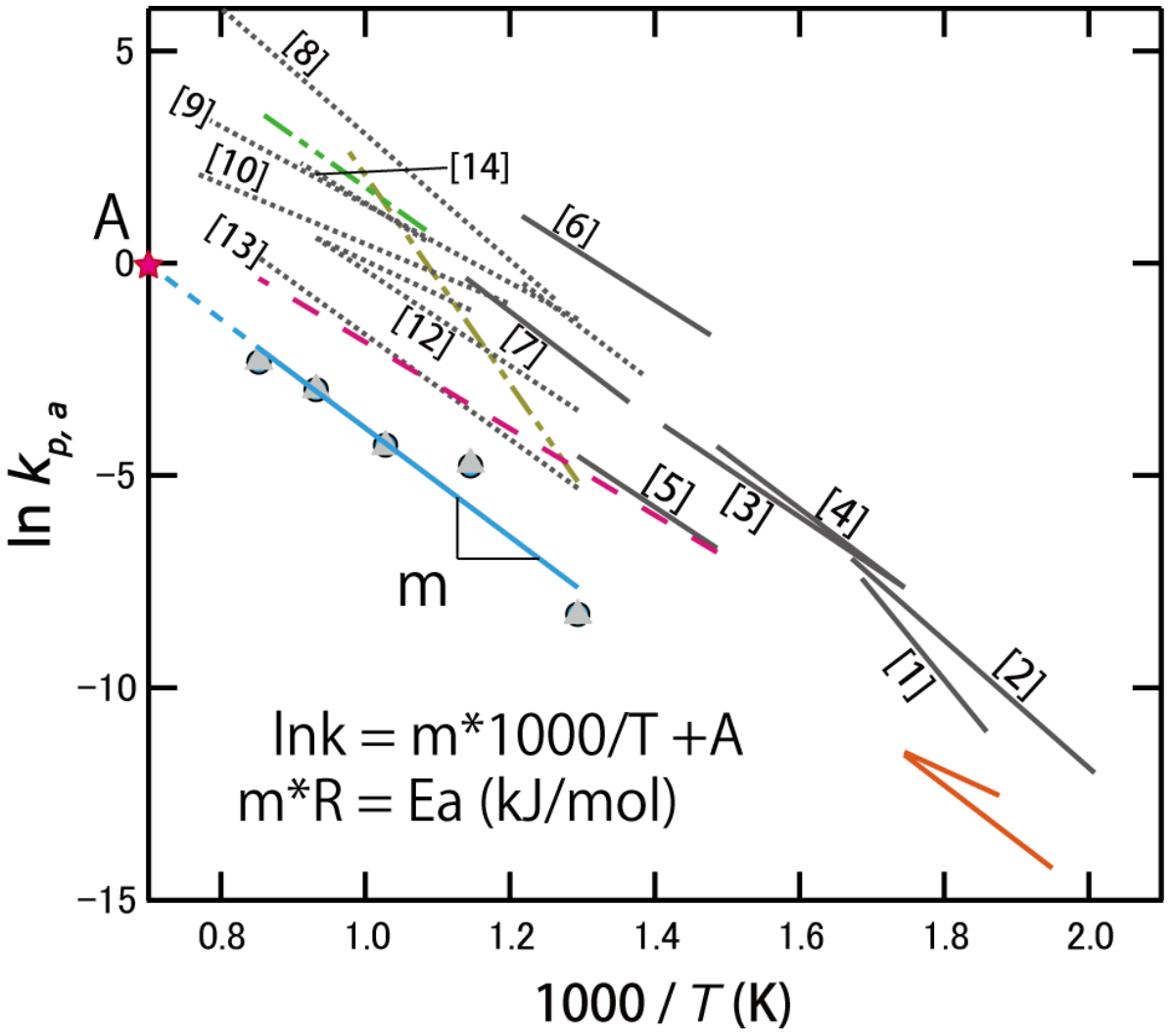

Figure A4. An example for solving the activation energy in Arrhenius plot. The effective activation energy is calculated by the slope multiply by gas constant.

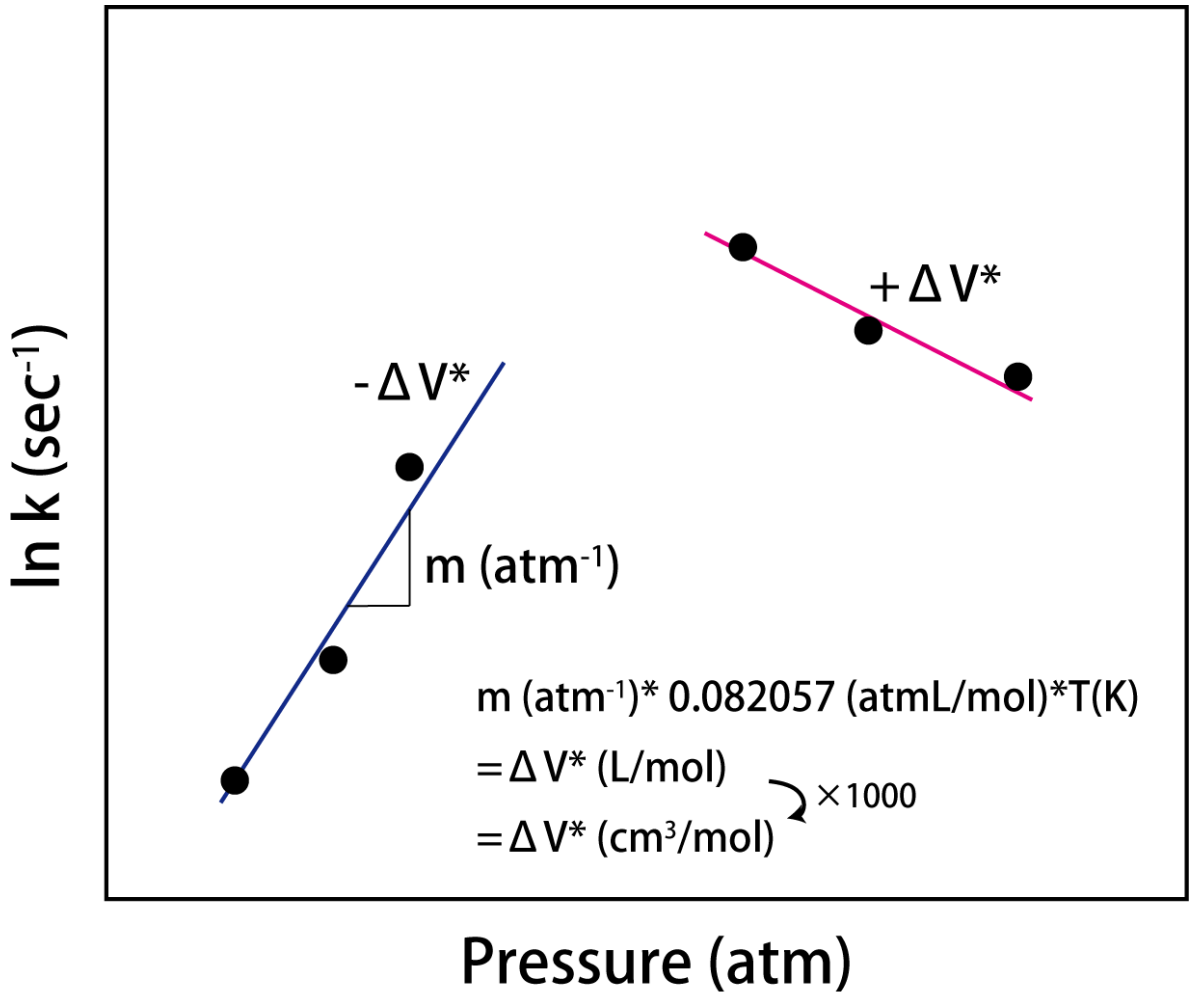

Figure A5. An example for solving the activation vomle in pressure vs. ln k plot. The effective activation volume is calculated by the slope multiply by gas constant and abusolute temperature.

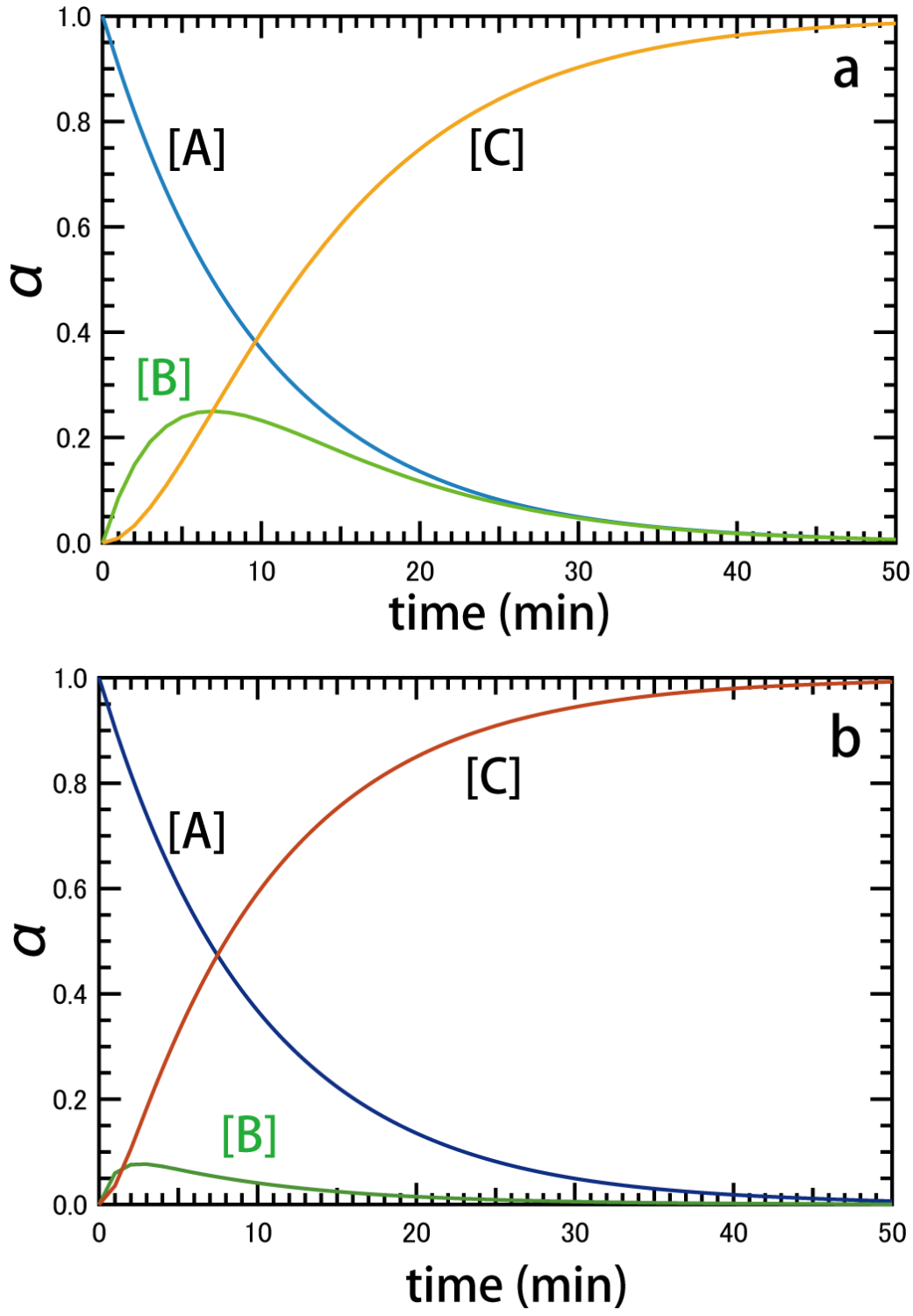

Figure A6. Series first order reactions in concentration of A, B, and C. The case where $[A]_0$ = 1.00, k_1 = 0.1 min^{-1}, k_2= 0.2 min^{-1} **(a)**, and $[A]_0$ = 1.00, k_1 = 0.1 min^{-1}, k_2= 0.2 min^{-1} **(b)** was used in the calculations.

APPENDIX III

Experimental kinetic study of structural evolution of CM

A3.1. Preliminary HTHP experiments for synthesis of graphite

It is well known that synthesis of graphite required a large activation energy of ca. 1000 kJ/mol (e.g., Fischbach 1971). If it attains at 1 atm, kinetic experiments are forced to run at over 3000 K under an anoxic condition. Table A1 shows summary of previous kinetic studies on graphitization. On the other hand, some researchers pointed out that the pressure effect dramatically decrease the heating temperature to form a synthetic graphite (Noda and Kato, 1965; Kamiya et al. 1970; Beyssac et al. 2003; Zhao et al. 2009). Inagaki et al. (1968) reported that graphite can be synthesized at 1500 °C under a 5 kbar using a piston-cylinder type high pressure apparatus. In addition, Beyssac et al. (2003) also reported the synthesized graphite at 1200 °C for 95 hours under a pressure of 1 GPa. These experiments suggest that pressure effects on graphitization can be remarkable at over 5 kb. Based on numerous literatures, I firstly synthesized graphite using natural CM at 1000 to 1500 °C under a pressure 1 GPa. The pressure of 1 GPa is the most reasonable in the case of a piston cylinder-type and a DIA-type high pressure apparatus. Figure A7 displayed the failed run products at various temperatures and heating duration. In the case of encapsulating in cylindrical MgO, almost all natural CM reacted and produced a reaction zone between samples and MgO vessel (Figs. A7a-c). In particular, natural CM in Shimanto accretionary complex completely converted to a white mineral by HPHT experiments. After *HPHT* experiments, I analyzed the white mineral using XRD, micro-Raman spectroscopy, and SEM observations (Figs. A8, A9, A10). The results of XRD and

micro-Raman spectroscopy found that it neither matched magnesia, nor carbonate, brucite, carbide minerals. Under the SEM observations, the reaction zone demonstrated the symplectite textures which comprised newly grown microlite with MgO (Figs. A10d-f). Such reaction zone consists of MgO, graphite and fluoride minerals. Chemical composition mapping of Al-F-Mg shows Al and F zonation from rim to core, suggesting the mineralization of Al-rich and pure fluorides. The fluorides are originated from the residues when I extracted from the natural mudstones using HF-HCl treatment. This suggests that it is important to eliminate the fluorides in starting material as much as possible before experiments. For high temperature experiments, almost all natural CMs have disappeared owing to the reaction with MgO (Figs. A7e and A11). Under a SEM, small amount of graphite with fluoride can be seen in the restricted grain boundaries of MgO (Fig. A11b).

The preliminary experiments suggested two important prerequisites for graphitization experiments using natural CMs; (1) the purity and (2) cell material. Figure A12 displays XRD profiles of starting materials I have used for preliminary experiments. Both samples contained a lot of fluorides in the residues, therefore, they converted to fluoride microlite in an MgO cell. In addition, previous studies on kinetic experiments used Pt tubes as a protection from the reaction between sample and MgO. For these reasons, I firstly tried to concentrate the CM as much as possible by repeating HF-HCl treatments (see details in APPENDIX I). Thereafter, I started to use different sizes of Pt tubes (φ2.0mm and φ3.0mm).

A3.2. Experimental conditions of high pressure apparatus

All experiments were carried out with both starting materials together in a single run so as to reduce any apparent difference in absolute temperature conditions. After welding

and encapsulating, the platinum capsules were placed in three different pressure apparatus for appropriate treatment of temperature and time; (1) The piston-cylinder (PC) high-pressure apparatus (Fig. A13a) (2) The DIA-type high-pressure apparatus (AMAGAEL; Fig. A13b) (3) The Kawai-type high-pressure apparatus (Fig. A13c). For the PC experiments, the assembly was composed of a talc-Pyrex-graphite furnace with MgO disks as pressure medium (3/4 inch diameter; Fig. A14b). Two platinum capsules were placed at the center of graphite heater. Experimental temperature was measured by type S (Pt-Pt_{90}-Re_{10}) thermocouples. For experiments using the DIA-type high-pressure apparatus, the cubic pyrophyllite with edge length of 21 mm was adopted as pressure medium and the tungsten carbide anvils with top edge length was 15 mm for runs at 1 and 2 GPa (Fig. A14a). Temperature was monitored using $W_{97}Re_3$-$W_{75}Re_{25}$ thermocouples with Al_2O_3 insulating sleeves, whose junction was placed in contact with the center of MgO disk. For experiments using the Kawai-type high-pressure apparatus, pressure media was composed of a Cr_2O_3-doped MgO octahedron with 18 mm edge length for run at 4 and 8 GPa (Fig. A14c). The powder samples encapsulated by Pt tube were placed at the center of graphite heater with MgO disk. Temperature was monitored using $W_{97}Re_3$-$W_{75}Re_{25}$ thermocouples with Al_2O_3 insulating sleeves, whose junction was placed at the contact between two Pt tubes. The pressure cell assembly was compressed using tungsten carbide cubes with 11 mm truncation edge lengths for runs at 4 and 8 GPa.

A3.2. Temperature-power rations

Annealing temperatures of all experiments were monitored using $W_{97}Re_3$-$W_{75}Re_{25}$ thermocouples. It is important to avoid the graphite heater using Al_2O_3 insulating sleeves because tungsten thermocouples can be easily converted to a carbide under a HPHT condition. In this study, experimental temperatures were controlled utilizing a

temperature control method. Temperature is proportional to the supply of power and shows a linear relationship, therefore, I carefully checked the temperature-power relations (Fig. A15). There are some differences of linear relation between temperature and power at the same temperatures, resulting from the error of temperature measurement, thermal insulation properties, load pressure, and cell assembly. The experiments were carried out with a heating rate of about 100 °C/min and quenching by switching off the furnace power.

Figures in APPENDIX III

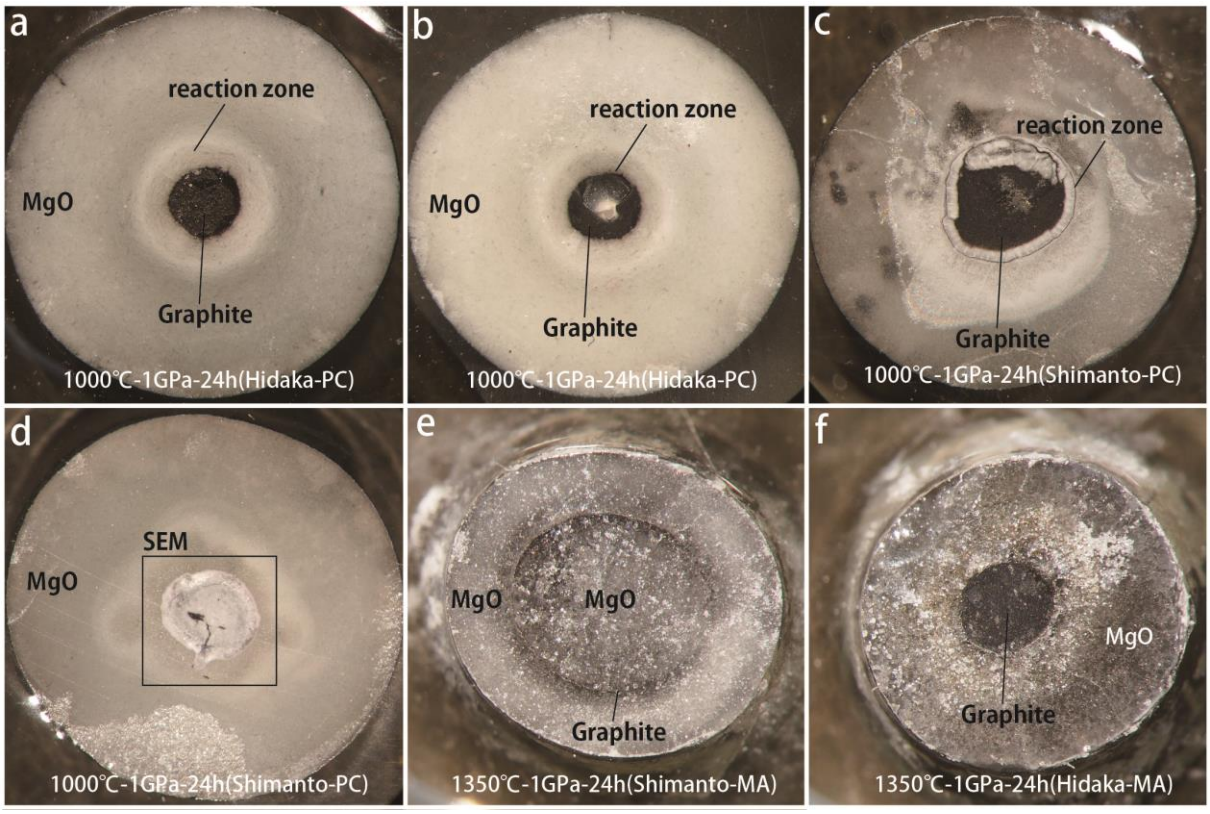

Figure A7. Photomicrographs of polished run products. These samples were recovered from failed experiments of HMB **(a, b)** and SM **(c, d)** at 1000 °C for 24 hours using piston-cylinder type high pressure apparatus. The SM **(e)** and HMB **(f)** samples within MgO capsules were recovered at 1350 °C for 24 hours using a DIA-type high pressure apparatus.

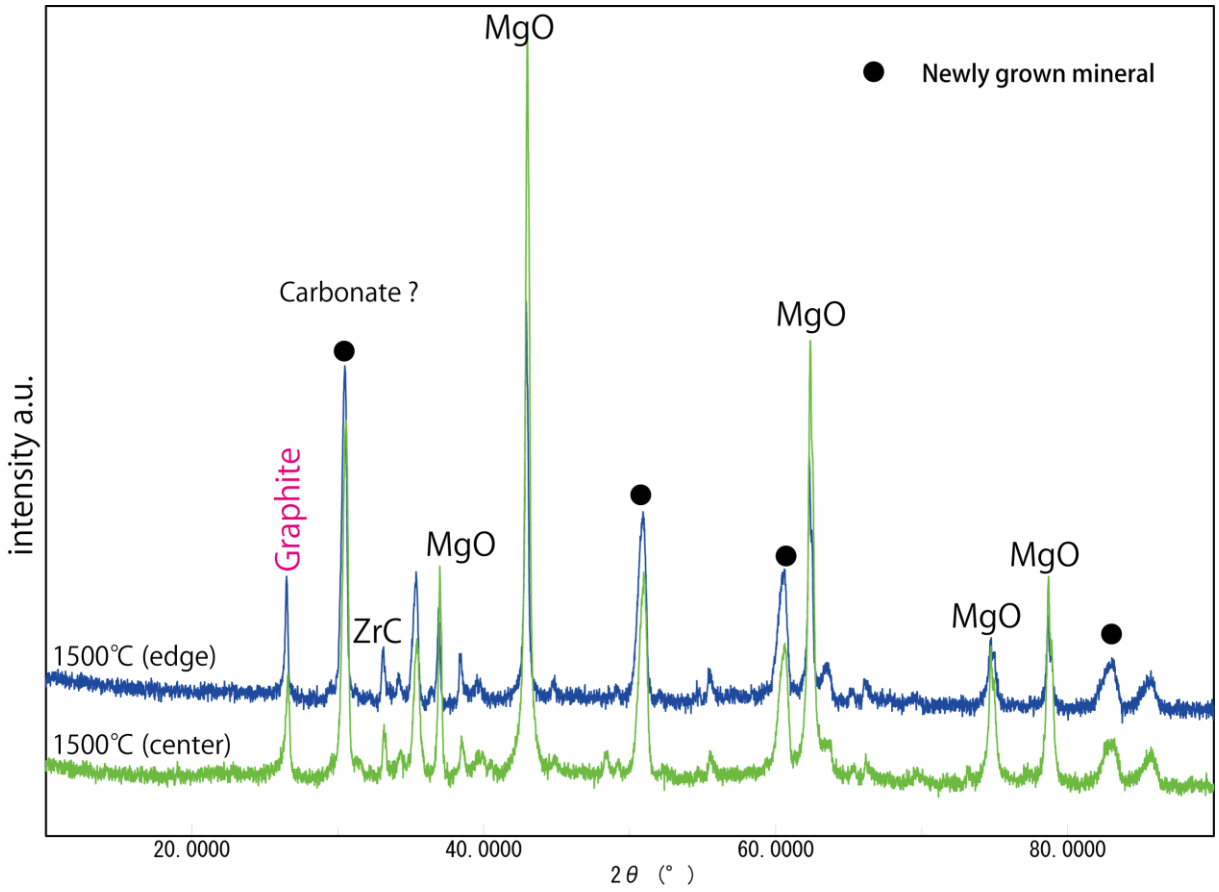

Figure A8. XRD profiles of run products, recovered from the edge part (blue) and center part (green) of starting material.

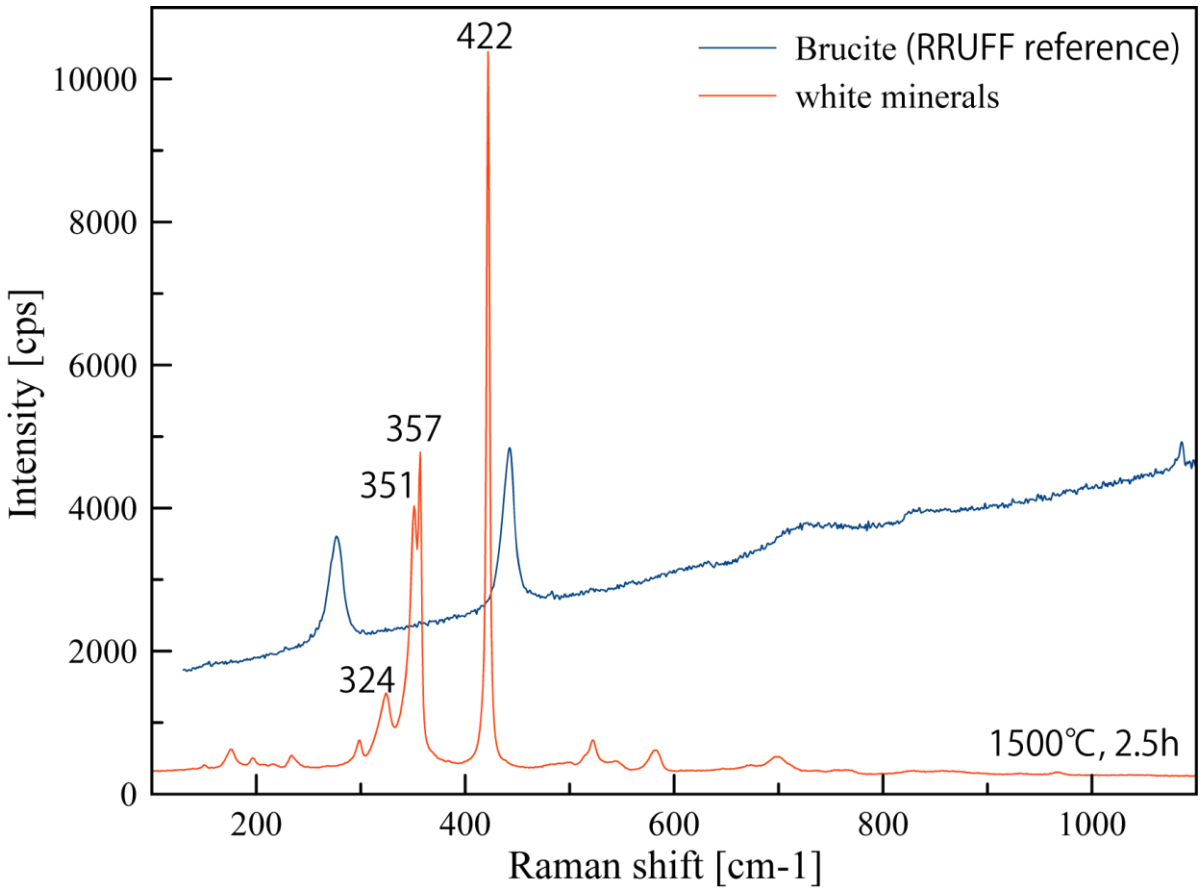

Figure A9. Raman profile of white mineral in the run product, which synthesized at 1500 °C for 2.5 hours. Blue profile of brucite cited from RRIFF are superposed for reference.

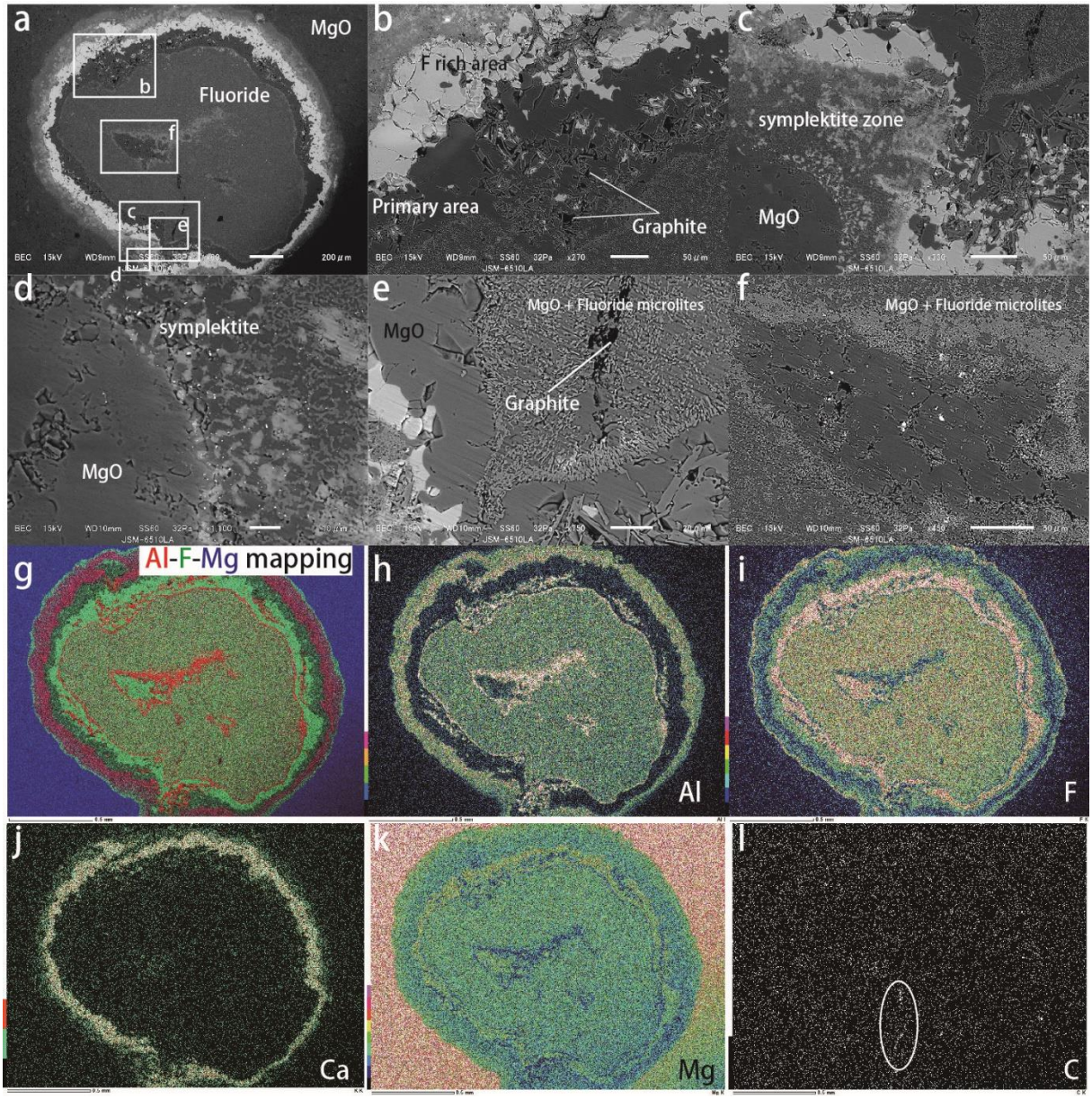

Figure A10. SEM observations of polished run products at 1000 °C for 24 hours. **(a)** Back scattered (BSE) image of reaction zone in MgO capsules. White box shows the analysis area for EDS mapping. **(b)** BSE image of reaction zone under high magnification. **(c)** BSE image of symplectite zone and **(d)** its high magnification image. **(e, f)** Fluoride microlites with graphite in MgO capsule. **(g)** Qualitative map by EDS analysis constructed with Al (red), F (green) and Mg (blue). Intensity map of Al **(h)**, F **(i)**, Ca **(j)**, Mg **(k)**, C **(l)** using a SEM-EDS analysis.

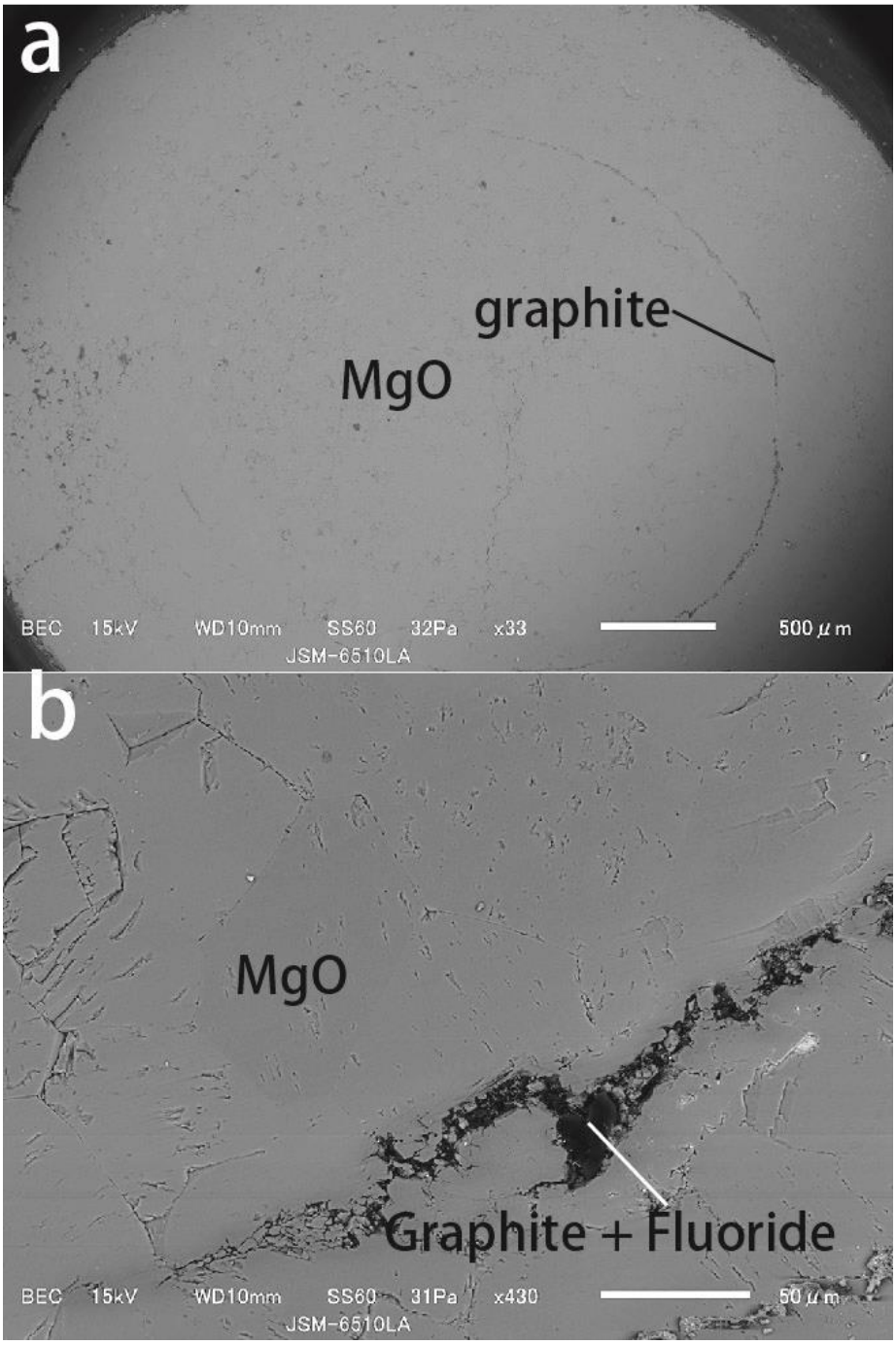

Figure A11. (a) BSE image of the run product at 1350 °C for 24 hours. **(b)** BSE image of same sample under high magnification, showing graphite and fluoride within MgO crystal.

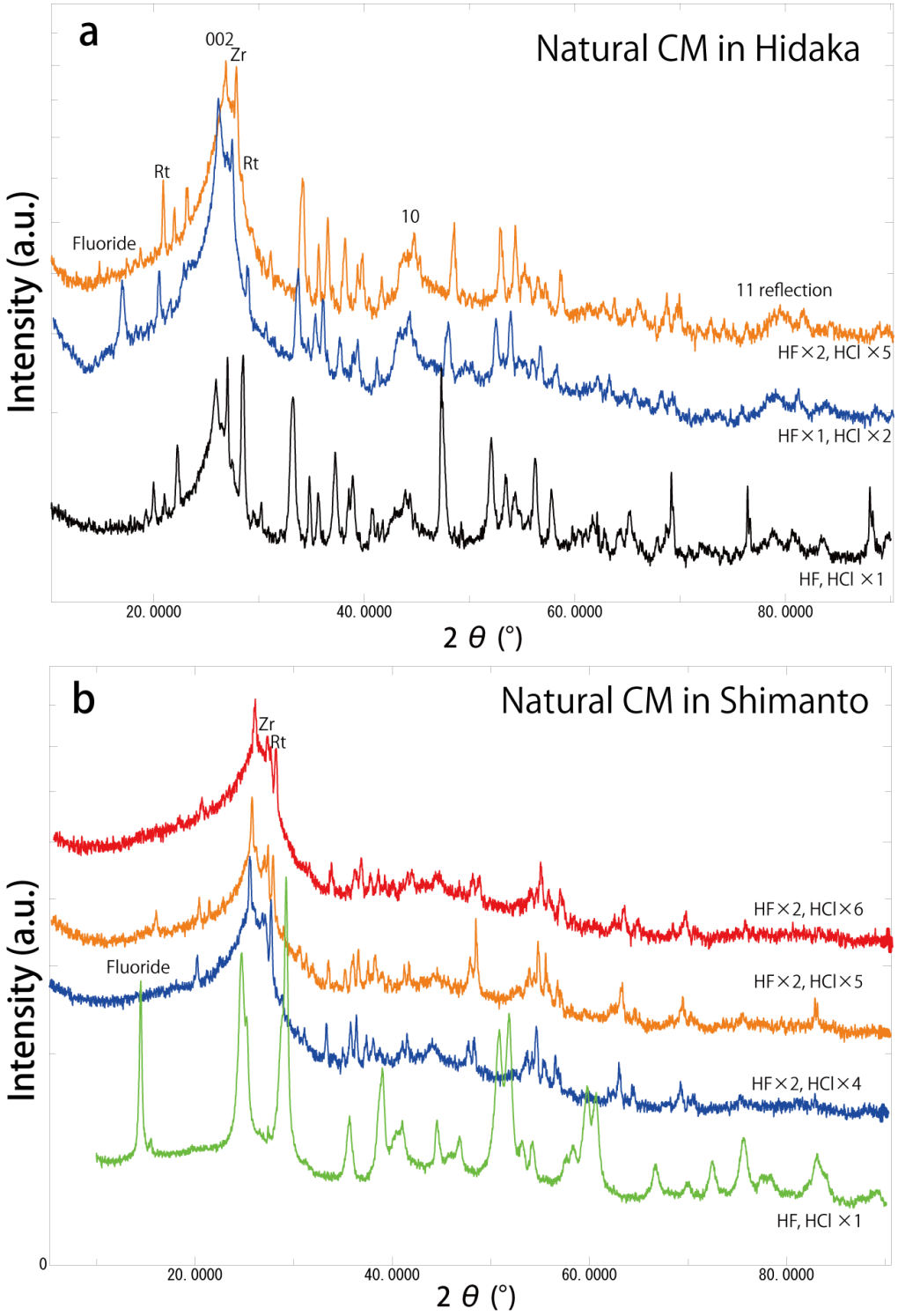

Figure A12. XRD profiles of a sequence of products after the chemical extraction by HF and HCl. Both samples are purified from 1 to 6 times using HF and HCl solutions.

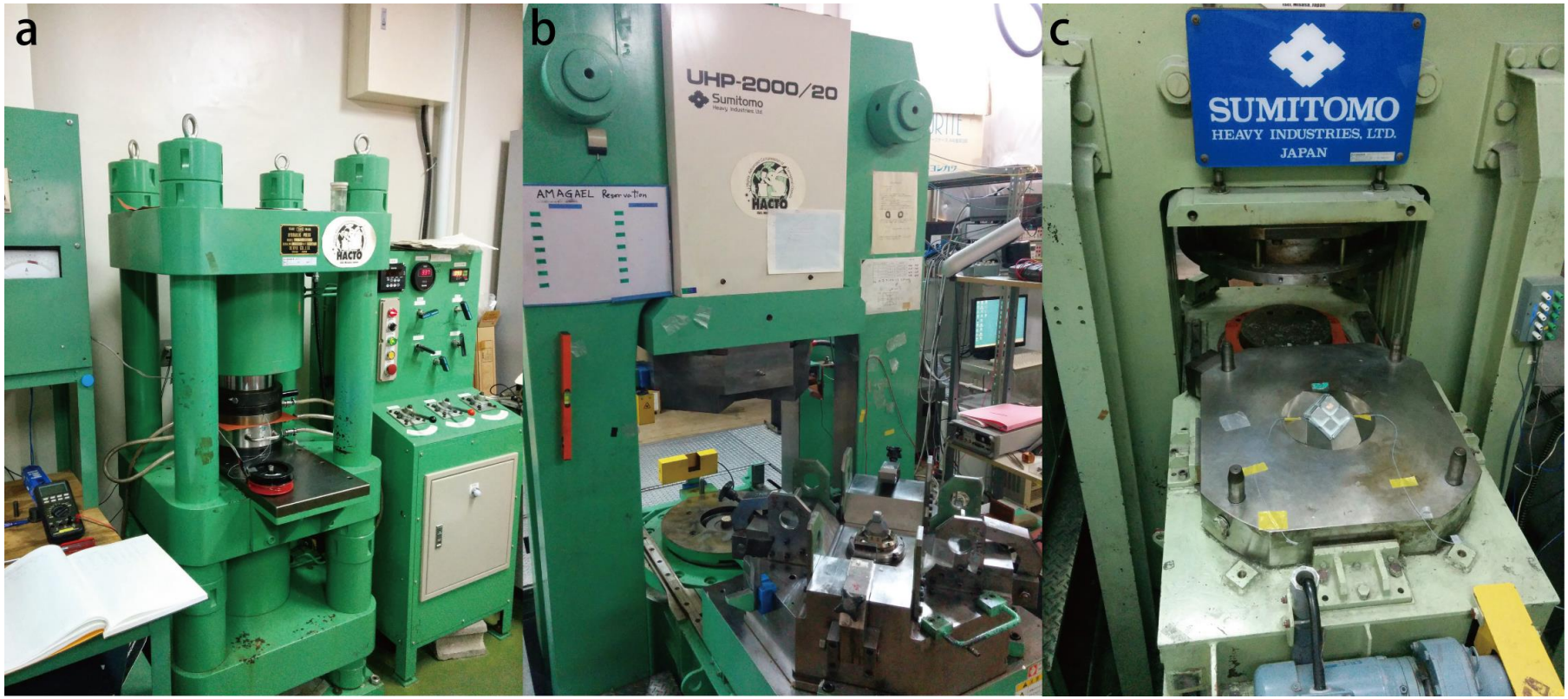

Figure A13. Photographs of high pressure apparatus used in this study. All three types are installed at the Institute for Planetary Materials, Okayama University at Misasa. **(a)** Piston cylinder-type high pressure apparatus. **(b)** DIA-type 2000 *t* multianvil press **(c)** Kawai-type 1000 *t* multi anvil press.

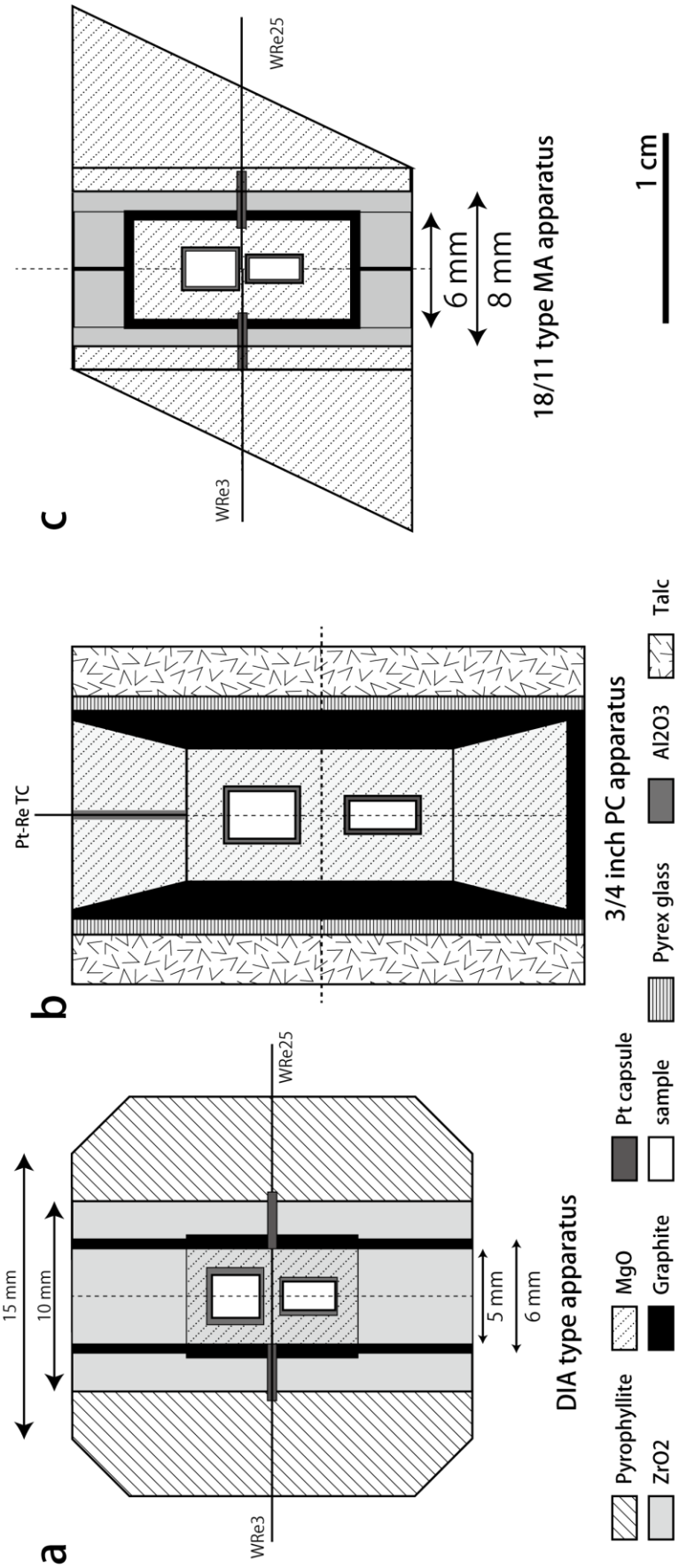

Figure A14. Schematic cross-sections of the sample assembly for **(a)** the piston–cylinder apparatus, **(b)** the DIA-type multi anvil apparatus, and **(c)** the Kawai-type multi anvil apparatus.

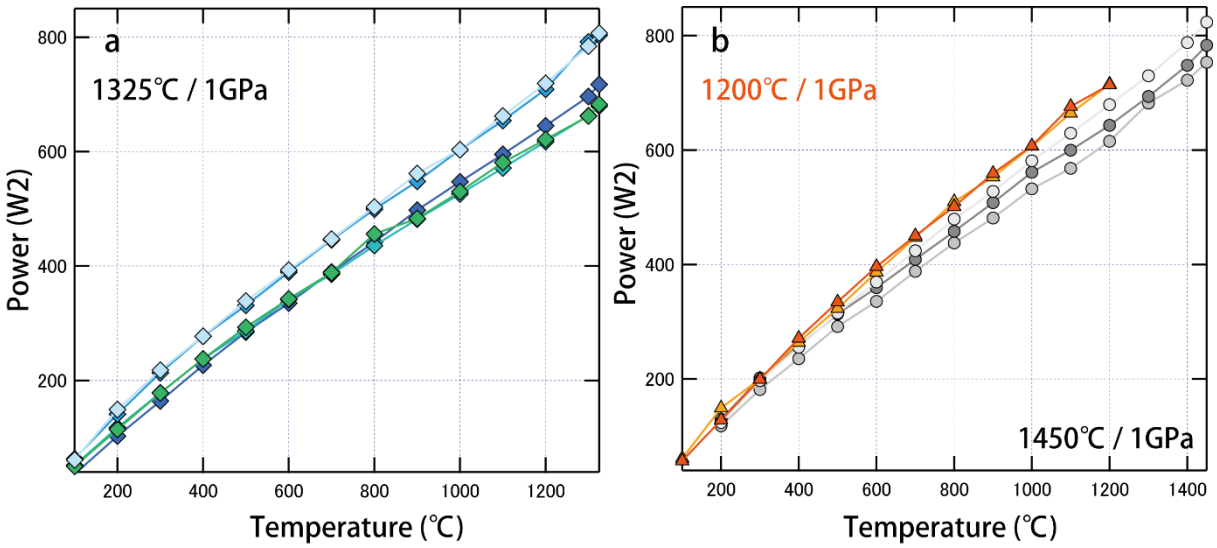

Figure A15. Temperature-power relations at 1325 °C **(a)**, 1200 °C and 1450 **(b)** under a pressure of 1 GPa utilizing a DIA-type multianvil apparatus.

Table 1. Illite and chrolite crystallinity (IC and ChC) values corrected by JIC standards.

sample	mean (CIS-dry)	mean (CIS-EG)	ChC(002)-AD	ChC(002)-EG
lw11081301	0.378	0.350	0.169	0.171
lw11081300	0.348	0.358	0.170	0.196
lw11080805	0.563	0.544	0.370	0.460
lw11080804	0.602	0.597	0.356	0.390
lw11080802	0.453	0.519	0.310	0.350
lw11080801	0.390	0.389	0.228	0.213
lw11081108	0.349	0.352	0.218	0.170
lw11081105	0.356	0.403	0.150	0.157
lw11081103	0.294	0.270	0.145	0.107
lw11081304	0.327	0.350	0.159	0.162
lw11081303	0.300	0.252	0.127	0.135
lw11081302	0.292	0.308	0.124	0.122
lw11062601	0.326	0.391	0.179	0.194
31s11080908	0.264	0.252	0.130	0.109
31s11080906	0.241	0.255	0.111	0.114
31s11080903	0.231	0.226	0.122	0.140
lw11081112	0.274	0.281	0.132	0.143
lw11081111	0.294	0.333	0.168	0.192
Og11070712	0.388	0.375	0.170	0.159
Og1070709	0.463	0.415	0.217	0.235
Og070707	0.370	0.399	0.156	0.158
Og070706	0.439	0.433	0.248	0.235
Og11070703	0.336	0.345	0.139	0.150
lw11070202	0.447	0.368	0.166	0.176
kp11082408	0.425	0.461	0.161	0.154
Kp11082404	0.522	0.452	0.193	0.206
Kp11070507	0.513	0.467	0.256	0.264
Kp11070505	0.416	0.406	0.173	0.178
Kp11070503	0.631	0.399	0.366	0.159
Kp11070501	0.664	0.457	0.389	0.250
kp11082409	0.456	0.373	0.135	0.165
2s11081902	0.354	0.377	0.198	0.181
UD12071400	0.738	0.650	0.398	0.477
UD12071401	0.631	0.551	0.340	0.375
UD12071402	0.535	0.511	0.325	0.272
UD12071404	0.590	0.485	0.298	0.270
UD12071106	0.623	0.534	0.291	0.300
UD12071110	0.517	0.465	0.276	0.330
UD12071113	0.476	0.381	0.204	0.212
130s12071115	0.413	0.374	0.228	0.243
130s12071116	0.393	0.413	0.215	0.233
130s12071117	0.309	0.334	0.110	0.106
130s12071120	0.460	0.389	0.248	0.235

Note: They are mean values analyzed by a glass slide method.

Table 1 (continued). Illite and chrolite crystallinity (IC and ChC) values corrected by JIC standa

sample	mean (CIS-dry)	mean (CIS-EG)	ChC(002)-AD	ChC(002)-EG
130s12071124	0.598	0.547	0.325	0.374
130s12071125.5	0.510	0.391	0.239	0.263
130s12071127	0.494	0.443	0.238	0.258
130s12071129	0.469	0.404	0.227	0.225
131s12071401	0.477	0.459	0.229	0.259
131s12071402	0.301	0.280	0.113	0.151
131s12071404	0.455	0.481	0.221	0.240
131s12071406	0.343	0.333	0.164	0.220
131s12071408.5	0.377	0.410	0.210	0.191
131s12071410	0.183	0.257	0.105	0.099
131s12071413	0.298	0.280	0.152	0.126
131s12071415	0.362	0.343	0.146	0.144
131s12071417	0.392	0.373	0.164	0.114
Kp12070602	0.564	0.564	0.269	0.269
Kp12070606	0.525	0.426	0.285	0.307
Kp12070609	0.819	0.742	0.287	0.450
Kpf12070601	1.275	0.888	0.365	0.560
Kpf12070602	0.604	0.505	0.307	0.280
Kpf12070603	0.762	0.584	0.377	0.420
Kpf12070604	0.671	0.624	0.318	0.370
14072101	0.289	0.309	0.164	0.157
14072102	0.377	0.379	0.204	0.194
14072103	0.597	0.597	0.393	0.345
14072104	0.799	0.821	0.650	0.562
15091600	0.776	0.678	0.282	0.280
15091601	0.590	0.567	0.313	0.375
15091603	0.731	0.697	0.406	0.652
15091604	1.073	0.870	0.466	0.570
15091606	0.912	0.627	0.486	0.655
15091607	0.671	0.616	0.444	0.630
15091608	0.711	0.746	0.490	0.500
15091701	0.926	0.763	0.299	0.318
15091704	1.199	0.946	0.317	0.392
15091705	0.718	0.712	0.323	0.402
15091706	0.729	0.675	0.364	0.499
15091707	0.671	0.692	0.535	0.410
15091708	0.704	0.637	0.373	0.422
15091709	0.987	0.810	0.455	0.415
15091710	0.772	0.740	0.383	0.485
15091711	0.684	0.708	0.425	0.450
15091712	0.820	0.659	0.409	0.374
15091713	0.664	0.640	0.311	0.320
P57	0.674	0.702	0.470	0.470
P58	0.684	0.613	0.325	0.367

Note: They are mean values analyzed by a glass slide method.

Table 2. XRF whole rock major elements of metasediments in this study area.

	ks11091602 Bt-Ms gneiss	ks12082516 Bt-Ms schist	N42 Pelitic rocks	N78 Pssamitic rocks	mean	1σ
SiO_2	60.67	57.60	64.33	66.15	62.19	3.81
TiO_2	0.82	0.89	0.92	0.62	0.81	0.13
Al_2O_3	17.56	18.45	17.66	13.65	16.83	2.16
Fe_2O_3*	5.93	6.82	4.95	4.83	5.63	0.93
MnO	0.08	0.09	0.06	0.07	0.07	0.01
MgO	3.13	3.64	2.54	2.89	3.05	0.46
CaO	1.77	1.97	1.47	1.68	1.72	0.21
Na_2O	2.85	3.36	2.73	3.60	3.13	0.41
K_2O	4.03	4.29	3.64	1.97	3.48	1.04
P_2O_5	0.12	0.15	0.17	0.11	0.14	0.03
L.O.I	2.59	2.36	1.84	4.73	2.88	1.28
Total	99.55	99.61	100.31	100.31	99.94	0.42

Table 3. The crystal parameters of natural carbonaceous materials by XRD study.

Sample	Distance	d(002)	FWHM	Lc(002)	d(110)	FWHM	La(110)	d(004)	FWHM	Lc(004)	d(112)	FWHM	La(112)	d(006)	FWHM	Lc(006)
15091704	-6599	3.509	4.45	20.35												
15091604	-5995	3.459	5.14	17.63												
31s11080606	-2222	3.454	4.83	18.76	1.221	2.33	89.94									
lw11081302	-2476	3.422	4.46	20.33												
lw11081303	-2291	3.439	2.8	32.36												
lw11081103	-2024	3.397	2.27	39.96												
lw11081105	-1880	3.399	2.37	38.27												
lw11081108	-1574	3.403	1.59	57.05	1.230	0.79	264.04									
lw11081111	-1243	3.429	2.87	31.59												
lw11081112	-1303	3.439	2.43	37.31												
4s11080101	-66	3.394	1.99	45.59												
4s11080102	-134	3.366	1.27	71.46												
5s11080606	-334	3.381	2.66	34.11												
Pt11091503	-1086	3.415	3.09	29.35												
Pt11073108	-906	3.434	3.7	24.50												
Pt11073102	-311	3.391	2.06	44.04	1.229	1.41	148.01									
15091802	-557	3.405	2.2	41.23												
15091803	-149	3.364	1.535	59.13	1.231	0.63	331.02									
15091804	143	3.369	1.183	76.71												
Sn11073004	156	3.382	0.93	97.56	1.231	0.92	226.68									
Sn11080104	193	3.374	1.217	74.56	1.232	0.79	263.82	1.691	0.63	157.57						
Sn11080504	216	3.361	1.092	83.12	1.232	1.06	196.62	1.688	0.92	107.99						
Sn11080503	160	3.380	1.32	68.74	1.232	0.83	251.09									
Sn11073001	243	3.373	1.299	69.86	1.232	0.65	320.66	1.678	1.4	71.03						
Sn11080105	208	3.363	1.169	77.64	1.232	0.63	331.37	1.688	1.14	87.11						
Sn11080501	420	3.368	1.11	81.76	1.232	0.70	297.65	1.689	0.62	160.19						
R11081801	494	3.378	1.306	69.48												
Ks11091301	573	3.361	0.82	110.69												
Ks11091302	650	3.362	0.838	108.31	1.232	0.57	365.65	1.682	0.65275	152.31						
Ks11091303	750	3.369	0.94	96.55	1.239	0.54	384.48	1.660	0.67	148.94						
Ks11091304	1221	3.365	0.49	185.22	1.230	0.53	393.59	1.666	0.96	103.34						
Ks11091305	1301	3.358	0.469	193.54	1.235	0.52	400.03	1.682	0.44	200.79						
Ks11062814	1024	3.356	0.783	115.93				1.684	0.7	142.02						
Ks1s11080204	972	3.365	0.445	203.95				1.683	0.74	134.36						
Ks1s11080209	1343	3.359	0.489	185.62	1.232	0.34	612.96	1.681	0.58	171.42	1.160	2.30	51.41			
Ks11091307	1615	3.353	0.436	208.20	1.231	0.40	521.15	1.685	0.62	160.33	1.157	0.87	136.15			
Ks11091308	1790	3.360	0.291	311.91	1.230	0.29	719.15	1.682	0.43	231.21	1.153	1.61	73.78			
Ks11091309	2192	3.357	0.2874	315.84	1.232	0.31	672.38	1.680	0.403	246.80	1.157	0.98	120.86	1.087	0.40	313.13
Ks12082516	2900	3.359	0.199	456.21	1.232	0.14	1543.70	1.679	0.211	471.30	1.157	0.55	215.41	1.087	0.40	313.29
Ks11091404	2295	3.365	0.191	475.17	1.232	0.22	947.42	1.682	0.23	432.34	1.157	0.75	158.01			
Ks11091600	3422	3.350	0.2182	416.04	1.231	0.18	1158.08	1.690	0.167	594.80	1.156	0.22	538.94	1.086	0.27	464.60
ks11091602	3967	3.357	0.108	840.46	1.232	0.12	1694.27	1.681	0.115	864.73	1.156	0.12	987.68	1.086	0.13	964.42

Table 4. The graphitization parameters of micro-Raman spectroscopy in Hidaka metamorphic belt.

Sample name	Latitude	Longitude	Distance * (m)	micro-Raman spectroscopy																								
				G band [cm^{-1}]	1σ	G FWHM	1σ	D1band [cm^{-1}]	1σ	D1 FWHM	1σ	R1 ratio	1σ	R2 ratio	1σ	RA1	1σ	RA2	1σ	I_{D3+D4}/I_G	1σ	La (Å)	T^1 (°C)	T^2 (°C)	T^3 (°C)	T^4 (°C)	T^5 (°C)	T^6 (°C)	N
Karupesinape River route																												
Kp11070505	42.61368	142.92545	-3804	1596	2.64	47.70	4.57	1334.70	2.45	100.40	4.20	1.09	0.10	0.68	0.01	0.66	0.01	1.96	0.11	0.26	0.04	<20		267.33		357.21	375.25	262.14	26
Kp11070504	42.61354	142.92626	-4006	1597	4.46	49.29	8.51	1335.39	1.80	93.89	6.79	1.21	0.13	0.67	0.02	0.67	0.01	1.99	0.11	0.24	0.06	<20		291.27		361.81	382.51	276.13	26
Kp11070501	42.61326	142.92814	-4163	1597	3.74	50.76	6.09	1333.32	2.30	103.65	6.39	1.11	0.12	0.67	0.01	0.65	0.02	1.89	0.13	0.25	0.07	<20		278.01		346.95	360.31	255.15	26
kp11082409	42.61507	142.91581	-3397	1601	2.60	44.13	7.84	1340.28	0.98	83.47	2.81	1.18	0.15	0.68	0.04	0.66	0.02	1.94	0.16	0.24	0.05	<20		282.61		354.08	371.49	298.53	24
Kp12070602	42.61500	142.92749	-4169	1598	3.74	42.71	5.65	1333.24	2.58	99.21	7.60	0.94	0.11	0.67	0.02	0.66	0.01	1.90	0.09	0.21	0.05	<20		257.09		349.20	362.88	264.69	25
Kp12070606	42.61718	142.92700	-4270	1599	2.96	42.47	6.72	1333.20	2.67	102.97	9.36	0.90	0.11	0.68	0.03	0.65	0.02	1.89	0.12	0.25	0.10	<20		237.21		346.87	359.90	256.61	25
Kp12070609	42.61996	142.92659	-4388	1597	2.71	45.64	5.23	1331.58	1.48	110.32	8.74	0.91	0.08	0.67	0.01	0.65	0.02	1.85	0.13	0.25	0.07	<20		242.58		340.18	350.27	240.82	25
Kpf12070601	42.60979	142.92930	-4194	1599	3.04	44.73	6.59	1336.67	2.43	99.94	8.61	1.03	0.12	0.69	0.03	0.67	0.02	2.03	0.21	0.23	0.06	<20		244.50		365.91	390.80	263.13	25
Kpf12070602	42.60559	142.93381	-4156	1600	3.71	41.65	6.52	1334.49	2.33	104.59	8.24	0.94	0.15	0.70	0.05	0.67	0.03	2.05	0.30	0.22	0.07	<20		222.01		368.10	396.63	253.14	25
Kpf12070603	42.60172	142.93849	-4344	1600	3.31	41.19	5.90	1334.48	3.55	102.75	10.82	0.86	0.14	0.67	0.02	0.65	0.01	1.86	0.11	0.22	0.07	<20		238.65		341.93	352.41	257.09	25
Kpf12070604	42.60051	142.94423	-4755	1597	4.37	47.65	7.13	1333.62	2.03	119.27	11.23	0.87	0.09	0.67	0.03	0.63	0.03	1.70	0.17	0.33	0.10	<20		235.73		314.60	316.78	221.57	25
Ueda River route																												
Iw15091701	42.64095	142.94730	-6923	1604	0.74	45.63	2.35	1357.17	3.35	115.99	5.29	0.53	0.02	0.59	0.02	0.58	0.02	1.38	0.13	0.41	0.02							228.63	28
Iw15091702	42.64384	142.94726	-7087	1601	1.12	53.71	5.40	1358.18	7.45	134.73	10.70	0.64	0.09	0.62	0.02	0.60	0.03	1.48	0.16	0.31	0.03							188.32	24
Iw15091703	42.64787	142.94314	-6931	1598	2.03	64.01	6.48	1367.33	5.43	153.58	10.70	0.67	0.07	0.62	0.01	0.64	0.04	1.79	0.28	0.29	0.05							147.79	29
Iw15091705	42.64973	142.93189	-6130	1606	0.55	35.56	2.70	1344.76	4.95	100.17	4.33	0.48	0.06	0.59	0.04	0.63	0.02	1.72	0.19	0.29	0.07							262.64	28
P58	42.65239	142.92466	-5695	1605	0.46	36.49	1.49	1347.02	3.08	100.69	3.51	0.46	0.04	0.57	0.02	0.62	0.02	1.64	0.11	0.34	0.04							261.52	30
Iw15091706	42.65558	142.92146	-5585	1606	0.55	34.11	1.48	1344.51	1.38	100.40	3.61	0.49	0.03	0.60	0.02	0.62	0.03	1.64	0.19	0.30	0.03							262.14	26
Iw15091709	42.66440	142.92039	-5747	1606	0.53	34.69	1.03	1344.43	1.72	99.84	3.71	0.48	0.02	0.59	0.01	0.62	0.02	1.61	0.10	0.28	0.03							263.34	26
Iw15091710	42.66592	142.91992	-5893	1606	0.50	34.15	0.97	1343.09	2.14	100.05	4.03	0.49	0.03	0.60	0.02	0.63	0.02	1.68	0.12	0.27	0.04							262.89	25
Iw15091712	42.66953	142.91906	-5907	1605	0.54	34.45	1.05	1340.74	0.66	101.65	3.47	0.57	0.02	0.63	0.01	0.64	0.01	1.76	0.07	0.26	0.02							259.45	26
Iw15091713	42.67163	142.91900	-5926	1606	0.43	36.03	1.03	1339.97	1.03	103.27	4.24	0.61	0.04	0.64	0.02	0.63	0.02	1.70	0.13	0.26	0.03							255.96	27
UD12071100	42.65744	142.91577	-4895	1600	2.20	48.51	4.03	1336.18	1.42	114.98	6.33	0.91	0.09	0.67	0.01	0.64	0.01	1.74	0.08	0.30	0.05	<20		245.93		324.30	327.47	230.79	25
UD12071104	42.65963	142.90672	-4223	1598	2.90	46.08	4.90	1332.87	2.06	113.26	7.28	0.93	0.10	0.69	0.02	0.65	0.01	1.90	0.08	0.27	0.05	<20		233.16		348.33	361.35	234.49	25
UD12071106	42.65921	142.90574	-4140	1599	2.19	42.04	5.38	1332.42	1.44	106.26	4.27	0.88	0.11	0.67	0.01	0.66	0.01	1.90	0.07	0.21	0.04	<20		242.16		349.30	362.67	249.55	25
UD12071110	42.65852	142.90083	-3532	1599	2.45	43.10	4.17	1333.23	1.96	104.52	5.20	0.95	0.10	0.68	0.01	0.66	0.01	1.95	0.09	0.21	0.04	<20		243.82		355.48	372.29	253.28	25
UD12071113	42.65896	142.89795	-3420	1595	2.35	44.74	3.41	1341.94	1.72	80.69	7.00	1.46	0.14	0.69	0.01	0.68	0.01	2.11	0.07	0.20	0.05	<20		294.49		378.39	409.30	304.51	25
UD12071115	42.65930	142.89652	-3417	1598	2.87	48.57	5.48	1338.58	1.85	93.48	5.61	1.19	0.14	0.69	0.02	0.67	0.01	2.00	0.11	0.26	0.05	<20		272.85		362.58	383.62	277.03	24
UD12071116	42.66096	142.89618	-3483	1591	3.92	47.78	5.47	1343.54	1.97	70.58	8.71	1.62	0.14	0.68	0.03	0.67	0.02	2.03	0.19	0.21	0.06	27		325.18		366.76	392.17	326.26	25
UD12071117	42.66200	142.89547	-3375	1588	3.34	53.74	3.46	1343.11	2.21	66.01	5.98	1.94	0.15	0.68	0.01	0.68	0.02	2.11	0.18	0.22	0.06	23		327.92		376.72	408.50	336.08	25
UD12071120	42.66303	142.89430	-3275	1586	2.94	54.11	3.39	1343.84	1.43	62.37	3.20	1.81	0.11	0.65	0.02	0.65	0.02	1.89	0.15	0.21	0.02	24		358.32		346.47	359.75	343.90	25
UD12071122	42.66385	142.89324	-3325	1585	2.91	56.42	3.56	1342.58	2.27	64.18	7.47	1.93	0.13	0.67	0.01	0.67	0.01	2.02	0.10	0.20	0.03	23		340.69		365.17	387.79	340.02	23
UD12071124	42.66447	142.89285	-3525	1596	4.02	47.05	5.33	1333.53	2.31	113.66	5.27	0.97	0.11	0.69	0.02	0.66	0.02	1.91	0.15	0.29	0.05	<20		232.09		349.36	364.06	233.62	25
UD12071125.5	42.66494	142.89208	-2975	1598	2.95	51.44	3.59	1344.28	1.48	93.37	6.21	1.31	0.09	0.70	0.01	0.68	0.01	2.10	0.12	0.25	0.04	<20		268.15		376.15	406.19	277.26	27
UD12071127	42.66661	142.89033	-2869	1593	3.22	55.81	2.62	1344.18	1.13	81.22	5.68	1.49	0.10	0.68	0.01	0.64	0.03	1.80	0.21	0.30	0.05	<20		315.40		331.52	340.24	303.38	26
UD12071129	42.66741	142.88681	-2700	1595	2.22	48.72	2.47	1346.11	1.40	62.12	6.79	1.91	0.19	0.68	0.01	0.68	0.02	2.17	0.21	0.21	0.04	23		327.50		385.12	423.28	344.45	23
131s12071401	42.65829	142.89678	-3054	1598	2.80	46.16	4.53	1342.03	2.05	84.38	9.69	1.28	0.13	0.69	0.02	0.68	0.01	2.09	0.10	0.22	0.04	<20		280.71		375.85	405.30	296.58	27
131s12071402	42.65773	142.89588	-2961	1595	3.52	50.78	4.96	1340.17	2.18	90.46	7.04	1.30	0.08	0.69	0.01	0.67	0.01	2.05	0.09	0.27	0.03	<20		279.91		369.76	395.00	283.50	27
131s12071404	42.65820	142.89413	-2884	1596	3.20	48.73	4.43	1341.97	2.04	82.63	8.13	1.40	0.12	0.70	0.01	0.68	0.01	2.11	0.08	0.23	0.03	<20		286.09		377.42	407.81	300.34	24
131s12071406	42.65722	142.89307	-2806	1585	3.12	52.68	3.67	1342.53	2.58	65.71	8.04	2.05	0.18	0.70	0.02	0.69	0.02	2.22	0.24	0.19	0.05	<20		311.38		390.05	432.91	336.73	23
131s12071408.5	42.65669	142.89177	-2715	1585	3.53	51.33	3.50	1344.53	2.30	57.64	5.82	1.91	0.13	0.65	0.01	0.66	0.02	1.94	0.16	0.18	0.04	23		357.20		353.82	371.10	354.08	24
131s12071413	42.65471	142.88656	-2342	1584	3.35	51.65	4.31	1344.74	2.06	58.78	5.25	1.80	0.13	0.65	0.02	0.65	0.03	1.90	0.22	0.16	0.07	24		363.06		346.52	361.92	351.63	26
131s12071415	42.65513	142.88339	-2130	1590	2.94	56.72	3.58	1344.25	1.86	65.76	4.91	1.89	0.10	0.67	0.02	0.67	0.02	2.01	0.16	0.24	0.04	23		336.74		363.93	387.03	336.61	26
131s12071417	42.65499	142.88091	-1933	1589	2.27	53.93	4.09	1345.51	1.42	56.70	4.31	2.11	0.15	0.67	0.02	0.67	0.02	2.08	0.16	0.17	0.04	21		337.57		373.58	402.62	356.09	26

Table 4 (continued). The graphitization parameters of micro-Raman spectroscopy in Hidaka metamorphic belt.

Sample name	Latitude	Longitude	Distance * (m)	micro-Raman spectroscopy																		La (Å)	T^{1} (°C)	T^{2} (°C)	T^{3} (°C)	T^{4} (°C)	T^{5} (°C)	T^{6} (°C)	N
				G band [cm^{-1}]	1σ	G FWHM	1σ	D1band [cm^{-1}]	1σ	D1 FWHM	1σ	R1 ratio	1σ	R2 ratio	1σ	RA1	1σ	RA2	1σ	I_{D3+D4}/I_G	1σ								
Iwanai River route																													
Iw15091600	42.63941	142.94754	-6900	1603	0.57	45.06	2.04	1356.32	4.00	112.65	3.03	0.53	0.04	0.59	0.02	0.59	0.02	1.45	0.13	0.42	0.04			258.51				235.79	30
Iw15091601	42.63939	142.94582	-6750	1604	0.95	42.83	3.32	1353.49	6.90	112.30	4.04	0.52	0.05	0.60	0.05	0.61	0.02	1.54	0.16	0.37	0.06			241.61				236.56	29
Iw15091602	42.64087	142.94204	-6513	1604	0.69	42.24	1.32	1353.60	2.51	106.34	3.21	0.49	0.02	0.57	0.01	0.60	0.01	1.53	0.07	0.41	0.02			267.80				249.36	30
Iw15091603	42.64095	142.93649	-6112	1604	0.99	39.40	2.72	1348.55	4.01	103.84	4.04	0.48	0.04	0.57	0.03	0.61	0.01	1.57	0.09	0.37	0.03			263.83				254.75	30
Iw15091604	42.64288	142.93352	-5995	1603	1.01	43.82	3.38	1354.85	6.20	111.83	6.31	0.52	0.03	0.59	0.02	0.58	0.03	1.38	0.17	0.40	0.05			253.74				237.57	28
Iw15091606	42.63753	142.94957	-6954	1603	0.52	48.85	1.97	1360.57	2.51	122.71	3.31	0.52	0.01	0.59	0.01	0.57	0.02	1.32	0.09	0.42	0.02			255.17				214.18	29
Iw15091607	42.63737	142.95327	-7141	1603	1.06	50.94	2.37	1360.11	2.00	123.01	4.94	0.56	0.03	0.59	0.01	0.58	0.03	1.42	0.16	0.44	0.03			258.22				213.54	25
Iw15091608	42.63854	142.95567	-7373	1604	1.06	46.32	4.23	1356.38	5.25	119.08	7.08	0.54	0.03	0.60	0.02	0.56	0.03	1.29	0.15	0.40	0.04			245.62				221.98	26
Iw11081301	42.63886	142.89353	-2755	1586	4.00	58.13	5.67	1343.08	1.94	72.33	8.93	1.73	0.19	0.65	0.02	0.64	0.03	1.77	0.22	0.27	0.05	25		354.62		325.56	332.63	322.48	25
Iw11081108	42.64094	142.87666	-1574	1580	2.76	35.28	2.15	1346.83	1.76	42.90	1.98	1.21	0.15	0.57	0.02	0.57	0.06	1.36	0.28	0.03	0.05	36		398.95		242.44	241.62	385.78	25
Iw11081105	42.64271	142.87830	-1880	1580	2.98	40.29	3.62	1346.22	1.91	45.86	3.10	1.43	0.19	0.59	0.03	0.57	0.06	1.37	0.32	0.14	0.07	31		405.75		243.19	244.15	379.40	26
Iw11081103	42.64341	142.88064	-2024	1581	2.89	41.36	4.41	1346.26	1.95	47.32	5.69	1.59	0.18	0.61	0.02	0.61	0.05	1.62	0.29	0.11	0.07	28		392.06		297.08	300.59	376.25	25
Iw11081304	42.64251	142.88302	-2190	1588	3.15	53.61	4.74	1344.22	1.97	60.25	5.66	2.09	0.14	0.67	0.02	0.66	0.03	1.93	0.26	0.23	0.05	21		337.26		350.33	369.10	348.46	24
Iw11081303	42.63958	142.88629	-2291	1585	3.94	56.26	5.38	1342.14	2.33	67.90	7.26	1.81	0.19	0.65	0.02	0.63	0.04	1.73	0.28	0.24	0.05	24		355.38		317.39	324.53	332.01	26
Iw11081302	42.63877	142.88981	-2476	1586	3.53	58.07	4.27	1342.82	2.20	67.62	7.35	1.89	0.16	0.66	0.01	0.66	0.02	1.92	0.16	0.25	0.03	23		350.02		350.40	365.93	332.63	26
31s11080906	42.63588	142.88788	-2222	1589	2.04	50.57	5.92	1346.51	1.20	52.09	4.30	2.14	0.23	0.65	0.03	0.67	0.04	2.05	0.39	0.21	0.09	21		356.80		363.20	394.74	366.01	24
Iw11081112	42.64186	142.87256	-1303	1581	3.12	46.35	5.66	1345.73	1.75	49.68	4.62	1.73	0.24	0.62	0.04	0.59	0.06	1.49	0.32	0.19	0.10	25		392.51		270.38	271.86	371.20	26
Iw11081111	42.64315	142.87177	-1243	1581	2.16	41.06	1.95	1345.94	1.43	47.07	1.95	1.59	0.08	0.61	0.01	0.60	0.03	1.51	0.21	0.13	0.05	28		391.55		278.59	275.28	376.80	25
Iw11080802	42.64111	142.91493	-3572	1598	2.64	42.21	3.85	1333.54	3.03	112.62	5.36	0.87	0.07	0.69	0.02	0.66	0.02	1.96	0.14	0.24	0.07	<20		217.35		356.96	375.54	235.87	25
Og11070706	42.63356	142.90230	-2525	1597	2.39	46.03	3.32	1341.64	1.64	81.45	6.80	1.36	0.08	0.70	0.02	0.68	0.01	2.14	0.11	0.24	0.06	<20		278.37		381.48	415.16	302.89	25
Satsunai River route																													
Sn14072101	42.58223	142.90862	-1091	1599	2.94	39.90	3.47	1343.25	1.91	76.53	6.24	1.32	0.13	0.69	0.02	0.68	0.01	2.15	0.12	0.18	0.04	<20		283.60		382.85	417.82	313.45	
Sn14072102	42.58621	142.91625	-1650	1594	3.58	48.52	4.36	1348.26	1.56	57.70	6.24	1.88	0.18	0.66	0.03	0.64	0.07	1.93	0.58	0.23	0.08	<20		346.51		336.34	367.88	353.95	
Sn14072103	42.58637	142.92734	-2327	1597	2.33	48.64	2.85	1346.91	1.56	76.93	10.01	1.44	0.19	0.67	0.02	0.65	0.03	1.91	0.28	0.23	0.06	<20		322.15		347.87	365.45	312.60	
Sn14072104	42.59455	142.95281	-4123	1600	1.82	48.18	4.62	1341.35	1.31	114.74	4.31	0.77	0.11	0.63	0.02	0.61	0.01	1.59	0.08	0.37	0.05	<20		263.36		297.83	294.06	231.31	
Sn04091901	42.62569	142.85864	538	1579	2.51	30.83	1.91	1346.98	2.02	38.24	2.17	0.90	0.10	0.51	0.02							49	415.03	419.58	417.39				25
Sn11082801	42.62785	142.85439	688	1576	2.91	26.72	2.98	1345.07	3.09	48.07	4.42	0.30	0.09	0.32	0.07							148	498.95	485.21	508.04				24
Snf11090101	42.62923	142.83335	2263	1575	2.61	18.04	1.74	1345.56	2.75	47.37	5.17	0.12	0.05	0.20	0.07							373	551.66	559.80	568.30				24
Sn11082803	42.62998	142.85333	699	1578	3.24	24.56	2.81	1348.78	2.67	46.22	3.26	0.25	0.06	0.30	0.04							176	509.62	497.64	520.03				25
Snf11090102	42.62950	142.84029	1715	1574	2.54	19.85	3.05	1345.22	2.71	48.27	4.34	0.15	0.07	0.25	0.12							299	527.63	510.94	540.51				25
Sn11082804	42.63200	142.85080	802	1576	2.39	25.51	2.27	1346.51	1.67	47.00	3.83	0.35	0.06	0.36	0.04							125	480.39	454.84	487.43				25
Snf11091002	42.62794	142.84434	1505	1577	2.78	20.96	3.15	1347.97	3.77	48.15	4.70	0.16	0.04	0.24	0.07							278	533.89	529.29	547.69				25
Sn11082805	42.63111	142.84849	1005	1576	3.33	26.21	2.84	1346.51	3.15	48.04	3.03	0.28	0.07	0.30	0.06							157	505.65	496.33	515.55				26
Sn11082806	42.62925	142.84677	1197	1575	2.47	24.29	3.29	1347.21	2.84	50.10	6.01	0.22	0.06	0.30	0.11							199	505.46	479.20	515.33				25
Snf11091001	42.62905	142.83180	2398	1577	1.42	17.58	1.32	1347.36	2.81	47.24	4.64	0.14	0.05	0.24	0.06							321	533.80	522.69	547.59				25
Sn11082606	42.61733	142.86820	105	1579	2.68	35.49	3.68	1346.08	1.97	43.37	3.77	1.13	0.14	0.55	0.03							39	395.59	408.43	397.31				25
Sn11082102	42.62273	142.86287	278	1578	3.07	31.60	2.00	1346.39	2.34	39.87	2.96	0.82	0.11	0.49	0.03							54	422.51	422.23	425.19				25
Sn11082103	42.62401	142.86075	389	1578	3.38	30.61	2.52	1346.58	2.57	38.69	3.00	0.79	0.10	0.48	0.03							56	427.55	428.69	430.49				24
Mt11081904	42.61981	142.85849	756	1579	2.62	28.33	2.08	1347.97	2.18	39.95	3.00	0.57	0.09	0.42	0.03							77	452.17	441.06	456.70				25
Sn11082101	42.61780	142.86577	297	1580	3.00	31.30	2.21	1348.07	2.28	38.91	2.25	0.98	0.10	0.53	0.02							45	404.44	407.51	406.40				25
Mt11081901	42.62268	142.85919	572	1577	2.92	28.92	2.44	1346.11	2.15	39.41	3.35	0.65	0.13	0.44	0.04							68	443.24	437.72	447.12				25
Mt11081903	42.62123	142.85875	688	1577	2.75	29.40	1.92	1345.90	2.13	38.96	3.17	0.61	0.09	0.43	0.04							72	449.07	443.62	453.36				25
Sn11073004	42.59615	142.88187	156	1580	2.55	29.14	2.71	1348.00	2.27	38.03	3.13	0.77	0.08	0.47	0.03							57	430.47	432.65	433.57				25
Sn11080102	42.60307	142.87851	38	1579	3.19	36.44	5.58	1347.26	1.95	42.39	5.90	1.03	0.20	0.52	0.04							43	410.08	428.51	412.24				24
Sn11073001	42.59826	142.87846	243	1577	2.43	33.76	3.59	1345.66	1.85	41.37	3.28	0.82	0.11	0.48	0.04							53	429.31	439.14	432.35				25
Sn11080105	42.60395	142.87442	208	1579	2.95	31.89	3.22	1347.03	2.30	40.31	2.98	0.88	0.13	0.50	0.03							50	416.47	419.29	418.89				25
Sn11080104	42.60267	142.87534	193	1577	2.68	31.73	2.96	1345.88	2.06	41.35	2.36	0.82	0.13	0.50	0.04							54	420.30	416.61	422.89				25
Sn11080503	42.61093	142.87105	160	1576	3.63	32.97	1.74	1344.92	2.65	41.50	1.91	0.98	0.12	0.53	0.02							45	404.49	407.76	406.45				24
Sn11080504	42.61198	142.86960	216	1579	2.86	32.37	2.95	1346.97	2.08	40.43	2.85	0.93	0.15	0.52	0.03							47	411.35	415.36	413.56				25
Sn11080501	42.60686	142.86993	420	1577	2.98	31.15	2.22	1346.24	2.23	41.10	2.15	0.75	0.08	0.48	0.03							58	428.93	424.56	431.95				25
3s11083101	42.58425	142.88708	257	1578	2.75	29.73	2.22	1346.60	2.19	38.31	2.85	0.69	0.10	0.45	0.03							64	442.59	444.72	446.43				24
Sn04091901	42.60685	142.86816	538	1579	2.51	30.83	1.91	1346.98	2.02	38.24	2.17	0.90	0.10	0.51	0.02							49	415.03	419.58	417.39				25
Md11081201	42.58823	142.88319	386	1578	2.78	29.18	2.37	1346.97	2.20	38.87	2.81	0.73	0.09	0.48	0.02							60	429.21	421.74	432.24				23
R11081801	42.59173	142.88047	494	1577	3.29	30.23	2.37	1346.20	2.26	41.30	2.86	0.70	0.15	0.46	0.03							63	434.08	426.15	437.39				24
3s11083102	42.58271	142.88600	432	1575	3.57	29.56	2.60	1345.20	2.73	41.69	3.16	0.58	0.13	0.42	0.04							75	452.60	445.49	457.16				25
Sn04090301	42.63944	142.82221	2611	1581	0.70	15.72	1.76	1346.66	2.64	44.48	4.01	0.06	0.06	0.11	0.11							777	592.88	639.84	617.22				25
Sn04092011	42.63835	142.81570	3138	1580	1.74	15.97	1.75	1349.02	2.10	42.37	2.02	0.06	0.05	0.11	0.08							727	593.10	641.56	617.48				24
Sn04091704	42.64349	142.80927	3560	1580	0.59	16.28	1.59	1349.78	1.41	43.09	5.66	0.07	0.07	0.13	0.11							590	582.28	619.98	604.48				24

Table 4 (continued). The graphitization parameters of micro-Raman spectroscopy in Hidaka metamorphic belt.

Sample name	Latitude	Longitude	Distance * (m)	micro-Raman spectroscopy																								
				G band [cm^{-1}]	1σ	G FWHM	1σ	D1band [cm^{-1}]	1σ	D1 FWHM	1σ	R1 ratio	1σ	R2 ratio	1σ	RA1	1σ	RA2	1σ	I_{D3+D4}/I_G	1σ	La (Å)	T^1 (°C)	T^2 (°C)	T^3 (°C)	T^4 (°C)	T^5 (°C)	T^6 (°C)	N
Pitoitoppi river route																												
Pt11091501	42.60870	142.88703	-748	1577	0.77	34.75	1.81	1345.40	0.54	49.84	2.43	1.10	0.12	0.58	0.02	0.58	0.03	1.40	0.16	0.07	0.02	40	383.89	376.55	385.40			370.84	25
Pt11091503	42.60905	142.88934	-1086	1584	2.91	42.87	3.65	1346.44	2.14	46.98	4.71	2.05	0.23	0.66	0.02	0.67	0.02	2.01	0.14	0.11	0.05	21	347.44	352.36	349.09			377.00	24
Pt11073108	42.60914	142.88669	-906	1582	2.84	40.03	3.12	1346.48	1.86	45.49	3.74	1.75	0.20	0.64	0.02	0.62	0.03	1.67	0.20	0.08	0.05	25	356.25	369.32	357.76			380.20	24
Pt11073106a	42.60697	142.88308	-531	1581	3.84	40.46	3.48	1346.16	2.68	47.16	5.38	1.62	0.21	0.62	0.02	0.62	0.04	1.62	0.26	0.07	0.04	27	362.93	378.80	364.37			376.61	24
Ks15091802	42.60690	142.88301	-557	1585	1.11	37.58	3.98	1349.77	1.26	41.88	3.66	1.65	0.19	0.61	0.02	0.63	0.10	1.85	0.72	0.13	0.06		370.02	397.56	371.44			387.95	26
Pt11073102	42.60504	142.88042	-311	1579	2.46	36.46	3.20	1346.18	1.65	44.38	3.75	1.37	0.20	0.60	0.03	0.58	0.04	1.39	0.19	0.04	0.02	32	374.32	385.65	375.75			382.58	24
Ks15091803	42.60313	142.88008	-149	1582	0.93	31.74	1.48	1349.21	1.09	40.39	2.19	1.10	0.15	0.56	0.02	0.53	0.07	1.18	0.30	0.07	0.04		394.00	400.88	395.68			391.16	28
Ks15091804	42.59995	142.87836	143	1582	1.19	29.98	2.00	1349.74	1.10	37.34	1.78	0.99	0.18	0.53	0.03	0.54	0.03	1.18	0.16	0.02	0.02		406.63	413.51	408.66			397.72	28
4 no sawa route																												
4s11080102	42.60065	142.88236	-134	1580	2.98	37.58	4.47	1346.50	1.91	44.64	3.90	1.27	0.18	0.57	0.04	0.56	0.04	1.31	0.18	0.08	0.04	35	386.89	405.29	388.43			382.03	25
5 no sawa route																												
5s11080602	42.61891	142.86894	-64	1581	2.75	35.33	2.85	1347.78	1.95	43.12	3.14	1.29	0.16	0.58	0.02	0.58	0.06	1.44	0.27	0.05	0.06	34	381.87	396.13	383.35			385.30	25
5s11080606	42.61916	142.87297	-334	1584	1.95	42.81	5.88	1347.67	1.48	46.31	5.76	1.94	0.18	0.64	0.02	0.64	0.04	1.79	0.26	0.11	0.08	23	354.03	368.30	355.56			378.44	17
5s11082604	42.62339	142.87181	-422	1584	3.40	41.20	3.74	1347.39	2.40	48.50	6.22	1.98	0.21	0.66	0.03	0.65	0.02	1.84	0.14	0.12	0.04	22	347.38	352.53	349.04			373.72	25
5s11082603	42.62244	142.87133	-313	1584	1.74	40.02	1.76	1347.80	1.07	44.32	1.99	1.90	0.15	0.65	0.02	0.65	0.02	1.87	0.15	0.03	0.03	23	352.04	363.04	353.60			382.71	25
6 no sawa route																												
6s110829t	42.63427	142.83191	2138	1577	2.70	19.81	1.83	1347.72	2.94	47.42	3.21	0.16	0.07	0.24	0.07							275	532.93	527.41	546.59				25
6s111082901	42.63557	142.83189	2075	1576	2.20	20.39	2.40	1347.66	2.43	46.73	2.55	0.15	0.05	0.22	0.07							301	543.11	547.79	558.35				25
6s11082902	42.63659	142.83229	1955	1576	2.69	21.44	3.24	1347.46	3.62	48.26	3.06	0.16	0.07	0.23	0.08							275	538.21	540.17	552.68				25
6s11082910	42.64323	142.84937	420	1578	2.04	29.62	2.57	1346.38	2.22	39.84	4.83	0.72	0.12	0.46	0.04							61	435.58	434.96	438.98				23
6s110882801	42.63283	142.83742	1790	1576	2.69	21.58	2.64	1346.63	3.20	48.38	3.85	0.20	0.08	0.28	0.10							219	518.11	503.75	529.64				24
6s11082802	42.63315	142.83465	2014	1576	2.62	20.79	2.36	1347.22	2.90	49.48	3.87	0.15	0.04	0.24	0.07							292	533.08	525.06	546.76				24
6s11082803	42.63401	142.83248	2126	1576	2.63	19.37	1.77	1346.17	2.78	47.84	4.30	0.13	0.06	0.21	0.07							350	548.79	555.24	564.96				24
6s11082908	42.64210	142.84552	833	1577	3.24	28.62	3.36	1346.68	2.73	39.27	4.12	0.52	0.08	0.40	0.03							84	462.78	455.73	468.17				25
6s11082909	42.64169	142.84928	521	1580	2.09	27.26	2.21	1348.61	1.67	35.88	2.29	0.69	0.10	0.45	0.03							64	439.81	438.08	443.48				25
6s11082905	42.64188	142.83856	1286	1578	2.73	24.81	2.25	1348.06	2.72	46.50	4.21	0.26	0.07	0.30	0.08							172	507.93	495.20	518.12				23
6s14072201	42.64689	142.84999	235	1580	2.76	31.26	1.94	1348.27	2.37	37.71	2.81	0.95	0.11	0.51	0.02							46	411.99	420.60	414.22				
6s14072202	42.64890	142.84834	286	1579	3.24	29.86	2.03	1347.77	2.53	38.19	2.99	0.70	0.11	0.46	0.03							63	437.81	434.94	441.35				
6s14072202.5	42.64994	142.84737	332	1577	4.00	28.14	3.94	1346.37	3.19	36.99	4.71	0.66	0.15	0.45	0.05							66	441.80	437.14	445.60				
6s14072203	42.65250	142.84681	335	1578	3.65	29.39	3.33	1346.83	2.82	38.78	4.06	0.67	0.14	0.43	0.09							66	448.22	454.18	452.46				
6s14072204	42.65580	142.84599	329	1576	3.03	28.54	3.03	1346.41	2.15	40.17	3.51	0.59	0.09	0.42	0.09							74	452.74	447.39	457.31				
6s14072205	42.65824	142.84591	281	1580	2.15	28.79	2.21	1348.30	1.84	36.56	2.50	0.75	0.14	0.45	0.10							59	439.49	448.80	443.13				
6s14072206	42.66225	142.84790	285	1581	2.57	29.60	3.10	1349.49	2.17	38.18	2.78	0.76	0.09	0.48	0.02							58	428.22	424.84	431.20				
6s14072207	42.66165	142.84342	649	1581	1.98	26.65	1.79	1349.73	1.52	36.89	2.61	0.59	0.09	0.42	0.09							75	456.28	455.18	461.13				
6s14072208	42.66211	142.84005	1009	1580	1.72	26.34	2.08	1349.42	1.71	38.30	2.62	0.58	0.14	0.42	0.05							75	453.77	448.47	458.43				
7 no sawa route																												
7s11091001	42.63180	142.82487	3137	1580	1.78	16.61	1.35	1349.18	2.19	44.70	2.94	0.09	0.04	0.18	0.07							500	562.30	576.18	580.77				25
7s11082706	42.61734	142.82715	3235	1578	2.41	17.62	1.20	1347.31	2.12	45.52	4.04	0.13	0.06	0.23	0.07							337	537.20	528.89	551.51				23
7s14072003	42.60404	142.82342	4088	1580	0.67	13.00	1.45	1349.98	1.96	37.03	16.01	0.05	0.05	0.09	0.09							975	600.80	655.22	626.79				23
7s14072004	42.60954	142.82233	3903	1580	0.63	15.73	1.86	1349.65	2.62	41.41	2.65	0.06	0.05	0.10	0.09							731	594.55	644.95	619.23				24
7s14072006	42.61722	142.82334	3533	1580	0.72	15.69	1.56	1349.25	2.29	41.45	3.80	0.09	0.07	0.14	0.10							514	576.95	610.60	598.13				24

Table 4 (continued). The graphitization parameters of micro-Raman spectroscopy in Hidaka metamorphic belt.

Sample name	Latitude	Longitude	Distance * (m)	micro-Raman spectroscopy																								
				G band [cm^{-1}]	1σ	G FWHM	1σ	D1band [cm^{-1}]	1σ	D1 FWHM	1σ	R1 ratio	1σ	R2 ratio	1σ	RA1	1σ	RA2	1σ	I_{D3+D4}/I_G	1σ	La (Å)	T^1 (°C)	T^2 (°C)	T^3 (°C)	T^4 (°C)	T^5 (°C)	T^6 (°C)	N
Koikakushu-Satsunai River route																												
Ks15091805	42.59782	142.87550	511	1581	0.84	29.17	1.47	1349.71	0.81	36.60	1.16	0.88	0.10	0.51	0.02	0.50	0.06	1.02	0.20	0.04	0.04		414.67	414.86	417.01				28
Ks11091301	42.59700	142.87455	573	1576	3.22	30.68	2.18	1345.76	3.39	41.69	1.90	0.67	0.09	0.45	0.03							65	441.97	439.91	445.77				25
Ks11091302	42.59664	142.87403	650	1575	3.29	29.52	2.18	1345.87	3.34	41.71	2.96	0.57	0.09	0.41	0.03							78	457.46	453.32	462.41				25
Ks05091301	42.59676	142.87413	613	1580	2.47	29.39	2.64	1348.50	2.20	38.68	3.97	0.73	0.20	0.47	0.04							60	431.41	426.94	434.56				25
Ks05091302	42.59676	142.87273	674	1576	3.00	29.31	2.69	1346.45	2.33	41.19	4.41	0.58	0.14	0.42	0.06							76	453.03	445.74	457.63				25
Ks11091303	42.59644	142.87320	750	1579	2.68	29.07	2.25	1348.41	2.36	39.18	3.12	0.65	0.10	0.44	0.03							68	443.57	437.92	447.48				25
Ks05091305	42.59503	142.86768	1229	1580	3.02	29.03	2.52	1348.51	2.59	38.33	2.30	0.68	0.08	0.46	0.03							65	438.10	431.87	441.65				24
Ks11062806	42.59616	142.87083	835	1578	2.08	29.92	2.66	1347.00	1.75	39.09	2.97	0.72	0.10	0.46	0.03							61	436.88	436.54	440.36				25
Ks11062814	42.59599	142.86994	1024	1581	3.57	30.26	2.32	1349.68	2.69	40.96	3.03	0.68	0.12	0.46	0.04							65	437.70	430.77	441.23				25
Ks1s11080201.5	42.59887	142.87042	779	1577	3.25	30.03	2.04	1346.34	2.58	39.89	3.46	0.66	0.13	0.44	0.04							67	443.36	440.42	447.26				25
Ks1s11080202	42.59930	142.86924	835	1577	2.43	22.98	3.33	1345.22	2.48	49.43	4.44	0.22	0.07	0.30	0.08							197	509.66	489.98	520.08				23
Ks1s11080204	42.60014	142.86674	972	1578	2.50	27.19	1.92	1347.87	1.97	39.30	2.75	0.57	0.11	0.43	0.03							78	449.87	435.16	454.23				25
Ks1s11080205	42.60022	142.86579	1048	1577	3.21	23.67	3.58	1348.45	3.48	51.59	3.85	0.22	0.06	0.29	0.05							202	513.48	497.70	524.39				25
Ks11091304	42.59443	142.86815	1221	1578	4.10	27.65	2.05	1348.65	3.32	43.99	3.38	0.38	0.06	0.36	0.04							117	481.98	465.13	489.18				25
Ks1s11080206	42.60090	142.86489	1096	1576	3.03	27.72	2.12	1345.43	2.52	41.21	3.09	0.48	0.08	0.40	0.04							92	465.17	450.37	470.77				23
Ks11091305	42.59533	142.86588	1301	1577	3.18	26.21	2.81	1346.24	2.65	43.59	3.71	0.38	0.07	0.36	0.05							114	479.49	461.44	486.43				25
Ks11091608	42.59548	142.86447	1416	1578	2.84	26.68	2.00	1348.37	2.71	44.15	3.82	0.38	0.11	0.37	0.05							116	478.30	457.24	485.12				24
Ks1s11080209	42.60174	142.86108	1343	1576	2.95	26.33	1.51	1344.91	2.99	44.95	2.91	0.34	0.04	0.35	0.03							128	485.92	466.32	493.53				25
Ks05091309	42.59591	142.86089	1628	1577	2.23	24.96	2.17	1347.92	2.25	46.84	3.68	0.28	0.06	0.31	0.05							159	504.67	492.98	514.45				25
Ks05091308	42.59487	142.85975	1770	1580	1.51	23.41	1.43	1350.47	1.45	45.65	3.72	0.30	0.05	0.34	0.05							148	491.79	467.66	500.04				24
Ks11091307	42.59540	142.86129	1615	1576	2.37	26.38	3.67	1345.82	2.39	48.79	4.81	0.27	0.07	0.32	0.07							161	498.33	477.05	507.34				23
Ks11091308	42.59578	142.85909	1790	1576	3.05	22.29	2.51	1347.42	2.48	49.67	3.57	0.20	0.05	0.27	0.06							224	520.91	509.33	532.83				23
Ks2s11082004	42.59097	142.85998	1957	1576	2.86	24.78	3.82	1346.27	4.05	52.74	6.89	0.22	0.07	0.28	0.08							202	515.18	501.73	526.31				24
Ks2s11082004.5	42.58923	142.85949	2104	1577	1.89	22.43	3.34	1348.80	2.42	48.06	3.71	0.20	0.06	0.27	0.06							219	519.88	508.14	531.66				25
Ks05091307	42.59477	142.85687	1982	1577	3.26	20.29	1.88	1348.99	2.89	46.88	3.61	0.20	0.05	0.28	0.05							222	515.22	496.08	526.36				25
Ks05091306c	42.59462	142.85528	2103	1578	1.48	20.92	2.41	1349.77	1.43	49.31	5.64	0.22	0.06	0.33	0.05							196	495.97	457.45	504.70				24
Ks04080504	42.59414	142.85519	2135	1577	2.05	21.74	3.05	1348.44	3.22	49.55	4.70	0.21	0.03	0.30	0.04							211	508.79	483.82	519.09				24
Ks11091309	42.59473	142.85584	2192	1575	2.89	24.60	4.91	1346.17	2.92	48.20	4.35	0.22	0.08	0.30	0.11							197	509.15	488.73	519.49				23
Ks11091404	42.59633	142.85126	2295	1576	2.04	19.91	1.96	1346.53	2.31	46.67	3.96	0.17	0.06	0.26	0.07							255	526.90	516.73	539.68				24
Ks11083003	42.59233	142.84992	2629	1576	2.14	18.97	2.00	1346.82	2.41	46.52	3.61	0.15	0.08	0.24	0.08							291	536.05	532.35	550.18				24
Ks11083004	42.59220	142.84822	2785	1577	2.39	18.82	2.13	1346.56	2.49	47.03	2.96	0.15	0.06	0.24	0.08							298	535.97	531.06	550.10				24
Ks12082516	42.59246	142.85094	2900	1575	2.41	18.58	2.18	1349.01	2.08	46.01	2.95	0.06	0.03	0.17	0.05							739	565.35	574.73	584.37				25
Ks04081407	42.59178	142.84534	2959	1576	2.80	20.74	1.86	1348.03	2.11	45.75	2.49	0.20	0.03	0.27	0.05							223	522.86	514.17	535.06				25
Ks11091407	42.59074	142.84407	3257	1580	1.12	17.39	1.26	1349.76	1.03	43.87	1.59	0.15	0.05	0.24	0.07							285	532.43	524.62	546.02				25
Ks11091600	42.58967	142.84082	3422	1578	2.64	17.52	1.76	1347.37	3.31	43.94	5.12	0.11	0.05	0.20	0.07							396	553.80	562.84	570.80				25
Ks04092314	42.58948	142.83990	3626	1579	1.77	16.23	1.79	1348.33	1.10	42.78	2.15	0.16	0.05	0.26	0.05							283	523.56	503.74	535.86				25
Ks11091601	42.58884	142.83701	3763	1580	1.69	16.57	1.25	1349.97	1.78	43.53	1.68	0.09	0.04	0.16	0.07							503	568.31	590.45	587.86				25
Ks04092603	42.58687	142.83526	3936	1580	0.41	16.43	0.84	1349.02	0.91	41.08	0.98	0.10	0.04	0.17	0.05							446	563.50	582.33	582.19				25
Ks11091602	42.58771	142.83576	3967	1580	1.00	16.11	1.35	1349.60	2.03	49.55	3.32	0.08	0.05	0.16	0.08							568	571.02	593.90	591.08				25
Ks12071502	42.58615	142.83475	4001	1576	3.42	16.79	1.46	1348.21	3.99	50.33	4.87	0.04	0.02	0.10	0.06							993	595.98	643.42	620.96				25
Ks11091606	42.58100	142.83536	4273	1578	1.89	16.67	1.44	1346.39	2.60	45.87	4.64	0.07	0.02	0.15	0.04							631	573.84	598.25	594.43				23
Ks11091607	42.58832	142.83003	4209	1579	2.75	17.05	0.88	1348.34	2.15	43.66	2.68	0.10	0.04	0.18	0.06							425	558.84	572.63	576.70				25
Mt.Ks11080405	42.58369	142.82827	4658	1579	2.29	16.85	0.87	1348.07	2.61	43.57	2.06	0.12	0.05	0.21	0.08							366	547.47	550.46	563.42				23
Mt.Ks11080403	42.57367	142.82102	5733	1580	0.99	16.06	1.30	1349.09	2.42	42.98	2.39	0.08	0.04	0.16	0.07							563	570.85	593.67	590.87				23
Mt.Ks11080401	42.57074	142.82496	5600	1579	2.01	16.62	0.92	1347.67	1.90	43.38	1.15	0.08	0.04	0.15	0.07							554	575.08	604.19	595.90				25

Table 5. Summary of Raman spectroscopic results of graphite and metamorphic mineral assemblages in host rocks.

Sample name	Distance from biotite isograd (m)	Lithology	Mineral assemblages							Raman data									
			Chl	Ms	Bt	BtP	MsP	Kfs	Crd	G band (cm^{-1})	1 σ	G band FWHM (cm^{-1})	1 σ	R1 ratio	1 σ	R2 ratio	1 σ	*T (°C)*	La (Å)
Pt11091503	-1086	Psammitic rock	++	+	–	–	–	–	–	1584	2.91	42.9	3.65	2.05	0.23	0.66	0.02	347	21
Pt11091501	-1015	Pelitic rock	++	+	–	–	–	–	–	1582	2.87	40.6	2.56	1.95	0.17	0.66	0.02	349	23
Pt11073108	-906	Pelitic rock	++	++	–	–	–	–	–	1582	2.84	40.0	3.12	1.75	0.20	0.64	0.02	356	25
Pt11073106a	-531	Psammitic rock	+	+	–	–	–	–	–	1581	3.84	40.5	3.48	1.62	0.21	0.62	0.02	363	27
Pt11073102	-311	Pelitic rock	+	+	–	–	–	–	–	1579	2.46	36.5	3.20	1.37	0.20	0.60	0.03	374	32
2s11081902	-204	Psammitic rock	+	+	–	–	–	–	–	1580	3.21	42.0	5.65	1.42	0.17	0.59	0.03	380	31
4s11080102	-134	Pelitic rock	+	+	–	–	–	–	–	1580	2.98	37.6	4.47	1.27	0.18	0.57	0.04	387	35
Sn11073004	156	Ms–Bt metasediment	+	+	+	–	–	–	–	1580	2.55	29.1	2.71	0.77	0.08	0.47	0.03	430	57
Sn11080102	38	Ms–Bt metasediment	+	+	+	–	–	–	–	1579	3.19	36.4	5.58	1.03	0.20	0.52	0.04	410	43
Sn11073001	243	Ms–Bt metasediment	+	+	+	–	–	–	–	1577	2.43	33.8	3.59	0.82	0.11	0.48	0.04	429	53
Sn11080105	208	Ms–Bt metasediment	+	+	+	–	–	–	–	1579	2.95	31.9	3.22	0.88	0.13	0.50	0.03	416	50
Sn11080104	193	Ms–Bt metasediment	+	+	+	–	–	–	–	1577	2.68	31.7	2.96	0.82	0.13	0.50	0.04	420	54
Sn11080503	160	Ms–Bt metasediment	+	+	+	–	–	–	–	1576	3.63	33.0	1.74	0.98	0.12	0.53	0.02	404	45
Sn11080504	216	Ms–Bt metasediment	+	+	+	–	–	–	–	1579	2.86	32.4	2.95	0.93	0.15	0.52	0.03	411	47
Sn11080501	420	Ms–Bt metasediment	+	+	+	–	–	–	–	1577	2.98	31.1	2.22	0.75	0.08	0.48	0.03	429	58
3s11083101	257	Ms–Bt metasediment	+	+	+	–	–	–	–	1578	3.07	29.8	2.19	0.68	0.10	0.45	0.03	443	64
Sn04091901	538	Ms–Bt metasediment	+	+	+	–	–	–	–	1579	2.51	30.8	1.91	0.90	0.10	0.51	0.02	415	49
Md11081201	386	Ms–Bt metasediment	+	+	+	–	–	–	–	1578	2.78	29.2	2.37	0.73	0.09	0.48	0.02	429	60
R11081801	494	Ms–Bt metasediment	+	+	+	–	–	–	–	1577	3.29	30.2	2.37	0.70	0.15	0.46	0.03	434	63
3s11083102	432	Ms–Bt metasediment	+	+	+	–	–	–	–	1575	3.57	29.6	2.60	0.58	0.13	0.42	0.04	453	75
Ks11091301	573	Ms–Bt metasediment	+	+	+	–	–	–	–	1574	2.76	30.7	2.18	0.67	0.09	0.45	0.03	442	65
Ks11091302	650	Ms–Bt metasediment	+	+	++	–	–	–	–	1574	2.76	29.5	2.18	0.57	0.09	0.41	0.03	457	78
Ks05091301	613	Ms–Bt metasediment	+	+	+	–	–	–	–	1580	2.47	29.4	2.64	0.73	0.20	0.47	0.04	431	60
Ks05091302	674	Ms–Bt metasediment	+	+	+	–	–	–	–	1576	3.00	29.3	2.69	0.58	0.14	0.42	0.06	453	76
Ks11091303	750	Ms–Bt metasediment	+	+	++	–	–	–	–	1579	2.68	29.1	2.25	0.65	0.10	0.44	0.03	444	68
Ks05091305	1229	Ms–Bt metasediment	×	+	+	–	–	–	–	1580	3.02	29.0	2.52	0.68	0.08	0.46	0.03	438	65
Ks11062806	835	Ms–Bt metasediment	×	+	+	–	–	–	–	1578	2.08	29.9	2.66	0.72	0.10	0.46	0.03	437	61
Ks11062814	1024	Ms–Bt metasediment	×	+	+	–	–	–	–	1581	3.57	30.3	2.32	0.68	0.12	0.46	0.04	438	65
Ks1s11080201	779	Ms–Bt metasediment	×	+	+	–	–	–	–	1577	3.25	30.0	2.04	0.66	0.13	0.44	0.04	443	67
Ks1s11080202	835	Ms–Bt metasediment	×	+	+	–	–	–	–	1575	3.26	23.0	3.33	0.22	0.07	0.30	0.08	510	197
Ks1s11080204	972	Ms–Bt metasediment	×	+	+	–	–	–	–	1578	3.70	27.2	1.92	0.57	0.11	0.43	0.03	450	78

Note; ++, Abundant; +, Moderate; ×, Poor; –, Absent; Chl, Chlorite; Ms, Muscovite; Bt, Biotite; BtP, Biotite porphyroblast; MsP, Muscovite porphyroblast; Kfs, K-feldspar; Crd, Cordierite. All samples include abundant quartz and plagioclase. Distance from the biotite isograd is measured from geological map. Mean values of *T* (°C) and La(Å) are calculated by the Raman spectroscopy of carbonaceous materials thermometry and crystal size following Beyssac et al. (2002a) and Tuinstra and Koenig (1970), respectively.

Table 5 (Continued). ummary of Raman spectroscopic results of graphite and metamorphic mineral assemblages in host rocks.

Sample name	Distance from biotite isograd (m)	Lithology	Mineral assemblages							Raman data									
			Chl	Ms	Bt	BtP	MsP	Kfs	Crd	G band (cm^{-1})	1 σ	G band FWHM (cm^{-1})	1 σ	R1 ratio	1 σ	R2 ratio	1 σ	T (°C)	La (Å)
Ks1s11080205	1048	Ms–Bt metasediment	×	+	++	–	–	–	–	1576	4.47	23.7	3.58	0.22	0.06	0.29	0.05	513	202
Ks11091304	1221	Ms–Bt metasediment	×	+	+	–	–	–	–	1577	4.56	27.6	2.05	0.38	0.06	0.36	0.04	482	117
Ks1s11080206	1096	Ms–Bt metasediment	×	+	+	–	–	–	–	1576	3.03	27.7	2.12	0.48	0.08	0.40	0.04	465	92
Ks11091305	1301	Ms–Bt metasediment	–	+	+	–	+	–	–	1577	3.58	26.2	2.81	0.38	0.07	0.36	0.05	479	114
Ks11091608	1416	Ms–Bt metasediment	–	+	+	–	–	–	–	1577	3.12	26.7	2.00	0.38	0.11	0.37	0.05	478	116
Ks05091309	1628	Ms–Bt metasediment	–	+	+	–	–	–	–	1575	2.97	25.0	2.17	0.28	0.06	0.31	0.05	505	159
Ks05091308	1770	Ms–Bt metasediment	–	+	+	–	–	–	–	1580	1.51	23.4	1.43	0.30	0.05	0.34	0.05	492	148
Ks11091307	1615	Ms–Bt metasediment	–	+	+	–	–	–	–	1575	2.54	26.4	3.67	0.27	0.07	0.32	0.07	498	161
Ks11091308	1790	Ms–Bt metasediment	–	+	+	++	–	–	–	1576	3.75	22.3	2.51	0.20	0.05	0.27	0.06	521	224
Ks2s11082004	1957	Ms–Bt metasediment	–	+	+	+	–	–	–	1573	4.08	24.8	3.82	0.22	0.07	0.28	0.08	515	202
Ks2s11082005	2104	Ms–Bt metasediment	–	+	+	++	–	–	–	1575	3.72	22.4	3.34	0.20	0.06	0.27	0.06	520	219
Ks05091307	1982	Ms–Bt metasediment	–	+	+	++	–	–	–	1577	4.36	20.3	1.88	0.20	0.05	0.28	0.05	515	222
Ks05091306c	2103	Ms–Bt metasediment	–	+	+	++	–	–	–	1578	1.48	20.9	2.41	0.22	0.06	0.33	0.05	496	196
Ks04080504	2135	Ms–Bt metasediment	–	+	+	++	–	–	–	1576	3.10	21.7	3.05	0.21	0.03	0.30	0.04	509	211
Ks11091309	2192	Ms–Bt metasediment	–	+	+	+	–	–	–	1575	3.04	24.6	4.91	0.22	0.08	0.30	0.11	509	197
Ks11083003	2629	Ms–Bt schist	–	+	+	+	–	+	–	1575	3.75	19.0	2.00	0.15	0.08	0.24	0.08	536	291
Ks11083004	2785	Ms–Bt schist	–	+	+	+	–	+	–	1575	4.67	18.8	2.13	0.15	0.06	0.24	0.08	536	298
Ks12082516	2900	Ms–Bt schist	–	++	+	+	++	+	–	1578	2.17	18.6	2.18	0.06	0.03	0.17	0.05	565	739
Ks04081407	2959	Ms–Bt gneiss	–	+	+	++	–	+	–	1576	2.80	20.7	1.86	0.20	0.03	0.27	0.05	523	223
Ks11091407	3257	Ms–Bt gneiss	–	+	+	++	++	+	–	1580	1.12	17.4	1.26	0.15	0.05	0.24	0.07	532	285
Ks04092314	3626	Ms–Bt gneiss	–	+	+	++	+	+	–	1579	1.77	16.2	1.79	0.16	0.05	0.26	0.05	524	283
Ks11091601	3763	Ms–Bt gneiss	–	+	+	++	+	+	–	1580	1.69	16.6	1.25	0.09	0.04	0.16	0.07	568	503
Ks04092603	3936	Ms–Bt gneiss	–	+	+	++	+	+	–	1580	0.41	16.4	0.84	0.10	0.04	0.17	0.05	564	446
Ks11091602	3967	Ms–Bt gneiss	–	+	+	++	+	+	+	1580	1.00	16.1	1.35	0.08	0.05	0.16	0.08	571	568
Ks12071502	4001	Ms–Bt gneiss	–	+	+	+	+	+	–	1575	5.70	16.8	1.46	0.04	0.02	0.10	0.06	596	993
Ks11091606	4273	Ms–Bt gneiss	–	++	+	++	+	+	–	1578	1.89	16.7	1.44	0.07	0.02	0.15	0.04	574	631
Ks11091607	4209	Ms–Bt gneiss	–	+	+	++	+	+	–	1579	2.75	17.0	0.88	0.10	0.04	0.18	0.06	559	425
Mt.Ks11080405	4658	Ms–Bt gneiss	–	+	+	++	+	+	–	1579	2.29	16.8	0.87	0.12	0.05	0.21	0.08	547	366
Mt.Ks11080403	5733	Ms–Bt gneiss	–	+	+	++	+	+	–	1579	2.17	16.1	1.30	0.08	0.04	0.16	0.07	571	563
Mt.Ks11080401	5600	Ms–Bt gneiss	–	+	+	++	+	+	–	1578	3.66	16.6	0.92	0.08	0.04	0.15	0.07	575	554

Note; ++, Abundant; +, Moderate; ×, Poor; –, Absent; Chl, Chlorite; Ms, Muscovite; Bt, Biotite; BtP, Biotite porphyroblast; MsP, Muscovite porphyroblast; Kfs, K-feldspar; Crd, Cordierite. All samples include abundant quartz and plagioclase. Distance from the biotite isograd is measured from geological map. Mean values of *T* (°C) and La(Å) are calculated by the Raman spectroscopy of carbonaceous materials thermometry and crystal size following Beyssac et al. (2002a) and Tuinstra and Koenig (1970), respectively.

Table 6. Summary of Raman spectroscopic results of graphite in fault rocks

Sample name	Host rock	Fault rock	Condition	Raman results								
				G band (cm^{-1})	1 σ	G band FWHM (cm^{-1})	1 σ	R1 ratio	1 σ	R2 ratio	1 σ	La (Å)
4a11080101	Pelitic rock	Cataclasite	bulk	1575	3.14	45	8.82	0.78	0.18	0.42	0.07	57
Ks05091306	Ms-Bt schist	Cataclasite	bulk	1579	2.53	31	3.03	0.79	0.13	0.47	0.04	56
Ks11083002	Ms-Bt schist	Ultracataclasite	vein	1579	1.88	25	1.74	0.64	0.11	0.50	0.03	69
Ks12082603	Ms-Bt schist	Cataclasite	bulk	1580	1.49	25	3.24	0.67	0.15	0.52	0.05	66
		Pseudotachylyte	vein	1580	1.51	25	1.34	0.88	0.13	0.58	0.02	50
		Ultracataclasite	vein	1581	1.48	27	1.43	1.14	0.08	0.61	0.01	39
		Pseudotachylyte	vein	1580	1.38	27	1.29	1.32	0.12	0.64	0.01	33
		Pseudotachylyte	vein	1580	1.45	28	2.02	1.39	0.12	0.64	0.02	32
Ks12082608	Ms-Bt gneiss	Cat + Pst	bulk	1575	1.87	22	1.08	0.23	0.03	0.31	0.03	195
Ks11091603	Ms-Bt gneiss	Cataclasite	bulk	1577	4.42	23	4.64	0.38	0.23	0.37	0.11	117
Ks12082607	Ms-Bt gneiss	Cataclasite	bulk	1576	2.62	23	2.42	0.38	0.12	0.41	0.05	115
Ks12082606	Ms-Bt gneiss	Cat + Pst	bulk	1578	3.12	20	1.79	0.27	0.05	0.34	0.03	163
		Cataclasite	vein	1579	0.48	18	0.65	0.29	0.05	0.35	0.03	154
		Pseudotachylyte	vein	1582	0.80	30	2.95	1.24	0.14	0.61	0.03	35
		Pseudotachylyte	vein	1581	0.71	32	3.21	1.41	0.12	0.64	0.02	31
		Ultracataclasite	vein	1577	2.71	30	5.35	1.01	0.35	0.55	0.06	44
		Pseudotachylyte	vein	1577	3.27	32	3.91	1.10	0.28	0.57	0.04	40
Ks1s11080209	Ms-Bt metasediment	mylonite	bulk	1575	3.61	26.3	1.51	0.34	0.04	0.35	0.03	128
Ks11091404	Ms-Bt schist	mylonite	bulk	1575	3.37	19.9	1.96	0.17	0.06	0.26	0.07	255
Ks11091600	Ms-Bt gneiss	mylonite	bulk	1578	4.12	17.5	1.76	0.11	0.05	0.20	0.07	396

Note; Raman spectroscopic measurements were done under petrographic thin sections for cataclasite, ultracataclasite, and pseudotachylyte vein (condition; vein) and for residues after HF–HCl treatment (condition; bulk), respectively.

Table 7. Summary of XRD results of graphite in fault rocks and metamorphic rocks

Sample name	Lithology	*d (00l) reflections*									*d (10l) reflection*			*d(11l) reflections*					Lattice strain ε*
		d_{002} (Å)	FWHM (Δ°2θ)	Lc (002) (Å)	d_{004} (Å)	FWHM (Δ°2θ)	Lc (004) (Å)	d_{006} (Å)	FWHM (Δ°2θ)	Lc (006) (Å)	d_{100} (Å)	FWHM (Δ°2θ)	La (100) (Å)	d_{110} (Å)	FWHM (Δ°2θ)	d_{112} (Å)	FWHM (Δ°2θ)	La (110) (Å)	
Host metamorphic rocks																			
Pt11091503	Psammitic rock	3.415	3.07	30	–	–	–	–	–	–	2.113	2.46	39	–	–	–	–	–	-
Pt11091501	Pelitic rock	3.409	2.94	23	–	–	–	–	–	–	–	–	–	–	–	–	–	–	-
Pt11073108	Pelitic rock	3.402	2.71	22	–	–	–	–	–	–	2.115	1.93	49	–	–	–	–	–	-
Pt11073102	Pelitic rock	3.403	1.93	47	–	–	–	–	–	–	2.133	2.50	38	–	–	–	–	–	-
4s11080102	Pelitic rock	3.373	1.42	64	–	–	–	–	–	–	–	–	–	–	–	–	–	–	-
Sn11073004	Ms-Bt metasediment	3.381	0.93	97	–	–	–	–	–	–	–	–	–	–	–	–	–	–	-
Sn11080104	Ms-Bt metasediment	3.365	1.00	91	1.686	1.45	68	–	–	–	2.113	2.95	32	0.790	0.81	–	–	140	0.1142
Sn11080503	Ms-Bt metasediment	3.379	1.43	60	–	–	–	–	–	–	–	–	–	–	–	–	–	–	-
Sn11080504	Ms-Bt metasediment	3.361	1.16	79	–	–	–	–	–	–	–	–	–	–	–	–	–	–	-
Sn11080501	Ms-Bt metasediment	3.383	1.05	81	1.688	0.83	120	–	–	–	2.112	2.48	38	0.790	0.68	–	–	167	0.1016
R11081801	Ms-Bt metasediment	3.379	1.30	70	–	–	–	–	–	–	–	–	–	–	–	–	–	–	-
Ks11091301	Ms-Bt metasediment	3.359	0.82	92	–	–	–	–	–	–	–	–	–	–	–	–	–	–	-
Ks11091302	Ms-Bt metasediment	3.354	0.96	94	1.679	1.35	74	–	–	–	2.121	2.70	35	0.789	0.42	0.776	1.39	270	0.1279
Ks11091303	Ms-Bt metasediment	3.353	0.27	341	–	–	–	–	–	–	–	–	–	–	–	–	–	–	-
Ks11062814	Ms-Bt metasediment	3.359	0.61	148	–	–	–	–	–	–	–	–	–	–	–	–	–	–	-
Ks1s11080204	Ms-Bt metasediment	3.365	0.44	206	1.679	0.99	100	–	–	–	2.123	1.40	68	–	–	–	–	–	-
Ks11091304	Ms-Bt metasediment	3.358	0.44	207	1.679	0.83	120	–	–	–	2.120	2.36	40	0.789	0.39	–	–	291	0.1102
Ks11091305	Ms-Bt metasediment	3.358	0.47	193	1.682	0.71	140	–	–	–	–	–	–	0.789	0.44	–	–	259	0.0400
Ks11091307	Ms-Bt metasediment	3.356	0.41	222	1.681	0.65	152	–	–	–	2.126	0.49	193	0.790	0.43	0.776	0.96	263	0.0157
Ks11091308	Ms-Bt metasediment	3.362	0.25	363	1.678	0.49	203	–	–	–	–	–	–	0.790	0.38	0.776	0.95	298	0.0147
Ks11091309	Ms-Bt metasediment	3.356	0.29	315	1.678	0.40	249	1.121	0.60	203	2.128	0.27	355	0.790	0.29	0.776	1.01	391	0.0252
Ks11083003	Ms-Bt schist	3.355	0.18	505	1.679	0.32	314	1.120	0.30	406	2.127	0.23	412	0.790	0.19	0.776	0.72	602	0.0151
Ks12082516	Ms-Bt schist	3.353	0.19	473	1.678	0.22	450	1.120	0.42	290	2.130	0.15	623	0.790	0.14	0.776	0.49	839	0.0132
Ks11091602	Ms-Bt gneiss	3.355	0.20	461	1.679	0.11	880	1.120	0.13	937	2.133	0.12	789	0.790	0.12	0.776	0.10	944	0.0004
Ks12071502	Ms-Bt gneiss	3.354	0.23	395	–	–	–	–	–	–	–	–	–	–	–	–	–	–	-
Cataclasite																			
4a11080101	catclasite	3.379	1.96	46	–	–	–	–	–	–	–	–	–	–	–	–	–	–	-
Ks11091603	catclasite	3.356	0.34	334	–	–	–	–	–	–	–	–	–	–	–	–	–	–	-
Pseudotachylyte-bearing cataclasite																			
Ks12082608	pseudotachylyte	3.364	0.56	162	1.676	0.65	153	1.124	0.70	173	2.128	0.30	316	0.790	0.27	0.776	1.25	424	0.0364
Ks12082603	pseudotachylyte	3.362	0.96	94	1.680	0.73	136	–	–	–	–	–	–	–	–	–	–	–	-
Ks12082607	pseudotachylyte	3.354	0.53	171	1.682	0.70	142	–	–	–	2.124	0.36	263	0.790	0.36	0.776	1.58	315	0.0423
Ks12082606	pseudotachylyte	3.354	0.48	189	1.687	0.62	160	–	–	–	2.122	0.54	176	0.790	0.37	0.776	1.30	306	0.0225
Ks12071505	pseudotachylyte	3.360	0.93	98	1.681	0.60	166	–	–	–	2.128	0.70	135	0.790	0.36	0.776	1.40	314	0.0235
Mylonite																			
Ks1s11080209	mylonite (Bt-Ms schist)	3.361	0.50	181	–	–	–	–	–	–	2.125	0.60	158	0.793	0.34	0.776	2.10	330	0.0486
Ks11091404	mylonite (Bt-Ms schist)	3.365	0.19	475	1.679	0.24	414	–	–	–	2.129	0.16	592	0.790	0.22	0.776	0.76	515	0.0195
Ks11091600	mylonite (Bt-Ms gneiss)	3.351	0.22	416	1.676	0.20	507	1.123	0.21	580	2.128	0.16	592	0.790	0.14	0.776	0.20	833	0.0032

Note; –, not detected in XRD profile. Each value of d-spacing is calibrated by internal standard (Silicon; 2θ = 28.462°) and Lc (002), Lc(004), Lc (006), La(100) and La(110) are estimated by Scherrar equation (K=1.0). All XRD measurements were done after HF –HCl treatment.

Table 8. Results of stable carbon isotope measurement of graphite and TOC values for the fault/host rocks (n = 30)

Sample name	host rock	type	$\delta^{13}C$ grp-host (‰)	TOC value (wt.%)	1σ	fault rock	type	$\delta^{13}C$ grp-fault (‰)	TOC value (wt.%)	1σ
ks11091302	metasediment	Bulk	–24.19							
ks11091308	Bt-Ms schist	Bulk	–24.16							
ks11091309	Bt-Ms schist	Bulk	–23.56	0.75	0.04					
ks11091404	Bt-Ms schist	Bulk	–25.79							
4a11080101	Pelitic rock					Cataclasite	Bulk	–25.32		
						Cataclasite	Bulk	–25.66		
ks11083002	Bt-Ms schist					Cataclasite	Bulk	–24.10		
ks12071502	Bt-Ms gneiss					Pseudotachylyte	Bulk	–25.92		
ks12082607	Bt-Ms gneiss	Bulk	–25.21	0.31	0.02	Cataclasite	Bulk	–25.45	0.66	0.01
	Bt-Ms gneiss	Bulk	–25.30			Pseudotachylyte	Bulk	–25.63		
ks12082608	Bt-Ms gneiss					Pseudotachylyte	Bulk	–26.16		
						Pseudotachylyte	Bulk	–26.17		
ks11091603	Bt-Ms gneiss					Cataclasite	Bulk	–25.04	0.31	0.03
						Cataclasite	Bulk	–24.67		
ks12082606	Bt-Ms gneiss	Bulk	–24.78	0.61	0.10	Pseudotachylyte	Bulk	–26.15		
	Bt-Ms gneiss	Bulk	–24.67			Pseudotachylyte	Bulk	–26.07		
						Ultracataclasite	Bulk	–25.78		
						Pseudotachylyte	cutting	–25.11		
						Ultracataclasite	cutting	–23.64	1.01	0.03
ks12082603	Bt-Ms schist	Bulk	–24.88			Pseudotachylyte	cutting	–25.82	1.04	0.04
		Bulk	–25.29	0.90	0.06	Pseudotachylyte	cutting	–25.19	1.53	0.18
						Ultracataclasite	cutting	–25.82	1.37	0.10
						Pseudotachylyte	Bulk	–25.78		
						Ultracataclasite	Bulk	–24.81		

Table 9. Microprobe analytical results of lithic fragments (plagioclase), microlite, spherulites and matrix in pseudotachylyte.

	Biotite		Biotite		microlite			Plagioclase		Pst I matrix		Pst II matrix		Spherulite		Rapakivi rim*		Rapakivi core		Patch texture		Patch texture	
	n = 17		*n = 18*		*n = 21*			*n = 21*		*n = 32*		*n = 34*		*n = 23*		*n = 26*		*n = 106*		*n = 27*		*n = 17*	
	Avg	Std	Avg	Std	Avg	Std		Avg	Std	Avg	Std	Avg	Std	Avg	Std	Avg	Std	Avg	Std	Avg	Std	Avg	Std
SiO2	35.90	0.48	36.01	0.56	39.96	4.35	SiO2	61.53	0.83	64.15	4.69	63.77	3.19	64.91	2.78	64.59	1.72	64.38	1.73	62.00	2.36	62.70	2.16
TiO2	2.20	0.14	1.98	0.24	0.14	0.09	TiO2	0.02	0.01	0.60	0.37	0.50	0.65	0.59	0.57	0.09	0.04	0.24	0.11	0.48	0.66	0.33	0.11
Al2O3	18.93	0.40	18.82	0.29	21.13	0.96	Al2O3	23.57	0.43	17.03	2.42	17.97	1.22	18.26	0.84	21.20	0.68	19.54	0.64	19.80	0.69	18.81	0.30
Cr2O3	0.08	0.03	0.00	0.00	0.05	0.02	Cr2O3	0.00	0.00	0.04	0.04	0.03	0.02	0.02	0.03	0.00	0.00	0.00	0.00	0.00	0.01	0.00	0.00
FeO	18.27	0.68	15.01	0.34	14.79	3.33	FeO	0.06	0.03	1.81	1.66	2.00	1.63	1.98	1.23	2.35	1.42	1.66	0.82	4.04	1.98	2.88	1.24
MnO	0.30	0.03	0.21	0.04	0.17	0.07	MnO	0.01	0.01	0.03	0.03	0.01	0.02	0.01	0.01	0.01	0.01	0.00	0.00	0.04	0.03	0.09	0.06
MgO	10.37	0.23	11.43	0.24	10.21	2.32	MgO	0.00	0.00	0.79	0.95	1.09	0.98	1.07	0.67	0.83	0.34	0.70	0.38	1.73	0.86	1.55	0.71
CaO	0.03	0.04	0.00	0.00	0.24	0.10	CaO	5.17	0.54	0.69	0.57	0.39	0.43	0.72	0.55	1.94	0.39	0.29	0.17	1.52	1.25	0.33	0.10
Na2O	0.12	0.01	0.11	0.05	0.05	0.06	Na2O	7.77	0.20	0.45	0.34	0.35	0.26	0.37	0.25	6.94	0.65	0.38	0.39	4.41	1.73	0.26	0.10
K2O	9.20	0.21	9.34	0.11	3.56	1.49	K2O	0.15	0.05	11.99	2.11	11.92	1.25	12.87	1.48	1.37	0.97	12.89	0.90	4.47	3.28	12.23	0.92
NiO	0.06	0.03	0.00	0.00	0.05	0.05	NiO	0.06	0.03	0.01	0.02	0.06	0.03	0.00	0.01	0.01	0.02	0.00	0.00	0.04	0.03	0.03	0.03
BaO	0.15	0.09	0.12	0.04	0.12	0.05	BaO	0.01	0.02	0.38	0.17	0.45	0.20	0.35	0.23	0.03	0.06	0.26	0.16	0.19	0.10	0.27	0.09
Total	95.63	0.91	93.04	1.02	90.47	2.06	Total	98.36	0.67	97.96	2.18	98.53	2.45	101.16	2.28	99.32	1.75	100.08	1.60	98.48	2.57	99.17	1.50
Si	5.42		5.50		5.93		Si	2.76		3.00		2.97		2.96		2.88		2.94		2.84		2.91	
Al^{IV}	2.58		2.50		2.07		Ti	0.00		0.02		0.02		0.02		0.00		0.01		0.02		0.01	
							Al	1.25		0.94		0.99		0.98		1.11		1.05		1.07		1.03	
Ti	0.25		0.23		0.02		Cr	0.00		0.00		0.00		0.00		0.00		0.00		0.00		0.00	
Al^{VI}	0.79		0.88		1.63		Fe	0.00		0.07		0.08		0.08		0.09		0.06		0.16		0.11	
Cr	0.01		0.00		0.01		Mn	0.00		0.00		0.00		0.00		0.00		0.00		0.00		0.00	
Fe	2.31		1.92		1.85		Ni	0.00		0.00		0.00		0.00		0.00		0.00		0.00		0.00	
Mn	0.04		0.03		0.02		Mg	0.00		0.06		0.08		0.07		0.06		0.05		0.12		0.11	
Ni	0.01		0.00		0.01		Ca	0.25		0.03		0.02		0.04		0.09		0.01		0.07		0.02	
Mg	2.33		2.60		2.28		Na	0.68		0.04		0.03		0.03		0.60		0.03		0.39		0.02	
							K	0.01		0.72		0.71		0.75		0.08		0.75		0.26		0.72	
Ca	0.01		0.00		0.04		Total	4.95		4.89		4.89		4.92		4.90		4.91		4.93		4.94	
Na	0.04		0.03		0.01																		
K	1.77		1.82		0.67																		
total	15.55		15.51		14.54		An%	26.57		4.53		2.57		4.30		12.00		1.75		9.99		2.13	
							Ab%	72.50		5.10		4.13		4.14		77.76		4.14		53.88		3.08	
Annite %	0.50		0.42		0.45		Or%	0.93		90.37		93.30		91.56		10.24		94.10		36.13		94.79	

Note: Biotite1 and biotite2 are selected from biotite schist and gneiss, respectively.

Table 10. Microprobe analysis of sulfide minerals in pseudotachylyte.

	No.	Pst I matrix							Pst II matrix						
		1	4	7	9	10	11	1	1	2	4	5	6	7	9
wt.%	Si	0.08	0.63	0.06	0.26	0.65	0.15	0.06	0.02	0.05	0.15	0.03	0.03	0.08	0.67
	Ti	0.70	0.67	0.67	0.78	0.66	0.71	0.65	0.65	0.68	0.72	0.69	0.67	0.68	0.67
	S	39.24	39.06	39.68	39.35	38.72	39.46	40.00	38.62	39.22	38.51	38.81	39.47	38.99	36.97
	Fe	58.76	58.74	60.07	58.74	58.34	59.22	59.38	60.07	59.21	59.59	59.43	58.78	58.88	57.73
	Co	0.20	0.21	0.30	0.23	0.19	0.20	0.23	0.14	0.14	0.13	0.17	0.13	0.13	0.07
	Ni	0.18	0.17	0.17	0.14	0.17	0.24	0.15	0.20	0.17	0.21	0.22	0.21	0.26	0.15
	Cu	0.07	0.00	0.00	0.00	0.04	0.00	0.05	0.00	0.00	0.00	0.00	0.00	0.00	0.01
	Total	99.22	99.47	100.95	99.49	98.76	99.98	100.52	99.70	99.47	99.31	99.35	99.28	99.02	96.27
atm. %	Si	0.00	0.01	0.00	0.00	0.01	0.00	0.00	0.00	0.00	0.00	0.00	0.00	0.00	0.01
	Ti	0.01	0.01	0.01	0.01	0.01	0.01	0.01	0.01	0.01	0.01	0.01	0.01	0.01	0.01
	S	0.53	0.53	0.53	0.53	0.53	0.53	0.53	0.52	0.53	0.52	0.53	0.53	0.53	0.52
	Fe	0.46	0.45	0.46	0.46	0.46	0.46	0.46	0.47	0.46	0.47	0.46	0.46	0.46	0.46
	Co	0.00	0.00	0.00	0.00	0.00	0.00	0.00	0.00	0.00	0.00	0.00	0.00	0.00	0.00
	Ni	0.00	0.00	0.00	0.00	0.00	0.00	0.00	0.00	0.00	0.00	0.00	0.00	0.00	0.00
	Cu	0.00	0.00	0.00	0.00	0.00	0.00	0.00	0.00	0.00	0.00	0.00	0.00	0.00	0.00
Cation	Si	0.00	0.02	0.00	0.01	0.02	0.00	0.00	0.00	0.00	0.00	0.00	0.00	0.00	0.02
(S = 1)	Ti	0.01	0.01	0.01	0.01	0.01	0.01	0.01	0.01	0.01	0.01	0.01	0.01	0.01	0.01
	Fe	0.86	0.86	0.87	0.86	0.87	0.86	0.85	0.89	0.87	0.89	0.88	0.86	0.87	0.90
	Co	0.00	0.00	0.00	0.00	0.00	0.00	0.00	0.00	0.00	0.00	0.00	0.00	0.00	0.00
	Ni	0.00	0.00	0.00	0.00	0.00	0.00	0.00	0.00	0.00	0.00	0.00	0.00	0.00	0.00
	Cu	0.00	0.00	0.00	0.00	0.00	0.00	0.00	0.00	0.00	0.00	0.00	0.00	0.00	0.00
	S	1.00	1.00	1.00	1.00	1.00	1.00	1.00	1.00	1.00	1.00	1.00	1.00	1.00	1.00
	atm %	0.860	0.864	0.869	0.857	0.865	0.862	0.852	0.893	0.867	0.888	0.879	0.855	0.867	0.897
	N_{FeS}	0.925	0.927	0.930	0.923	0.928	0.926	0.920	0.943	0.929	0.941	0.936	0.922	0.929	0.945
	XFeS	0.462	0.463	0.465	0.462	0.464	0.463	0.460	0.472	0.464	0.470	0.468	0.461	0.464	0.473
	fS_2*	-1.863	-2.037	-2.302	-1.744	-2.108	-1.950	-1.527	-3.525	-2.192	-3.279	-2.798	-1.652	-2.209	-3.721
	fS_2**	-0.820	-0.972	-1.205	-0.715	-1.034	-0.896	-0.524	-2.280	-1.108	-2.064	-1.641	-0.634	-1.124	-2.453

Note: fS_2* and fS_2** are calculated using the equation of Toulmin and Barton (1964) and Froese and Gunter (1976) at 600 and 700 °C, respectively.

Table 11. The concentrations of trace element (ppm) in the Pst II, Pst I and protolith.

	Pseudotachylyte II				Pseudotachylyte I					Protolith	
	Pst IIMD	Pst IIMD	Pst IIMD	Pst II SD	PstI	PstI	PstI	PstI	Cataclasite	Schist	gneiss
Li	41.36	83.86	34.21	64.87	32.79	13.67	25.82	5.68	56.38	34.65	55.14
B	48.66	41.92	36.47	51.48	19.74	21.04	24.64	14.54	15.83	489.85	8.78
Sc	24.57	29.72	15.50	25.88	25.47	25.37	20.90	24.64	15.16	18.32	18.00
V	174.90	216.72	208.21	308.93	235.39	265.46	246.44	230.63	102.59	154.54	136.54
Cr	121.92	145.73	128.73	205.46	183.93	143.63	60.54	137.86	45.71	95.64	159.08
Co	101.99	75.91	143.05	153.72	44.55	269.29	21.59	33.81	84.84	19.88	150.69
Zn	139.80	221.72	142.59	326.02	131.37	46.64	45.97	31.53	58.38	78.67	84.18
Ga	17.25	15.68	13.82	25.16	11.94	9.81	16.67	10.63	14.23	17.03	15.50
Ge	1.15	1.18	0.39	0.74	0.47	0.48	0.84	0.11	0.51	0.80	0.88
Rb	253.51	202.13	271.94	361.67	270.05	316.59	260.68	307.48	115.88	83.96	88.45
Sr	453.39	434.95	478.83	769.65	811.49	560.33	610.93	815.93	352.97	466.35	255.50
Y	28.45	33.52	16.97	45.64	24.77	25.66	26.43	18.00	17.68	22.89	18.58
Zr	171.06	178.90	157.92	254.45	210.56	198.80	209.55	202.88	117.52	137.98	129.49
Nb	5.82	8.22	6.71	13.25	10.52	10.12	9.85	10.17	6.08	6.58	6.85
Cs	10.88	9.92	6.57	13.08	7.28	11.27	9.08	7.33	1.77	5.49	5.92
Ba	1532.27	1220.73	1458.04	2481.34	2067.77	4187.40	1675.54	2889.18	807.54	952.63	662.26
La	14.73	15.39	13.28	29.27	25.96	26.29	25.45	19.62	17.05	21.78	17.30
Ce	26.13	25.83	25.05	56.45	45.98	43.33	46.40	38.06	25.87	38.92	28.66
Pr	3.40	3.50	3.03	7.75	5.56	5.03	5.67	4.10	3.92	4.93	4.10
Nd	13.46	14.32	12.82	30.22	20.52	20.47	21.27	16.34	14.84	19.35	16.02
Sm	3.09	3.06	2.63	6.54	4.07	3.59	4.62	2.82	2.77	3.93	2.91
Eu	0.74	0.79	0.78	1.63	1.00	1.09	1.21	0.84	0.83	0.81	0.96
Gd	3.32	3.45	3.04	7.19	4.55	4.02	4.23	2.91	2.91	3.66	2.90
Tb	0.55	0.62	0.45	1.13	0.72	0.70	0.91	0.54	0.54	0.58	0.49
Dy	3.48	3.67	2.59	6.59	4.17	4.14	4.92	2.89	2.66	3.73	2.98
Ho	0.78	0.85	0.58	1.46	0.99	1.01	1.03	0.70	0.57	0.75	0.66
Er	2.30	2.66	1.66	4.41	2.83	2.86	3.10	2.33	1.76	2.25	1.92
Tm	0.38	0.41	0.34	0.66	0.46	0.47	0.47	0.33	0.31	0.32	0.33
Yb	2.08	2.16	1.59	2.97	2.62	2.33	2.18	1.51	1.28	1.93	1.73
Lu	0.30	0.51	0.34	0.51	0.43	0.45	0.42	0.41	0.23	0.32	0.25
Hf	4.39	4.37	3.68	6.68	5.13	5.07	5.70	5.25	3.16	3.44	3.12
Ta	6.74	4.14	0.51	7.73	0.58	0.76	1.41	2.78	7.14	0.65	9.82
Pb	6.91	7.37	7.92	14.94	10.82	18.04	10.59	23.09	7.61	10.22	10.78
Th	7.87	7.14	5.65	12.19	9.20	8.54	8.62	8.66	5.08	7.14	6.18
U	1.15	1.32	1.34	2.94	1.63	1.51	1.27	1.55	1.08	1.41	1.30

Note: All sample powders were cut from slab sections using a tungseten drill, and thus the values for W, Co, and Ta are unreliable.

Table 12. Results of stable carbon isotope measurements of graphite and TOC values for e

sample	lithologhy	method	$\delta^{13}C$ [‰]	TOC [wt.%]	1σ
ks11091602	host rocks	bulk	-25.21	0.31	0.02
Ks12082516	host rocks	bulk	-24.88	0.90	0.06
Ks11091600	host rocks	bulk	-24.67	0.61	0.10
Ks11091600	host rocks	bulk	-24.78		
Ks11091404-1	host rocks	bulk	-25.79		
ks11091308-2	host rocks	bulk	-24.16		
ks11091602	host rocks	bulk	-25.30		
ks12082516	host rocks	bulk	-25.29		
ks11091309	host rocks	bulk	-23.56	0.75	0.04
KS11091302	host rocks	bulk	-24.19	0.63	0.02
Sn11080104	host rocks	bulk	-25.12		
lw11081111	host rocks	bulk	-24.55		
PT091503	host rocks	bulk	-25.73		
ks12071505	cataclasite	bulk	-25.92		
ks11091603	cataclasite	bulk	-25.04	0.31	0.03
ks11091603	cataclasite	bulk	-24.67		
4s11080101a	cataclasite	bulk	-25.32		
4s11080101b	cataclasite	bulk	-25.66		
ks12083002-1	cataclasite	bulk	-24.10		
Ks12082606	Pst bearing cataclasite	bulk	-26.15		
ks12082607	Pst bearing cataclasite	bulk	-25.45	0.66	0.01
Ks12082608	Pst bearing cataclasite	bulk	-26.16		
Ks12082606-crash	Pst bearing cataclasite	bulk	-26.07		
Ks12082606-bulk	Pst bearing cataclasite	bulk	-25.78		
ks12082607-bulk	Pst bearing cataclasite	bulk	-25.63		
ks12082608-bulk	Pst bearing cataclasite	bulk	-26.17		
ks12082603-2	Pst bearing cataclasite	bulk	-27.00		
ks12071504	Pst bearing cataclasite	bulk	-26.78		
ks12082603-3	Pst bearing cataclasite	bulk	-22.50		
ks12071404type1	Pst bearing cataclasite	bulk	-27.14		
ks12082603-3-1-2	cataclasite	cutting	-25.78		
ks12082603-3-1-5	cataclasite	cutting	-24.81		
ks12082603-Ucat	ultracataclasite	cutting	-25.82	1.37	0.10
Ulcat-15-2	ultracataclasite	cutting	-23.64	1.01	0.03
ks12082603-3-1-1	pseudotachhylyte I	cutting	-25.82	1.04	0.04
ks12082603-3-1-3	pseudotachhylyte I	cutting	-25.19	1.53	0.18
2603-BD-06	pseudotachhylyte I	cutting	-24.55	0.85	0.04
PatII-17-MD	pseudotachylyte II	cutting	-20.94		
2606-Sph-1-1	pseudotachylyte II	cutting	-21.74		
2606-pstII-11	pseudotachylyte II	cutting	-21.46		
130922-PD	pseudotachylyte II	cutting	-18.19	1.52	0.04
130922-MD	pseudotachylyte II	cutting	-21.49	1.00	0.20
2606-SD-03	pseudotachylyte II	cutting	-21.02	0.89	0.06
2606-sp-2-1	pseudotachylyte II	cutting	-24.34		
2606-in	pseudotachylyte II	cutting	-25.11		
2606-SD-04	pseudotachylyte II	cutting	-24.88	0.83	0.04
2603-MD-05	pseudotachylyte II	cutting	-23.61	0.84	0.06
130922-MD	pseudotachylyte II	cutting	-25.40		
15012703-SD-1	pseudotachylyte II	cutting	-21.57		
15012702-SD-2	pseudotachylyte II	cutting	-21.64		
15012703-VD	pseudotachylyte II	cutting	-19.90		

Table 13. Summary of Raman spectroscopic results of carbonaceous materials in mudstone

Samples	Line	Units	Lithology	Distance* (m)	*n*	G position (cm^{-1})	1σ	G band FWHM (cm^{-1})	1σ	D1 band (cm^{-1})	1σ	D1 band FWHM (cm^{-1})	1σ	I_D/I_G	1σ	A_{D1+D4} / A_{D3+G}	1σ	T^1 (℃)	T^2 (℃)
R01	B	Tochidani	coherent	21620	25	1602.2	0.76	56.13	3.26	1357.1	4.32	133.29	4.96	0.60	0.02	1.49	0.11	191	154
R02	B	Tochidani	coherent	20864	26	1602.0	0.79	54.79	3.02	1354.8	4.90	132.23	5.98	0.61	0.03	1.57	0.09	194	163
R03	B	Hinotani	coherent	18823	25	1603.0	0.65	51.39	3.81	1352.8	5.59	129.41	8.37	0.60	0.03	1.64	0.09	200	187
R04	B	Hinotani	coherent	18017	31	1601.9	0.68	54.98	3.68	1358.5	5.06	133.66	3.65	0.58	0.03	1.55	0.20	191	162
R05	B	Hinotani	coherent	17185	25	1602.1	0.68	52.05	3.14	1354.7	5.90	131.26	7.40	0.58	0.03	1.61	0.08	196	182
R06	B	Osodani	coherent	15951	29	1602.9	1.00	48.07	3.35	1353.7	5.21	127.13	5.85	0.56	0.02	1.72	0.10	205	209
R07	B	Osodani	coherent	15295	28	1602.7	0.62	46.12	2.40	1353.1	5.05	124.67	6.77	0.54	0.02	1.82	0.04	210	222
R08	A	Osodani	coherent	11944	29	1603.3	0.41	38.94	1.47	1347.4	4.46	110.42	6.81	0.50	0.02	1.84	0.03	241	271
R09	A	Osodani	coherent	12574	27	1602.7	0.77	44.34	2.53	1352.1	5.14	120.68	7.25	0.53	0.03	1.79	0.09	219	234
R10	B	Osodani	coherent	12927	28	1602.6	0.74	43.09	2.54	1351.0	4.43	118.14	5.87	0.52	0.02	1.82	0.05	224	243
R11	B	Osodani	coherent	14388	31	1604.2	2.08	42.92	2.36	1348.4	2.96	108.43	4.57	0.54	0.03	1.61	0.13	245	244
R12	C	Taniyama	melange	13532	30	1605.4	0.38	37.31	0.98	1340.0	0.91	103.24	3.64	0.57	0.02	1.68	0.08	256	282
R13	D	Hinotani	coherent	18048	28	1601.2	0.56	52.83	3.43	1356.3	5.63	131.29	4.23	0.57	0.03	1.65	0.10	196	177
R14	D	Osodani	coherent	15004	32	1601.2	0.84	50.46	2.56	1355.2	4.22	130.23	4.91	0.56	0.02	1.72	0.08	198	193
R15	D	Taniyama	melange	11650	29	1602.7	0.79	40.15	2.14	1347.0	4.07	109.86	6.50	0.52	0.02	1.79	0.06	242	263
R16	D	Hiwasa	coherent	10064	28	1600.3	0.47	58.44	3.20	1358.3	4.91	138.25	2.78	0.57	0.03	1.43	0.20	181	139
R17	D	Taniyama	melange	10458	25	1604.5	1.30	36.73	1.99	1341.3	2.51	103.57	6.03	0.55	0.03	1.78	0.08	255	286
R18	C	Hiwasa	melange	9794	29	1603.5	1.24	50.80	3.27	1356.4	4.74	134.03	6.64	0.56	0.02	1.69	0.07	190	191
R19	A	Taniyama	melange	8416	30	1603.5	0.70	47.15	1.33	1356.3	2.31	124.55	2.29	0.55	0.01	1.81	0.04	210	215
R20	A	Hiwasa	coherent	7585	28	1604.3	0.72	43.19	2.22	1351.9	3.35	114.95	6.48	0.56	0.02	1.80	0.05	231	242
R21	A	Hiwasa	coherent	6602	31	1604.3	0.49	41.28	0.68	1348.8	1.07	112.54	2.20	0.54	0.01	1.78	0.04	236	255
R22	A	Mugi	Cataclasite	3528	28	1605.9	0.26	40.24	0.70	1341.7	0.52	112.17	2.36	0.59	0.01	1.64	0.05	237	262
R23	A	Mugi	melange	1411	31	1604.9	1.87	42.76	1.59	1340.4	2.02	98.62	2.70	0.70	0.03	1.47	0.06	266	245
R24	A	Mugi	melange	714	31	1605.4	0.96	41.02	1.42	1339.4	1.42	97.57	3.69	0.67	0.03	1.47	0.07	268	257
R25	A	Mugi	phyllite	227	36	1606.1	0.23	39.29	0.60	1337.4	0.85	91.93	3.04	0.69	0.02	1.56	0.03	280	269
R26	A	Mugi	coherent	350	26	1604.0	0.69	43.77	1.39	1348.6	2.73	116.55	4.53	0.57	0.03	1.76	0.09	227	238
R27	A	Mugi	phyllite	515	26	1605.2	0.30	39.58	0.87	1339.6	1.11	100.24	3.26	0.65	0.04	1.63	0.08	262	267
R28	A	Mugi	phyllite	584	29	1604.0	3.14	37.35	2.56	1335.7	2.13	95.41	4.32	0.60	0.03	1.63	0.06	273	282
R29	A	Mugi	melange	192	26	1603.8	0.68	42.35	1.25	1348.7	1.83	114.56	3.32	0.56	0.02	1.74	0.07	232	248
R30	A	Naharigawa	melange	73	25	1603.3	0.49	42.60	2.11	1347.1	3.82	114.12	7.57	0.57	0.02	1.81	0.05	233	246
R31	A	Naharigawa	coherent	-1058	27	1605.4	1.09	40.12	1.39	1345.6	2.31	109.50	4.22	0.56	0.02	1.72	0.04	243	263

Note: T^1 (D1 band FWHM) and T^2 (G (D2) band FWHM) are estimated by the equation of Kouketsu et al. (2014).

Table 13 (continued). Summary of Raman spectroscopic results of carbonaceous materials in mudstone

Samples	Line	Units	Lithology	Distance* (m)	*n*	G position (cm^{-1})	1σ	G band FWHM (cm^{-1})	1σ	D1 band (cm^{-1})	1σ	D1 band FWHM (cm^{-1})	1σ	I_D/I_G	1σ	A_{D1+D4} / A_{D3+G}	1σ	T^1 (℃)	T^2 (℃)
HG01	A	Naharigawa	coherent	-333	28	1605.6	0.41	39.81	0.73	1346.1	1.16	109.18	1.86	0.54	0.01	1.67	0.09	243	265
HG02	A	Naharigawa	melange	-96	28	1604.7	0.34	40.42	0.84	1346.3	2.40	109.16	3.56	0.56	0.01	1.79	0.05	243	261
HG03	A	Naharigawa	melange	-41	27	1604.5	0.29	40.95	1.09	1346.8	2.66	109.31	4.18	0.56	0.02	1.76	0.04	243	257
HG06	A	Mugi	melange	152	28	1604.0	0.42	42.60	0.99	1348.8	2.88	112.47	4.08	0.56	0.01	1.76	0.05	236	246
HG07	A	Mugi	melange	333	28	1604.2	0.21	43.06	1.20	1349.8	2.59	113.57	3.66	0.56	0.01	1.76	0.05	234	243
HG09-13	A	Mugi	melange	401	27	1604.6	0.56	42.30	1.15	1347.9	1.83	108.72	4.27	0.59	0.01	1.73	0.07	244	248
HG09-17	A	Mugi	melange	405	30	1605.2	0.33	41.11	0.96	1347.9	1.84	108.82	3.20	0.57	0.01	1.79	0.04	244	256
HG12	A	Naharigawa	coherent	-460	28	1604.9	0.47	39.38	0.66	1345.2	0.99	108.68	2.09	0.55	0.01	1.74	0.05	244	268
NG01	A	Mugi	melange	110	28	1605.9	0.20	37.54	0.70	1339.5	1.11	95.32	3.22	0.59	0.01	1.63	0.05	273	280
NG02	A	Mugi	melange	233	29	1605.3	0.18	36.83	0.89	1338.2	0.95	96.10	3.67	0.61	0.02	1.76	0.06	271	285
NG04	A	Mugi	melange	329	29	1605.9	0.20	36.90	0.85	1339.4	0.93	95.21	2.98	0.58	0.02	1.70	0.07	273	285
NG05e	A	Mugi	melange	373	30	1605.0	0.30	36.32	1.04	1337.3	1.29	93.40	4.38	0.59	0.02	1.61	0.07	277	289
NG5c	A	Mugi	Sandstone	390	30	1606.1	0.72	37.12	0.84	1338.9	0.88	96.68	2.80	0.58	0.02	1.66	0.04	270	283
NG06	A	Mugi	phyllite	422	30	1606.1	0.30	35.81	0.65	1337.8	0.66	92.43	2.58	0.59	0.01	1.69	0.06	279	292
NG07	A	Mugi	phyllite	474	30	1605.3	0.37	35.57	0.65	1337.9	0.99	92.66	3.57	0.58	0.02	1.76	0.06	279	294
NG08	A	Naharigawa	coherent	-191	30	1605.0	0.51	41.85	1.07	1347.4	2.36	115.07	4.22	0.56	0.02	1.74	0.05	231	251
NG09	A	Naharigawa	coherent	-781	30	1605.1	0.54	41.29	1.32	1348.9	2.96	112.67	3.97	0.55	0.02	1.74	0.07	236	255
NG10	A	Naharigawa	coherent	-1306	29	1605.0	0.51	42.22	1.11	1348.9	2.40	111.98	3.66	0.56	0.01	1.78	0.05	237	249
YN02	A	Mugi	melange	126	29	1604.6	0.60	42.72	1.65	1349.5	3.08	109.55	5.54	0.58	0.02	1.72	0.06	242	245
YN04	A	Mugi	melange	248	28	1605.3	0.30	37.09	0.75	1338.7	1.24	94.87	3.43	0.58	0.02	1.65	0.06	274	284
YN07	A	Hiwasa	coherent	5871	27	1604.5	0.28	37.75	0.78	1343.6	1.65	103.51	2.89	0.54	0.02	1.80	0.06	255	279
YN08	A	Hiwasa	coherent	4888	28	1604.8	0.32	37.51	2.31	1338.9	2.30	98.48	5.74	0.61	0.02	1.76	0.06	266	281
YN09	A	Naharigawa	coherent	-3167	27	1604.6	0.37	40.40	0.62	1344.8	1.51	111.34	2.03	0.57	0.02	1.74	0.08	239	261
YN10	A	Mugi	melange	4025	29	1606.2	0.39	35.82	0.94	1338.7	1.53	94.56	4.72	0.60	0.02	1.78	0.06	275	292
YN11	A	Mugi	melange	2696	31	1606.4	0.24	37.62	0.72	1342.0	1.82	97.95	3.11	0.57	0.02	1.73	0.04	267	280
YN12	A	Mugi	melange	2047	33	1606.8	0.27	37.73	1.10	1339.6	1.09	96.86	3.67	0.60	0.02	1.63	0.05	270	279
YN13	A	Mugi	melange	1191	28	1607.2	0.34	39.05	1.09	1339.0	1.18	95.01	3.48	0.64	0.02	1.56	0.05	274	270
YN14	A	Naharigawa	coherent	-1732	27	1606.1	0.33	39.40	0.92	1344.4	1.79	108.78	4.56	0.56	0.02	1.72	0.07	244	268
YN15	A	Naharigawa	coherent	-2293	33	1605.3	0.44	45.32	3.20	1349.6	2.96	116.82	4.88	0.61	0.02	1.69	0.07	227	228
YD01	A	Naharigawa	coherent	-2997	27	1603.2	0.38	45.91	1.60	1352.8	3.46	119.36	4.05	0.57	0.02	1.76	0.07	221	224

Note: T^1 (D1 band FWHM) and T^2 (G (D2) band FWHM) are estimated by the equation of Kouketsu et al. (2014).

Table 14. Summary of micro-Raman spectroscopic data on kinetic experiments for 10 to 2880 min.

Run No.	T (°C)	t (min)	t (sec)	n	G position (cm^{-1})	1σ	G band FWHM (cm^{-1})	1σ	D1 band (cm^{-1})	1σ	D1 band FWHM (cm^{-1})	1σ	I_D/I_G	1σ	A_{D1+D4} / A_{D3+G}	1σ	α
HTT1	500	10	600	19	1597.8	1.46	60.74	1.20	1359.2	1.59	130.70	1.47	0.55	0.01	1.21	0.06	0.0033
HTT2	500	60	3600	20	1598.1	1.36	59.69	1.82	1357.7	2.45	131.96	1.71	0.56	0.01	1.23	0.06	0.0092
HTT3	500	180	10800	19	1598.0	1.41	59.63	0.87	1357.6	1.94	132.97	1.46	0.57	0.01	1.22	0.05	0.0130
HTT4	500	360	21600	21	1600.0	1.33	59.62	1.14	1358.7	1.45	137.32	2.42	0.58	0.01	1.29	0.06	0.0166
HTT5	500	1440	86400	19	1599.8	1.12	58.89	0.97	1356.4	1.31	138.20	3.26	0.60	0.01	1.32	0.07	0.0279
HTT6	600	10	600	17	1599.5	1.79	59.85	2.37	1356.7	2.25	137.31	3.77	0.59	0.02	1.28	0.09	0.0257
HTT7	600	60	3600	13	1599.6	1.43	59.96	0.97	1353.7	1.32	143.75	4.09	0.63	0.01	1.39	0.07	0.0460
HTT8	600	180	10800	17	1600.2	1.63	58.70	1.42	1351.4	1.84	141.06	3.48	0.64	0.02	1.40	0.09	0.0510
HTT9	600	360	21600	14	1600.9	0.68	58.48	0.61	1350.2	1.13	139.61	2.89	0.65	0.01	1.32	0.06	0.0548
HTT10	600	720	43200	16	1601.2	1.62	58.18	1.69	1349.5	1.28	133.19	2.95	0.66	0.03	1.28	0.07	0.0618
HTT11	600	1440	86400	16	1600.8	1.11	58.82	1.28	1348.2	1.45	132.45	3.50	0.67	0.02	1.26	0.05	0.0692
HTT12	600	2880	172800	15	1601.8	1.10	58.21	0.76	1348.2	1.73	129.66	3.55	0.69	0.03	1.22	0.09	0.0770
HTT13	700	10	600	16	1601.0	1.20	60.22	1.34	1351.9	1.30	135.62	2.15	0.63	0.02	1.16	0.07	0.0452
HTT14	700	60	3600	17	1601.0	1.20	59.22	1.53	1348.8	1.56	129.97	2.43	0.68	0.02	1.12	0.05	0.0744
HTT15	700	180	10800	17	1601.4	0.92	59.40	0.69	1348.9	1.10	128.61	1.30	0.71	0.02	1.11	0.03	0.0896
HTT16	700	360	21600	19	1601.8	1.11	59.43	0.95	1349.0	1.24	127.13	2.13	0.73	0.01	1.11	0.05	0.0991
HTT17	700	1800	108000	20	1603.5	1.32	60.92	1.71	1351.1	1.48	126.41	2.36	0.78	0.02	1.19	0.05	0.1277
HTT18	800	10	600	15	1602.1	0.63	64.04	0.98	1351.8	1.71	135.55	2.37	0.73	0.02	1.14	0.04	0.1022
HTT19	800	60	3600	15	1602.7	0.78	63.83	1.06	1351.6	1.29	130.99	2.68	0.80	0.02	1.17	0.03	0.1377
HTT20	800	180	10800	13	1603.1	0.68	64.84	1.55	1351.8	1.47	128.30	2.29	0.84	0.02	1.18	0.03	0.1592
HTT21	800	360	21600	15	1603.8	0.73	65.01	2.07	1353.5	2.10	126.40	2.83	0.85	0.02	1.24	0.11	0.1656
HTT22	800	1440	86400	15	1603.9	1.44	68.65	1.80	1355.1	1.60	128.84	2.71	0.88	0.02	1.19	0.04	0.1819
HTT23	900	10	600	20	1603.4	1.03	66.05	1.61	1353.0	2.21	129.56	2.32	0.85	0.02	1.20	0.03	0.1670
HTT24	900	60	3600	22	1603.5	0.85	67.49	1.34	1354.2	1.30	126.79	1.51	0.90	0.01	1.21	0.04	0.1932
HTT25	900	180	10800	21	1602.1	2.31	69.67	1.98	1354.2	2.27	124.86	2.50	0.95	0.02	1.20	0.05	0.2169
HTT26	900	360	21600	15	1602.9	0.98	71.01	1.39	1354.5	1.40	123.48	1.55	0.98	0.01	1.23	0.04	0.2369
HTT27	900	1440	86400	17	1604.0	1.25	74.29	1.74	1356.1	1.08	123.03	2.78	1.01	0.03	1.35	0.16	0.2500

Table 15. Summary of kinetic parameters of natural carbonaceous material in pyrolysis experiments

T (℃)	T(k)	1000/T	*Power rate model*			*Avrami-Erofeev model*		
			ln$k$	n	R^2	ln$k$	n	R^2
500	773	1.294	-8.272	0.419	0.983	-8.286	0.421	0.984
600	873	1.145	-4.772	0.189	0.949	-4.729	0.186	0.957
700	973	1.028	-4.286	0.197	0.974	-4.317	0.205	0.976
800	1073	0.932	-2.978	0.117	0.949	-2.981	0.126	0.952
900	1173	0.853	-2.331	0.086	0.977	-2.311	0.096	0.978

Table 16. Summary of rate paramters calculated from power rate and Avrami-Erofeev models

Crystal parameter	Kinetic model	m	ln*A*	Ea (kJ/mol)	1σ	R^2
I_{D1}/I_G	power rate	12.777	8.892	106	16.63	0.932
I_{D1}/I_G	Avrami-Erofeev	12.797	8.916	106	17.13	0.928

Table 17. Experimental conditions and XRD parameters of the run products at 1 GPa.

Run No.	Temp (°C)	Time (min)	XRD analysis							
			d_{002} (Å)	FWHM	L_c(002) (Å)	g* (%)	d_{002} (Å)	FWHM	L_c(002) (Å)	g* (%)
			CM in Hidaka metamorphic belt				*CM in Shimanto accretionary complex*			
PC478	1000	10	3.432	2.58	35	0.019	3.491	5.33	17	0.035
PC475	1000	60	3.426	2.39	38	0.099	3.495	4.67	19	0.008
PC473	1000	360	3.420	2.39	38	0.170	3.483	4.75	20	0.093
PC471	1000	1440	3.406	2.19	41	0.356	3.471	3.59	25	0.186
PC470	1000	2880	3.402	2.12	43	0.416	3.471	3.48	26	0.184
PC482	1200	0.017	3.430	2.45	37	0.044	3.436	4.04	22	0.439
PC477	1200	10	3.427	1.93	47	0.083	3.430	2.91	31	0.483
PC479	1200	30	3.417	1.93	47	0.212	3.437	2.43	37	0.436
PC476	1200	60	3.416	1.66	55	0.226	3.420	2.55	36	0.556
PC485	1200	180	3.396	1.19	69	0.492	3.396	1.38	65	0.739
PC474	1200	360	3.393	1.14	80	0.538	3.396	1.51	60	0.738
PC462	1200	1440	3.387	0.89	107	0.619	3.382	0.72	127	0.840
PC461	1200	6900	3.359	0.40	225	0.989	3.368	0.70	129	0.941
A2590	1325	10	3.404	1.40	65	0.390	3.422	2.31	39	0.543
A2588	1325	60	3.387	1.20	76	0.607	3.400	0.76	119	0.708
A2583	1325	360	3.369	0.80	113	0.853	3.372	0.62	147	0.915
A2581	1325	720	3.362	0.61	146	0.947	3.368	0.64	154	0.938
A2582	1325	1440	3.368	0.63	144	0.868	3.370	0.59	143	0.926
A2580	1325	2880	3.367	0.45	201	0.875	3.368	0.60	152	0.938
PC481	1450	0.017	3.407	1.47	62	0.351	3.425	1.17	37	0.523
A2589	1450	10	3.388	1.25	72	0.607	3.383	0.57	77	0.831
A2587	1450	60	3.365	0.79	115	0.903	3.375	0.55	159	0.891
A2586	1450	360	3.364	0.67	136	0.927	3.373	0.51	179	0.906
A2584	1450	1440	3.367	0.40	228	0.881	3.363	0.49	184	0.975

Note: L_c(002) is calculated by the Scherrer equation (K = 1.0)

g* (%) is the calculated degree of crystallinity using initial and final values of d_{002} spacing

Table 18. Micro-Raman spectroscopic data for center and edge part of CM obtained by the peak deconvolution.

Run No.	*Temp* (°C)	*time* (min)	Raman spectroscopy (center)									Raman spectroscopy (Edge)								
			D1 band (cm^{-1})	D1 band FWHM	G band (cm^{-1})	G band FWHM	R1 ratio	R2 ratio	AR	*La* (Å)	*n*	D1 band (cm^{-1})	D1 band FWHM	G band (cm^{-1})	G band FWHM	R1 ratio	R2 ratio	AR	*La* (Å)	*n*
Center part of CM in Hidaka metamorphic belt												*Edge part of CM in Hidaka metamorphic belt*								
PC478	1000	10	1342 (1)	54.0 (2.8)	1574 (1)	42.2 (2.2)	1.54 (11)	0.62 (1)	1.68 (9)	29	20	1343 (2)	51.3 (1.9)	1576 (3)	41.6 (2.0)	1.59 (17)	0.62 (2)	1.67 (13)	28	14
PC475	1000	60	1343 (1)	55.2 (4.0)	1575 (2)	45.4 (4.5)	1.48 (13)	0.61 (2)	1.55 (11)	30	17	1342 (1)	55.8 (4.8)	1573 (2)	44.0 (3.5)	1.35 (15)	0.60 (2)	1.47 (11)	32	16
PC473	1000	360	1342 (2)	54.3 (2.7)	1576 (3)	43.2 (2.1)	1.31 (15)	0.59 (2)	1.43 (10)	34	15	1343 (2)	54.4 (3.1)	1574 (4)	45.3 (4.3)	1.44 (24)	0.60 (3)	1.48 (17)	30	16
PC471	1000	1440	1343 (2)	54.8 (2.7)	1574 (3)	45.8 (3.2)	1.35 (15)	0.59 (2)	1.48 (13)	33	15	1343 (2)	55.5 (3.6)	1575 (3)	46.0 (2.3)	1.38 (13)	0.59 (1)	1.51 (10)	32	16
PC470	1000	2880	1343 (2)	55.8 (3.4)	1576 (3)	46.9 (3.9)	1.47 (16)	0.61 (1)	1.55 (10)	30	16	1344 (2)	53.7 (3.1)	1576 (4)	47.1 (3.4)	1.49 (16)	0.60 (2)	1.51 (11)	30	17
PC482	1200	0.02	1343 (2)	53.3 (3.6)	1575 (3)	43.5 (3.5)	1.46 (19)	0.61 (2)	1.61 (15)	30	16	1343 (1)	53.7 (4.1)	1576 (2)	44.3 (3.6)	1.43 (14)	0.61 (2)	1.60 (12)	31	17
PC477	1200	10	1342 (2)	53.0 (3.2)	1574 (2)	44.0 (2.9)	1.31 (15)	0.58 (2)	1.40 (12)	34	15	1341 (2)	54.3 (3.3)	1575 (3)	43.8 (2.0)	1.27 (15)	0.58 (2)	1.38 (8)	35	17
PC479	1200	30	1343 (2)	50.3 (2.0)	1574 (3)	39.8 (2.8)	1.26 (16)	0.58 (2)	1.39 (10)	35	16	1343 (2)	51.1 (3.0)	1574 (3)	41.7 (1.6)	1.30 (11)	0.58 (1)	1.36 (6)	34	15
PC476	1200	60	1343 (2)	50.2 (2.1)	1574 (2)	39.9 (2.7)	1.09 (13)	0.55 (2)	1.20 (10)	40	17	1344 (2)	49.5 (2.5)	1575 (3)	40.0 (3.1)	1.15 (19)	0.55 (3)	1.25 (13)	38	16
PC485	1200	180	1345 (2)	43.1 (3.3)	1577 (3)	33.6 (3.5)	1.08 (12)	0.55 (2)	1.30 (14)	41	16	1344 (2)	44.2 (2.7)	1575 (2)	35.3 (4.2)	1.05 (19)	0.54 (2)	1.27 (16)	42	15
PC474	1200	360	1345 (2)	45.0 (1.8)	1576 (3)	31.9 (2.5)	0.81 (12)	0.50 (3)	1.05 (11)	54	16	1347 (2)	45.0 (2.5)	1578 (2)	33.1 (3.4)	0.91 (15)	0.52 (2)	1.14 (12)	48	16
PC462	1200	1440	1345 (2)	42.7 (3.0)	1577 (3)	33.3 (3.2)	0.95 (12)	0.52 (2)	1.16 (9)	46	12	1346 (2)	43.2 (2.7)	1578 (3)	32.6 (3.5)	0.97 (16)	0.54 (3)	1.21 (17)	45	13
PC461	1200	6900	1347 (2)	42.9 (2.8)	1577 (4)	22.7 (1.5)	0.28 (7)	0.33 (5)	0.53 (12)	156	15	1347 (2)	43.6 (2.3)	1575 (4)	22.8 (2.6)	0.22 (7)	0.28 (6)	0.47 (17)	196	20
A2590	1325	10	1343 (3)	47.9 (3.1)	1574 (4)	38.7 (4.3)	1.11 (15)	0.55 (2)	1.26 (10)	40	16	1342 (3)	48.9 (2.8)	1577 (4)	38.7 (3.7)	1.11 (19)	0.55 (3)	1.21 (15)	40	16
A2588	1325	60	1343 (2)	47.6 (2.9)	1574 (3)	36.5 (3.8)	0.97 (19)	0.52 (3)	1.13 (12)	46	17	1344 (2)	48.1 (2.4)	1574 (3)	39.3 (3.8)	1.05 (19)	0.54 (3)	1.20 (12)	42	11
A2583	1325	360	1344 (2)	43.6 (2.0)	1575 (4)	31.2 (2.0)	0.82 (14)	0.50 (5)	1.04 (13)	54	14	1346 (1)	42.9 (2.5)	1577 (2)	31.2 (2.8)	0.83 (12)	0.50 (2)	1.05 (10)	53	14
A2581	1325	720	1347 (3)	42.1 (1.9)	1577 (4)	28.8 (2.6)	0.63 (17)	0.45 (6)	0.84 (18)	70	14	1346 (2)	42.4 (3.7)	1575 (3)	28.8 (3.6)	0.57 (19)	0.42 (7)	0.80 (16)	77	14
A2582	1325	1440	1344 (2)	43.6 (1.9)	1574 (3)	31.3 (3.0)	0.66 (10)	0.46 (2)	0.88 (9)	66	17	1344 (2)	43.6 (2.0)	1573 (3)	29.8 (3.2)	0.66 (9)	0.46 (2)	0.89 (9)	67	16
A2580	1325	2880	1346 (2)	40.3 (2.4)	1577 (3)	23.6 (2.2)	0.37 (6)	0.37 (3)	0.62 (7)	119	14	1347 (2)	39.3 (2.8)	1578 (3)	22.9 (1.5)	0.34 (6)	0.35 (3)	0.57 (10)	129	15
PC481	1450	0.02	1346 (2)	45.4 (2.5)	1579 (3)	38.4 (2.8)	1.33 (18)	0.58 (2)	1.40 (14)	33	16	1348 (1)	43.7 (2.3)	1581 (2)	37.5 (2.9)	1.40 (17)	0.58 (3)	1.41 (14)	32	18
A2589	1450	10	1344 (2)	46.4 (2.3)	1577 (3)	40.3 (2.7)	1.30 (18)	0.57 (2)	1.40 (12)	34	16	1345 (2)	46.3 (2.9)	1577 (3)	39.6 (3.8)	1.35 (21)	0.58 (3)	1.46 (16)	33	17
A2587	1450	60	1344 (2)	43.6 (2.3)	1576 (4)	33.1 (3.4)	0.92 (13)	0.52 (3)	1.13 (13)	48	15	1346 (2)	42.1 (2.7)	1576 (4)	30.7 (3.7)	0.84 (18)	0.51 (3)	1.07 (15)	52	16
A2586	1450	360	1343 (3)	45.5 (3.3)	1574 (4)	33.3 (4.4)	0.74 (15)	0.48 (3)	1.01 (14)	59	16	1344 (3)	44.6 (2.9)	1574 (4)	32.6 (3.8)	0.79 (13)	0.50 (3)	1.04 (11)	56	15
A2584	1450	1440	1348 (2)	43.2 (3.3)	1579 (2)	22.3 (3.3)	0.27 (8)	0.31 (5)	0.62 (15)	164	15	1349 (3)	47.1 (5.3)	1579 (3)	24.0 (2.7)	0.27 (8)	0.32 (7)	0.56 (16)	160	16

Note; AR is the area ratio of (D1+D4 bands) / (D2+D3+G bands).

Table 18 (continued). Micro-Raman spectroscopic data for center and edge part of CM obtained by the peak deconvolution.

Run No.	*Temp* (°C)	*time* (min)	Raman spectroscopy (center) D1 band (cm^{-1})	D1 band FWHM	G band (cm^{-1})	G band FWHM	R1 ratio	R2 ratio	AR	*La* (Å)	*n*	Raman spectroscopy (Edge) D1 band (cm^{-1})	D1 band FWHM	G band (cm^{-1})	G band FWHM	R1 ratio	R2 ratio	AR	*La* (Å)	*n*
Center part of CM in Shimanto accretionary complex												*Edge part of CM in Shimanto accretionary complex*								
PC478	1000	10	1345 (2)	83.0 (6.2)	1593 (3)	57.1 (4.4)	1.83 (9)	0.72 (1)	2.17 (12)	24	16	1346 (2)	86.7 (5.0)	1596 (4)	57.7 (5.4)	1.79 (12)	0.72 (2)	2.20 (14)	25	17
PC475	1000	60	1347 (1)	76.6 (3.8)	1595 (2)	58.3 (4.6)	1.86 (17)	0.70 (2)	2.03 (22)	24	15	1348 (1)	82.1 (4.0)	1598 (2)	58.3 (2.9)	1.76 (14)	0.71 (2)	2.09 (15)	25	17
PC473	1000	360	1346 (1)	81.0 (4.9)	1591 (3)	67.3 (3.9)	1.70 (19)	0.68 (2)	1.79 (19)	26	16	1346 (1)	87.5 (8.7)	1589 (3)	69.9 (5.0)	1.65 (24)	0.67 (3)	1.57 (23)	27	15
PC471	1000	1440	1345 (1)	81.4 (4.7)	1589 (3)	68.8 (3.4)	1.74 (21)	0.67 (2)	1.81 (15)	25	16	1346 (2)	88.6 (6.0)	1592 (3)	68.6 (3.4)	1.72 (16)	0.70 (1)	2.02 (10)	26	15
PC470	1000	2880	1346 (1)	75.9 (6.5)	1590 (4)	65.7 (4.6)	1.89 (23)	0.68 (2)	1.98 (16)	23	17	1346 (2)	84.5 (6.5)	1591 (3)	65.7 (3.9)	1.74 (20)	0.69 (2)	1.86 (19)	25	16
PC482	1200	0.02	1345 (2)	72.4 (6.3)	1589 (4)	63.4 (3.2)	1.97 (22)	0.69 (2)	2.05 (13)	22	16	1345 (1)	72.7 (4.6)	1584 (3)	66.8 (7.2)	1.97 (18)	0.66 (3)	1.89 (13)	22	15
PC477	1200	10	1345 (2)	64.4 (2.6)	1585 (3)	56.8 (2.8)	2.14 (17)	0.68 (2)	1.98 (13)	21	16	1345 (1)	65.3 (3.2)	1584 (2)	61.9 (3.4)	1.98 (16)	0.66 (2)	1.94 (14)	22	16
PC479	1200	30	1345 (1)	61.7 (3.9)	1586 (4)	57.7 (5.3)	2.15 (28)	0.68 (2)	2.09 (17)	20	16	1345 (1)	63.9 (2.2)	1588 (3)	62.5 (2.2)	2.05 (13)	0.68 (2)	1.99 (12)	22	18
PC476	1200	60	1345 (1)	61.1 (3.4)	1583 (4)	54.1 (3.4)	2.08 (22)	0.67 (3)	1.89 (16)	21	17	1345 (1)	63.9 (3.9)	1584 (3)	59.0 (4.0)	2.02 (24)	0.66 (2)	1.81 (15)	22	19
PC485	1200	180	1346 (1)	55.2 (3.4)	1583 (3)	52.5 (4.5)	2.10 (29)	0.66 (2)	2.13 (31)	21	16	1346 (1)	58.8 (2.9)	1586 (4)	57.9 (3.3)	2.15 (22)	0.67 (2)	1.98 (20)	20	14
PC474	1200	360	1346 (1)	59.1 (2.0)	1582 (4)	51.4 (6.3)	1.93 (32)	0.65 (3)	1.82 (20)	23	16	1346 (1)	61.3 (2.3)	1582 (5)	51.4 (5.7)	1.84 (26)	0.65 (2)	1.79 (16)	24	18
PC462	1200	1440	1348 (1)	36.0 (2.1)	1579 (1)	24.8 (1.1)	0.57 (9)	0.43 (3)	0.83 (9)	77	17	1347 (2)	37.2 (2.4)	1578 (3)	25.1 (1.6)	0.48 (8)	0.40 (3)	0.73 (11)	91	16
PC461	1200	6900	1346 (2)	37.1 (2.3)	1576 (3)	24.7 (1.6)	0.46 (8)	0.39 (4)	0.70 (10)	97	15	1346 (2)	37.5 (2.4)	1575 (3)	25.6 (1.9)	0.49 (10)	0.40 (4)	0.73 (12)	90	16
A2590	1325	10	1344 (1)	59.3 (3.0)	1582 (2)	59.1 (3.6)	1.97 (18)	0.65 (1)	1.81 (13)	22	17	1344 (1)	59.1 (3.2)	1580 (3)	56.2 (5.2)	1.85 (20)	0.64 (1)	1.77 (14)	24	16
A2588	1325	60	1345 (2)	45.3 (6.7)	1575 (3)	29.3 (4.6)	0.85 (26)	0.52 (6)	1.12 (23)	52	16	1347 (2)	42.4 (7.7)	1578 (2)	28.0 (5.2)	0.82 (32)	0.49 (10)	1.22 (29)	54	15
A2583	1325	360	1348 (2)	38.5 (2.0)	1578 (3)	24.3 (1.6)	0.39 (6)	0.37 (3)	0.63 (8)	112	12	1347 (2)	38.0 (2.6)	1577 (3)	24.8 (2.9)	0.39 (7)	0.37 (3)	0.65 (14)	112	11
A2581	1325	720	1347 (2)	39.3 (1.9)	1578 (3)	24.8 (2.2)	0.40 (6)	0.38 (2)	0.65 (8)	109	17	1348 (1)	38.3 (2.1)	1579 (2)	23.4 (1.1)	0.41 (6)	0.39 (3)	0.67 (8)	106	17
A2582	1325	1440	1348 (2)	38.4 (2.7)	1578 (3)	23.8 (1.0)	0.40 (6)	0.38 (3)	0.63 (7)	109	18	1348 (2)	38.4 (2.7)	1578 (3)	23.8 (1.0)	0.40 (6)	0.38 (3)	0.63 (7)	109	18
A2580	1325	2880	1348 (2)	38.9 (1.6)	1578 (3)	24.3 (2.3)	0.38 (3)	0.37 (2)	0.62 (6)	115	16	1348 (3)	39.1 (2.7)	1578 (3)	24.7 (2.7)	0.37 (6)	0.36 (3)	0.59 (8)	120	17
PC481	1450	0.02	1346 (2)	60.8 (2.7)	1585 (4)	58.1 (3.7)	2.1 (18)	0.67 (2)	1.92 (15)	21	19	1345 (2)	63.2 (2.9)	1584 (5)	56.9 (3.7)	2.01 (23)	0.67 (2)	1.89 (16)	22	20
A2589	1450	10	1345 (1)	55.6 (2.0)	1581 (2)	56.2 (4.0)	1.96 (24)	0.64 (2)	1.82 (20)	23	16	1345 (2)	54.8 (3.1)	1581 (3)	54.8 (4.9)	1.90 (27)	0.63 (2)	1.73 (13)	23	16
A2587	1450	60	1347 (2)	37.5 (1.7)	1577 (3)	24.0 (1.3)	0.43 (6)	0.39 (3)	0.72 (16)	101	16	1347 (2)	36.4 (2.1)	1578 (2)	22.9 (1.3)	0.41 (6)	0.37 (2)	0.67 (11)	109	16
A2586	1450	360	1346 (2)	38.9 (2.4)	1576 (4)	23.5 (2.5)	0.38 (8)	0.37 (4)	0.69 (18)	115	15	1346 (2)	38.6 (3.0)	1577 (3)	23.5 (2.1)	0.43 (7)	0.39 (3)	0.78 (16)	101	16
A2584	1450	1440	1349 (2)	37.7 (3.4)	1579 (3)	20.7 (2.3)	0.23 (6)	0.28 (5)	0.47 (20)	189	15	1349 (1)	40.1 (2.4)	1578 (3)	21.1 (2.8)	0.23 (7)	0.28 (5)	0.47 (15)	189	15

Note; AR is the area ratio of (D1+D4 bands) / (D2+D3+G bands).

Table 19. Summary of rate paramters calculated from power rate and JMA models

Crystal parameter	Kinetic model	*m*	ln*A (s)*	*Ea (kJmol^{-1})*	R^2
d_{002} spacing-HMB	power rate	–31103 (3070)	17.27 (2.06)	259 (26)	0.981
d_{002} spacing-SM	power rate	–32569 (7560)	19.21 (5.08)	271 (63)	0.903
d_{002} spacing-HMB	JMA	–32414 (7040)	17.50 (4.73)	269 (59)	0.914
d_{002} spacing-SM	JMA	–32886 (5620)	19.12 (3.78)	273 (47)	0.945

Table 20. Summary of calculated E_a values and fitting results

Parameters	Samples	Fitting data (sigmoid function)					Arrhenius plots				
		C_{min}	C_{max}	h	t_{half}	R^2	m	ln$A$	lnA_1 [b]	E_a (kJ mol^{-1})	R^2
d_{002} *spacing*	HMB	6.859 (6)	6.725 (4)	0.86 (12)	3577	0.982	–31893 (2230)	24.86	–16.680	265 (19)	0.990
FWHM	HMB	2.60 (14)	0.36 (14)	0.57 (12)	8482	0.964	–35641 (2380)	28.20	–19.154	296 (20)	0.990
Area ratio	HMB	1.60 (10)	0.10*	0.39 (8)	247240	0.878	–32776 (2930)	26.00	–13.563	272 (24)	0.984
d_{002} *spacing*	SM	6.992 (17)	6.731 (11)	0.69 (14)	5905	0.957	–40813 (2750)	32.23	–23.546	339 (23)	0.991
FWHM	SM	5.34 (32)	0.42 (16)	0.60 (11)	3358	0.969	–43416 (860)	34.17	–26.050	361(7)	0.999
L_c(002)	SM	21.98 (6.4)	163.7 (7.4)	1.09 (26)	33813	0.956	–40198 (1090)	31.54	–21.104	334 (9)	0.999
Area ratio	SM	2.11 (11)	0.10*	0.61 (10)	95374	0.906	–38508 (2110)	30.27	–18.808	320 (18)	0.994
		Fitting data (Power function [a])									
		c	A	b	R^2						
L_c(002)	HMB	23.9 (13.6)	2.9	0.31 (6)	0.961		–31312 (1520)	24.70		260 (13)	0.995

[a] $f(t) = Aexp(bt) + c$ [b] lnA_1 is calculated from the intercept of the Arrhenius plot ($1/T$ vs. lnt_{half})

*Both C_{max} of area ratio is held

Table 21. Experimental conditions and XRD profiles of the run products at 1200 °C

Run No.	Type	Temp. (°C)	Pressure (GPa)	Time (sec)	XRD analysis							
					d_{002} (Å)	FWHM	L_c(002) (Å)	g* (%)	d_{002} (Å)	FWHM	L_c(002) (Å)	g* (%)
					CM in Hidaka metamorphic belt				*CM in Shimanto accretionary complex*			
PC586	PC	1200	0.5	600	3.419	1.932	47	0.242	3.484	3.72	24	0.085
A2614	DIA	1200	0.5	3600	3.413	2.090	43	0.317	3.477	3.50	26	0.138
PC585	PC	1200	0.5	21600	3.413	2.060	44	0.310	3.474	3.09	29	0.163
PC589	PC	1200	0.5	43200	3.404	1.585	57	0.417	3.424	2.69	34	0.531
PC587	PC	1200	0.5	86400	3.390	1.480	61	0.584	3.394	2.66	34	0.753
A2634	DIA	1200	2	600	3.397	1.440	63	0.500	3.384	1.11	82	0.826
A2613	DIA	1200	2	3600	3.394	1.230	74	0.534	3.389	1.76	51	0.795
A2637	DIA	1200	2	21600	3.386	1.029	88	0.630	3.369	0.69	131	0.937
A2615	DIA	1200	2	86400	3.374	0.936	97	0.769	3.370	0.98	97	0.928
PC590	PC	1200	1.5	3600	3.391	1.390	65	0.568	3.392	1.38	66	0.768
1k2640	MA	1200	4	3600	3.365	0.822	110	0.868	3.380	0.75	121	0.855
1k2641	MA	1200	8	3600	3.364	0.730	223	0.882	3.364	0.41	223	0.970

Note: L_c(002) is calculated by the Scherrer equation ($K = 1$. g* (%) is the calculated degree of crystallinity using initial and final values of d_{002} spacing

TABLE 22. Micro-Raman spectroscopic data for center and edge part of CM obtained by the peak deconvolution at 1200 °C.

Run No.	*Pressure* (GPa)	*time* (min)	Raman spectroscopy (center)														
			D1 band (cm^{-1})		D1 band FWHM		G band (cm^{-1})		G band FWHM		R1 ratio		R2 ratio		AR		*n*
Center part of CM in Hidaka metamorphic belt																	
PC586	0.5	10	1343.86	1.57	53.38	3.79	1575.63	2.34	45.06	4.01	1.27	0.11	0.57	0.01	1.36	0.08	23
A2614	0.5	60	1346.73	2.52	51.01	4.93	1579.00	3.24	44.50	4.69	1.31	0.10	0.57	0.02	1.35	0.13	14
PC585	0.5	360	1342.77	1.62	55.39	2.89	1574.78	2.70	48.83	3.44	1.32	0.14	0.57	0.02	1.36	0.08	20
PC589	0.5	720	1341.84	1.09	53.28	1.94	1573.11	1.34	43.30	2.65	1.21	0.09	0.57	0.01	1.33	0.06	21
PC587	0.5	1440	1342.89	1.59	51.48	1.88	1573.73	2.27	40.55	3.24	1.11	0.12	0.55	0.02	1.23	0.07	20
A2634	2	10	1343.24	1.40	49.75	3.13	1574.16	2.35	38.79	3.14	1.17	0.13	0.57	0.02	1.32	0.11	19
A2613	2	60	1346.42	2.91	45.15	3.38	1578.50	4.31	35.94	3.78	1.24	0.15	0.58	0.02	1.46	0.14	15
A2637	2	360	1345.28	2.01	44.90	2.27	1575.63	3.01	33.40	2.41	0.86	0.10	0.51	0.02	1.08	0.11	20
A2615	2	1440	1345.43	5.72	38.66	3.86	1575.93	7.66	24.53	2.53	0.56	0.08	0.44	0.02	0.82	0.07	11
PC590	1.5	60	1343.15	1.58	48.40	1.94	1574.71	2.39	40.03	2.99	1.20	0.12	0.56	0.02	1.37	0.11	19
1k2640	4	60	1349.45	0.98	37.38	1.94	1580.62	0.96	23.13	2.00	0.77	0.18	0.51	0.04	1.16	0.23	18
1k2641	8	60	1349.19	0.98	40.59	1.07	1579.44	1.35	22.18	1.21	0.59	0.07	0.48	0.02	0.98	0.10	22
Center part of CM in Shimanto accretionary complex																	
PC586	0.5	10	1347.28	1.40	105.43	3.36	1596.18	2.95	72.40	3.21	1.37	0.07	0.67	0.02	1.69	0.12	19
A2614	0.5	60	1347.07	2.21	84.71	4.37	1591.36	3.08	71.78	4.98	1.65	0.16	0.67	0.01	1.85	0.13	16
PC585	0.5	360	1343.50	1.78	86.64	5.43	1585.72	4.52	71.49	4.17	1.57	0.12	0.66	0.02	1.78	0.17	22
PC589	0.5	720	1346.80	1.39	76.95	2.67	1591.39	1.23	68.93	3.48	1.84	0.12	0.67	0.01	1.93	0.09	21
PC587	0.5	1440	1345.93	1.91	88.01	4.31	1591.90	1.96	71.70	2.71	1.82	0.16	0.68	0.01	2.00	0.10	20
A2634	2	10	1343.84	1.58	58.34	2.81	1579.75	3.34	55.90	5.00	1.93	0.17	0.64	0.01	1.82	0.11	17
A2613	2	60	1345.73	3.12	56.11	5.61	1581.81	4.99	51.56	6.68	1.91	0.24	0.65	0.02	1.89	0.15	15
A2637	2	360	1349.41	0.96	37.66	1.61	1580.04	0.99	24.60	0.81	0.54	0.08	0.43	0.03	0.81	0.08	17
A2615	2	1440	1347.33	1.32	35.57	2.41	1579.06	1.53	25.92	1.85	0.87	0.07	0.52	0.02	1.16	0.10	20
PC590	1.5	60	1349.43	0.82	52.44	2.23	1586.47	2.19	48.61	5.79	2.11	0.22	0.66	0.01	2.08	0.13	19
1k2640	4	60	1350.31	0.56	35.49	1.28	1581.72	0.72	24.84	0.86	1.06	0.09	0.57	0.02	1.36	0.08	18
1k2641	8	60	1349.99	0.74	44.11	1.39	1580.66	1.11	25.44	1.41	0.74	0.12	0.52	0.02	1.16	0.12	20

Note: AR is the area ratio of (D1 + D4 bands) / (D2 + D3 + G bands).

TABLE 22 (continued). Micro-Raman spectroscopic data for center and edge part of CM obtained by the peak deconvolution at 1200 °C.

Run No.	*Pressure* (GPa)	*time* (min)	Raman spectroscopy (Edge)														
			D1 band (cm^{-1})		D1 band FWHM		G band (cm^{-1})		G band FWHM		R1 ratio		R2 ratio		AR		*n*
Center part of CM in Hidaka metamorp			*Edge part of CM in Hidaka metamorphic belt*														
PC586	0.5	10	1343.62	1.40	53.42	3.75	1575.23	1.72	44.45	3.37	1.26	0.09	0.57	0.01	1.36	0.06	20
A2614	0.5	60	1346.80	2.11	49.56	5.26	1579.06	3.75	42.58	5.42	1.28	0.26	0.57	0.04	1.38	0.26	12
PC585	0.5	360	1342.27	2.78	56.12	4.33	1574.95	4.02	48.86	4.30	1.38	0.15	0.58	0.02	1.43	0.10	20
PC589	0.5	720	1341.97	1.31	52.09	1.65	1573.01	1.81	42.56	2.38	1.18	0.10	0.56	0.01	1.29	0.07	20
PC587	0.5	1440	1342.11	0.91	53.65	2.14	1572.93	1.50	42.40	2.76	1.10	0.08	0.55	0.01	1.24	0.05	22
A2634	2	10	1343.81	1.51	50.25	2.68	1574.30	2.12	39.89	2.65	1.10	0.08	0.55	0.01	1.25	0.05	19
A2613	2	60	1344.28	3.40	47.67	4.32	1574.79	5.13	36.28	3.46	1.02	0.19	0.54	0.04	1.25	0.22	14
A2637	2	360	1346.63	1.66	43.72	2.46	1577.46	2.74	32.14	2.61	0.91	0.09	0.52	0.02	1.16	0.09	19
A2615	2	1440	1348.48	1.14	37.64	2.61	1579.48	2.04	23.33	3.76	0.48	0.08	0.41	0.03	0.75	0.09	19
PC590	1.5	60	1344.58	1.95	46.62	3.73	1575.95	2.95	36.63	4.12	1.13	0.13	0.56	0.02	1.31	0.12	18
1k2640	4	60	1348.92	0.70	36.73	1.34	1579.96	0.68	22.00	1.13	0.73	0.08	0.51	0.02	1.10	0.11	18
1k2641	8	60	1348.45	1.24	39.42	1.00	1578.92	1.60	22.25	0.80	0.67	0.05	0.50	0.01	1.10	0.11	23
Center part of CM in Shimanto accretic			*Edge part of CM in Hidaka metamorphic belt*														
PC586	0.5	10	1347.46	1.19	109.34	4.27	1595.63	2.57	74.34	3.30	1.34	0.05	0.67	0.01	1.69	0.08	19
A2614	0.5	60	1348.81	2.18	89.22	4.84	1593.97	3.67	72.02	5.35	1.73	0.18	0.68	0.01	1.95	0.14	20
PC585	0.5	360	1344.35	1.33	88.16	4.89	1589.81	4.09	71.22	3.18	1.53	0.09	0.67	0.02	1.74	0.12	26
PC589	0.5	720	1347.03	1.34	79.00	4.13	1592.33	1.74	68.85	3.59	1.90	0.15	0.68	0.01	2.01	0.10	20
PC587	0.5	1440	1346.65	1.98	87.40	5.71	1592.14	2.31	72.60	3.84	1.83	0.14	0.68	0.01	1.98	0.09	18
A2634	2	10	1344.51	1.20	57.90	2.79	1580.37	3.37	56.60	5.54	1.91	0.18	0.64	0.02	1.78	0.12	19
A2613	2	60	1348.13	2.17	56.49	3.98	1584.21	5.28	50.92	5.96	1.88	0.31	0.64	0.02	1.89	0.17	15
A2637	2	360	1348.82	1.68	38.40	2.08	1578.94	2.31	24.64	1.70	0.45	0.04	0.40	0.02	0.72	0.06	17
A2615	2	1440	1347.15	1.99	35.17	3.33	1578.41	2.88	25.06	2.55	0.75	0.08	0.49	0.02	1.01	0.09	20
PC590	1.5	60	1345.64	1.62	63.59	3.89	1585.07	3.04	59.74	3.97	2.00	0.23	0.66	0.02	1.77	0.17	18
1k2640	4	60	1349.63	0.95	35.83	0.98	1580.95	1.16	24.98	0.93	1.05	0.08	0.57	0.01	1.39	0.13	19
1k2641	8	60	1349.22	1.37	43.01	1.22	1580.51	1.92	27.07	1.21	0.88	0.13	0.54	0.03	1.26	0.12	20

Note: AR is the area ratio of (D1 + D4 bands) / (D2 + D3 + G bands).

Table 23. Summary of rate paramters calculated from power rate and JMAK models

Crystal parameter	Kinetic model	*Slope* (10^{-4})	*lnA*	$\Delta V^{\ddagger}$ (cm^3/mol)	R^2
d_{002} spacing-HMB	power rate	1.771 (279)	– 4.907 (0.37)	– 22 (3.4)	0.976
d_{002} spacing-HMB	JMA	2.050 (792)	– 5.664(1.03)	– 25 (9.6)	0.870
d_{002} spacing-SM	power rate	2.975 (159)	– 5.909 (2.10)	– 36 (19.5)	0.778
d_{002} spacing-SM	JMA	3.634 (145)	– 6.956(1.89)	– 44 (17.5)	0.863

Table A1. Summary of previous kinetic studies

Reference	Material	Preheat *T*	Measurement (°C)	Pressure	Parameter	⊿H kcal/mol	⊿H kJ/mol	Analytical method
Graphitization								
Noda et al. (1965)	Pet. coke	1300	1900-2400	Ar or N_2	d002 spacing	180	753	superposition
Inagaki et al. (1968)	PVC coke	680	1880-2300	Ar or N_2	d002 spacing	150 +/- 10	628	superposition
		1500	2060-2360	Ar or N_2	d002 spacing	175 +/- 25	732	superposition
		2060	2060-2270	Ar or N_2	d002 spacing	200 +/- 20	837	superposition
		1500+2060	2060-2270	Ar or N_2	d002 spacing	235 +/- 25	983	superposition
Pacault & Gasparoux (1967)	Pitch coke	1100	1820-2265	Ar or N_2	χ, La	164	686	superposition
Gasparoux (1965)	Pitch coke	1100	2120-2200	Ar or N_2	d002 spacing	260	1088	superposition
			1720-1930	Ar or N_2	χ	175	732	superposition
			1930-2475	Ar or N_2	χ	240	1004	superposition
Massa (1964)	Pitch coke	1100	1420-1720	Ar or N_2	χ	120-200	500-840	superposition
			1720-2850	Ar or N_2	χ	280	1172	superposition
Forchioni et al. (1964)	Pitch coke	1100	1420-1720	Ar or N_2	Hall coeff.	120-200	500-840	superposition
			1720-2850	Ar or N_2	Hall coeff.	280	1172	superposition
Massa et al. (1964)	Pitch coke	1100	1520-1720	Ar or N_2	d002 spacing, La	175-200	730-840	superposition
			1720-2850	Ar or N_2	d002 spacing, La	250	1046	superposition
Roulin (1967)	Anthrace coke	1000	2140-2250	Ar or N_2	χ, d002 spacing	220 +/- 40	920	superposition
	PC	2100	2550-2650	Ar or N_2	d002 spacing, La	270 +/- 50	1130	superposition
Fair & Collins (1961)	Coke-pitch comp.	800	2000-3000	Ar or N_2	d002 spacing	260	1088	superposition
Tarpinian & Tedmon (1960)	Pet. coke	2057	2057-2727	Ar or N_2	Lc	90	377	Initial rate
Richardson & Zehms (1963)	PC	2150	2600-3000	Ar or N_2	d002 spacing	260	1088	superposition
Fischbach (1963, 1964)	Pet. coke	2000	2200-3000	Ar or N_2	d002 spacing	250 +/- 30	1046	superposition
	Pitch coke			Ar or N_2	d002 spacing	250 +/- 30	1046	superposition
	Coke-pitch comp.			Ar or N_2	d002 spacing, χT	250 +/- 30	1046	superposition
Fischbach (1966,1963,1964)	PC	2150	2400-3000	Ar or N_2	d002, χT, P.O.	270 +/- 30	1046	superposition
		1800-2200	2400-3000	Ar or N_2	d002, χT	247-279	1033	superposition
Deformation								
Kotlensky (1966)	PC	2800	2400-2760	Ar or N_2	Tensile creep curve	257	1075	superposition
						242	1013	superposition
Fischbach & Kotlensky (1967)	PC	2900-3000	2500-2900	Ar or N_2	Basal sheaerε vs. σ	270	1130	σflow vs ε, T
Fischbach (1968, 1969)	PC	2150	2500-3000	Ar or N_2	Tensile creep rate	250 +/- 40	1046	Unispecimen ⊿T
Zukas & Green (1968)	ZTA (Stress recryst coke-pitch composite)	>2500	2500	Ar or N_2	Creep rate	277	1159	Unispecimen ⊿T
Ross & Bustin (1990)		-	350-600	5 kbar	Stress difference vs strain rate	16.41	69	power-law creep equation
Carbonization								
Smith et al. (1980)	Bituminous coal	-	25-900	Air	DTGA	69.28	290	?
Honda et al. (1970)	Coal tar pitch	-	390-450	?	Lc, TGA	35-45	146	superposition
Huang (1996)	Lignite	-	300-450	0.5 kbar	VR	5.97	25	emprical power rate model
Torre et al. (1997)	Lignite	-	200-350	0.5-20 kbar	VR	5.63-6.64	24	emprical power rate model

Table A2. Summary of kinetic functions based on the acceleratory, deceleratory and sigmoidal rate equations.

Abbreviation	Kinetic function		Description		*n*
	g (α) = *kt (integration form)*	*f* (α) = $k^{-d\alpha/dt}$ (differential form)			
$F_{1/3}$	1-(1-α)^2/3	(3/2)(1-α)^1/3	Chemical process or mechanism non-invoking equations	one-third order	1/3
$F_{3/4}$	1-(1-α)^1/4	4(1-α)^3/4		three quarters order	3/4
$F_{2/3}$	1-(1-α)^-1/2 -1	2(1-α)^3/2		one and half order	1+1/2
F_2	1-(1-α)^-1 -1	(1-α)^2		second order	2
F_3	1-(1-α)^-2 -1	(1/2)(1-α)^3		third order	3
$P_{3/2}$	α^3/2	(2/3)α^-1/2	Acceleratory rate equations	Mampel's power law	
$P_{1/2}$	α^1/2	2α^1/2			2
$P_{1/3}$	α^1/3	3α^2/3			3
$P_{1/4}$	α^1/4	4α^3/4			4
E_1	lnα	α		Exponential law	
A_1, F_1	-ln(1-α)	(1-α)	Sigmoidal rate equations or random nucleation and subsequent growth		1
$A_{2/3}$	-ln(1-α)^2/3	2/3(1-α)[-ln(1-α)]^1/3			1+1/2
A_2	-ln(1-α)^1/2	2(1-α)[-ln(1-α)]^1/2		JMAK equation	2
A_3	-ln(1-α)^1/3	3(1-α)[-ln(1-α)]^2/3			3
A_4	-ln(1-α)^1/4	4(1-α)[-ln(1-α)]^3/4			4
A_u	ln(α/(1-α))	α(1-α)		Prout-Tomkins equation	
R_1, F_0, P_1	α	(1-α)^0	Deceleratory rate equations based on boundary reactions	Contracting disk	
R_2, $F_{1/2}$	1-(1-α)^1/2	2(1-α)^1/2		contracting cylinder	2
R_3, $F_{2/3}$	1-(1-α)^1/3	2(1-α)^2/3		contracting sphere	3
D_1	α^2	1/2α	Deceleratory rate equation based on diffusion mechanim	Parabolic rate law	
D_2	α+(1-α)ln(1-α)	[-ln(1-α)]^-1		Valensi equation	
D_3	(1-(1-α)^1/3)^2	3/2(1-α)^2/3[1-(1-α)^1/3]^-1		Jander equation	
D_4	1-(2α/3)-(1+α)^2/3	3/2[(1-α)^-1/3-1]^-1		G-B euation	
D_5	((1-α)^-1/3-1)^2	3/2(1-α)^4/3[(1-α)^-1/3-1]^-1		ZLT euation	
D_6	((1+α)^1/3-1)^2	3/2(1-α)^2/3[1-(1-α)^1/3-1]^-1		Anti-Jander equation	
D_7	1+(2α/3)-(1+α)^2/3	3/2(1+α)^-1/3-1]^-1		Anti-GB equation	
D_8	((1+α)^-1/3-1)^2	3/2(1+α)^4/3[(1+α)^-1/3-1]^-1		Anti-ZLT equation	